

Feb 98

19980223 019

## FINAL TECHNICAL REPORT

Contract Title: **Growth and Characterization of Reduced Dimensionality Superconductor-Related Phases by Molecular Beam Epitaxy**

Performing Organization: **The Pennsylvania State University**

Principal Investigator: **Darrell G. Schlom**  
    ~~T~~ (814) 863-8579  
    Fax: (814) 865-2917  
    e-mail: schlom@ems.psu.edu

Contract Number: **N00014-93-1-0512 (and AASERT N00014-94-1-0690)**

R & T Project Number: **400x125yip01**

ONR Scientific Officer: **Kristl B. Hathaway**

### Executive Summary

#### DISTRIBUTION STATEMENT A

Approved for public release,  
Distribution Unlimited

This contract played a major role in enhancing the understanding and capabilities of reactive molecular beam epitaxy (MBE) to assemble oxide heterostructures with unit cell layering precision.

The specific compounds grown under its support included (Ba,K)BiO<sub>3</sub>, YBa<sub>2</sub>Cu<sub>3</sub>O<sub>7-8</sub>, SrTiO<sub>3</sub>, PbTiO<sub>3</sub>, Bi<sub>4</sub>Ti<sub>3</sub>O<sub>12</sub>, and superlattices of these compounds. Several of these materials had never before been grown by MBE and in addition to achieving an enhanced understanding of the underlying growth mechanisms of these compounds, the structural and electrical properties of the thin films and superlattices surpass those achieved by other thin film techniques. For example, our MBE-grown Bi<sub>4</sub>Ti<sub>3</sub>O<sub>12</sub> films have the lowest RBS minimum channeling yield ( $\chi_{min}$ ) and exhibit remanent polarization values of ~3  $\mu$ C/cm<sup>2</sup> along the *c*-axis which is approximately the value observed in this same measurement direction for bulk single crystals (~4  $\mu$ C/cm<sup>2</sup>) and significantly exceeds the highest value previously reported for epitaxial films of this material (i.e., ~1  $\mu$ C/cm<sup>2</sup> reported by R. Ramesh *et al.*, Science **252** (1991) 944). We have identified adsorption-controlled growth conditions, analogous to those used for the preparation of III-V and II-VI semiconductors by MBE, for the synthesis of PbTiO<sub>3</sub> and Bi<sub>4</sub>Ti<sub>3</sub>O<sub>12</sub> and assessed the thermodynamics of why this occurs. In addition this contract supported work related to the integration of oxides with silicon.

This contract supported two (U.S. citizen) graduate students, both of whom completed their M.S. degrees under its support.

- Christopher D. Theis, "Investigation of Growth and Domain Structure of Epitaxial Lead Titanate Thin Films," M.S. Thesis (1996).
- Charles J. Kraisinger, "Design and Evaluation of a Nozzle for Efficient Delivery of Oxidizing Gases During High Vacuum Deposition," M.S. Thesis (1996).

One of them (Chris D. Theis) is nearing the completion of his Ph.D. degree and has won numerous awards for his research supported by this program including:

- Xerox Award (1996) for the best M.S. Thesis at Penn State in materials.
- International Society for Hybrid Microelectronics (ISHM) Educational Foundation Grant (1996-1997).

An undergraduate who completed his B.S. thesis associated with this project (Kevin J. Hubbard) is now employed by EPI, the only remaining domestic vendor of MBE equipment.

This work led to the publications and presentations listed below. Copies of all the publications supported by this contract (and its AASERT supplement) are attached.

DOE QUALITY INSPECTED

## **1. Papers Published in Refereed Journals**

1. A. Catana, D.G. Schlom, J. Mannhart, and J.G. Bednorz, "*a/c*  $\text{YBa}_2\text{Cu}_3\text{O}_7$  Boundaries: Preferential Sites for the Nucleation of Epitaxial  $\text{Y}_2\text{O}_3$  Precipitates," *Applied Physics Letters* **61** (1992) 720-722.
2. J. Mannhart, J.G. Bednorz, K.A. Müller, D.G. Schlom, and J. Ströbel, "Electric Field Effect in High- $T_c$  Superconductors," *Journal of Alloys and Compounds* **195** (1993) 519-526.
3. A. Catana, J.G. Bednorz, Ch. Gerber, J. Mannhart, and D.G. Schlom, "Surface Outgrowths on Sputtered  $\text{YBa}_2\text{Cu}_3\text{O}_{7-x}$  Films: A Combined Atomic Force Microscopy and Transmission Electron Microscopy Study," *Applied Physics Letters* **63** (1993) 553-555.
4. D.G. Schlom, D. Anselmetti, J.G. Bednorz, Ch. Gerber, and J. Mannhart, "Epitaxial Growth of Cuprate Superconductors from the Gas Phase," *Journal of Crystal Growth* **137** (1994) 259-267.
5. N. Chandrasekhar and D.G. Schlom, "Evidence for Surface Melting During the Growth of High  $T_c$  Thin Films," *Physica C* **235-240** (1994) 697-698.
6. K.J. Hubbard and D.G. Schlom, "Thermodynamic Stability of Binary Oxides in Contact with Silicon," *Journal of Materials Research* **11** (1996) 2757-2776.
7. D.G. Schlom, E.S. Hellman, E.H. Hartford, Jr., C.B. Eom, J.C. Clark, and J. Mannhart, "Origin of the  $\phi \sim \pm 9^\circ$  Peaks in  $\text{YBa}_2\text{Cu}_3\text{O}_{7-\delta}$  Films Grown on Cubic Zirconia Substrates," *Journal of Materials Research* **11** (1996) 1336-1348.
8. C.D. Theis and D.G. Schlom, "Domain Structure of Epitaxial  $\text{PbTiO}_3$  Films Grown on Vicinal (001)  $\text{SrTiO}_3$ ," *Journal of Materials Research* **12** (1997) 1297-1305.
9. C.D. Theis and D.G. Schlom, "Epitaxial Lead Titanate Grown by MBE," *Journal of Crystal Growth* **174** (1997) 473-479.
10. D.G. Schlom, C.D. Theis, and M.E. Hawley, "The Growth of Oxide Heterostructures by MBE," submitted to *JOM*.
11. C.D. Theis, J. Yeh, D.G. Schlom, M.E. Hawley, and G.W. Brown, "Adsorption-Controlled Growth of  $\text{Bi}_4\text{Ti}_3\text{O}_{12}$  by Reactive Molecular Beam Epitaxy," submitted to *Applied Physics Letters*.
12. C.D. Theis, J. Yeh, D.G. Schlom, M.E. Hawley, and G.W. Brown, "Adsorption-Controlled Growth of  $\text{PbTiO}_3$  by Reactive Molecular Beam Epitaxy," to be published in *Thin Solid Films*.
13. C.J. Kraisinger and D.G. Schlom, "The Distribution of Gas Emitted by a Ring-Shaped Orifice in the Molecular Flow Regime," submitted to the *Journal of Vacuum Science and Technology A*.

## **2. Non-Refereed Publications and Published Technical Reports**

1. D.G. Schlom, D. Anselmetti, J.G. Bednorz, Ch. Gerber, and J. Mannhart, "Defect-Mediated Growth of  $\text{YBa}_2\text{Cu}_3\text{O}_{7-\delta}$  Films," in: *Evolution of Surface and Thin Film Microstructure*, edited by H.A. Atwater, E.H. Chason, M.L. Grabow, and M.G. Lagally, Vol. 280 (Materials Research Society, Pittsburgh, 1993), pp. 341-344.

2. K.J. Hubbard and D.G. Schlom, "Thermodynamic Stability of Binary Oxides in Contact with Silicon," in: *Structure and Properties of Interfaces in Ceramics*, edited by D.A. Bonnell, U. Chowdhry, and M. Rühle, Vol. 357 (Materials Research Society, Pittsburgh, 1995), pp. 331-336.
3. K.J. Hubbard and D.G. Schlom, "Thermodynamic Stability of Binary Oxides in Contact with Silicon," in: *Epitaxial Oxide Thin Films II* edited by J.S. Speck, D.K. Fork, R.M. Wolf, and T. Shiosaki, Vol. 401 (Materials Research Society, Pittsburgh, 1996), pp. 33-38.
4. C.J. Kraisinger, D.M. Fusina, and D.G. Schlom, "Computer Simulation, Design, and Characterization of a Nozzle for More Effective Delivery of Oxidizing Gases," in: *Epitaxial Oxide Thin Films II* edited by J.S. Speck, D.K. Fork, R.M. Wolf, and T. Shiosaki, Vol. 401 (Materials Research Society, Pittsburgh, 1996), pp. 387-392.
5. C.D. Theis and D.G. Schlom, "Epitaxy of PbTiO<sub>3</sub> on (100) SrTiO<sub>3</sub> and Vicinal (100) SrTiO<sub>3</sub> by Pulsed Laser Deposition," in: *Epitaxial Oxide Thin Films II* edited by J.S. Speck, D.K. Fork, R.M. Wolf, and T. Shiosaki, Vol. 401 (Materials Research Society, Pittsburgh, 1996), pp. 171-176.
6. S. Trolier-McKinstry, C.A. Randall, J.P. Maria, C. Theis, D.G. Schlom, J. Shepard, Jr., and K. Yamakawa, "Size Effects and Domains in Ferroelectric Thin Film Actuators," in: *Ferroelectric Thin Films V* edited by S.B. Desu, R. Ramesh, B.A. Tuttle, R.E. Jones, and I.K. Yoo, Vol. 433 (Materials Research Society, Pittsburgh, 1996), pp. 363-374.
7. C.D. Theis and D.G. Schlom, "Domain Structure of Epitaxial PbTiO<sub>3</sub> Films Grown on Vicinal (001) SrTiO<sub>3</sub>," in: *ISAF '96: Proceedings of the Tenth IEEE International Symposium on Applications of Ferroelectrics*, vol. 1 (IEEE, Piscataway, 1996), pp. 491-494.
8. C.D. Theis, J. Yeh, M.E. Hawley, G.W. Brown, and D.G. Schlom, "Adsorption-Controlled Growth of Ferroelectric PbTiO<sub>3</sub> and Bi<sub>4</sub>Ti<sub>3</sub>O<sub>12</sub> Films for Nonvolatile Memory Applications by MBE," in: *Epitaxial Oxide Thin Films III* edited by D.G. Schlom, C.B. Eom, M.E. Hawley, C.M. Foster, and J.S. Speck, Vol. 474 (Materials Research Society, Pittsburgh, 1997), pp. 297-302.
9. D.G. Schlom, C.D. Theis, and M.E. Hawley, "The Controlled Growth of Perovskite Thin Films: Opportunities, Challenges, and Synthesis," to be published in the *Transactions of the American Ceramic Society 99th Annual Symposium*.
10. C.D. Theis and D.G. Schlom, "The Reactivity of Ozone Incident onto the Surface of Perovskite Thin Films Grown by MBE," in: *High Temperature Materials Chemistry IX*, edited by K.E. Spear, Vol. 97-39 (Electrochemical Society, Pennington, 1997) pp. 610-616.

### **3 . Presentations**

#### **a. Invited**

1. D.G. Schlom, "Epitaxial Growth of Cuprate Superconductors from the Gas Phase," presented at the Ninth American Conference on Crystal Growth (ACCG-9) in Baltimore, Maryland (1993).
2. D.G. Schlom, "Epitaxial Growth of Oxide Superconductors and Related Phases," presented at the IBM T. J. Watson Research Center on 9-24-93.
3. D.G. Schlom, "Epitaxial Growth of Cuprate Superconductors from the Gas Phase," presented at the University of Maryland on 9-30-93.

4. D.G. Schlom, "Epitaxial Growth of Oxide Superconductors and Related Phases," presented at the Pennsylvania State University (Physics Department, Condensed Matter Physics Seminar) on 12-13-93.
5. D.G. Schlom, J. Mannhart, and J.G. Bednorz, "High- $T_c$  Superconductor Field-Effect Microstructures: An Overview," presented at the SPIE OE/LASE '94 International Symposium in Los Angeles, California (1994).
6. D.G. Schlom, "Epitaxial Growth of Oxide Superconductors and Related Phases," presented at the Naval Command, Control and Ocean Surveillance Center Research, Development, Test and Evaluation Division (NRaD) on 1-28-94.
7. D.G. Schlom, "High-Temperature Superconductors," presented at the Pennsylvania State University (Department of Geosciences, Ore Deposits Research Section Seminar) on 2-2-95.
8. D.G. Schlom, "Epitaxial Growth of Oxide Superconductors and Related Phases," presented at the National Institute of Standards and Technology (NIST) in Gaithersburg, MD on 5-15-95.
9. D.G. Schlom, "Superconductivity," presented at the Pennsylvania State University (Department of Materials Science and Engineering, NSF-REU Seminar Series) on 6-15-95.
10. D.G. Schlom, "The Customized Growth of Oxides, including Superconductors, by MBE," presented at the Pennsylvania State University (U.S. DOE-BES Contractor's Meeting) on 9-15-95.
11. D.G. Schlom, "Overview of High Temperature Superconductors," presented at the Pennsylvania State University (Department of Materials Science and Engineering, NSF-REU Seminar Series) on 6-13-96.
12. D.G. Schlom, "The Controlled Growth of Perovskite Thin Films: Opportunities, Challenges, and Synthesis," presented at Clarkson University (Department of Chemical Engineering) on 10-17-96.
13. D.G. Schlom, "The Controlled Growth of Perovskite Thin Films: Opportunities, Challenges, and Synthesis," presented at the California Institute of Technology (Materials Research Lecture Series) on 11-13-96.
14. D.G. Schlom, C.D. Theis, and C.J. Kraisinger "MBE Growth of Perovskite Thin Films using Real-Time Atomic Absorption Composition Control," presented at *The First Yamazaki International Symposium on Oxide Materials with Optoelectronic Functions and 3<sup>rd</sup> International Symposium on Oxide Electronics* in Tokyo, Japan (1996).
15. D.G. Schlom, "The Controlled Growth of Perovskite Thin Films: Opportunities, Challenges, and Synthesis," presented at Los Alamos National Laboratory (Center for Materials Science Seminar Series) on 3-13-97.
16. D.G. Schlom, C.D. Theis, and M.E. Hawley, "The Controlled Growth of Perovskite Thin Films: Opportunities, Challenges, and Synthesis," presented at the *American Ceramic Society 99<sup>th</sup> Annual Meeting & Exposition* in Cincinnati, Ohio (1997).
17. D.G. Schlom, "The Controlled Growth of Perovskite Thin Films: Opportunities, Challenges, and Synthesis," presented at Northwestern University (Department of Materials Science and Engineering) on 5-13-97.

**b. Contributed**

1. D.G. Schlom, D. Anselmetti, J.G. Bednorz, Ch. Gerber, and J. Mannhart, "Defect-Mediated Growth of  $\text{YBa}_2\text{Cu}_3\text{O}_{7-\delta}$  Films," presented at the Fall 1992 MRS meeting symposium B: *Evolution of Surface and Thin Film Microstructure*, in Boston, Massachusetts (1992).
2. D.G. Schlom, E.S. Hellman, E.H. Hartford, Jr., and J. Mannhart, "Origin of the  $\phi \approx \pm 9^\circ$  Peaks in  $\text{YBa}_2\text{Cu}_3\text{O}_{7-\delta}$  Films Grown on Cubic Zirconia Substrates," presented at the *Fall '93 Materials Research Society Meeting* in Boston, Massachusetts (1993).
3. K.J. Hubbard and D.G. Schlom, "Thermodynamic Stability of Binary Oxides in Contact with Silicon," presented at the *Fall '94 Materials Research Society Meeting* in Boston Massachusetts (1994).
4. C.D. Theis and D.G. Schlom, "Domain Structure of Epitaxial  $\text{PbTiO}_3$  Films Grown on Vicinal (001)  $\text{SrTiO}_3$ ," presented at the *10th IEEE International Symposium on Applications of Ferroelectrics* in Piscataway, New Jersey (1996).
5. C.D. Theis and D.G. Schlom, "Growth of Epitaxial  $\text{PbTiO}_3$  Films on Vicinal  $\text{SrTiO}_3$  Surfaces," presented at *The Tenth American Conference on Crystal Growth* in conjunction with *The Ninth International Conference on Vapor Growth & Epitaxy (ACCG-10/ICVGE-9)* in Vail, Colorado (1996).
6. C.D. Theis and D.G. Schlom, "Domain Structure of  $\text{PbTiO}_3$  Films Grown on Vicinal (001)  $\text{SrTiO}_3$ ," presented at *The Tenth International Symposium on the Applications of Ferroelectrics (ISAF '96)* in East Brunswick, New Jersey (1996).
7. D.G. Schlom, C.D. Theis, C.J. Kraisinger, B.J. Gibbons, and S. Trolier-McKinstry "MBE Growth of  $\text{YBa}_2\text{Cu}_3\text{O}_{7-\delta}$  Interfaces using Real-Time Atomic Absorption Composition Control," presented at the *Fall '96 Materials Research Society Meeting* in Boston, Massachusetts (1996).
8. C.J. Kraisinger and D.G. Schlom, "Optimized Delivery of Gases in Oxide MBE: Simulation and Characterization of Optimized Nozzles," presented at the *Fall '96 Materials Research Society Meeting* in Boston, Massachusetts (1996).
9. C.D. Theis and D.G. Schlom, "MBE Growth of  $\text{PbTiO}_3$  with *In Situ* Atomic Absorption Composition Control," presented at the *Fall '96 Materials Research Society Meeting* in Boston, Massachusetts (1996).
10. C.D. Theis, J. Yeh, M.E. Hawley, G.W. Brown, and D.G. Schlom, "Adsorption-Controlled Growth of Ferroelectric  $\text{PbTiO}_3$  and  $\text{Bi}_4\text{Ti}_3\text{O}_{12}$  Films for Nonvolatile Memory Applications by MBE," presented at the *Spring '97 Materials Research Society Meeting* in San Francisco, California (1997).
11. C.D. Theis and D.G. Schlom, "The Reactivity of Ozone Incident onto the Surface of Perovskite Thin Films Grown by MBE," presented at the *High Temperature Materials Chemistry (HTMC IX)* conference of the Electrochemical Society in University Park, Pennsylvania (1997).

#### **4. Books (and sections thereof)**

1. J. Mannhart, J.G. Bednorz, A. Catana, Ch. Gerber, and D.G. Schlom, "High- $T_c$  Thin Films. Growth Modes—Structure—Applications," in: *Materials and Crystallographic Aspects of HT<sub>c</sub>-Superconductivity*, edited by E. Kaldis (Kluwer, Erice, 1994), pp. 453-470.
2. D.G. Schlom and J.S. Harris, Jr., "MBE Growth of High  $T_c$  Superconductors," in: *Molecular Beam Epitaxy: Applications to Key Materials*, edited by R.F.C. Farrow (Noyes, Park Ridge, 1995), pp. 505-622.

# **a/c YBa<sub>2</sub>Cu<sub>3</sub>O<sub>7</sub> boundaries: Preferential sites for the nucleation of epitaxial Y<sub>2</sub>O<sub>3</sub> precipitates**

A. Catana, D. G. Schlom, J. Mannhart, and J. G. Bednorz  
IBM Research Division, Zurich Research Laboratory, 8803 Rüschlikon, Switzerland

(Received 12 March 1992; accepted for publication 26 May 1992)

Y<sub>2</sub>O<sub>3</sub> precipitates with typical sizes between 70 and 300 nm<sup>2</sup> have been identified by high-resolution electron microscopy and image calculations in mixed *a*- and *c*-axis oriented YBa<sub>2</sub>Cu<sub>3</sub>O<sub>7</sub> sputtered films. The precipitates are densely distributed ( $10^{15}$  cm<sup>-3</sup>), have tabular shape and grow epitaxially at boundaries between *a*- and *c*-axis oriented grains, with the (001) Y<sub>2</sub>O<sub>3</sub> plane parallel to the *a,b* plane of the *a*-axis oriented grain and the (110) Y<sub>2</sub>O<sub>3</sub> plane parallel to the *a,b* plane of the *c*-axis oriented grain. Their largest interfacial facet lies parallel to the *a,b* plane of the *a*-axis oriented regions. Lattice-matching arguments show that energetically this situation is the most favorable one, which explains the nucleation of precipitates at *a/c* boundaries.

The understanding of the microstructure of high  $T_c$  films is not only essential for applications, but should also provide valuable insights into the growth mechanisms. Defects play an essential role in controlling the growth process, the superconducting and non-superconducting properties of such films. This motivates the study of the structure and morphology of impurity phases, their formation and their impact on the resulting structure of slightly nonstoichiometric films. Concerning the surfaces of such films, it has been shown that they are strongly dependent on composition.<sup>1,2</sup> However, off-stoichiometry also results in features embedded inside the films, such as line and point defects, stacking faults and precipitates. To investigate how stoichiometry and processing parameters influence the distribution of second phases and other features embedded inside the films, a detailed structural characterization is required.

A number of studies have focused on the characterization of second phases that are incorporated in YBCO films which were grown by various techniques. In particular, it has been reported that in sputtered and laser-ablated films, YBa<sub>2</sub>Cu<sub>3</sub>O<sub>7</sub> precipitates are present at boundaries between *a*- and *c*-axis YBCO domains where it was suggested that they act as nucleation sites for *a,b* domains.<sup>3</sup> Other groups have reported on other impurity phases: Y<sub>2</sub>O<sub>3</sub>, CuO, Y<sub>2</sub>Cu<sub>2</sub>O<sub>5</sub>, and Y<sub>2</sub>BaCuO<sub>5</sub> in laser-ablated films,<sup>4</sup> Y<sub>2</sub>O<sub>3</sub> in sputtered films,<sup>5</sup> and CuYO<sub>2</sub> in films prepared by electron beam coevaporation.<sup>6,7</sup>

Y<sub>2</sub>O<sub>3</sub> is cubic ( $a=1.06$  nm) and belongs to the space *Ia3*. The dominant orientation of Y<sub>2</sub>O<sub>3</sub> particles with respect to pure *c*-axis oriented films was determined to be [100]Y<sub>2</sub>O<sub>3</sub> || [110]YBCO, (001) Y<sub>2</sub>O<sub>3</sub> || (001) YBCO.<sup>5</sup> It has been shown that this orientation relationship also describes Y<sub>2</sub>O<sub>3</sub> buffer layers grown on *c*-axis oriented YBCO.<sup>8,9</sup>

This letter focuses on Y<sub>2</sub>O<sub>3</sub> inclusions in mixed *a*- and *c*-axis oriented YBa<sub>2</sub>Cu<sub>3</sub>O<sub>7</sub> (YBCO) films, thereby presenting complementary results to those for *c*-axis films.<sup>5</sup> We report on the structure of the precipitates and on their epitaxial orientations with respect to YBCO, as obtained from electron diffraction, high-resolution electron micro-

copy (HREM) and image calculations. In addition, the present relevance of second phases for the growth of domains having their *a* or *b* axis normal to the substrate surface (*a*-axis domains)<sup>3</sup> is investigated.

The YBCO films were grown by dc hollow cathode magnetron sputtering<sup>10</sup> on SrTiO<sub>3</sub> (001) and Sr<sub>2</sub>RuO<sub>4</sub> (001)<sup>11</sup> substrates at substrate heater block temperatures ( $T_{\text{sub}}$ ) ranging from 650 to 750 °C. The sputtering pressure was 650 mTorr (Ar/O<sub>2</sub>=2:1), the plasma discharge was operated at 450 mA and 150–170 V, and after growth, the films were cooled at room temperature within 1 h in 0.15 bar O<sub>2</sub>.

Transmission electron microscopy samples were prepared for both planar and cross-sectional views by standard mechanical polishing and ion milling with liquid nitrogen cooling. The observations were performed on a JEOL JEM-2010 operating at 200 kV. Image calculations were performed using the EMS software package developed by Stadelmann.<sup>12</sup>

Figure 1(a) shows low-magnification HREM image of a mixed *a*- and *c*-axis oriented YBCO film; about 50% of the film is a *a*-axis oriented. Precipitates with sizes between 70 and 300 nm<sup>2</sup> and density of the order of  $10^{15}$  cm<sup>-3</sup> are observed at both *a/c* and *a/a* (90° in-plane rotation twins) boundaries. The precipitates predominantly exhibit tabular habit; they are elongated along the *a,b* plane of the *a*-axis regions [Fig. 1(b)]. At *a/a* boundaries the thickness/width ratio and the precipitate size (up to 600 nm<sup>2</sup>) increase. The corresponding electron diffraction pattern [Fig. 1(c)] is consistent with the precipitates being Y<sub>2</sub>O<sub>3</sub>. Their dominant epitaxial relationship with respect to the *c*-axis oriented regions is [110] Y<sub>2</sub>O<sub>3</sub> || [001] YBCO, (001) Y<sub>2</sub>O<sub>3</sub> || (100) YBCO, which is different from the orientation of those particles that are fully embedded in regions of this type.<sup>5</sup>

The nucleation of the precipitates can be explained on the basis of lattice-matching arguments. The *a,b* plane of YBCO has the smallest lattice mismatch to (001) Y<sub>2</sub>O<sub>3</sub>: 3% along [110] Y<sub>2</sub>O<sub>3</sub> || [100] YBCO, with a nearly coincident unit cell area of 1.1 nm<sup>2</sup> [Fig. 2(a)]. The lattice match of the (110) Y<sub>2</sub>O<sub>3</sub> plane to the *a,b* plane of YBCO is not as

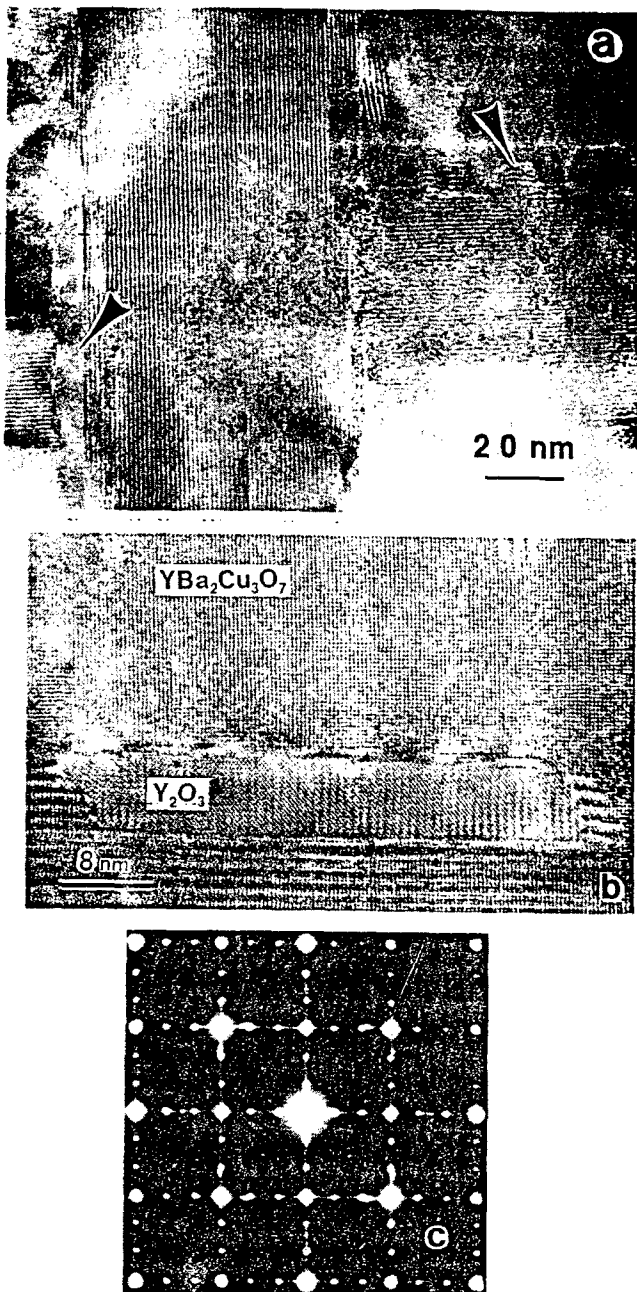


FIG. 1. (a) Planar-view micrograph of mixed  $a$  and  $c$  YBCO domains and second-phase inclusions (arrows). (b) HREM image of a  $\text{Y}_2\text{O}_3$  precipitate with tabular shape at an  $a/c$  boundary. (c) Electron diffraction pattern along the substrate normal;  $\text{Y}_2\text{O}_3$  100- and 110-type reflections overlap with YBCO 100-type spots.

favorable: 9% along  $[001]\text{Y}_2\text{O}_3 \parallel [010]\text{YBCO}$  and 3% along  $[110]\text{Y}_2\text{O}_3 \parallel [100]\text{YBCO}$ , with a nearly coincident unit cell area of  $1.7\text{ nm}^2$  [Fig. 2(b)]. Hence, joining  $(110)\text{Y}_2\text{O}_3$  to the  $a,b$  plane of YBCO requires larger nearly coincident cells and deformations and is thus energetically less favorable than joining  $(001)\text{Y}_2\text{O}_3$  to the  $a,b$  plane. The high density of atomic coincidences in this latter plane as well as minimal strain promote growth, which in turn leads to the formation of larger interfacial areas and to the observed precipitate elongation.

It is interesting to note that precipitates have not been observed to grow inside  $a$ -axis domains. This is partly due to the poor matching between  $[001]\text{Y}_2\text{O}_3$  and  $[001]\text{YBCO}$

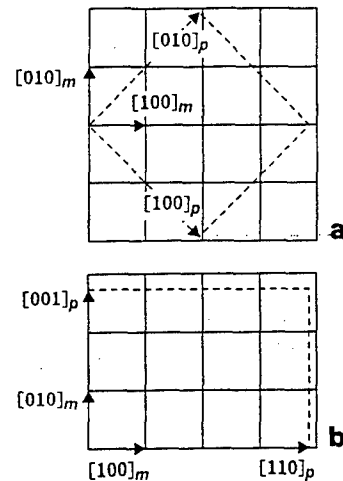


FIG. 2. Superimposed lattice points indicating nearly coincident unit cells in the interfacial planes: (a)  $(001)\text{Y}_2\text{O}_3 \parallel (001)\text{YBCO}$  and (b)  $(110)\text{Y}_2\text{O}_3 \parallel (001)\text{YBCO}$ . At  $a/c$  boundaries the precipitates have interface of type (a) along the  $a$ -axis grain and of type (b) along the  $c$ -axis grain. Solid lines and  $m$  (matrix) subscripts indicate YBCO, dashed lines and  $p$  (precipitate) subscripts  $\text{Y}_2\text{O}_3$ .

(10%). However, lattice matching arguments alone cannot explain this feature since such precipitates have been observed to nucleate inside  $c$ -axis films deposited at higher temperatures.<sup>5</sup> Other features such as the growth kinetics of the  $a$ -axis oriented grains ought to be considered to explain the growth of these second phases. Particularly, the large number of domain boundaries present in mixed  $a$ - and  $c$ -oriented films, providing favorable sites for the segregation of second phases, seems to be relevant.

For an unambiguous identification of these precipitates, we compared HREM micrographs to calculated images. The  $[110]$  projection of the  $\text{Y}_2\text{O}_3$  unit cell is displayed in Fig. 3(a). Figure 3(b) shows a HREM micrograph of  $\text{Y}_2\text{O}_3$  and, superimposed, the matching calculated image obtained with the Bloch wave algorithm of the EMS software package.<sup>12</sup> The sample thickness was estimated to be 6 nm, while the focusing conditions ( $66\text{ nm}^{-1}$ ) were determined on the basis of diffractograms. For the calculation parameters used, the image favorably matches the experimental micrograph: it clearly shows the projection of the face-centered substructure of the Y atoms (bright dots) for which the  $(111)$  planes cross at an angle of  $70.5^\circ$ .

In addition to the observation of epitaxial  $\text{Y}_2\text{O}_3$  pre-

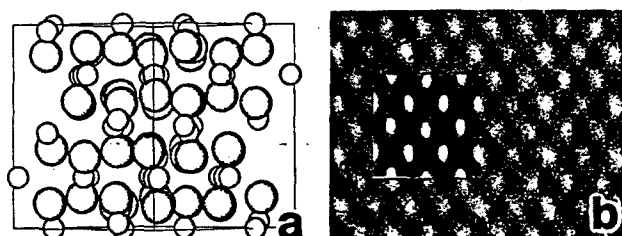


FIG. 3. (a)  $[110]$  projection of the  $\text{Y}_2\text{O}_3$  structure (small circles represent metal atoms). (b) HREM micrograph of  $(110)\text{Y}_2\text{O}_3$  and matching calculated image (inset). The microscope parameters are: spherical aberration coefficient = 0.5 mm, spread of focus = 8 nm, beam semiconvergence = 0.8 mrad, defocus = 66 nm; sample thickness = 6 nm.

cipitates in films produced by laser ablation<sup>4</sup> and sputtering, there is also evidence of such precipitates in films grown by e-beam evaporation.<sup>6,7</sup> Although these impurities were not explicitly identified as  $\text{Y}_2\text{O}_3$  in this case, regions in the HREM micrographs closely match the calculated image [Fig. 3(b)]. Unassigned x-ray peaks<sup>7</sup> also corroborate the presence of  $\text{Y}_2\text{O}_3$ . On the basis of these results, we suggest that in addition to  $\text{CuYO}_2$  also the occurrence of  $\text{Y}_2\text{O}_3$  should be considered in films by electron-beam co-evaporation. That  $\text{Y}_2\text{O}_3$  forms and persists in contact with YBCO is unexpected from the equilibrium phase diagram, which indicates that even at low oxygen pressures the two phases should react to produce  $\text{Y}_2\text{BaCuO}_5$  and either  $\text{CuO}$ ,  $\text{Cu}_2\text{O}$ , or  $\text{BaCu}_2\text{O}_2$ , depending on the oxygen pressure.<sup>13</sup> The existence of  $\text{Y}_2\text{O}_3/\text{YBCO}$  interfaces in films may be due to the kinetic hindrance of the nucleation and growth of the expected phases (mainly  $\text{Y}_2\text{CuO}_5$ ) or to lower interfacial energies between YBCO and  $\text{Y}_2\text{O}_3$  than between YBCO and  $\text{Y}_2\text{BaCuO}_5$ . Considering the lattice-matching considerations presented and the highly oriented growth observed, this latter explanation appears more likely.

In summary,  $\text{Y}_2\text{O}_3$  precipitates in sputtered mixed  $a$ - and  $c$ -axis oriented YBCO films on  $\text{SrTiO}_3$  substrates have been identified by HREM and image calculations. They exhibit tabular shape and grow epitaxially at  $a/c$  as well as at  $a/a$  boundaries. The orientation relationship with respect to the  $c$ -axis regions is  $[110] \text{Y}_2\text{O}_3 \parallel [001] \text{YBCO}$ ,  $(001) \text{Y}_2\text{O}_3 \parallel (100) \text{YBCO}$ . Their largest interfacial facet lies parallel to the  $a,b$  plane of the  $a$ -axis regions, in agreement with predictions based on lattice-matching arguments. Although these results present additional evidence for the presence of second phases at  $a/c$  boundaries, it is

not concluded at this point that such inclusions directly influence the nucleation of  $a$ -axis oriented domains. Specifically, the predominance of  $(001) \text{Y}_2\text{O}_3 \parallel (001) \text{YBCO}$  of  $a$ -axis oriented grains over  $c$ -axis oriented grains suggests that these precipitations nucleate on preexisting  $a$ -axis grains rather than causing their formation. In addition, the observation of  $\text{Y}_2\text{O}_3$  precipitates indicates that a straight line joins  $\text{Y}_2\text{O}_3$  to YBCO in the phase diagram that applies to our deposition conditions.

The authors gratefully acknowledge F. Lichtenberg for providing the  $\text{Sr}_2\text{RuO}_4$  substrates and R. F. Broom for his valuable support, as well as the financial support of the Swiss National Science Foundation.

- <sup>1</sup>J. A. Edwards, N. G. Chew, S. W. Goodyear, S. E. Blenkinsop, and R. G. Humphries, *J. Less-Common Metals* **164**, 414 (1990).
- <sup>2</sup>J. Zhao, C. S. Chern, Y. Q. Li, P. Norris, B. Gallois, B. Kear, X. D. Wu, and R. E. Münchhausen, *Appl. Phys. Lett.* **58**, 2839 (1991).
- <sup>3</sup>R. Ramesh, A. Inam, D. M. Hwang, T. D. Sands, C. C. Chang, and D. L. Hart, *Appl. Phys. Lett.* **58**, 1557 (1991).
- <sup>4</sup>O. Eibl and B. Roas, *J. Mater. Res.* **5**, 2620 (1990).
- <sup>5</sup>A. Catana, R. F. Broom, J. G. Bednorz, J. Mannhart, and D. G. Schlom, *Appl. Phys. Lett.* **60**, 1016 (1992).
- <sup>6</sup>A. F. Marshall, V. Matijasevic, P. Rosenthal, K. Shinohara, R. H. Hammond, and M. R. Beasley, *Appl. Phys. Lett.* **57**, 1158 (1990).
- <sup>7</sup>V. Matijasevic, P. Rosenthal, K. Shinohara, A. F. Marshall, R. H. Hammond, and M. R. Beasley, *J. Mater. Res.* **6**, 682 (1991).
- <sup>8</sup>K. Hirata, K. Yamaoto, K. Iijima, J. Takada, T. Terashima, Y. Bando, and H. Mizaki, *Appl. Phys. Lett.* **56**, 683 (1990).
- <sup>9</sup>Q. Y. Ying, C. Hilbert, N. Kumar, D. Eichman, M. Thompson, K. Kroger, and D. M. Hwang, *Appl. Phys. Lett.* **59**, 3036 (1991).
- <sup>10</sup>X. X. Xi, G. Linker, O. Meyer, E. Nold, B. Obst, F. Ratzel, R. Smithey, B. Strehlau, F. Weschenfelder, and J. Geerk, *Z. Phys. B* **74**, 13 (1989).
- <sup>11</sup>F. Lichtenberg, A. Catana, J. Mannhart, and D. G. Schlom, *Appl. Phys. Lett.* **60**, 1138 (1992).
- <sup>12</sup>P. Stadelmann, *Ultramicroscopy* **21**, 131 (1987).
- <sup>13</sup>R. Beyers and B. T. Ahn, *Annu. Rev. Mater. Sci.* **21**, 335 (1991).

## Electric Field Effect in High- $T_c$ Superconductors

J. Mannhart, J.G. Bednorz, K.A. Müller, D.G. Schlom,<sup>a</sup> and J. Ströbel<sup>b</sup>

IBM Research Division, Zurich Research Laboratory, 8803 Rüschlikon, Switzerland

<sup>a</sup>Present address: Penn State University, Pennsylvania, USA

<sup>b</sup>Also at the Physikalisches Institut, Universität Erlangen-Nürnberg, Erwin-Rommel-Str. 1, D-W 8520 Erlangen, Germany

### Abstract

A brief summary of electric field effects on the normal and the superconducting state of high- $T_c$  superconductors is given. Novel experiments are presented in which electric fields are used to modulate the transport properties of weak links. Analogies between the effects of electric and magnetic fields on superconductivity are emphasized.

### 1. Introduction

Since the beginning of the 1960's there has been an ongoing effort to use electric fields to control the transport properties of superconducting films [1-5]. These activities were extended both experimentally and theoretically to the high- $T_c$  cuprates shortly after the discovery of these materials [6-14] because they are exceptionally well suited for field effect studies. Their relatively low carrier density  $n$  in conjunction with a sizable dielectric constant  $\epsilon_{r,\text{sc}}^{\text{sc}}$  results in relatively large electric penetration depths  $\lambda_z^{\text{el}}$ . Furthermore, their small coherence lengths  $\xi$  allow the fabrication of ultrathin superconducting films in which the total carrier density can be modulated to a substantial extent. These properties are not only helpful from a technological perspective, but are also essential for the field effect from a fundamental point of view [15,16]. If a superconductor is penetrated by an electric field, its response to the field will depend sensitively on the value of the parameter  $\tau$

$$\tau(T) = \frac{\lambda_z^{\text{el}}(T)}{\xi_z(T)},$$

where  $\lambda_z^{\text{el}}(T)$  is the temperature-dependent electrical penetration depth and  $\xi_z(T)$  is the coherence length in field direction. Comparable to the Ginzburg-Landau parameter  $\kappa$ , which classifies the response of a superconductor to applied magnetic fields, the parameter  $\tau$  classifies the response of a superconductor to electric fields by differentiating between  $\tau < 1$  and  $\tau > 1$  superconductors. In both cases the field is shielded approximately exponentially from the interior of the superconductor, with the shielding length given by  $\lambda_z^{\text{el}}$ . Thus, the thickness of the layer in which the carrier density can be modulated is of the order of  $\lambda_z^{\text{el}}$ . For superconductors with  $\tau < 1$ , however, the superconducting properties are controlled by a layer of thick-

ness  $\xi_z$  and will thus barely respond to the field. If  $\tau > 1$ , the coherence length  $\xi_z$  is small enough for the superconducting order parameter to adjust to the modified carrier density. Therefore, in superconductors with  $\tau > 1$  the superconducting properties of the field penetrated layer can be altered sensitively by the applied field.

Remarkably, standard low- $T_c$  superconductors are small  $\tau$  superconductors. For niobium at 4.2 K, for instance,  $\tau = 3 \times 10^{-3}$ , as  $\lambda_{\text{el}} < 1 \text{ \AA}$  and  $\xi(4.2 \text{ K}) \approx 380 \text{ \AA}$ . In the high- $T_c$  cuprates, however, both  $\lambda_z^{\text{el}}$  and  $\xi_z$  equal a few angstroms, thus  $\tau \approx 1$ . This is the basis of the large electric field effects in the high- $T_c$  cuprates.

In this contribution field effect experiments performed with  $\text{YBa}_2\text{Cu}_3\text{O}_{7-\delta}$  films at the IBM Zurich Research Laboratory shall be discussed. For reviews of work performed by other groups the reader is referred to Refs. 16 and 17. After an introduction to sample preparation, the effect of electrostatic fields on the normal state transport, on  $T_c$ , and on the superconducting state will be presented. A separate chapter is devoted to the influence of applied electric fields on the transport properties of weak links in high- $T_c$  superconductors. For weakly linked samples, shifts of  $T_{c0}$  of more than 10 K are reported. By way of summary, analogies between the roles of magnetic and electric fields in superconductors will be considered.

### 2. Sample Preparation and Measurement Technique

The standard sample configuration used in the experiments is shown in Fig. 1 [18]. An  $n$ -type {100}-oriented 0.05% Nb-doped  $\text{SrTiO}_3$  single crystal grown with the zone-melting technique [19] is used as the substrate and gate electrode. As a thin insulating surface layer, which is detrimental to sample performance, forms on the surface of such crystals, 1-5 nm thin Pt films were grown on the doped  $\text{SrTiO}_3$  by

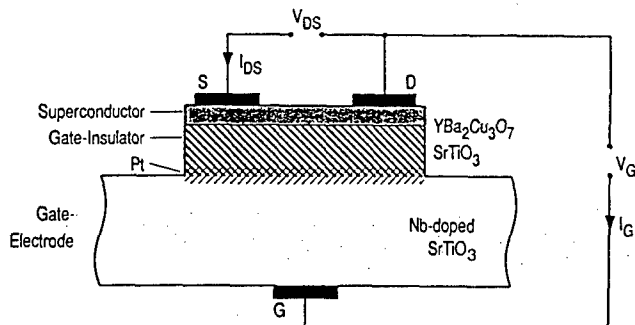


Fig. 1: Standard sample configuration used for the study of field effects. From [11].

electron beam evaporation. On top of the Pt layer, {100}-oriented and highly insulating layers of  $\text{SrTiO}_3$  were epitaxially deposited by reactive rf-magnetron sputtering at 0.05 Torr in an  $\text{O}_2/\text{Ar}$  atmosphere at  $\approx 650^\circ\text{C}$  (temperature of the sample holder).  $\text{SrTiO}_3$  was chosen as the material for the gate barrier because it is compatible in growth with  $\text{YBa}_2\text{Cu}_3\text{O}_{7-\delta}$  and it offers high dielectric constants without becoming ferroelectric at low temperatures where it is in a quantum paraelectric state [20]. Finally,  $\text{YBa}_2\text{Cu}_3\text{O}_{7-\delta}$  films were sputter deposited with a hollow cathode magnetron. Contacts were made to the  $\text{YBa}_2\text{Cu}_3\text{O}_{7-\delta}$  layer by sputtered Au pads and to the conducting substrate by diffusing silver into the Nb-doped  $\text{SrTiO}_3$ . To avoid leakage through pinholes, relatively thick ( $\approx 500$  nm) insulating  $\text{SrTiO}_3$  layers were used, whereas the  $\text{YBa}_2\text{Cu}_3\text{O}_{7-\delta}$  films were fabricated as thin as possible to achieve large  $\Delta n/n$  ratios. The thinnest  $\text{YBa}_2\text{Cu}_3\text{O}_{7-\delta}$  films found to be superconducting had an average thickness of  $\approx 4.5$  nm as determined from the extrapolated sputter rate. STM studies of similar films [21] revealed a thickness variation of  $\approx 2.8$  nm. Contamination of the interfaces was limited by performing all crucial steps of the sample preparation *in situ* in a specially designed vacuum system.

To rule out problems due to voltage pickup, all measurements were done in dc-mode. For each data point the drain source current  $I_{DS}$  was repeatedly reversed and the results were averaged.

### 3. Experiments

Through use of such samples, the transport properties of  $\text{YBa}_2\text{Cu}_3\text{O}_{7-\delta}$  can be modified by the electric field in the normal as well as in the superconducting state as exemplified in Figures 2-4. Before these results are described in detail it has to be clarified whether these effects are field effects at all. As described in detail elsewhere [12], this is done by eliminating alternative explanations. By studying the effects as a function of gate and drain source current, for instance, it has been shown that they are not

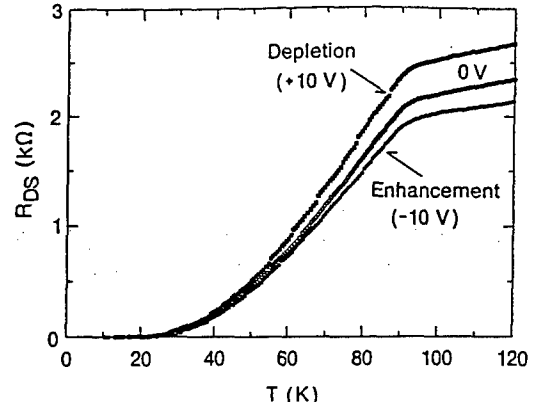


Fig. 2: Temperature dependence of the drain source resistance  $R_{DS}$  of an  $\approx 7$  nm thick  $\text{YBa}_2\text{Cu}_3\text{O}_{7-\delta}$  film for three gate voltages applied: +10 V (solid squares), 0 V (open circles), and -10 V (solid circles). From [13].

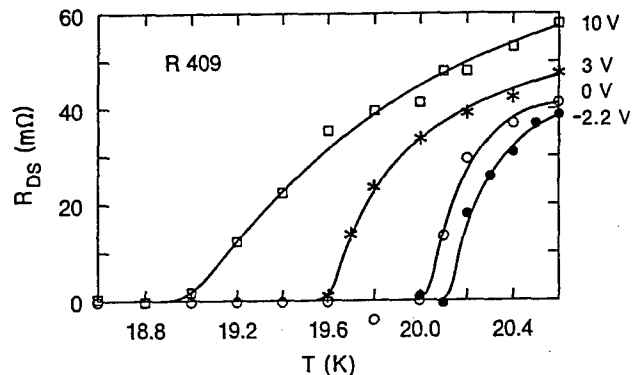


Fig. 3: Temperature dependence (close to  $T_{c0}$ ) of the drain source resistance  $R_{DS}$  of an  $\approx 10$  nm thick  $\text{YBa}_2\text{Cu}_3\text{O}_{7-\delta}$  film for four gate voltages: +10 V (depletion, open squares), +3 V (depletion, stars), 0 V (open circles), and -2.2 V (enhancement, solid circles). For this sample  $R_{DS}(300\text{ K}) \approx 3600\text{ }\Omega$ . From [13].

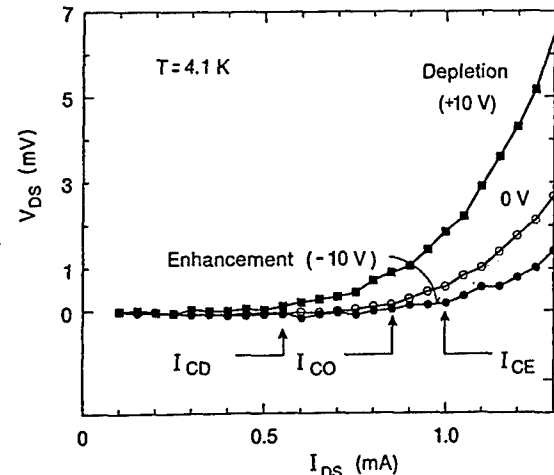


Fig. 4: Current dependence of the drain source voltage  $V_{DS}$  of the  $\text{YBa}_2\text{Cu}_3\text{O}_{7-\delta}$  film shown in Fig. 2 for three applied gate voltages: +10 V (solid squares), 0 V (open circles), and -10 V (solid circles). From [18].

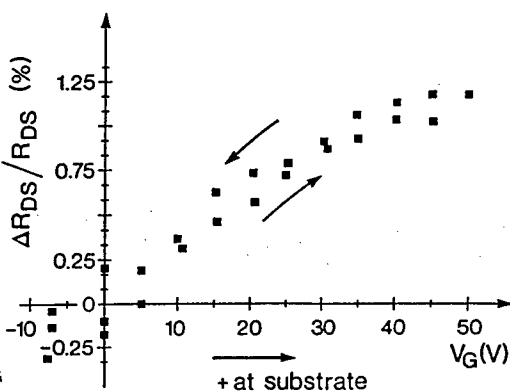


Fig. 5: Change of the drain source resistance  $R_{DS}$  caused by an applied gate voltage  $V_G$  of an  $\approx 10$  nm thick  $\text{YBa}_2\text{Cu}_3\text{O}_{7-\delta}$  film. The change of resistance has been normalized to  $R_{DS}(V_G=0 \text{ V})$ . The data have been taken at 300 K. From [11].

caused by heating or by quasiparticle injection and that voltages induced in the drain source channel or in the contacts are irrelevant. Similarly, by fabricating samples of different structures [12] and by studying the response as a function of channel thickness it is concluded that electrostriction or piezoelectricity of the gate barrier play a minor role at most.

In general the data obtained agree with the most simple field effect prediction [6,12] as shall be demonstrated with the dependence of  $R_{DS}$  on the gate voltage  $V_G$  of an early sample which had an effect of  $\Delta n/n \approx 10^{-2}$ . As shown in Fig. 5 the  $R_{DS}(V_G)$  dependence is approximately linear,  $\Delta R_{DS}$  changes sign when the gate voltage is reversed and the polarity agrees with the one expected for depletion and enhancement of holes. It is pointed out that for *n*-type  $\text{NdCeCuO}$  films the opposite polarity has been reported [22], in agreement with depletion and enhancement of electrons. The measured value of  $R_{DS}(V_G)$  corresponds to expectations: due to a gate capacitance of  $2 \times 10^{-7} \text{ F/cm}^2$ ,  $V_G = 30 \text{ V}$  changes the electron density in the electrodes by  $4 \times 10^{13}/\text{cm}^2$ . Because the carrier density of  $\text{YBa}_2\text{Cu}_3\text{O}_{7-\delta}$  is  $3.5 \times 10^{21}/\text{cm}^3$ , an areal density of mobile holes in the 10 nm thick channel layer of  $3.5 \times 10^{15}/\text{cm}^2$  is derived. This means that within experimental error, a change of the free carrier density of  $\approx 1\%$  results in an equal change of  $R_{DS}$ , as expected for a standard field effect.

Thus it is summarized that the effects seen are generally consistent with a field-induced change of the superconductor carrier density close to the gate interface. It is important to realize that the electric field predominantly affects this interface layer which, at least for standard samples, is expected to have a higher defect density than the rest of the film. Therefore, by analyzing field effect experiments one has to take into account that they reflect properties of a

superconductor rich in defects. These defects may exhibit an additional electrostatic life of their own and be susceptible to charging.

#### 4. Field Effect Behavior

##### 1) $T > T_c$

By applying the electric field the normal state resistance changes as described above. As demonstrated in Fig. 5, a linear  $R_{DS}(V_G)$  characteristic is observed that sometimes shows a slight saturation behavior at higher fields [12], in agreement with observations by X.X. Xi et al. [23]. Hysteresis effects are present [12] which are attributed to the trapping of charges at the interface states. As a function of temperature, for  $T > T_c$ , the relative change of the drain source resistance  $\Delta R_{DS}/R_{DS}$  is constant, which, in accordance with A.F. Fiory et al. [6], is interpreted as evidence for a temperature-independent carrier density.

##### 2) $T = T_c$

Approaching  $T_c$  from above, the relative change of the drain source resistance  $\Delta R_{DS}/R_{DS}$  diverges, indicating a field-induced shift of  $T_c$ . The  $T_c$  shift becomes evident if the behavior at  $T_{c0}$  is analyzed. As demonstrated by Fig. 3, gate voltages of the order of 10 V, can shift  $T_{c0}$  by more than 1 K [18]. It is pointed out that similar results have been obtained by X.X. Xi et al. using samples of another configuration prepared with different thin film techniques [13,23].

##### 3) $T < T_c$

Below  $T_c$ , the current voltage characteristics  $I_{DS}(V_{DS})$  of the drain source channel are modified by the electric field as shown in Fig. 4. The  $V_{DS}$  ( $I_{DS}$ ) curve is well rounded and there is no marked kink that could serve as a definition of the critical current  $I_c$ . Smooth  $I(V)$  curves are a characteristic of epitaxial films [24]; in these ultrathin samples the smoothness is even enhanced by the thickness variations of the  $\text{YBa}_2\text{Cu}_3\text{O}_{7-\delta}$  films mentioned above. This implies that  $I_c$  has to be defined with some arbitrary criterion, which was chosen to be  $R(100 \text{ K})/10^4 \approx 200 \text{ m}\Omega$ .

As shown in Fig. 4,  $I_c$  depends sensitively on  $E$ , and can be shifted by a surprising 50% at 4.1 K. Because the sample in Fig. 4 had a  $T_c$  of  $\approx 14$  K, the shift of  $I_c$  is not regarded as a secondary effect resulting from a  $T_c$  shift. Remarkably, the magnetic field dependence of the critical current  $I_c(B)$  of the sample shown in Fig. 4 is the same as that of conventional, 100 nm thick  $\text{YBa}_2\text{Cu}_3\text{O}_{7-\delta}$  films which are known to be limited by depinning. This suggests that also for this ultrathin film,  $I_c$  is depinning-limited and that the electric field changes the strength of the pinning force, probably by altering the depths of the pinning potentials [16,18].

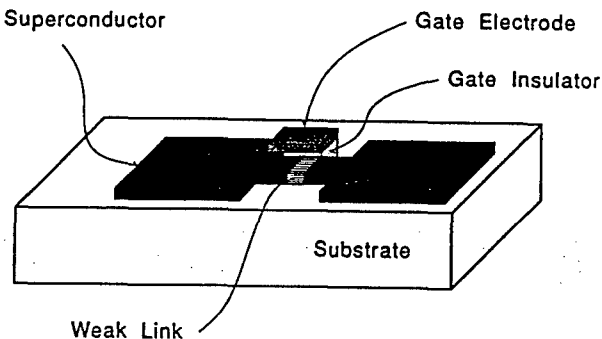


Fig. 6. Sketch of a sample where a superconducting weak link is controlled by an electric field. From [26].

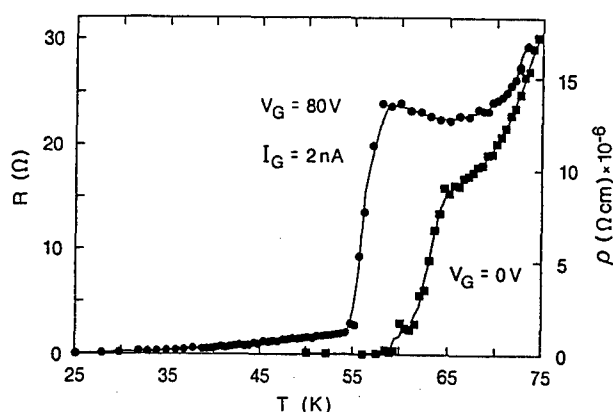


Fig. 7.  $R_{DS}(T)$  curves of an  $\text{YBa}_2\text{Cu}_3\text{O}_{7-\delta}$  film containing weak links for  $I_{DS} = 200 \text{ nA}$  and gate voltages (a)  $V_G = 0 \text{ V}$ , and (b)  $V_G = 80 \text{ V}$  ( $I_G = 2 \text{ nA}$ ). From [26].

### 5. Electric Field Effects in $\text{YBa}_2\text{Cu}_3\text{O}_{7-\delta}$ Films Containing Weak Links

As described above, electrostatic screening counteracts the propagation of electric fields into the interior of the superconducting film and thus reduces the field effects. This suggests that an additional reduction in screening, attained for example by using samples into which weak links have been incorporated (Fig. 6), would help increase  $\tau$  and thus result in even larger field effects. Besides their sensitivity to electric fields, such weak link structures may have another interesting feature. If the weak links are Josephson junctions, three terminal Josephson junctions (JOFETs) are obtained, and their gate voltage can be used for control, switching and trimming purposes. This is of interest for a wide range of applications.

As large-angle grain boundaries in  $\text{YBa}_2\text{Cu}_3\text{O}_{7-\delta}$  films have been shown to act as Josephson junctions [25], one way to incorporate weak links is to add grain boundaries to the drain-source channel of standard field effect structures. Thus we have prepared numerous samples into which grain boundaries were

inserted by using substrates with vicinal surfaces, by employing substrates with sharp edges or small grooves, or by fabricating bicrystalline drain-source channels.

In the following we focus on the behavior of samples for which submicron grooves were used to create the weak links.

The trenches in the substrate surface were produced by polishing the substrates with  $1 \mu\text{m}$  diamond paste on a soft plastic foil, which yields a fine network of submicron grooves on the substrate surface. The groove density was of the order of  $10^4/\text{cm}^2$  and the average depth and width of the trenches on top of the sputtered  $\text{SrTiO}_3$  film were found by atomic force microscopy to be  $\approx 300 \text{ \AA}$  and  $\approx 500 \text{ \AA}$ , respectively. Since it is known that grooves and edges on substrate surfaces provoke grain boundaries in  $\text{YBa}_2\text{Cu}_3\text{O}_{7-\delta}$  films, it is supposed in our case that the modified substrate surfaces give rise to grain boundary networks in the drain-source channels.

To demonstrate the large field effects obtainable, we present the behavior of one particular sample with large field effects. Further data can be found in Ref. 26.

Figure 7 shows the  $DS$ -resistance of this sample near  $T_{c0}$  as a function of temperature, measured with a  $DS$ -current of  $200 \text{ nA}$  for gate voltages of  $V_G = 0 \text{ V}$  and  $V_G = 80 \text{ V}$  (depletion). As shown, the transition temperature  $T_{c0} \approx 60 \text{ K}$  is shifted by more than  $10 \text{ K}$  with  $V_G = 80 \text{ V}$  and a gate current of  $I_G = 2 \text{ nA}$ .

Samples of this type differ from conventional samples only with respect to the presence of weak links, yet they show a much greater shift of  $T_{c0}$ . The large field effects are therefore attributed to the weak links. Evidently, the shifts are induced in the weak links predominantly by the applied electric fields and not by  $I_G$ , first because they scale with  $V_G$ , second because large shifts have been obtained with small gate currents ( $\leq 1 \text{ nA}$ ), and third because  $T_c$  is increased in the enhancement mode (by  $0.65 \text{ K}$  for  $V_G = 4.5 \text{ V}$ ). As the polarity of the effects is consistent with the movement of holes in the weak links, in contrast to the polarity observed for moving oxygen ions [27], it is suggested that the effects are primarily based on the change of the hole density.

$I_G$  increases exponentially with  $V_G$ . Thus for gate voltages  $V_G$  above  $100 \text{ V}$ , the value of  $I_G$  could be varied significantly while causing only slight electric field variations. As only a small change of  $V_G$  caused the  $R(T)$  curves to shift noticeably in this parameter regime, it is concluded that these shifts are based in part on the higher gate currents involved. Since these currents were still small compared to the critical current, the enhancement effect is tentatively attributed to non-equilibrium effects caused by quasiparticle injection into the grain boundaries.

It is noted that the enhanced  $\tau$  for samples containing weak links allows the achievement of consider-

**Table I: Electromagnetic Fields and Superconductivity**

Magnetic Fields	Electric Fields
$\lambda_m = \left( \frac{m^*}{\mu_0 n^* e^{*2}} \right)^{1/2}$	$\lambda_{el} = \left( \frac{\varepsilon_r^{sc} \varepsilon_0}{e^2 \frac{dN}{dE} (E_F)} \right)^{1/2}$
$\kappa = \frac{\lambda_m(T)}{\xi(T)}$	$\iota(T) = \frac{\lambda_{el}(T)}{\xi(T)}$
$\begin{cases} < 1/\sqrt{2} \\ > 1/\sqrt{2} \end{cases}$ Type I Type II	$\begin{cases} < 1 \\ > 1 \end{cases}$ E effects are averaged out $\psi$ is sensitive to E
in bulk: $h/2e$	$e$
$\mathbf{B}$ affects $\vec{\nabla}\psi$	E affects $ \psi $
Physics: magnetic flux structures and their interactions with the superconductor	Influence of $\frac{n}{E_F}$ on any superconducting property $\Delta$ $U_{con}$
Devices: $I$ and $B$ controlled small signal devices (Squids, FFTs), power transmission, magnets...	Voltage controlled FETs phonon generators detectors...

able field effects with high- $T_c$  thicker than standard drain source channels and thus have a higher  $T_c$ , which is of importance for potential applications.

## 6. Comparison of the Effects of Electric and Magnetic Fields on Superconductors

There is a remarkable analogy between the effects of electric and of magnetic fields on superconductivity which shall be elucidated in this chapter (see also Table 1).

First of all, by generating self-fields a superconductor shields its interior against electric or magnetic fields, generally damping them exponentially. For magnetic fields oriented in the z-direction, the corresponding shielding length is given by the Ginzburg-Landau penetration depth  $\lambda_{ab}''(T)$ , for electric fields this is given by the much smaller electric penetration depth  $\lambda_{el}'(T)$ .

The response of a superconductor to magnetic fields is characterized by the Ginzburg-Landau parameter  $\kappa = \lambda_{ab}''(T)/\xi_{ab}(T)$ . For type I superconductors,

$\kappa < 1/\sqrt{2}$  and the magnetic fields penetrate superconductors as flux tubes containing many vortices; for type II materials,  $\kappa > 1/\sqrt{2}$  and the superconductor lets the field penetrate as single flux quanta.

The response of a superconductor to electric fields is classified in a similar way by the parameter  $\iota(T) = \lambda_{el}'/\xi_z(T)$ . As described above, if  $\iota < 1$ , the electric field can influence the carrier density, but only in a region that is too small for the superconducting order parameter to respond to. Only if  $\iota(T) > 1$  can the superconducting order parameter adapt to the modified carrier density and will depend sensitively on the applied field in this zone.

Next it is noted that both types of field may penetrate deeply into a superconductor, their sources being quantized in both cases. For magnetic fields, the quanta are flux lines with a charge of  $h/2e$ , for electric fields the quantum of the field source is the electronic charge  $e$ .

The analogy can be carried further by noting that the magnetic fields affect the gradient of the superconducting order parameter  $\vec{\nabla}\Psi$  which is exploited in

phase-sensitive devices like SQUIDS, whereas electric fields change the order parameter's magnitude  $|\Psi|$ . Therefore electric fields are interesting for devices that exploit the value of the superconducting gap [28].

## 7. Summary

Owing to their low carrier densities, their high dielectric constants and their small coherence lengths the high- $T_c$  cuprates are destined to change their transport properties with applied electric fields. In various experiments, field effects have been reported that agree in general with a model in which the electric field acts on the superconductor by changing its density of mobile carriers via band bending. Field effects have been reported for the normal state as well as for the superconducting phase. Concerning the latter it has been found that in epitaxial  $\text{YBa}_2\text{Cu}_3\text{O}_{7-\delta}$  films the critical temperature of ultrathin films can be shifted by 1 K and that their pinning energy and hence their critical current can be varied up to 50% by gate voltages of the order of 10 V. In the case that weak links are incorporated into the high- $T_c$  films,  $T_{c0}$  shifts can be enhanced to 10 K or more.

It is hoped that applied electric fields will be a key to basic studies of the influence of the carrier concentration on such fundamental properties of high- $T_c$  superconductors as  $T_c(n)$ ,  $\lambda(n)$ , and  $\xi(n)$ , and may provide new access to the macroscopic quantum state of superconductivity.

## 8. Acknowledgments

The authors gratefully acknowledge helpful valuable discussions with A. Baratoff, C.C. Chi, H.M. Christen and A. Kleinsasser. One of the authors (J.S.) is thankful to the Bundesministerium f. Forschung und Technologie and the Bayerische Forschungsstiftung Forsupra for financial support.

## References

- 1 R.E. Glover and M.D. Sherrill, *Phys. Rev. Lett.* **5** (1960) 248.
- 2 H.L. Stadler, *Phys. Rev. Lett.* **14** (1965) 979.
- 3 A.T. Fiory and A.F. Hebard, *Phys. Rev. Lett.* **52** (1984) 2057.
- 4 M. Gurvitch, H.L. Stormer, R.C. Dynes, J.M. Graybeal, and D.C. Jacobson, *Extended Abstracts, Proceedings of Symposium S*, ed. J. Bevk and A.I. Braginski (MRS, 1986) p. 47-49.
- 5 V.V. Bogatko and Yu.N. Venetsev, *Sov. Phys. Solid State* **29** (1988) 1654.
- 6 A.T. Fiory, A.F. Hebard, R.H. Eick, P.M. Mankiewich, R.E. Howard, and M.L. O'Malley, *Phys. Rev. Lett.* **65** (1990) 3441.
- 7 Yu.V. Gomeniuk, N.I. Kliuy, V.Z. Lozovski, V.S. Lysenko, A.Yu. Prokofiev, B.N. Romaniuk, T.N. Sytenko, and I.P. Tyagulski, *Sverkhprovodimost: fiz., khim., tekhn.*, **4**, 762 (1991).
- 8 A. Levy, J.P. Falck, M.A. Kastner, W.J. Gallagher, A. Gupta, and A.W. Kleinsasser, *J. Appl. Phys.* **69** (1991) 4439.
- 9 D.F. Moore, "Superconducting Thin Films for Device Applications," *Proc. 2nd Workshop on High- $T_c$  Electron Devices*, R&D Association for Future Electron Devices, June 7-9, 1989, in Shikabe, Japan, pp. 281-284.
- 10 Y. Tarutani, S. Saitoh, T. Fukazawa, U. Kawabe, *J. Appl. Phys.* **69** (1991) 1778.
- 11 U. Kabasawa, K. Asano, and T. Kobayashi, *Jpn. J. Appl. Phys.* **29** (1990) L86.
- 12 J. Mannhart, J.G. Bednorz, K.A. Müller, and D.G. Schlom, *Z. Phys. B* **83** (1991) 307.
- 13 X.X. Xi, Q.Li, C. Doughty, C. Kwon, S. Bhattacharya, A.T. Finkoglou, and T. Venkatesan, *Appl. Phys. Lett.* **59** (1991) 3470.
- 14 T. Fujii, K. Sakuta, T. Awaji, K. Matsui, T. Hirano, Y. Ogawa and T. Kobayashi, *Jpn. J. Appl. Phys.* **31**, L612 (1992).
- 15 B.Ya. Shapiro, *Sov. State Comm.*, **53**, 673 (1985).
- 16 J. Mannhart, *Mod. Phys. Lett. B* **6** (1992) 555.
- 17 A. Kleinsasser, in "Superconducting Field Effect Devices," *Proc. of NATO ASI "The New Superconducting Electronics,"* Waterville Valley, August 9-19, 1992 (Kluwer Academic Publishers, Dordrecht, The Netherlands);
- 18 J. Mannhart, D.G. Schlom, J.G. Bednorz, and K.A. Müller, *Phys. Rev. Lett.* **67** (1991) 2099.
- 19 J.G. Bednorz and H. Arend, *J. Cryst. Growth* **67** (1984) 660.
- 20 K.A. Müller and H. Burkard, *Phys. Rev. B* **19** (1979) 3593.
- 21 C. Gerber, D. Anselmetti, J.G. Bednorz, J. Mannhart and D.G. Schlom, *Nature* **350** (1991) 279; D.G. Schlom, D. Anselmetti, J.G. Bednorz, R.F. Broom, A. Catana, T. Frey, Ch. Gerber, H.-J. Güntherodt, H.P. Lang, and J. Mannhart, *Z. Phys. B* **86** (1992) 163.
- 22 X.X. Xi, "Field-Induced Hole-Density Modulation in Ultrathin YNCO-Films," March Meeting of the American Physical Society, Indianapolis, March 20, 1992.
- 23 X.X. Xi, C. Doughty, A. Walkenhorst, C. Kwon, Q. Li, and T. Venkatesan, *Phys. Rev. Lett.* **68** (1992) 1240.
- 24 J. Mannhart, P. Chaudhari, D. Dimos, C.C. Tsuei and T.R. McGuire, *Phys. Rev. Lett.* **61** (1988) 2476.
- 25 D. Dimos, P. Chaudhari, J. Mannhart, and F.K. LeGoues, *Phys. Rev. Lett.*, **61**, 219 (1988).
- 26 J. Mannhart, J. Ströbel, J.G. Bednorz and Ch. Gerber, "Large Electric Field Effects in  $\text{YBa}_2\text{Cu}_3\text{O}_{7-\delta}$  Films Containing Weak Links", submitted to *Appl. Phys. Lett.*

- 27 A.V. Mitlin, N.E. Alekseevskii, and E.P. Khlybov,  
Physica C, 199, 351 (1992).
- 28 J. Mannhart and A. Kleinsasser "Electric Field  
Effect in High- $T_c$  Superconductors, Field Induced

Superconductivity and Device Applications," to be  
published in *Proc. 1992 Spring Meeting of the  
MRS, Symposium S*, San Francisco, April 27-May  
1, 1992.

# Surface outgrowths on sputtered $\text{YBa}_2\text{Cu}_3\text{O}_{7-x}$ films: A combined atomic force microscopy and transmission electron microscopy study

A. Catana,<sup>a)</sup> J. G. Bednorz, Ch. Gerber, J. Mannhart, and D. G. Schlom<sup>b)</sup>  
IBM Research Division, Zurich Research Laboratory, 8803 Rüschlikon, Switzerland

(Received 2 December 1992; accepted for publication 10 May 1993)

We have structurally and morphologically characterized the surface of sputtered  $\text{YBa}_2\text{Cu}_3\text{O}_{7-x}$  films on (001)  $\text{SrTiO}_3$  using atomic force microscopy and transmission electron microscopy. Atomic force microscopy reveals three types of outgrowths with different shapes and heights between 2 and 200 nm: type I exhibits cubic habit, type II tabular habit, and type III is an agglomerate of no particular shape. Some of the type-III outgrowths are located at the center of growth spirals where the screw dislocation intersects the film surface, suggesting that in  $\text{YBa}_2\text{Cu}_3\text{O}_{7-x}$  films these defects promote the occurrence of one another. Using high-resolution electron microscopy and electron diffraction the surface outgrowths have been identified as follows: type I is  $\text{Y}_2\text{O}_3$ , type II  $\text{Y}_2\text{O}_3$  and  $\text{CuYO}_2$ , and type III  $\text{YBa}_2\text{Cu}_3\text{O}_{7-x}$ ,  $\text{CuO}$ , and  $\text{Y}_2\text{O}_3$ . In contrast to types-I and -II outgrowths which are both epitaxially related to the surrounding  $\text{YBa}_2\text{Cu}_3\text{O}_{7-x}$ , the large type-III agglomerates consist of epitaxial and nonepitaxial grains. As it is found that the outgrowing nonepitaxial phases emanate from screw dislocations and from  $a,b$ -axis domain boundaries, it is suggested that both internal stresses and high interfacial energies promote such outgrowths on  $\text{YBa}_2\text{Cu}_3\text{O}_{7-x}$  films.

Analysis of the surface morphology and of embedded microstructural features in  $\text{YBa}_2\text{Cu}_3\text{O}_{7-x}$  (YBCO) films has provided valuable clues for the understanding of film growth mechanisms.<sup>1-4</sup> Surface morphology and bulk microstructure are also essential aspects for the growth and investigation of multilayers as well as for microelectronic applications.

Previous studies have shown that outgrowths formed on  $\text{YBa}_2\text{Cu}_3\text{O}_{7-x}$  films and other surface features are sensitive to composition and deposition conditions,<sup>5-7</sup> but have not identified the structure of the out-growing second phases. Off-stoichiometry is also present inside the films, where it causes line and point defects, stacking faults, and precipitates.<sup>4,8-12</sup> Recently, by using scanning electron microscopy (SEM) and transmission electron microscopy (TEM), Ramesh and co-workers found that surface outgrowths ( $\text{YBa}_2\text{Cu}_3\text{O}_{7-x}$ ) and  $a,b$ -axis domains are correlated in sputtered and laser-ablated YBCO films.<sup>13</sup> In other work it was found that films with a high density of growth spirals contain a high number of  $\text{Y}_2\text{O}_3$  precipitates.<sup>4</sup> All these investigations suggest a close connection between surface features and the bulk structure of the films.

In this letter, atomic force microscopy (AFM) and TEM studies of surface outgrowths on sputtered YBCO films are presented. The shape and composition of three types of outgrowths are identified and their epitaxial orientations and the connection to the surface microstructure are discussed.

The YBCO films, about 100 nm thick, were grown by dc hollow cathode magnetron sputtering on  $\text{SrTiO}_3$ (001) substrates at substrate heater block temperatures ( $T_{\text{sub}}$ ) of approximately 750 °C. The sputtering pressure was 650

mTorr ( $\text{Ar}/\text{O}_2 = 2:1$ ), the plasma discharge was operated at 450 mA and 150–170 V, and after growth, the films were cooled to room temperature within an hour in 0.5 bar of  $\text{O}_2$ .

AFM images were obtained with a commercially available instrument (Nanoscope III, Digital Instruments) using optical beam deflection to monitor the displacement of a microfabricated  $\text{Si}_3\text{N}_4$ -type cantilever having a spring constant of 0.1 N/m. Images were recorded in the constant force mode with typical forces of  $10^{-8}$  N between tip and sample.

TEM samples of the same films analyzed by AFM were prepared for both planar and cross-sectional views by standard mechanical polishing and subsequent ion milling with liquid nitrogen cooling. The observations were made on a JEOL JEM-2010 operated at 200 kV.

Figure 1 shows AFM images of the film surface which emphasize the presence of three typical surface outgrowths. Type-I outgrowths, as labeled in Fig. 1, are small precipitates densely distributed ( $\approx 10^{10}/\text{cm}^2$ ) over the film surface. The size of these precipitates is about  $(20-25) \times (20-25) \times (2-8)$  nm.<sup>3</sup> Type-II outgrowths [typically  $(200-300) \times (170-230) \times (30-50)$  nm<sup>3</sup>] have a characteristic tabular habit and are preferentially oriented with the long edges parallel to the in-plane  $\langle 100 \rangle$  axes of the film (Fig. 1), suggesting that these orientations are energetically favorable. Type-III outgrowths (Fig. 1) are large agglomerates with typical heights of 200 nm. Although the majority of the constituent grains of type-III outgrowths have irregular shapes, in most cases a platelet-like grain (A in Fig. 1) separates them from the surrounding YBCO matrix. The center of growth spirals has been observed to be a second nucleation site (B in Fig. 1), suggesting a correlation between screw dislocations and the nucleation and agglomeration of second phases.

To identify the structure of the various types of out-

<sup>a)</sup>Present address: EPFL, Prospective and Research, 1015 Lausanne, Switzerland.

<sup>b)</sup>Present address: Department of Materials Science and Engineering, The Pennsylvania State University, University Park, PA 16802-5505.

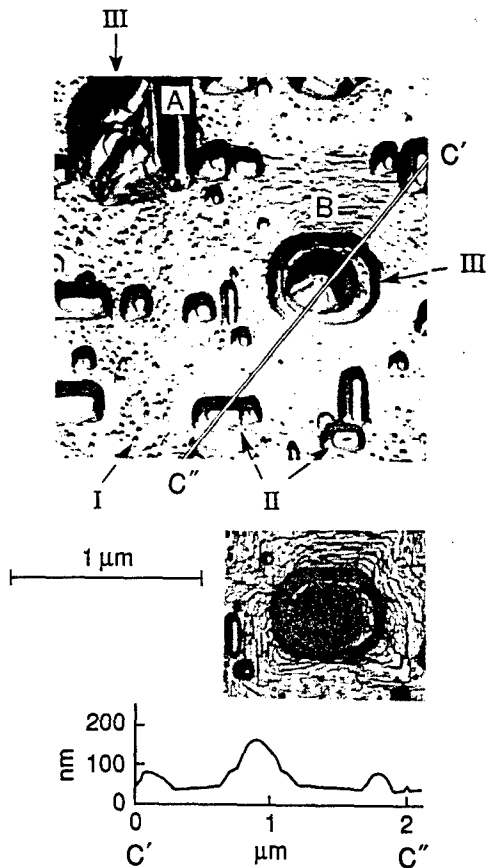


FIG. 1. AFM image of the YBCO film surface showing densely distributed outgrowths of types I-III (arrows). A refers to the YBCO platelets and B to a growth spiral. The growth spiral is shown once more in the small micrograph, in which the growth steps (one unit cell high) are clearly visible. At the bottom a height profile along the line C'-C'' is shown.

growths, high-resolution electron microscopy (HREM) and electron diffraction were employed.

Type-I particles are epitaxial  $\text{Y}_2\text{O}_3$  grains of cube shape. Their orientation with respect to YBCO is  $\langle 100 \rangle \text{Y}_2\text{O}_3 \parallel \langle 110 \rangle \text{YBCO}$  and  $\{001\} \text{Y}_2\text{O}_3 \parallel \{001\} \text{YBCO}$ , in agreement with previous studies.<sup>4,10</sup> A cross-sectional HREM micrograph of a  $\text{Y}_2\text{O}_3$  surface precipitate is shown in Fig. 2. Occasionally,  $\text{Y}_2\text{O}_3$  outgrowths with  $\{110\}$  planes parallel to  $(001)$  YBCO nucleate in the bulk of the film. In this case they frequently separate  $c$ -axis from  $a,b$ -axis YBCO regions as shown in Fig. 3. Owing to favorable matching conditions between  $\{110\} \text{Y}_2\text{O}_3$  and  $(001)$  YBCO, the presence of  $(001)$  planes of YBCO parallel to the substrate normal favors the nucleation and enhances the growth rate of  $\text{Y}_2\text{O}_3$  with this particular orientation, as suggested previously.<sup>14</sup>

$\text{Y}_2\text{O}_3$  precipitates oriented in the latter manner ( $\{110\} \text{Y}_2\text{O}_3 \parallel \{001\} \text{YBCO}$ ) occur on the film surface, and together with  $\text{CuYO}_2$  precipitates give rise to the type-II surface features.  $\text{CuYO}_2$  grows with its [421] axis parallel to [001] YBCO (Fig. 4), which is different from previously reported results.<sup>11</sup> Just as the nucleation of  $\text{Y}_2\text{O}_3$  precipitates has been explained on the basis of lattice-matching arguments,<sup>4,14</sup> the orientation of  $\text{CuYO}_2$  also relates to lattice match. Indeed, the observed orientation relationship is

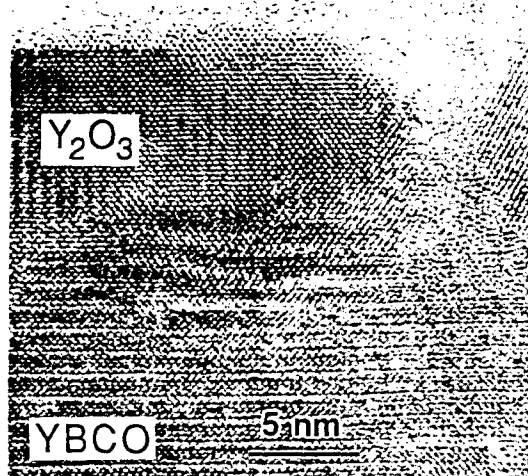


FIG. 2. Cross-sectional HREM micrograph of an epitaxial  $\text{Y}_2\text{O}_3$  surface precipitate with the orientational relationship:  $\{001\} \text{Y}_2\text{O}_3 \parallel \{001\} \text{YBCO}$ ,  $\{110\} \text{Y}_2\text{O}_3 \parallel \{100\} \text{YBCO}$ .

such that  $(112)$  and  $(012)$   $\text{CuYO}_2$  planes are almost parallel to  $(110)$  YBCO planes, the mismatch being only 1.2%. In addition to these two phases, diffraction patterns indicate the presence of other phases not yet identified.

The larger polycrystalline agglomerates (type-III outgrowths) consist of both epitaxial and nonepitaxial grains. They are predominantly correlated with YBCO  $a,b$ -axis plates (Fig. 5), which may serve as nucleation sites, or are located at the center of growth spirals, which were identified by AFM and scanning tunneling microscopy (Fig. 1). Different diffraction patterns obtained on the constituent grains of the agglomerates provide evidence for epitaxial grains, namely YBCO (i.e., the  $a,b$ -axis platelets mentioned above), CuO and  $\text{Y}_2\text{O}_3$ , as well as for unidentified constituents.

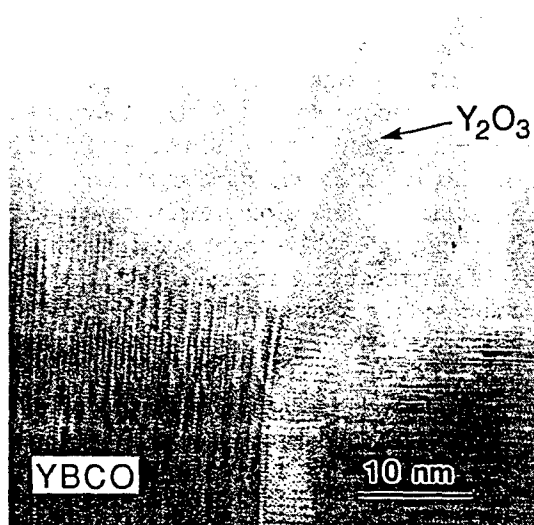


FIG. 3. Cross-sectional HREM micrograph of an epitaxial  $\text{Y}_2\text{O}_3$  outgrowth at a domain boundary between  $a,b$ -axis YBCO (on the left) and  $c$ -axis YBCO (on the right) with  $\{110\} \text{Y}_2\text{O}_3 \parallel \{001\} \text{YBCO}$  and  $\{100\} \text{Y}_2\text{O}_3 \parallel \{100\} \text{YBCO}$  of the  $a,b$ -axis YBCO domain.

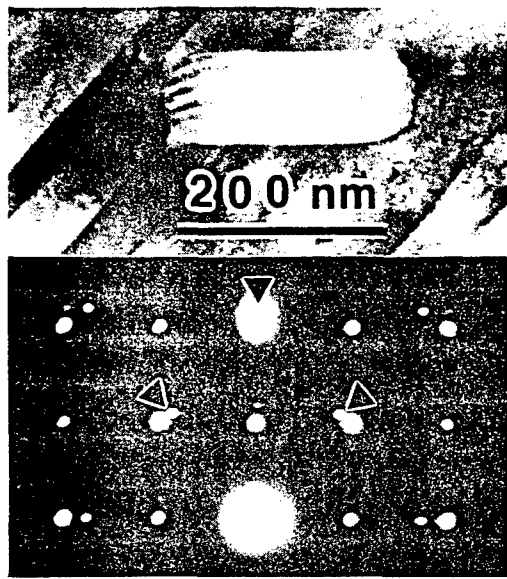


FIG. 4. Planar-view HREM micrograph of a  $\text{CuYO}_2$  precipitate and corresponding selected area diffraction pattern. The epitaxial orientation is such that [001]  $\text{YBCO} \parallel$  [421]  $\text{CuYO}_2$ , (100)  $\text{YBCO} \parallel$  (120)  $\text{CuYO}_2$ . Arrows indicate 421  $\text{CuYO}_2$  reflections.

The locations and the structure of type-III precipitate agglomerates are correlated with  $a,b$ -axis outgrowths and with the intersections of screw dislocations with the film surface, suggesting that these defects promote one another. Precipitates have been shown to cause the nucleation of

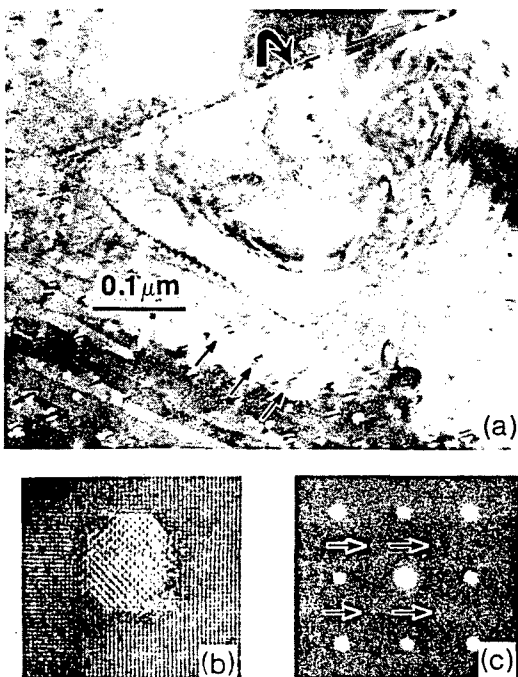


FIG. 5. (a) Planar-view TEM micrograph demonstrating the coexistence of small  $\text{Y}_2\text{O}_3$  particles (type I) and larger agglomerates (type III). Three  $\text{Y}_2\text{O}_3$  precipitates are marked by the parallel arrows. A  $\text{YBCO}$  platelet separating the agglomerate from the film matrix is indicated by the curved arrow. (b) HREM image of a typical  $\text{Y}_2\text{O}_3$  precipitate and (c) corresponding selected area diffraction pattern (the four arrows indicate 100  $\text{Y}_2\text{O}_3$  reflections).

screw dislocations in the growth of other layered materials.<sup>15,16</sup> High interfacial energies and internal stresses between nonepitaxial precipitates and the  $\text{YBCO}$  matrix provide a driving force for the transport of impurity species to energetically more favorable nucleation or attachment sites, for example, to locations where defects such as dislocations, grain boundaries, or out-of-phase boundaries intersect the film surface. Surface outgrowths, induced by compressive stresses, are known to occur in thin films; these stresses are relieved by the transport of material along easy diffusion paths given by the defects mentioned above to unstressed regions.<sup>17</sup> In addition, outgrowths may form adjacent to already existing outgrowths of a different type, for example, at  $a,b$ -axis  $\text{YBCO}$  domains which provide favorable nucleation sites.<sup>14</sup>

In summary, three types of outgrowths, which are predominantly epitaxial with respect to the  $\text{YBCO}$  matrix, have been observed by AFM on sputtered  $\text{YBCO}$  films grown on (001)  $\text{SrTiO}_3$ . Type I are cube-shaped  $\text{Y}_2\text{O}_3$  grains, type II have tabular habit and consist of either  $\text{Y}_2\text{O}_3$  or  $\text{CuYO}_2$  precipitates, whereas type III are agglomerate in which  $\text{YBCO}$ ,  $\text{CuO}$ , and  $\text{Y}_2\text{O}_3$  grains have been identified. Type-III outgrowths are correlated with  $a,b$ -axis platelets or with the center of growth spirals. These results show that  $a/c$ -domain boundaries and screw dislocations are favorable sites for the nucleation and agglomeration of second phases and suggest that such outgrowths on  $\text{YBa}_2\text{Cu}_3\text{O}_{7-x}$  films are promoted by high interfacial energies and by internal stress.

The authors gratefully acknowledge R. F. Broom for his valuable aid, P. Chaudhari for fruitful discussions, and the Swiss National Science Foundation for financial support.

- <sup>1</sup>Ch. Gerber, D. Anselmetti, J. G. Bednorz, J. Mannhart, and D. G. Schlom, *Nature* **350**, 279 (1991).
- <sup>2</sup>M. Hawley, I. D. Raistrick, J. G. Beery, and R. J. Houlton, *Science* **251**, 1587 (1991).
- <sup>3</sup>D. G. Schlom, D. Anselmetti, J. G. Bednorz, R. F. Broom, A. Catana, T. Frey, Ch. Gerber, H.-J. Güntherodt, H. P. Lang, and J. Mannhart, *Z. Phys. B* **86**, 163 (1992).
- <sup>4</sup>A. Catana, R. F. Broom, J. G. Bednorz, J. Mannhart, and D. G. Schlom, *Appl. Phys. Lett.* **60**, 1016 (1992).
- <sup>5</sup>J. A. Edwards, N. G. Chew, S. W. Goodyear, S. E. Blenkinsop, and R. G. Humphries, *J. Less-Common Metals* **164**, 414 (1990).
- <sup>6</sup>J. Zhao, C. S. Chern, Y. Q. Li, P. Norris, B. Gallois, B. Kear, X. D. Wu, and R. E. Münchhausen, *Appl. Phys. Lett.* **58**, 2839 (1991).
- <sup>7</sup>C. C. Chang, X. D. Wu, R. Ramesh, X. X. Xi, T. S. Ravi, T. Venkatesan, D. M. Hwang, R. E. Münchhausen, S. Foltyn, and N. S. Nogar, *Appl. Phys. Lett.* **57**, 1814 (1990).
- <sup>8</sup>F. K. LeGoues, *Philos. Mag. B* **57**, 167 (1988).
- <sup>9</sup>O. Eibl and B. Roas, *J. Mater. Res.* **5**, 2620 (1990).
- <sup>10</sup>P. Lu, Y. Q. Li, J. Zhao, C. S. Chern, B. Gallois, P. Norris, P. Kear, and F. Cosandey, *Appl. Phys. Lett.* **60**, 1265 (1992).
- <sup>11</sup>A. F. Marshall, V. Matijasevic, P. Rosenthal, K. Shinohara, R. H. Hammond, and M. R. Beasley, *Appl. Phys. Lett.* **57**, 1158 (1990).
- <sup>12</sup>T. I. Selinder, U. Helmersson, Z. Han, J.-E. Sundgren, H. Sjöström, and L. R. Wallenberg, *Physica C* **202**, 69 (1992).
- <sup>13</sup>R. Ramesh, A. Inam, D. M. Hwang, T. D. Sands, C. C. Chang, and D. L. Hart, *Appl. Phys. Lett.* **58**, 1557 (1991).
- <sup>14</sup>A. Catana, D. G. Schlom, J. Mannhart, and J. G. Bednorz, *Appl. Phys. Lett.* **61**, 720 (1992).
- <sup>15</sup>A. Baronnet, *J. Cryst. Growth* **19**, 193 (1973).
- <sup>16</sup>M. I. Kozlovskii, *Sov. Phys. Crystallogr.* **3**, 206 (1958).
- <sup>17</sup>P. Chaudhari, *J. Appl. Phys.* **45**, 4339 (1974).

**Reprinted from**

JOURNAL OF

# **CRYSTAL GROWTH**

---

Journal of Crystal Growth 137 (1994) 259-267

## **Epitaxial growth of cuprate superconductors from the gas phase**

D.G. Schlom <sup>a,\*</sup>, D. Anselmetti <sup>b</sup>, J.G. Bednorz <sup>c</sup>, Ch. Gerber <sup>c</sup>, J. Mannhart <sup>c</sup>

<sup>a</sup> *The Pennsylvania State University, Department of Materials Science and Engineering, University Park, Pennsylvania 16802-5005, USA*

<sup>b</sup> *University of Basel, Institute of Physics, Klingelbergstrasse 82, CH-4056 Basel, Switzerland*

<sup>c</sup> *IBM Research Division, Zurich Research Laboratory, CH-8803 Rüschlikon, Switzerland*



## EDITORIAL BOARD

M. SCHIEBER (Principal Editor)  
Dept. Materials Science,  
School Appl. Sci. & Technol.  
Hebrew University, Jerusalem 91904, Israel  
Telefax: +972-2-666 804

R. KERN  
CRMC<sup>2</sup>, CNRS, Campus Luminy, Case 913  
F-13288 Marseille Cedex 9, France  
Telefax: +33-91-418 916

R.S. FEIGELSON  
Ctr. Materials Res., 105 McCullough Bldg.  
Stanford Univ., Stanford, CA 94305-4045, USA  
Telefax: +1-415-723 3044

D.T.J. HURLE  
H.H. Wills Physics Laboratory  
Univ. Bristol, Tyndall Avenue  
Bristol BS8 1TL, UK

T. NISHINAGA  
Dept. Electronic Engineering, University of Tokyo  
7-3-1, Hongo, Bunkyo-ku, Tokyo 113, Japan  
Telefax: +81-3-5684-3974

G.B. STRINGFELLOW  
Dept. Materials Science, 304 EMRO  
University of Utah  
Salt Lake City, UT 84112, USA  
Telefax: +1-801-581 4816

## ASSOCIATE EDITORS

Y. BANDO (*Superconductivity*)  
Lab. of Solid State Chemistry  
Inst. for Chemical Research, Kyoto Univ.  
Uji, Kyoto-fu 611, Japan

A. BARONNET (*Industrial, Biological and Molecular Crystals*)  
CRMC<sup>2</sup>, CNRS, Campus Luminy, Case 913  
F-13288 Marseille Cedex 9, France  
Telefax: +33-91-418 916

K.W. BENZ (*Microgravity, Electronic Materials*)  
Kristallographisches Inst., Universität  
Hebelstr. 25, D-7W-7800 Freiburg, Germany  
Telefax: +49-761-203 4369

G.M. BLOM (*Liquid Phase Epitaxy*)  
Philips Laboratories, 345 Scarborough Road  
Briarcliff Manor, NY 10510, USA  
Telefax: +1-914-945 6375

A.A. CHERNOV (*Kinetics of Crystallization*)  
Inst. Crystallography, Acad. of Sciences  
Leninskii Prospekt, Moscow 117333, Russian Fed.  
Telefax: +7-095-135 1011

J. CHIKAWA (*Perfection of Crystals*)  
Faculty of Science, Himeji Inst. Technology  
Harima Garden City, Kamigori-chyo  
Hyogo 678-12, Japan

A.Y. CHO (*Molecular Beam Epitaxy*)  
Room 1C-323, AT & T Bell Laboratories  
Murray Hill, NJ 07974-2070, USA  
Telefax: +1-908-582 2043

B. COCKAYNE (*Review Articles, IOCG News*)  
DRA Malvern, St. Andrews Road,  
Great Malvern, Worcs. WR14 3PS, UK  
Telefax: +44-684-894 540

D. ELWELL (*Priority Communications, Superconductivity*)  
Hughes Aircraft Company  
P.O. Box H, M/S E2103, 500 Superior Avenue  
New Port Beach, CA 92658-8908, USA  
Telefax: +1-714-759 2868

M.A.G. HALLIWELL (*X-ray Diffraction*)  
Philips Analytical X-ray, Lelyweg 1  
7602 EA Almelo, Netherlands

K.A. JACKSON (*Theory*)  
Arizona Materials Laboratory  
4715 E Fort Lowell Road, Tucson, AZ 85712, USA

E. KALDIS (*Chemical Transport*)  
Institut für Festkörperforschung, ETH  
Hönggerberg, CH-8093 Zürich, Switzerland  
Telefax: +41-1-371 5989

S. KIMURA (*Oxide Crystals*)  
National Inst. Res. Inorg. Materials  
1-1 Namiki, Tsukuba, Ibaraki 305, Japan  
Telefax: +81-298-52 7449

T.F. KUECH (*Thin Films and Electronic and Optical Devices*)  
Dept. Chemical Engineering  
Univ. Wisconsin-Madison  
Madison, WI 53706, USA  
Telefax: +1-608-262 5434

H. KUKIMOTO (*Thin Films, Epitaxy*)  
Imaging Science & Eng. Lab.  
Tokyo Inst. of Technology  
4259 Nagatsuda, Midori-ku  
Yokohama 227, Japan  
Telefax: +81-45-921-1492

A. MCPHERSON (*Protein Growth*)  
Dept. Biochemistry, Univ. of California  
Riverside, CA 92521, USA  
Telefax: +1-909-787 3790

J.B. MULLIN (*Semiconductors*)  
EMC, "The Hoe", Brookhill Road  
West Malvern, Worcs. WR14 4DL, UK  
Telefax: +44-684-575 591

K. PLOOG (*Molecular Beam Epitaxy*)  
Paul-Drude-Inst. für Festkörperforschung  
Hausvogteiplatz 5-7, D-10117 Berlin, Germany  
Telefax: +49-30-203 77201

F. ROSENBERGER (*Vapor Growth, Fluid Dynamics*)  
Center for Microgravity and Materials Research  
Univ. Alabama, Huntsville, AL 35899, USA  
Telefax: +1-205-895 6791

R.W. ROUSSEAU (*Solution Growth, Industrial Crystallization*)  
School of Chemical Engineering  
Georgia Institute of Technology  
Atlanta, GA 30332-0100, USA  
Telefax: +1-404-894 2866

L.F. SCHNEEMAYER (*Superconductivity, Oxides, Novel Materials*)  
Room 1A-363, AT & T Bell Laboratories  
Murray Hill, NJ 07974-2070, USA  
Telefax: +1-908-582 2521

R.F. SEKERKA (*Theory*)  
6319 Wean Hall, Carnegie Mellon University  
Pittsburgh, PA 15213, USA  
Telefax: +1-412-681 0648

D.W. SHAW (*Semiconductors, Epitaxy, Devices*)  
Texas Instruments Inc., P.O. Box 655936, MS 147  
Dallas, TX 75265, USA  
Telefax: +1-214-995 5539

I. SUNAGAWA (*Morphology and Minerals*)  
3-54-2 Kashiwa-cho, Tachikawa-shi  
Tokyo 190, Japan  
Telefax: +81-425-35 3637

T. SUREK (*Materials for Energy Conversion and Photovoltaics*)  
National Renewable Energy Lab.  
1617 Cole Blvd., Golden, CO 80401, USA  
Telefax: +1-303-231 1030

G. VAN TENDELOO (*Electron Microscopy, Fullerenes, Superconductivity*)  
University of Antwerp, RUCA  
Groenenborgerlaan 171  
B-2030 Antwerp, Belgium  
Telefax: +32-3-2180 217

A.F. WITT (*Semiconductor Crystals*)  
Dept. of Metallurgy & Materials Science  
Massachusetts Institute of Technology  
Cambridge, MA 02139, USA  
Telefax: +1-617-253 5827

Technical Editor: F.Y. Verploegh Chassé, Elsevier/North-Holland, P.O. Box 103, 1000 AC Amsterdam, Netherlands,  
Telefax: +31-20-5862 775

Elsevier Science B.V.: All rights reserved. No part of this publication may be reproduced, stored in a retrieval system or transmitted in any form or by any means, electronic, mechanical, photocopying, recording or otherwise, without the written permission of the publisher, Elsevier Science B.V., P.O. Box 103, 1000 AC Amsterdam, Netherlands.

*Special regulations for authors* ~ Upon acceptance of an article by the journal, the author(s) will be asked to transfer copyright of the article to the publisher. This transfer will ensure the widest possible dissemination of information.

*Special regulations for readers in the USA* ~ This journal has been registered with the Copyright Clearance Center, Inc. Consent is given for copying of articles for personal or internal use, or for the personal use of specific clients. This consent is given on the condition that the copier pays through the Center the per-copy fee stated in the code on the first page of each article for copying beyond that permitted by Sections 107 or 108 of the US Copyright Law. The appropriate fee should be forwarded with a copy of the first page of the article to the Copyright Clearance Center, Inc., 27 Congress Street, Salem, MA 01970, USA. If no code appears in an article, the author has not given broad consent to copy and permission to copy must be obtained directly from the author. The fee indicated on the first page of an article in this issue will apply retroactively to all articles published in the journal, regardless of the year of publication. This consent does not extend to other kinds of copying, such as for general distribution, resale, advertising and promotion purposes, or for creating new collective works. Special written permission must be obtained from the publisher for such copying.

No responsibility is assumed by the Publisher for any injury and/or damage to persons or property as a matter of products liability, negligence or otherwise, or from any use or operation of any methods, products, instructions or ideas contained in the material herein. Although all advertising material is expected to conform to ethical standards, inclusion in this publication does not constitute a guarantee or endorsement of the quality or value of such product or of the claims made of it by its manufacturer.

*US mailing notice* ~ Journal of Crystal Growth (ISSN 0022-0248) is published monthly by Elsevier Science, Molenwerf 1, P.O. Box 211, 1000 AE Amsterdam, Netherlands. Annual subscription price in the USA is US \$4822 (valid in North, Central and South America only), including air speed delivery. Second class postage paid at Jamaica NY 11431.

**USA POSTMASTERS:** Send address changes to Journal of Crystal Growth, Publications Expediting, Inc., 200 Meacham Avenue, Elmont NY 11003. Airfreight and mailing in the USA by Publications Expediting.



ELSEVIER

JOURNAL OF CRYSTAL GROWTH

Journal of Crystal Growth 137 (1994) 259-267

## Epitaxial growth of cuprate superconductors from the gas phase

D.G. Schlom <sup>a,\*</sup>, D. Anselmetti <sup>b</sup>, J.G. Bednorz <sup>c</sup>, Ch. Gerber <sup>c</sup>, J. Mannhart <sup>c</sup>

<sup>a</sup> The Pennsylvania State University, Department of Materials Science and Engineering, University Park, Pennsylvania 16802-5005, USA

<sup>b</sup> University of Basel, Institute of Physics, Klingelbergstrasse 82, CH-4056 Basel, Switzerland

<sup>c</sup> IBM Research Division, Zurich Research Laboratory, CH-8803 Rüschlikon, Switzerland

### Abstract

The growth mechanism of *c*-axis oriented thin epitaxial films of the most widely studied cuprate superconductor,  $\text{YBa}_2\text{Cu}_3\text{O}_{7-\delta}$ , formed by a variety of gas phase codeposition methods on common substrate materials is described. The evolution of the surface microstructure, as revealed by scanning tunneling microscopy (STM), indicates that growth is dominated by the accommodation of depositing species at ledges. These ledges, which provide energetically favorable positions for this process, lie either along growth spirals emanating from screw dislocations, or, when a vicinal substrate is used, separate the low energy (001) planes at the film surface. If the substrate is misoriented sufficiently, growth occurs by step propagation. Otherwise, a high density of screw dislocations ( $\sim 10^9 \text{ cm}^{-2}$ ) is nucleated during the initial stages of growth, providing a continual supply of ledge incorporation sites for the depositing species. Two likely mechanisms for the generation of these screw dislocations are described. The surface evolution reported appears to be an intrinsic feature of *c*-axis oriented  $\text{YBa}_2\text{Cu}_3\text{O}_{7-\delta}$  films for a wide range of growth conditions, irrespective of the substrate material or vapor phase deposition method.

### 1. Introduction

Vapor phase deposition techniques have achieved immense success in preparing epitaxial thin films of cuprate superconductors with transport properties superior to those made by bulk synthesis methods. A consequence of the extremely short coherence lengths in these superconductors, typically a few ångströms, is that the electrical characteristics of these materials are particularly sensitive to their underlying microstructure. This microstructure is in turn de-

pendent on the film growth mechanism, which is the subject of this paper.

Efforts to understand the growth mechanism of oxide superconductor films have profited substantially from atomic-scale imaging techniques [1-3], in particular scanning tunneling microscopy (STM) and atomic force microscopy (AFM) [4,5]. Since experimental data elucidating the growth mechanism of high temperature superconductors by gas phase codeposition methods are predominantly for  $\text{YBa}_2\text{Cu}_3\text{O}_{7-\delta}$  films oriented with their *c*-axes normal to the substrate, this material will be the focus of this paper. The applicability of the inferred growth mechanism to other high temperature superconductors is briefly addressed, based on the limited data available.

\* Corresponding author.

## 2. Microstructure of $\text{YBa}_2\text{Cu}_3\text{O}_{7-\delta}$ films

Despite the obvious differences in the vapor phase growth techniques used to produce high quality superconductor thin films, the specific conditions used by different research groups, and the range of lattice match, crystal structure, substrate perfection, and surface preparation of the substrate materials used, the microstructures of the films grown by different methods exhibit remarkable similarity, indicating that the same growth mechanism is operative. The *c*-axis oriented  $\text{YBa}_2\text{Cu}_3\text{O}_{7-\delta}$  films discussed here are grown by sputtering [6,7], off-axis magnetron sputtering [4,5,8–16], pulsed laser deposition (PLD) [3,6,15–27], thermal coevaporation [6,28], chemical vapor deposition (CVD) [6,16,27,29], and

molecular beam epitaxy (MBE) [30,31] ( $\text{DyBa}_2\text{Cu}_3\text{O}_{7-\delta}$  films) on  $\text{SrTiO}_3$  {100} [3–7,9,12,14–16,19,23–27,29–31],  $\text{MgO}$  {100} [3,5,6,8,9,13,15–19,27,28,31],  $\text{LaAlO}_3$  {100} [6,9,20,22], yttria-stabilized cubic zirconia  $\text{Y}_2\text{O}_3\text{-ZrO}_2$  {100} [21], oxidized Zr sheets [27],  $\text{NdGaO}_3$  (001) [10,31], and  $\text{Mg}_2\text{TiO}_4$  {100} [23]. STM and AFM images of these films reveal a surface morphology containing closely spaced steps [3–29]. These steps, which have a height equal to the *c*-axis length of  $\text{YBa}_2\text{Cu}_3\text{O}_{7-\delta}$  (11.7 Å) or an integral multiple of it, separate (001)  $\text{YBa}_2\text{Cu}_3\text{O}_{7-\delta}$  terraces. These terraces are typically only a few hundred ångströms wide [3,13,15,20,22,26,29], indicating the length scale over which (001) oriented  $\text{YBa}_2\text{Cu}_3\text{O}_{7-\delta}$  films are atomically flat. The high density of steps, which appears to be a common



Fig. 1. STM image of a *c*-axis oriented, 1300 Å thick  $\text{YBa}_2\text{Cu}_3\text{O}_{7-\delta}$  film grown on  $\text{SrTiO}_3$  (100) by sputter deposition. Growth spirals emanating from both left- and right-handed screw dislocations indicate a screw dislocation density of  $(12.5 \pm 1) \times 10^8 \text{ cm}^{-2}$  at the film surface.

feature of *c*-axis oriented  $\text{YBa}_2\text{Cu}_3\text{O}_{7-\delta}$  films grown by vapor phase methods, exposes *a*-axis faces. These typically amount to 5%–10% of the surface area of the  $\text{YBa}_2\text{Cu}_3\text{O}_{7-\delta}$  films [12].

The microstructure of *c*-axis oriented  $\text{YBa}_2\text{Cu}_3\text{O}_{7-\delta}$  films is distinctly different for films grown on well-oriented (100) substrates (Fig. 1), compared to vicinal surfaces (Fig. 2). Irrespective of the substrate material and deposition method used, on well-oriented (100) substrates, a high density of screw dislocations ( $10^8$ – $10^{10} \text{ cm}^{-2}$ ) is seen in films more than a few hundred ångströms thick, whereas for growth on substrates with vicinal surfaces the stepped nature of the substrate surface is preserved and a much lower density of screw dislocations ( $< 10^8 \text{ cm}^{-2}$ ) is found. These screw dislocations not only may be strong vortex pinning sites which enhance the critical current densities of the thin films [32], but also reveal the film growth mechanism [12,14,15]. Films with much lower screw dislocation densities have been grown on vicinal  $\text{SrTiO}_3$  (100) [15] and  $\text{LaAlO}_3$  (100) [26] surfaces by sputtering [15] and PLD [26]. As the orientation of the substrate deviates

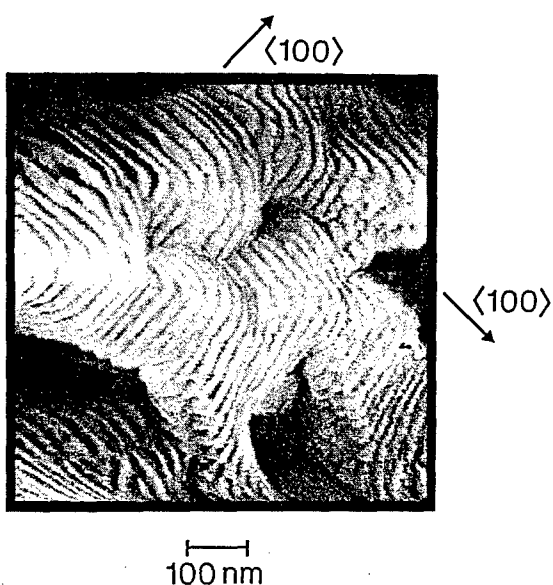


Fig. 2. STM image of a *c*-axis oriented, 1300 Å thick  $\text{YBa}_2\text{Cu}_3\text{O}_{7-\delta}$  film grown on a vicinal  $\text{SrTiO}_3$  (100) substrate by sputter deposition. The surface morphology is dominated by steps between (001)  $\text{YBa}_2\text{Cu}_3\text{O}_{7-\delta}$  terraces which accommodate the substrate tilt (from Ref. [15]).

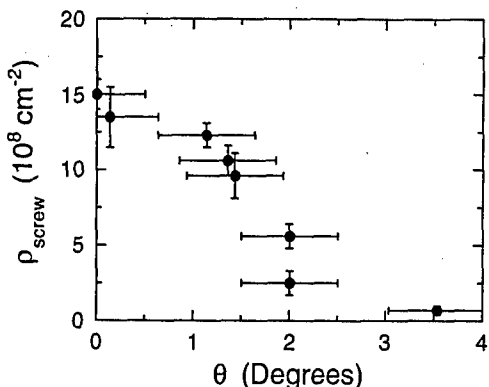


Fig. 3. Screw dislocation density ( $\rho_{\text{screw}}$ ) as a function of substrate misorientation angle ( $\theta$ ) for sputtered 1000–1500 Å thick  $\text{YBa}_2\text{Cu}_3\text{O}_{7-\delta}$  films grown at  $T_{\text{sub}} \approx 750^\circ\text{C}$  and a growth rate of 0.5–1.8 Å/s on nominally (100) oriented  $\text{SrTiO}_3$  substrates (from Ref. [15]).

from (100) and becomes increasingly misoriented, a continual cross-over in dislocation density as a function of misorientation is observed (Fig. 3). Increased growth temperature and decreased growth rate cause a similar effect, as discussed below [4,15].

The STM images shown are not only representative of the hundreds of such images that we have taken of our own films formed by direct current (DC) magnetron sputtering [4,12,14,15], but are characteristic of the topological features reported by many other researchers using the variety of gas phase preparation techniques and substrates listed above [3–31]. A lower magnification STM image of a sputtered film grown on a well-oriented  $\text{SrTiO}_3$  (100) substrate is shown in Fig. 4. The terrace widths on films grown on well-oriented substrates are comparable to the maximum terrace width observed on films grown on vicinal substrates under the same growth conditions at film thicknesses where the growth spirals emanating from screw dislocations have become well established. As described below, the growth spirals typically appear after the growth of a  $\text{YBa}_2\text{Cu}_3\text{O}_{7-\delta}$  film about 8–10 unit cells thick on  $\text{SrTiO}_3$  (100) [4,6,15] or  $\text{MgO}$  (100) [3,19]. These are the only two substrate materials for which studies of the development of growth spirals with film thickness have been published.

### 3. Growth mechanism

The presence of a high density of growth spirals emanating from screw dislocations in *c*-axis oriented  $\text{YBa}_2\text{Cu}_3\text{O}_{7-\delta}$  films [3–29] indicates that film growth takes place by accommodating species along the spiral-shaped growth steps. The growth process of *c*-axis oriented  $\text{YBa}_2\text{Cu}_3\text{O}_{7-\delta}$  films may thus be described as ledge growth, emphasizing the energetic preference of the depositing species to attach to existing ledges (step edges), which propagate laterally across the substrate surface as they accommodate species. This process and the various types of ledge sites available for attachment are schematically shown in Fig. 5. As the spacing between existing ledges on

the growth surface is increased, the supersaturation at positions far from the ledges becomes high enough for two-dimensional nucleation to occur on terraces.

At the initiation of growth, the only available ledge sites on a vicinal, but otherwise perfect, surface are surface steps. Indeed transmission electron microscopy (TEM) studies show that the initial nucleation occurs predominantly there [2]. If the substrate is sufficiently well oriented and the substrate temperature low enough that the supersaturation on the terrace can reach the level required for two-dimensional nucleation, growth will take place by the nucleation of new layers (two-dimensional nucleation) in regions far from ledges. However, if a sufficient density of screw

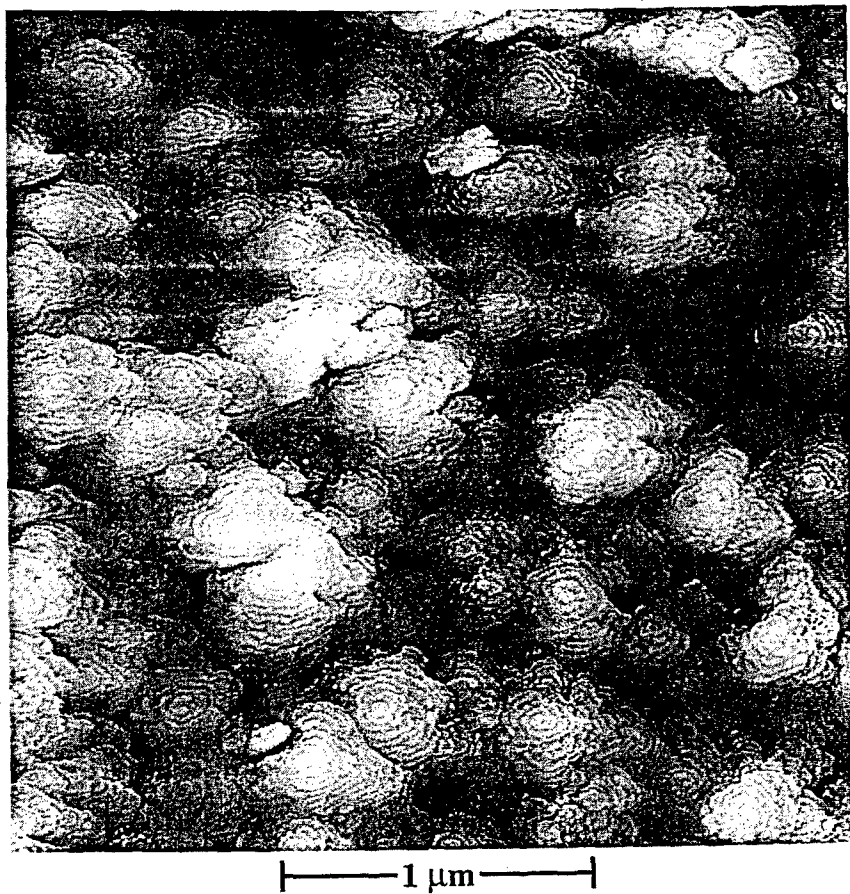


Fig. 4. STM image of a *c*-axis oriented, 1200 Å thick  $\text{YBa}_2\text{Cu}_3\text{O}_{7-\delta}$  film grown on  $\text{SrTiO}_3$  (100) by sputter deposition. Growth spirals emanating from both left- and right-handed screw dislocations indicate a screw dislocation density of  $(13.5 \pm 2) \times 10^8 \text{ cm}^{-2}$  at the film surface.

dislocations were to be generated, possible mechanisms for which are described below, an endless supply of attachment sites would be available to accommodate the depositing species. Direct morphological evidence from STM and AFM studies [3,4,6,15,19] as well as indirect evidence from reflection high energy electron diffraction (RHEED) intensity oscillations [33,34] indicate that two-dimensional nucleation is only dominant for the first 100 to 200 Å of film growth. By this thickness high densities of screw dislocations are present in  $\text{YBa}_2\text{Cu}_3\text{O}_{7-\delta}$  films grown on well oriented substrates, dominating the growth process from then on. Only in a few cases has growth dominated by two-dimensional nucleation been documented for thicker films [8,35,36]. The surface morphology of these films, which has been described as "Tower of Hanoi" [35] or "layer-cake-like" [36] exhibits narrow terraces with widths comparable to other *c*-axis oriented  $\text{YBa}_2\text{Cu}_3\text{O}_{7-\delta}$  films, with the exception that these films appear to be devoid of screw dislocations at the tops of the stacks of concentric  $\text{YBa}_2\text{Cu}_3\text{O}_{7-\delta}$  layers. The growth parameters

which appear to impede the nucleation of screw dislocations and lead to continued two-dimensional nucleation for the growth of thick films are as yet unclear.

RHEED intensity oscillations are not expected for growth occurring by the addition of species to established growth spirals or to a propagating sequence of surface steps, since the surface step density is then essentially time independent. Indeed, the observation of RHEED intensity oscillations has only been reported [33,34] to occur during the initial stages of growth (for thickness  $\leq 200$  Å for  $\text{YBa}_2\text{Cu}_3\text{O}_{7-\delta}$  films) on bare substrates, indicative of the time necessary for a steady-state surface step density to become established. On thicker films, no RHEED intensity oscillations are seen, even if the growth is briefly interrupted [33,34], nor are RHEED oscillations observed for growth on sufficiently vicinal surfaces [37].

When slightly misoriented from (100), a sequence of steps separating (100) terraces is present on the surface of the substrate. Although the substrate step height does not match the layer

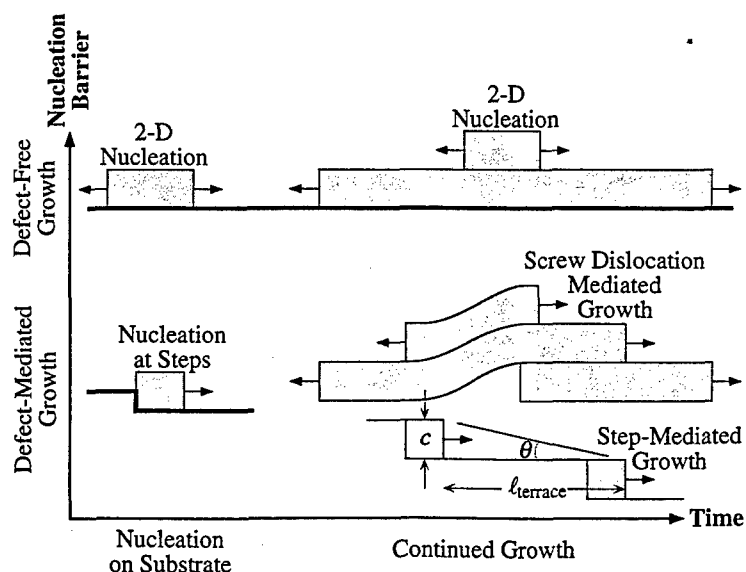


Fig. 5. Schematic representation of the ledge growth process inferred from the growth of *c*-axis oriented  $\text{YBa}_2\text{Cu}_3\text{O}_{7-\delta}$  films. The high nucleation barrier to forming a new layer by two-dimensional nucleation requires a high supersaturation to be reached for such nucleation to take place. The presence of more energetically favorable ledge attachment sites in the vicinity of the depositing species (e.g., emanating from screw dislocations or those present on vicinal substrates) accommodates the depositing species and reduces the supersaturation such that after the initial stages of growth, two-dimensional nucleation is rare.

height of  $\text{YBa}_2\text{Cu}_3\text{O}_{7-\delta}$ , steps develop, separating (001)  $\text{YBa}_2\text{Cu}_3\text{O}_{7-\delta}$  terraces and accommodating the tilt of the substrate. The amount of substrate tilt necessary to achieve growth mainly by this step propagation growth mechanism is presumably that which causes the steps to be spaced sufficiently close together that the depositing species diffuse to and are accommodated by the ledges without reaching a supersaturation on the terrace sufficient for two-dimensional nucleation [38]. Experimentally, a cross-over from screw dislocation mediated growth to step propagation, shown in Fig. 3, has been observed on vicinal  $\text{SrTiO}_3$  (100) surfaces [15]. Under these growth conditions, the transition occurs at about  $\theta_c \approx 2^\circ$ , corresponding to an average terrace spacing of about 30 nm. Growth on less misoriented substrates under the same growth conditions results in a comparable terrace spacing ( $\sim 20$  nm [15]) between turns of the growth spirals, as is to be expected for this analogous ledge-mediated growth process. The influence of substrate orientation on the film growth mechanism explains the apparently disparate results of several studies (in which substrate misorientations were not reported) where nominally identical growth conditions yielded drastically different growth morphologies [7,8].

#### 4. Nucleation of screw dislocations

An important, but so far unresolved issue is the mechanism of nucleation of the screw dislocations. One possibility is that they are simply inherited from the substrate. Although the bulk dislocation densities of the substrates used vary significantly and are in general orders of magnitude lower than the screw dislocation densities observed in *c*-axis oriented  $\text{YBa}_2\text{Cu}_3\text{O}_{7-\delta}$  films [4,15,20], AFM studies have revealed that polishing damage can result in screw dislocation densities at the substrate surface comparable ( $\sim 10^9$   $\text{cm}^{-2}$ ) to what is observed in  $\text{YBa}_2\text{Cu}_3\text{O}_{7-\delta}$  films [39]. Although screw dislocation inheritance from the substrate is likely to occur to some extent, it appears incapable of explaining the rather consistently observed screw dislocation densities ( $10^8$ –

$10^{10}$   $\text{cm}^{-2}$ ) reported also for growth on annealed or cleaved substrates. For example,  $\text{YBa}_2\text{Cu}_3\text{O}_{7-\delta}$  films grown on  $\text{MgO}$  (100) substrates that were annealed at 1100°C for 12 h in oxygen prior to growth [8], conditions under which reordering of the substrate surface occurs [2,40,41], exhibited screw dislocation densities in the  $10^8$ – $10^{10}$   $\text{cm}^{-2}$  range, despite this significant difference in substrate surface preparation. The same is true for  $\text{YBa}_2\text{Cu}_3\text{O}_{7-\delta}$  films grown on cleaved surfaces of  $\text{MgO}$ , which underwent heating to 1250°C, followed by a topotactic solid state reaction with  $\text{TiO}_2$  at 1100°C to form  $\text{Mg}_2\text{TiO}_4$  substrates, a process known to bury any defects which might have been present on the initial  $\text{MgO}$  surface [23,42]. Another proposed mechanism for the introduction of screw dislocations involves the nucleation of dislocation half-loops at the film surface, which then glide to the substrate interface to relieve the lattice mismatch between the  $\text{YBa}_2\text{Cu}_3\text{O}_{7-\delta}$  film and the substrate [3,19,22]. Although the Burgers vector of the proposed dislocation half-loops was not explicitly stated, note that if  $b = c[001]$  (i.e., the ends of the dislocation loop intersecting the film surface are pure screw), the pure edge interfacial segment of this loop does *not* relieve any of the mismatch between the film and the substrate. Choosing a Burgers vector which would relieve interfacial misfit (i.e., one that contains an  $a[100]$  or  $b[010]$  component), results in an even longer Burgers vector; energetically such a dislocation would be favored to dissociate (i.e., into dislocations with  $b = c[001]$  and  $b = a[100]$  or  $b[010]$ ).

Two likely mechanisms for the generation of screw dislocations, first proposed by Fisher et al. [43] and observed in the growth of layered micaeous materials [44–47], are (1) the coalescence of two separate growth fronts having inclined surfaces with respect to each other, and (2) the recombination of two branches of a single growth front offset in layer height. This second mechanism is shown schematically in Fig. 6. The ability of  $\text{YBa}_2\text{Cu}_3\text{O}_{7-\delta}$  to flow over irregularities [1] (creating offsets in layer height) is facilitated by the ledge growth mechanism. The first mechanism of screw dislocation nucleation is likely to occur during the coalescence of nuclei that form

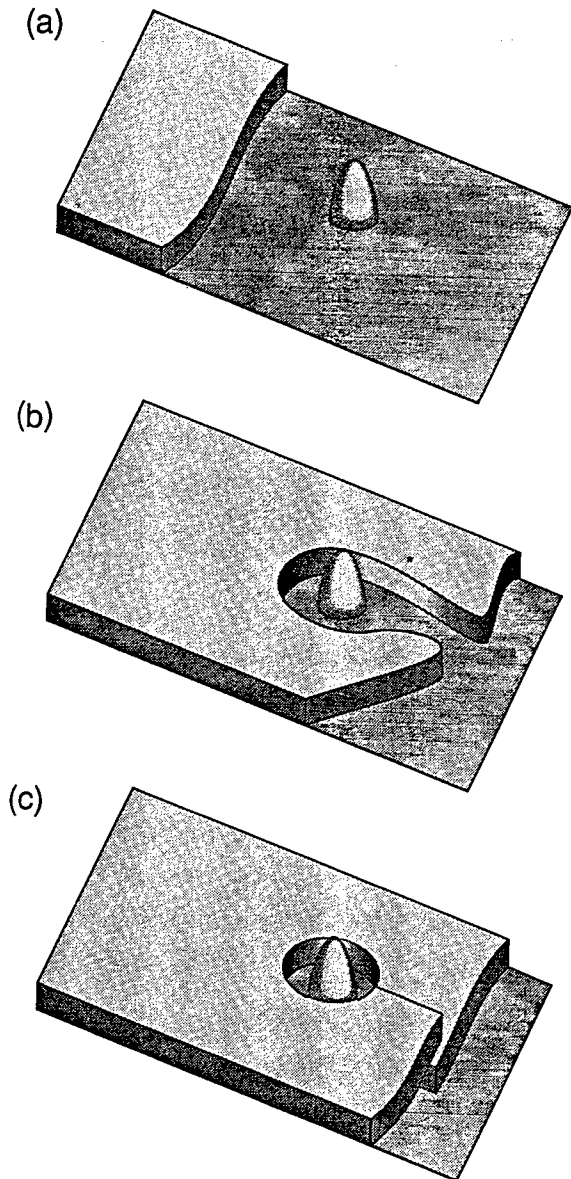


Fig. 6. Schematic illustration of screw dislocation nucleation by the incoherent meeting of growth fronts (from Ref. [14]).

on the substrate surface. Obstacles leading to the second mechanism of screw dislocation nucleation may include impurity particles or even steps on the substrate surface. For example, nanometer-size  $\text{Y}_2\text{O}_3$  precipitates with concentrations over two orders of magnitude higher than the surface screw dislocation density have been identified in  $\text{YBa}_2\text{Cu}_3\text{O}_{7-\delta}$  films [14,48,49]. In-plane

alignment of the coalescing nuclei is necessary for the first nucleation mechanism to occur, and this is made possible by the epitaxial alignment of the individual nuclei to the underlying substrate. TEM, STM, and AFM images of ultra-thin  $\text{YBa}_2\text{Cu}_3\text{O}_{7-\delta}$  films contain features suggestive of these two nucleation mechanisms [6,50,51].

## 5. Other cuprate superconductors

Although the nucleation and growth of other cuprate materials have not been as intensively studied as  $\text{YBa}_2\text{Cu}_3\text{O}_{7-\delta}$ , the presence of screw dislocations and their associated growth spirals have been reported for (001) oriented films of other  $\text{ReBa}_2\text{Cu}_3\text{O}_{7-\delta}$  materials grown by vapor phase deposition methods, where  $\text{Re} = \text{Sm}$  [6,52],  $\text{Dy}$  [30,31], and  $\text{Ho}$  [35]; screw dislocations with  $c$ -axis Burgers vectors have also been reported for bulk  $\text{Bi}_2\text{Sr}_2\text{CaCu}_2\text{O}_8$  [53,54] and  $\text{Pb}_2\text{Sr}_2(\text{Y}, \text{Ca})\text{Cu}_3\text{O}_{8+\delta}$  crystals [55]. Due to the analogous layered nature of all the known cuprate superconductors, it is anticipated that a ledge growth mechanism is applicable to  $c$ -axis oriented films of all layered cuprate superconductors. The minimum substrate tilt necessary for growth to take place by step propagation (the cross-over shown in Fig. 3) depends on surface diffusion, which is a function of the growth conditions and the particular layered cuprate superconductor material.

## 6. Acknowledgements

We gratefully acknowledge informative discussions with A. Catana, N. Chandrasekhar, T. Frey, H.P. Lang, I. Maggio-Aprile, A.F. Marshall, and S.K. Streiffer. The work at Penn State is supported by ONR through contract N00014-93-1-0512.

## 7. References

- [1] See, for example: S.K. Streiffer, B.M. Lairson, C.B. Eom, B.M. Clemens, J.C. Bravman and T.H. Geballe, Phys. Rev. B 43 (1991) 13007.

- [2] M.G. Norton and C.B. Carter, *J. Crystal Growth* 110 (1991) 641.
- [3] S.J. Pennycook, M.F. Chisholm, D.E. Jesson, R. Feenstra, S. Zhu, X.Y. Zheng and D.J. Lowndes, *Physica C* 202 (1992) 1.
- [4] Ch. Gerber, D. Anselmetti, J.G. Bednorz, J. Mannhart and D.G. Schlom, *Nature* 350 (1991) 279.
- [5] M. Hawley, I.D. Raistrick, J.G. Beery and R.J. Houlton, *Science* 251 (1991) 1587.
- [6] J. Burger, I: Aufbau eines Rastertunnelmikroskops für tiefe Temperaturen und äußere Magnetfelder; II: Oberflächenuntersuchungen und Wachstumsstudien an epitaktischen Hochtemperatursupraleiter-Dünnfilmen und -Einkristallen mit dem Rastertunnel- und Kraftmikroskop, PhD Thesis, University of Erlangen, Erlangen, 1992, see in particular, pp. 58–86, 107–133 (in German).
- [7] I. Maggio-Aprile, A.D. Kent, Ph. Niedermann, Ch. Renner, L. Antognazza, L. Miéville, O. Brunner, J.-M. Triscione and Ø. Fischer, *Ultramicroscopy* 42–44 (1992) 728.
- [8] J. Moreland, P. Rice, S.E. Russek, B. Jeanneret, A. Roshko, R.H. Ono and D.A. Rudman, *Appl. Phys. Letters* 59 (1991) 3039.
- [9] I.D. Raistrick, M. Hawley, J.G. Beery, F.H. Garzon and R.J. Houlton, *Appl. Phys. Letters* 59 (1991) 3177.
- [10] M.E. Hawley, I.D. Raistrick, R.J. Houlton, F.H. Garzon and M. Piza, *Ultramicroscopy* 42–44 (1992) 705.
- [11] I. Heyvaert, E. Osquigui, C. Van Haesendonck and Y. Bruynseraeede, *Appl. Phys. Letters* 61 (1992) 111.
- [12] D.G. Schlom, in: International Workshop on Superconductivity Co-Sponsored by ISTEC and MRS: Controlled Growth of Single- and Poly-Crystals of High Temperature Superconductors (ISTEC/MRS, Honolulu, 1992) p. 34.
- [13] J.R. Sheats and P. Merchant, *Appl. Phys. Letters* 62 (1993) 99.
- [14] J. Mannhart, J.G. Bednorz, A. Catana, Ch. Gerber and D.G. Schlom, in: NATO ASI Course on Materials and Crystallographic Aspects of High  $T_c$  Superconductivity (Kluwer, Erice), to be published.
- [15] D.G. Schlom, D. Anselmetti, J.G. Bednorz, R.F. Broom, A. Catana, T. Frey, Ch. Gerber, H.-J. Güntherodt, H.P. Lang and J. Mannhart, *Z. Phys. B* 86 (1992) 163.
- [16] J. Burger, P. Bauer, M. Veith and G. Saemann-Ischenko, *Ultramicroscopy* 42–44 (1992) 721.
- [17] H.P. Lang, T. Frey and H.-J. Güntherodt, *Europhys. Letters* 15 (1991) 667.
- [18] H.U. Krebs, Ch. Krauns, X. Yang and U. Geyer, *Appl. Phys. Letters* 59 (1991) 2180.
- [19] X.-Y. Zheng, D.H. Lowndes, S. Zhu, J.D. Budai and R.J. Warmack, *Phys. Rev. B* (1992) 7584.
- [20] M. McElfresh, T.G. Miller, D.M. Schaefer, R. Reifenberger, R.E. Muenchhausen, M. Hawley, S.R. Folty and X.D. Wu, *J. Appl. Phys.* 71 (1992) 5099.
- [21] H. Olin, G. Brorsson, P. Davidsson, Z.G. Ivanov, P.-Å. Nilsson and T. Claeson, *Ultramicroscopy* 42–44 (1992) 734.
- [22] H.P. Lang, H. Haefke, G. Leemann and H.-J. Güntherodt, *Physica C* 194 (1992) 81.
- [23] H.P. Lang, H. Haefke, R. Sum, H.-J. Güntherodt, L. Berthold and D. Hesse, *Physica C* 202 (1992) 289.
- [24] M. Kawasaki, J.P. Gong, M. Nantoh, T. Hasegawa, K. Kitazawa, M. Kumagai, K. Hirai, K. Horiguchi, M. Yoshimoto and H. Koinuma, *Japan. J. Appl. Phys.*, to be published.
- [25] B. Holzapfel, B. Roas, L. Schultz, P. Bauer and G. Saemann-Ischenko, *Appl. Phys. Letters* 61 (1992) 3178.
- [26] D.H. Lowndes, X.-Y. Zheng, S. Zhu, J.D. Budai and R.J. Warmack, *Appl. Phys. Letters* 61 (1992) 852.
- [27] U. Geyer, Rastertunnelmikroskopie an  $\text{YBa}_2\text{Cu}_3\text{O}_{7-\delta}$ -Schichten: Interpretation der Bilder und der spektroskopischen Ergebnisse, PhD Thesis, University of Göttingen, Göttingen, 1992, see in particular pp. 91–120 (in German).
- [28] F. Baudenbacher, K. Hirata, P. Berberich, H. Kinder, W. Assmann and H.P. Lang, *Physica C* 185–189 (1991) 2177.
- [29] L. Luo, M.E. Hawley, C.J. Maggiore, R.C. Dye, R.E. Muenchhausen, L. Chen, B. Schmidt and A.E. Kaloyerous, *Appl. Phys. Letters* 62 (1993) 485.
- [30] N. Chandrasekhar, V. Agrawal, V.S. Achutharaman and A.M. Goldman, *Appl. Phys. Letters* 60 (1992) 2424.
- [31] H.S. Wang, D. Eissler, W. Dietsche, A. Fischer and K. Ploog, *J. Crystal Growth* 126 (1993) 565.
- [32] J. Mannhart, D. Anselmetti, J.G. Bednorz, A. Catana, Ch. Gerber, K.A. Müller and D.G. Schlom, *Z. Phys. B* 86 (1992) 177.
- [33] N. Chandrasekhar for the growth of  $\text{YBa}_2\text{Cu}_3\text{O}_{7-\delta}$  by MBE, private communication.
- [34] T. Frey for the growth of  $\text{YBa}_2\text{Cu}_3\text{O}_{7-\delta}$  by PLD, private communication.
- [35] H.P. Lang, T. Frey, R. Sum and H.-J. Güntherodt, in: High  $T_c$  Superconductor Thin Films, Ed. L. Correra (Elsevier, Amsterdam, 1992) p. 789.
- [36] M.A. Harmer, C.R. Fincher and B.A. Parkinson, *J. Appl. Phys.* 70 (1991) 2760.
- [37] H. Karl and B. Stritzker, *Phys. Rev. Letters* 69 (1992) 2939.
- [38] T. Nishinaga, T. Shitara, K. Mochizuki and K.I. Cho, *J. Crystal Growth* 99 (1990) 482.
- [39] D. Eissler, H.S. Wang and W. Dietsche, *Appl. Phys. Letters* 62 (1993) 1292.
- [40] B.H. Moeckly, S.E. Russek, D.K. Lathrop, R.A. Buhrman, J. Li and J.W. Mayer, *Appl. Phys. Letters* 57 (1990) 1687.
- [41] R.G. Humphreys, J.S. Satchell, N.G. Chew, J.A. Edwards, S.W. Goodyear, M.N. Keene and S.J. Hedges, *Mater. Sci. Eng. B* 10 (1991) 293.
- [42] D. Hesse, L. Berthold, H. Haefke, H.P. Lang, R. Sum and H.-J. Güntherodt, *Physica C* 202 (1992) 277.
- [43] J.C. Fisher, R.L. Fullman and G.W. Sears, *Acta Met.* 2 (1954) 344.
- [44] G.G. Lemlein and E.D. Dukova, *Soviet Phys. Cryst.* 1 (1956) 269.
- [45] M.I. Kozlovskii, *Soviet Phys. Cryst.* 3 (1958) 206.
- [46] M.I. Kozlovskii, *Soviet Phys. Cryst.* 3 (1958) 236.

- [47] A. Baronnet, J. Crystal Growth 19 (1973) 193.
- [48] A. Catana, R.F. Broom, J.G. Bednorz, J. Mannhart and D.G. Schlom, Appl. Phys. Letters 60 (1992) 1016.
- [49] A. Catana, J.G. Bednorz, Ch. Gerber, J. Mannhart and D.G. Schlom, Appl. Phys. Letters 63 (1993) 553.
- [50] S.K. Streiffer, in: Proc. 49th Annu. Meeting of the Electron Microscopy Society of America, Ed. G.W. Bailey (EMSA, San Francisco, 1991) p. 1070.
- [51] I. Maggio-Aprile, private communication.
- [52] W. Schindler, P. van Hasselt, P. Tontsch, J. Markl, J. Burger, P. Bauer and G. Saemann-Ischenko, J. Crystal Growth 127 (1993) 1088.
- [53] J.M. Liang, L. Chang, S.F. Tang, Y.C. Chen, P.T. Wu and L.J. Chen, Appl. Phys. Letters 53 (1988) 913.
- [54] A.V. Narlikar, P.K. Dutta, S.B. Samanta, O.N. Srivastava, P. Ramasamy, S.C. Sabarwal, M.K. Gupta and B.D. Padalia, J. Crystal Growth 116 (1992) 37.
- [55] P.K. Dutta, S.B. Samanta, A.V. Narlikar, C. Chen, J.W. Hodby and B.M. Wanklyn, Phil. Mag. A 66 (1992) 507.

# 1994 PHYSICS and MATERIALS SCIENCE JOURNALS

## Applied Surface Science

Volumes 72-81 in 40 issues. Price: US \$ 2114.00 / Dfl. 3910.00

## Astroparticle Physics

Volume 2 in 4 issues. Price: US \$ 182.00 / Dfl. 336.00

## Computational Materials Science

Volume 2 in 4 issues. Price: US \$ 211.00 / Dfl. 391.00

## Computer Physics Communications

Volumes 79-85 in 21 issues. Price: US \$ 2236.00 / Dfl. 4137.00

## International Journal of Applied

## Electromagnetics In Materials

Volume 5 in 4 issues. Price: US \$ 203.00 / Dfl. 376.00

## Journal of Crystal Growth

Volumes 135-145 in 44 issues. Price: US \$ 4822.00 / Dfl. 8921.00

## Journal of Geometry and Physics

Volumes 13 and 14 in 8 issues. Price: US \$ 358.00 / Dfl. 662.00

## Journal of Luminescence

Volumes 59-62 in 24 issues. Price: US \$ 1083.00 / Dfl. 2004.00

## Journal of Magnetism and Magnetic Materials

Volumes 126-137 in 36 issues. Price: US \$ 3347.00 / Dfl. 6192.00

## Journal of Non-Crystalline Solids

Volumes 162-176 in 45 issues. Price: US \$ 3535.00 / Dfl. 6540.00

## Journal of Nuclear Materials

Volumes 206-216 in 33 issues. Price: US \$ 3098.00 / Dfl. 5731.00

## Materials Letters

Volumes 19-22 in 24 issues. Price: US \$ 899.00 / Dfl. 1664.00

## Nuclear Instruments and Methods In Physics

### Research - Section A

### Accelerators, Spectrometers, Detectors & Associated Equipment

Volumes 337-351 in 45 issues. Price: US \$ 5441.00 / Dfl. 10,065.00

## Nuclear Instruments and Methods In Physics

### Research - Section B

### Beam Interactions with Materials and Atoms

Volumes 83-94 in 48 issues. Price: US \$ 4352.00 / Dfl. 8052.00

*Reduced combined 1994 subscription price* to Nuclear Instruments and Methods - A and B: US \$ 9063.00 / Dfl. 16,767.00

## Nuclear Physics A

Volumes 566-580 in 60 issues. Price: US \$ 4792.00 / Dfl. 8865.00

## Nuclear Physics B

Volumes 409-432 in 72 issues. Price: US \$ 7537.00 / Dfl. 13,944.00

## Nuclear Physics B - Proceedings Supplements

Volumes 34-38 in 15 issues. Price: US \$ 881.00 / Dfl. 1630.00

*Reduced combined 1994 subscription price* to Nuclear Physics A + Nuclear Physics B + NPB-Proceedings

Supplements: US \$ 11,202.00 / Dfl. 20,724.00

## Optical Materials

Volume 3 in 4 issues. Price: US \$ 206.00 / Dfl. 381.00

## Optics Communications

Volumes 103-111 in 54 issues. Price: US \$ 2121.00 / Dfl. 3924.00

## Physica A - Statistical and Theoretical Physics

Volumes 201-211 in 44 issues. Price: US \$ 2503.00 / Dfl. 4631.00\*

## Physica B - Condensed Matter Physics

Volumes 192-202 in 44 issues. Price: US \$ 2503.00 / Dfl. 4631.00\*

## Physica C - Superconductivity

Volumes 219-236 in 72 issues. Price: US \$ 4096.00 / Dfl. 7578.00\*

## Physica D - Nonlinear Phenomena

Volumes 70-78 in 36 issues. Price: US \$ 2048.00 / Dfl. 3789.00\*

*\*Reduced rates are available for combined subscriptions to Physica; please contact the publisher for details.*

## Physics Letters A

Volumes 185-197 in 78 issues. Price: US \$ 2537.00 / Dfl. 4693.00

## Physics Letters B

Volumes 317-340 in 96 issues. Price: US \$ 4683.00 / Dfl. 8664.00

## Physics Reports

Volumes 240-251 in 72 issues. Price: US \$ 2342.00 / Dfl. 4332.00

*Reduced combined 1994 subscription price* to Physics Letters A, Physics Letters B + Physics Reports: US \$ 8502.00 / Dfl. 15,729.00

## Solid State Ionics

Volumes 68-76 in 36 issues. Price: US \$ 1805.00 / Dfl. 3339.00

## Surface Science

(including Surface Science Letters)

Volumes 296-318 in 69 issues. Price: US \$ 6104.00 / Dfl. 11,293.00

## Surface Science Reports

Volumes 18-20 in 24 issues. Price: US \$ 618.00 / Dfl. 1143.00

*Reduced combined 1994 subscription price* to Surface Science (including Surface Science Letters), Applied Surface Science and Surface Science Reports: US \$ 8192.00 / Dfl. 15,156.00

## Ultramicroscopy

Volumes 52-56 in 20 issues. Price: US \$ 1151.00 / Dfl. 2130.00

Dutch Guilder price(s) quoted applies worldwide, except in the Americas (North, Central and South America). US Dollar price(s) quoted applies in the Americas only. Journals are sent by Surface Mail to all countries except to the following where Air Delivery via SAL mail is ensured at no extra cost to the subscriber: Argentina, Australia/New Zealand, Brazil, Hong Kong, India, Israel, Japan, Malaysia, Mexico, Pakistan, P.R. China, Singapore, S. Africa, S. Korea, Taiwan, Thailand, USA & Canada. Customers in the European Community should add the appropriate VAT rate applicable in their country to the price(s).



# ELSEVIER SCIENCE B.V.

P.O. Box 103, 1000 AC Amsterdam, The Netherlands

Elsevier Science Inc., Journal Information Center, PO Box 882,  
Madison Square Station, New York, NY 10159, U.S.A.

## Evidence for surface melting during the growth of high $T_c$ thin films

N. Chandrasekhar<sup>a</sup> and Darrell G. Schlom<sup>b</sup>

<sup>a</sup>Physics Department, Indian Institute of Science,  
Bangalore 560 012, INDIA.

<sup>b</sup>Department of Materials Science and Engineering,  
Pennsylvania State University, University Park, PA 16802, USA.

We present reflection high energy electron diffraction (RHEED) spot profile analyses, which show anomalous broadening over very short time scales. Our data can only be interpreted in terms of surface melting. The conclusions are consistent with the thermodynamic phase diagrams and with the vapor-liquid-solid (VLS) mechanism of crystal growth.

### 1. Introduction

Lower oxygen pressures allow the formation of YBCO films at lower temperatures, thereby minimizing interdiffusion and reaction with the substrate and improving film morphology. The quaternary phase relations in YBCO in reduced oxygen pressures has been determined [1].

### 2. EXPERIMENTAL

All RHEED data during the growth of YBCO thin films by molecular beam epitaxy (MBE) were obtained at 10 kV and a grazing angle of 28 mrad ( $1.5^\circ$ ). The RHEED patterns were photographed with high sensitivity film (1000 ASA) and the RHEED intensity oscillations of selected spots monitored.

We study the (11) spot. The intensity oscillations of the specular spot have been published [2, 3]. A computer controlled densitometer was used to analyse the spot profiles[4].

### 3. RESULTS

Figure 1 shows the oscillations in the intensity of the (11) diffracted spot as a function of time. We draw attention to the precipitous drop in the intensity immediately following the first maximum, caused by a surface process with a very small time constant. Fig. 2 is a plot of the intensity profile across the (11) diffracted spot which probes extent of ordering in the plane of the surface. There are two sets of data in this figure,

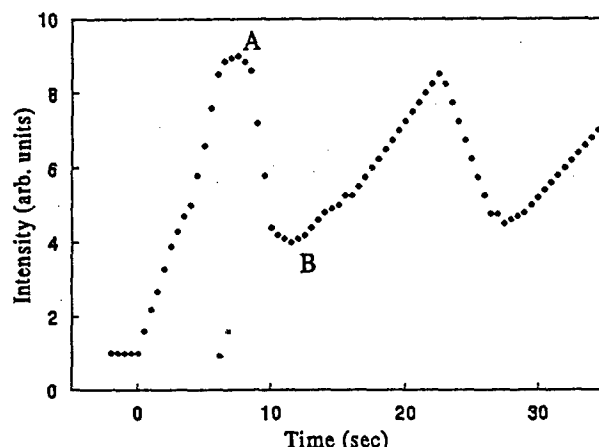


Figure 1. Intensity oscillations of (11) spot.

with the closed circles indicating the profile at the point A (the point of the first maximum in the RHEED intensity oscillations of Fig. 1) and the triangles indicating the intensity profile at the point B (the first minimum immediately following point A). The spot profile is substantially broader at B than at A, and accompanied by a concomitant drop in the intensity. There is substantial Lorentzian broadening. One would ideally expect disorder to induce Gaussian broadening. The increase of the FWHM by a factor of 5 is hard to explain in terms of the birth-death model [5].

Activation energies may be deduced from RHEED intensity oscillation recovery profiles. We obtain a value of 0.8 eV, which is consis-

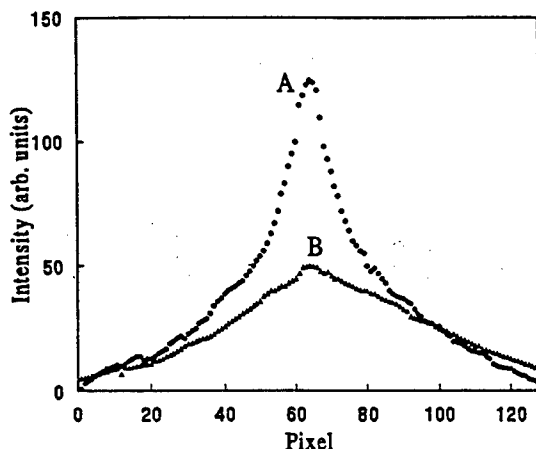


Figure 2. (11) spot profile (see text).

tent with that reported in the literature by various groups. All the cation fluxes are turned off, with only the oxygen being on. Hence, if some species is being incorporated in the film it can be nothing but oxygen. We also note here that this activation energy is independent of the process used, i.e. MBE, sputtering and laser ablation all yield the same number, a remarkable independence of the process energy and fluence. Further, surface diffusion coefficients are in the range of  $10^{-12} \text{ cm}^2 \text{s}^{-1}$ . These values are comparable to those for oxygen.

#### 4. DISCUSSION

Wagner *et al.* [7] have proposed a vapor-liquid-solid (VLS) mechanism of crystal growth. In this mechanism, a liquid solution coexists with the crystalline material to be grown from the vapor. Crystal growth occurs by precipitation from the supersaturated liquid at the liquid-solid interface. A crystalline defect such as a screw dislocation is not essential for the VLS mechanism to operate. Deposition may be directly on a solid substrate in a vapor-solid system. An example is the epitaxial deposition of thin films [8].

Since the oxygen flux is always on during any measurement of RHEED relaxation profiles, it is not surprising that the activation energy measured is of the same order as that of oxygen diffusion and is independent of the process. This also explains the coincidence of the diffusion co-

efficient. Since the slowest process in this case is the diffusion of oxygen, it is reasonable to conclude that there is a lower activation energy for all the cationic species present on the surface along with some oxygen, which is a must for charge neutrality of the ionic compounds considered in this work.

Despite the problems associated with the measurements of  $p$  and  $T$  in vacuum, it is reasonable to assert that the  $p$  is between 0.1 to 0.3 atmospheres and that  $T$  is known to accuracies of at least 10 to 20°. Comparing with the published thermodynamic data, the substrate temperatures that are encountered in thin film growth are consistently higher than those for bulk material. This suggests that there may be a liquid phase present during the growth of thin films of these materials.

#### 5. CONCLUSIONS

In summary, we have presented data that confirm the existence of a liquid phase on the surface during the growth of YBCO thin films. These observations seem to indicate that the operative mechanism for the growth of high  $T_c$  thin films is the VLS mechanism of growth [7]. These observations mandate extreme caution in interpreting layer-by-layer growth in these materials.

#### REFERENCES

1. R. Beyers and B. T. Ahn, Ann. Rev. Mat. Sci., (1991).
2. H. Karl and B. Stritzker, Phys. Rev. Lett., 69 (1992) 2939.
3. N. Chandrasekhar *et al.* Phys. Rev. B 46 (1992) 8565.
4. J. Venables *et al.*, Phys. Rev. B39 (1989) 415.
5. C. S. Lent and P. I. Cohen, Surf. Sci., 139 (1984) 121.
6. L. M. Peng and M. J. Whelan, Proc. R. Soc. Lond. A435 (1991) 269.
7. R. S. Wagner and W. C. Ellis, Trans. Met. Soc. AIME, 233 (1965) 1053.
8. H. C. Theurer, J. Electrochem. Soc., 108 (1961) 649.

# Thermodynamic stability of binary oxides in contact with silicon

K. J. Hubbard<sup>a)</sup> and D. G. Schlom

Department of Materials Science and Engineering, The Pennsylvania State University,  
University Park, Pennsylvania 16802-5005.

(Received 8 June 1995; accepted 26 April 1996)

Using tabulated thermodynamic data, a comprehensive investigation of the thermodynamic stability of binary oxides in contact with silicon at 1000 K was conducted. Reactions between silicon and each binary oxide at 1000 K, including those involving ternary phases, were considered. Sufficient data exist to conclude that all binary oxides except the following are thermodynamically unstable in contact with silicon at 1000 K: Li<sub>2</sub>O, most of the alkaline earth oxides (BeO, MgO, CaO, and SrO), the column IIIB oxides (Sc<sub>2</sub>O<sub>3</sub>, Y<sub>2</sub>O<sub>3</sub>, and *Re*<sub>2</sub>O<sub>3</sub>, where *Re* is a rare earth), ThO<sub>2</sub>, UO<sub>2</sub>, ZrO<sub>2</sub>, HfO<sub>2</sub>, and Al<sub>2</sub>O<sub>3</sub>. Of these remaining oxides, sufficient data exist to conclude that BeO, MgO, and ZrO<sub>2</sub> are thermodynamically stable in contact with silicon at 1000 K. Our results are consistent with reported investigations of silicon/binary oxide interfaces and identify candidate materials for future investigations.

## I. INTRODUCTION

The fabrication of oxide thin-film microstructures on silicon substrates offers tremendous opportunities for the future of microelectronic devices. Such microstructures would allow oxide layers to be fully integrated with silicon circuitry and the broad variety of optical, electronic, and magnetic properties of oxides to be utilized on-chip. If high dielectric constant ( $\epsilon_r$ ) oxides, ferroelectric oxides, high transition temperature ( $T_c$ ) superconducting oxides, or magnetic oxides could be combined with existing semiconductor technology, the materials properties available for use in microelectronics would be drastically enhanced, allowing improved functionality and performance to be realized. Unfortunately, direct growth of these oxides on silicon is frequently accompanied by extensive interdiffusion or chemical reactions that degrade the properties of the oxide, the underlying silicon, or both.<sup>1-8</sup> Consequently, the focus of a great deal of materials research has been devoted to overcoming these obstacles through the identification of compatible buffer layers for use between silicon and the desired oxide layers.<sup>7-9</sup>

Several factors must be considered in selecting materials for use as buffer layers between silicon and a particular oxide: chemical reactions, interdiffusion, thermal expansion match, crystal structure, and lattice match are some of the most important.<sup>8-10</sup> Extensive chemical reaction between the buffer layer material and silicon or between the buffer layer material and the overlying oxide can result in the formation of interfacial phases that often result in a loss of epitaxy. Interdiffusion

among silicon, the buffer layer, and the overlying oxide can severely degrade the desired properties of these materials. For example, impurities diffusing into an oxide superconductor film can lower the  $T_c$ , reduce the temperature coefficient of resistivity, and increase the normal-state resistivity.<sup>11</sup> Impurities diffusing into the silicon substrate, especially those that produce deep levels such as the yttrium, barium, and copper constituents of the YBa<sub>2</sub>Cu<sub>3</sub>O<sub>7- $\delta$</sub>  high  $T_c$  superconductor, dramatically alter carrier concentration profiles and lower carrier lifetimes in the silicon.<sup>7,12</sup> Thermal expansion mismatch must be minimized to prevent cracking due to thermally induced strains upon cooling after growth, especially if these strains lead to a state of tension in the overgrown oxide films, which is typically the case due to the low thermal expansion coefficient of silicon. In addition, the crystal structure and lattice match between each of the layers must be considered when epitaxy is desired. Ideally, a buffer layer for the growth of an oxide on silicon should provide a nonreactive diffusion barrier and a stable nucleation template for the subsequent epitaxial growth of the overlying desired oxide.

This paper addresses the issue of chemical reaction between silicon and binary oxide buffer layers. Specifically the thermodynamic stability of binary oxides in contact with silicon for potential use as epitaxial buffer layers between silicon and oxide thin films was examined at 1000 K, since this is a typical deposition temperature for the epitaxial growth of oxides. Thermodynamic instability is a necessary, but insufficient criterion to conclude that an interface *will* react. It indicates the presence of a driving force for reaction, but it is possible for a kinetic barrier to limit the extent of reaction or even prevent a thermodynamically unstable interface from reacting at all. Of course, at the relatively high

<sup>a)</sup>Present address: EPI, Chorus Corporation, St. Paul, Minnesota 55110.

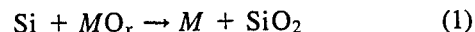
temperature considered, 1000 K, such kinetic barriers must be significant to prevent interaction. Reactions involving gaseous species were not considered as it was desired to test the stability of the interface between two solids (silicon and the binary oxide) and there is thus no free volume in which a gas can exist. Most of the binary oxides considered in this comprehensive study were determined to be thermodynamically unstable in contact with silicon and consequently were eliminated. For many of the remaining materials the calculations were unable to be completed due to the lack of thermodynamic data for silicides, ternary phases, or both. These materials could neither be eliminated nor determined to be stable. Existing experimental results indicate that many of these remaining materials are stable in contact with silicon; those that have not been reported warrant experimental investigation. Finally, sufficient data exist to conclude that BeO, MgO, and ZrO<sub>2</sub> are thermodynamically compatible with silicon.

## II. METHOD

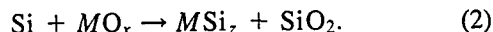
In order to narrow down the list of binary oxides that could be stable in contact with silicon at 1000 K, possible reactions between each binary oxide and silicon, for which thermodynamic data existed, were considered. Any reaction leading to a lowering of the Gibbs free energy of the system ( $\Delta G < 0$ ) allowed the binary oxide to be eliminated from further consideration. This is not to say that the reaction found was the most favorable of all possible reactions, but the identification of any reaction products more stable than silicon in contact with the binary oxide implies that the latter interface is thermodynamically unstable. Identification of the most stable reaction products was not our goal, and in many cases cannot be accomplished due to insufficient thermodynamic data. The method employed is the same as that used by Beyers<sup>13-16</sup> to determine the *M-Si-O* phase diagrams for *M* = Ti, Zr, Ta, Mo, and W. Here it is applied to all elements of the periodic table in order to identify prudent choices of silicon-compatible binary oxides for subsequent experimental studies.<sup>17</sup>

Although there are many possible reactions, several key reactions can be identified by considering the phase diagram of a *M-Si-O* system. This phase diagram contains silicon, the binary oxide under consideration, *MO<sub>x</sub>*, and all the possible products of a reaction between silicon and the binary oxide. In general this phase diagram will contain ternary *M-Si-O* phases, but due to the lack of thermodynamic data for ternary phases, we first consider the phase diagram of a *M-Si-O* system free of ternary phases and containing only one binary oxide (*MO<sub>x</sub>*) of the element *M*, as shown in Fig. 1.<sup>15,16</sup> Ti-Si-O is an example of a system free of ternary phases. For the binary oxide to be stable in contact with silicon, a tie-line must exist between *MO<sub>x</sub>* and silicon. The existence of such a stable

tie-line constrains the rest of the phase diagram, since the crossing of tie-lines is forbidden (a consequence of the Gibbs phase rule as described in the Appendix). There are only three possible types of *M-Si-O* phase diagrams. These are shown in Fig. 1 and referred to as "metal oxide dominant," "SiO<sub>2</sub> dominant," and "no phase dominant."<sup>18</sup> following the work of Beyers.<sup>15,16</sup> In this study we are interested only in the metal oxide dominant-type, since it is the only type having a tie-line between *MO<sub>x</sub>* and silicon. Thermodynamic data may be used to determine which of these three types of phase diagrams a particular *M-Si-O* system belongs to. A reaction flowchart allowing this determination is given in Fig. 2. For the purposes of the present study, any system that fails ( $\Delta G < 0$ ) a reaction along the path to the metal oxide dominant-type system can be eliminated from further consideration. The (unbalanced) reactions along this path are

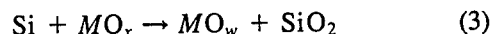


and

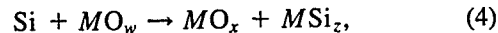


if an element has multiple silicides, the most silicon-rich silicide (*MSi<sub>z</sub>*) should be used in Eq. (2).<sup>19</sup> Any system that fails Eq. (1) can be eliminated from further consideration. Any system that passes ( $\Delta G > 0$ ) Eq. (1) but fails Eq. (2) can also be eliminated. This conclusion is true even if the *M-Si-O* system contains ternary phases or multiple binary oxides *MO<sub>x</sub>*, because failing Eq. (1) or (2) implies that silicon is thermodynamically unstable in contact with the binary oxide.

If the *M-Si-O* system contains more than one *MO<sub>x</sub>* binary oxide, then after passing ( $\Delta G > 0$ ) Eqs. (1) and (2), reactions involving *MO<sub>x</sub>* binary oxides on both sides of the equation must also be tested. The *M-Si-O* systems that passed Eqs. (1) and (2) had at most two *MO<sub>x</sub>* binary oxides. For systems containing two binary oxides the additional (unbalanced) reactions to be tested are



and



where *MO<sub>x</sub>* and *MO<sub>w</sub>* are the two binary oxides (*MO<sub>x</sub>* being the more oxygen-rich), at least one of which has passed Eqs. (1) and (2). Equation (3) needs to be tested only when *MO<sub>x</sub>* has passed Eqs. (1) and (2). Similarly, Eq. (4) needs to be tested only when *MO<sub>w</sub>* has passed Eqs. (1) and (2). If an element has multiple silicides, the most silicon-rich silicide (*MSi<sub>z</sub>*) should be used in Eq. (4).<sup>20</sup> If the *M-Si-O* system fails ( $\Delta G < 0$ ) Eq. (3), then a stable tie-line does not exist between silicon and *MO<sub>x</sub>* and it may be eliminated from further consideration. Similarly, if it fails Eq. (4), then a stable tie-line does not

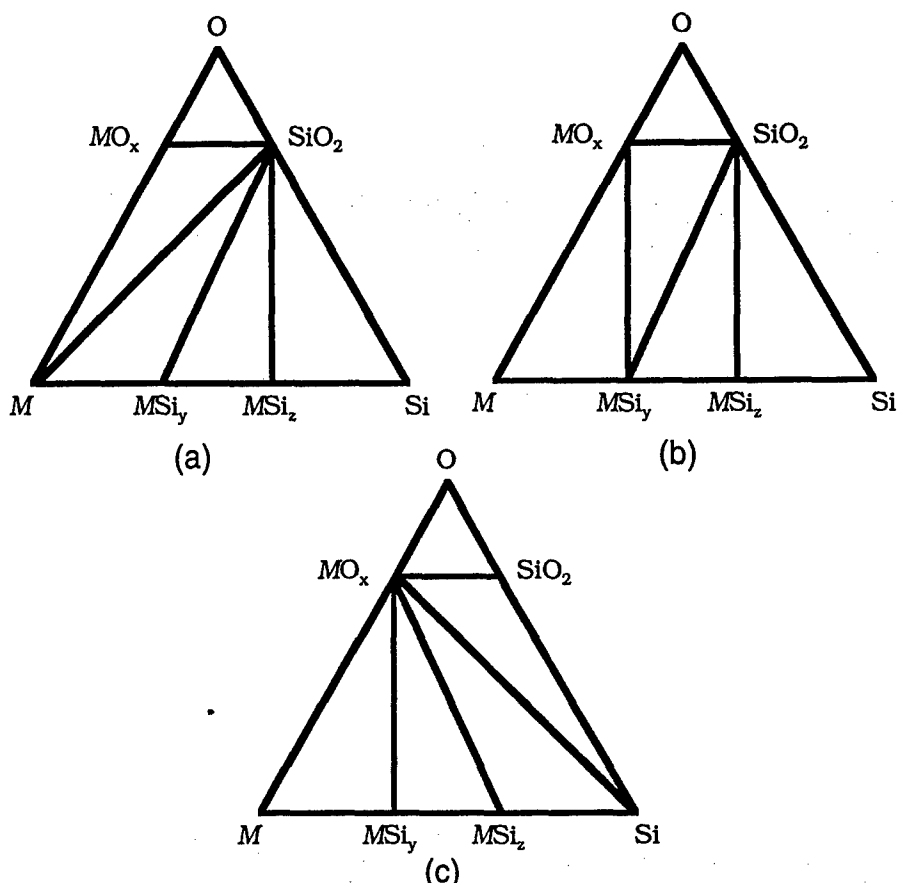


FIG. 1. The three types of  $M\text{-Si}\text{-O}$  phase diagrams at fixed temperature and pressure: (a)  $\text{SiO}_2$  dominant, (b) no phase dominant, and (c) metal oxide dominant (after Ref. 13).

exist between silicon and  $MO_x$  and it may be eliminated. A flowchart showing these reactions and the resulting phase diagrams is given in Fig. 3.<sup>21</sup>

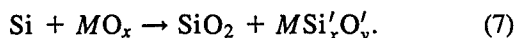
If the  $M\text{-Si}\text{-O}$  system contains ternary phases, then after passing ( $\Delta G > 0$ ) Eqs. (1) and (2) [and Eqs. (3) or (4) if the system contains more than one  $MO_x$  binary oxide], further reactions involving ternary products must be tested. In general, the relevant reaction to test is that at the crossing of two potential tie-lines. For the case at hand, the relevant crossing is between the  $\text{Si}-MO_x$  tie-line with one dictated by the location of the ternary phase(s). If a ternary phase ( $MSi_xO_y$ ) which exists at 1000 K lies on the tie-line between silicon and the binary oxide ( $MO_x$ ), silicon will not be thermodynamically stable in contact with  $MO_x$  and the system can be eliminated from further consideration. No such examples were found. If all of the ternary phases existing at 1000 K are on only one side or the other of the  $\text{Si}-MO_x$  tie-line, the relevant reactions depend on which side they occur, as shown in Fig. 4. If all of the ternary phases lie above the  $\text{Si}-MO_x$  tie-line [as shown in Fig. 4(a)], the relevant (unbalanced) reactions are



and



whereas if all of the ternary phases lie below the  $\text{Si}-MO_x$  tie-line [as shown in Fig. 4(b)], the relevant (unbalanced) reaction is



Equations (5) and (6) need to be evaluated only for those ternary oxides ( $MSi_xO_y$ ) that are positioned such that the triangle  $MSi_xO_y\text{-}MO_x\text{-Si}$  does not contain any other ternary oxides.<sup>22</sup> Those ternary oxides satisfying this condition are shown as solid dots in Fig. 4(a). Equation (5) needs to be evaluated only for the most silicon-rich silicide ( $MSi_z$ ).<sup>23</sup> Only if Eqs. (5) and (6) are passed ( $\Delta G > 0$ ) by all such ternary oxides, can the  $\text{Si}-MO_x$  tie-line be concluded to be thermodynamically stable. Similarly, Eq. (7) needs to be evaluated only for those ternary oxides ( $MSi'_xO'_y$ ) that are positioned such that the triangle  $MSi'_xO'_y\text{-}MO_x\text{-Si}$  does not contain any other ternary oxides.<sup>22</sup> The ternary oxides satisfying this condition are shown as solid dots in Fig. 4(b). Only if Eq. (7) is passed by all such ternary oxides, can the  $\text{Si}-MO_x$  tie-line be concluded to be thermodynamically

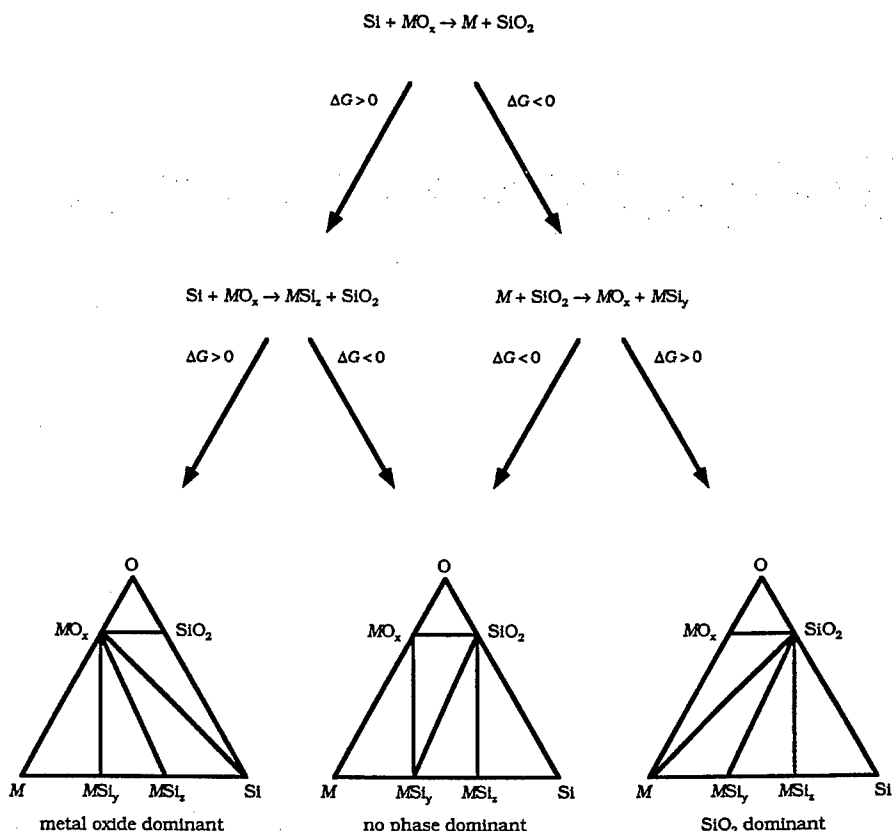
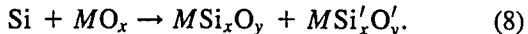


FIG. 2. A reaction flowchart showing what two reactions (unbalanced as shown) can be used to determine which of the three types of phase diagrams a particular  $M\text{-Si-O}$  system belongs to if the system contains no ternary phases ( $\text{MSi}_x\text{O}_y$ ) and only one  $M_x$  phase.

stable. For all but one of the  $M\text{-Si-O}$  systems that passed Eqs. (1) and (2), all of the ternary phases lay above the  $\text{Si-MO}_x$  tie-line.

If the  $M\text{-Si-O}$  system contains ternary phases on both sides of the  $\text{Si-MO}_x$  tie-line, then in addition to Eqs. (5), (6), and (7), reactions with ternary products lying above ( $\text{MSi}_x\text{O}_y$ ) and below ( $\text{MSi}'_x\text{O}_y$ ) the  $\text{Si-MO}_x$  tie-line must also be tested:



The only system of this type that passed ( $\Delta G > 0$ ) Eqs. (1) and (2) was the  $\text{Si-Sc-O}$  system.

The Gibbs free energy change at 1000 K ( $\Delta G_{1000}^\circ$ ) was calculated for each of the above reactions using the available free energies of formation at 1000 K ( $G_{f,1000}^\circ$ ) of each element ( $M$ ), binary oxide ( $\text{MO}_x$ ), silicide ( $\text{MSi}_z$ ), ternary phases ( $\text{MSi}_x\text{O}_y$ ), and of silicon and  $\text{SiO}_2$  (quartz). The values of  $G_{f,1000}^\circ$  were taken from Refs. 24, 25, and 26. All the data for a single calculation were taken from either Refs. 24 and 25 or from Ref. 26 to maintain consistency. Note that there are slight discrepancies in the tabulated values in these different sources for the same material. No single calculation was made with data from both sources. For the calculations involving  $\text{Sc}_2\text{O}_3$ ,  $\text{La}_2\text{O}_3$ ,  $\text{Nd}_2\text{O}_3$ , and  $\text{Gd}_2\text{O}_3$ , Refs. 24 and 25 were used for the values of  $G_{f,1000}^\circ$  for silicon,  $\text{MO}_x$ ,  $\text{MSi}_x\text{O}_y$ , and  $\text{SiO}_2$ , while

Ref. 27 was used in determining the values of  $G_{f,1000}^\circ$  for the corresponding silicides.

For each reaction (appropriately balanced for the particular binary oxide,  $\text{MO}_x$ , with coefficients  $\nu$ )  $\Delta G_{f,1000}^\circ$  for the complete reaction was determined by subtracting the sum of the free energies of formation of the reactants from the sum of the free energies of formation of the products<sup>28</sup>:

$$\Delta G_{1000}^\circ = \sum_{\text{Products}} \nu G_{f,1000}^\circ - \sum_{\text{Reactants}} \nu G_{f,1000}^\circ. \quad (9)$$

The magnitude of  $\Delta G_{f,1000}^\circ$  indicates the direction of the reaction. A negative value for  $\Delta G_{f,1000}^\circ$  indicates that it is thermodynamically favorable for the reaction to proceed to its products. Thus, when it was determined that  $\Delta G_{f,1000}^\circ$  for one of the above reactions was negative, indicating that silicon and  $\text{MO}_x$  are not thermodynamically stable in contact with each other, the respective binary oxide was eliminated from further consideration.

In cases where  $\Delta G_{f,1000}^\circ$  is close to zero, it is important to consider the accuracy of the thermodynamic data. When the magnitude of  $\Delta G_{f,1000}^\circ$  is less than this accuracy, no conclusion of thermodynamic stability or instability can be made. Unfortunately, the accuracy of thermodynamic data is frequently not given. References 24 and 25 do give an indication of the accuracy of their

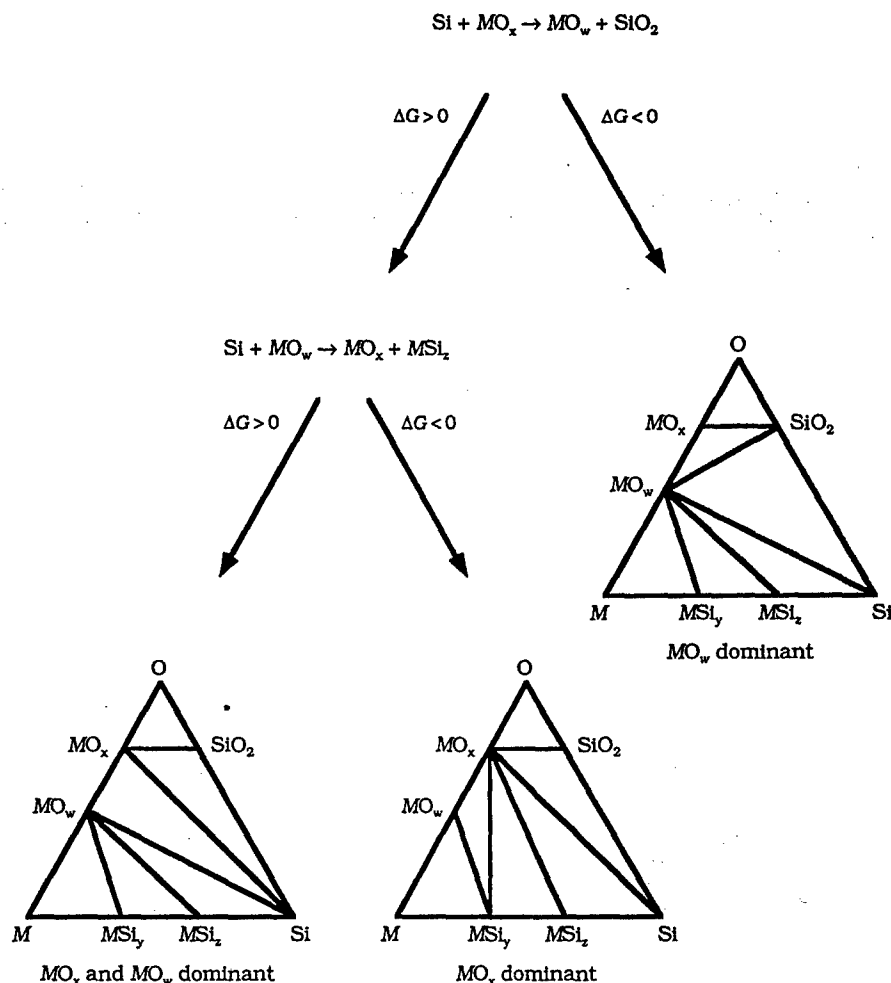


FIG. 3. A reaction flowchart showing what two reactions (unbalanced as shown) can be used to determine which of the three types of phase diagrams a particular  $M-\text{Si}-\text{O}$  system belongs to if the system is free of ternary phases ( $\text{MSi}_z\text{O}_y$ ) and contains two metal oxide phases,  $\text{MO}_w$  and  $\text{MO}_x$ , both of which have passed Eqs. (1) and (2).

tabulated thermodynamic data, and for this reason these references were used whenever possible. With the exception of  $\text{TiSi}_2$  and  $\text{ZrSi}_2$ , all of the thermodynamic data from Refs. 24 and 25 used in the calculations given have a stated accuracy of "C" or better, for those cases where the accuracy was given. This means that the accuracy of the  $G_f^\circ$ ,<sub>1000</sub> values themselves are better than  $\pm 2.3$  kcal/mol at  $T = 1000$  K,<sup>24,25</sup> and implies that the accuracy of the  $G_f^\circ$ ,<sub>1000</sub> values for the reactions evaluated using these data is better than about  $\pm 5$  kcal/mol. The magnitudes of nearly all the reactions calculated are well above this approximate accuracy. For those reactions evaluated using Refs. 24 and 25 where the magnitude of  $\Delta G_f^\circ$ ,<sub>1000</sub> is less than 5 kcal/mol, the approximate accuracy of the calculated  $\Delta G_f^\circ$ ,<sub>1000</sub> value is given adjacent to it, based on the stated accuracy of the reference data.

The reactions listed above were used (in the order given) to determine  $\Delta G_f^\circ$ ,<sub>1000</sub> for each of the binary oxides under consideration in this study (see Table II). Equation (1) was used to determine  $\Delta G_f^\circ$ ,<sub>1000</sub> for the bi-

nary oxides listed in Table II. Those with a negative value for  $\Delta G_f^\circ$ ,<sub>1000</sub> were eliminated from further consideration. The remaining materials (see Table III) were tested using Eq. (2). Note that for many of these remaining binary oxides Eq. (2) could not be completed due to the lack of data for the relevant  $\text{MSi}_z$  phase. Those materials with no known silicides are identified. Equations (3) and (4) were applied to those remaining systems containing multiple binary oxides (see Table IV). Those that failed (a negative value for  $\Delta G_f^\circ$ ,<sub>1000</sub>) were eliminated from further consideration.

Using Ref. 29, all known ternary phases ( $\text{MSi}_z\text{O}_y$ ) for the  $M-\text{Si}-\text{O}$  systems of the remaining binary oxides were identified and are listed in Table V. Using Eqs. (5) and (6)  $\Delta G_f^\circ$ ,<sub>1000</sub> for the remaining binary oxides (for which thermodynamic data for  $\text{MSi}_z\text{O}_y$  phases were available) was calculated and is given in Table VI. A summary of the remaining binary oxides that were not able to be eliminated on thermodynamic grounds is given in Table VII. For three of these sufficient thermodynamic

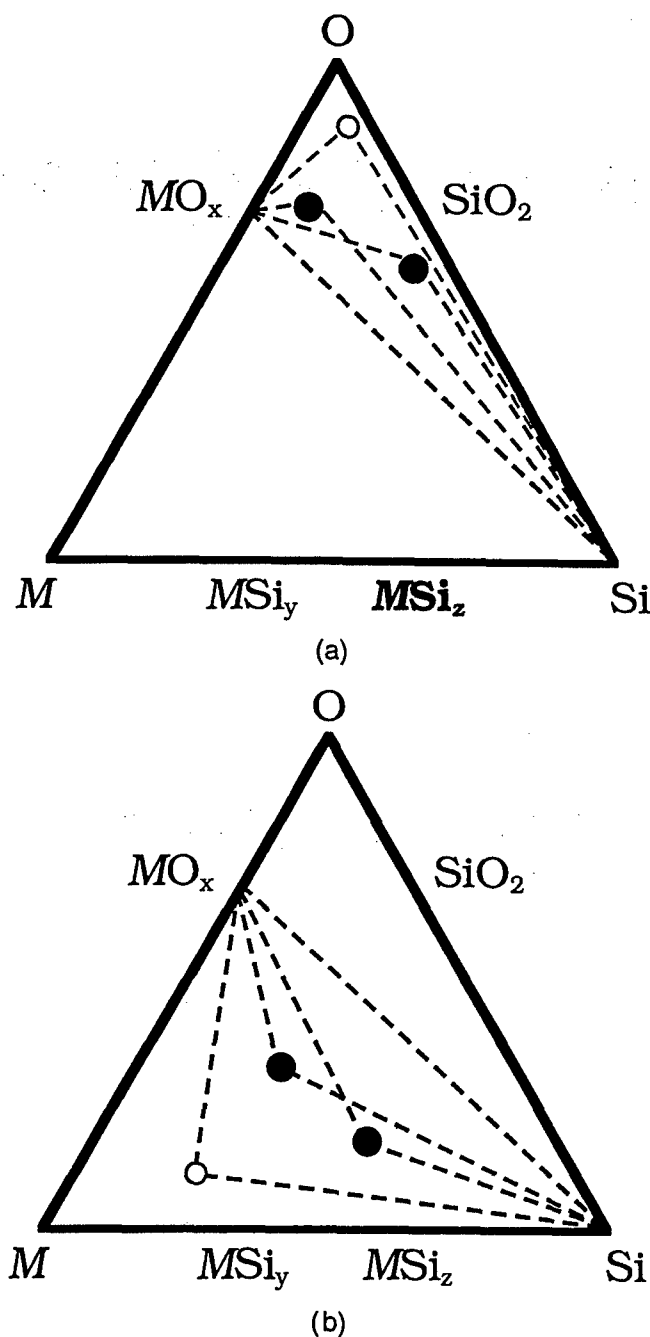


FIG. 4.  $M\text{-Si}\text{-O}$  phase diagrams containing one or more ternary phases ( $MSi_xO_y$ , at position of dots) located (a) above the  $\text{Si}\text{-}MO_x$  tie-line and (b) beneath the  $\text{Si}\text{-}MO_x$  tie-line. For case (a) Eqs. (5) and (6) should be used to test the stability of the  $\text{Si}\text{-}MO_x$  tie-line with the ternary phases ( $MSi_xO_y$ ) indicated by a solid dot. For case (b) Eq. (7) should be used with those ternary phases ( $MSi'_xO'_y$ ) indicated by a solid dot. Ternary phases indicated by hollow dots (those that are positioned such that the triangle  $MSi_xO_y\text{-}MO_x\text{-Si}$  or  $MSi'_xO'_y\text{-}MO_x\text{-Si}$  contains other ternary oxides) do not need to be considered.

data existed to complete the thermodynamic calculations and conclude stability. The remaining 23 materials *might* be stable in contact with silicon at 1000 K. Many of these

materials have already been investigated; the remaining materials warrant study.

### III. RESULTS

#### A. Initial considerations

The goal of this study was to identify potentially compatible binary oxides for use as effective buffer layers or as epitaxial thin films on silicon, by eliminating those that are thermodynamically reactive with silicon. A binary oxide in contact with silicon must be stable not only at the temperature used for its growth, but also at the temperatures used for the growth of additional oxide layers on top of the binary oxide (e.g., oxide superconductors, high  $\epsilon_r$  insulators, ferroelectrics, ferromagnets, etc.). Typically, substrate temperatures ( $T_{\text{sub}}$ ) between 800 K and 1200 K are used, depending on the particular oxide. Consequently, the free energy calculations of this study were performed at 1000 K.

All naturally occurring elements ( $M$ ) that form binary oxides ( $MO_x$ ) listed in Ref. 30 were considered in this comprehensive study. Of these, only nonradioactive oxides that exist as solids at 1000 K were pertinent. Table I lists those binary oxides that were eliminated from further consideration according to these constraints. All the binary oxides remaining after those in Table I were eliminated are contained in Table II, with the exception of  $\text{SiO}_2$ , since it is the native oxide of silicon and is the trivial case of an oxide that is stable in contact with silicon.  $\text{SiO}_2$  might seem like the obvious choice for integration of silicon with oxide overlayers; however, the amorphous nature of overgrown  $\text{SiO}_2$  or  $\text{SiO}_2$  formed by the oxidation of silicon (for layers thicker than about 0.5 nm<sup>38</sup>) makes the growth of epitaxial oxide overlayers on  $\text{SiO}_2$  a formidable obstacle.<sup>39,40</sup>

#### B. Binary oxides eliminated by considering $\text{Si} + MO_x \rightarrow M + \text{SiO}_2$ at 1000 K

The binary oxides remaining after those in Table I were eliminated are listed in Table II. Those materials that have a negative  $\Delta G_f^\circ, 1000$  for the reaction  $\text{Si} + MO_x \rightarrow M + \text{SiO}_2$  at 1000 K [Eq. (1)] can be removed from the list of candidates since they are thermodynamically unstable in contact with silicon at 1000 K. From this reaction alone, the binary oxides of 30 elements can be eliminated. No attempt was made to determine the phase diagrams of those binary oxide systems that were dismissed.

#### C. Binary oxides eliminated by considering $\text{Si} + MO_x \rightarrow MSi_z + \text{SiO}_2$ at 1000 K

For those materials that passed ( $\Delta G > 0$ ) Eq. (1),  $\Delta G_f^\circ, 1000$  for the reaction  $\text{Si} + MO_x \rightarrow MSi_z + \text{SiO}_2$  at 1000 K [Eq. (2)] was determined in those cases where free

TABLE I. Binary oxides that were deemed unacceptable for integration with silicon at a growth temperature of approximately 1000 K.

Binary oxide ( $MO_x$ )	Reason unacceptable <sup>a</sup>	Binary oxide ( $MO_x$ )	Reason unacceptable <sup>a</sup>
$H_2O$	MP = 273 K	$Pt_3O_4$	<sup>b</sup>
$Na_2O_2$	DT = 733 K	$PtO_2$	MP = 723 K
$K_2O_2$	MP = 763 K	$PtO_3$	<sup>c</sup>
$K_2O_3$	MP = 703 K	$Ag_2O$	DT = 403 K
$KO_2$	MP = 653 K	$Ag_2O_2$	DT > 373 K
$Rb_2O$	DT = 673 K	$Au_2O_3$	DT = 433 K
$Rb_2O_2$	MP = 843 K	$Hg_2O$	DT = 373 K
$Rb_2O_3$	MP = 762 K	$HgO$	DT = 773 K
$RbO_2$	MP = 705 K	$Ga_2O$	MP > 933 K
$Rb_2O_4$	DT = 773 K	$In_2O$	<sup>c</sup>
$Cs_2O$	MP = 763 K	$InO$	<sup>c</sup>
$Cs_2O_2$	MP = 673 K	$Tl_2O$	MP = 852 K <sup>i</sup>
$Cs_2O_3$	MP = 673 K	$Tl_2O_2$	MP = 990 K
Oxides of Fr, Ra, Pm, the actinides (Ac to Lr), Tc, Po, At, and Rn	Radioactive	$B_2O_3$	MP = 723 K
$MgO_2$	DT = 361 K <sup>b</sup>	Oxides of C	BP < 280 K
$CaO_2$	DT = 548 K	$Pb_2O$	<sup>c</sup>
$SrO_2$	DT = 488 K	$Pb_2O_3$	DT = 643 K
$BaO_2$	MP = 723 K	Oxides of N	BP < 295 K
$V_2O_5$	MP = 963 K	$P_2O_3$	MP = 297 K
$Nb_2O_3$	<sup>c</sup>	$P_2O_4$	MP < 373 K
$Ta_2O_4$	<sup>d</sup>	$P_2O_5$	MP = 573 K
$CrO$	<sup>e</sup>	Oxides of Po	Radioactive
$CrO_2$	MP = 573 K	$As_2O_3$	MP = 585 K
$CrO_3$	MP = 469 K	$As_2O_5$	DT = 588 K
$Mo_2O_3$	<sup>c</sup>	$Sb_2O_3$	MP = 929 K
$Mo_2O_5$	<sup>c</sup>	$Sb_2O_5$	DT = 653 K
$W_2O_5$	<sup>c</sup>	$BiO$	DT = 453 K
$MnO_2$	DT = 808 K	$Bi_2O_5$	DT = 423 K
$Mn_2O_7$	MP = 279 K	Oxides of S	BP < 1000 K
$ReO_3$	DT = 673 K	$SeO_2$	MP = 391 K
$Re_2O_7$	MP = 570 K	$SeO_3$	MP = 590 K
$RuO_4$	MP = 299 K	$TeO$	DT = 643 K
$OsO$	<sup>c</sup>	$TeO_3$	DT = 668 K
$Os_2O_3$	<sup>c</sup>	Oxides of Br	MP < 373 K
$OsO_4$	MP = 313 K	$IO_2$	DT < 403 K
$Co_2O_3$	DT = 538 K <sup>f</sup>	$I_4O_9$	DT = 348 K
$RhO_2$	DT = 953 K <sup>g</sup>	$I_2O_5$	DT = 573–623 K
$PtO$	DT = 823 K	Oxides of At	Radioactive

<sup>a</sup>See Ref. 30. MP = Melting Point, BP = Boiling Point, DT = Decomposition Temperature.<sup>b</sup>See Ref. 31.<sup>c</sup>Not listed in Ref. 29.<sup>d</sup>Not stable as a pure phase. See Refs. 32 and 33.<sup>e</sup>Not a stable phase. See Refs. 33, 34, and 35.<sup>f</sup>See Ref. 36.<sup>g</sup>See Ref. 37.<sup>h</sup>High pressure phase ( $P_{O_2} \geq 40$  atm at 1000 K). See Ref. 37.<sup>i</sup>See Ref. 26.

energy data for the silicides were available (see Table III). Beryllium and aluminum do not form silicides,<sup>29,41</sup> obviating the need to evaluate Eqs. (2) and (5) for  $BeO$  and  $Al_2O_3$ . The results allowed  $CeO_2$ ,  $TiO$ ,  $Ti_2O_3$ , and  $TiO_2$  to be eliminated from consideration. The negative value of  $\Delta G_{f,1000}^\circ$  for the reactions involving  $TiO$ ,  $Ti_2O_3$ , and  $TiO_2$  indicates that the Ti–Si–O system is a no phase dominant system [see Fig. 1(b)], in agreement with the results of Beyers.<sup>13</sup> Due to the lack of free energy data for pertinent

silicides, Eq. (2) could not be evaluated for many of the remaining binary oxides.

#### D. Binary oxides eliminated by considering reactions involving another binary oxide

Reactions involving multiple binary oxides  $MO_x$  were considered next. The  $M$ –Si–O systems that passed ( $\Delta G > 0$ ) Eqs. (1) and (2) had at most two  $MO_x$  binary oxides.

TABLE II. Gibbs free energy change at 1000 K ( $\Delta G_{1000}^\circ$ ) for the reaction  $\text{Si} + \text{MO}_x \rightarrow M + \text{SiO}_2$  (balanced appropriately) for each of the binary oxides remaining after those in Table I were eliminated.

Binary oxide ( $\text{MO}_x$ )	$\Delta G_{1000}^\circ$ per $\text{MO}_x$ for $\text{Si} + \text{MO}_x \rightarrow M + \text{SiO}_2$ (balanced appropriately) (kcal/mol)	Reference(s)	Binary oxide ( $\text{MO}_x$ )	$\Delta G_{1000}^\circ$ per $\text{MO}_x$ for $\text{Si} + \text{MO}_x \rightarrow M + \text{SiO}_2$ (balanced appropriately) (kcal/mol)	Reference(s)
$\text{Li}_2\text{O}$	+ 24.298	24	$\text{Nb}_2\text{O}_5$	- 86.228	24
$\text{Na}_2\text{O}$	- 20.061	24	$\text{Ta}_2\text{O}_5$	- 52.533	24, 25
$\text{K}_2\text{O}$	- 33.749	24	$\text{Cr}_2\text{O}_3$	- 55.275	24, 25
$\text{BeO}$	+ 32.405	24, 25	$\text{MoO}_2$	- 76.902	24, 25
$\text{MgO}$	+ 30.572	24, 25	$\text{MoO}_3$	- 143.782	24, 25
$\text{CaO}$	+ 39.914	24, 25	$\text{WO}_2$	- 77.126	24
$\text{SrO}$	+ 30.821	24, 25	$\text{WO}_{2.72}$	- 107.195	24
$\text{BaO}$	+ 21.338	24	$\text{WO}_3$	- 121.814	24
$\text{Sc}_2\text{O}_3$	+ 123.105	24, 25	$\text{MnO}$	- 12.752	24, 25
$\text{Y}_2\text{O}_3$	+ 116.823	24	$\text{Mn}_3\text{O}_4$	- 100.598	24, 25
$\text{La}_2\text{O}_3$	+ 98.470	24, 25	$\text{Mn}_2\text{O}_3$	- 94.689	24, 25
$\text{Ce}_2\text{O}_3$	+ 104.946	24, 25	$\text{TcO}_2^a$	- 112.914	24, 25
$\text{CeO}_2$	+ 36.290	24, 25	$\text{ReO}_2$	- 126.662	26
$\text{Pr}_2\text{O}_3$	+ 105.768	24, 25	$\text{FeO}$	- 37.774	24, 25
$\text{PrO}_2$	+ 13.559	24, 25	$\text{Fe}_3\text{O}_4$	- 160.084	24, 25
$\text{Nd}_2\text{O}_3$	+ 101.692	24, 25	$\text{Fe}_2\text{O}_3$	- 127.471	24, 25
$\text{Sm}_2\text{O}_3$	+ 103.941	26	$\text{RuO}_2$	- 142.270	26
$\text{EuO}$	+ 33.238	26	$\text{OsO}_2$	- 147.245	24, 25
$\text{Eu}_2\text{O}_3$	+ 61.901	26	$\text{CoO}$	- 48.041	24, 25
$\text{Gd}_2\text{O}_3$	+ 101.549	24	$\text{Co}_3\text{O}_4$	- 227.374	24, 25
$\text{Tb}_2\text{O}_3$	+ 114.762	24, 25	$\text{Rh}_2\text{O}_3$	- 235.152	24, 25
$\text{TbO}_{1.72}$	+ 38.273	24, 25	$\text{IrO}_2$	- 159.465	24, 25
$\text{Dy}_2\text{O}_3$	+ 112.435	26	$\text{NiO}$	- 51.377	24, 25
$\text{Ho}_2\text{O}_3$	+ 118.450	26	$\text{PdO}$	- 86.066	24
$\text{Er}_2\text{O}_3$	+ 122.030	26	$\text{Cu}_2\text{O}$	- 64.284	24, 25
$\text{Tm}_2\text{O}_3$	+ 116.654	26	$\text{CuO}$	- 71.375	24, 25
$\text{Yb}_2\text{O}_3$	+ 103.830	26	$\text{ZnO}$	- 28.461	24, 25
$\text{Lu}_2\text{O}_3$	+ 116.965	26	$\text{CdO}$	- 49.433	24, 25
$\text{ThO}_2^a$	+ 75.513	26	$\text{Al}_2\text{O}_3$	+ 63.399	24, 25
$\text{UO}_2^a$	+ 43.670	24, 25	$\text{Ga}_2\text{O}_3$	- 79.411	24, 25
$\text{TiO}$	+ 17.849	24	$\text{In}_2\text{O}_3$	- 117.722	26
$\text{Ti}_2\text{O}_3$	+ 35.432	24	$\text{GeO}_2$	- 82.124	26
$\text{TiO}_2$	+ 7.527	24	$\text{SnO}$	- 43.514	24, 25
$\text{ZrO}_2$	+ 42.326	24	$\text{SnO}_2$	- 84.977	24, 25
$\text{HfO}_2$	+ 47.648	24, 25	$\text{PbO}$	- 59.249	24, 25
$\text{VO}$	- 5.314	24, 25	$\text{Pb}_3\text{O}_4$	- 269.624	24, 25
$\text{V}_2\text{O}_3$	- 30.197	24, 25	$\text{PbO}_2$	- 155.786	24, 25
$\text{VO}_2$	- 43.280	24, 25	$\text{SbO}_2$	- 110.523	24, 25
$\text{NbO}$	- 10.132	24	$\text{Bi}_2\text{O}_3$	- 191.853	24, 25
$\text{NbO}_2$	- 13.872	24	$\text{TeO}_2$	- 140.949	24, 25

<sup>a</sup>Radioactive, but still considered since thermodynamic data exist.

Equations (3) and (4) were applied to these systems and the results are given in Table IV. The results allowed  $\text{PrO}_2$ ,  $\text{Eu}_2\text{O}_3$ , and  $\text{TbO}_{1.72}$  ( $\text{Tb}_7\text{O}_{12}$ ) to be eliminated from consideration.

### E. Binary oxides eliminated by considering reactions involving ternary phases

The presence of ternary phases at 1000 K in the remaining candidate  $M$ -Si-O systems is now considered. Table V lists the ternary phases known to exist<sup>29</sup> in the systems remaining under consideration and the values of

$G_{f,1000}^\circ$  for those phases for which data exist.<sup>24,25</sup> Note that all of the remaining  $M$ -Si-O systems under consideration contain ternary phases. For systems in which data on the relevant thermodynamic phases were not available, Eqs. (5) and (6) were evaluated for all phases for which data were available. Although thermodynamic data for the relevant phases are required to conclude thermodynamic stability, if any of the ternary phases leads to a negative  $\Delta G_{f,1000}^\circ$  in Eqs. (5) or (6), the binary oxide can be eliminated.

Table VI contains the results of the relevant thermodynamic calculations [Eqs. (5) and (6)] involving ternary

TABLE III. Gibbs free energy change at 1000 K ( $\Delta G_{1000}^\circ$ ) for the reaction  $\text{Si} + \text{MO}_x \rightarrow \text{MSi}_z + \text{SiO}_2$  (balanced appropriately) for each of the binary oxides in Table II that had a positive  $\Delta G_{1000}^\circ$  for the reaction  $\text{Si} + \text{MO}_x \rightarrow M + \text{SiO}_2$  (balanced appropriately).

Binary oxide ( $\text{MO}_x$ )	$\Delta G_{1000}^\circ$ per $\text{MO}_x$ for $\text{Si} + \text{MO}_x \rightarrow \text{MSi}_z + \text{SiO}_2$ (balanced appropriately) (kcal/mol)	Relevant silicide ( $\text{MSi}_z$ ) <sup>a</sup>	Reference(s)
$\text{Li}_2\text{O}$	b	$\text{Li}_{21}\text{Si}_8$	...
$\text{BeO}$	c	c	29
$\text{MgO}$	+23.385	$\text{Mg}_2\text{Si}$	26
$\text{CaO}$	+17.582	$\text{CaSi}_2$	24, 25
$\text{SrO}$	b	$\text{SrSi}_2$	...
$\text{BaO}$	b	$\text{BaSi}_2$	...
$\text{Sc}_2\text{O}_3$	+91.297	$\text{ScSi}$	24, 25, 27
$\text{Y}_2\text{O}_3$	b	$\text{YSi}_2$	...
$\text{La}_2\text{O}_3$	+66.372	$\text{LaSi}_{1.69}$	24, 25, 27
$\text{Ce}_2\text{O}_3$	+17.896	$\text{CeSi}_2$	24, 25
$\text{CeO}_2$	-7.908	$\text{CeSi}_2$	24, 25
$\text{Pr}_2\text{O}_3$	b	$\text{PrSi}_2$	...
$\text{PrO}_2$	b	$\text{PrSi}_2$	...
$\text{Nd}_2\text{O}_3$	+76.974	$\text{NdSi}_{1.8}$	24, 25, 27
$\text{Sm}_2\text{O}_3$	b	$\text{SmSi}_{1.4}$	...
$\text{EuO}$	b	$\text{EuSi}_2$	...
$\text{Eu}_2\text{O}_3$	b	$\text{EuSi}_2$	...
$\text{Gd}_2\text{O}_3$	+88.582	$\text{GdSi}_{1.89}$	24, 25, 27
$\text{Tb}_2\text{O}_3$	b	$\text{TbSi}_2$	...
$\text{TbO}_{1.72}$	b	$\text{TbSi}_2$	...
$\text{Dy}_2\text{O}_3$	b	$\text{DySi}_{1.4}$	...
$\text{Ho}_2\text{O}_3$	b	$\text{HoSi}_2$	...
$\text{Er}_2\text{O}_3$	b	$\text{ErSi}_2$	...
$\text{Tm}_2\text{O}_3$	b	$\text{TmSi}_{2-x}$	...
$\text{Yb}_2\text{O}_3$	b	$\text{YbSi}_{2-x}$	...
$\text{Lu}_2\text{O}_3$	b	$\text{Lu}_2\text{Si}_3$	...
$\text{ThO}_2^d$	b	$\text{ThSi}_2$	...
$\text{UO}_2^d$	+12.066	$\text{USi}_3$	24, 25
$\text{TiO}$	-12.693	$\text{TiSi}_2$	24, 25
$\text{Ti}_2\text{O}_3$	-25.651	$\text{TiSi}_2$	24, 25
$\text{TiO}_2$	-23.014	$\text{TiSi}_2$	24, 25
$\text{ZrO}_2$	+5.914	$\text{ZrSi}_2$	24, 25
$\text{HfO}_2$	b	$\text{HfSi}_2$	...
$\text{Al}_2\text{O}_3$	c	c	29

<sup>a</sup>See Refs. 27 and 29.

<sup>b</sup>Free energy data for the silicide(s) were unavailable.

<sup>c</sup>No known silicides.

<sup>d</sup>Radioactive, but still considered since thermodynamic data exist.

phases. The values of  $\Delta G_{1000}^\circ$  for reactions involving  $\text{Li}_2\text{O}$ ,  $\text{CaO}$ , and  $\text{BaO}$  were negative. However, for the reactions involving  $\text{Li}_2\text{O}$  and  $\text{CaO}$ , the magnitude of the negative  $\Delta G_{1000}^\circ$  is within the uncertainty of the thermodynamic data. Hence the results allowed only  $\text{BaO}$  to be eliminated from consideration. In most cases these calculations could not be completed due to the lack of free energy data for pertinent ternary phases or silicides.

For three of the systems under consideration, the data for the relevant known ternary phases were available and the calculations were completed. The results of these thermodynamic calculations indicated that  $\text{BeO}$ ,

$\text{MgO}$ , and  $\text{ZrO}_2$  are thermodynamically stable in contact with silicon at 1000 K, as summarized in Table VII. Beyers' thermodynamic calculations<sup>16</sup> previously showed  $\text{ZrO}_2$  to have a stable tie-line with silicon at 1000 K; the calculations of the present study confirm Beyers' findings.

#### IV. COMPARISON TO EXPERIMENTAL OBSERVATIONS

Both the growth of binary oxides on silicon as well as silicon on binary oxides have been reported. Most of the recent work with the aim of integrating oxides, other than  $\text{SiO}_2$ , with silicon technology has focused on the integration of oxide superconductors with silicon. Due to the extensive reaction that accompanies direct integration,<sup>1,2,4,5</sup> many researchers have been working to fabricate superconducting thin films on silicon by depositing a nonreactive epitaxial buffer layer between the silicon substrate and the superconducting oxide.<sup>7,9</sup> In order to preserve the crystalline template of silicon, the growth of binary oxides on silicon is usually initiated in a vacuum or oxygen-deficient atmosphere.<sup>42-49</sup> Following nucleation of the binary oxide, growth of the binary oxide is continued in an oxygen-rich atmosphere. The excess-oxygen environment may lead to the oxidation of the silicon (or of the silicides or other interfacial reaction products) underlying the binary oxide, if the binary oxide is sufficiently permeable to oxygen. Although the effects of this additional oxidation are not considered in our thermodynamic reactivity analysis, the stability of the initial binary oxide/silicon interface is. The stability of this interface is an important consideration for epitaxial growth. In addition to the recent efforts to integrate oxide superconductors with silicon, the effort (primarily in the 1960s) to develop an epitaxial silicon-on-insulator (SOI) technology has also led to the experimental investigation of silicon deposited on binary oxides.<sup>50,51</sup> Below we compare these experimental observations with the thermodynamic stability of each binary oxide/silicon interface.

The results of this study are remarkably consistent with experimental reports. With the possible exception of  $\text{BaO}$ ,  $\text{PrO}_2$ , and  $\text{IrO}_2$ , for which detailed analysis of the interface with silicon is lacking as described below, the only binary oxides found to be free of reaction layers with silicon are all among the list of candidate materials identified in this study. The integration of several of the candidate materials with silicon, i.e.,  $\text{Li}_2\text{O}$ ,  $\text{Sc}_2\text{O}_3$ , most of the  $\text{Re}_2\text{O}_3$  oxides, and  $\text{HfO}_2$ ,<sup>52</sup> has not been experimentally reported and warrants investigation. Below we compare the experimental observations of all reported binary oxide/silicon couples, both the growth of the binary oxide on silicon, as well as the growth of silicon on the binary oxide, with the results of our thermodynamic analysis.

TABLE IV. Gibbs free energy change at 1000 K ( $\Delta G_{1000}^\circ$ ) for the reactions [Eqs. (3) and (4)] involving multiple  $MO_x$  binary oxides for each of the binary oxides in Table III that had a positive  $\Delta G_{1000}^\circ$  for the reaction  $Si + MO_x \rightarrow MSi_z + SiO_2$  (balanced appropriately) and multiple  $MO_x$  binary oxides.

Binary oxide ( $MO_x$ or $MO_w$ )	$\Delta G_{1000}^\circ$ per $MO_x$ for $Si + MO_x \rightarrow MO_w + SiO_2$ (balanced appropriately) (kcal/mol)	$\Delta G_{1000}^\circ$ per $MO_w$ for $Si + MO_w \rightarrow MO_x + MSi_z$ (balanced appropriately) (kcal/mol)	Reference(s)
Ce <sub>2</sub> O <sub>3</sub>	...	+29.758	24, 25
Pr <sub>2</sub> O <sub>3</sub>	...	a	...
PrO <sub>2</sub>	-39.325	...	24, 25
EuO	...	a	...
Eu <sub>2</sub> O <sub>3</sub>	-4.575	...	26
Tb <sub>2</sub> O <sub>3</sub>	...	a	...
TbO <sub>1.72</sub>	-19.108	...	24, 25

<sup>a</sup>Free energy data for the silicide(s) were unavailable.

### A. Reported binary oxide/silicon reactions

Relatively few examples of reactions of binary oxides with silicon have been reported. This may at first seem surprising considering that the vast majority of binary oxides are thermodynamically unstable in contact with silicon at 1000 K, but a nonreactive barrier layer is clearly more newsworthy than a reactive one. What few reports exist are often relegated to brief remarks or footnotes in the description of an otherwise successful experiment.

Reaction between silicon and Gd<sub>2</sub>O<sub>3</sub> (at  $T_{sub}$  between 923 K and 1023 K),<sup>9</sup> SnO<sub>2</sub> (at  $T_{sub}$  above 1273 K),<sup>50</sup> and PbO (at  $T_{sub}$  = 783 K)<sup>3</sup> have been noted. All of these, except Gd<sub>2</sub>O<sub>3</sub>, are expected from our thermodynamic calculations. Although we were unable to complete our thermodynamic calculations for Gd<sub>2</sub>O<sub>3</sub> due to the lack of thermodynamic data, Gd<sub>2</sub>O<sub>3</sub> passed ( $\Delta G > 0$ ) the two reactions for which sufficient data were available [Eqs. (1) and (2)]. Tarsa *et al.*<sup>9</sup> suggested that Gd<sub>2</sub>O<sub>3</sub> reacts with silicon to form GdO<sub>2</sub>. Unfortunately, we were unable to assess if this reaction is thermodynamically favored due to the absence of thermodynamic data for GdO<sub>2</sub>.

An equivalent means of showing that a  $MO_x/Si$  interface is thermodynamically unstable is to demonstrate the stability of another interface in the  $M-Si-O$  phase diagram that would necessarily cross the  $Si-MO_x$  tie-line. For example, the stability of  $M/SiO_2$  interfaces has been experimentally (and thermodynamically) studied.<sup>53</sup> A stable  $M/SiO_2$  interface in a given  $M-Si-O$  system implies that the  $MO_x/Si$  interface in that system must be thermodynamically unstable, since the crossing of tie-lines is forbidden. The experiments of Pretorius *et al.*<sup>53</sup> showed the metals Cr, Mn, Fe, Co, Ni, Pd, Pt, and Cu to be stable in contact with SiO<sub>2</sub> at 1073 K signifying that the corresponding metal-oxides are all thermodynamically unstable in contact with silicon. Similarly, experiments showing the stability of molybdenum and tungsten in contact with SiO<sub>2</sub> at 1273 K to 1573 K,<sup>54</sup> the stability of TiSi and TiSi<sub>2</sub> in contact with SiO<sub>2</sub> at

1273 K,<sup>13,55</sup> the stability of V<sub>3</sub>Si in contact with SiO<sub>2</sub> at 1273 K,<sup>56</sup> and the stability of TaSi<sub>2</sub> in contact with SiO<sub>2</sub> at temperatures between 1173 K and 1323 K,<sup>55,57</sup> indicate that the corresponding metal-oxides are all thermodynamically unstable in contact with silicon. These results are all in agreement with our thermodynamic calculations.

### B. Reported nonreactive binary oxide-silicon interfaces

#### 1. BeO/Si

Our thermodynamic calculations indicate that BeO is stable in contact with silicon at 1000 K. This is consistent with the experimental observations of Manasevit *et al.*<sup>58</sup> who reported the epitaxial growth of silicon on several faces of BeO single crystals at substrate temperatures near 1450 K.

#### 2. MgO/Si

Based on the thermodynamic calculations of this study, MgO and silicon are stable in contact with each other at 1000 K. Reports of reaction-free MgO/Si interfaces confirm our thermodynamic calculations.<sup>59,60</sup> In particular, Fork *et al.*<sup>59</sup> have examined an epitaxial MgO/Si interface of a film grown at a substrate temperature of 773 K by high-resolution cross-sectional transmission electron microscopy (TEM) and show that it is abrupt and free from reaction layers or noticeable interdiffusion. Cross-sectional TEM studies of polycrystalline MgO films grown on silicon have revealed either no interfacial reaction ( $T_{sub}$  = 923 K)<sup>60</sup> or a thin amorphous interfacial layer ( $T_{sub}$  = 673 K to 773 K).<sup>61</sup> In light of the absence of an interfacial layer in the epitaxial MgO films,<sup>59</sup> the latter observation of an amorphous interlayer<sup>61</sup> is more likely attributed to incomplete removal of the native oxide on the silicon substrate prior to growth or oxidation of the silicon by O<sup>2-</sup> ion transport through the polycrystalline

TABLE V. Ternary phases present in the metal-silicon-oxygen systems for each of the binary oxides in Table III that had a positive  $\Delta G_{1000}^{\circ}$  for the reaction  $\text{Si} + \text{MO}_x \rightarrow \text{MSi}_z + \text{SiO}_2$  (balanced appropriately). The known free energies of formation at 1000 K ( $G_{f,1000}^{\circ}$ ) for these phases are also given. The relevant ternary phases for Eqs. (5) and (6) are shown in bold.

Ternary phase <sup>a</sup> ( $\text{MSi}_x\text{O}_y$ )	Free energy of formation ( $G_{f,1000}^{\circ}$ ) (kcal/mol)	Ternary phase <sup>a</sup> ( $\text{MSi}_x\text{O}_y$ )	Free energy of formation ( $G_{f,1000}^{\circ}$ ) (kcal/mol) <sup>b</sup>
$\text{Li}_3\text{SiO}_6$	c	$\text{Eu}_3\text{SiO}_5$	c
$\text{Li}_2\text{SiO}_4$	-605.954	$\text{Eu}_2\text{SiO}_4$	c
$\text{Li}_2\text{Si}_2\text{O}_7$	c	$\text{Eu}_2\text{SiO}_5$	c
$\text{Li}_2\text{SiO}_3$	-428.439	$\text{Eu}_3\text{Si}_2\text{O}_7$	c
$\text{Li}_2\text{Si}_2\text{O}_5$	-664.434	$\text{EuSiO}_3$	c
$\text{Li}_2\text{Si}_3\text{O}_7$	c	$\text{Eu}_2\text{Si}_2\text{O}_7$	c
$\text{Be}_2\text{SiO}_4$	-543.542	$\text{Gd}_2\text{SiO}_5$	c
$\text{Mg}_2\text{SiO}_4$	-560.595	$\text{Gd}_2\text{Si}_2\text{O}_7$	c
$\text{MgSiO}_3$	-398.377	$\text{Tb}_2\text{SiO}_5$	c
$\text{Ca}_3\text{SiO}_5$	-753.050	$\text{Tb}_2\text{Si}_2\text{O}_7$	c
$\text{Ca}_2\text{SiO}_4$	-586.443	$\text{Dy}_2\text{SiO}_5$	c
$\text{Ca}_8\text{Si}_5\text{O}_{18}$	c	$\text{Dy}_2\text{Si}_2\text{O}_7$	c
$\text{Ca}_3\text{Si}_2\text{O}_7$	-1023.100	$\text{Ho}_2\text{SiO}_5$	c
$\text{CaSiO}_3$	-422.822	$\text{Ho}_4\text{Si}_3\text{O}_{12}$	c
$\text{CaSi}_2\text{O}_5$	c	$\text{Ho}_2\text{Si}_2\text{O}_7$	c
$\text{Sr}_3\text{SiO}_5$	c	$\text{Ho}_2\text{Si}_3\text{O}_9$	c
$\text{Sr}_2\text{SiO}_4$	-605.164	$\text{Ho}_2\text{Si}_6\text{O}_9$	c
$\text{SrSiO}_3$	-426.295	$\text{Er}_2\text{SiO}_5$	c
$\text{Ba}_3\text{SiO}_5$	c	$\text{Er}_2\text{Si}_2\text{O}_7$	c
$\text{Ba}_2\text{SiO}_4$	-608.939	$\text{Tm}_2\text{SiO}_5$	c
$\text{BaSiO}_3$	-427.257	$\text{Tm}_2\text{Si}_2\text{O}_7$	c
$\text{Ba}_2\text{Si}_3\text{O}_8$	c	$\text{Yb}_3\text{SiO}_5$	c
$\text{Ba}_5\text{Si}_8\text{O}_{21}$	c	$\text{Yb}_3\text{SiO}_7$	c
$\text{Ba}_3\text{Si}_5\text{O}_{13}$	c	$\text{Yb}_2\text{SiO}_4$	c
$\text{BaSi}_2\text{O}_5$	c	$\text{Yb}_2\text{SiO}_5$	c
$\text{BaSi}_4\text{O}_9$	c	$\text{YbSiO}_3$	c
$\text{ScSi}_{0.02}\text{O}_{0.98}$	c	$\text{Yb}_2\text{Si}_2\text{O}_7$	c
$\text{Sc}_2\text{SiO}_5$	c	$\text{Lu}_2\text{SiO}_5$	c
$\text{Sc}_2\text{Si}_2\text{O}_7$	c	$\text{Lu}_2\text{SiO}_7$	c
$\text{Y}_2\text{SiO}_5$	c	$\text{Lu}_2\text{Si}_2\text{O}_7$	c
$\text{Y}_4\text{Si}_3\text{O}_{12}$	c	$\text{ThSiO}_4$	c
$\text{Y}_2\text{Si}_2\text{O}_7$	c	$\text{USiO}_4$	c
$\text{La}_2\text{SiO}_5$	c	$\text{USi}_7\text{O}_{17}$	c
$\text{La}_2\text{Si}_2\text{O}_7$	c	$\text{ZrSiO}_4$	-520.307
$\text{Ce}_2\text{SiO}_5$	c	$\text{HfSiO}_4$	c
$\text{Ce}_2\text{Si}_2\text{O}_7$	c	$\text{Al}_{1.90}\text{Si}_{0.05}\text{O}_{2.95}$	c
$\text{Pr}_2\text{SiO}_5$	c	$\text{Al}_{1.70}\text{Si}_{0.15}\text{O}_{2.85}$	c
$\text{Pr}_8\text{Si}_6\text{O}_{24}$	c	$\text{Al}_{1.40}\text{Si}_{0.30}\text{O}_{2.70}$	c
$\text{Nd}_2\text{SiO}_5$	c	$\text{Al}_6\text{Si}_2\text{O}_{13}$	-1736.172
$\text{Nd}_4\text{Si}_3\text{O}_{12}$	c	$\text{Al}_2\text{SiO}_5$	-660.925
$\text{Nd}_2\text{Si}_2\text{O}_7$	c	$\text{Al}_{0.50}\text{Si}_{0.75}\text{O}_{2.25}$	c
$\text{Sm}_2\text{SiO}_4$	c	$\text{Al}_2\text{Si}_4\text{O}_{10}$	c
$\text{Sm}_2\text{SiO}_5$	c		
$\text{Sm}_4\text{Si}_3\text{O}_{12}$	c		
$\text{SmSiO}_3$	c		
$\text{Sm}_2\text{Si}_2\text{O}_7$	c		

<sup>a</sup>Free energy data from Refs. 24 and 25.

<sup>b</sup>Ternary phase data from Ref. 29.

<sup>c</sup>Free energy data not given in Refs. 24 and 25.

MgO film (e.g., along grain boundaries) during growth, than to a reaction between MgO and silicon.

### 3. CaO/Si

Sufficient data existed to complete the thermodynamic calculations for CaO. The calculations indicated

that CaO and silicon would react at 1000 K ( $\Delta G_{1000}^{\circ} < 0$ ) to form  $\text{CaSi}_2$  and  $\text{Ca}_3\text{SiO}_5$ . However, the magnitude of this reaction (-1.519 kcal/mol) is close to the approximate uncertainty of the thermodynamic data ( $\pm 1$  kcal/mol). Consequently, the instability of the CaO/Si interface cannot be asserted. The growth of CaO

TABLE VI. Gibbs free energy change at 1000 K ( $\Delta G_{1000}^\circ$ ) for the reactions [Eqs. (5) and (6)] involving relevant ternary phases (bold) for which data were available (Table V) for each of the binary oxides in Table III that had a positive  $\Delta G_{1000}^\circ$  for the reaction  $\text{Si} + \text{MO}_x \rightarrow \text{MSi}_z + \text{SiO}_2$  (balanced appropriately).

Ternary phase ( $\text{MSi}_z \text{O}_y$ )	$\Delta G_{1000}^\circ$ per $\text{MO}_x$ for $\text{Si} + \text{MO}_x \rightarrow$ $\text{MSi}_z + \text{MSi}_x \text{O}_y$ (balanced appropriately)	$\Delta G_{1000}^\circ$ per $\text{MO}_x$ for $\text{Si} + \text{MO}_x \rightarrow$ $\text{M} + \text{MSi}_x \text{O}_y$ (balanced appropriately)
	(kcal/mol)	(kcal/mol)
$\text{Li}_4\text{SiO}_4$	a	-0.493 <sup>c</sup> ( $\pm 0.8$ ) <sup>d</sup>
$\text{Li}_2\text{SiO}_3$	a	+5.049
$\text{Li}_2\text{Si}_2\text{O}_5$	a	+12.467
$\text{Be}_2\text{SiO}_4$	b	+14.414
$\text{Mg}_2\text{SiO}_4$	+7.951	+11.544
$\text{Ca}_3\text{SiO}_5$	-1.519 <sup>c</sup> ( $\pm 1.0$ ) <sup>d</sup>	+10.155
$\text{Sr}_2\text{SiO}_4$	a	+3.041 ( $\pm 1.4$ ) <sup>d</sup>
$\text{SrSiO}_3$	a	+4.807 ( $\pm 1.4$ ) <sup>d</sup>
$\text{Ba}_2\text{SiO}_4$	a	-4.831 ( $\pm 0.8$ ) <sup>d</sup>
$\text{BaSiO}_3$	a	+2.359 ( $\pm 0.9$ ) <sup>d</sup>
$\text{ZrSiO}_4$	+1.253 <sup>c</sup> ( $\pm 2.1$ ) <sup>d</sup>	+19.459
$\text{Al}_6\text{Si}_2\text{O}_{13}$	b	+19.050
$\text{Al}_2\text{SiO}_5$	b	+24.443

<sup>a</sup>Free energy data for the silicide(s) were unavailable.

<sup>b</sup>No known silicides.

<sup>c</sup>The magnitude of this reaction is close to the approximate uncertainty of the thermodynamic data, making its result inconclusive.

<sup>d</sup>The approximate uncertainty given is a lowerbound on the error; approximate errors were not given in Refs. 24 and 25 for some of the terms involved in the calculation of this  $\Delta G_{1000}^\circ$  value.

on silicon at a substrate temperature of 673 K has been reported by Soerensen and Gygax.<sup>62</sup> They used Auger depth profiling to analyze a 50 Å thick CaO film grown on silicon and reported that the CaO/Si interface was on the order of 20 Å wide. This suggests that the CaO/Si interface is free of reaction layers.

#### 4. SrO/Si

Although the thermodynamic calculations for SrO in contact with silicon at 1000 K could not be completed due to the absence of thermodynamic data for  $\text{SrSi}_2$  and  $\text{Sr}_3\text{SiO}_5$ , it is believed that SrO and silicon are thermodynamically stable in contact at 1000 K based on experimental observations. Kado and Arita<sup>63,64</sup> grew both epitaxial SrO films on silicon and epitaxial silicon films on SrO by molecular beam epitaxy (MBE) at substrate temperatures between 923 K and 1053 K. They used Auger electron spectroscopy (AES) to depth-profile the SrO/Si interface(s) and reported both the absence of noticeable interdiffusion at the interface(s) and the absence of Auger peaks due to  $\text{SiO}_2$ . Similarly, Soerensen and Gygax<sup>62</sup> also reported reaction-free SrO/Si interfaces for films grown at  $T_{\text{sub}} = 673$  K. It has also been shown that it is not necessary to completely remove the thin native oxide ( $\text{SiO}_2$ ) layer from the silicon substrate in order to achieve an epitaxial SrO layer.<sup>42</sup> The

residual  $\text{SiO}_2$  may be reduced (to Si or volatile  $\text{SiO}$ ) and the excess strontium metal oxidized (to SrO) by initiating the growth with strontium metal in an oxygen-deficient atmosphere.<sup>42</sup> This observation is consistent with the absence of a stable tie-line between strontium metal and  $\text{SiO}_2$  [e.g., the  $\text{SiO}_2$  dominant system shown in Fig. 1(a)], and together with the other experimental observations is consistent with the presence of a stable tie-line between silicon and SrO.

#### 5. BaO/Si

Our thermodynamic calculations indicate that it is energetically favorable for BaO to react with silicon [e.g., to form barium metal and  $\text{Ba}_2\text{SiO}_4$ , Eq. (6)]. However, experimental evidence does not support this conclusion. Kado and Arita<sup>64</sup> grew epitaxial BaO films on silicon by MBE at a substrate temperature of 1053 K and reported a Rutherford backscattering spectrometry (RBS) channeling yield,  $\chi_{\text{min}}$ , of about 7%. McKee *et al.*<sup>43</sup> have also reported the MBE growth of epitaxial BaO layers on silicon substrates by a more involved route, involving the formation of a one monolayer thick  $\text{BaSi}_2$  layer on top of the silicon prior to the deposition of BaO. This later result demonstrates the existence of a stable tie-line between  $\text{BaSi}_2$  and BaO, which, in the absence of the existence of ternary phases, would mandate a stable tie-line between silicon and BaO [i.e., the metal oxide dominant system shown in Fig. 1(c)]. Analysis of the BaO/ $\text{BaSi}_2$ /silicon interfaces after growth has not been reported, leaving it unclear if the one monolayer thick  $\text{BaSi}_2$  layer survives intact or if the final interface is simply between BaO and silicon as the prior work of Kado and Arita<sup>64</sup> suggests is stable. Such interfacial characterization would help to resolve the discrepancy between our thermodynamic calculations and reported observations. It is possible that interfacial energies favor the BaO/silicon interface due to its more favorable lattice match. Interfacial energies not included in our thermodynamic calculations are likely important in cases where the magnitude of the free energy change of an interfacial reaction is small, as in this case and also for  $\text{Li}_2\text{O}$ /silicon, CaO/silicon, SrO/silicon, and  $\text{ZrO}_2$ /silicon (see Table VI).

#### 6. $\text{Y}_2\text{O}_3$ /Si

The epitaxial growth of  $\text{Y}_2\text{O}_3$  on silicon<sup>44–46,65–67</sup> and silicon on  $\text{Y}_2\text{O}_3$ <sup>68</sup> has been demonstrated at substrate temperatures ranging from 1003 K to 1073 K. Reaction between the silicon and  $\text{Y}_2\text{O}_3$  has not been reported, despite *in situ* monitoring of the deposition process with reflection high-energy electron diffraction (RHEED) during growth.<sup>44,65–68</sup> High-resolution cross-sectional TEM micrographs of the  $\text{Y}_2\text{O}_3$ /Si interface have also been obtained.<sup>46</sup> Therefore, even though our thermodynamic calculations could not be completed due to the absence

TABLE VII. Summary of the remaining binary oxides that were not able to be eliminated on thermodynamic grounds. These are the only binary oxides that *may* be stable in contact with silicon. Due to the lack of free energy data for relevant silicides, ternary phases, or both, only for a limited number of binary oxides (shown in bold) could thermodynamic stability with silicon be concluded.

Oxide	Magnitude of $\Delta G_{1000}^\circ$ per $MO_x$ for Reaction 1 <sup>a</sup> (kcal/mol)	Magnitude of $\Delta G_{1000}^\circ$ per $MO_x$ for Reaction 2 <sup>a</sup> (kcal/mol)	Magnitude of $\Delta G_{1000}^\circ$ per $MO_x$ for Reaction 5 <sup>a</sup> (kcal/mol)	Magnitude of $\Delta G_{1000}^\circ$ per $MO_x$ for Reaction 6 <sup>a</sup> (kcal/mol)
Li <sub>2</sub> O	+ 24.298	b	b	- 0.493 <sup>g</sup> ( $\pm 0.8$ ) <sup>h</sup>
BeO	+ 32.405	c	c	+14.414 <sup>f</sup>
MgO	+ 30.572	+23.385	+7.951 <sup>f</sup>	+11.544 <sup>f</sup>
CaO	+ 39.914	+17.582	-1.519 <sup>g</sup> ( $\pm 1.0$ ) <sup>h</sup>	+10.155 <sup>f</sup>
SrO	+ 30.821	b	b	Positive <sup>e</sup>
Sc <sub>2</sub> O <sub>3</sub>	+123.105	+91.297	d	d
Y <sub>2</sub> O <sub>3</sub>	+116.823	b	bd	d
La <sub>2</sub> O <sub>3</sub>	+ 98.470	+66.372	d	d
Ce <sub>2</sub> O <sub>3</sub>	+104.946	+17.896	d	d
Pr <sub>2</sub> O <sub>3</sub>	+105.768	b	bd	d
Nd <sub>2</sub> O <sub>3</sub>	+101.692	+76.974	d	d
Sm <sub>2</sub> O <sub>3</sub>	+103.941	b	bd	d
EuO	+ 33.238	b	bd	d
Gd <sub>2</sub> O <sub>3</sub>	+101.549	+88.582	d	d
Tb <sub>2</sub> O <sub>3</sub>	+114.762	b	bd	d
Dy <sub>2</sub> O <sub>3</sub>	+112.435	b	bd	d
Ho <sub>2</sub> O <sub>3</sub>	+118.450	b	bd	d
Er <sub>2</sub> O <sub>3</sub>	+122.030	b	bd	d
Tm <sub>2</sub> O <sub>3</sub>	+116.654	b	bd	d
Yb <sub>2</sub> O <sub>3</sub>	+103.830	b	bd	d
Lu <sub>2</sub> O <sub>3</sub>	+116.965	b	bd	d
ThO <sub>2</sub> <sup>i</sup>	+ 75.513	b	bd	d
UO <sub>2</sub> <sup>i</sup>	+ 43.670	+12.066	d	d
ZrO <sub>2</sub>	+ 42.326	+ 5.914	+1.253 <sup>g</sup> ( $\pm 2.1$ ) <sup>h</sup>	+19.459 <sup>f</sup>
HfO <sub>2</sub>	+ 47.648	b	bd	d
Al <sub>2</sub> O <sub>3</sub>	+ 63.399	c	c	Positive <sup>e</sup>

<sup>a</sup>Reactions (balanced appropriately)

- 1: Si +  $MO_x \rightarrow M + SiO_2$  at 1000 K (Table II).
- 2: Si +  $MO_x \rightarrow MSi_z + SiO_2$  at 1000 K (Table III).
- 5: Si +  $MO_x \rightarrow MSi_z + MSi_xO_y$  at 1000 K (Table VI).
- 6: Si +  $MO_x \rightarrow M + MSi_xO_y$  at 1000 K (Table VI).

<sup>b</sup>Free energy data for the silicide(s) were unavailable.

<sup>c</sup>No known silicides.

<sup>d</sup>Free energy data for the relevant ternary phase(s) were unavailable.

<sup>e</sup>Free energy data for the relevant ternary phase(s) were not available. The free energy change at 1000 K ( $\Delta G_{1000}^\circ$ ) for each of the phases for which data were available was positive.

<sup>f</sup>Free energy data for the relevant ternary phase(s) were available and reactions 5 and 6 were positive in all cases.

<sup>g</sup>The magnitude of this reaction is close to the approximate uncertainty of the thermodynamic data, making its result inconclusive.

<sup>h</sup>The approximate uncertainty given is a lowerbound on the error; approximate errors were not given in Refs. 24 and 25 for some of the terms involved in the calculation of this  $\Delta G_{1000}^\circ$  value.

<sup>i</sup>Radioactive, but still considered since thermodynamic data exist.

of free energy data for  $YSi_2$  and  $Y_2SiO_5$ , it is believed that these calculations, if completed, would confirm the thermodynamic stability of  $Y_2O_3$  in contact with silicon. Analogous to the case of epitaxial SrO/Si growth, it has been shown that it is not necessary to completely remove the thin native oxide ( $SiO_2$ ) layer from the silicon substrate in order to achieve an epitaxial  $Y_2O_3$  layer.<sup>44-46</sup> By initiating growth with the deposition of yttrium metal in an oxygen-deficient atmosphere, the residual  $SiO_2$  may be converted to  $Y_2O_3$  and volatile  $SiO$ .<sup>44</sup> This observation is consistent with the absence of a stable tie-line between

yttrium metal and  $SiO_2$  [e.g., the  $SiO_2$  dominant system shown in Fig. 1(a)].

## 7. CeO<sub>2</sub>/Si

CeO<sub>2</sub> has been epitaxially grown on silicon at temperatures ranging from 293 K to 1123 K.<sup>69-73</sup> This result is unexpected from a thermodynamic standpoint as the calculations presented show that CeO<sub>2</sub> is thermodynamically unstable in contact with silicon [ $\Delta G_{1000}^\circ$  for Eq. (2) is *negative* for CeO<sub>2</sub>]. As the magnitude of

$\Delta G_{1000}^\circ$  for Eq. (2) involving  $\text{CeO}_2$ ,  $-7.908 \text{ kcal/mol}$ , is not appreciably greater than the approximate accuracy of this calculation (approximately  $\pm 2.7 \text{ kcal/mol}$ ),<sup>74</sup> Eq. (3) was also applied to see if the thermodynamic instability of  $\text{CeO}_2$  with silicon could be more conclusively shown from existing thermodynamic data. The resulting  $\Delta G_{1000}^\circ$  for Eq. (3) is  $-16.856 \text{ kcal/mol}$ .<sup>24,25</sup> This result is sufficiently greater than the possible error in the thermodynamic data to rule out the possible thermodynamic stability of  $\text{CeO}_2$  in contact with silicon.

Although from a thermodynamic standpoint the calculations presented show that  $\text{CeO}_2$  is thermodynamically unstable in contact with silicon,  $\text{Ce}_2\text{O}_3$  is potentially stable in contact with silicon. This apparent discrepancy between experimental observation and the present thermodynamic calculations would be absent if at the silicon interface the  $\text{CeO}_2$  were locally reduced to  $\text{Ce}_2\text{O}_3$ , yielding a stable  $\text{Si}/\text{Ce}_2\text{O}_3/\text{CeO}_2$  interface. Indeed both *in situ* x-ray photoelectron spectroscopy (XPS) measurements<sup>71,72</sup> and *ex situ* cross-sectional TEM investigations<sup>73</sup> of epitaxial  $\text{CeO}_2$  films deposited on silicon indicate the presence of a mixed-valence<sup>71,72</sup> ( $\text{Ce}^{4+}$  and  $\text{Ce}^{3+}$ ), oxygen-deficient<sup>73</sup> ( $\text{CeO}_{2-x}$ ) region in the vicinity of the  $\text{CeO}_2/\text{Si}$  interface. Using cross-sectional TEM Chikyow *et al.*<sup>73</sup> examined several epitaxial  $\text{CeO}_2/\text{Si}$  interfaces prepared under different conditions, yet nowhere did they find  $\text{CeO}_2$  in direct contact with silicon. Similarly, the cross-sectional TEM images of as-grown  $\text{CeO}_2/\text{Si}$  films reported by Inoue *et al.*<sup>75</sup> do not show  $\text{CeO}_2$  in direct contact with silicon. Instead, these TEM studies reveal an amorphous layer between the silicon and overgrown  $\text{CeO}_2$ .<sup>73,75</sup> Inoue *et al.*<sup>75</sup> attribute this layer to amorphous  $\text{SiO}_2$ , while Chikyow *et al.*<sup>73</sup> conclude that this amorphous interlayer consists of  $\text{SiO}_2$  and oxygen-deficient  $\text{CeO}_{2-x}$ . The thickness of this layer depends on the growth conditions,<sup>75</sup> but it is typically a few nanometers in thickness. This suggests, since epitaxy occurs, that the amorphous  $\text{SiO}_2$  layer is formed after the initial stages of growth due to  $\text{O}^{2-}$  ion conduction through the growing  $\text{CeO}_2$  (and  $\text{CeO}_{2-x}$ ),<sup>75</sup> much as the amorphous  $\text{SiO}_2$  layer forms at the yttria-stabilized zirconia (YSZ)/Si interface observed by Fenner *et al.*<sup>1</sup>

## 8. $\text{PrO}_2/\text{Si}$

Despite our conclusion that  $\text{PrO}_2$  is thermodynamically unstable in contact with silicon at 1000 K [ $\Delta G_{1000}^\circ$  for Eq. (3) is *negative* for  $\text{PrO}_2$ ], Fork *et al.*<sup>76</sup> have grown epitaxial  $\text{PrO}_2$  on silicon at substrate temperatures between 823 K and 923 K. At these lower growth temperatures,  $\Delta G^\circ$  for Eq. (3) is still negative; in fact, it becomes even more negative than it is at 1000 K. The reported results would be in complete agreement with our thermodynamic analysis if during the initial stages of

growth a stable  $\text{PrO}_2/\text{Pr}_2\text{O}_3/\text{Si}$  interface is formed; such a situation is analogous to the thermodynamically unstable  $\text{CeO}_2/\text{Si}$  interface at which interfacial reaction occurs. Unfortunately, cross-sectional TEM studies of  $\text{PrO}_2/\text{Si}$  interfaces have not been reported.

## 9. $\text{Pr}_2\text{O}_3/\text{Si}$

Without thermodynamic data for  $\text{PrSi}_2$  and  $\text{Pr}_2\text{SiO}_5$  it is not possible to determine the thermodynamic stability of  $\text{Pr}_2\text{O}_3$  in contact with silicon. However, Tarsa *et al.*<sup>77</sup> have grown epitaxial  $\text{Pr}_2\text{O}_3$  films on silicon and epitaxial silicon films on  $\text{Pr}_2\text{O}_3$  at a substrate temperature of 873 K. Their study, which includes *in situ* RHEED analysis during growth and *ex situ* cross-sectional TEM analysis, contains no evidence suggestive of reaction at the  $\text{Pr}_2\text{O}_3/\text{Si}$  interfaces. It is thus believed that  $\text{Pr}_2\text{O}_3$  is thermodynamically stable in contact with silicon.

## 10. $\text{Nd}_2\text{O}_3/\text{Si}$

Due to the lack of thermodynamic data for  $\text{Nd}_2\text{SiO}_5$ , we were unable to complete our thermodynamic analysis of the stability of  $\text{Nd}_2\text{O}_3$  in contact with silicon at 1000 K. Nagata *et al.*<sup>71</sup> have reported the epitaxial growth of  $\text{Nd}_2\text{O}_3$  films on silicon at substrate temperatures between 873 K and 973 K, which would be consistent with the thermodynamic stability of  $\text{Nd}_2\text{O}_3$  in contact with silicon.

## 11. $\text{ThO}_2/\text{Si}$

Although the thermodynamic calculations for  $\text{ThO}_2$  could not be completed due to the absence of thermodynamic data for  $\text{ThSi}_2$  and  $\text{ThSiO}_4$ , it is believed that  $\text{ThO}_2$  and silicon are thermodynamically stable in contact at 1000 K based on experimental observations. The cube-on-cube epitaxial growth of silicon on  $\text{ThO}_2$  single crystals has been reported for substrate temperatures between 1373 K and 1423 K.<sup>50,78</sup> Although it appears that the  $\text{ThO}_2/\text{Si}$  interface is stable, the practicality of using  $\text{ThO}_2$  as a buffer layer is unlikely because of its radioactive nature.

## 12. $\text{ZrO}_2/\text{Si}$

There are many reports of the epitaxial growth of  $\text{ZrO}_2$  films on silicon at substrate temperatures ranging from 923 K to 1153 K,<sup>47,66,79-81</sup> but no reports of interfacial reaction between  $\text{ZrO}_2$  and silicon. These results are in agreement with the thermodynamic calculations presented in this study in which we find the  $\text{ZrO}_2/\text{Si}$  interface to be stable at 1000 K.

Although the successful integration of yttria-stabilized cubic zirconia ( $\text{Y}_2\text{O}_3-\text{ZrO}_2$ ) with silicon has been widely demonstrated (both the epitaxial growth of silicon on  $\text{Y}_2\text{O}_3-\text{ZrO}_2$ <sup>66,68,82</sup> and vice versa<sup>1,44-46,48,65,66,68,80,83-86</sup>), calculating the thermodynamic stability of this ternary

oxide is beyond the scope of the calculations that we present here for binary oxides. Just as it has been shown possible to grow epitaxial SrO and epitaxial Y<sub>2</sub>O<sub>3</sub> films on silicon without first removing the thin native oxide (SiO<sub>2</sub>) from the silicon substrate,<sup>42,44-46</sup> epitaxial ZrO<sub>2</sub><sup>47</sup> and Y<sub>2</sub>O<sub>3</sub>-ZrO<sub>2</sub><sup>44-46,48,49</sup> films have been grown on silicon by initiating growth in an oxygen-deficient atmosphere. This results in the reduction of the residual SiO<sub>2</sub> (to Si or volatile SiO) and oxidation of the excess metallic zirconium and yttrium. Additionally, the Y<sub>2</sub>O<sub>3</sub>-ZrO<sub>2</sub>/Si interface is one of the few thermodynamically compatible oxide/Si interfaces for which interdiffusion has been studied. Zirconium diffusion into the silicon was observed to have a decay length of 20 nm per decade of concentration decrease and silicon diffusion into the Y<sub>2</sub>O<sub>3</sub>-ZrO<sub>2</sub> was observed to have a decay length of 7 nm per decade.<sup>86</sup>

### 13. HfO<sub>2</sub>/Si

Although there are no reports characterizing the HfO<sub>2</sub>/Si interface,<sup>52</sup> the oxidation of HfSi<sub>2</sub> has been studied.<sup>87</sup> When HfSi<sub>2</sub> undergoes oxidation at temperatures between 773 K and 1273 K, SiO<sub>2</sub> is not found in contact with it,<sup>87</sup> implying the absence of a tie-line between HfSi<sub>2</sub> and SiO<sub>2</sub>. This implies that silicon is stable in contact with either HfO<sub>2</sub> or HfSiO<sub>4</sub>. This is consistent with the results of our thermodynamic calculations, which could not be completed due to the absence of thermodynamic data for HfSi<sub>2</sub> and HfSiO<sub>4</sub>.

### 14. RuO<sub>2</sub>/Si

In contrast to our calculations indicating that silicon is *not* thermodynamically stable in contact with RuO<sub>2</sub>, initial experimental studies came to the opposite conclusion. Green *et al.*<sup>88</sup> reported stable RuO<sub>2</sub>/Si interfaces for polycrystalline RuO<sub>2</sub> films grown on silicon wafers at substrate temperatures ranging from 848 to 873 K. AES depth-profiling and (low-resolution) TEM gave no indication of reaction or interdiffusion at the interface. This reaction-free result was also concluded by others using AES depth-profiling<sup>89</sup> or RBS<sup>90,91</sup> to characterize the RuO<sub>2</sub>/Si interface. The reportedly stable RuO<sub>2</sub>/Si interface is, however, contrary to other experimental results presented in one of these same initial studies<sup>88</sup> and to more recent high-resolution TEM investigations.<sup>92,93</sup> In addition to studying the RuO<sub>2</sub>/Si interface, Green *et al.*<sup>88</sup> analyzed Ru/SiO<sub>2</sub> interfaces by AES depth-profiling, TEM, and RBS and reported that they were also reaction-free. These two experimental results are contradictory in that they simultaneously imply stable RuO<sub>2</sub>-Si and Ru-SiO<sub>2</sub> tie-lines, an impossibility since it would require the crossing of tie-lines and thus violate the Gibbs phase rule. In contrast to the above experimental results, a thin (~3 nm) SiO<sub>2</sub> layer, undetected by the comparatively

low-resolution interface characterization methods mentioned above, was revealed by high-resolution TEM at the RuO<sub>2</sub>/Si interface.<sup>92,93</sup> It was present in the as-deposited polycrystalline RuO<sub>2</sub> films grown on silicon substrates and did not change appreciably in thickness after annealing these samples at temperatures between 723 K and 973 K.<sup>92,93</sup> In addition to the thin SiO<sub>2</sub> layer, Charai *et al.*<sup>93</sup> also observed Ru<sub>2</sub>Si precipitates at the RuO<sub>2</sub>/Si interface and interpreted their results to indicate that the reaction  $3\text{Si} + 2\text{RuO}_2 \rightarrow \text{Ru}_2\text{Si} + 2\text{SiO}_2$  [i.e., Eq. (2)] is favorable at 773 K. The presence of this reaction layer is in agreement with our thermodynamic calculations as well as prior thermodynamic calculations predicting Ru-SiO<sub>2</sub> to be the stable tie-line<sup>53</sup> in this system.

The reason that early experimental investigations did not reveal the presence of reaction products is due to the small size of the reaction products compared to the resolution of the interface analysis techniques utilized. At the relatively low reaction temperatures used, the interface reaction is not extensive.

### 15. IrO<sub>2</sub>/Si

Using secondary ion mass spectrometry (SIMS) and x-ray diffraction, Nakamura *et al.*<sup>94</sup> concluded that the interface between polycrystalline silicon and polycrystalline IrO<sub>2</sub> is nonreactive at processing temperatures up to 1073 K. Our thermodynamic calculations lead to the opposite conclusion; IrO<sub>2</sub> fails ( $\Delta G < 0$ ) Eq. (1). Unfortunately, in the SIMS analysis presented by Nakamura *et al.*<sup>94</sup> the IrO<sub>2</sub>/Si interface occurred at about 0.6  $\mu\text{m}$  below the sample surface, lowering the resolution at which the interface was chemically profiled. They also reported electrical continuity between the IrO<sub>2</sub> layer and underlying silicon layer. However, interfacial reaction does not preclude electrical continuity. For example, if one of the reaction products forms a conductive percolation path between the underlying silicon and IrO<sub>2</sub>, or if the thickness of the insulating reactant(s) (e.g., SiO<sub>2</sub>) is very thin (increasing the probability of electron tunneling), continuity will still be observed. Prior thermodynamic calculations predict the Ir/SiO<sub>2</sub> interface to be stable,<sup>53</sup> which implies, in agreement with our calculations, that the IrO<sub>2</sub>/Si interface is thermodynamically unstable. Further experimental investigation, e.g., high-resolution TEM, is needed to resolve this discrepancy. Such studies would be enhanced by using higher reaction temperatures to increase the extent of the reaction layer, if one, and facilitate its detection and analysis.

### 16. Al<sub>2</sub>O<sub>3</sub>/Si

Silicon-on-sapphire is an extensively studied system.<sup>50,51,95</sup> Among other techniques, high-resolution

TEM has been used to probe the Si/Al<sub>2</sub>O<sub>3</sub> interface, revealing it to be abrupt and free of reaction layers.<sup>96</sup> Epitaxial Al<sub>2</sub>O<sub>3</sub> films on silicon substrates have also been prepared,<sup>97,98</sup> as have epitaxial Si/Al<sub>2</sub>O<sub>3</sub>/Si heterostructures.<sup>99</sup> The substrate temperatures used for the synthesis of these epitaxial interfaces range from 723 K to about 1423 K.<sup>50,97</sup> Although the thermodynamic calculations of this study could not be completed due to the lack of free energy data for Al<sub>1.90</sub>Si<sub>0.05</sub>O<sub>2.95</sub> and Al<sub>2</sub>Si<sub>4</sub>O<sub>10</sub>, the success by the above researchers in establishing reaction-free Al<sub>2</sub>O<sub>3</sub>/Si interfaces suggests that they are indeed thermodynamically compatible materials. Note that the well-known reaction between silicon and Al<sub>2</sub>O<sub>3</sub>, Al<sub>2</sub>O<sub>3</sub> + 2Si → 2SiO + Al<sub>2</sub>O,<sup>95,100</sup> is not relevant to this study because it involves gaseous products.

### 17. In<sub>2</sub>O<sub>3</sub>/Si

Although our thermodynamic calculations indicate that the In<sub>2</sub>O<sub>3</sub>/Si interface is thermodynamically unstable at 1000 K, initial studies of the interface between polycrystalline In<sub>2</sub>O<sub>3</sub> films and the underlying silicon substrate reported it to be reaction-free after processing at temperatures of 873 K<sup>101</sup> and 923 K.<sup>102</sup> This was likely due to the relatively low resolution of the AES depth-profiling,<sup>102</sup> RBS interface analysis,<sup>102</sup> and scanning transmission electron microscopy (STEM)<sup>101</sup> methods employed and the relatively low reaction temperatures. In contrast to these initial results, a high-resolution TEM study revealed the presence of a thin (3.5 nm to 5 nm) SiO<sub>2</sub> layer at the In<sub>2</sub>O<sub>3</sub>/Si interface both in as-deposited polycrystalline In<sub>2</sub>O<sub>3</sub> films on silicon and after annealing these films at 873 K.<sup>103</sup> This result is in agreement with our thermodynamic calculations.

## C. Discussion

An important practical result of our calculations is that there are not any conducting binary oxides that are thermodynamically stable in contact with silicon at 1000 K. In applications where it is desired to provide a stable electrical contact between an oxide electrode and the underlying silicon (e.g., in DRAM's incorporating high  $\epsilon_r$  materials), the most straightforward and processing-tolerant method for achieving such a contact would be to use a conductive oxide that is stable in contact with silicon. Since no such binary oxides exist, integration routes other than Si/conducting MO<sub>x</sub>/insulator will probably be needed to provide reliable conducting contacts. Potential examples include Si/MSi<sub>2</sub>/conducting MO<sub>x</sub>/insulator [where M is chosen from an appropriate "no phase dominant" system of the type shown in Fig. 1(b)] or Si/MSi<sub>z</sub>/MSi<sub>y</sub>/M/conducting MO<sub>x</sub>/insulator. This latter route involves moving from Si to MO<sub>x</sub> along the edges of the Si-M-O phase diagram triangle, a path

that traverses only conducting elements, silicides, and oxides. A thermodynamically stable contact scheme involves a sequence of layers, between each of which a tie-line exists; i.e., each interface is thermodynamically stable. Of course, even if reaction occurs, it is possible to maintain electrical conduction between the silicon overlying conducting oxide if, for example, one of the reaction products is conductive and forms a conductive path between the silicon and conductive oxide or if the thickness of the insulating reactants is thin enough to allow sufficient conduction by electron tunneling. But obtaining such a conductive path is very dependent on reaction kinetics, and puts limits on the tolerable processing conditions.

In those cases where the thermodynamic stability of a particular binary oxide in contact with silicon could not be assessed due to insufficient thermodynamic data, an alternative to determining the free energy of the relevant phase(s) is to perform bulk or thin-film experiments to determine key tie-lines in the M-Si-O phase diagram.<sup>13-16</sup> Conceptually the MO<sub>x</sub>/Si interface itself is the most relevant to study. However, experimental difficulties associated with this interface may make other interfaces more tractable. For example, the MO<sub>x</sub>/Si interface must be prepared using experimental conditions yielding silicon that is free of even a thin native oxide layer (i.e., SiO<sub>2</sub>) being brought into initial contact with the binary oxide. Another potential complication is that excess oxygen during the fabrication process can lead to oxidation of the silicon surface, even though the MO<sub>x</sub>/Si interface is stable, as has been observed for the CeO<sub>2-x</sub>/Si and YSZ/Si interfaces by TEM.<sup>1,75</sup>

For these reasons it is often experimentally more convenient to select a potential reaction other than that between MO<sub>x</sub> and silicon to determine the key tie-lines in the M-Si-O phase diagram. Regardless if one is using thermodynamic data or experimental methods, the relevant reaction to test is one lying at the crossing of two potential tie-lines. The thermodynamic stability of all of the binary oxides, except Sc<sub>2</sub>O<sub>3</sub>, remaining in Table VII in contact with silicon could be established if Eqs. (2), (5), and (6) were evaluated. A simple bulk or thin-film means to experimentally evaluate the tie-line addressed by Eqs. (2) and (5) is to see if MSi<sub>x</sub> is stable in contact with SiO<sub>2</sub> or MSi<sub>x</sub>O<sub>y</sub>. For example, MSi<sub>z</sub> could be oxidized and the interface examined to see if MSi<sub>z</sub> exists in contact with either SiO<sub>2</sub> or MSi<sub>x</sub>O<sub>y</sub>. Such an observation, as has been experimentally noted between SiO<sub>2</sub> and TiSi<sub>2</sub>,<sup>13,55</sup> V<sub>3</sub>Si,<sup>56</sup> and TaSi<sub>2</sub>,<sup>55,57</sup> indicates the existence of a stable tie-line between MSi<sub>z</sub> and SiO<sub>2</sub>, and consequently implies the absence of a stable Si-MO<sub>x</sub> tie-line. Similarly, Eq. (6) can be experimentally probed by depositing the metal M on the silicate MSi<sub>x</sub>O<sub>y</sub> and heating to see if a reaction takes place between these materials.

## V. EXTENSION OF APPROACH TO TERNARY OXIDES

A thermodynamic analysis of the type used here to test the stability of binary oxides in contact with silicon can be readily extended to ternary oxides. Below we apply it to the case of  $\text{SrTiO}_3$  in contact with silicon. Not only does sufficient data exist to show that  $\text{SrTiO}_3$  is thermodynamically unstable in contact with silicon at 1000 K, but this interface has also been extensively studied experimentally. However, the use of this method to comprehensively investigate ternary oxides with the goal of identifying candidate buffer layers for use between silicon and overlying oxides is precluded by the lack of thermodynamic data.

Any reaction between  $\text{SrTiO}_3$  and silicon with  $\Delta G < 0$  is sufficient to show that the  $\text{SrTiO}_3/\text{Si}$  interface is thermodynamically unstable. One such reaction is



with  $\Delta G_{1000}^{\circ} = -19.133 \text{ kcal/mol}$ .<sup>24,25</sup> Although this reaction may not be the most favorable of all possible reactions, its existence indicates that the  $\text{SrTiO}_3/\text{Si}$  interface is thermodynamically unstable at 1000 K. Several researchers have noted a reaction at the  $\text{SrTiO}_3/\text{Si}$  interface at substrate temperatures ranging from 473 K to 873 K.<sup>104–106</sup> This reaction interferes with the direct epitaxial growth of  $\text{SrTiO}_3$  on silicon.<sup>106–108</sup> One route leading to epitaxial  $\text{SrTiO}_3$  films on silicon substrates has employed an intermediate epitaxial  $\text{SrO}$  buffer layer.<sup>108</sup> This is an excellent example of how a stable binary oxide buffer layer can enable the successful integration of oxides with silicon, i.e.,  $\text{SrTiO}_3/\text{SrO}/\text{Si}$ .

A rule of thumb for choosing potential ternary or higher multicomponent oxides for direct integration with silicon is to choose those made of combinations of binary oxides that are all thermodynamically compatible with silicon.<sup>109</sup> Examples that follow this simple guide that have been experimentally demonstrated to be compatible with silicon are yttria-stabilized cubic zirconia ( $\text{Y}_2\text{O}_3-\text{ZrO}_2$ ),<sup>1,44–46,48,49,65,66,68,80,82–86</sup>  $(\text{Ba}, \text{Sr})\text{O}$ ,<sup>64,110</sup>  $\text{LaAlO}_3$ ,<sup>50,78</sup>  $\text{ZrSiO}_4$ ,<sup>50,78</sup>  $\text{Al}_2\text{BeO}_4$ ,<sup>58</sup> and  $\text{MgAl}_2\text{O}_4$ ,<sup>50,51,111–113</sup> whereas  $\text{SrTiO}_3$  is not since  $\text{TiO}_2$  is thermodynamically unstable in contact with silicon, as shown above.

## VI. CONCLUSIONS

Thermodynamic data indicate that  $\text{BeO}$ ,  $\text{MgO}$ , and  $\text{ZrO}_2$  are thermodynamically stable in contact with silicon at 1000 K. There are no thermodynamic data available to show that  $\text{Li}_2\text{O}$ , most of the alkaline earth oxides ( $\text{BeO}$ ,  $\text{MgO}$ ,  $\text{CaO}$ , and  $\text{SrO}$ ), the column IIIB oxides ( $\text{Sc}_2\text{O}_3$ ,  $\text{Y}_2\text{O}_3$ , and  $\text{Re}_2\text{O}_3$ , where  $\text{Re}$  is a rare earth),  $\text{ThO}_2$ ,  $\text{UO}_2$ ,  $\text{ZrO}_2$ ,  $\text{HfO}_2$ , and  $\text{Al}_2\text{O}_3$  are not thermodynamically stable in contact with silicon. Of these materials,  $\text{BeO}$ ,  $\text{MgO}$ ,

$\text{CaO}$ ,  $\text{SrO}$ ,  $\text{Y}_2\text{O}_3$ ,  $\text{Pr}_2\text{O}_3$ ,  $\text{Nd}_2\text{O}_3$ ,  $\text{ThO}_2$ ,  $\text{ZrO}_2$ , and  $\text{Al}_2\text{O}_3$  have been integrated with silicon and appear to be free of reaction layers. The remaining materials ( $\text{Li}_2\text{O}$ ,  $\text{Sc}_2\text{O}_3$ , most of the  $\text{Re}_2\text{O}_3$  oxides, and  $\text{HfO}_2$ ) are candidates for future experimental investigations. Note that all of these remaining binary oxides (both those determined to be compatible and those that are potentially compatible) are insulating materials, with  $\epsilon_r$  value ranging from 3.0 for  $\text{CaO}$  to 21 for  $\text{La}_2\text{O}_3$ .<sup>31</sup>

For the successful integration of oxide overlayers (e.g., high  $T_c$  superconductors, ferroelectrics, etc.) on top of the binary oxides identified in this study as being stable or potentially stable in contact with silicon, compatibility between the overlayer and the binary oxide is also necessary. Although such stability was not the subject of this study, the limited number of binary oxides identified as being compatible or potentially compatible with silicon greatly limits the possibilities for a single binary oxide interlayer between the desired overlayer and a silicon substrate.

## ACKNOWLEDGMENTS

We gratefully acknowledge Robby Beyers for stimulating discussions, Melissa Emery for double-checking all of the calculated values in the tables, and the financial support of ONR through contracts N00014-93-1-0512 and N00014-94-1-0690.

## REFERENCES

- D. B. Fenner, A. M. Viano, D. K. Fork, G. A. N. Connell, J. B. Boyce, F. A. Ponce,\* and J. C. Tramontana, *J. Appl. Phys.* **69**, 2176 (1991).
- C. Ziegler, F. Baudenbacher, H. Karl, H. Kinder, and W. Göpel, *Fresenius J. Anal. Chem.* **341**, 308 (1991).
- Y. Shichi, S. Tanimoto, T. Goto, K. Kuroiwa, and Y. Tarui, *Jpn. J. Appl. Phys.* **33**, 5172 (1994).
- M. Scheib, H. Goebel, L. Hofmann, B. Lengeler, H. Oechsner, and G. Zorn, *Thin Solid Films* **174**, 5 (1989).
- J. K. G. Panitz and C. C. Hu, *J. Vac. Sci. Technol.* **16**, 315 (1979).
- V. S. Dharmadhikari and W. W. Grannemann, *J. Vac. Sci. Technol. A* **1**, 483 (1983).
- A. Mogro-Campero, *Supercond. Sci. Technol.* **3**, 155 (1990).
- D. K. Fork, in *Pulsed Laser Deposition of Thin Films*, edited by D. B. Chrisey and G. K. Hubler (Wiley, New York, 1994), p. 393.
- E. J. Tarsa, K. L. McCormick, and J. S. Speck, in *Epitaxial Oxide Thin Films and Heterostructures*, edited by D. K. Fork, J. M. Phillips, R. Ramesh, and R. M. Wolf (Mater. Res. Soc. Symp. Proc. **341**, Pittsburgh, PA, 1994), p. 73.
- J. M. Phillips, *MRS Bulletin* **20**, 35 (April 1995); J. M. Phillips, to be published in *Processing and Properties of High  $T_c$  Superconductors, Volume 2: Thin Films*, edited by S. Jin and D. K. Christen (World Scientific).
- M. Gurvitch and A. T. Fiory, *Appl. Phys. Lett.* **51**, 1027 (1987).
- Q. X. Jia, K. L. Jiao, and W. A. Anderson, *J. Appl. Phys.* **70**, 3364 (1991).
- R. Beyers, *J. Appl. Phys.* **56**, 147 (1984).
- R. Beyers, R. Sinclair, and M. E. Thomas, *J. Vac. Sci. Technol. B* **2**, 781 (1984).

15. R. Beyers, K.B. Kim, and R. Sinclair, *J. Appl. Phys.* **61**, 2195 (1987).
16. R. Beyers, Ph.D. Thesis, Stanford University, 1989, pp. 38–76.
17. K.J. Hubbard, B.S. Thesis, The Pennsylvania State University, 1993.
18. Note that if the  $M\text{-Si-O}$  system contains more than one metal-silicide phase, there will be several phase diagram possibilities within the “no phase dominant” type; if the system contains no metal-silicide phases, there will not be a “no phase dominant” type.
19. Of all the silicides, only the most silicon-rich ( $MSi_2$ ) lies on a tie-line between  $MSi_2$  and  $SiO_2$  in *all* of the possible no phase dominant phase diagrams, making the preference of this tie-line or the one between silicon and  $MO_x$ , Eq. (2), the critical test of metal oxide dominant versus no phase dominant.
20. Of all the silicides, only the most silicon-rich ( $MSi_2$ ) lies on a tie-line between  $MSi_2$  and  $MO_x$  in *all* of the possible  $MO_x$  dominant type (see Fig. 3) phase diagrams, making the preference of this tie-line or the one between silicon and  $MO_w$ , Eq. (4), the critical test of  $MO_x$  and  $MO_w$  dominant versus  $MO_x$  dominant.
21. Note that if the  $M\text{-Si-O}$  system contains more than one metal-silicide phase, there will be several phase diagram possibilities within the  $MO_x$  dominant type (see Fig. 3); if the system contains no metal-silicide phases, there will not be a  $MO_x$  dominant type.
22. These are the potential compatibility triangles that would accompany a tie-line between silicon and  $MO_x$ . The ternary phases lying on these compatibility triangles are the only ones relevant to the existence of the tie-line being tested by Eqs. (5), (6), and (7).
23. If a tie-line between silicon and  $MO_x$  does not exist, a tie-line from the relevant  $MSi_xO_y$  phase(s) that crosses the silicon– $MO_x$  tie-line position must exist. Such a tie-line must connect with either  $M$  or  $MSi_2$  since a  $MSi_2\text{-SiO}_2$  tie-line is known not to exist [in order to reach Eq. (5),  $\Delta G$  had to be positive for Eq. (2)].
24. I. Barin and O. Knacke, *Thermochemical Properties of Inorganic Substances* (Springer-Verlag, Berlin, 1973).
25. I. Barin, O. Knacke, and O. Kubaschewski, *Thermochemical Properties of Inorganic Substances, Supplement* (Springer-Verlag, Berlin, 1977).
26. *Thermodynamic Properties of Elements and Oxides* (United States Bureau of Mines Bulletin 672, U.S. Government Printing Office, Washington, DC, 1982).
27. G.M. Lukashenko, R.I. Polotskaya, and V.R. Sidorko, *J. Alloys Compd.* **179**, 299 (1992).
28. See, for example, R.E. Dickerson, *Molecular Thermodynamics* (Benjamin/Cummings, Menlo Park, 1969).
29. *Powder Diffraction File: Inorganic Phases* (JCPDS International Centre for Diffraction Data, Swarthmore, PA, 1992).
30. *CRC Handbook of Chemistry and Physics*, 71st ed. (CRC Press, Cleveland, OH, 1990/91).
31. *The Oxide Handbook*, 2nd ed., edited by G.V. Samsonov (IFI/Plenum, New York, 1982).
32. *Landolt-Börnstein: Numerical Data and Functional Relationships in Science and Technology, New Series*, Group III, Vol. 7b, edited by K.H. Hellwege (Springer-Verlag, Berlin, 1975), p. 456.
33. W.J. Kramers and J.R. Smith, *Trans. Brit. Ceram. Soc.* **56**, 590 (1957).
34. *Landolt-Börnstein: Numerical Data and Functional Relationships in Science and Technology, New Series*, Group III, Vol. 27g, edited by O. Madelung (Springer-Verlag, Berlin, 1992), p. 4.
35. G. Brauer, H. Reuther, H. Walz, and K.H. Zapp, *Z. Anorg. Allg. Chem.* **369**, 144 (1969).
36. G. Natta and M. Strada, *Gazzetta Chimica Italiana* **58**, 419 (1928).
37. O. Muller and R. Roy, *J. Less-Common Met.* **16**, 129 (1968).
38. A. Ourmazd, D.W. Taylor, J.A. Rentschler, and J. Bevk, *Phys. Rev. Lett.* **59**, 213 (1987).
39. E.I. Givargizov, *Oriented Crystallization on Amorphous Substrates* (Plenum Press, New York, 1991).
40. R.P. Reade, P. Berdahl, R.E. Russo, and L.W. Schaper, *Appl. Phys. Lett.* **66**, 2001 (1995).
41. H.J. Goldschmidt, *Interstitial Alloys* (Plenum Press, New York, 1967), p. 296.
42. H. Mori and H. Ishiwara, *Jpn. J. Appl. Phys.* **30**, L1415 (1991); H. Ishiwara, H. Mori, K. Jyokyu, and S. Ueno, in *Silicon Molecular Beam Epitaxy*, edited by J.C. Bean, S.S. Iyer, and K.L. Wang (Mater. Res. Soc. Symp. Proc. **220**, Pittsburgh, PA, 1991), p. 595; H. Ishiwara, N. Tsuji, H. Mori, and H. Nohira, *Appl. Phys. Lett.* **61**, 1459 (1992).
43. R.A. McKee, F.J. Walker, J.R. Conner, E.D. Specht, and D.E. Zelmon, *Appl. Phys. Lett.* **59**, 782 (1991); R.A. McKee, F.J. Walker, J.R. Conner, and R. Raj, *Appl. Phys. Lett.* **63**, 2818 (1993).
44. H. Behner, J. Wecker, Th. Matthée, and K. Samwer, *Surf. Interface Anal.* **18**, 685 (1992).
45. Th. Matthée, J. Wecker, H. Behner, G. Friedl, O. Eibl, and K. Samwer, *Appl. Phys. Lett.* **61**, 1240 (1992).
46. A. Bardal, O. Eibl, Th. Matthée, G. Friedl, and J. Wecker, *J. Mater. Res.* **8**, 2112 (1993).
47. S.I. Krasnosvobodtsev and E.V. Pechen, *Physica C* **185–189**, 2097 (1991).
48. H. Behner, J. Wecker, and B. Heines, in *High  $T_c$  Superconductor Thin Films*, edited by L. Correra (North-Holland, Amsterdam, 1992), p. 623.
49. E.V. Pechen, R. Schoenberger, B. Brunner, S. Ritzinger, K.F. Renk, M.V. Sidorov, and S.R. Oktyabrsky, *J. Appl. Phys.* **74**, 3614 (1993).
50. J.D. Filby and S. Nielsen, *Br. J. Appl. Phys.* **18**, 1357 (1967).
51. H.M. Manasevit, *J. Cryst. Growth* **22**, 125 (1974).
52. The growth of  $HfO_2$  layers on silicon has been reported by R. de Reus, F.W. Saris, G.J. van der Kolk, C. Witmer, B. Dam, D.H.A. Blank, D.J. Adelerhof, and J. Flokstra, *Mater. Sci. Engr. B* **7**, 135 (1990). From RBS analyses, these researchers report  $HfO_2$  to be inert in contact with silicon at temperatures up to 1073 K. However, as in many reports of the deposition of oxides on silicon, no mention is given in this work of the method used to remove the native oxide from the (100) Si wafer prior to growth. It is thus likely that the stable interfaces studied were actually  $HfO_2/SiO_2/Si$ , which does not indicate whether the  $HfO_2/Si$  interface is stable or unstable. It is for this same reason that other reports of the growth of binary oxides on silicon, in which the removal of the native oxide prior to growth is unclear, are not considered in our comparisons.
53. R. Pretorius, J.M. Harris, and M-A. Nicolet, *Solid-State Electron.* **21**, 667 (1978).
54. D.M. Brown, W.E. Engeler, M. Garfinkel, and P.V. Gray, *Solid-State Electron.* **11**, 1105 (1968).
55. S.P. Murarka, *J. Vac. Sci. Technol.* **17**, 775 (1980); S.P. Murarka, *Silicides for VLSI Applications* (Academic Press, New York, 1983), pp. 138–140.
56. K.E. Spear, P.W. Gilles, and H. Schäfer, *J. Less-Common Met.* **14**, 69 (1968).
57. S.P. Murarka, D.B. Fraser, W.S. Lindenberger, and A.K. Sinha, *J. Appl. Phys.* **51**, 3241 (1980).
58. H.M. Manasevit, D.H. Forbes, and I.B. Cadoff, *Trans. Metall. Soc. AIME* **236**, 275 (1966).
59. D.K. Fork, F.A. Ponce, J.C. Tramontana, and T.H. Geballe, *Appl. Phys. Lett.* **58**, 2294 (1991).
60. P. Tiwari, S. Sharan, and J. Narayan, *J. Appl. Phys.* **69**, 8358 (1991).
61. S.H. Rou, T.M. Graettinger, A.F. Chow, C.N. Soble, II, D.J. Lichtenwalner, O. Auciello, and A.I. Kingon, in *Ferroelectric*

- Thin Films II*, edited by A. I. Kingon, E. R. Myers, and B. Tuttle (Mater. Res. Soc. Symp. Proc. 243, Pittsburgh, PA, 1992), p. 81.
62. G. Soerensen and S. Gygax, *Physica B* **169**, 673 (1991).
  63. Y. Kado and Y. Arita, *J. Appl. Phys.* **61**, 2398 (1987); Y. Kado and Y. Arita, in *Extended Abstracts of the 18th (1986 International) Conference on Solid State Devices and Materials* (Tokyo, 1986), p. 45.
  64. Y. Kado and Y. Arita, in *Extended Abstracts of the 20th (1988 International) Conference on Solid State Devices and Materials* (Tokyo, 1988), p. 181.
  65. H. Fukumoto, T. Imura, and Y. Osaka, *Appl. Phys. Lett.* **55**, 360 (1989).
  66. H. Fukumoto, M. Yamamoto, and Y. Osaka, *Proc. Electrochem. Soc.* **90**, 239 (1990).
  67. K. Harada, H. Nakanishi, H. Itozaki, and S. Yazu, *Jpn. J. Appl. Phys.* **30**, 934 (1991).
  68. M. Yamamoto, H. Fukumoto, and Y. Osaka, in *Heteroepitaxy of Dissimilar Materials*, edited by R. F. C. Farrow, J. P. Harbison, P. S. Peercy, and A. Zangwill (Mater. Res. Soc. Symp. Proc. 221, Pittsburgh, PA, 1991), p. 35.
  69. T. Inoue, Y. Yamamoto, S. Koyama, S. Suzuki, and Y. Ueda, *Appl. Phys. Lett.* **56**, 1332 (1990); T. Inoue, M. Osonoe, H. Tohda, M. Hiramatsu, Y. Yamamoto, A. Yamanaka, and T. Nakayama, *J. Appl. Phys.* **69**, 8313 (1991); L. Luo, X. D. Wu, R. C. Dye, R. E. Muenchhausen, S. R. Folty, Y. Coulter, C. J. Maggiore, and T. Inoue, *Appl. Phys. Lett.* **59**, 2043 (1991); T. Inoue, T. Ohsuna, L. Luo, X. D. Wu, C. J. Maggiore, Y. Yamamoto, Y. Sakurai, and J. H. Chang, *Appl. Phys. Lett.* **59**, 3604 (1991); T. Inoue, T. Ohsuna, Y. Yamada, K. Wakamatsu, Y. Itoh, T. Nozawa, E. Sasaki, Y. Yamamoto, and Y. Sakurai, *Jpn. J. Appl. Phys.* **31**, L1736 (1992); Y. Yamamoto, M. Satoh, Y. Sakurai, S. Nakajima, T. Inoue, and T. Ohsuna, *Jpn. J. Appl. Phys.* **32**, L620 (1993).
  70. M. Yoshimoto, H. Nagata, T. Tsukahara, and H. Koinuma, *Jpn. J. Appl. Phys.* **29**, L1199 (1990); H. Nagata, M. Yoshimoto, H. Koinuma, E. Min, and N. Haga, *J. Cryst. Growth* **123**, 1 (1992); M. Yoshimoto, K. Shimozono, T. Maeda, T. Ohnishi, M. Kumagai, T. Chikyow, O. Ishiyama, M. Shinohara, and H. Koinuma, *Jpn. J. Appl. Phys.* **34**, L688 (1995).
  71. H. Nagata, M. Yoshimoto, T. Tsukahara, S. Gonda, and H. Koinuma, in *Evolution of Thin-Film and Surface Microstructure*, edited by C. V. Thompson, J. Y. Tsao, and D. J. Srolovitz (Mater. Res. Soc. Symp. Proc. 202, Pittsburgh, PA, 1991), p. 445.
  72. H. Koinuma, H. Nagata, T. Tsukahara, S. Gonda, and M. Yoshimoto, *Appl. Phys. Lett.* **58**, 2027 (1991).
  73. T. Chikyow, S. M. Bedair, L. Tye, and N. A. El-Masry, *Appl. Phys. Lett.* **65**, 1030 (1994); L. Tye, T. Chikyow, N. A. El-Masry, and S. M. Bedair, in *Epitaxial Oxide Thin Films and Heterostructures*, edited by D. K. Fork, J. M. Phillips, R. Ramesh, and R. M. Wolf (Mater. Res. Soc. Symp. Proc. 341, Pittsburgh, PA, 1994), p. 107; L. Tye, N. A. El-Masry, T. Chikyow, P. McLarty, and S. M. Bedair, *Appl. Phys. Lett.* **65**, 3081 (1994).
  74. The approximate error stated is calculated from the "B" quality data for  $\text{SiO}_2$ , the "B-C" quality data for  $\text{CeO}_2$ , and the "C" quality data for  $\text{CeSi}_2$  given in Ref. 24 and 25.
  75. T. Inoue, T. Ohsuna, Y. Obara, Y. Yamamoto, M. Satoh, and Y. Sakurai, *Jpn. J. Appl. Phys.* **32**, 1765 (1993).
  76. D. K. Fork, D. B. Fenner, and T. H. Geballe, *J. Appl. Phys.* **68**, 4316 (1990).
  77. E. J. Tarsa, J. S. Speck, and McD. Robinson, *Appl. Phys. Lett.* **63**, 539 (1993).
  78. T. L. Chu, M. H. Francombe, G. A. Gruber, J. J. Oberly, and R. L. Tallman, *Deposition of Silicon on Insulating Substrates*, Report No. AFCRL-65-574 (Westinghouse Research Laboratories, Pittsburgh, PA, 1965). See especially pp. 31–34 and pp. 41–44. (NTIS ID No. AD-619 992).
  79. M. Morita, H. Fukumoto, T. Imura, Y. Osaka, and M. Ichihara, *J. Appl. Phys.* **58**, 2407 (1985); Y. Osaka, T. Imura, Y. Nishibayashi, and F. Nishiyama, *J. Appl. Phys.* **63**, 581 (1988).
  80. H. Myoren, Y. Nishiyama, H. Fukumoto, H. Nasu, and Y. Osaka, *Jpn. J. Appl. Phys.* **28**, 351 (1989).
  81. A. Lubig, Ch. Buchal, J. Schubert, C. Copetti, D. Guggi, C. L. Jia, and B. Stritzker, *J. Appl. Phys.* **71**, 5560 (1992); A. Lubig, Ch. Buchal, D. Guggi, C. L. Jia, and B. Stritzker, *Thin Solid Films* **217**, 125 (1992).
  82. I. Golecki, H. M. Manasevit, L. A. Moudy, J. J. Yang, and J. E. Mee, *Appl. Phys. Lett.* **42**, 501 (1983); H. M. Manasevit, I. Golecki, L. A. Moudy, J. J. Yang, and J. E. Mee, *J. Electrochem. Soc.* **130**, 1752 (1983); A. L. Lin, and I. Golecki, *J. Electrochem. Soc.* **132**, 239 (1985).
  83. P. Legagneux, G. Garry, D. Dieumegard, C. Schwebel, C. Pellet, G. Gautherin, and J. Siejka, *Appl. Phys. Lett.* **53**, 1506 (1988).
  84. H. Fukumoto, T. Imura, and Y. Osaka, *Jpn. J. Appl. Phys.* **27**, L1404 (1988); H. Fukumoto, M. Yamamoto, Y. Osaka, and F. Nishiyama, *J. Appl. Phys.* **67**, 2447 (1990); H. Fukumoto, M. Yamamoto, and Y. Osaka, *J. Appl. Phys.* **69**, 8130 (1991).
  85. D. K. Fork, D. B. Fenner, G. A. N. Connell, J. M. Phillips, and T. H. Geballe, *Appl. Phys. Lett.* **57**, 1137 (1990); D. K. Fork, D. B. Fenner, R. W. Barton, J. M. Phillips, G. A. N. Connell, J. B. Boyce, and T. H. Geballe, *Appl. Phys. Lett.* **57**, 1161 (1990); D. K. Fork, F. A. Ponce, J. C. Tramontana, N. Newman, J. M. Phillips, and T. H. Geballe, *Appl. Phys. Lett.* **58**, 2432 (1991).
  86. W. Pursseit, S. Corsépius, M. Zwerger, P. Berberich, H. Kinder, O. Eibl, C. Jaekel, U. Breuer, and H. Kurz, *Physica C* **201**, 249 (1992).
  87. S. P. Murarka and C. C. Chang, *Appl. Phys. Lett.* **37**, 639 (1980).
  88. M. L. Green, M. E. Gross, L. E. Papa, K. J. Schnoes, and D. Brasen, *J. Electrochem. Soc.* **132**, 2677 (1985).
  89. Q. X. Jia and W. A. Anderson, *Appl. Phys. Lett.* **57**, 304 (1990).
  90. E. Kolawa, F. C. T. So, E. T-S. Pan, and M-A. Nicolet, *Appl. Phys. Lett.* **50**, 854 (1987).
  91. L. Krusin-Elbaum, M. Wittmer, and D. S. Yee, *Appl. Phys. Lett.* **50**, 1879 (1987).
  92. C. W. Nieh, E. Kolawa, F. C. T. So, and M-A. Nicolet, *Mater. Lett.* **6**, 177 (1988).
  93. A. Charai, S. E. Hörnström, O. Thomas, P. M. Fryer, and J. M. E. Harper, *J. Vac. Sci. Technol. A* **7**, 784 (1989).
  94. T. Nakamura, Y. Nakao, A. Kamisawa, and H. Takasu, *Appl. Phys. Lett.* **65**, 1522 (1994); T. Nakamura, Y. Nakao, A. Kamisawa, and H. Takasu, *Jpn. J. Appl. Phys.* **33**, 5207 (1994).
  95. H. M. Manasevit and W. J. Simpson, *J. Appl. Phys.* **35**, 1349 (1964); H. M. Manasevit, A. Miller, F. L. Morritz, and R. Nolder, *Trans. Metall. Soc. AIME* **233**, 540 (1965).
  96. F. A. Ponce, *Appl. Phys. Lett.* **41**, 371 (1982).
  97. M. Ishida, I. Katakabe, T. Nakamura, and N. Ohtake, *Appl. Phys. Lett.* **52**, 1326 (1988); K. Sawada, M. Ishida, T. Nakamura, and N. Ohtake, *Appl. Phys. Lett.* **52**, 1672 (1988); K. Sawada, M. Ishida, T. Nakamura, and T. Suzuki, *J. Cryst. Growth* **95**, 494 (1989).
  98. H. Iizuka, K. Yokoo, and S. Ono, *Appl. Phys. Lett.* **61**, 2978 (1992).
  99. M. Ishida, K. Sawada, S. Yamaguchi, T. Nakamura, and T. Suzuki, *Appl. Phys. Lett.* **55**, 556 (1989); M. Ishida, S. Yamaguchi, Y. Masa, T. Nakamura, and Y. Hikita, *J. Appl. Phys.* **69**, 8408 (1991).
  100. G. Grube, A. Schneider, U. Esch, and M. Flad, *Z. Anorg. Chem.* **260**, 120 (1949).

101. E. Kolawa, C. Garland, L. Tran, C. W. Nieh, J. M. Molarius, W. Flick, M-A. Nicolet, and J. Wei, *Appl. Phys. Lett.* **53**, 2644 (1988).
102. Y. Zeng, Z. Zhang, W. Luo, N. Yang, Y. Cai, Z. Hua, and X. Shen, *Thin Solid Films* **214**, 235 (1992); Z. Zhang, Y. Zeng, W. Lou, Y. Cai, Y. Sun, Z-Y. Hua, and X. Shen, *Vacuum* **43**, 1033 (1992).
103. E. Kolawa, C. W. Nieh, J. M. Molarius, L. Tran, C. Garland, W. Flick, M-A. Nicolet, F. C. T. So, and J. C. S. Wei, *Thin Solid Films* **166**, 15 (1988).
104. W. B. Pennebaker, *IBM J. Res. Develop.* **13**, 686 (Nov. 1969).
105. S. Matsubara, T. Sakuma, S. Yamamichi, H. Yamaguchi, and Y. Miyasaka, in *Ferroelectric Thin Films*, edited by E. R. Myers and A. I. Kingon (Mater. Res. Soc. Symp. Proc. **200**, Pittsburgh, PA, 1990), p. 243; T. Sakuma, S. Yamamichi, S. Matsubara, H. Yamaguchi, and Y. Miyasaka, *Appl. Phys. Lett.* **57**, 2431 (1990); H. Yamaguchi, S. Matsubara, and Y. Miyasaka, *Jpn. J. Appl. Phys.* **30**, 2197 (1991).
106. H. Nagata, T. Tsukahara, S. Gonda, M. Yoshimoto, and H. Koinuma, *Jpn. J. Appl. Phys.* **30**, L1136 (1991).
107. H. Ishiwara and K. Azuma, in *Heteroepitaxy on Silicon; Fundamentals, Structure, and Devices*, edited by H. K. Choi, R. Hull, H. Ishiwara, and R. J. Nemanich (Mater. Res. Soc. Symp. Proc. **116**, Pittsburgh, PA, 1988), p. 369.
108. H. Mori, and H. Ishiwara, *Jpn. J. Appl. Phys.* **30**, L1415 (1991); H. Ishiwara, H. Mori, K. Jyoky, and S. Ueno, in *Silicon Molecular Beam Epitaxy*, edited by J. C. Bean, S. S. Iyer, and K. L. Wang (Mater. Res. Soc. Symp. Proc. **220**, Pittsburgh, PA, 1991), p. 595.
109. Since the free energy of the ternary or higher, multicomponent oxide must be lower than its binary constituents in order for it to form, and the binary constituents selected are individually compatible with silicon, the only potential reactions with silicon (i.e., where  $\Delta G < 0$ ) involve ternary or higher, multicomponent products (e.g.,  $MM'_xO_z$ ,  $MM'_xSi_y$ , or  $MM'_xSi_yO_z$  phases). Although this greatly reduces the number of reactions that need to be tested to establish thermodynamic stability, thermodynamic data for these relevant multicomponent materials are often lacking.
110. Y. Kado and Y. Arita, in *Extended Abstracts of the 21st Conference on Solid State Devices and Materials* (Tokyo, 1989), p. 45.
111. H. M. Manasevit and D. H. Forbes, *J. Appl. Phys.* **37**, 734 (1966).
112. H. Seiter and Ch. Zaminer, *Z. Angew Phys.* **20**, 158 (1965).
113. M. Ihara, Y. Arimoto, M. Jifuku, T. Kimura, S. Kodama, H. Yamawaki, and T. Yamaoka, *J. Electrochem. Soc.* **129**, 2569 (1982); M. Ihara, *Microelectron. Eng.* **1**, 161 (1983).

## APPENDIX: TERNARY PHASE DIAGRAMS

The construction of phase diagrams must be in accordance with the Gibbs phase rule:<sup>28</sup>

$$f = c + 2 - p, \quad (11)$$

where  $f$  is the number of degrees of freedom (number of independent intensive variables),  $c$  is the number of components in the system (i.e., the minimum number of independent constituents sufficient to form all the phases in the phase diagram), and  $p$  is the number of phases in equilibrium. This phase rule is readily deduced by subtracting the total number of independent equations involving the intensive variables from the total number of intensive variables.

The three-component phase diagrams,  $M\text{-Si}\text{-O}$ , considered in this paper are all at fixed temperature and pressure. With these two intensive variables fixed, the Gibbs phase rule implies that the maximum number (i.e., when  $f = 0$ ) of phases that can coexist in equilibrium is three. Consequently,  $M\text{-Si}\text{-O}$  phase diagrams are constrained to contain only one, two, and at most three-phase regions. A one-phase region exists at the vertex of any of the triangles within the phase diagram; a two-phase region exists on any tie-line; and the interior to any triangle is a three-phase region. Crossing tie-lines are not allowed because at the point of their intersection the simultaneous coexistence of four phases (two from each tie-line) would be implied, whereas a maximum of three phases in coexistence is mandated by the Gibbs phase rule.

## Origin of the $\phi \sim \pm 9^\circ$ peaks in $\text{YBa}_2\text{Cu}_3\text{O}_{7-\delta}$ films grown on cubic zirconia substrates

D. G. Schlom

*Department of Materials Science and Engineering, The Pennsylvania State University, University Park, Pennsylvania 16802-5005*

E. S. Hellman, E. H. Hartford, Jr., and C. B. Eom<sup>a)</sup>

*AT&T Bell Laboratories, Murray Hill, New Jersey 07974-0636*

J. C. Clark

*Department of Materials Science and Engineering, The Pennsylvania State University, University Park, Pennsylvania 16802-5005*

J. Mannhart

*IBM Research Division, Zurich Research Laboratory, CH-8803 Rüschlikon, Switzerland*

(Received 26 September 1995; accepted 3 January 1996)

The *c*-axis oriented  $\text{YBa}_2\text{Cu}_3\text{O}_{7-\delta}$  films grown on (001) yttria-stabilized cubic zirconia (YSZ) substrates often contain domains whose in-plane alignment is rotated approximately  $9^\circ$  from the cube-on-cube epitaxial relationship, in addition to the more commonly observed  $0^\circ$  and  $45^\circ$  in-plane rotations. We have investigated the origin of this  $\sim 9^\circ$  orientation using *in situ* electron diffraction during growth and *ex situ* 4-circle x-ray diffraction. Our results indicate that the  $\sim 9^\circ$  orientation provides the most favorable lattice match between the interfacial (110)-oriented  $\text{BaZrO}_3$  epitaxial reaction layer, which forms between  $\text{YBa}_2\text{Cu}_3\text{O}_{7-\delta}$  and the YSZ substrate. If epitaxy occurs directly between  $\text{YBa}_2\text{Cu}_3\text{O}_{7-\delta}$  and the YSZ substrate, i.e., before the  $\text{BaZrO}_3$  epitaxial reaction layer is formed, the  $0^\circ$  and  $45^\circ$  domains have the most favorable lattice match. However, growth conditions that favor the formation of the  $\text{BaZrO}_3$  reaction layer prior to the nucleation of  $\text{YBa}_2\text{Cu}_3\text{O}_{7-\delta}$  lead to an increase in  $\sim 9^\circ$  domains. The observed phenomenon, which results from epitaxial alignment between the diagonal of a square surface net and the diagonal of a rectangular surface net, is a general method for producing in-plane misorientations, and has also been observed for the heteroepitaxial growth of other materials, including (Ba, K) $\text{BiO}_3$ /LaAlO<sub>3</sub>. The  $\text{YBa}_2\text{Cu}_3\text{O}_{7-\delta}$ /YSZ case involves epitaxial alignment between  $[\bar{1}11]_{\text{BaZrO}_3}$  and  $[110]_{\text{YSZ}}$ , resulting in an expected in-plane rotation of  $11.3^\circ$  to  $9.7^\circ$  for fully commensurate and for fully relaxed  $(110)_{\text{BaZrO}_3}$  on  $(001)_{\text{YSZ}}$ , respectively.

### I. INTRODUCTION

Controlling the types and locations of grain boundaries between single crystals is not only useful for developing a detailed understanding of the effects of grain boundaries on the physical properties of a material, but in many instances it is useful for device purposes. Grain boundaries lie at the heart of many electroceramic devices, e.g., varistors, positive temperature coefficient (PTC) thermistors and internal-barrier-layer capacitors.<sup>1</sup> They influence the motion of domain boundaries in ferroelectrics and disrupt superconductivity in oxide superconductors, causing "weak links" and Josephson junctions. The ability to introduce grain boundaries of chosen

orientation at specific locations into epitaxial oxide films is thus very important for microelectronic applications. One example of grain boundary engineering is the "bi-epitaxy" process used to introduce  $45^\circ$  grain boundaries into epitaxial oxide superconductor films.<sup>2,3</sup> This process has been utilized to make superconducting quantum-interference devices (SQUID's).<sup>4</sup>

Just as it is important to engineer the location and orientation of introduced-grain boundaries, it is vital for many device applications to have the remaining regions free of grain boundaries. It is for these reasons that we studied the origin of the  $\phi \sim 9^\circ$  peaks observed<sup>5-11</sup> in x-ray diffraction studies of epitaxial films of  $\text{YBa}_2\text{Cu}_3\text{O}_{7-\delta}$  grown with their *c*-axis aligned normal to the plane of the (001) yttria-stabilized cubic zirconia (YSZ) substrates (*c*-axis oriented  $\text{YBa}_2\text{Cu}_3\text{O}_{7-\delta}$  films). Four-circle x-ray diffraction is often used to characterize the

<sup>a)</sup>Present address: Department of Mechanical Engineering and Materials Science, Duke University, Durham, North Carolina 27708-0300.

in-plane orientation of films. X-ray diffraction peaks at  $\phi \sim 9^\circ$  signify grain boundaries that, in their present uncontrolled state, are unwanted as they degrade the critical current density and microwave surface resistance of the superconducting  $\text{YBa}_2\text{Cu}_3\text{O}_{7-\delta}$  film.<sup>6,9,12-14</sup> If understood and controllable, these  $\sim 9^\circ$  boundaries (and  $45^\circ - 9^\circ = 36^\circ$  grain boundaries) would be a significant improvement over  $45^\circ$  bi-epitaxy boundaries for many applications because of the higher critical current densities of the Josephson junctions formed at these lower-angle boundaries.

## II. BACKGROUND

To clarify the lattice match discussions that follow, the crystal structures of  $\text{YBa}_2\text{Cu}_3\text{O}_{7-\delta}$ , YSZ, and  $\text{BaZrO}_3$  are shown in Fig. 1 and their lattice parameters are given in Table I.  $\text{YBa}_2\text{Cu}_3\text{O}_{7-\delta}$  has a layered perovskite-related structure, YSZ has the fluorite structure, and  $\text{BaZrO}_3$  is a simple-cubic perovskite.

Multiple in-plane orientations have been reported in *c*-axis oriented  $\text{YBa}_2\text{Cu}_3\text{O}_{7-\delta}$  films grown on (001)

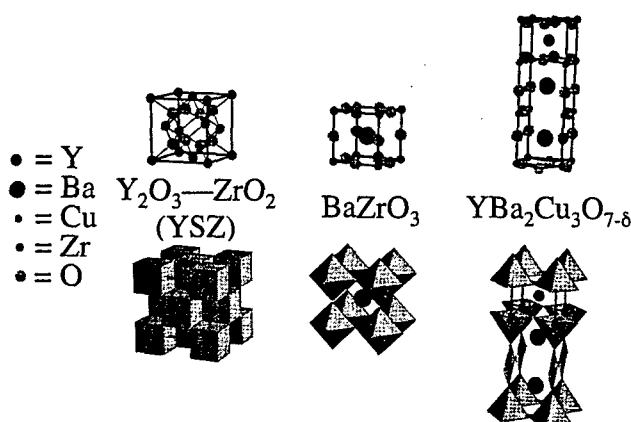


FIG. 1. The crystal structures of YSZ,  $\text{BaZrO}_3$ , and  $\text{YBa}_2\text{Cu}_3\text{O}_{7-\delta}$ . Two equivalent representations of these crystal structures are shown: the atomic positions (above) and the coordination polyhedra (below). The oxygen atoms occupy the vertices of the coordination polyhedra. The relative sizes of the atoms reflect their relative ionic radii, as given by Ref. 15. The origins of the unit cells have been chosen to illustrate the similarities between the structures.

TABLE I. Lattice constants of YSZ,  $\text{BaZrO}_3$ , and  $\text{YBa}_2\text{Cu}_3\text{O}_{7-\delta}$ .

Material	Lattice constant(s) at 25 °C (Å)	Space group	Reference
$(\text{Y}_2\text{O}_3)_x(\text{ZrO}_2)_{1-x}$ (YSZ) ( $x \approx 0.095$ )	$a = 5.140$	$Fm\bar{3}m$	16
$\text{BaZrO}_3$	$a = 4.193$	$Pm\bar{3}m$	17
$\text{YBa}_2\text{Cu}_3\text{O}_{7-\delta}$ ( $\delta \approx 0$ )	$a = 3.820$ $b = 3.885$ $c = 11.68$	$Pmmm$	18
$\text{YBa}_2\text{Cu}_3\text{O}_{7-\delta}$ ( $\delta \approx 1$ )	$a = 3.857$ $c = 11.82$	$P4/mmm$	18

YSZ substrates.<sup>3,5-11,14,19,20</sup> The most common orientations observed are rotated  $0^\circ$  and  $45^\circ$  from the cube-on-cube orientation relationship. Specifically, the  $0^\circ$  in-plane rotation from cube-on-cube refers to

$$(001)_{\text{YBa}_2\text{Cu}_3\text{O}_{7-\delta}} \parallel (001)_{\text{YSZ}}$$

$$\text{and } [100]_{\text{YBa}_2\text{Cu}_3\text{O}_{7-\delta}} \parallel [100]_{\text{YSZ}},$$

and the  $45^\circ$  in-plane rotation denotes

$$(001)_{\text{YBa}_2\text{Cu}_3\text{O}_{7-\delta}} \parallel (001)_{\text{YSZ}}$$

$$\text{and } [110]_{\text{YBa}_2\text{Cu}_3\text{O}_{7-\delta}} \parallel [100]_{\text{YSZ}}.$$

The  $45^\circ$  in-plane rotation is typically dominant in films grown at lower substrate temperatures, while the  $0^\circ$  in-plane rotation is dominant for higher growth temperatures.<sup>3,6,7</sup> These two orientations have been understood in terms of the competition between surface mobility and lattice match.<sup>6</sup> The  $45^\circ$  in-plane rotation has a lattice mismatch<sup>21</sup> of about  $-5.7\%$  with a near-coincident site surface mesh cell area of  $0.14 \text{ nm}^2$ . The  $0^\circ$  (cube-on-cube) in-plane rotation is better lattice matched, 0.1%, but the near-coincident site surface mesh cell area is much larger,  $2.38 \text{ nm}^2$ . Hence, under growth conditions where there is sufficient surface mobility (e.g., high substrate temperature), the dominant orientation relationship observed is the  $0^\circ$ , cube-on-cube, orientation relationship because of its lower lattice mismatch. Similarly, under conditions of low surface mobility, the  $45^\circ$  in-plane rotation is dominant. In addition, nucleation at surface steps on (001) YSZ substrates has been found to favor the  $45^\circ$  in-plane rotation,<sup>9</sup> an example of graphoepitaxy.

Besides these frequently observed orientations, in-plane rotations in the vicinity of  $9^\circ$  from the cube-on-cube orientation relationship have also been observed.<sup>5-11</sup> The first detailed report<sup>7</sup> of the  $\phi \sim 9^\circ$  peaks was accompanied by a possible explanation for their occurrence involving a near-coincident site lattice model.<sup>7,8,11</sup> However, no experimental evidence for such a mechanism has been reported, and our investigation of this phenomenon supports an alternative explanation, which is described below.<sup>23</sup> This alternate explanation was also independently proposed by Boikov

*et al.*,<sup>10</sup> although beyond suggesting this mechanism no supporting data was given. Here we present *in situ* characterization demonstrating the formation of a  $\sim 9^\circ$  in-plane-rotated (110)-oriented  $\text{BaZrO}_3$  epitaxial reaction layer at the surfaces of (001) YSZ and (110) YSZ substrates exposed to  $\text{BaO}$ , and demonstrate that  $\sim 9^\circ$  in-plane rotations of  $\text{YBa}_2\text{Cu}_3\text{O}_{7-\delta}$  grains occur on both of these YSZ substrate orientations at high substrate temperatures in agreement with our model. The formation of  $\sim 9^\circ$  in-plane-rotated domains in *c*-axis oriented  $\text{YBa}_2\text{Cu}_3\text{O}_{7-\delta}$  films grown on (001) YSZ and (110) YSZ are examples of a general phenomena; examples of this same phenomena in the heteroepitaxial growth of other materials are also presented.

It has been widely shown that  $\text{YBa}_2\text{Cu}_3\text{O}_{7-\delta}$  reacts with YSZ to form  $\text{BaZrO}_3$ ,<sup>24-28</sup> and thin interfacial layers of  $\text{BaZrO}_3$  are routinely observed between epitaxial  $\text{YBa}_2\text{Cu}_3\text{O}_{7-\delta}$  films and the underlying YSZ substrates.<sup>8,14,19,29-34</sup> For the case of *c*-axis oriented  $\text{YBa}_2\text{Cu}_3\text{O}_{7-\delta}$  films on (001) YSZ, both (001)-<sup>8,14,19,33,34</sup> and (110)-oriented<sup>3,19,29,31</sup>  $\text{BaZrO}_3$  reaction layers have been seen at the  $\text{YBa}_2\text{Cu}_3\text{O}_{7-\delta}$ /YSZ interface by cross-sectional transmission electron microscopy (TEM).

In previous studies of  $0^\circ$  and  $45^\circ$  in-plane-rotated  $\text{YBa}_2\text{Cu}_3\text{O}_{7-\delta}$  films grown on (001) YSZ substrates in which a  $\text{BaZrO}_3$  epitaxial reaction layer has been seen, the researchers concluded that the  $\text{BaZrO}_3$  layer formed *after* the orientation of the overlying  $\text{YBa}_2\text{Cu}_3\text{O}_{7-\delta}$  layer was established.<sup>19,34</sup> In this paper we show that if the growth conditions are such that a  $\text{BaZrO}_3$  epitaxial-reaction layer forms *before* the nucleation of the overlying  $\text{YBa}_2\text{Cu}_3\text{O}_{7-\delta}$  layer,  $\sim 9^\circ$  in-plane rotations of the overlying  $\text{YBa}_2\text{Cu}_3\text{O}_{7-\delta}$  layer are favored.

The orientation of the  $\text{BaZrO}_3$  layers formed by epitaxial reaction is different depending on whether the  $\text{BaZrO}_3$  is formed before or after the nucleation of the overlying  $\text{YBa}_2\text{Cu}_3\text{O}_{7-\delta}$  layer. In the former unconstrained case, the  $\text{BaZrO}_3$  is oriented (as we demonstrate below) with

$$(110)_{\text{BaZrO}_3} \parallel (001)_{\text{YSZ}} \text{ and } [\bar{1}11]_{\text{BaZrO}_3} \parallel [110]_{\text{YSZ}},$$

whereas in the latter constrained case the  $\text{BaZrO}_3$  is oriented with

$$(001)_{\text{BaZrO}_3} \parallel (001)_{\text{YSZ}} \text{ and } [100]_{\text{BaZrO}_3} \parallel [100]_{\text{YSZ}},^{8,19,33,34}$$

or

$$(001)_{\text{BaZrO}_3} \parallel (001)_{\text{YSZ}} \text{ and } [110]_{\text{BaZrO}_3} \parallel [100]_{\text{YSZ}},^{8,14}$$

or

$$(110)_{\text{BaZrO}_3} \parallel (001)_{\text{YSZ}} \text{ and } [001]_{\text{BaZrO}_3} \parallel [100]_{\text{YSZ}}.^{19,31}$$

The unconstrained orientation leads to in-plane rotations of  $\sim 9^\circ$ , while the constrained orientations lead to  $0^\circ$  and  $45^\circ$  in-plane-rotated  $\text{YBa}_2\text{Cu}_3\text{O}_{7-\delta}$  grains.

### III. EXPERIMENTAL

Two orientations of YSZ substrates, (001) and (110), both containing 9.5 mol %  $\text{Y}_2\text{O}_3$  [i.e.,  $(\text{Y}_2\text{O}_3)_{0.095}(\text{ZrO}_2)_{0.905}$ ] were used in this study.<sup>35</sup> Prior to growth the substrates were chem-mechanically polished,<sup>36</sup> degreased in acetone and alcohol, and mounted onto a substrate holder using silver paint for the sputtered samples or indium for the samples prepared by molecular beam epitaxy (MBE). The samples grown by off-axis pulsed laser deposition (PLD) were radiatively heated and loosely held by their sides, allowing both sides to be coated simultaneously. The  $\text{YBa}_2\text{Cu}_3\text{O}_{7-\delta}$  layers were grown by dc hollow-cathode magnetron sputtering<sup>37</sup> and off-axis PLD.<sup>38</sup> The sputtered  $\text{YBa}_2\text{Cu}_3\text{O}_{7-\delta}$  films were grown at a substrate heater block temperature of 750–780 °C, a total pressure ( $\text{Ar}/\text{O}_2 = 2:1$ ) of 650 mTorr, and an after-growth cooldown in  $\sim 0.5$  bar  $\text{O}_2$  lasting  $\sim 1$  h. Additional  $\text{YBa}_2\text{Cu}_3\text{O}_{7-\delta}$  films were grown by off-axis PLD at a substrate temperature of 780 °C in 20 mTorr oxygen/ozone mixture ( $\sim 5\%$   $\text{O}_3$ ) and an after-growth cooldown in 1 bar  $\text{O}_2$  lasting  $\sim 1$  h. The  $\text{BaO}$  and  $(\text{Ba}, \text{K})\text{BiO}_3$  layers were grown by MBE at substrate temperatures of 660–680 °C and 270–280 °C, respectively. An oxygen plasma generated in a tube (20 W rf power and an oxygen pressure of 90 mTorr) flowed into the MBE system, resulting in a background pressure of  $5 \times 10^{-5}$  to  $10^{-4}$  Torr during growth.<sup>39</sup> The crystalline structure of the film surface was monitored by *in situ* reflection high-energy electron diffraction (RHEED) during growth. The  $\text{BaZrO}_3$  films were grown by 90° off-axis magnetron sputtering at a substrate temperature of 650 °C and a total pressure of 100 mTorr ( $\text{Ar}/\text{O}_2 = 3:2$ ).<sup>40</sup>

The orientation relationships between the  $\text{YBa}_2\text{Cu}_3\text{O}_{7-\delta}$  films and YSZ substrates were determined using 4-circle x-ray diffraction in the Bragg–Brentano geometry and radiation from a copper x-ray tube. A schematic of the 4-circle geometry used is shown in Fig. 2.  $\theta$ - $2\theta$  scans with the diffraction vector normal to the wafer surface were first used to establish which plane of the  $\text{YBa}_2\text{Cu}_3\text{O}_{7-\delta}$  film lay parallel to the (001) YSZ substrate. This was the (001)  $\text{YBa}_2\text{Cu}_3\text{O}_{7-\delta}$  plane for all of the growths discussed here (i.e., all are *c*-axis oriented  $\text{YBa}_2\text{Cu}_3\text{O}_{7-\delta}$  films). Then  $\phi$ -scans of  $\text{YBa}_2\text{Cu}_3\text{O}_{7-\delta}$  103 reflections were used to establish the

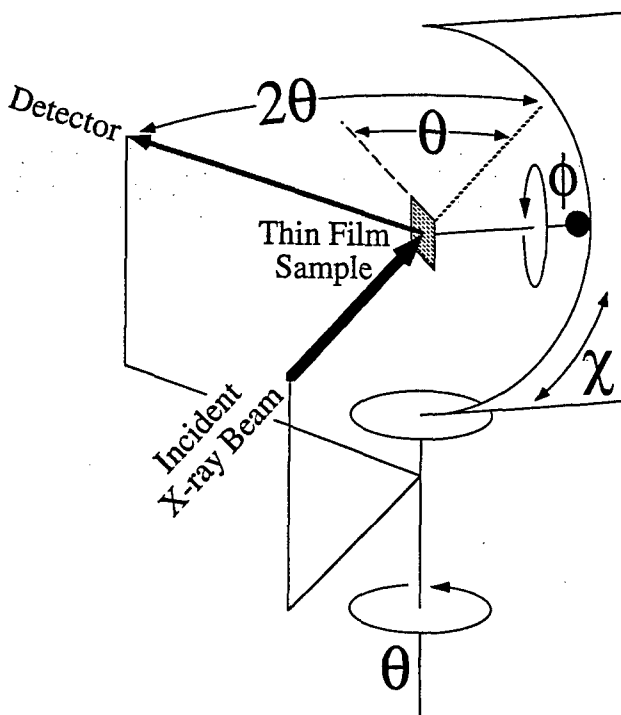


FIG. 2. A schematic diagram of a 4-circle x-ray diffractometer used to determine the epitaxial relationship between a film and a substrate.<sup>41</sup>

in-plane orientation relationship of the films with respect to the underlying substrate. As this is an inclined plane (asymmetric reflection), a component of the diffraction vector lies in the plane of the substrate. For all scans  $\phi = 0^\circ$  was set parallel to the [100] YSZ direction for (001) YSZ substrates and parallel to the [001] YSZ direction for (110) YSZ substrates. This in-plane direction ( $\phi = 0^\circ$ ) was ascertained from the location of the 011 YSZ reflection for (001) YSZ substrates and from the 100 YSZ reflection for (110) YSZ substrates. No distinction is made between the [100]  $\text{YBa}_2\text{Cu}_3\text{O}_{7-\delta}$  and [010]  $\text{YBa}_2\text{Cu}_3\text{O}_{7-\delta}$  directions in the x-ray scans nor in the deduced orientation relationships because the in-plane alignment of the [100] and [010]  $\text{YBa}_2\text{Cu}_3\text{O}_{7-\delta}$  directions is determined during growth while the  $\text{YBa}_2\text{Cu}_3\text{O}_{7-\delta}$  is tetragonal and the [100] and [010]  $\text{YBa}_2\text{Cu}_3\text{O}_{7-\delta}$  directions are equivalent.

#### IV. RESULTS

In order to determine the origin of the  $\phi \sim \pm 9^\circ$  peaks in  $\text{YBa}_2\text{Cu}_3\text{O}_{7-\delta}$  films grown on YSZ substrates, we begin by examining in detail the observation of Fork *et al.*<sup>7</sup> that the deposition of a thin (~0.3 nm) BaO buffer layer prior to  $\text{YBa}_2\text{Cu}_3\text{O}_{7-\delta}$  deposition leads to a dominance of ~9° in-plane-rotated  $\text{YBa}_2\text{Cu}_3\text{O}_{7-\delta}$  grains. We present *in situ* RHEED characterization showing that the deposited BaO reacts with the YSZ substrate to form a ~9° in-plane-rotated (110)-oriented

$\text{BaZrO}_3$  epitaxial reaction layer. This ~9° in-plane-rotated epitaxial alignment occurs on both (001) YSZ and (110) YSZ substrates and involves the diagonal of a rectangular surface net aligning with the diagonal of a square surface net.

We then show that at high substrate temperatures *c*-axis oriented  $\text{YBa}_2\text{Cu}_3\text{O}_{7-\delta}$  films grown on both (001) YSZ and (110) YSZ contain ~9° in-plane-rotated  $\text{YBa}_2\text{Cu}_3\text{O}_{7-\delta}$  domains. This implies that the ~9° rotation of the  $\text{YBa}_2\text{Cu}_3\text{O}_{7-\delta}$  domains is inherited from the underlying ~9°-rotated  $\text{BaZrO}_3$  reaction layer; growth conditions (e.g., high substrate temperatures and low growth rates) favoring the formation of the ~9°-rotated  $\text{BaZrO}_3$  reaction layer prior to the nucleation of the overlying  $\text{YBa}_2\text{Cu}_3\text{O}_{7-\delta}$  lead to an increase in ~9°-rotated  $\text{YBa}_2\text{Cu}_3\text{O}_{7-\delta}$  domains.

Finally, we consider the underlying general mechanism leading to this in-plane rotation. Ideal lattice constant ratios where this in-plane rotation provides the most favorable lattice match to a heteroepitaxial system are given and two additional examples of this general phenomenon, (110)  $(\text{Ba}, \text{K})\text{BiO}_3/(001)$  YSZ and (110)  $(\text{Ba}, \text{K})\text{BiO}_3/(001)$   $\text{LaAlO}_3$ , are presented.

#### A. Epitaxial reaction between BaO and YSZ

Due to the dramatic ability of a thin BaO buffer layer to cause ~9° in-plane rotations in the overgrown  $\text{YBa}_2\text{Cu}_3\text{O}_{7-\delta}$  layer, as demonstrated by Fork *et al.*,<sup>7</sup> we began by examining the effect of such a thin BaO layer on the surface structure of (001) YSZ using *in situ* RHEED. Figure 3 shows the RHEED pattern observed at a ~9° in-plane rotation off the [100] YSZ azimuth after the deposition of ~1.4 nm<sup>42</sup> of BaO on a (001) YSZ substrate at  $T_{\text{sub}} \sim 665^\circ\text{C}$ . The pattern cannot be indexed by BaO or YSZ reflections, but it can be by  $\text{BaZrO}_3$  reflections. The RHEED pattern indicates the presence of a (110)-oriented  $\text{BaZrO}_3$  epitaxial reaction layer with two different in-plane orientations:  $[\bar{1}10]_{\text{BaZrO}_3}$  and  $[001]_{\text{BaZrO}_3}$ , parallel to the ~9° off [100] YSZ azimuth. An identical RHEED pattern is observed at an in-plane rotation of ~9° the other way from the [100] YSZ azimuth as well as at ~±9° from the [010] YSZ azimuth. This indicates the presence of a total of four equivalent in-plane (110)  $\text{BaZrO}_3$  orientations, as shown in Fig. 4(a). The lattice mismatch of these four equivalent orientation relationships is about -0.1% along the  $[\bar{1}11]_{\text{BaZrO}_3} \parallel [\bar{1}10]_{\text{YSZ}}$  edge and 6.0% along the  $[\bar{1}1\bar{2}]_{\text{BaZrO}_3} \parallel [\bar{1}\bar{1}0]_{\text{YSZ}}$  edge of the near-coincident site surface mesh cell with area 0.77 nm<sup>2</sup>, as shown for one of these equivalent orientations in Fig. 4(b). The observed orientation relationship between (110)  $\text{BaZrO}_3$  and (001) YSZ has the most favorable lattice match of all possible near-coincident surface mesh cells of equal or smaller area.

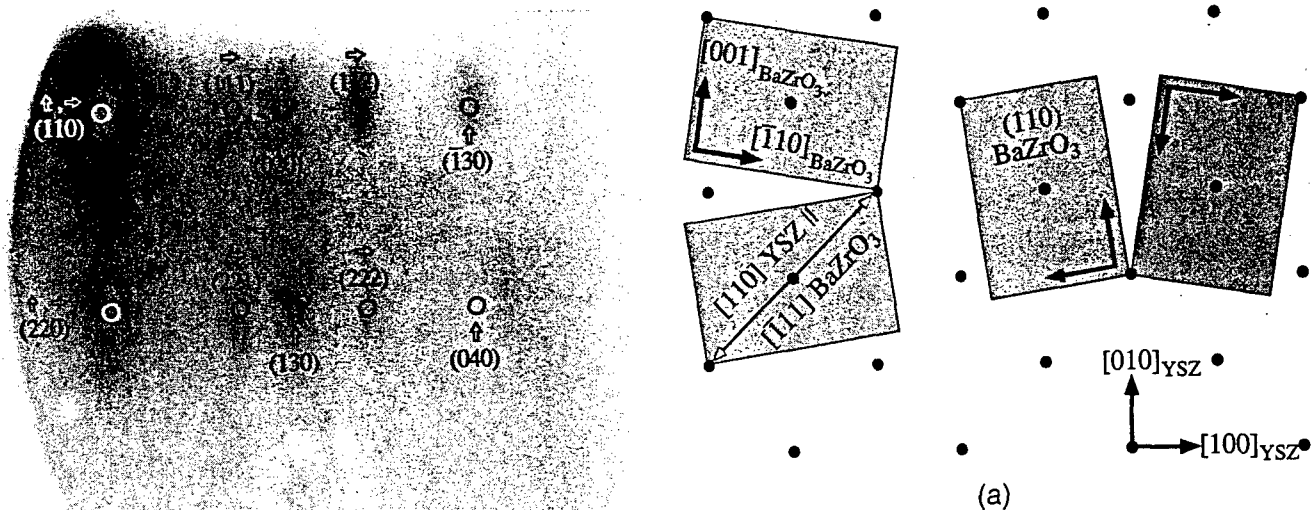


FIG. 3. RHEED pattern observed  $\sim 9^\circ$  off the [100] YSZ azimuth after the deposition of 1.4 nm of BaO on (001) YSZ at  $T_{\text{sub}} \sim 665^\circ\text{C}$ . A superposition of two (110)  $\text{BaZrO}_3$  orientations,  $[\bar{1}10]_{\text{BaZrO}_3}$   $\text{BaZrO}_3$  azimuth (↑) and [001]  $\text{BaZrO}_3$  azimuth (→), are indexed.

The in-plane rotation angle,  $\phi$ , expected for these orientations was calculated from the lattice parameters of  $\text{BaZrO}_3$  and YSZ for two limiting cases: (i) where the  $\text{BaZrO}_3$  layer is strained to be fully commensurate with the underlying YSZ substrate and (ii) where the  $\text{BaZrO}_3$  layer has fully relaxed. The result is  $\phi$  values of  $\pm 11.3^\circ$  for fully commensurate and  $\pm 9.7^\circ$  for fully relaxed  $\text{BaZrO}_3$  layers. As described below, it is this  $\sim 9^\circ$  in-plane rotation of the (110)  $\text{BaZrO}_3$  layers that leads to the  $\sim 9^\circ$  in-plane rotation of the overgrown  $\text{YBa}_2\text{Cu}_3\text{O}_{7-\delta}$  layers. Note that this angular value depends on the lattice constant of  $\text{BaZrO}_3$ . As significant ( $\sim 10\%$ ) variations in the lattice constant of (110)  $\text{BaZrO}_3$  epitaxial reaction layers on YSZ have been observed,<sup>31</sup> the peaks at  $\sim \pm 9^\circ$  observed in  $\phi$ -scans of  $\text{YBa}_2\text{Cu}_3\text{O}_{7-\delta}$  are in qualitatively good agreement with our expectations based on this orientation relationship.

The orientation relationship shown in Fig. 4 involves the epitaxial alignment between the diagonal of a square surface net and the diagonal of a rectangular surface net (specifically the epitaxial alignment between  $\langle 111 \rangle_{\text{BaZrO}_3}$  and  $\langle 110 \rangle_{\text{YSZ}}$ ). To test the generality of this epitaxial alignment, we also performed experiments on another orientation of YSZ containing an in-plane  $\langle 110 \rangle$ -type direction: (110) YSZ. In analogy to our results on (001) YSZ, we would expect the deposition of BaO on (110) YSZ to result in the formation of a (110)-oriented  $\text{BaZrO}_3$  epitaxial reaction layer with

$$\langle 110 \rangle_{\text{BaZrO}_3} \parallel \langle 110 \rangle_{\text{YSZ}} \text{ and } [\bar{1}11]_{\text{BaZrO}_3} \parallel [\bar{1}10]_{\text{YSZ}}.$$

The two equivalent ways in which  $\langle 111 \rangle_{\text{BaZrO}_3}$  can align with  $\langle 110 \rangle_{\text{YSZ}}$  in the nucleation of a (110)  $\text{BaZrO}_3$

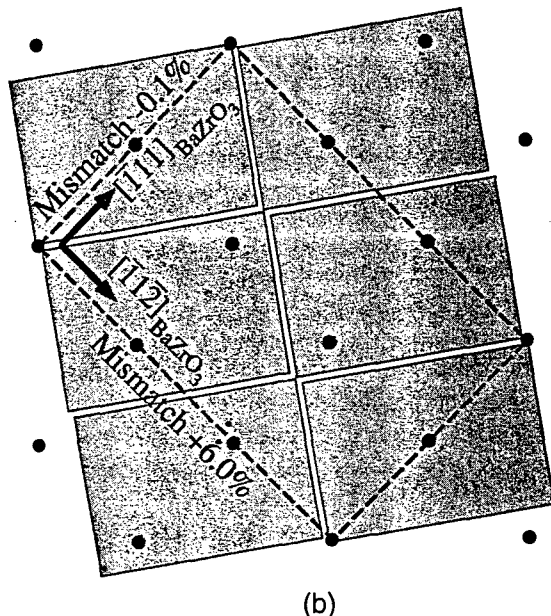


FIG. 4. Epitaxial relationship between (110)  $\text{BaZrO}_3$  and (001) YSZ showing (a) the four equivalent domains with  $[\bar{1}11]_{\text{BaZrO}_3} \parallel [\bar{1}10]_{\text{YSZ}}$  and (b) the near-coincident site surface mesh cell (dashed) and its lattice match for one of the four equivalent orientations. The rectangles indicate the relaxed dimensions of the (110)  $\text{BaZrO}_3$  surface mesh with respect to the (001) YSZ substrate surface mesh (dots).

layer on (110) YSZ are shown in Fig. 5(a). As shown for one of these equivalent orientations in Fig. 5(b), the lattice mismatch of these orientation relationships is about  $-0.1\%$  along both edges of the near-coincident site surface mesh cell with area  $0.75 \text{ nm}^2$ . This lattice match is even more favorable than that for (110)  $\text{BaZrO}_3$  on (001) YSZ and is also the most favorable lattice match of all possible near-coincident surface mesh cells of equal or smaller area. This excellent lattice match results in the expected in-plane rotation angle,  $\phi$ , between [001]  $\text{BaZrO}_3$  and [001] YSZ to be

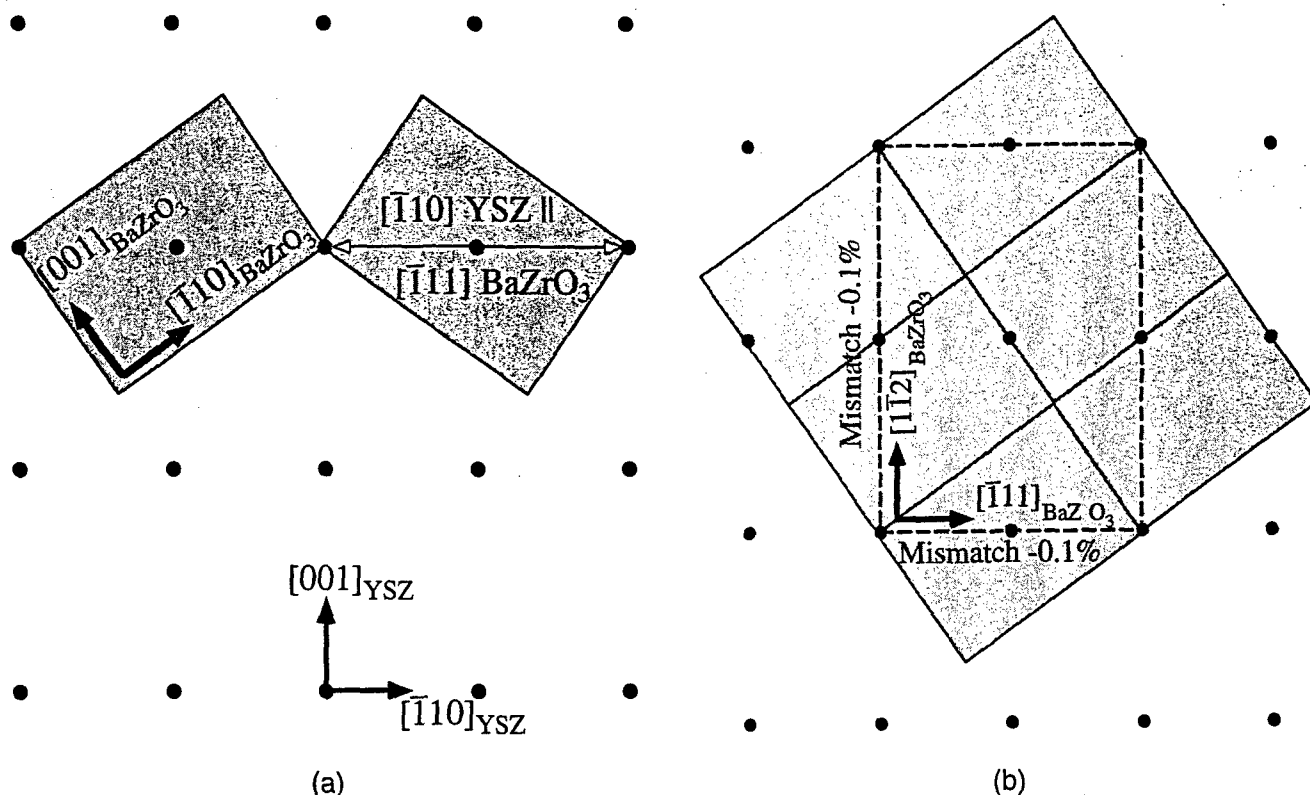


FIG. 5. Epitaxial relationship between (110) BaZrO<sub>3</sub> and (110) YSZ showing (a) the two equivalent domains with  $[\bar{1}11]_{\text{BaZrO}_3} \parallel [\bar{1}10]_{\text{YSZ}}$  and (b) the near-coincident site surface mesh cell (dashed) and its lattice match for one of the two equivalent orientations. The rectangles indicate the relaxed dimensions of the (110) BaZrO<sub>3</sub> surface mesh with respect to the (110) YSZ substrate surface mesh (dots).

$\pm 35.3^\circ$  regardless of whether the (110) BaZrO<sub>3</sub> layer is fully commensurate or fully relaxed.

The RHEED pattern observed along the [001] YSZ azimuth after the deposition of  $\sim 1.4$  nm of BaO on (110) YSZ at  $T_{\text{sub}} \sim 665^\circ\text{C}$  is shown in Fig. 6. When viewed along the [001] BaZrO<sub>3</sub> azimuth ( $\sim \pm 35^\circ$  off the [001] YSZ azimuth) or the [110] BaZrO<sub>3</sub> azimuth ( $\sim \pm 125^\circ$  off the [001] YSZ azimuth), the RHEED pattern looked identical to the corresponding BaZrO<sub>3</sub> azimuths shown superimposed in Fig. 3. The observed RHEED patterns are consistent with the orientation relationship shown in Fig. 5. Note that for the growth of (110) BaZrO<sub>3</sub> on (110) YSZ there are only two equivalent in-plane orientations because of the 2-fold symmetry of the substrate, compared to the four equivalent in-plane orientations on a (001) YSZ substrate.

### B. $\phi \sim 9^\circ$ peaks in $\text{YBa}_2\text{Cu}_3\text{O}_{7-\delta}$ on (001) YSZ

Having determined how a thin BaO buffer layer dramatically alters the surface structure of (001) YSZ and (110) YSZ substrates, yielding a  $\sim 9^\circ$ -rotated (110) BaZrO<sub>3</sub> layer, we now consider the origin of the  $\sim 9^\circ$  rotations observed in  $\text{YBa}_2\text{Cu}_3\text{O}_{7-\delta}$  films grown on these substrates.

In agreement with previous reports,<sup>10,11</sup> we found  $\phi \sim 9^\circ$  peaks to be most prevalent in  $\text{YBa}_2\text{Cu}_3\text{O}_{7-\delta}$

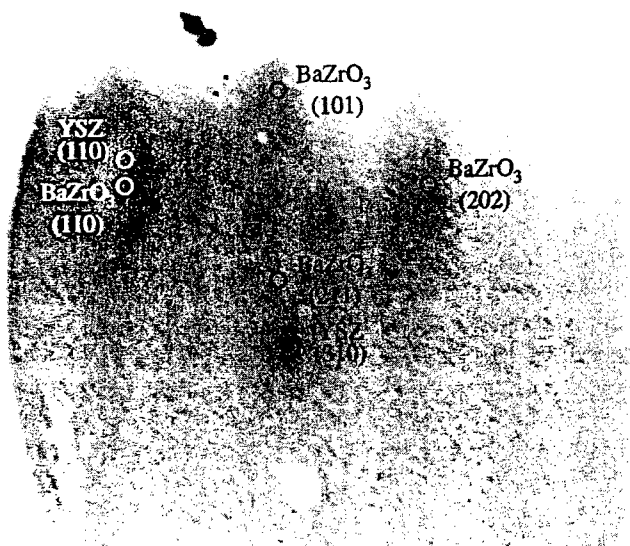


FIG. 6. RHEED pattern observed along the [001] YSZ azimuth after the deposition of 1.4 nm of BaO on (110) YSZ at  $T_{\text{sub}} \sim 665^\circ\text{C}$ . Along this azimuth, both of the equivalent (110) BaZrO<sub>3</sub> orientations shown in Fig. 5 give rise to the same set of spots. These BaZrO<sub>3</sub> spots are indexed, as well as two spots due to the YSZ substrate.

films grown at high substrate temperatures. With increasing substrate temperature, the reaction between  $\text{YBa}_2\text{Cu}_3\text{O}_{7-\delta}$  and YSZ occurs more rapidly, until at

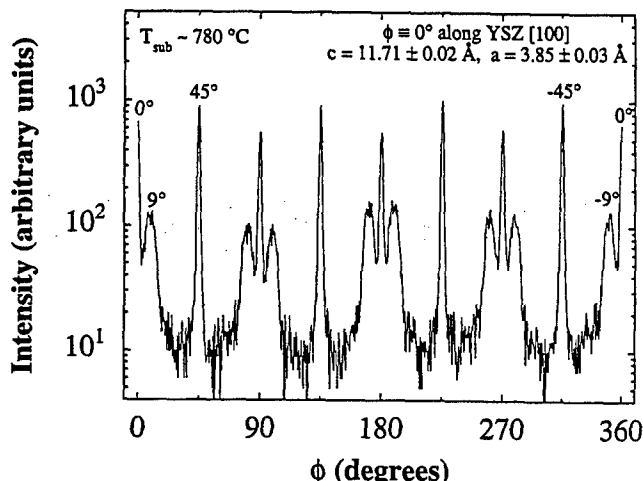


FIG. 7.  $\phi$ -scan of 103  $\text{YBa}_2\text{Cu}_3\text{O}_{7-\delta}$  peaks of *c*-axis oriented  $\text{YBa}_2\text{Cu}_3\text{O}_{7-\delta}$  film grown on (001) YSZ grown by PLD at  $T_{\text{sub}} \sim 780$  °C.

some point the  $\text{BaZrO}_3$  reaction layer forms *prior* to the nucleation of the  $\text{YBa}_2\text{Cu}_3\text{O}_{7-\delta}$ . The same event will occur at a fixed growth temperature as the growth rate is lowered, since the reaction then has more time to transpire. Such an event will lead to  $\sim 9^\circ$  in-plane rotations of (110)  $\text{BaZrO}_3$  grains; the epitaxial sequence is identical to the  $\text{BaO} + \text{YSZ}$  case described above. Of course, microscopically there may be regions where the  $\text{YBa}_2\text{Cu}_3\text{O}_{7-\delta}$  nucleates prior to the formation of  $\text{BaZrO}_3$  and regions where  $\text{BaZrO}_3$  nucleates prior to the  $\text{YBa}_2\text{Cu}_3\text{O}_{7-\delta}$ . In such cases, a mixture of  $0^\circ$ ,  $45^\circ$ , and  $\sim 9^\circ$  in-plane rotations can be expected to occur. This is the typical observation for  $\text{YBa}_2\text{Cu}_3\text{O}_{7-\delta}$  films grown on (001) YSZ substrates at high temperatures, an example of which is shown in Fig. 7.

The results of Fork *et al.*<sup>7</sup> on how thin BaO buffer layers deposited on YSZ (001) lead to a dramatic increase in  $\sim 9^\circ$  in-plane-rotated  $\text{YBa}_2\text{Cu}_3\text{O}_{7-\delta}$  grains, together with the above *in situ* observations of the ensuing epitaxial reaction, indicate the full orientation relationship between the *c*-axis oriented  $\text{YBa}_2\text{Cu}_3\text{O}_{7-\delta}$ , the (110)  $\text{BaZrO}_3$  epitaxial reaction layer, and the underlying (001) YSZ substrate is

$$(001)_{\text{YBa}_2\text{Cu}_3\text{O}_{7-\delta}} \parallel (110)_{\text{BaZrO}_3} \parallel (001)_{\text{YSZ}}, \\ [100]_{\text{YBa}_2\text{Cu}_3\text{O}_{7-\delta}} \parallel [001]_{\text{BaZrO}_3}, \\ \text{and } [\bar{1}\bar{1}\bar{1}]_{\text{BaZrO}_3} \parallel [110]_{\text{YSZ}}.$$

Cross-sectional TEM studies have shown that constrained (110)-oriented  $\text{BaZrO}_3$ , i.e.,  $\text{BaZrO}_3$  formed *after* the epitaxial alignment between  $\text{YBa}_2\text{Cu}_3\text{O}_{7-\delta}$  and YSZ is established, epitaxially aligns with *c*-axis oriented  $\text{YBa}_2\text{Cu}_3\text{O}_{7-\delta}$  in the following manner<sup>19,31</sup>:

$$(001)_{\text{YBa}_2\text{Cu}_3\text{O}_{7-\delta}} \parallel (110)_{\text{BaZrO}_3}, \\ \text{and } [110]_{\text{YBa}_2\text{Cu}_3\text{O}_{7-\delta}} \parallel [001]_{\text{BaZrO}_3}.$$

This orientation relationship is not the same as that inferred from the in-plane orientation of the  $\sim 9^\circ$  domains in *c*-axis  $\text{YBa}_2\text{Cu}_3\text{O}_{7-\delta}$  films grown on (001) YSZ. The above orientation relationship would be manifested by peaks at  $\phi \sim 36^\circ$  and equivalent angles, rather than the observed peaks at  $\phi \sim 9^\circ$ . Our *in situ* observations of the in-plane orientation of (110)  $\text{BaZrO}_3$  on (001) YSZ together with the observation of peaks at  $\phi \sim 9^\circ$  and symmetrically equivalent angles indicate that the orientation relationship between unconstrained (110)-oriented  $\text{BaZrO}_3$  and *c*-axis oriented  $\text{YBa}_2\text{Cu}_3\text{O}_{7-\delta}$  is

$$(001)_{\text{YBa}_2\text{Cu}_3\text{O}_{7-\delta}} \parallel (110)_{\text{BaZrO}_3}, \\ \text{and } [100]_{\text{YBa}_2\text{Cu}_3\text{O}_{7-\delta}} \parallel [001]_{\text{BaZrO}_3}$$

on (001) YSZ substrates. Interestingly, both of these variants have *identical* lattice match<sup>19</sup> (2.6% and 8.8% mismatch along the surface mesh cell edge directions), as shown in Fig. 8. The near-coincident site surface mesh cell area is  $0.94 \text{ nm}^2$  for the former orientation relationship and half this for the latter orientation relationship. Because of its smaller area,<sup>43</sup> the latter orientation relationship (indicated by peaks at  $\phi \sim 9^\circ$ , rather than  $\phi \sim 36^\circ$ ) is dominant, as expected. As described below, sometimes both variants are seen in the same film, yielding not only peaks at  $\phi \sim 9^\circ$ , but also peaks at  $\phi \sim (45^\circ - 9^\circ) = 36^\circ$ .<sup>11</sup>

### C. $\phi \sim 9^\circ$ peaks in $\text{YBa}_2\text{Cu}_3\text{O}_{7-\delta}$ on (110) YSZ

In our model the origin of  $\sim 9^\circ$  in-plane-rotated  $\text{YBa}_2\text{Cu}_3\text{O}_{7-\delta}$  domains is due to a  $\sim 9^\circ$ -rotated (110)  $\text{BaZrO}_3$  epitaxial reaction layer. As shown above (Fig. 5), a  $\sim 9^\circ$  in-plane-rotated (110)  $\text{BaZrO}_3$  layer also occurs on (110) YSZ substrates. We thus investigated the growth of (001)  $\text{YBa}_2\text{Cu}_3\text{O}_{7-\delta}$  on (110) YSZ to see if, at growth conditions favoring the formation of a  $\text{BaZrO}_3$  reaction layer prior to the nucleation of the overlying  $\text{YBa}_2\text{Cu}_3\text{O}_{7-\delta}$ , in-plane rotation of the  $\text{YBa}_2\text{Cu}_3\text{O}_{7-\delta}$  domains would also be observed, as predicted by our model.

The growth of *c*-axis oriented  $\text{YBa}_2\text{Cu}_3\text{O}_{7-\delta}$  films has been reported on (001)-, (110)-, and (111)-oriented YSZ substrates as well as on misoriented YSZ substrates.<sup>8,20,30,32,44</sup> However, the in-plane orientation of  $\text{YBa}_2\text{Cu}_3\text{O}_{7-\delta}$  deposited on (110) YSZ substrates has not been previously reported. As shown in Figs. 9 and 10,  $\text{YBa}_2\text{Cu}_3\text{O}_{7-\delta}$  grows *c*-axis oriented with in-plane rotations of  $0^\circ$ ,  $\sim 9^\circ$ , and  $45^\circ$  on (110) YSZ. The relative fraction of these in-plane orientations depends on the substrate temperature during growth. At lower temperature, Fig. 10(a), the  $\phi = 0^\circ$  peaks dominate; at higher substrate temperature, Fig. 10(b), peaks at  $\sim 9^\circ$  and  $45^\circ$  are also observed. The  $0^\circ$  and  $45^\circ$  in-plane rotations are the orientations expected from lattice match considerations when  $\text{YBa}_2\text{Cu}_3\text{O}_{7-\delta}$  nucleates

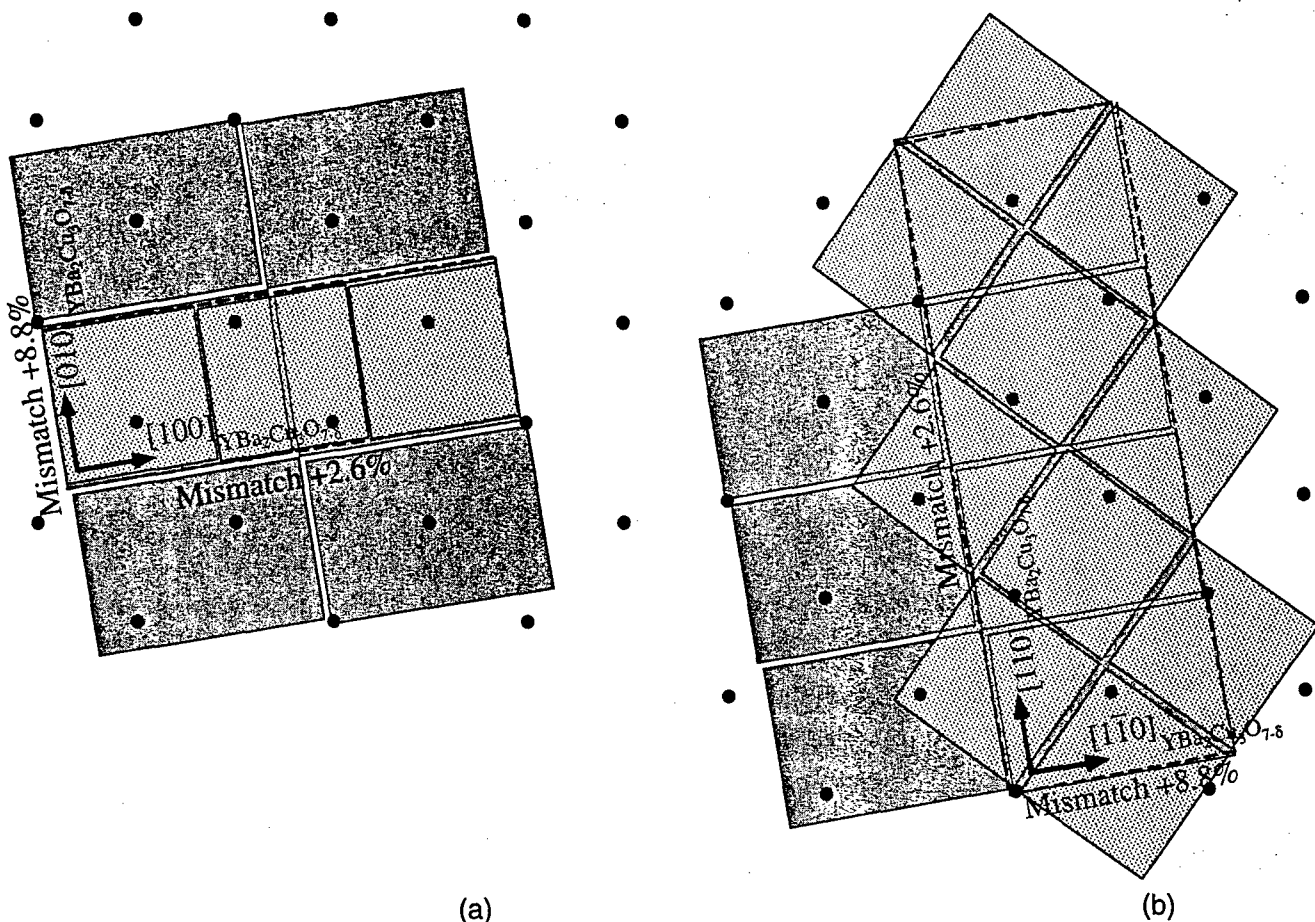


FIG. 8. Epitaxial relationship between (001)  $\text{YBa}_2\text{Cu}_3\text{O}_{7-\delta}$  and (110)  $\text{BaZrO}_3$  showing the near-coincident site surface mesh cell (dashed) and its lattice match for (a)  $[010]_{\text{YBa}_2\text{Cu}_3\text{O}_{7-\delta}} \parallel [001]_{\text{BaZrO}_3}$ , and (b)  $[110]_{\text{YBa}_2\text{Cu}_3\text{O}_{7-\delta}} \parallel [001]_{\text{BaZrO}_3}$ . The squares indicate the relaxed dimensions of the (001)  $\text{YBa}_2\text{Cu}_3\text{O}_{7-\delta}$  surface mesh with respect to the (110)  $\text{BaZrO}_3$  surface mesh (rectangles) on the (001) YSZ substrate surface mesh (dots).

directly on (110) YSZ. As shown in Fig. 11, the  $0^\circ$  relationship has a lattice mismatch of  $-5.7\%$  along the  $[100]_{\text{YBa}_2\text{Cu}_3\text{O}_{7-\delta}} \parallel [110]_{\text{YSZ}}$  edge and a mismatch of  $0.1\%$  along the  $[010]_{\text{YBa}_2\text{Cu}_3\text{O}_{7-\delta}} \parallel [001]_{\text{YSZ}}$  edge of a near-coincident site surface mesh cell with area  $0.58 \text{ nm}^2$ . The  $45^\circ$  relationship has the identical lattice mismatch and near-coincident site surface mesh cell area:  $-5.7\%$  along the  $[110]_{\text{YBa}_2\text{Cu}_3\text{O}_{7-\delta}} \parallel [001]_{\text{YSZ}}$  edge,  $0.1\%$  along the  $[110]_{\text{YBa}_2\text{Cu}_3\text{O}_{7-\delta}} \parallel [110]_{\text{YSZ}}$  edge, and an area of  $0.58 \text{ nm}^2$ . However, if only the oxygen sublattice is considered, the  $0^\circ$  orientation relationship has a near-coincident site surface mesh cell area half the size ( $0.29 \text{ nm}^2$ ) of the  $45^\circ$  orientation relationship, explaining the dominance of the  $0^\circ$  peaks compared to the  $45^\circ$  peaks in the  $\phi$ -scans. The observation of more  $\sim 9^\circ$  peaks at higher substrate temperature is analogous to the growth of  $\text{YBa}_2\text{Cu}_3\text{O}_{7-\delta}$  on (001) YSZ and expected from the increased likelihood of (110)  $\text{BaZrO}_3$  formation before nucleation of the overlying  $\text{YBa}_2\text{Cu}_3\text{O}_{7-\delta}$ .

Combining the RHEED results indicating the epitaxial orientation of the (110)  $\text{BaZrO}_3$  layer on (110) YSZ (see Fig. 5) with the  $\phi$ -scan results [see Fig. 10(b)],

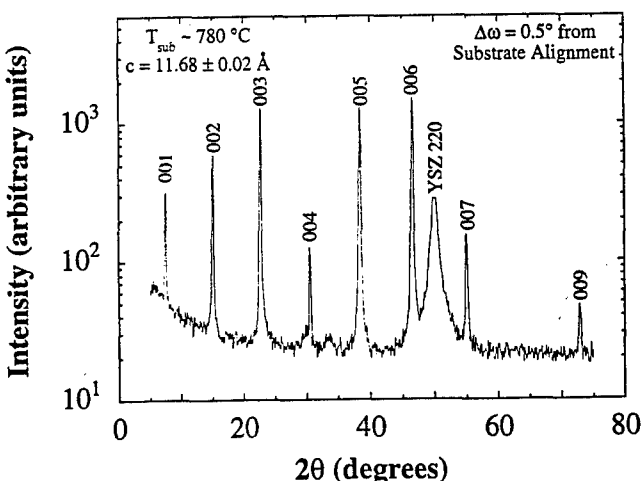


FIG. 9.  $\theta$ - $2\theta$  scan of a  $c$ -axis oriented  $\text{YBa}_2\text{Cu}_3\text{O}_{7-\delta}$  film grown on (110) YSZ by sputtering at  $T_{\text{sub}} \sim 780^\circ\text{C}$ . This scan was made after rocking  $0.5^\circ$  in omega off alignment to the (110) YSZ substrate.

the following orientation relationship is implied between the  $c$ -axis oriented  $\text{YBa}_2\text{Cu}_3\text{O}_{7-\delta}$ , the (110)  $\text{BaZrO}_3$  epitaxial reaction layer, and the underlying (110) YSZ

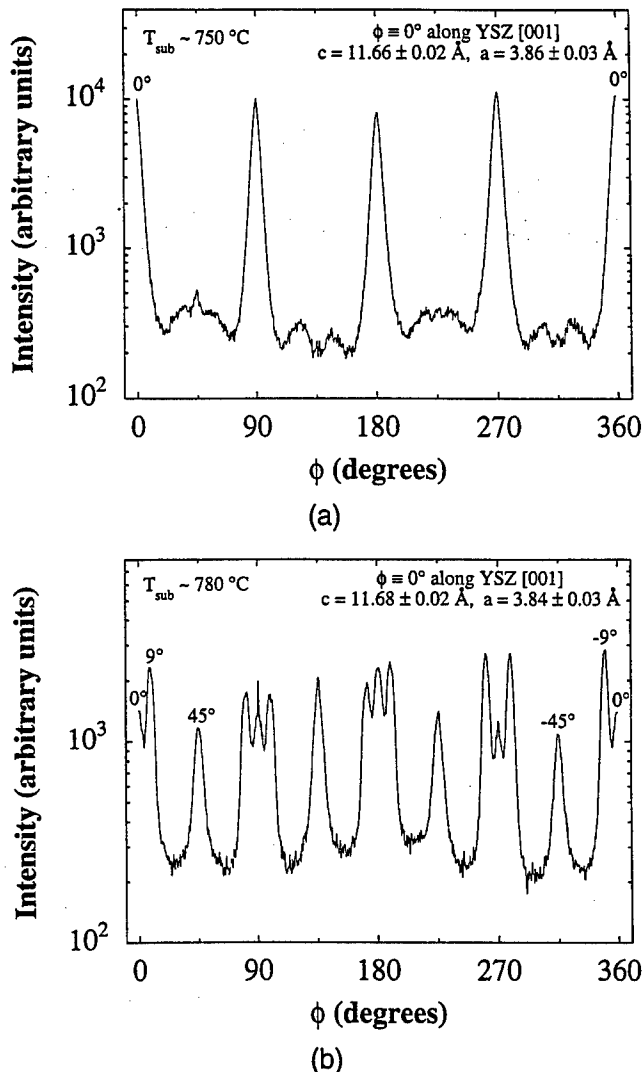


FIG. 10.  $\phi$ -scans of 103  $\text{YBa}_2\text{Cu}_3\text{O}_{7-\delta}$  peaks of  $c$ -axis oriented  $\text{YBa}_2\text{Cu}_3\text{O}_{7-\delta}$  films grown on (110) YSZ by sputtering at (a)  $T_{\text{sub}} \sim 750^\circ\text{C}$  and (b)  $T_{\text{sub}} \sim 780^\circ\text{C}$ .

substrate:

$$\begin{aligned} (001)_{\text{YBa}_2\text{Cu}_3\text{O}_{7-\delta}} &\parallel (110)_{\text{BaZrO}_3} \parallel (110)_{\text{YSZ}}, \\ [110]_{\text{YBa}_2\text{Cu}_3\text{O}_{7-\delta}} &\parallel [001]_{\text{BaZrO}_3}, \\ \text{and } [\bar{1}\bar{1}1]_{\text{BaZrO}_3} &\parallel [\bar{1}\bar{1}0]_{\text{YSZ}}. \end{aligned}$$

Note that the in-plane orientation between  $\text{YBa}_2\text{Cu}_3\text{O}_{7-\delta}$  and  $\text{BaZrO}_3$  differs by a  $45^\circ$  in-plane rotation from that observed on (001) YSZ. Although the lattice mismatch is identical for both of these orientation relationships, the reason for the preference of the variant with the larger near-coincident site surface mesh cell area<sup>43</sup> on (110) YSZ is unclear. In both cases, (001)  $\text{YBa}_2\text{Cu}_3\text{O}_{7-\delta}$  is nucleating on (110)  $\text{BaZrO}_3$ . The clear dependence of the orientation relationship on the layer underlying the (110)  $\text{BaZrO}_3$  [i.e., (001) YSZ or (110) YSZ] leads us to speculate that the step structure of the (110)  $\text{BaZrO}_3$  layer, which is in turn dependent on the step structure of

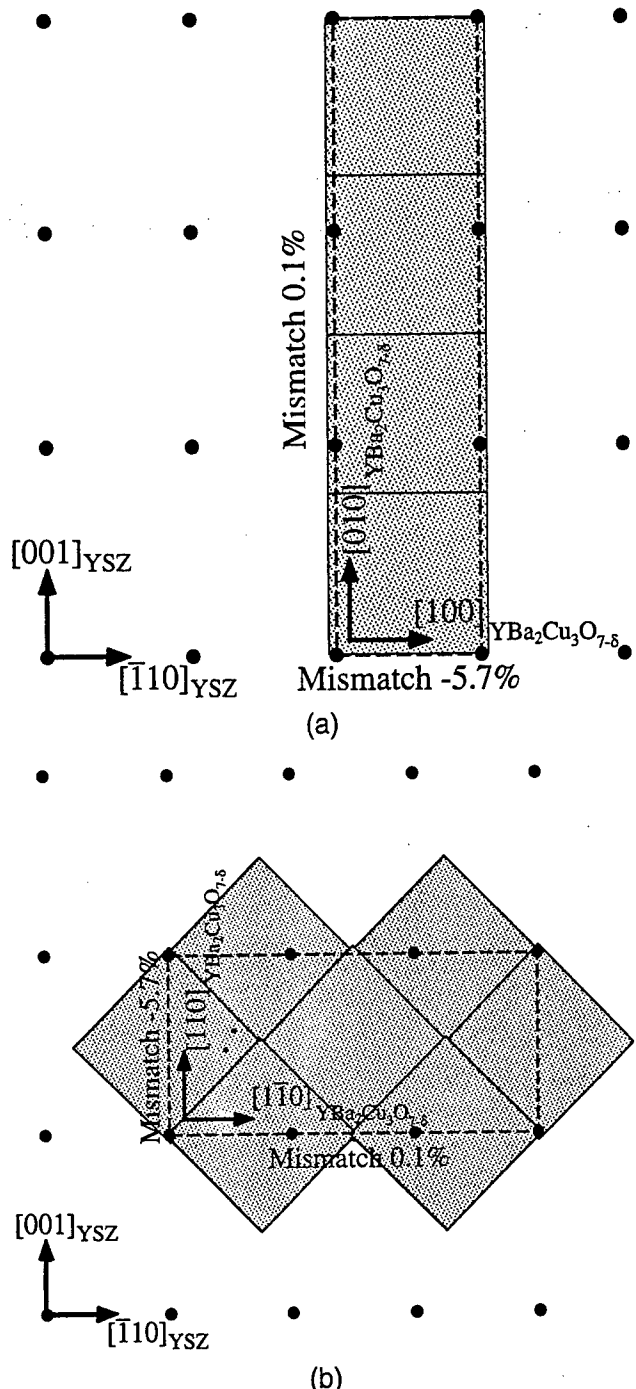


FIG. 11. Epitaxial relationship between (001)  $\text{YBa}_2\text{Cu}_3\text{O}_{7-\delta}$  and (110) YSZ showing the near-coincident site surface mesh cell (dashed) and its lattice match for (a)  $[010]_{\text{YBa}_2\text{Cu}_3\text{O}_{7-\delta}} \parallel [001]_{\text{YSZ}}$  and (b)  $[110]_{\text{YBa}_2\text{Cu}_3\text{O}_{7-\delta}} \parallel [001]_{\text{YSZ}}$ . The squares indicate the relaxed dimensions of the (001)  $\text{YBa}_2\text{Cu}_3\text{O}_{7-\delta}$  surface mesh with respect to the (110) YSZ substrate surface mesh (dots).

the underlying YSZ substrate orientation, is responsible for the dominance of one orientation relationship over the other. The importance of graphoepitaxy on the  $45^\circ$  in-plane orientation of (001)  $\text{YBa}_2\text{Cu}_3\text{O}_{7-\delta}$  on (001) YSZ has been noted.<sup>9</sup> We believe that graphoepitaxy is also playing a role in the  $\sim 9^\circ$  in-plane orientation.

The in-plane orientation observations are in accord with our model and difficult to explain by other means. For example, just as a near-coincident site lattice model between (001)  $\text{YBa}_2\text{Cu}_3\text{O}_{7-\delta}$  and (001) YSZ [i.e., without the prior formation of an intermediate (110)  $\text{BaZrO}_3$  reaction layer] was inadequate to explain the occurrence of the  $\sim 9^\circ$  orientation,<sup>11</sup> it is also incapable of predicting  $\sim 9^\circ$  domains in (001)  $\text{YBa}_2\text{Cu}_3\text{O}_{7-\delta}$  on (110) YSZ. The low-mismatch, low- $\Sigma$  criterion used to select favorable orientations from near-coincident site lattices and meshes leads to the prediction that other orientations that are not seen should be observed, rather than the observed  $\sim 9^\circ$  in-plane-rotated orientation.

#### D. Other examples of general phenomenon

The formation of  $\sim 9^\circ$  in-plane-rotated domains in  $c$ -axis oriented  $\text{YBa}_2\text{Cu}_3\text{O}_{7-\delta}$  films grown on (001) YSZ and (110) YSZ are just two examples of a general heteroepitaxial phenomenon. This phenomenon, involving the epitaxial alignment between the diagonal of a square surface mesh and the diagonal of a rectangular surface mesh, is a general method for producing in-plane misorientations. Here we describe the ideal lattice constant ratios where this phenomenon is expected to occur for a (110)/(001) interface between two cubic structures. Extension of this epitaxial alignment concept to the relevant surface meshes of other planes and lattices is straightforward. Additional examples of this phenomenon are then presented.

For a (110)-oriented film of a material with a simple cubic lattice with lattice constant  $a_{\text{film}}$  on a (001)-oriented substrate having a face-centered cubic (fcc) lattice with lattice constant  $a_{\text{fcc sub}}$ , this match along the diagonals occurs when  $\sqrt{3}a_{\text{film}} = \sqrt{2}a_{\text{fcc sub}}$ , or  $a_{\text{film}} \approx 0.816 a_{\text{fcc sub}}$ . For comparison, the  $a_{\text{film}}/a_{\text{fcc sub}}$  ratio for (110)  $\text{BaZrO}_3$  on (001) YSZ is 0.816 (at room temperature). However, minimizing the mismatch along the diagonal does not minimize the lattice mismatch of the near-coincident site surface mesh. To minimize the latter, it is desired to minimize the lattice mismatch along two orthogonal directions, as can be seen from Fig. 4(b). The ideal lattice constant of the film (that minimizes the lattice match along two orthogonal directions) is attained when  $a_{\text{film}} = 2\sqrt{3}(3\sqrt{2} - 4)a_{\text{fcc sub}}$ , or  $a_{\text{film}} \approx 0.841 a_{\text{fcc sub}}$ . Alternatively, if the (001)-oriented substrate has a simple cubic lattice with lattice constant  $a_{\text{sub}}$ , the corresponding value is  $a_{\text{film}} = 4\sqrt{3}(3 - 2\sqrt{2})a_{\text{sub}}$ , or  $a_{\text{film}} \approx 1.189 a_{\text{sub}}$ . In both of these cases, the minimized lattice mismatch is 2.9% (+2.9% in one direction and -2.9% in the perpendicular direction).

A more favorable lattice match can be achieved along two orthogonal directions when this phenomenon occurs between a (110)-oriented film and a (110)-oriented substrate of two cubic materials. In this case, the ideal lattice constant of the film is attained in two

orthogonal directions at the same time (i.e., perfect lattice match) when  $a_{\text{film}} = \sqrt{2/3}a_{\text{fcc sub}}$ , or  $a_{\text{film}} \approx 0.816 a_{\text{fcc sub}}$ . As Fig. 5(b) shows, (110)  $\text{BaZrO}_3$  on (110) YSZ is nearly this ideal case:  $a_{\text{film}}/a_{\text{fcc sub}} = 0.816$  (at room temperature). Alternatively, if the (110)-oriented substrate has a simple cubic lattice, the ideal value is  $a_{\text{film}} = (2/\sqrt{3})a_{\text{sub}}$ , or  $a_{\text{film}} \approx 1.155 a_{\text{sub}}$ .

From the above discussion, the ideal lattice parameter of a (110)-oriented simple cubic material for growth on (001) YSZ in order to observe this phenomenon is 4.319 Å.  $\text{Ba}_{1-x}\text{K}_x\text{BiO}_3$  has a lattice constant of 4.322 Å to 4.287 Å over the composition range where its structure is simple cubic ( $0.1 \leq x \leq 0.4$ ).<sup>45,46</sup> In hopes of observing another example of this phenomenon, involving the epitaxial alignment between the diagonal of a square surface mesh and the diagonal of a rectangular surface mesh, (110)  $(\text{Ba}, \text{K})\text{BiO}_3$  was grown on (001) YSZ. This growth was initiated at  $T_{\text{sub}} \sim 550^\circ\text{C}$  with the nucleation of  $\text{BaBi}_x\text{O}_y$  ( $x \sim 1$ ) for 5 min (~10 nm).<sup>39,47</sup> Then the substrate temperature was lowered to  $\sim 270^\circ\text{C}$  and  $(\text{Ba}, \text{K})\text{BiO}_3$  was grown. As expected, sharp peaks at  $\phi \sim \pm 9^\circ$  were observed [see Fig. 12(a)]. Note, however, that the lattice parameter of  $(\text{Ba}, \text{K})\text{BiO}_3$  is quite close to that of  $\text{BaZrO}_3$  (4.193 Å).<sup>17</sup> Although no x-ray diffraction peaks arising from (110)  $\text{BaZrO}_3$  were detected, it is possible that an epitaxial reaction occurred between  $(\text{Ba}, \text{K})\text{BiO}_3$  and YSZ forming a thin (110)  $\text{BaZrO}_3$  reaction layer, upon which the  $(\text{Ba}, \text{K})\text{BiO}_3$  layer subsequently grew.

An example of this same epitaxial phenomena between a simple cubic substrate and simple cubic film is (110)  $(\text{Ba}, \text{K})\text{BiO}_3$  on (001)  $\text{LaAlO}_3$ ,<sup>48</sup> as shown in Fig. 12(b). Although the epitaxial alignment giving rise to the in-plane rotation is the same as that shown for YSZ in Fig. 4, here the peaks occur at  $\phi \sim (45 - 9) = 36^\circ$  because the  $\text{LaAlO}_3$  surface mesh is not centered, resulting in a 45° rotation of the in-plane axes compared to the (001) YSZ surface mesh. The  $a_{\text{film}}/a_{\text{sub}}$  ratio for (110)  $(\text{Ba}, \text{K})\text{BiO}_3$  on (001)  $\text{LaAlO}_3$  is 1.13, compared to the ideal value of 1.189 discussed above.

## V. DISCUSSION

Having investigated the origin of the  $\phi \sim \pm 9^\circ$  peaks, we reexamine the results presented by others related to  $\sim 9^\circ$  peaks in (001)  $\text{YBa}_2\text{Cu}_3\text{O}_{7-\delta}$  films deposited on (001) YSZ. Our explanation, involving the epitaxial alignment between the diagonal of a square surface mesh and the diagonal of a rectangular surface mesh, is consistent with prior results and clarifies unexplained and previously unexpected observations. For example, Fork *et al.*<sup>7</sup> showed that the in-plane orientation of overlying  $\text{YBa}_2\text{Cu}_3\text{O}_{7-\delta}$  layers was sensitively dependent on the deposition of extremely thin

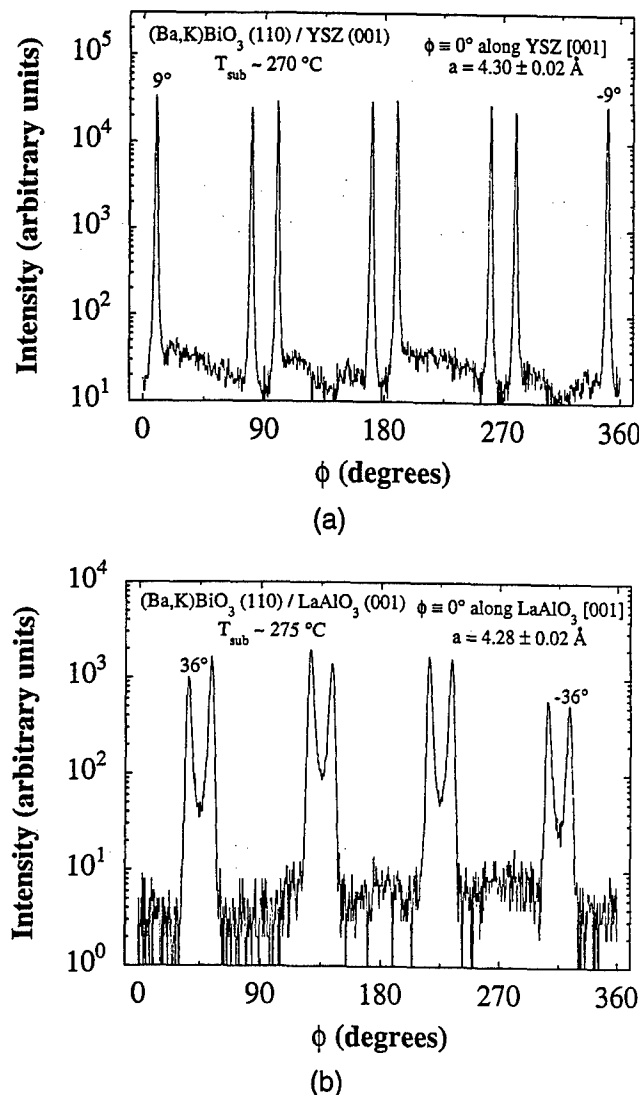


FIG. 12.  $\phi$ -scans of 200 (Ba,K)BiO<sub>3</sub> peaks of (110)-oriented (Ba,K)BiO<sub>3</sub> films grown by MBE on (a) (001) YSZ at  $T_{\text{sub}} \sim 270^\circ\text{C}$  and (b) (001) LaAlO<sub>3</sub> at  $T_{\text{sub}} \sim 275^\circ\text{C}$ .

layers ( $\sim 0.3$  nm) of BaO, CuO, Y<sub>2</sub>O<sub>3</sub>, or BaZrO<sub>3</sub> on (001) YSZ substrates, or on (001) YSZ substrates upon which a homoepitaxial YSZ layer was grown. The thin CuO, Y<sub>2</sub>O<sub>3</sub>, and BaZrO<sub>3</sub> layers and the homoepitaxial YSZ layer favored the  $45^\circ$  in-plane rotation, whereas the BaO layer led to the  $\sim 9^\circ$  in-plane rotation. Although this previous study lacked *in situ* characterization during the deposition of these thin layers, our *in situ* RHEED observations indicate the reason for the extreme sensitivity of the in-plane orientation to BaO deposition: it leads to a  $\sim 9^\circ$  rotated (110) BaZrO<sub>3</sub> epitaxial reaction layer, which subsequently determines the in-plane orientation of the YBa<sub>2</sub>Cu<sub>3</sub>O<sub>7-δ</sub> overlayer. We have not studied the interfacial reactions of CuO or Y<sub>2</sub>O<sub>3</sub> overlayers, but in contrast to the BaO-ZrO<sub>2</sub> case, the CuO-ZrO<sub>2</sub> phase diagram<sup>49</sup> is free of intermediate phases and the Y<sub>2</sub>O<sub>3</sub>-ZrO<sub>2</sub> phase diagram<sup>50</sup> not only

contains a very wide solid solution region (up to 40 mol % Y<sub>2</sub>O<sub>3</sub>), but the only intermediate compound,<sup>50</sup> Zr<sub>3</sub>Y<sub>4</sub>O<sub>12</sub>, forms so sluggishly that single-phase YSZ films with up to 78 mol % Y<sub>2</sub>O<sub>3</sub> have been reported.<sup>51</sup> Thus, of the thin layers deposited by Fork *et al.*,<sup>7</sup> an interfacial reaction layer is expected only for the case of BaO. The resultant (110)-oriented BaZrO<sub>3</sub> reaction layer subsequently leads to the dominant  $\sim 9^\circ$  in-plane rotation observed in the overgrown YBa<sub>2</sub>Cu<sub>3</sub>O<sub>7-δ</sub> film.

Given the strong influence of the (110) BaZrO<sub>3</sub> interfacial reaction layer on the resulting in-plane orientation of the YBa<sub>2</sub>Cu<sub>3</sub>O<sub>7-δ</sub>, it may seem surprising that the thin BaZrO<sub>3</sub> layer deposited in the aforementioned study<sup>7</sup> did not also lead to YBa<sub>2</sub>Cu<sub>3</sub>O<sub>7-δ</sub> domains with a  $\sim 9^\circ$  in-plane rotation. We attribute this to the growth of a non-(110) oriented BaZrO<sub>3</sub> layer. Fork *et al.*<sup>7</sup> did not report the orientation of their thin BaZrO<sub>3</sub> layers. However, we found that BaZrO<sub>3</sub> films deposited on (001) YSZ were mainly oriented in the cube-on-cube orientation, i.e., with (001) BaZrO<sub>3</sub> parallel to (001) YSZ, in contrast to the (110) BaZrO<sub>3</sub> orientation formed by epitaxial reaction. Others have reported (110)-oriented BaZrO<sub>3</sub> films deposited on (001) YSZ,<sup>3,52</sup> but they also report that the inverted interface, i.e., (001) YSZ deposited on (001) BaZrO<sub>3</sub>, grows cube-on-cube.<sup>3</sup> As the epitaxial relationship obtained for the growth of BaZrO<sub>3</sub> on (001) YSZ and vice versa varies significantly with deposition conditions, it would appear from the absence of  $\sim 9^\circ$  domains in the YBa<sub>2</sub>Cu<sub>3</sub>O<sub>7-δ</sub> films grown on top of a BaZrO<sub>3</sub> buffer layer by Fork *et al.*<sup>7</sup> that their BaZrO<sub>3</sub> layer was not (110)-oriented.

The predominant  $45^\circ$  in-plane rotation observed by Fork *et al.*<sup>7</sup> for YBa<sub>2</sub>Cu<sub>3</sub>O<sub>7-δ</sub> films grown on (001) YSZ substrates with homoepitaxial YSZ buffer layers is consistent with the work of Brorsson *et al.*<sup>9</sup> Brorsson *et al.*<sup>9</sup> showed that homoepitaxial YSZ layers, grown under conditions similar to those used by Fork *et al.*,<sup>7</sup> have an increased surface step density compared to the underlying YSZ substrate. They found that an increased step density on the surface of (001) YSZ, regardless of whether it was from a homoepitaxial YSZ film or a result of high temperature annealing of the substrate, led to an increased fraction of  $45^\circ$  in-plane-rotated YBa<sub>2</sub>Cu<sub>3</sub>O<sub>7-δ</sub> grains in the overlying film. Brorsson *et al.*<sup>9</sup> interpreted this result to imply that step edges on (001) YSZ substrates act as favorable nucleation sites for  $45^\circ$ -oriented YBa<sub>2</sub>Cu<sub>3</sub>O<sub>7-δ</sub>.<sup>9</sup> Since no reactions between the thin ( $\sim 0.3$  nm) CuO and Y<sub>2</sub>O<sub>3</sub> layers deposited by Fork *et al.*<sup>7</sup> on (001) YSZ are expected, an analogous surface roughening and graphoepitaxial mechanism may take place, leading to the observed increase in  $45^\circ$  in-plane-rotated YBa<sub>2</sub>Cu<sub>3</sub>O<sub>7-δ</sub> grains for these buffer layers as well.

Similar to the growth temperature effect reported for the growth of YBa<sub>2</sub>Cu<sub>3</sub>O<sub>7-δ</sub> on (001) YSZ,<sup>10,11</sup>

in our growths on (110) YSZ substrates, the  $\phi \sim 9^\circ$  domains were observed at higher growth temperatures. This is consistent with the epitaxial relationship of the  $\text{YBa}_2\text{Cu}_3\text{O}_{7-\delta}$  layer being established after the formation of the  $\text{BaZrO}_3$  interfacial layer. Lower growth temperatures were free of  $\phi \sim 9^\circ$  domains, consistent with the epitaxial relationship of the  $\text{YBa}_2\text{Cu}_3\text{O}_{7-\delta}$  layer being established before the formation of the  $\text{BaZrO}_3$  layer.

Wen *et al.*<sup>8</sup> present a cross-sectional TEM image (Fig. 6 in Ref. 8) of a  $\text{BaZrO}_3$  epitaxial in-plane reaction product between (001)  $\text{YBa}_2\text{Cu}_3\text{O}_{7-\delta}$  and (001) YSZ that appears to be close to the  $\sim 9^\circ$  rotation that we have seen by RHEED. Their cross-sectional TEM image is along the [100] YSZ zone axis, and they state that this substrate zone-axis is approximately parallel to the [331] direction of the  $\text{BaZrO}_3$  layer. This is within  $3.5^\circ$  of the (irrational) direction in  $\text{BaZrO}_3$  that lies parallel to [100] YSZ (see Fig. 4) for fully relaxed  $\text{BaZrO}_3$ . Unfortunately, Wen *et al.*<sup>8</sup> do not indicate if the  $\text{BaZrO}_3$  layer is (110)-oriented. However, it is clear that it must be different than the (001)-oriented  $\text{BaZrO}_3$  layers that are present in the remainder of their TEM images as {001} cannot be perpendicular to [331].

Recently peaks at  $\phi \sim \pm 37^\circ$  have also been reported in *c*-axis oriented  $\text{YBa}_2\text{Cu}_3\text{O}_{7-\delta}$  films grown on (001) YSZ, indicating the presence of  $\text{YBa}_2\text{Cu}_3\text{O}_{7-\delta}$  grains with in-plane rotations of about  $37^\circ$ .<sup>11</sup> These peaks are observed in films grown under conditions similar to those in which peaks at  $\phi \sim 9^\circ$  occur (i.e., high substrate temperatures). In fact, both the  $\phi \sim 9^\circ$  peaks and the  $\phi \sim 37^\circ$  peaks were observed in the same film by Skofronick *et al.*<sup>11</sup> The origin of these  $\sim 37^\circ$  in-plane-rotated grains is likely the same as that of the  $\sim 9^\circ$  rotated grains. *c*-axis oriented  $\text{YBa}_2\text{Cu}_3\text{O}_{7-\delta}$  is known to align epitaxially with (110)-oriented  $\text{BaZrO}_3$  in two manners, related by a  $45^\circ$  in-plane rotation. The first is

$$(001)_{\text{YBa}_2\text{Cu}_3\text{O}_{7-\delta}} \parallel (110)_{\text{BaZrO}_3} \\ \text{and } [100]_{\text{YBa}_2\text{Cu}_3\text{O}_{7-\delta}} \parallel [001]_{\text{BaZrO}_3},$$

as we have found to be dominant for the nucleation of  $\text{YBa}_2\text{Cu}_3\text{O}_{7-\delta}$  on  $\text{BaZrO}_3$  on (001) YSZ, and the second is

$$(001)_{\text{YBa}_2\text{Cu}_3\text{O}_{7-\delta}} \parallel (110)_{\text{BaZrO}_3} \\ \text{and } [110]_{\text{YBa}_2\text{Cu}_3\text{O}_{7-\delta}} \parallel [001]_{\text{BaZrO}_3}$$

as others<sup>19,31</sup> have observed for  $\text{BaZrO}_3$  formed after the epitaxial alignment between  $\text{YBa}_2\text{Cu}_3\text{O}_{7-\delta}$  and YSZ is established. We have found the second to be dominant for the nucleation of  $\text{YBa}_2\text{Cu}_3\text{O}_{7-\delta}$  on  $\text{BaZrO}_3$  on (110) YSZ. As discussed earlier, both of these orientation relationships have identical lattice match, and we speculate that the dominance of a particular one is due to a graphoepitaxial contribution. The presence of both  $\sim 9^\circ$  and  $\sim 37^\circ$  in-plane

rotations in the  $\text{YBa}_2\text{Cu}_3\text{O}_{7-\delta}$  films of Skofronick *et al.*,<sup>11</sup> in contrast to the more frequent observation of solely  $\phi \sim 9^\circ$  peaks, provides further evidence that an influencing factor other than lattice match alone is active. The more frequent observation of the  $\phi \sim 9^\circ$  peaks compared to the  $\phi \sim 37^\circ$  (or  $45^\circ - 9^\circ = 36^\circ$ ) peaks indicates that the  $[100]_{\text{YBa}_2\text{Cu}_3\text{O}_{7-\delta}} \parallel [001]_{\text{BaZrO}_3}$  orientation is dominant for the growth conditions most frequently used to deposit (001)  $\text{YBa}_2\text{Cu}_3\text{O}_{7-\delta}$  on (001) YSZ.

## VI. CONCLUSIONS

The epitaxial alignment between the diagonal of a square surface mesh and the diagonal of a rectangular surface mesh is a general method for producing in-plane misorientations. The model presented explains why diffraction peaks at  $\phi \sim 9^\circ$  are observed in *c*-axis oriented  $\text{YBa}_2\text{Cu}_3\text{O}_{7-\delta}$  grown on (001) YSZ as well as on (110) YSZ substrates, and has been used to select other epitaxial systems to demonstrate this phenomenon. If a means could be found to suppress all but one of the  $\sim 9^\circ$  in-plane-rotated domains, this technique could provide a significant advantage in grain boundary engineering over the bi-epitaxy process for the growth of  $\text{YBa}_2\text{Cu}_3\text{O}_{7-\delta}$ -based and (Ba, K) $\text{BiO}_3$ -based Josephson junctions.

## ACKNOWLEDGMENTS

We gratefully acknowledge helpful interactions with J. Ströbel, G. L. Skofronick, and A. H. Carim, and Joe Wenckus for generously supplying yttria-stabilized cubic zirconia crystals. DGS acknowledges the financial support of ONR through Contract N00014-93-1-0512. JCC acknowledges the financial support of NSF through Grant DMR-9357614.

## REFERENCES

1. A. J. Moulson and J. M. Herbert, *Electroceramics: Materials • Applications* (Chapman & Hall, London, 1990).
2. K. Char, M. S. Colclough, S. M. Garrison, N. Newman, and G. Zaharchuk, *Appl. Phys. Lett.* **59**, 733 (1991); K. Char, M. S. Colclough, L. P. Lee, and G. Zaharchuk, *Appl. Phys. Lett.* **59**, 2177 (1991).
3. X. D. Wu, L. Luo, R. E. Muenchausen, K. N. Springer, and S. Folty, *Appl. Phys. Lett.* **60**, 1381 (1992).
4. L. P. Lee, K. Char, M. S. Colclough, and G. Zaharchuk, *Appl. Phys. Lett.* **59**, 3051 (1991).
5. D. K. Fork, A. Barrera, T. H. Geballe, A. M. Viano, and D. B. Fenner, *Appl. Phys. Lett.* **57**, 2504 (1990).
6. S. M. Garrison, N. Newman, B. F. Cole, K. Char, and R. W. Barton, *Appl. Phys. Lett.* **58**, 2168 (1991); S. M. Garrison, N. Newman, B. F. Cole, K. Char, and R. W. Barton, *Appl. Phys. Lett.* **59**, 3060 (1991).
7. D. K. Fork, S. M. Garrison, M. Hawley, and T. H. Geballe, *J. Mater. Res.* **7**, 1641 (1992).
8. J. G. Wen, C. Traeholt, H. W. Zandbergen, K. Joosse, E. M. C. M. Reuvekamp, and H. Rogalla, *Physica C* **218**, 29 (1993).

9. G. Brorsson, E. Olsson, Z. G. Ivanov, E. A. Stepansov, J. A. Alarco, Y. Boikov, T. Claeson, P. Berastegui, V. Langer, and M. Löfgren, *J. Appl. Phys.* **75**, 7958 (1994).
10. Y. Boikov, Z. G. Ivanov, G. Brorsson, and T. Claeson, *Supercond. Sci. Technol.* **7**, 281 (1994).
11. G. L. Skofronick, A. H. Carim, S. R. Foltyn, and R. E. Muenchhausen, *J. Appl. Phys.* **76**, 4753 (1994).
12. D. Dimos, P. Chaudhari, and J. Mannhart, *Phys. Rev. B* **41**, 4038 (1990).
13. S. S. Laderman, R. C. Taber, R. D. Jacobowitz, J. L. Moll, C. B. Eom, T. L. Hylton, A. F. Marshall, T. H. Geballe, and M. R. Beasley, *Phys. Rev. B* **43**, 2922 (1991).
14. J. A. Alarco, G. Brorsson, Z. G. Ivanov, P.-Å. Nilsson, E. Olsson, and M. Löfgren, *Appl. Phys. Lett.* **61**, 723 (1992).
15. R. D. Shannon, *Acta Crystallogr. A* **32**, 751 (1976).
16. R. P. Ingel and D. Lewis, III, *J. Am. Ceram. Soc.* **69**, 325 (1986).
17. JCPDS card 6-399 (JCPDS International Centre for Diffraction Data, Swarthmore, PA).
18. R. Beyers and T. M. Shaw, *Solid State Phys.* **42**, 135 (1989), and references therein.
19. G. L. Skofronick, A. H. Carim, S. R. Foltyn, and R. E. Muenchhausen, *J. Mater. Res.* **8**, 2785 (1993).
20. C. H. Mueller, P. H. Holloway, J. D. Budai, F. A. Miranda, and K. B. Bhasin, *J. Mater. Res.* **10**, 810 (1995).
21. The lattice mismatch values given throughout this article are calculated by the formula  $(a_{\text{sub}} - a_{\text{film}}/a_{\text{film}})$ .<sup>22</sup> Although the lattice constants vary with temperature and composition ( $0.095 \leq x \leq 0.6$  in  $(\text{Y}_2\text{O}_3)_x(\text{ZrO}_2)_{1-x}$  and  $0 \leq \delta \leq 1$  in  $\text{YBa}_2\text{Cu}_3\text{O}_{7-\delta}$ ) and it would be most appropriate to report the lattice mismatch for the specific growth conditions used, for simplicity we report the lattice mismatch at room temperature,  $x \sim 0.095^{16}$  and  $\delta \sim 0.1^8$ . These approximate values are adequate for the relatively qualitative reasoning that lattice mismatch considerations allow.
22. See, for example, J. W. Matthews in *Epitaxial Growth, Part B*, edited by J. W. Matthews (Academic Press, New York, 1975), pp. 559–609.
23. D. G. Schlom, E. S. Hellman, E. H. Hartford, Jr., and J. Mannhart, presented at the Fall '93 Materials Research Society Meeting in Boston, MA, 1993 (unpublished).
24. J. J. Cuomo, M. F. Chisholm, D. S. Yee, D. J. Mikalsen, P. B. Madakson, R. A. Roy, E. Giess, and G. Scilla, in *Thin Film Processing and Characterization of High-Temperature Superconductors*, AIP Conference Proceedings No. 165, edited by J. M. E. Harper, R. J. Colton, and L. C. Feldman (American Institute of Physics, New York, 1988), pp. 141–148.
25. T. Komatsu, O. Tanaka, K. Matusita, M. Takata, and T. Yamashita, *Jpn. J. Appl. Phys.* **27**, L1025 (1988).
26. H. Koinuma, K. Fukuda, T. Hashimoto, and K. Fueki, *Jpn. J. Appl. Phys.* **27**, L1216 (1988).
27. M. J. Cima, J. S. Schneider, S. C. Peterson, and W. Coblenz, *Appl. Phys. Lett.* **53**, 710 (1988).
28. C. T. Cheung and E. Ruckenstein, *J. Mater. Res.* **4**, 1 (1989).
29. L. A. Tietz, C. B. Carter, D. K. Lathrop, S. E. Russek, R. A. Buhrman, and J. R. Michael, *J. Mater. Res.* **4**, 1072 (1989). The 0.3 nm fringe spacing reported for the intermediate reaction layer in the cross-sectional TEM image (identified as being possibly  $\text{BaZrO}_3$ ) indicates that the  $\text{BaZrO}_3$  is (110)-oriented.
30. M. J. Shapiro, K. L. More, W. J. Lackey, J. A. Hanigofsky, D. N. Hill, W. B. Carter, E. K. Barefield, E. A. Judson, D. F. O'Brien, R. Patrick, Y. S. Chung, and T. S. Moss, *J. Am. Ceram. Soc.* **74**, 2021 (1991).
31. D. M. Hwang, Q. Y. Ying, and H. S. Kwok, *Appl. Phys. Lett.* **58**, 2429 (1991).
32. M. J. Casanove, A. Alimoussa, C. Roucau, C. Escribe-Filippini, P. L. Reydet, and P. Marcus, *Physica C* **175**, 285 (1991).
33. O. Eibl, K. Hradil, and H. Schmidt, *Physica C* **177**, 89 (1991).
34. J. A. Alarco, G. Brorsson, H. Olin, and E. Olsson, *J. Appl. Phys.* **75**, 3202 (1994).
35. Ceres Corp., N. Billerica, Massachusetts.
36. Commercial Crystal Laboratories, Naples, Florida.
37. X. X. Xi, G. Linker, O. Meyer, E. Nold, B. Obst, F. Ratzel, R. Smits, B. Strehlau, F. Weschenfelder, and J. Geerk, *Z. Phys. B* **74**, 13 (1989).
38. B. Holzapfel, B. Roas, L. Schultz, P. Bauer, and G. Saemann-Ischenko, *Appl. Phys. Lett.* **61**, 3178 (1992).
39. E. S. Hellman, E. H. Hartford, and E. M. Gyorgy, *Appl. Phys. Lett.* **58**, 1335 (1991).
40. C. B. Eom, J. Z. Sun, K. Yamamoto, A. F. Marshall, K. E. Luther, T. H. Geballe, and S. S. Laderman, *Appl. Phys. Lett.* **55**, 595 (1989).
41. L. V. Azároff, *Elements of X-Ray Crystallography* (McGraw-Hill, New York, 1968), pp. 360–389.
42. With the oxygen plasma on, the sample was exposed to the barium beam for 40 s. RBS measurement of the resulting  $\text{BaO}$  film thickness deposited on a comounted  $\text{MgO}$  substrate ( $T_{\text{sub}} \sim 660^\circ\text{C}$ ) indicated an average  $\text{BaO}$  film thickness of 1.4 nm.
43. Note that depending on the surface termination of the (110)  $\text{BaZrO}_3$  layer, the oxygen sublattice of this latter orientation relationship ( $[110]_{\text{YBa}_2\text{Cu}_3\text{O}_{7-\delta}} \parallel [001]_{\text{BaZrO}_3}$ ) could have the same surface mesh area as the oxygen sublattice of the former orientation relationship ( $[100]_{\text{YBa}_2\text{Cu}_3\text{O}_{7-\delta}} \parallel [001]_{\text{BaZrO}_3}$ ). There are two distinct (110)  $\text{BaZrO}_3$  planes, neither of which is charge neutral:  $\text{BaZrO}$  and  $\text{O}_2$ . If the latter is the terminating layer, the oxygen sublattice of the near-coincident site surface mesh cell shown in Fig. 8 is centered, and the primitive cell would have an area of  $0.47 \text{ nm}^2$ .
44. C. Escribe-Filippini, P. L. Reydet, J. Marcus, and M. Burnel, *J. Less-Comm. Met.* **151**, 263 (1989).
45. L. F. Schneemeyer, J. K. Thomas, T. Siegrist, B. Batlogg, L. W. Rupp, R. L. Opila, R. J. Cava, and D. W. Murphy, *Nature (London)* **335**, 421 (1988).
46. J. P. Wignacourt, J. S. Swinnea, H. Steinfink, and J. B. Goode-nough, *Appl. Phys. Lett.* **53**, 1753 (1988).
47. M. G. Norton, E. S. Hellman, E. H. Hartford, Jr., and C. B. Carter, *Physica C* **205**, 347 (1993); M. G. Norton, E. S. Hellman, E. H. Hartford, Jr., and C. B. Carter, *J. Cryst. Growth* **113**, 716 (1991).
48. Landolt-Börstein: *Numerical Data and Functional Relationships in Science and Technology, New Series*, Group III, Vol. 12a, edited by K.-H. Hellwege (Springer-Verlag, Berlin, 1978), p. 160. At room temperature  $\text{LaAlO}_3$  is rhombohedral (not simple cubic). However, the distortion from simple cubic is extremely small ( $\alpha = 60.1^\circ$ ) vs.  $\alpha = 60^\circ$  for cubic). Furthermore, at the substrate temperature at which growth was initiated,  $T_{\text{sub}} \sim 550^\circ\text{C}$ ,  $\text{LaAlO}_3$  is cubic.
49. A. M. M. Gadalla and J. White, *Trans. Brit. Ceram. Soc.* **65**, 383 (1966).
50. V. S. Stubician, R. C. Hink, and S. P. Ray, *J. Am. Ceram. Soc.* **61**, 17 (1978); V. S. Stubician and J. R. Hellmann, in *Science and Technology of Zirconia*, Vol. 3 in *Advances in Ceramics* series, edited by A. H. Heuer and L. W. Hobbs (American Ceramic Society, Westerville, OH, 1981), pp. 25–36.
51. H. Holzschuh and H. Suhr, *Appl. Phys. Lett.* **59**, 470 (1991).
52. D. K. Fork (private communication). These (110)  $\text{BaZrO}_3$  films were deposited on (001)  $\text{YSZ}$  on (001) Si. They were much thicker than the  $\sim 0.3 \text{ nm}$   $\text{BaZrO}_3$  buffer layers studied in Ref. 7. Interestingly, a  $\phi$ -scan of these (110)-oriented  $\text{BaZrO}_3$  films on (001)  $\text{YSZ}$  revealed two in-plane orientation variants rotated with respect to one another by  $9.5^\circ$ .

# Domain structure of epitaxial PbTiO<sub>3</sub> films grown on vicinal (001) SrTiO<sub>3</sub>

C. D. Theis and D. G. Schlom

Department of Materials Science and Engineering, The Pennsylvania State University,  
University Park, Pennsylvania 16802-5005

(Received 22 February 1996; accepted 3 January 1997)

Epitaxial PbTiO<sub>3</sub> films have been grown on vicinal (001) SrTiO<sub>3</sub> substrates by pulsed laser deposition. Vicinal SrTiO<sub>3</sub> substrates with misorientations up to 9° from (001) were used, and the influence of the direction of misorientation on the resulting domain structure was studied. 4-circle x-ray diffraction analysis indicates that thin (40 nm) PbTiO<sub>3</sub> films are completely *c*-axis oriented [rocking curve full-width-at-half-maximum (FWHM) of 0.25° for the 002 reflection] and that thicker films (~200 nm) contain mixed *a*-axis and *c*-axis PbTiO<sub>3</sub> domains due to twinning along {011} planes. The [100] axis of the *a*-axis domains is misoriented by 2.1° to 3.3° toward {100} substrate directions with respect to the substrate normal. In contrast to growth on well-oriented (001) SrTiO<sub>3</sub> surfaces where the four equivalent tilts of the [100] axis of the *a*-axis domains are equally likely, on vicinal SrTiO<sub>3</sub> the *a*-axis domains are preferentially oriented in an uphill direction with respect to the crystallographic miscut.

## I. INTRODUCTION

Lead titanate has become an extensively studied ferroelectric material. It has a variety of potential applications, including ultrasonic sensors, infrared detectors, and ferroelectric random access memories.<sup>1</sup> Growth of PbTiO<sub>3</sub> has been hampered by problems with lead volatility.<sup>2,3</sup> However, high quality films have been made by metal-organic chemical-vapor deposition (MOCVD),<sup>4–7</sup> laser ablation,<sup>8–10</sup> sputtering,<sup>3,11</sup> and through the use of solution precursors.<sup>2</sup> Because of the anisotropic nature of lead titanate, many of its properties, including remanent polarization, pyroelectric coefficient, and coefficient of second harmonic generation, are dependent on its crystallographic orientation. For most of these applications, it is desirable to have a single-domain film with the PbTiO<sub>3</sub> *c*-axis normal to the substrate surface. To date, the growth of relatively thick films ( $\geq 50$  nm) of pure *c*-axis oriented epitaxial lead titanate has been hampered by the formation of {011} domain boundaries, resulting in mixed *c*- and *a*-domain films.<sup>2,4–6,9,10–14</sup> Researchers have shown that the introduction of domain boundaries in PbTiO<sub>3</sub> films grown on SrTiO<sub>3</sub> is favored to reduce strains that arise from the PbTiO<sub>3</sub> phase transition, lattice mismatch, and differences in thermal expansion between the film and substrate upon cooling.<sup>15–17</sup> In order to more fully understand the mechanisms that contribute to the ultimate population and orientation of these *a*-domains, we have grown epitaxial lead titanate films on vicinal (001) SrTiO<sub>3</sub> substrates.

The heteroepitaxial growth of anisotropic oxides on vicinal surfaces of isotropic oxide substrates

has been studied extensively: Bi<sub>2</sub>Sn<sub>2</sub>Ca<sub>n-1</sub>Cu<sub>n</sub>O<sub>2n+4</sub>/SrTiO<sub>3</sub>,<sup>18–20</sup> Bi<sub>2</sub>Sn<sub>2</sub>Ca<sub>n-1</sub>Cu<sub>n</sub>O<sub>2n+4</sub>/MgO,<sup>21,22</sup> YBa<sub>2</sub>Cu<sub>3</sub>O<sub>7-δ</sub>/SrTiO<sub>3</sub>,<sup>23–25</sup> YBa<sub>2</sub>Cu<sub>3</sub>O<sub>7-δ</sub>/MgO,<sup>26–28</sup> YBa<sub>2</sub>Cu<sub>3</sub>O<sub>7-δ</sub>/(Y<sub>2</sub>O<sub>3</sub>–ZrO<sub>2</sub>),<sup>29</sup> (La, Sr)-CuO<sub>4</sub>/SrTiO<sub>3</sub>,<sup>30</sup> and SrRuO<sub>3</sub>/SrTiO<sub>3</sub>.<sup>31</sup> However, in all of these cases, the relaxed state of the film at the growth temperatures involved is anisotropic. Here we describe the results of our investigation of the growth of a material that is isotropic and well lattice-matched to the underlying vicinal isotropic substrate at the growth temperature. However, after the film growth is complete and as the sample cools, the isotropic film undergoes a structural phase transition and becomes anisotropic. Similar behavior is expected in other isotropic epitaxial systems that undergo a phase transition after growth, e.g., BaTiO<sub>3</sub>, KNbO<sub>3</sub>, Pb(Zr, Ti)O<sub>3</sub>, (Pb, La)(Zr, Ti)O<sub>3</sub>, etc. However, the large tetragonal distortion in PbTiO<sub>3</sub> is an advantage for measuring the effect that a vicinal substrate surface has on the domain formation process that occurs *after growth*, making it an excellent model system on which to carry out this study. In the study described below, the films are all grown at temperatures higher than the Curie temperature and the domains are formed after growth is complete as the films cool. We have investigated the influence of vicinal (001) SrTiO<sub>3</sub> substrates on the domain structure of epitaxial PbTiO<sub>3</sub> films.

## II. BACKGROUND

The presence of PbTiO<sub>3</sub> grains oriented with their *a*-axis perpendicular to the (001) SrTiO<sub>3</sub> substrate (*a*-axis oriented PbTiO<sub>3</sub>) mixed with grains oriented with

their *c*-axis perpendicular to the substrate (*c*-axis oriented PbTiO<sub>3</sub>) have been seen in films grown from solution precursors,<sup>2</sup> and grown by MOCVD<sup>12</sup> and laser ablation.<sup>9</sup> Seifert *et al.*<sup>2</sup> reported a relative tilt of 3.5° between the [100] axis of *a*-oriented PbTiO<sub>3</sub> grains and the [001] axis of *c*-oriented PbTiO<sub>3</sub> grains caused by twinning along {011} planes. Similarly, Li *et al.*<sup>12</sup> saw a 3.0° tilt of the *a*-axis of *a*-oriented PbTiO<sub>3</sub> grains away from the substrate normal. They reported that below a thickness of 150 nm, the x-ray intensity associated with the *a*-axis oriented PbTiO<sub>3</sub> domains disappears,<sup>12</sup> indicating that thinner films are completely *c*-axis oriented. Films thicker than 150 nm grown on (001) SrTiO<sub>3</sub> display mixed *a*-axis and *c*-axis orientation.<sup>12</sup> Hsu and Raj<sup>9</sup> reported a relative tilt of 2.65 ± 0.5° of the *a*-axis of *a*-oriented PbTiO<sub>3</sub> grains away from the (001) SrTiO<sub>3</sub> substrate normal. This tilt angle remains independent of thickness from 50 to 350 nm, and the volume fraction of *a*-oriented material increases continuously as a function of thickness.<sup>9</sup> Below a thickness of 37 nm they reported that there are no longer *a*-oriented domains present based on x-ray diffraction analysis.<sup>9</sup>

Prior TEM<sup>32,33</sup> and STM<sup>34–36</sup> studies of vicinal (001) SrTiO<sub>3</sub> surfaces have established that the edges of the steps on such surfaces are primarily faceted along ⟨100⟩ directions<sup>32–34</sup> (i.e., the step edges run along ⟨100⟩ directions) and that the height of the steps are integral multiples of the unit cell height of SrTiO<sub>3</sub>.<sup>34–36</sup> Additionally, TEM studies of the PbTiO<sub>3</sub>/substrate interface have shown that the {011} domain boundaries begin at the interface and extend into the film.<sup>2,12–14</sup> The importance of these observations, and an explanation of the apparent discrepancies in the reported tilt angle of *a*-oriented PbTiO<sub>3</sub>/(001) SrTiO<sub>3</sub>, will be discussed in conjunction with the structure of thick epitaxial PbTiO<sub>3</sub> films grown on vicinal (001) SrTiO<sub>3</sub> substrates.

To date, the use of vicinal substrates for the growth of PbTiO<sub>3</sub> has been limited. Kim *et al.*<sup>37</sup> report the use of vicinal (5.5° miscut) MgO substrates for the growth of PbTiO<sub>3</sub> by rf sputtering. They note that the *c*-domains are misoriented by 1.0° away from the MgO(001), and the *a*-domains are misoriented by 0.5° from the MgO(001). Both the *a*- and *c*-domains are reported to be tilted toward the macroscopic surface normal, or equivalently downhill as defined by the macroscopic tilt of the substrate surface with respect to the (001) MgO plane [see inset to Fig. 1(c)]. Additionally, Kim *et al.*<sup>37</sup> note that the presence of MgO step edges has no influence on the in-plane orientation of the *a*-oriented domains. That is, equal volume fractions of *a*-domains were measured with the *c*-axis parallel to and perpendicular to the MgO step edges.<sup>37</sup> Kim *et al.*<sup>37</sup> found that the PbTiO<sub>3</sub> film crystalline quality improved dramatically using vicinal MgO substrates. They reported an improvement in the FWHM of the PbTiO<sub>3</sub>(001) rocking curve width from

2.28° to 1.64° for growth on nominal and vicinal (5.5° miscut) MgO substrates, respectively.<sup>37</sup>

Similarly, Wasa *et al.*<sup>38</sup> deposited PbTiO<sub>3</sub> films on vicinal (1.7° miscut) SrTiO<sub>3</sub> using rf sputtering. The substrates were miscut toward the [010] crystalline axis. These films were found to have extremely smooth surfaces, root mean square (RMS) roughness less than 3 nm for a film thickness of 100 nm.<sup>38</sup>

### III. EXPERIMENTAL

PbTiO<sub>3</sub> targets (2.5 cm diameter) are synthesized in-house using a traditional ceramic synthesis route. Powders of PbCO<sub>3</sub> and PbTiO<sub>3</sub> are ball milled in water for 36 h using a polymer dispersant. The slurry is dried and calcined at 450 °C to remove all CO<sub>2</sub> and pressed in a uniaxial press to 1500 psi (10 MPa) in order to achieve sufficient green strength to transport the pellet to a cold isostatic press. The pellet is then cold isostatically pressed to 40,000 psi (276 MPa). Sintering occurs in a lead-rich atmosphere (to prevent lead loss) at 770 °C for 4 h. Using this synthesis route we are able to achieve densities in excess of 98% of theoretical while minimizing lead loss (<0.5% by weight). The target employed in this study has a 75% to 25% molar ratio of PbTiO<sub>3</sub> to PbO, respectively.

Our deposition system consists of a rotating target which is ablated by a 248 nm KrF excimer laser. The substrate is radiatively heated by an alumina furnace with a Kanthal®<sup>39</sup> A-1 heating element which surrounds the substrate and allows for easy switching between off-axis and on-axis geometries.<sup>40</sup> Typical deposition temperatures for PbTiO<sub>3</sub> are ~775 °C using SrTiO<sub>3</sub>(001) and vicinal (001) SrTiO<sub>3</sub> single-crystal substrates.<sup>41</sup> All thick films grown in this study were deposited on-axis with the substrate located 6–7 cm from the target in an oxygen/ozone (~5% O<sub>3</sub>) ambient of 5–30 mTorr. The laser is focused to achieve an energy density of 2 J/cm<sup>2</sup> with a repetition frequency of 20–30 Hz.

Structural analysis was performed using a Picker 4-circle x-ray diffractometer equipped with a graphite incident-beam monochromator. A small solid state laser is employed to align the sample surface with the geometrical center of the diffractometer sphere. The laser is mounted in place of the detector at a symmetric reflection angle. The laser mount is designed to reflect the laser beam off of the sample surface in a path identical to (but in the reverse direction of) the collimated Cu K $\alpha$  radiation. Using this alignment technique we are able to reproducibly align the macroscopic surface of the sample to ±0.2°. After the sample surface is accurately aligned on the diffractometer using the laser, the angle and direction of miscut are readily determined using x-ray diffraction. The thickness of the samples in this study was determined by Rutherford backscattering

spectrometry (RBS) and spectroscopic ellipsometry (SE) measurements.

## IV. RESULTS AND DISCUSSION

### A. X-ray diffraction analysis of domain structure

On well-oriented (100) SrTiO<sub>3</sub> substrates, we routinely achieve high-quality epitaxial PbTiO<sub>3</sub> films.<sup>42</sup> For example, x-ray diffraction analysis of a 40 nm thick PbTiO<sub>3</sub> film deposited on (001) SrTiO<sub>3</sub> by 90° off-axis pulsed laser deposition (PLD) shows intense (00ℓ) peaks, indicating that the film is pure *c*-axis oriented PbTiO<sub>3</sub>. Additional scans show that no other orientations are present. The rocking curve FWHM of the PbTiO<sub>3</sub> 002 reflection is measured to be 0.25°, showing excellent out-of-plane alignment. An azimuthal scan of the 101 PbTiO<sub>3</sub> reflections of this same film shows a cube-on-cube orientational relationship between the PbTiO<sub>3</sub> film and the SrTiO<sub>3</sub> substrate with a FWHM of 0.4° in  $\phi$ , indicating little variation in the in-plane alignment. These peak widths are all comparable to the instrument resolution of our Picker 4-circle diffractometer. This film contains no *a*-axis grains caused by {011} twin boundaries, in agreement with the findings for epitaxial PbTiO<sub>3</sub> films of comparable thickness grown on (001) SrTiO<sub>3</sub> by MOCVD.<sup>12</sup>

In order to more fully understand the factors that influence the formation of domain boundaries in thicker films, numerous samples having thicknesses of ~200 nm were grown under identical conditions with similar cooling rates (~10° C/min) on vicinal (001) SrTiO<sub>3</sub>. Vicinal (001) SrTiO<sub>3</sub> substrates miscut toward the [100] or [110] were utilized, and the degree of miscut was varied from less than 1° to more than 9°.<sup>41</sup>

Figure 1(a) shows the  $\theta$ -2θ x-ray diffraction scan of a 200 nm thick film of PbTiO<sub>3</sub> grown on miscut SrTiO<sub>3</sub>. This vicinal (001) SrTiO<sub>3</sub> is miscut by 3.2° toward  $\phi = 55^\circ$ , where  $\phi = 0^\circ$  is defined as the SrTiO<sub>3</sub> [100] direction and  $\phi = 90^\circ$  is the SrTiO<sub>3</sub> [010] direction. The *c*-axis of the PbTiO<sub>3</sub> in Fig. 1(a) is slightly, but resolvably (0.3°), misoriented from the substrate normal; the scan in Fig. 1(a) is aligned to the PbTiO<sub>3</sub> (001) planes, resulting in diminished substrate peak intensities. The *c*-axis oriented PbTiO<sub>3</sub> domains show good out-of-plane orientation with a rocking curve FWHM of 0.7° for the PbTiO<sub>3</sub> 002 reflection. The azimuthal scan of the PbTiO<sub>3</sub> 101 reflections of the *c*-axis grains in Fig. 1(b) shows only cube-on-cube orientations with a FWHM of 1.0° in  $\phi$ .

The peaks at  $\xi = 3.3^\circ$ ,  $\xi = -2.4^\circ$ ,  $\xi = 3.1^\circ$ , and  $\xi = -2.7^\circ$  in the rocking curves of the PbTiO<sub>3</sub> 200 reflections shown in Fig. 1(c) indicate the presence of *a*-oriented PbTiO<sub>3</sub> grains, where  $\xi$  is the angle of tilt between the *c*-axis of the *c*-domains and the *a*-axis of the *a*-domains. The diffraction patterns in

Fig. 1(c) are measured at an in-plane separation of  $\phi = 90^\circ$  from each other, along the SrTiO<sub>3</sub> [100] and [010] directions. The *a*-axis in both crystallographic directions is preferentially tilted uphill, as defined by the macroscopic tilt of the substrate surface with respect to the (001) SrTiO<sub>3</sub> plane and schematically indicated in the inset within Fig. 1(c). Because (001) SrTiO<sub>3</sub> has 4-fold rotational symmetry, we see four directions of *a*-axis tilt following the four equivalent {011} twin planes. Based on x-ray diffraction integrated intensity, 39 vol % of the *a*-oriented material is tilted uphill toward the [100], 5% tilts downhill toward the [100], 51% is tilted uphill toward the [010], and 5% is tilted downhill toward the [010]. This is in contrast to the equally likely (i.e., four peaks of equal intensity) {011} twin boundaries previously reported in PbTiO<sub>3</sub> films grown on well-oriented (001) SrTiO<sub>3</sub> substrates.<sup>29</sup> The *c*-domain in this film shows only one orientation and is tilted by 0.3° toward the direction of miscut ( $\phi = 55^\circ$ ). In essence, the entire film is tilted toward the direction of miscut (uphill) by 0.3° with the four *a*-domains tilted orthogonally to the *c*-domain by the angles shown in Fig. 1(c). This spatial arrangement of domains was seen in all samples. As a result, all rocking curves performed were first aligned to the *c*-oriented domains. This sample is indicative of the trend seen in all PbTiO<sub>3</sub> films; as the relative volume fraction of *a*-oriented material tilted in a certain direction increases, the tilt between that *a*-domain and the *c*-domain increases (higher  $\xi$ ). Similarly, as the relative volume fraction of *a*-oriented material tilted in a certain direction decreases, the tilt between that *a*-domain and the *c*-domain decreases (lower  $\xi$ ).

### B. Model of preferred *a*-domain orientations

The preferential orientation of the *a*-axis PbTiO<sub>3</sub> domains can be explained by lattice matching considerations. As the film growth temperature is well above the Curie temperature (490 °C for bulk PbTiO<sub>3</sub>),<sup>43</sup> twinning of the PbTiO<sub>3</sub> must occur during cooling following film growth. The ⟨100⟩ directions of the SrTiO<sub>3</sub> substrate—both the in-plane directions of the (001) SrTiO<sub>3</sub> surface<sup>32–34</sup> as well as those of the integral-unit cell high step edges<sup>34–36</sup>—are much better lattice matched to the *a*-axis of PbTiO<sub>3</sub> than to its *c*-axis. Consequently, as schematically depicted in Fig. 2, it is energetically favorable for the regions of the PbTiO<sub>3</sub> film in contact with the {100} SrTiO<sub>3</sub> surfaces to be (001) PbTiO<sub>3</sub> surfaces. Such an orientational relationship provides excellent lattice matching between the in-plane ⟨100⟩ SrTiO<sub>3</sub> directions and the in-plane [100] and [010] PbTiO<sub>3</sub> directions. Specifically, the lattice mismatch between (001) PbTiO<sub>3</sub> and {100} SrTiO<sub>3</sub> is 0.1% along both the [100] PbTiO<sub>3</sub> || ⟨100⟩ SrTiO<sub>3</sub> and [010] PbTiO<sub>3</sub> || ⟨100⟩ SrTiO<sub>3</sub> directions at room temperature.

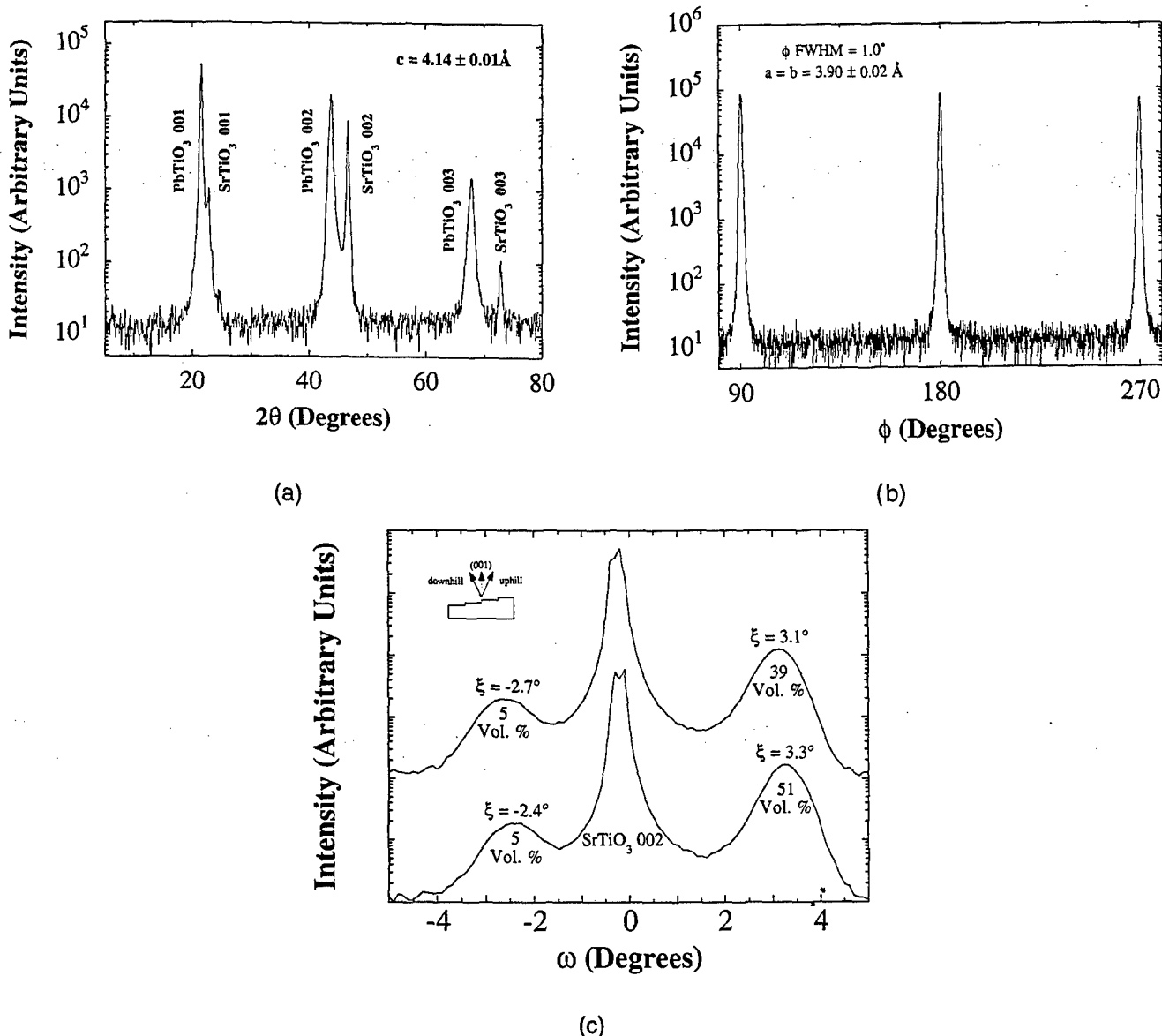


FIG. 1. (a) X-ray diffraction patterns of a 200 nm thick PbTiO<sub>3</sub> film grown on a vicinal (001) SrTiO<sub>3</sub> substrate miscut by 3.2° toward  $\phi = 55^\circ$ . (b)  $\phi$  scan of PbTiO<sub>3</sub> 101 reflections showing cube-on-cube orientation to the substrate, and (c)  $\omega$  scan of PbTiO<sub>3</sub> 200 reflections showing  $a$ -axis tilt angle  $\xi$  (upper scan is toward  $\phi = 0^\circ$ , and lower scan is toward  $\phi = 90^\circ$ ; these scans are offset from each other for clarity).

For comparison, the (100) PbTiO<sub>3</sub> || {100} SrTiO<sub>3</sub> and (010) PbTiO<sub>3</sub> || SrTiO<sub>3</sub> epitaxial orientations both have a lattice mismatch of -6% along [001] PbTiO<sub>3</sub> || <100> SrTiO<sub>3</sub> and 0.1% along <100> PbTiO<sub>3</sub> || <100> SrTiO<sub>3</sub> at room temperature.

On well-oriented (001) SrTiO<sub>3</sub> surfaces, there is not a dominance of any step edge, and all four types of {011} twin boundaries occur with equal likelihood. However, the vicinal (001) SrTiO<sub>3</sub> surface contains a dominant step edge direction, and the corresponding (011) twin boundary dominates as is schematically shown in Fig. 2. The tetragonality of PbTiO<sub>3</sub> has been exaggerated in this figure to clearly illustrate the geometrical cause of the tilt of the  $a$ -oriented material of PbTiO<sub>3</sub> with respect to the crystallographic normal. This explanation is consistent

with our observation that a preferred orientation of  $a$ -domains is found *only* on vicinal substrates. This indicates that the phenomenon is related to a dominance in the direction of the steps on the SrTiO<sub>3</sub> substrate.

The lattice-matching arguments presented above and depicted in Fig. 2 imply that the  $c$ -axis of all  $a$ -domains will lie parallel to the projection of the [100] axis of the  $a$ -domain onto the SrTiO<sub>3</sub> (001) surface and not perpendicular to this projection. Indeed, only this expected orientation of  $a$ -domains is observed by 4-circle x-ray diffraction. Unlike the orientation of  $a$ -domains on vicinal (100) MgO, where equal volume fractions were measured with their  $c$ -axis parallel and perpendicular to the MgO step edges,<sup>37</sup> on vicinal (100) SrTiO<sub>3</sub> the  $c$ -axis of  $a$ -domains lies solely perpendicular to the step edge.

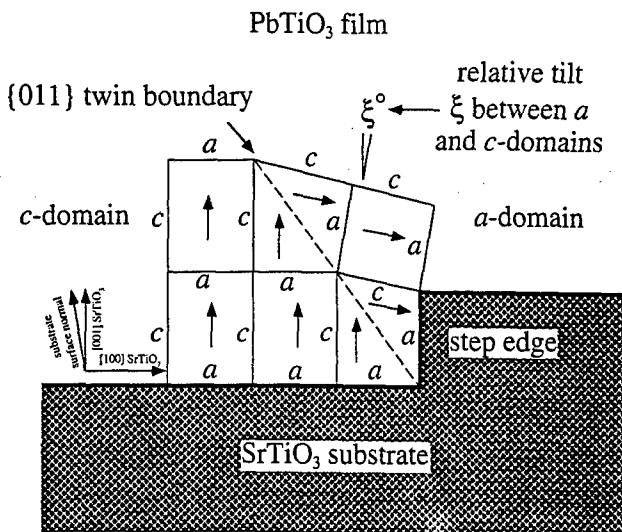


FIG. 2. Schematic showing how the presence of step edges on a vicinal (001) SrTiO<sub>3</sub> substrate may lead to the preferred nucleation of a PbTiO<sub>3</sub> (011) twin boundary. The arrows indicate the direction in which the PbTiO<sub>3</sub> *c*-axis lies. The tetragonality of PbTiO<sub>3</sub> has been exaggerated for clarity.

### C. Influence of terrace length on *a*-domain distribution

The effect of these SrTiO<sub>3</sub> step edges can be further understood if we consider the ratio of the volume fraction of material tilted uphill/downhill for a given crystallographic [100] or [010] direction as a function of the average distance between steps in that direction (Fig. 3). An uphill/downhill ratio of 1 (seen at low misorientations) indicates that the *a*-axis domains are equally populated. As the substrate misorientation increases beyond  $\sim 1^\circ$ , the dominance of the uphill *a*-domain clearly emerges. This threshold corresponds

to an average terrace length between steps of about 20 nm. Here the average distance between steps,  $d_{\text{avg}}$ , is calculated as  $d_{\text{avg}} = [a_{\text{SrTiO}_3} / \tan(\theta_m)]$ , where  $a_{\text{SrTiO}_3}$  is the lattice constant of SrTiO<sub>3</sub>, and  $\theta_m$  is the component of the misorientation angle of the substrate toward [100]. Other researchers have seen and measured the average width of *a*-domains in epitaxial PbTiO<sub>3</sub> on SrTiO<sub>3</sub> by TEM analysis.<sup>2,13,14</sup> Stemmer *et al.*<sup>13</sup> report an average width of  $19 \pm 1.6$  nm of the *a*-domains for a 200 nm film thickness of PbTiO<sub>3</sub> on SrTiO<sub>3</sub>. Similarly, Stemmer *et al.*<sup>14</sup> show an average width of  $18 \pm 0.9$  nm of the *a*-domains for a 150 nm PbTiO<sub>3</sub> film with a 30 nm SrTiO<sub>3</sub> interlayer on an MgO substrate. In Fig. 3 it is clear that as the average distance between step edges becomes large compared to the average *a*-domain width measured for the PbTiO<sub>3</sub>/SrTiO<sub>3</sub> system, the ratio of the volume fraction of *a*-oriented material tilted uphill/downhill approaches unity [i.e., the measured ratio for PbTiO<sub>3</sub> films on nominal (001) SrTiO<sub>3</sub> substrates]. The effect of vicinal substrates causing a preferred orientation in *a*-domain abundance appears to become significant when the average terrace length approaches the average *a*-domain width previously measured.<sup>13,14</sup> The points illustrated in Fig. 3 are meant only to show a trend as the error induced can be very large when measuring downhill volume fractions of less than  $\sim 5\%$  (i.e., at uphill/downhill ratios  $\geq 10$ ).

### D. Influence of *a*-domain distribution on tilt angle $\xi$

In Fig. 4, we have overlaid the rocking curve scans of several vicinal substrates and one nominal substrate. All scans are taken along a crystallographic [100] or [010] type direction and have been placed on a linear scale for clarity. The tilt angles in a downhill direction

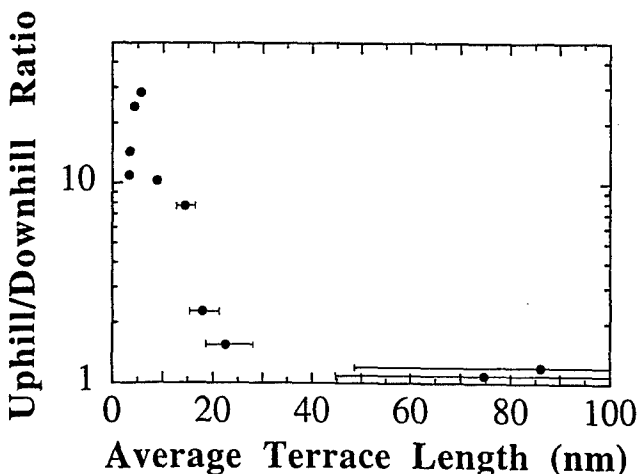


FIG. 3. Graph of the ratio of uphill/downhill *a*-axis volume fractions along a specific [100] or [010] crystallographic orientation as a function of the average terrace length in that direction.

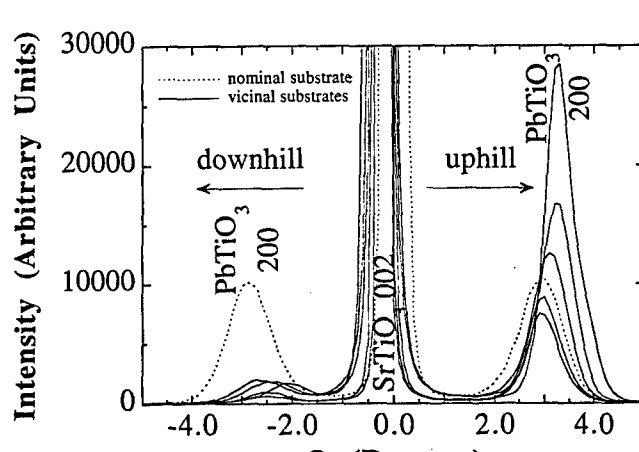


FIG. 4. Overlay of PbTiO<sub>3</sub> 200 rocking curve scans for several vicinal (001) SrTiO<sub>3</sub> substrates and one nominal (misorientation  $\leq 0.25^\circ$ ) substrate. All scans were aligned to the [001] axis of the PbTiO<sub>3</sub> *c*-domains.

range from  $\xi = 2.1^\circ$  up to  $2.9^\circ$  for the nominal substrate, and similarly in an uphill direction from  $\xi = 3.0^\circ$  for the nominal substrate up to  $3.3^\circ$  for the  $a$ -domains with the largest uphill relative volume fraction. Here the effect of vicinal substrates on creating an asymmetry in the  $a$ -domain populations can clearly be seen, as well as the influence this asymmetry has on the ultimate tilt angle ( $\xi$ ).

Figure 5 shows the  $a$ -domain tilt angle ( $\xi$ ) as a function of the relative volume percentage of  $a$ -oriented material. 100% indicates that all of the  $a$ -axis oriented PbTiO<sub>3</sub> domains are tilted in the same direction with respect to the [001] axis of the  $c$ -axis oriented PbTiO<sub>3</sub> domains. Here it is clear that the ultimate orientation of these  $a$ -domains is not only a function of the large  $c/a$  ratio (~1.06 for bulk PbTiO<sub>3</sub>),<sup>43</sup> but also the relative volume fraction of  $a$ -domains present in a specific orientation. Further, we have drawn a best-fit curve to this graph to direct the reader's eye to the fact that the effect on the tilt angle ( $\xi$ ) is more dramatic for smaller volume fractions of  $a$ -domains.

The magnitude of the tilt angle between the [100] axis of  $a$ -domains and the [001] axis of  $c$ -domains has been explained as being due to the tetragonal distortion of PbTiO<sub>3</sub>, specifically,

$$\xi = 90^\circ - 2 \tan^{-1} \left( \frac{a}{c} \right). \quad (1)$$

Using 4-circle x-ray diffraction, we have measured the lattice constants of the different domains comprising the PbTiO<sub>3</sub> films. We see up to five different PbTiO<sub>3</sub> domain types (one  $c$ -domain, and four  $a$ -domains tilted toward the [100], [ $\bar{1}00$ ], [010], and [0 $\bar{1}0$ ] SrTiO<sub>3</sub> directions). For each of these domains we have measured the in-plane and out-of-plane lattice constants. These lattice constants for the  $c$ -domains and  $a$ -domains of several films are summarized in Table I. From these lattice constants it is

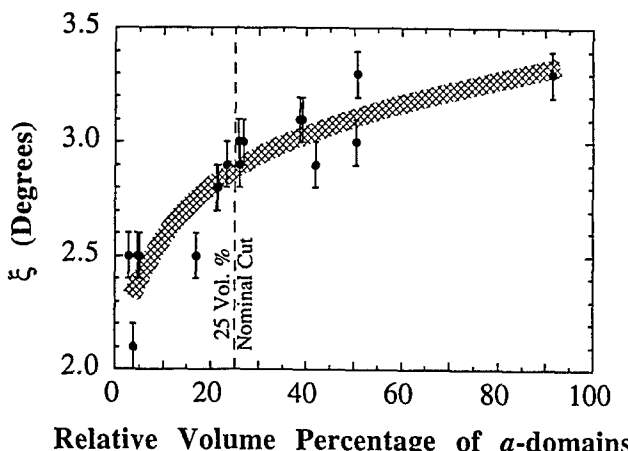


FIG. 5. Graph of the relative volume percentage of  $a$ -domains along a specific [100] or [010] crystallographic orientation as a function of the tilt angle  $\xi$ . The broad curve illustrates the trend of the data.

possible to calculate predicted  $a$ -domain tilt angles due to twins along {011} domain boundaries using the model shown in Fig. 6. The in-plane  $a$ -axis of the  $a$ -domains is not shown in this table as its value does not affect the calculated angle of the twin boundary. As mentioned previously, all  $a$ -domains are oriented with their in-plane  $c$ -axis parallel to the projection of the  $a$ -domain [100] axis onto the SrTiO<sub>3</sub>(001) surface (as shown in Fig. 2).

To calculate the tilt angle ( $\xi$ ), we first assume that the {011} domain is a mirror plane, and that the angles of the tetragonal unit cell are preserved at the domain boundary interface (i.e.,  $\alpha = \beta = 90^\circ$ ). It is then possible to calculate a tilt angle ( $\xi$ ) based solely on the lattice constants measured for one of the domains [this is equivalent to using Eq. (1)]. In Table I we have tabulated these values using the measured lattice constants from the  $c$ -domains and from the  $a$ -domains separately, and compare them to the actual measured values. Here we can see a general lack of agreement, and in most cases the calculated values are *larger* than the measured values. Next, we assume that the measured lattice constants for both the  $a$ - and  $c$ -domains are all preserved at the domain boundary interface, and similarly that the angles of the tetragonal unit cells are preserved (i.e.,  $\alpha = \beta = 90^\circ$ ). If we now attempt to calculate a tilt angle  $\xi$ , this model cannot produce a solution. There are no four-sided figures having sides equal to our measured lattice constants and two internal angles of  $90^\circ$ . Because x-ray diffraction is an averaging technique, the calculated lattice constants for the  $a$ - and  $c$ -domains are values averaged over the whole film. It is therefore concluded that the measured lattice constants and/or the  $90^\circ$  angles ( $\alpha$  and  $\beta$  from Fig. 6) of the tetragonal unit cell are *not preserved at or near* the domain boundary interface, resulting in the inability to calculate a tilt angle based solely on the measured average lattice constants of PbTiO<sub>3</sub>. In addition, we note that Eq. (1) is not in quantitative agreement with the observed tilt angles, nor does it include the clear influence of the relative volume fractions of  $a$ -domains shown in Fig. 5.

### E. Influence of $a$ -domain distribution on the $c$ -domain tilt

In all films grown on vicinal (001) SrTiO<sub>3</sub>, the PbTiO<sub>3</sub>  $c$ -oriented domains are observed to be tilted slightly ( $0.05^\circ$ – $0.4^\circ$ ) uphill from SrTiO<sub>3</sub> [001] toward the miscut direction (i.e., toward the dominant  $a$ -domain for a miscut toward a SrTiO<sub>3</sub> [100] direction or between two dominant  $a$ -domains if the miscut is toward a SrTiO<sub>3</sub> [110] direction).

Flynn<sup>44</sup> and Nagai<sup>45</sup> have proposed models describing tilted epitaxy on vicinal substrates. The model proposed by Flynn<sup>44</sup> describes tilt of the epitaxial layer as a

TABLE I. Comparison of calculated and measured tilt angles  $\xi$ .

Miscut angle	c-domain		a-domain		$\xi$ calculated from c-domains from Eq. (1)	$\xi$ calculated from a-domains from Eq. (1)	$\xi$ measured
	$c_{\perp}$	$a_{\text{in-plane}}$	$a_{\perp}$	$c_{\text{in-plane}}$			
7°	$4.12 \pm 0.01 \text{ \AA}$	$3.93 \pm 0.02 \text{ \AA}$	$3.89 \pm 0.01 \text{ \AA}$	$4.20 \pm 0.02 \text{ \AA}$	$2.7 \pm 0.4^\circ$	$4.4 \pm 0.4^\circ$	$2.9 \pm 0.1^\circ$
6.5°	$4.12 \pm 0.01 \text{ \AA}$	$3.93 \pm 0.02 \text{ \AA}$	$3.89 \pm 0.01 \text{ \AA}$	$4.19 \pm 0.02 \text{ \AA}$	$2.7 \pm 0.4^\circ$	$4.3 \pm 0.4^\circ$	$3.0 \pm 0.1^\circ$
2.6°	$4.14 \pm 0.01 \text{ \AA}$	$3.90 \pm 0.02 \text{ \AA}$	$3.89 \pm 0.01 \text{ \AA}$	$4.15 \pm 0.02 \text{ \AA}$	$3.4 \pm 0.4^\circ$	$3.7 \pm 0.4^\circ$	$3.3 \pm 0.1^\circ$
2.6°	$4.14 \pm 0.01 \text{ \AA}$	$3.90 \pm 0.02 \text{ \AA}$	$3.90 \pm 0.01 \text{ \AA}$	$4.11 \pm 0.02 \text{ \AA}$	$3.4 \pm 0.4^\circ$	$3.0 \pm 0.4^\circ$	$3.1 \pm 0.1^\circ$
1.9°	$4.14 \pm 0.01 \text{ \AA}$	$3.90 \pm 0.02 \text{ \AA}$	$3.89 \pm 0.01 \text{ \AA}$	$4.16 \pm 0.02 \text{ \AA}$	$3.4 \pm 0.4^\circ$	$3.8 \pm 0.4^\circ$	$2.4 \pm 0.1^\circ$

mechanism for relieving bulk strain by slightly increasing the effective in-plane lattice constant of the film to better match that of the substrate. In our case, this mechanism is not applicable to either the *c*-domains or the *a*-domains because, as Table I shows, the in-plane lattice constants of the PbTiO<sub>3</sub> films ( $c_{\text{in-plane}}$  and  $a_{\text{in-plane}}$ ) are both larger than  $a_{\text{SrTiO}_3}$ . Nagai<sup>45</sup> has proposed a model for a tetragonally distorted film having unit cell dimensions  $a \times a \times c$  on a vicinal cubic substrate with a lattice constant  $a_s$ . This model is appropriate for the *c*-domains in our film. Nagai's model assumes that the *c*-axis of the film is clamped at the substrate step edge and relaxes over the length of a terrace. The amount of *c*-axis tilt,  $\Delta\Phi$ , expected from Nagai's model is<sup>45</sup>

$$\Delta\Phi = \tan^{-1} \left( \frac{a_s - c}{a_s} \tan \Phi \right), \quad (2)$$

where  $\Phi$  is the angle of substrate miscut. This model predicts that the tilt should be in an uphill direction for  $c > a_s$  and in a downhill direction for  $c < a_s$ . We note that the predicted tilt direction is in qualitative agreement with our results. In Fig. 7 we show the *c*-axis tilt angle (the angle between [001] of the PbTiO<sub>3</sub> *c*-domains and [001] of the SrTiO<sub>3</sub> substrate) measured by 4-circle x-ray diffraction (solid dots) as a function of substrate misorientation. The line in Fig. 7 is the tilt calculated from Eq. (2) using the bulk lattice constants of PbTiO<sub>3</sub>. The triangles indicate the  $\Delta\Phi$  tilt angle calculated from Nagai's model when the lattice constants measured for the *c*-domains (Table I) are used in Eq. (2).

Nagai's model shows reasonable agreement with our results at relatively small miscut angles, but deviates at higher angles ( $> 5^\circ$ ). Nagai's model predicts the *c*-axis tilt angle to increase continuously as the misorientation of the substrate increases. However, as can be seen from Fig. 7, this trend does not continue for misorientations greater than about  $6^\circ$ . A similar threshold occurs in the tilt angle of the *a*-axis grains,  $\xi$ , as a function of substrate misorientations exceeding  $6^\circ$ . Both the *c*-axis tilt angle and the *a*-axis tilt angle are greatest when the relative volume fraction of *a*-domains is most unequal. This implies these tilt angles are strongly influenced by elastic effects arising from the dominant *a*-domain orientations.

Consideration of this overall *c*-axis tilt with respect to the substrate, and the fact that the tilt angles ( $\xi$ ) calculated in Table I are in general not achieved by the *a*-domains in the film, implies that there is a crystallographic "tug of war" between the direction in which the *c*-domains are oriented and the four different *a*-domain orientations. Further, since the measured lattice constants are averaged over the whole film, the inability to calculate the measured tilt angle  $\xi$  from these lattice constants indicates that distortion of the tetragonal unit cell occurs at or very close to the domain boundary interface. The ultimate tilt angle of the *c*-domain as well as the four *a*-domains appears to be driven by the large  $c/a$  ratio in PbTiO<sub>3</sub>, but are mutually constrained by the relative volume fractions of each of the four *a*-domains present at the specific cooling rate ( $\sim 10 \text{ }^\circ\text{C}/\text{min}$ ) employed in this work. It is possible that the presence of multiple *c*-domain orientations seen by other researchers<sup>2,5,6,11</sup> is the result of the choice of substrate material and/or a higher volume fraction of *a*-domains with respect to *c*-domains contained in the film, which has been shown to depend largely on the effective cooling rate.<sup>8,46</sup>

## V. CONCLUSIONS

We have grown high quality thin films (40 nm) of PbTiO<sub>3</sub> on SrTiO<sub>3</sub> with good epitaxial alignment that are free of *a*-axis domains. Thicker films ( $\sim 200 \text{ nm}$ ) grown on vicinal (up to  $9^\circ$  miscut) (001) SrTiO<sub>3</sub> substrates contain both *a*-axis and *c*-axis PbTiO<sub>3</sub> domains. The *a*-domains have a preferred orientation in an uphill direction with respect to the macroscopic substrate surface. The excellent lattice matching of the PbTiO<sub>3</sub> (001) planes to the SrTiO<sub>3</sub> {100} planes on both the substrate surface, and at the SrTiO<sub>3</sub> step edges make this an ideal location for the formation of PbTiO<sub>3</sub> {011} domain boundaries. The effect of a preferred *a*-axis orientation yields insight into the ultimate orientation of all domains upon cooling. The predicted tilt angle of the *a*-domains,  $90^\circ - 2 \tan^{-1}(a/c)$ , is not achieved. In our films where there is only one *c*-axis orientation, there appears to be a compromise between the *c*-domain orientation and the four equivalent *a*-domain orientations based on the respective volume fractions of *a*-domains present.

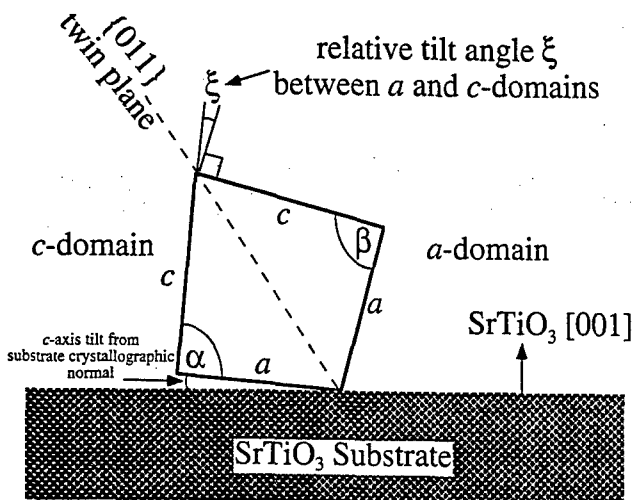


FIG. 6. Schematic illustrating the geometry used to calculate tilt angles  $\xi$  based on lattice constants measured by x-ray diffraction.

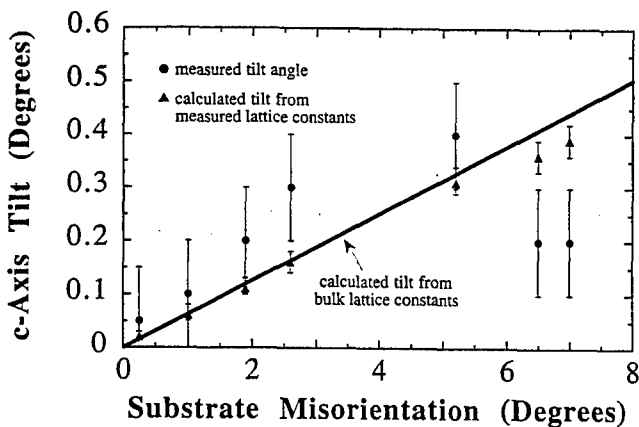


FIG. 7. Graph of measured c-axis tilt angle, tilt angle calculated from data on c-domains given in Table I [using Eq. (2)], and tilt angle calculated from bulk lattice constants [using Eq. (2)] as a function of substrate misorientation.

The effect of step edges in causing a preferred orientation in  $a$ -domain abundance exists, but becomes significant only when the average distance between these steps is on the order of or less than the average  $a$ -domain width.

## ACKNOWLEDGMENTS

We gratefully acknowledge Dr. S. Trolier-McKinstry for the SE measurements, Y. Narinder for help fabricating the ceramic targets, and the final support of the Office of Naval Research through Grant No. N00014-94-1-0690.

## REFERENCES

- J. F. Scott and D. A. Paz de Araujo, Science 246, 1400 (1989).
- A. Seifert, F. F. Lange, and J. S. Speck, J. Mater. Res. 10, 680 (1995).
- K. Iijima, I. Ueda, and K. Kugimiya, Jpn. J. Appl. Phys. 30, 2149 (1991).
- Y. Gao, G. Bai, K. L. Merkle, Y. Shi, H. L. M. Chang, Z. Shen, and D. J. Lam, J. Mater. Res. 8, 145 (1993).
- G. R. Bai, H. L. M. Chang, C. M. Foster, Z. Shen, and D. J. Lam, J. Mater. Res. 9, 156 (1994).
- Y.-F. Chen, T. Yu, J.-X. Chen, L. Shun, P. Li, and N.-B. Ming, Appl. Phys. Lett. 66, 148 (1995).
- C. M. Foster, Z. Li, M. Buckett, D. Miller, P. M. Baldo, L. E. Rehn, G. R. Bai, D. Guo, H. You, and K. L. Merkle, J. Appl. Phys. 78, 2607 (1995).
- H. Tabata, O. Murata, T. Kawai, S. Kawai, and M. Okuyama, Appl. Phys. Lett. 64, 428 (1994).
- W.-Y. Hsu and R. Raj, Appl. Phys. Lett. 67, 792 (1995).
- C. D. Theis and D. G. Schlom, in *Epitaxial Oxide Thin Films II*, edited by D. K. Fork, J. S. Speck, R. M. Wolf, and T. Shiosaki (Mater. Res. Soc. Symp. Proc. 401, Pittsburgh, PA, 1996), p. 171.
- K. Iijima, Y. Tomita, R. Takayama, and I. Ueda, J. Appl. Phys. 60, 361 (1986).
- Z. Li, C. M. Foster, D. Guo, H. Zhang, G. R. Bai, P. M. Baldo, and L. E. Rehn, Appl. Phys. Lett. 65, 1106 (1994).
- S. Stemmer, S. K. Streiffer, F. Ernst, M. Ruhle, W.-Y. Hsu, and R. Raj, Solid State Ionics 75, 43 (1995).
- S. Stemmer, S. K. Streiffer, W.-Y. Hsu, F. Ernst, R. Raj, and M. Ruhle, J. Mater. Res. 10, 791 (1995).
- J. S. Speck and W. Pompe, J. Appl. Phys. 76, 466 (1994).
- W. Pompe, X. Gong, Z. Suo, and J. S. Speck, J. Appl. Phys. 74, 6012 (1993).
- B. S. Kwak, A. Erbil, B. J. Wilkens, J. D. Budai, M. F. Chisholm, and L. A. Boatner, Phys. Rev. Lett. 68, 3733 (1992).
- J. N. Eckstein, I. Bozovic, D. G. Schlom, and J. S. Harris, Jr., Appl. Phys. Lett. 57, 1049 (1990).
- O. Wada, K. Kuroda, J. Tanimura, M. Kataoka, K. Kojima, T. Takami, K. Hamanaka, and T. Ogama, Jpn. J. Appl. Phys. 30, L1881 (1991).
- T. Satoh, J. Fujita, T. Yoshitake, and H. Igarashi, Physica C 191, 359 (1992).
- J. Fujita, T. Yoshitake, T. Satoh, T. Ichihashi, and H. Igarashi, IEEE Trans. Magn. 27, 1205 (1991).
- J. Tanimura, K. Kuroda, M. Kataoka, O. Wada, T. Takami, K. Kojima, and T. Ogama, Jpn. J. Appl. Phys. 32, L254 (1993).
- J. D. Budai, M. F. Chisholm, R. Feenstra, D. H. Lowndes, D. P. Norton, L. A. Boatner, and D. K. Christen, Appl. Phys. Lett. 58, 2174 (1991).
- W. A. M. Aarnink, E. M. C. M. Reuvekamp, M. A. J. Verhoeven, M. V. Pedyash, G. J. Gerritsma, A. van Silfhout, and H. Rogalla, Appl. Phys. Lett. 61, 607 (1992).
- D. G. Schlom, D. Anselmetti, J. G. Bednorz, R. F. Broom, A. Catana, T. Frey, Ch. Gerber, H.-J. Guntherodt, H. P. Lang, and J. Mannhart, Z. Phys. B 86, 163 (1992).
- S. K. Streiffer, B. M. Lairson, and J. C. Bravman, Appl. Phys. Lett. 57, 2501 (1990).
- B. H. Moeckly, S. E. Russek, D. K. Lathrop, R. A. Buhrman, M. G. Norton, and C. B. Carter, Appl. Phys. Lett. 57, 2951 (1990).
- M. Matsui, K. Yamamoto, and M. Nakajima, Phase Transitions 42, 103 (1993).
- C. H. Mueller, P. H. Holloway, J. D. Budai, F. A. Miranda, and K. B. Bhasin, J. Mater. Res. 10, 810 (1995).
- J. Kwo, R. M. Fleming, H. L. Kao, D. J. Werder, and C. H. Chen, Appl. Phys. Lett. 60, 1905 (1992).
- C. B. Eom, R. J. Cava, R. M. Fleming, J. M. Phillips, R. B. van Dover, J. H. Marshall, J. W. P. Hsu, J. J. Krajewski, and W. F. Peck, Jr., Science 258, 1766 (1992).
- N. G. Norton, S. R. Summerfield, and C. B. Carter, Appl. Phys. Lett. 56, 2246 (1990).

33. V. Argrawal, N. Chandrasekhar, Y. J. Zhang, V. S. Achutharaman, M. L. Mecartney, and A. M. Goldman, *J. Vac. Sci. Technol. A* **10**, 1531 (1992).
34. M. Kawasaki, K. Takahashi, T. Maeda, R. Tsuchiya, M. Shinozaki, O. Ishiyama, T. Yonezawa, M. Yoshimoto, and H. Koinuma, *Science* **266**, 1540 (1994).
35. Y. Liang and D. A. Bonnell, *Surf. Sci.* **310**, 128 (1994).
36. Q. D. Jiang and J. Zegenhagen, *Surf. Sci. Lett.* **338**, L882 (1995).
37. S. Kim, Y. Kang, and S. Baik, *Thin Solid Films* **256**, 240 (1995).
38. K. Wasa, Y. Haneda, T. Satoh, H. Adachi, S. Hayashi, and K. Setsune, *Jpn. J. Appl. Phys.* **34**, 5132 (1995).
39. Kanthal is a registered trademark of Kanthal AB, Sweden.
40. J. C. Clark, J. P. Maria, K. J. Hubbard, and D. G. Schlom, unpublished results.
41. Commercial Crystal Laboratories, Naples, FL.
42. C. D. Theis, M.S. Thesis, The Pennsylvania State University, University Park, PA.
43. *Landolt-Bornstein: Numerical Data and Functional Relationships in Science and Technology, New Series, Group III, Vol. 12*, edited by K-H. Hellwege (Springer-Verlag, Berlin, 1978), p. 156.
44. C. P. Flynn, *MRS Bull.* **16**, 30 (June 1991).
45. H. Nagai, *J. Appl. Phys.* **45**, 3789 (1974).
46. R. Ramesh, T. Sands, and V. G. Keramidas, *Appl. Phys. Lett.* **63**, 731 (1993).

Reprinted from

JOURNAL OF **CRYSTAL  
GROWTH**

---

Journal of Crystal Growth 174 (1997) 473–479

Epitaxial lead titanate grown by MBE

C.D. Theis, D.G. Schlom\*

*Department of Materials Science and Engineering, The Pennsylvania State University, University Park, Pennsylvania 16802-5005, USA*



# Journal of Crystal Growth

## EDITORIAL BOARD

M. SCHIEBER (Principal Editor)  
The Fredy and Nadine Herrmann  
Graduate School of Appl. Sci.  
Hebrew University, Jerusalem 91904, Israel  
Telefax: +972-2-566 3878

R. KERN  
CRMC<sup>2</sup>, CNRS, Campus Luminy, Case 913  
F-13288 Marseille Cedex 9, France  
Telefax: +33-91-4-418 916

R.S. FEIGELSON  
Ctr. Materials Res., 105 McCullough Bldg.  
Stanford Univ., Stanford, CA 94305-4045, USA  
Telefax: +1-415-723 3044

T. NISHINAGA  
Dept. Electron. Eng., Univ. of Tokyo  
7-3-1, Hongo, Bunkyo-ku, Tokyo 113, Japan  
Telefax: +81-3-5684-3974

D.T.J. HURLE  
H.H. Wills Phys. Lab., Univ. Bristol  
Tyndall Avenue  
Bristol BS8 1TL, UK

G.B. STRINGFELLOW  
Dept. Mater. Sci., 304 EMRO, Univ. of Utah  
Salt Lake City, UT 84112, USA  
Telefax: +1-801-581 4816

A. BARONNET (*Industrial, Biological, Molecular Crystals*)  
CRMC<sup>2</sup>, CNRS, Campus Luminy, Case 913  
F-13288 Marseille Cedex 9, France  
Telefax: +33-91-4-418 916

K.W. BENZ (*Microgravity, Electronic Materials*)  
Kristallographisches Inst., Universität  
Hebelstr. 25, D-79104 Freiburg, Germany  
Telefax: +49-761-203 4369

A.A. CHERNOV (*Kinetics of Crystallization, Protein Crystallization*)  
Inst. Crystallography, Acad. of Sciences  
Leminskii Prospekt, Moscow 117333, Russian Fed.  
Telefax: +7-095-135 011

A.Y. CHO (*Molecular Beam Epitaxy*)  
Room IC-323, AT&T Bell Laboratories  
Murray Hill, NJ 07974-2070, USA  
Telefax: +1-908-582 2043

B. COCKAYNE (*IOCG News*)  
School of Metallurgy and Mater.  
Univ. Birmingham, P.O. Box 363,  
Edgbaston, Birmingham, B15 2TT, UK  
Telefax: +44-121-471 2207

S.R. CORIELL (*Theory*)  
A153 Mater., Natl. Inst. of Standards & Technol.  
Gaithersburg, MD 20899-0001, USA  
Telefax: +1-301-975-4553

M.E. GLICKSMAN (*Solidification*)  
School of Eng., Mater. Eng. Dept.,  
Rensselaer Polytechnic Inst.  
Troy, NY 12180-3590, USA  
Telefax: +1-518-276 8554

M.A.G. HALLIWELL (*X-ray Diffraction*)  
Philips Analytical X-ray, Lelyweg 1  
7602 EA Almelo, The Netherlands

T. HIBIYA (*Oxides, Melt Thermophysical Properties, Microgravity*)  
Fundamental Res. Labs., NEC CORPORATION  
34, Miyukigaoka, Tsukuba 305, Japan  
Telefax: +81-298-566 136

H. KOMATSU (*Proteins Molecular Crystallization, Growth from Solutions*)  
Inst. Mater. Res., Tohoku Univ.  
Katahira 2-1-1, Sendai 980, Japan  
Telefax: +81-22-215 2011

T.F. KUECH (*Thin Films and Electronic and Optical Devices*)  
Dept. Chem. Eng., Univ. Wisconsin-Madison  
Madison, WI 53706, USA  
Telefax: +1-608-265 3782

A. MCPHERSON (*Protein Growth*)  
Dept. Biochemistry, Univ. of California  
Riverside, CA 92521, USA  
Telefax: +1-909-787 3790

P.A. MORRIS HOTSENPILLER (*Electrooptical Crystals, Book Reviews, Oxide Thin Films*)  
E.I. du Pont de Nemours & Co., Exp. Station  
Wilmington, DE 19888-0358, USA  
Telefax: +1-302-695 1664

J.B. MULLIN (*Semiconductors*)  
EMC, "The Hoe", Brockhill Road  
West Malvern, Worcs., WR14 4DL, UK  
Telefax: +44-1684-575 591

K. NAKAJIMA (*Liquid and Vapor Phase Epitaxy*)  
Integrated Mater. Lab., Fujitsu Labs. Ltd.  
Morinosato-Wakamiya 10-1, Atsugi 243-01, Japan  
Telefax: +81-462-48 3473

H. OHNO (*Epitaxy*)  
Research Inst. of Electrical Commun.  
Tohoku Univ., Sendai 980 77, Japan  
Telefax: +81-22-217 5553

K. PLOOG (*Molecular Beam Epitaxy*)  
Paul-Drude-Inst. für Festkörperelektronik  
Hausvogteiplatz 5-7, D-10117 Berlin, Germany  
Telefax: +49-30-203 77201

F. ROSENBERGER (*Protein Crystallization, Fluid Dynamics*)  
Center for Microgravity and Materials Research  
Univ. Alabama, Huntsville, AL 35899, USA  
Telefax: +1-205-890 6791

R.W. ROUSSEAU (*Solution Growth, Industrial Crystallization*)  
School of Chem. Eng., Georgia Inst. of Technol.  
Atlanta, GA 30332-0100, USA  
Telefax: +1-404-894 2866

K. SATO (*Biocrystallization and Organic Crystals*)  
Fac. Appl. Biol. Sci., Hiroshima Univ.  
Higashi-Hiroshima 724, Japan  
Telefax: +81-824-227 062

L.F. SCHNEEMAYER (*Superconductivity, Oxides, Novel Materials*)  
Room 1A-363, AT&T Bell Labs.  
Murray Hill, NJ 07974-2070, USA  
Telefax: +1-908-582 2521

D.W. SHAW (*Semiconductors, Epitaxy, Devices*)  
Texas Instruments Inc., P.O. Box 655936, MS 147  
Dallas, TX 75265, USA  
Telefax: +1-214-995 7785

I. SUNAGAWA (*Minerals*)  
3-54-2 Kashiba-cho, Tachikawa-shi  
Tokyo 190, Japan  
Telefax: +81-425-35 3637

G. VAN TENDELOO (*Electron Microscopy, Fullerenes, Superconductivity*)  
University of Antwerp, RUCA  
Groenenborgerlaan 171, B-2020 Antwerp-Belgium  
Telefax: +32-3-2180 217

A.F. WITT (*Semiconductor Crystals*)  
Dept. of Metall. & Mater. Sci., Massachusetts  
Inst. of Technol., Cambridge, MA 02139, USA  
Telefax: +1-617-253 5827

A. ZANGWILL (*Theory (Epitaxy)*)  
School of Physics, Georgia Inst. of Technol.  
Atlanta, GA 30332, USA  
Telefax: +1-404-894 9958

**Scope of the Journal**  
Experimental and theoretical contributions are invited in the following fields: Theory of nucleation and growth, molecular kinetics and transport phenomena, crystallization in viscous media such as polymers and glasses. Crystal growth of metals, minerals, semiconductors, magnetics, inorganic, organic and biological substances in bulk or as thin films. Apparatus instrumentation and techniques for crystal growth, and purification methods. Characterization of single crystals by physical and chemical methods.

**Abstracted/Indexed in:**  
Aluminium Industry Abstracts; Chemical Abstracts; Current Contents; Physical, Chemical and Earth Sciences; EI Compendex Plus; Engineered Materials Abstracts; Engineering Index; INSPEC; Metals Abstracts.

### Subscription Information 1997

Volumes 170-181 of *Journal of Crystal Growth* (ISSN 0022-0248) are scheduled for publication. (Frequency: semimonthly.) Prices are available from the publishers upon request. Subscriptions are accepted on a prepaid basis only. Issues are sent by SAL (Surface Air Lifted) mail wherever this service is available. Airmail rates are available upon request. Please address all enquiries regarding orders and subscriptions to:

Elsevier Science, B.V., Order Fulfilment Department  
P.O. Box 211, 1000 AE Amsterdam, The Netherlands  
Tel: +31 20 485 3642; Fax: +31 20 485 3598

Claims for issues not received should be made within six months of our publication (mailing) date.

**US mailing notice—Journal of Crystal Growth** (ISSN 0022-0248) is published semimonthly by Elsevier Science B.V., Molenwerf 1, P.O. Box 211, 1000 AE Amsterdam, The Netherlands. Annual subscription price in the USA is US \$7081 (valid in North, Central and South America only), including air speed delivery. Periodicals postage paid at Jamaica NY 11431.

US postmasters: Send address changes to *Journal of Crystal Growth*, Publications Expediting, Inc., 200 Meacham Avenue, Elmont NY 11003. Airfreight and mailing in the USA by Publications Expediting.

© The paper used in this publication meets the requirements of ANSI/NISO Z39.48-1992 (Permanence of Paper)

PRINTED IN THE NETHERLANDS

North-Holland, an imprint of Elsevier Science

## Epitaxial lead titanate grown by MBE

C.D. Theis, D.G. Schlom\*

Department of Materials Science and Engineering, The Pennsylvania State University, University Park, Pennsylvania 16802-5005, USA

### Abstract

Epitaxial  $\text{PbTiO}_3$  films have been grown by reactive molecular beam epitaxy (MBE) on (100)  $\text{LaAlO}_3$  substrates. Lead is supplied from a conventional effusion cell. Titanium is sublimated from a Ti-Ball<sup>TM</sup>, and oxygen is supplied in the form of purified ozone. Atomic layer-by-layer composition control is obtained using real-time atomic absorption spectroscopy (AA) feedback. The titanium flux is controlled with a shutter directly coupled to the titanium AA feedback to deliver a burst corresponding to one monolayer of titania. Similarly, lead is monitored in situ using an atomic absorption signal. An adsorption-controlled growth mechanism leads to the use of a lead overpressure to insure films with proper stoichiometries. Film structure is studied during growth using in situ RHEED. 4-circle X-ray diffraction analysis indicates that films grown on  $\text{LaAlO}_3$  are epitaxial and are mixed *a*- and *c*-axis oriented.

PACS: 81.15.Hi; 77.84.Dy

Keywords: MBE;  $\text{PbTiO}_3$ ; Epitaxy

### 1. Introduction

Lead titanate has become one of the most extensively studied ferroelectric materials. It has a variety of potential applications including optical switches, infrared detectors, and ferroelectric random access memories [1]. However, growth of  $\text{PbTiO}_3$  has been hampered by problems with lead volatility [2, 3]. Nonetheless, high quality films have been made by metal organic chemical vapor deposition (MOCVD) [4–7], pulsed laser depo-

sition (PLD) [8–10], sputtering [3, 11], and through the use of solution precursors [2]. Because of the anisotropic nature of lead titanate, many of its properties, including remanent polarization, pyroelectric coefficient, and coefficient of second harmonic generation, are dependent on its crystallographic orientation. For most of these applications it is desirable to have a single-domain film with the  $\text{PbTiO}_3$  *c*-axis normal to the substrate surface in order to fully utilize its anisotropic properties. Devices that use polycrystalline  $\text{PbTiO}_3$  films, in general, exhibit lower remanent polarizations and require higher coercive fields, as the electrical properties are diluted. Additionally, the growth of single crystal films offers the possibility of

\* Corresponding author. E-mail: schlom@ems.psu.edu.

integrating  $\text{PbTiO}_3$  with other structurally matched materials that have vastly different electrical and magnetic properties. As an example,  $\text{PbTiO}_3$  has the highest known remanent polarization ( $\sim 80 \mu\text{C}/\text{cm}^2$ ) [8, 12], and is potentially useful for altering the carrier concentration of structurally matched high  $T_c$  superconductors by electrical means. Ahn et al. [13] have fabricated a field effect device consisting of the oxide superconductor undoped parent material,  $\text{SrCuO}_2$ , epitaxially grown on a  $\text{Pb}(\text{Zr}_{0.52}\text{Ti}_{0.48})\text{O}_3$  ferroelectric layer. They measured a reversible and nonvolatile 3.5% change in the room temperature resistance of the  $\text{SrCuO}_2$  induced by poling the ferroelectric to generate charge carriers at the superconductor/ferroelectric interface [13]. With its higher remanent polarization,  $\text{PbTiO}_3$  could in principle be used to change the carrier concentration of an oxide superconductor film sufficiently to induce/destroy superconductivity. This is not only relevant to studying the effect of carrier concentration on superconductivity, but might also lead to new superconducting materials (where chemical doping to alter the carrier concentration is insufficient) and non-volatile superconducting field-effect transistors.

## 2. Background

Recent developments in thin film deposition techniques as well as the availability of compatible oxide substrate materials have fueled an explosion of research in the last few years on the growth of ferroelectric and electro-optic epitaxial thin films [14]. One of the most important factors in determining the structural quality of any epitaxial thin film is the choice of substrate material. In order to grow high quality epitaxial lead titanate films, it is desirable to have good lattice matching and a high degree of chemical compatibility between the substrate and film. Table 1 [15–20] shows some commonly chosen substrates, their lattice constants, thermal expansion coefficients, and relative lattice mismatch to the  $\text{PbTiO}_3(0\ 0\ 1)$  plane. Here it can be seen that  $\text{SrTiO}_3$  is most suited for the growth of lead titanate, as it has the smallest degree of lattice mismatch at room temperature ( $\sim 0.1\%$ ). The orientation of the  $\text{SrTiO}_3$  substrate also affects growth; small vicinal tilts away from  $(1\ 0\ 0)$   $\text{SrTiO}_3$  have been shown to have dramatic effects on the domain structure of  $\text{PbTiO}_3$  films [21].

Table 1

Commonly chosen substrates for  $\text{PbTiO}_3$  growth, their lattice constants, thermal expansion coefficients, and lattice mismatch to  $\text{PbTiO}_3$

Substrate material and lattice-matched orientation ( $hkl$ )	Lattice constants at 25°C (Å)	Thermal expansion coefficient ( $\alpha \times 10^6/\text{°C}$ ) <sup>b</sup>	Lattice mismatch of $\text{PbTiO}_3(0\ 0\ 1)$ to substrate ( $0\ 0\ 1$ ) at 25°C <sup>c</sup>
$\text{PbTiO}_3(0\ 0\ 1)$	$a = b = 3.904$ [16] $c = 4.152$	27 (a) [20] – 67 (c)	–
$\text{SrTiO}_3(0\ 0\ 1)$	$a = 3.905$ [19]	11 [20]	< 0.1%
$\text{MgO}(0\ 0\ 1)$	$a = 4.212$ [15]	14 [15]	7.3%
$\text{Pt}(0\ 0\ 1)$	$a = 3.924$ [17]	7.8 [17]	0.5%
$\text{LaAlO}_3(0\ 0\ 1)$	$a = 3.792^a$ [18]	11 [20]	– 2.9%

<sup>a</sup> Pseudocubic subcell;  $\text{LaAlO}_3$  is rhombohedral with  $a = 5.356 \text{ \AA}$  and  $\alpha = 60.10^\circ$  at 25°C.

<sup>b</sup> Thermal expansion coefficient from 25 to 490°C for  $\text{PbTiO}_3$ . All other materials are from 25 to 630°C, where

$$\bar{\alpha} = \frac{a_{\text{sub}, 630\text{ C}} - a_{\text{sub}, 25\text{ C}}}{a_{\text{sub}, 25\text{ C}} \times 605^\circ\text{C}}$$

$$\text{Percent lattice mismatch} = \frac{a_{\text{substrate}} - a_{\text{PbTiO}_3}}{a_{\text{substrate}}} \times 100\%$$

Despite the use of well suited substrates, the growth of high quality single-domain lead titanate films has been plagued with problems. Lead is an extremely volatile metal having a vapor pressure of  $10^{-3}$  Torr at  $627^{\circ}\text{C}$  [22]. For comparison, PbO has a vapor pressure of  $10^{-3}$  Torr at  $\sim 780^{\circ}\text{C}$  for congruent evaporation [23]. Phase diagram work done on the PbO-TiO<sub>2</sub> system by Holman [24] indicates that there exists a wide phase field in the lead-poor perovskite lead titanate region. The structure of PbTiO<sub>3</sub> is known to accommodate extremely large concentrations (up to 17 at%) of lead and oxygen vacancies [25]. In most physical and chemical vapor deposition techniques it is difficult to accurately compensate for lead loss in lead titanate films. Resulting PbTiO<sub>3</sub> structures are often filled with lead vacancies, V<sub>Pb</sub><sup>2-</sup>. In BaTiO<sub>3</sub>, it has been established that the electrical resistivity is extremely sensitive to oxygen deficiencies [26]. In lead titanate, however, the presence of a small number of lead vacancies has been shown to reduce the electrical resistivity by several orders of magnitude at room temperature due to uncompensated charge carriers [27]. Similarly, lead vacancies have been shown to depress the Curie point by up to  $100^{\circ}\text{C}$ , with a corresponding decrease in the unit cell volume [25].

Phase diagram work done by Eisa et al. [28] indicates that the perovskite lead titanate structure is also capable of accommodating large amounts of excess lead. They have identified a single-phase lead-rich perovskite lead titanate region extending to more than 15 at% excess lead. Previous experimental work done by the authors indicates that this region also exists in thin films [29]. Fig. 1 shows the *c*-axis lattice constant measured by 4-circle X-ray diffraction of several lead titanate films grown by PLD as a function of excess lead (beyond a 1 : 1 Pb : Ti ratio). These films were all grown under identical conditions at substrate temperatures varying from 710 to  $775^{\circ}\text{C}$  to investigate the effect of excess lead on the perovskite PbTiO<sub>3</sub> structure. Specifically, we employed an on-axis PLD geometry with a target to substrate distance of  $\sim 6.5$  cm. Films were grown using a background oxygen/ozone ( $\sim 5\%$  O<sub>3</sub>) ambient pressure of 15 mTorr. The ceramic target used in this study contained a 75/25% molar ratio of PbTiO<sub>3</sub>/PbO

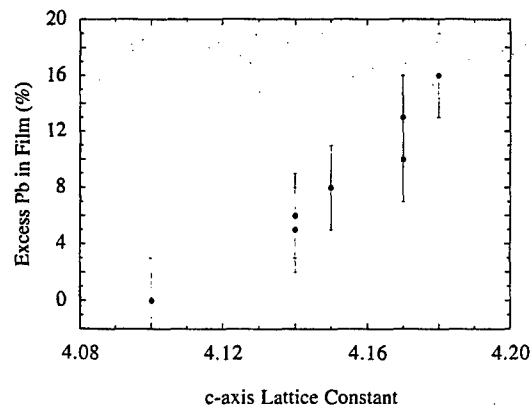


Fig. 1. Measured *c*-axis lattice constant for several PbTiO<sub>3</sub> films grown by laser ablation on (100) LaAlO<sub>3</sub> substrates as a function of excess lead content (measured by RBS).

and we used a focused energy density of  $\sim 2\text{ J/cm}^2$  incident from a KrF excimer laser. Film compositions were measured by Rutherford backscattering spectroscopy (RBS). Here it can be seen that there is a continuous expansion along PbTiO<sub>3</sub>[001] as the amount of excess lead increases. In all of these films there were no second phases, particularly crystalline PbO, discernible by X-ray diffraction. This fact, coupled with the continuous expansion of the *c*-axis of the unit cell as a function of excess lead in the film supports evidence that there must be not only a large single-phase lead-poor perovskite lead titanate region, but also a large single-phase lead-rich perovskite lead titanate region.

Many of the difficulties encountered in attempting to measure electrical properties of PbTiO<sub>3</sub> films are most likely due to the existence of these wide phase fields. Defects in the PbTiO<sub>3</sub> lattice give rise to conduction mechanisms that can drastically lower the room temperature resistivity and nullify the ferroelectric applications of this material. In this light, growth of high quality stoichiometric epitaxial films of PbTiO<sub>3</sub> demands the use of a technique such as MBE where precise control of the composition in the deposited film can be achieved.

MBE has not been widely applied to the growth of oxide ferroelectrics and has never been used to grow PbTiO<sub>3</sub> films. However, the recent success of MBE for the growth of multicomponent oxide superconductors [30] suggests that MBE is ideally

suited to growing titanates as well. An extensive literature search revealed only two examples of the use MBE to grow epitaxial oxide ferroelectric films:  $\text{LiNbO}_3$  [31] and  $\text{BaTiO}_3$  [32] films. However, in both cases the electrical characteristics of the films are not reported. The promise of applying MBE to ferroelectrics has occurred to those active in the ferroelectrics field, predating the availability of the MBE technique for the controlled growth of multi-component oxides. For example, Scott and Paz de Araujo in their review of the status of ferroelectric thin films state: "In order to make ultrapure ferroelectric memories with virtually no mobile ions, it would be extremely useful to fabricate ferroelectric memories by MBE techniques." [1]

### 3. Experimental procedure

Fig. 2 is a schematic of our MBE system. It is the first commercial MBE system containing ports for atomic absorption spectroscopy (AA) [33], allowing real-time monitoring of all the depositing fluxes. It also contains a retractable quartz crystal microbalance (QCM) to provide an absolute in situ flux measurement at the position of the wafer (prior to growth) for calibration of the AA signals. The depositing fluxes of all the sources (up to eight different elements simultaneously) are monitored during growth by AA [34]. The measured AA signal is fed into the MBE computer control system [35], which integrates the AA fluxes and closes the appropriate shutters after the desired dose has been delivered to the substrate. Purified ozone is used to provide sufficient oxidation, while maintaining the long mean free path necessary for MBE [30]. The highly oxidizing environment used in the MBE necessitated two major differences between this EPI 930 oxide MBE system [36] and conventional III-V MBE systems: (1) the replacement of all molybdenum parts that experience high temperatures with an oxidation-resistant stainless steel alloy (Haynes<sup>TM</sup>214 [37]), and (2) a substrate heater capable of radiatively heating the substrate block in an oxidizing environment. This second challenge was met by using quartz lamps in place of the bare tungsten or tantalum filaments conventionally used in MBE substrate heaters. In addition, the system

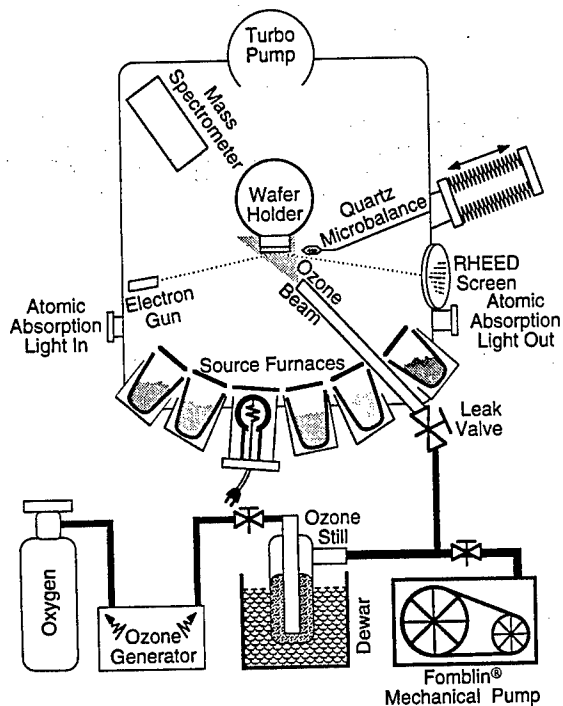


Fig. 2. Schematic of our MBE system equipped with atomic absorption ports for each of the eight sources present.

also contains ports allowing ellipsometry measurements (at two different angles of incidence, appropriate for transparent oxides and oxide superconductors), infrared reflectivity measurements, and through-the-wafer optical transmission measurements. The system also contains the standard features found in MBE systems: in situ reflection high energy electron diffraction (RHEED), a mass spectrometer, computer-controlled shutters and furnaces for 8 elemental sources, and a load-locked wafer introduction chamber. For the growth of titanates, a titanium sublimation pump is employed as a titanium source. The Ti-Ball<sup>TM</sup> [38] is available commercially from Varian Vacuum Products, and has proven to be a comparatively cheap and stable source of titanium. The stability and suitability of the Ti-Ball<sup>TM</sup> for an MBE source, as well as its compatibility with an oxidizing environment is described in more detail elsewhere [39].

The benefit of AA can be seen from Fig. 3 which shows an example of how the depositing flux of certain elements depends critically on the presence

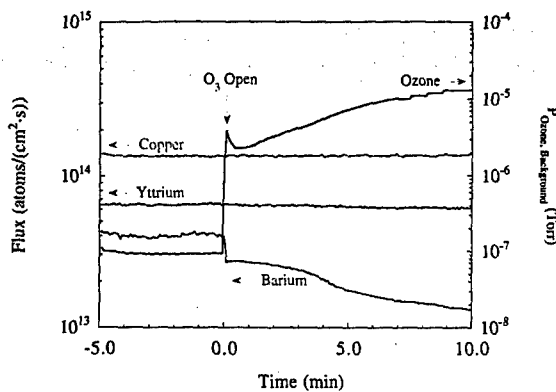


Fig. 3. Effect of ozone on the incident flux of several elemental species. Note the change in barium flux upon the introduction of ozone. Other fluxes, including strontium, show similar changes.

of ozone. Prior to this experiment, the AA signal was calibrated in situ using a QCM at the position of the substrate in the absence of ozone. By measuring the AA signal corresponding to different fluxes (measured by the QCM), the relationship between AA signal and flux (a nonlinear relationship at high fluxes [33]) was established. Note how the Ba flux drops by about 50% upon the introduction of ozone and continues to drop as the ozone flux is increased. When the ozone is turned off, the Ba flux slowly comes back to its initial value. Such changes can go unnoticed using conventional MBE flux measurement techniques in which the fluxes are measured before and after growth (e.g., using an ion gauge) and assuming that the fluxes remain constant during growth.

$\text{PbTiO}_3$  films ( $\sim 1000 \text{ \AA}$ ) thick were grown on  $(1\ 0\ 0)$   $\text{LaAlO}_3$  substrates. Films were grown using an incident lead flux of  $(1\text{--}2) \times 10^{14} \text{ atoms}/(\text{cm}^2 \text{ s})$  and ozone background pressures of  $5 \times 10^{-6}$  to  $5 \times 10^{-5}$  Torr. Substrate temperatures ranged from 570 to  $650^\circ\text{C}$  (measured by optical pyrometry). The best epitaxial  $\text{PbTiO}_3$  films were grown by supplying an overpressure of lead, and shuttering the titanium to provide bursts of titanium atoms which correspond to individual monolayers of  $\text{TiO}_2$ .

#### 4. Results and discussion

Fig. 4 shows the  $\theta\text{--}\theta$  X-ray diffraction pattern for a  $1000 \text{ \AA}$  thick  $\text{PbTiO}_3$  film grown on  $\text{LaAlO}_3$

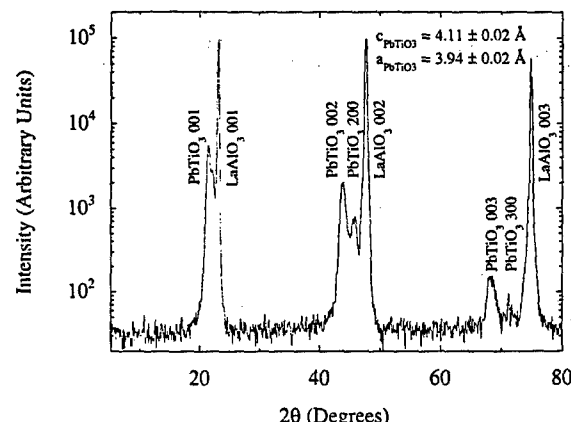


Fig. 4.  $\theta\text{--}\theta$  X-ray diffraction pattern of a  $1000 \text{ \AA}$  thick  $\text{PbTiO}_3$  film grown on  $(1\ 0\ 0)$   $\text{LaAlO}_3$  by MBE. This film was grown at a growth temperature of  $\sim 630^\circ\text{C}$ , in an ozone background pressure of  $5 \times 10^{-5}$  Torr, an incident Pb flux of  $1.5 \times 10^{14} \text{ atoms}/(\text{cm}^2 \text{ s})$ , and a shuttered titanium flux to deliver individual monolayers of titania. The growth rate for this film was  $\sim 0.3 \text{ \AA s}$ .

by MBE. The data indicate that some  $\text{PbTiO}_3$  domains are oriented with their *a*-axis oriented normal to the substrate (*a*-axis oriented), while others are oriented with their *c*-axis normal to the substrate (*c*-axis oriented). This configuration is expected due to the poor in-plane lattice match between  $\text{PbTiO}_3$  and the  $\text{LaAlO}_3$  substrate. Indeed, this pattern is virtually identical to X-ray diffraction patterns of stoichiometric (measured by RBS)  $\text{PbTiO}_3$  films grown on  $\text{LaAlO}_3$  substrates by PLD [29]. Fig. 5 shows the  $\phi$ -scan for the same film indicating alignment between the perovskite subcell axes of the film with those of the substrate. The film is epitaxial and no other in-plane orientations are present.

The growth of lead titanate by MBE depends critically on the ability to oxidize the lead. Initially, using ozone background pressures of  $5 \times 10^{-6}$  Torr, films were almost entirely  $\text{TiO}_2$  (anatase), independent of the incident lead flux and using growth temperatures as low as  $570^\circ\text{C}$ . At ozone background pressures of  $5 \times 10^{-5}$  Torr, films are entirely perovskite lead titanate at substrate temperatures ranging from  $600$  to  $650^\circ\text{C}$ . 4-circle X-ray diffraction analysis indicates that there is little variation in the film structure with temper-

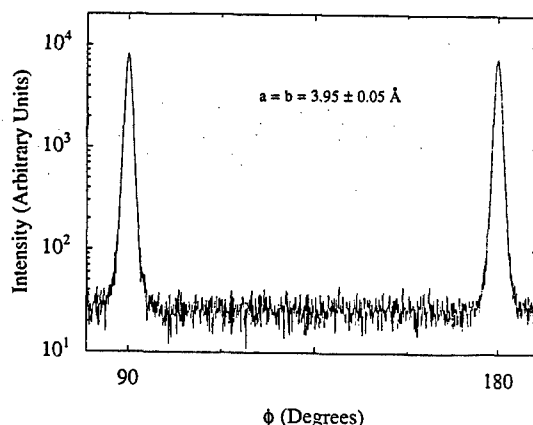


Fig. 5.  $\phi$ -scan of the  $\text{PbTiO}_3$  101 reflections for the *c*-axis grains oriented normal to the substrate surface for the film shown in Fig. 4.

ature (in the 600–650°C range) and incident  $\text{Pb} : \text{Ti}$  ratio (for  $\text{Pb} : \text{Ti}$  ratios greater than 2 : 1) at this higher ozone pressure. This result is evidence of an adsorption-controlled growth mechanism, i.e., the  $\text{PbTiO}_3$  is grown in an overpressure of  $\text{Pb}$  and  $\text{O}_3$ , and the excess of these species desorb. M. de Keijser et al. has shown that the same growth mechanism is operative for lead-based oxide thin films grown by metal-organic chemical vapor deposition (MOCVD) [40].

## 5. Conclusions

We have demonstrated the growth of lead titanate thin films on (100)  $\text{LaAlO}_3$  substrates for the first time by reactive MBE. These films are mixed *a*- and *c*-axis oriented as expected from lattice matching considerations. Initial results indicate that the formation of the perovskite phase is dependent on (1) the ability to oxidize the incident lead flux, and (2) an overabundance of lead present during growth to prevent the formation of lead vacancies or lead deficient phases.

## Acknowledgements

We gratefully acknowledge the financial support of ONR through contract N00014-94-1-0690. The

MBE system was made possible by support from NSF through grants ECS-9311146 and DMR-9357614.

## References

- [1] J.F. Scott and C. Paz de Araujo, *Science* 246 (1989) 1400.
- [2] A. Seifert, F.F. Lange and J.S. Speck, *J. Mater. Res.* 10 (1995) 680.
- [3] K. Iijima, I. Ueda and K. Kugimiya, *Jpn. J. Appl. Phys.* 30 (1991) 2149.
- [4] Y.-F. Chen, T. Yu, J.-X. Chen, L. Shun, P. Li and N.-B. Ming, *Appl. Phys. Lett.* 66 (1995) 148.
- [5] Y. Gao, G. Bai, K.L. Merkle, Y. Shi, H.L.M. Chang, Z. Shen and D.J. Lam, *J. Mater. Res.* 8 (1993) 145.
- [6] G.R. Bai, H.L.M. Chang, C.M. Foster, Z. Shen and D.J. Lam, *J. Mater. Res.* 9 (1994) 156.
- [7] C.M. Foster, Z. Li, M. Buckett, D. Miller, P.M. Baldo, L.E. Rehn, G.R. Bai, D. Guo, H. You and K.L. Merkle, *J. Appl. Phys.* 78 (1995) 2607.
- [8] H. Tabata, O. Murata, T. Kawai, S. Kawai and M. Okuyama, *Appl. Phys. Lett.* 64 (1994) 428.
- [9] W.-Y. Hsu and R. Raj, *Appl. Phys. Lett.* 67 (1995) 792.
- [10] C.D. Theis and D.G. Schlom, in: *Epitaxial Oxide Thin Films II*, Eds. D.K. Fork, J.S. Speck, R.M. Wolf and T. Shiosaki, *Mater. Res. Soc. Symp. Proc.*, Vol. 401 (Mater. Res. Soc., Pittsburgh, 1996) pp. 171–176.
- [11] K. Iijima, Y. Tomita, R. Takayama and I. Ueda, *J. Appl. Phys.* 60 (1986) 361.
- [12] E.C. Subbarao, *Ferroelectrics* 5 (1973) 267.
- [13] C.H. Ahn, J.-M. Triscone, N. Archibald, M. Decroux, R.H. Hammond, T.H. Geballe, O. Fischer and M.R. Beasley, *Science* 269 (1995) 373.
- [14] J.F. Scott, C. Paz de Araujo and G.W. Taylor, Eds., *Ferroelectric Thin Films: Synthesis and Basic Properties* (Gordon and Breach, New York, 1996).
- [15] K.-H. Hellwege, Ed., *Landolt-Bornstein. Numerical Data and Functional Relationships in Science and Technology*, New Series III, Vol. 7b1 (Springer, Berlin, 1975) pp. 26–27.
- [16] K.-H. Hellwege, Ed., *Landolt-Bornstein. Numerical Data and Functional Relationships in Science and Technology*, New Series III, Vol. 3 (Springer, Berlin, 1969) p. 59.
- [17] K.-H. Hellwege, Ed., *Landolt-Bornstein. Numerical Data and Functional Relationships in Science and Technology*, New Series III, Vol. 14a (Springer, Berlin, 1988) p. 30.
- [18] J.W. Dalziel and A.J.E. Welch, *Acta Cryst.* 13 (1960) 956.
- [19] K.-H. Hellwege, Ed., *Landolt-Bornstein. Numerical Data and Functional Relationships in Science and Technology*, New Series III, Vol. 7e (Springer, Berlin, 1976) p. 134.
- [20] D. Taylor, *Trans. J. Brit. Cer. Soc.* 84 (1985) 181.
- [21] C.D. Theis and D.G. Schlom, *J. Mater. Res.*, in press.
- [22] R.E. Honig and D.A. Kramer, *RCA Rev.* 30 (1969) 285.
- [23] R.H. Lamoreaux, D.L. Hildenbrand and L. Brewer, *J. Phys. Chem. Ref. Data* 16 (1987) 419.
- [24] R.L. Holman, *Ferroelectrics* 14 (1976) 675.

- [25] S. Shirasaki, Solid State Commun. 9 (1971) 1217.
- [26] J.P. Remeika, J. Am. Chem. Soc. 76 (1954) 940.
- [27] J.P. Remeika and A.M. Glass, Mater. Res. Bull. 5 (1970) 37.
- [28] M.A. Eisa, M.F. Abadir and A.M. Gadalla, Trans. J. Brit. Ceram. Soc. 79 (1980) 100.
- [29] C.D. Theis, Investigation of Growth and Domain Structure of Epitaxial Lead Titanate Thin Films, MS Thesis, The Pennsylvania State University, University Park, PA (1996).
- [30] D.G. Schlom and J.S. Harris, Jr., in: Molecular Beam Epitaxy: Applications to Key Materials, Ed. R.F.C. Farrow (Noyes, Park Ridge, 1995).
- [31] R.A. Betts and C.W. Pitt, Electron. Lett. 21 (1985) 960; M. Petrucci, C.W. Pitt and P.J. Dobson, Electron. Lett. 22 (1986) 954.
- [32] R.A. McKee, F.J. Walker, J.R. Conner, E.D. Specht and D.E. Zelmon, Appl. Phys. Lett. 59 (1991) 782.
- [33] C. Lu and Y. Guan, J. Vac. Sci. Technol. A 13 (1995) 1797.
- [34] Intelligent Sensor Technology, Mountain View, CA.
- [35] WeckTech Systems, Pleasanton, CA.
- [36] EPI, Chorus Corp., St. Paul, MN.
- [37] Haynes is a registered trademark of Haynes International, Kokomo, IN.
- [38] Ti-Ball is a registered trademark of Varian Vacuum Products, Lexington, MA.
- [39] C.D. Theis and D.G. Schlom, J. Vac. Sci. Technol. A 14 (1996) 2677.
- [40] M. de Keijser and G.J.M. Dormans, Mater. Res. Soc. Bull. 21 (1996) 37.

# Journal of Crystal Growth

## Instructions to Authors (short version)

### Submission of papers

Manuscripts (one original + two copies), should be sent to a member of the Editorial Board or preferably to an appropriate subject Associate Editor. News or announcements should be submitted through the Principal Editor; a duplicate should be sent directly to Elsevier Science B.V., address given below.

*Original material.* Submission of a manuscript implies it is not being simultaneously considered for publication elsewhere and that the authors have obtained the necessary authority for publication.

### Types of contributions

Original research papers, Letters to the Editors and Priority communications are welcome. They should contain an Abstract (of up to 200 words) and a Conclusion section, which particularly in the case of theoretical papers translates the results into terms readily accessible to most readers.

As a guideline: *experimental papers* should not be longer than 16 double-spaced typed pages, and 8 figures + tables; for *theoretical papers* a maximum of 20 pages and 10 figures + tables is suggested.

*Letters and Priority communications* should not be longer than 5 double-spaced typed pages, and 3 figures + tables. They will be given priority in both the refereeing and production processes. The faster production schedule may preclude sending proofs of Letters and Priority communications to authors.

### Manuscript preparation

Contributions may be written in English, French or German. They should have an abstract in English. The paper copies of the text should be prepared with double line spacing and wide margins, on numbered sheets.

*Structure.* Please adhere to the following order of presentation: Article title, Author(s), Affiliation(s), Abstract, PACS codes and keywords, Main text, Acknowledgements, Appendices, References, Figure captions, Tables.

*Corresponding author.* The name, complete postal address, telephone and fax numbers and the e-mail address of the corresponding author should be given on the first page of the manuscript.

*Classification codes/keywords.* Please supply one to four classification codes (PACS and/or MSC) and up to six keywords of your own choice that describe the content of your article in more detail.

*References.* References to other work should be consecutively numbered in the text using square brackets and listed by number in the Reference list. Please refer to the more detailed instructions for examples.

### Illustrations

Illustrations should also be submitted in triplicate: one master set and two sets of copies. The *line drawings* in the master set should be original laser printer or plotter output or drawn in black india ink, with careful lettering, large enough (3–5 mm) to remain legible after reduction for printing. The *photographs* should be originals, with somewhat more contrast than is required in the printed version. They should be unmounted unless part of a composite figure. Any scale markers should be inserted on the photograph itself, not drawn below it.

*Colour plates.* Figures may be published in colour, if this is judged essential by the Editor. The Publisher and the author will each bear part of the extra costs involved. Further information is available from the Publisher.

### After acceptance

*Important.* When page proofs of the accepted manuscripts are made and sent out to authors, this is in order to check that no undetected errors have arisen in the typesetting (or file conversion) process. At the proof stage only printer's errors may be corrected. No changes in, or additions to, the edited manuscript will be accepted.

*Notification.* The authors will receive the final answer of acceptance or rejection from the Office of the Principal Editor and will be invited to supply an electronic version of the accepted text, if this is not already available.

*Copyright transfer.* In the course of the production process you will be asked to transfer the copyright of the article to the Publisher. This transfer will ensure the widest possible dissemination of information.

### Electronic manuscripts

The Publisher welcomes the receipt of an electronic version of your accepted manuscript. If there is not already a copy of this (on diskette) with the journal editor at the time the manuscript is being refereed, you will be asked to send a file with the text of the accepted manuscript directly to the Publisher by e-mail or on diskette (allowed formats 3.5" or 5.25" MS-DOS, or 3.5" Macintosh) to the address given below. (When e-mailing a non-ASCII word-processor file, you should encode it, e.g. with UUENCODE or BinHex, so as to retain all formatting codes.) The name and version of the word-processing program and the type of operating system should always be indicated. Please note that no deviations from the version accepted by the Editor of the journal are permissible without the prior and explicit approval by the Editor. Such changes should be clearly indicated on an accompanying printout of the file.

### Author benefits

*No page charges.* Publishing in Journal of Crystal Growth is free.

*Free offprints.* The corresponding author will receive 50 offprints free of charge. An offprint order form will be supplied by the Publisher for ordering any additional paid offprints.

*Discount.* Contributors to Elsevier Science journals are entitled to a 30% discount on all Elsevier Science books.

### Further information (after acceptance)

Elsevier Science B.V., J. Crystal Growth  
Issue Management Physics  
and Materials Science  
P.O. Box 2759, 1000 CT Amsterdam  
The Netherlands  
Fax: +31 20 485 2319 / +31 20 485 2704  
E-mail: matsci-de-f@elsevier.nl

## The Growth of Oxide Heterostructures by MBE

D.G. Schlom and C.D. Theis

Department of Materials Science and Engineering  
Penn State University

and

M.E. Hawley  
Los Alamos National Laboratory

### ABSTRACT

The opportunities, challenges, and synthesis of oxide heterostructures by reactive molecular beam epitaxy (MBE) are described, with examples taken from the growth of oxide superconductors and oxide ferroelectrics.

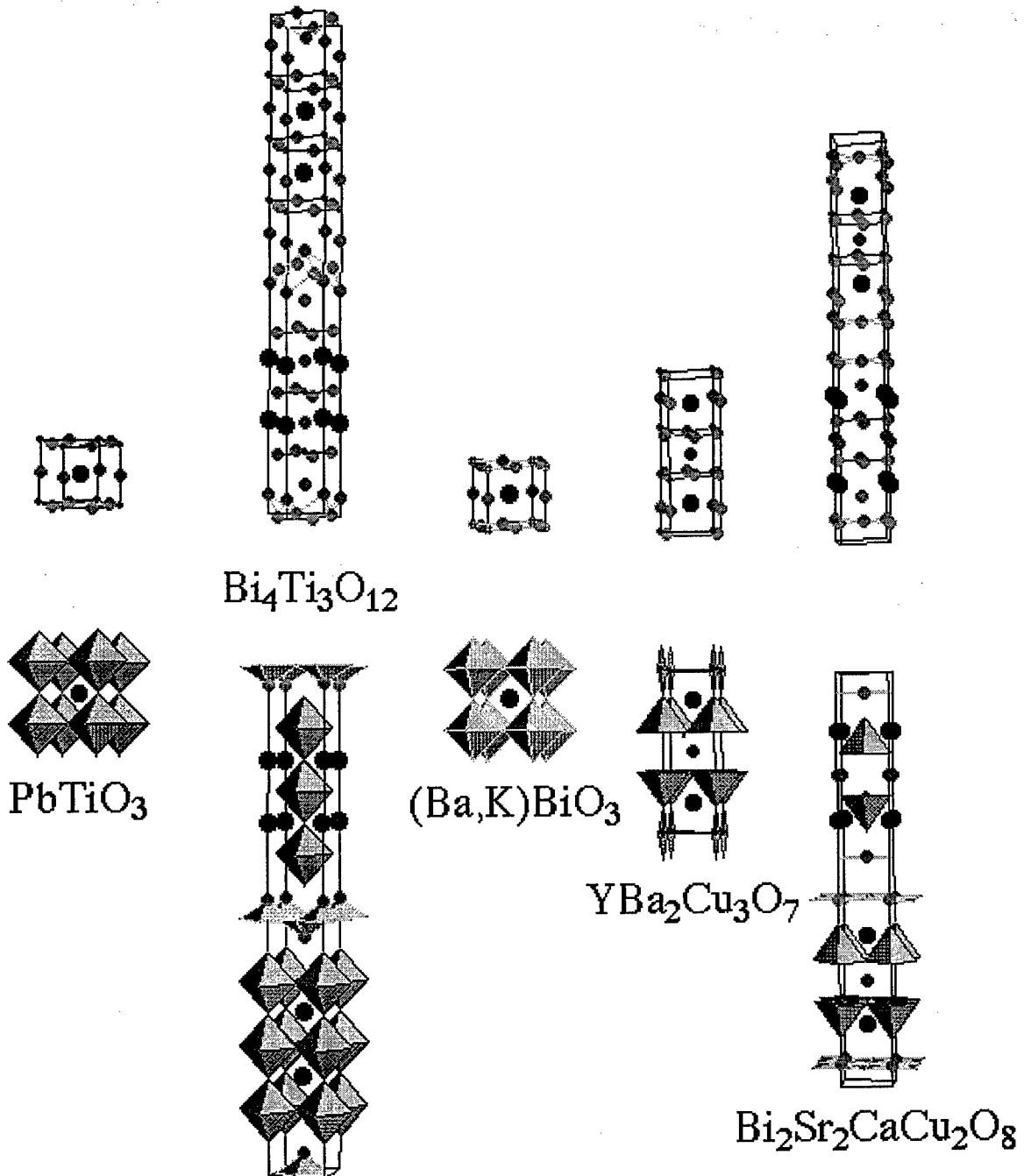
### INTRODUCTION

The broad spectrum of electronic and optical properties exhibited by oxides offers tremendous opportunities for microelectronic devices, especially when a combination of properties in a single device is desired. Oxides exhibit the full spectrum of electronic, optical, and magnetic behavior; insulating, semiconducting, metallic, high temperature superconducting, pyroelectric, piezoelectric, ferroelectric, ferromagnetic, and non-linear optical effects are all contained within structurally-compatible oxides (particularly perovskites). Examples are given in Table I and some of their crystal structures are shown in Fig. 1. The electroceramics industry, a more than \$20 billion/year industry, utilizes these electrical properties generally in single devices made primarily by bulk synthesis methods for capacitors, sensors, actuators, night vision and other applications. However, a significant opportunity exists to combine these properties together in oxide heterostructures where multiple properties can be utilized to yield a functional integrated device. Integration of epitaxial stacks of these oxide crystals is motivated by the similarity in crystal structure (the perovskite oxides listed in Table I all have perovskite subcell dimensions in the 3.8 Å to 4.0 Å range), the chemical compatibility that exists between many oxides, and the enhanced properties that these materials exhibit in single crystal form. The increase in performance can be by many orders of magnitude for the critical current density ( $J_c$ ) of a superconductor or the magnetoresistance effect. In addition to synthesizing oxide heterostructures that integrate relatively thick layers of different oxides together, in principle, new oxides can be engineered if structural control can be achieved at the atomic-layer level. Although now commonplace in the growth of semiconductors (i.e., by MBE), such an ability would be new to oxides and would likely result in the discovery/engineering of higher performance materials and possibly the exploitation of new

electrical phenomena. Numerous attempts by conventional solid-state techniques to synthesize oxide structures believed to be of significant scientific and technological importance have failed.

Table I: Examples of the properties of compatible (perovskite) oxides.

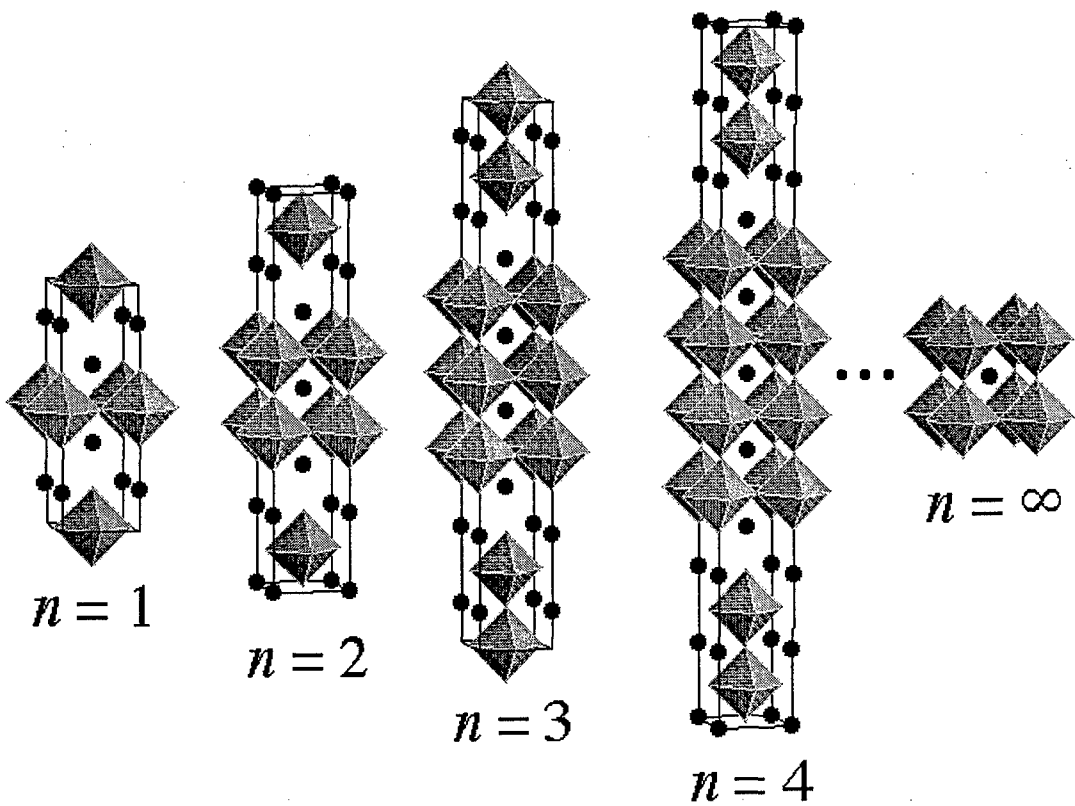
Property	Value	Oxide Material
High $\epsilon_r$ Insulators	$\rho \approx 1 \times 10^{11} \Omega \cdot \text{m}$ $\epsilon_r = 20000$ (4 K)	$\text{SrTiO}_3$
Low $\epsilon_r$ Insulators	$\epsilon_r = 16$ (77 K)	$\text{LaAlO}_3$
Conductors	$\rho \approx 1 \times 10^{-7} \Omega \cdot \text{m}$ (77 K)	$\text{Sr}_2\text{RuO}_4$
Superconductors	$\rho \approx 0$	$\text{YBa}_2\text{Cu}_3\text{O}_{7-\delta}$
Ferroelectrics	$P_r = 0.75 \text{ C/m}^2$	$\text{PbTiO}_3$
Pyroelectrics	$p_3 = 500 \frac{\mu\text{C}}{\text{m}^2 \text{K}}$	(Ba,Sr)TiO <sub>3</sub>
Piezoelectrics	$d_{15} = 600 \text{ pC/N}$	$\text{BaTiO}_3$
Ferromagnets	$M_s = 1.4 \mu_B$	$\text{SrRuO}_3$
Colossal Magnetoresistance	$\Delta R/R_H > 10^4$ (6 T)	(La,Sr)MnO <sub>3</sub>



**Fig. 1.** The crystal structure of some perovskite-related structures exhibiting the properties described in Table I. Two equivalent representations of these crystal structures are shown: the atomic positions (above) and the coordination polyhedra (below). The oxygen atoms occupy the vertices of the coordination polyhedra. The tetragonal subcells of the  $\text{Bi}_4\text{Ti}_3\text{O}_{12}$  and  $\text{Bi}_2\text{Sr}_2\text{CaCu}_2\text{O}_{8+\delta}$  structures are shown for clarity and to illustrate the similarities between these perovskite-related phases. The relative sizes of the atoms reflect their relative ionic radii as given by Ref. 1.

Just as MBE made possible the bandgap engineering of semiconductor heterostructures, reactive MBE shows great promise for the growth of oxide heterostructures with control down to the atomic layer level, i.e., atomic layer engineering of oxides.<sup>2</sup>

Structure-property relations have been studied for a great many oxides using solid-state synthesis methods. Many cases have been found where the property of a structurally-related family of oxides (i.e., a homologous series) changes drastically from one end to the other of the series. Examples include the  $\text{Sr}_{n+1}\text{Ru}_n\text{O}_{3n+1}$  Ruddlesden-Popper homologous series shown in Fig. 2. The  $n = 1$  ( $\text{Sr}_2\text{RuO}_4$ ) member of the series is paramagnetic and superconducting whereas the  $n = \infty$  ( $\text{SrRuO}_3$ ) member of the series is ferromagnetic. Many other equally fascinating homologous series exist in perovskite-related oxide structures showing interesting variation in ferromagnetic, ferroelectric, superconducting, or metal-insulator behavior. However, when the goal is to study the property variation with changing  $n$  in detail, solid-state synthesis methods fall short. Invariably researchers have only been able to find conditions of temperature and pressure yielding single-phase products for low values of  $n$  and for  $n = \infty$ . Attempts to make intermediate  $n$  values result in uncontrolled intergrowths. Thus, apart from theoretical calculations, little is known about how the properties of a series of structures vary with  $n$  as the dimensionality of the structure changes. A key advantage of the use of MBE for the preparation of oxide heterostructures is that single-phase epitaxial films with intermediate  $n$  values can often be synthesized even though nearby phases have similar formation energies. This is made possible by the ability to supply incident species in any desired sequence with submonolayer composition control. A particular phase can often be grown by supplying the constituents in an ordered sequence corresponding to the atomic arrangement of these constituents in the desired phase.



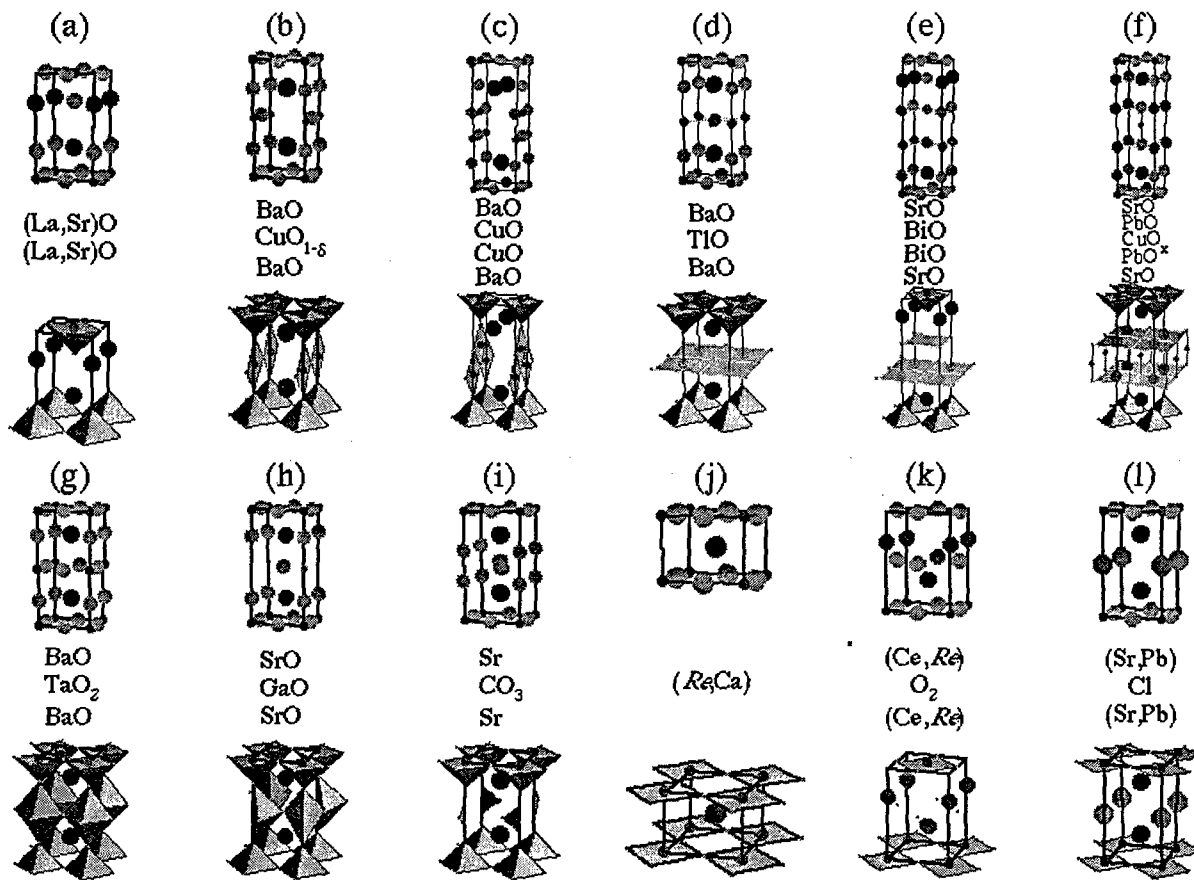
**Fig. 2.**  $n = 1$  ( $\text{Sr}_2\text{RuO}_4$ ),  $n = 2$  ( $\text{Sr}_3\text{Ru}_2\text{O}_7$ ),  $n = 3$  ( $\text{Sr}_4\text{Ru}_3\text{O}_{10}$ ),  $n = 4$  ( $\text{Sr}_5\text{Ru}_4\text{O}_{13}$ ), and  $n = \infty$  ( $\text{SrRuO}_3$ ) members of the homologous Ruddlesden-Popper series of compounds  $\text{Sr}_{n+1}\text{Ru}_n\text{O}_{3n+1}$ .

MBE even allows metastable phases to be formed by utilizing interfacial strain energies to favor the desired metastable phase over the equilibrium phase (epitaxial stabilization).<sup>3</sup> In contrast to bulk synthesis, in epitaxial growth, interfacial energies play a significant role. Specifically, strain energies due to interfacial mismatch are often sufficient to shift the energetics of which phase is most stable. In cases where the equilibrium structure has significantly different lattice spacing than a desired metastable structure, the formation of the metastable structure may be made favorable by selecting a substrate that is lattice matched to it rather than to the equilibrium structure. Numerous examples of epitaxially-stabilized phases exist in semiconductor, metal, and alkali halide systems.<sup>3-5</sup> Many of these examples have been grown by MBE.

Below the roadblock to the controlled synthesis of oxide heterostructures is first described, followed by examples indicating the promise and current capabilities of reactive MBE.

## UNCONTROLLED INTERGROWTHS

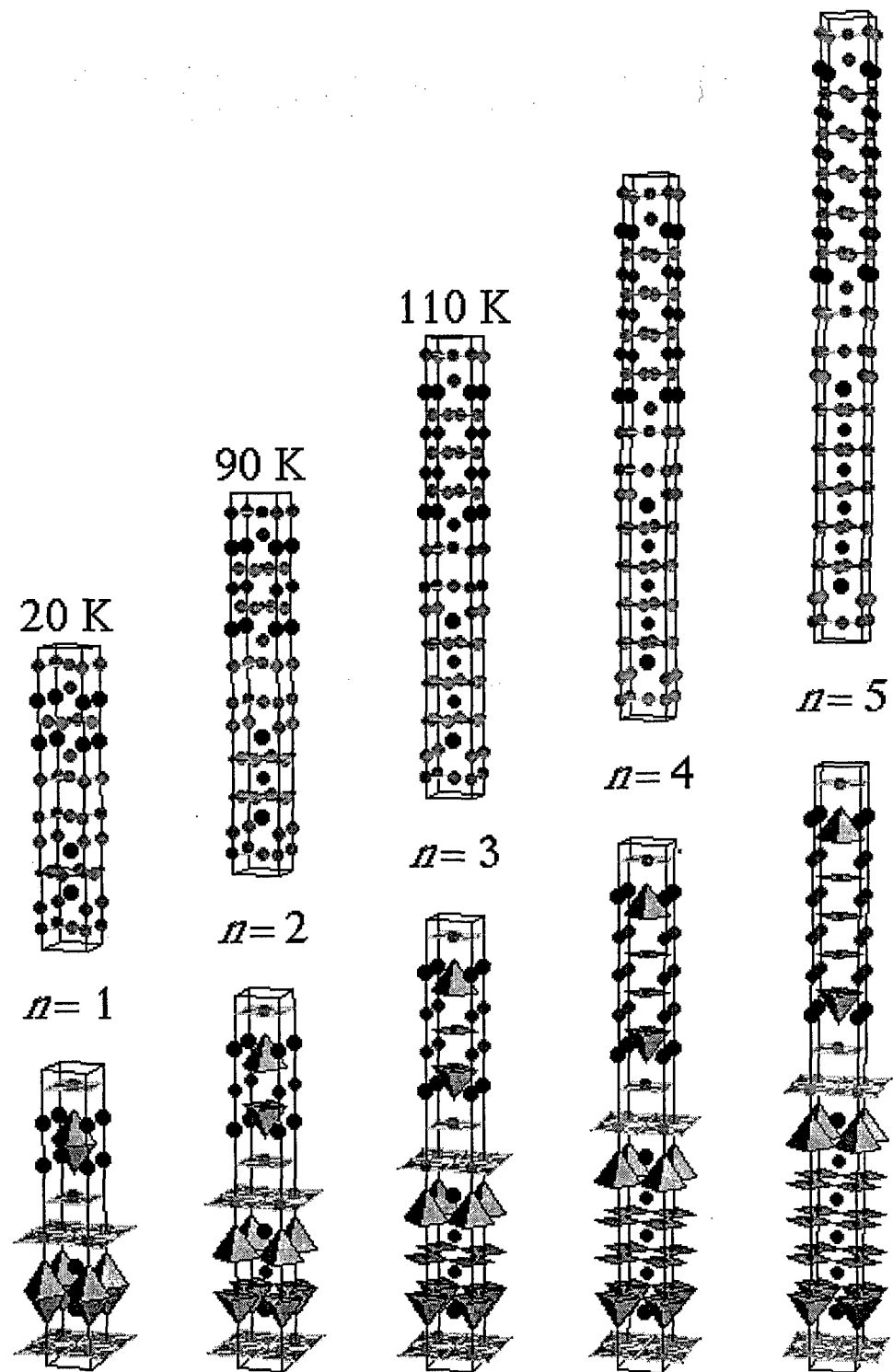
One example of this general problem involves the synthesis of oxide superconductors. The crystal structures of *all* known layered CuO<sub>2</sub>-containing compounds (including all of the known copper-containing high transition temperature (high  $T_c$ ) superconductors) can be constructed,<sup>6</sup> using CuO<sub>2</sub> layers and the layers shown in Fig. 3 as alternate building layers. Having identified the constituent layers, a great many additional structures can be imagined. However, the synthesis of such structures by conventional methods can be elusive and is often impossible, especially for structures with unit cells comprised of a large number of repeated building layers.



**Fig. 3.** The building layers of all known layered CuO<sub>2</sub> structures: (a) [(La,Sr)O-(La,Sr)O] or [(Sr,Ca)(Br,Cl)-(Sr,Ca)(Br,Cl)]\*, (b) [BaO-CuO<sub>1-δ</sub>-BaO], (c) [BaO-CuO-CuO-BaO], (d) [BaO-TiO-BaO] or [BaO-HgO<sub>x</sub>-BaO] or [SrO-(Bi,Cu)O<sub>x</sub>-SrO] or [SrO-(Bi,Cd)O-SrO] or [SrO-(Pb,Sr)O-SrO] or [SrO-(Pb,Cu)O<sub>x</sub>-SrO] or [SrO-(Pb,Cd)O-SrO] or [SrO-(Ce,Cu)O<sub>x</sub>-SrO]\* or [SrO-(Ce,Cd)O-SrO], (e) [BaO-TiO-TiO-BaO] or [BaO-HgO<sub>x</sub>-HgO<sub>x</sub>-BaO] or [SrO-BiO-BiO-SrO] or [(Ba,Sr)O-(Pb,Cu)O<sub>x</sub>-(Pb,Cu)O<sub>x</sub>-(Ba,Sr)O], (f) [SrO-PbO-CuO<sub>x</sub>-PbO-SrO], (g) [LaO-SnO<sub>2</sub>-LaO]\* or [BaO-TaO<sub>2</sub>-BaO]\* or [SrO-TaO<sub>2</sub>-SrO] or [SrO-NbO<sub>2</sub>-SrO], (h) [SrO-GaO-SrO] or [SrO-CoO-SrO]\* or [SrO-AlO-SrO]\*, (i) [Sr-CO<sub>3</sub>-Sr] or [(Re,Ba)-BO<sub>3</sub>-(Re,Ba)], (j) [(Re,Ca)],

(k) [(Ce,*Re*)-O<sub>2</sub>-(Ce,*Re*)], and (l) [(Sr,Pb)-Cl-(Sr,Pb)]\*. The tetragonal subcell of each building layer is outlined. CuO<sub>2</sub> layers are shown above and below each building layer to illustrate their attachment positions. Partial substitution for the constituents of these basic building layers is frequently possible and may be used for doping purposes (e.g., Bi ↔ Pb, Tl ↔ Pb, Sr ↔ Ba, Sr ↔ La, Ca ↔ *Re*). Most of these building layers are constituents of the copper-containing high *T<sub>c</sub>* superconductors discovered to date. Those intervening layers known to occur between CuO<sub>2</sub> layers, but so far not constituents of superconducting structures, are marked with an (\*) asterisk (after Ref. 6).

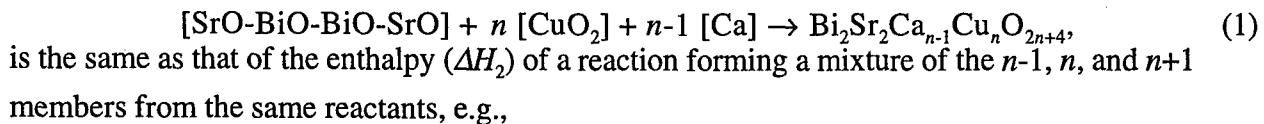
As a specific example, consider the Bi<sub>2</sub>Sr<sub>2</sub>Ca<sub>*n*-1</sub>Cu<sub>*n*</sub>O<sub>2*n*+4</sub> phases. The crystal structures of the Bi<sub>2</sub>Sr<sub>2</sub>Ca<sub>*n*-1</sub>Cu<sub>*n*</sub>O<sub>2*n*+4</sub> phases that have been synthesized in pure single-phase form by bulk methods (*n* = 1 to 3) are shown in Fig. 4 along with their approximate superconducting transition temperatures (*T<sub>c</sub>*). The synthesized structures are the first three members of a homologous series of phases. The members of such a series are related to each other by the addition or subtraction of a simple structural element, which in this case is comprised of a [CuO<sub>2</sub>] and a [Ca] building layer. The next two members of this series are also shown in Fig. 4. The striking empirical trend of increasing *T<sub>c</sub>* with the number of CuO<sub>2</sub> layers in the unit cell of these structures (a similar phenomena exists for TlBa<sub>2</sub>Ca<sub>*n*-1</sub>Cu<sub>*n*</sub>O<sub>2*n*+3</sub>, Tl<sub>2</sub>Ba<sub>2</sub>Ca<sub>*n*-1</sub>Cu<sub>*n*</sub>O<sub>2*n*+4</sub>, and HgBa<sub>2</sub>Ca<sub>*n*-1</sub>Cu<sub>*n*</sub>O<sub>2*n*+2</sub> phases) led many researchers to attempt to prepare higher order members by bulk methods. However, as the number of (CuO<sub>2</sub>)<sub>*n*</sub>Ca<sub>*n*-1</sub> layers in these structures becomes greater, pure single phase specimens become progressively more difficult to synthesize in bulk form, presumably because the differences between the free energies of formation of these phases become smaller and smaller.<sup>7</sup> Indeed, TEM studies of bulk samples reveal *uncontrolled* syntactic intergrowths of Bi<sub>2</sub>Sr<sub>2</sub>Ca<sub>*n*-1</sub>Cu<sub>*n*</sub>O<sub>2*n*+4</sub> phases when the bulk synthesis of *n* > 2 is attempted as shown in Fig. 5,<sup>8</sup> and of Tl<sub>2</sub>Ba<sub>2</sub>Ca<sub>*n*-1</sub>Cu<sub>*n*</sub>O<sub>2*n*+4</sub> phases for *n* > 3.<sup>9</sup> Analogous examples of uncontrolled intergrowths abound for the bulk synthesis of other high *T<sub>c</sub>* related homologous series, including the Y<sub>2</sub>Ba<sub>4</sub>Cu<sub>*n*+5</sub>O<sub>*n*+13</sub> phases for *n* > 3,<sup>10</sup> La<sub>4*n*+4</sub>Cu<sub>2*n*+8</sub>O<sub>8*n*+14</sub> phases for *n* > 3,<sup>11</sup> and Ba<sub>*n*+1</sub>(Pb,Bi)<sub>*n*</sub>O<sub>3*n*+1</sub> phases for *n* > 2.<sup>12</sup> The disordered nature of intergrowths is not limited to high *T<sub>c</sub>* systems; rather numerous examples have been documented for other homologous series of layered oxides.<sup>13</sup>

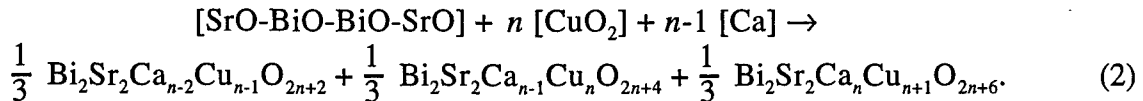


**Fig. 4.** The crystal structures of the  $\text{Bi}_2\text{Sr}_2\text{Ca}_{n-1}\text{Cu}_n\text{O}_{2n+4}$  phases for  $n = 1$  to 5. The tetragonal subcells are shown for clarity. The approximate superconducting transition temperatures of the phases that have been prepared by bulk methods are also shown. Some researchers, utilizing MBE to synthesize the  $n = 8$  member of this homologous series, suggest that this phase may exhibit a superconducting transition temperature ( $T_c$ ) of 250 K.<sup>14</sup> Other researchers have been unable to confirm this report.<sup>15</sup>

**Fig. 5.** A high resolution TEM image showing the structural disorder present in a bulk synthesis attempt of the  $\text{Bi}_2\text{Sr}_2\text{Ca}_2\text{Cu}_3\text{O}_{10}$  phase (from Ref. 8). X-ray diffraction indicates that  $\text{Bi}_2\text{Sr}_2\text{Ca}_2\text{Cu}_3\text{O}_{10}$ , the  $n = 3$   $\text{Bi}_2\text{Sr}_2\text{Ca}_{n-1}\text{Cu}_n\text{O}_{2n+4}$  phase, is the majority phase. However, high resolution TEM images of the microstructure reveal the presence of many *uncontrolled* intergrowths, where  $n$  is seen to vary from 1 to 7.

Uncontrolled intergrowths appear to be a general feature and fundamental limitation of using bulk synthesis methods to prepare complex layered oxide heterostructures. Bulk techniques rely on the existence of sufficiently deep reaction free energy minima to transform the starting materials into a single phase at a particular temperature and pressure. If the formation energies of other phases comprised of the same building layers (and therefore the same in-plane lattice constants) are nearly the same as the desired phase, the sample will contain uncontrolled syntactic intergrowths of these structurally related, but nearly energetically degenerate, phases. The increase in entropy of a syntactically intergrown phase, compared to a single phase sample, provides the free energy driving force for such intergrowths. This driving force increases with temperature and as the numerous examples cited above show, causes significant syntactic mixing at the high synthesis temperatures used in bulk synthesis methods. The overall sample composition is insufficient to determine the microscopic layering order when numerous syntactic members have nearly the same free energies; homologous series members containing fewer of the relevant structural building layers will be balanced out by those containing more in a randomly ordered syntactic mixture of these phases. For example, the  $\text{Bi}_2\text{Sr}_2\text{Ca}_{n-1}\text{Cu}_n\text{O}_{2n+4}$  phases are comprised of [SrO-BiO-BiO-SrO], [ $\text{CuO}_2$ ], and [Ca] building layers. If there is no energetic preference for the formation of the  $n$  member of this series over the  $n-1$  or  $n+1$  members (i.e.,  $\Delta H_f$  of  $\text{Bi}_2\text{Sr}_2\text{Ca}_{n-2}\text{Cu}_{n-1}\text{O}_{2n+2}$ ,  $\text{Bi}_2\text{Sr}_2\text{Ca}_{n-1}\text{Cu}_n\text{O}_{2n+4}$ , and  $\text{Bi}_2\text{Sr}_2\text{Ca}_n\text{Cu}_{n+1}\text{O}_{2n+6}$  are identical), then the enthalpy ( $\Delta H_1$ ) of the formation reaction of the  $n$  member,





Note that the free energy of the latter reaction ( $\Delta G_2$ ) will be lower than that of the former ( $\Delta G_1$ ) because of the increased entropy of the randomly layered mixture of the  $n-1$ ,  $n$ , and  $n+1$  members. Of course, equation (2) represents just one example of a random mixture composition that is energetically favored over the pure  $n$  member phase. In general, all of the members of the homologous series may participate and their fractions are free to vary such that the overall equation is balanced. As long as the enthalpies of formation of participating members are sufficiently equivalent, the free energy of the mixture will always be lower than that of the pure phase. Calculation of the energy of formation of several homologous series of layered oxide phases indicates that the differences in formation energy become smaller and smaller as more building layers are inserted into the parent structure (i.e., with increasing  $n$ ).<sup>†,16,17</sup>

The low growth temperature and atomic layering capability of MBE, widely utilized for the growth of metastable layered semiconductor superlattices, have enabled the *controlled* customized layering of high  $T_c$  phases whose phase-pure growth is unattainable by bulk synthesis methods.<sup>2</sup> These results demonstrate the capability of MBE to grow customized layered structures and metastable phases within *oxide* systems.

### MBE GROWTH APPARATUS

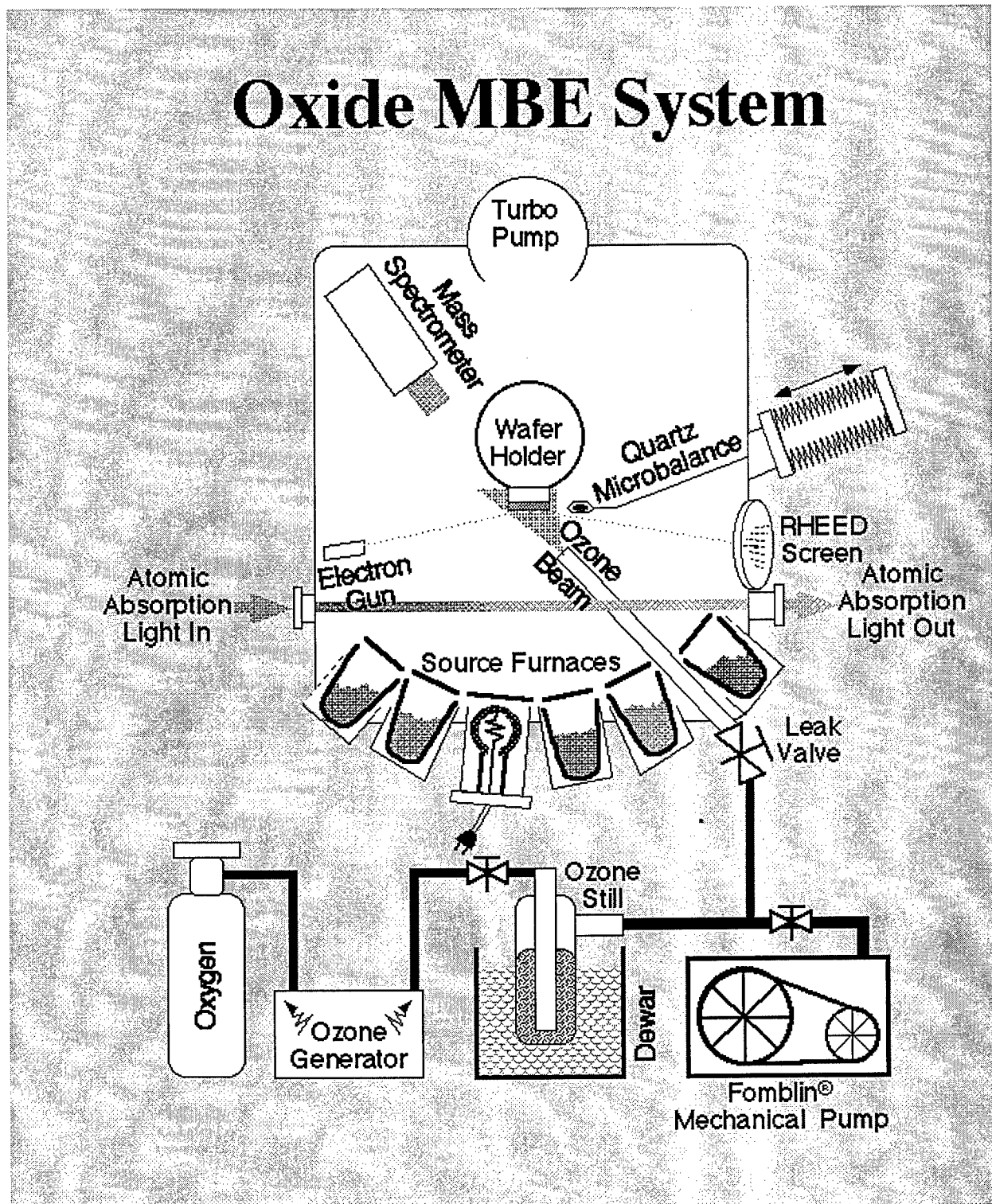
MBE machines for the growth of semiconductors (e.g., IV-IV, III-V, and II-VI materials systems) are present in many laboratories and the technique has enjoyed significant success in the preparation of semiconductor microstructures with nanoscale thickness control and exceptional device characteristics. The use of MBE for the controlled growth of multi-component oxides is relatively new.<sup>2</sup>

A schematic diagram of the growth chamber of the MBE machine<sup>18</sup> used by the authors is shown in Fig. 6. Eight independent shutters, controlled by a computer, supply elemental fluxes to the substrate either at the same time (codeposition) or separately (sequential deposition), as described below. Purified ozone is used to provide sufficient oxidation, while maintaining the long

<sup>†</sup> For example, in the  $\text{Sr}_{n+1}\text{Ti}_n\text{O}_{3n+1}$  homologous series of compounds (another perovskite-related series of compounds), calculations indicate that the formation enthalpy remains essentially constant for  $n > 2$ .<sup>16</sup> Since there is insufficient enthalpic driving force for forming a low entropy phase-pure compound, disordered intergrowths are to be expected in the synthesis of these compounds by bulk methods. Indeed, TEM images of these  $\text{Sr}_{n+1}\text{Ti}_n\text{O}_{3n+1}$  phases<sup>17</sup> show disordered syntactic intergrowths where  $n$  ranges from 2 to 8, as would be expected for the bulk preparation of essentially energetically degenerate phases.

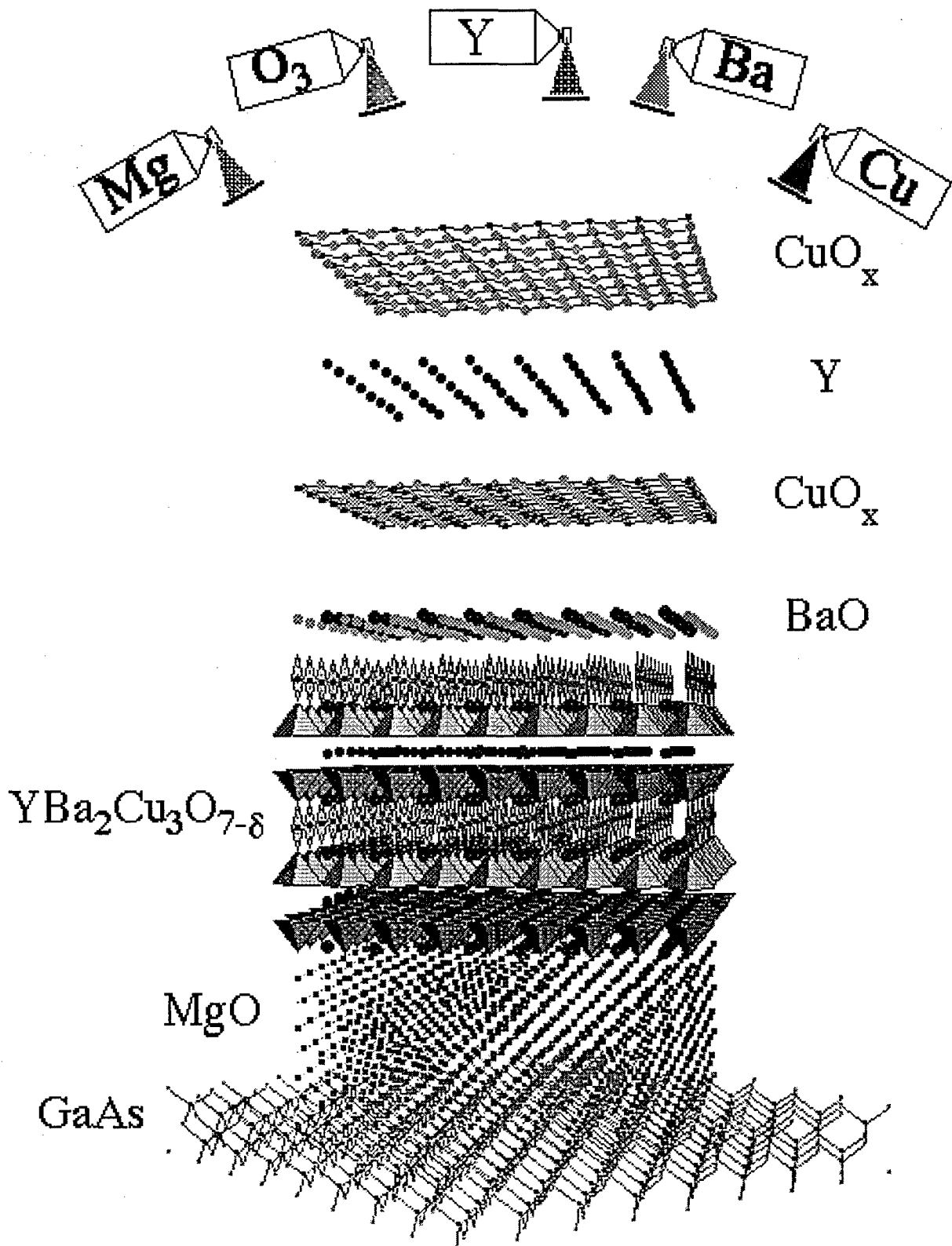
mean free path necessary for MBE.<sup>2</sup> A titanium sublimation pump, powered by a precision current supply, is used as a stable (flux variation of less than 1% per hour)<sup>19</sup> and economical titanium source.

The lack of adequate composition control has been a major problem for previous oxide MBE work.<sup>2</sup> The use of atomic absorption spectroscopy (AA) for oxide MBE composition control has allowed flux stability of better than 1% to be achieved.<sup>20</sup> The MBE system also contains a retractable quartz crystal microbalance to provide an absolute *in situ* flux measurement at the position of the wafer (prior to growth) for calibration of the AA signals. The depositing fluxes of *all* the sources (up to eight different elements simultaneously) are monitored during growth by AA.<sup>21</sup> The measured AA signal is fed into the MBE computer control system, which integrates the AA fluxes and closes the appropriate shutters after the desired dose has been delivered to the substrate.<sup>22</sup> In addition, the system also contains the standard features found in MBE systems: *in situ* reflection high energy electron diffraction (RHEED), a mass spectrometer, computer-controlled shutters and furnaces for eight elemental sources, and a load-locked wafer introduction chamber.



**Fig. 6:** A schematic diagram of the growth chamber of an MBE system dedicated to the controlled synthesis of oxide heterostructures.

The MBE method of thin film growth may be thought of as atomic spray painting, as shown in Fig. 7 in which an oxide heterostructure consisting of the superconductor  $\text{YBa}_2\text{Cu}_3\text{O}_{7-\delta}$  is schematically assembled layer-by-layer on an  $\text{MgO}$  buffer layer grown on  $\text{GaAs}$ . The flux of spray from each atomic or molecular beam is controlled by the temperature (and thus vapor pressure) of the effusion cell in which each species is contained. The duration of spray is individually controlled for each beam by shutters, which control not only the open time (and thus dose), but also the sequence in which species reach the growth surface. By controlling the shutters and temperature of the evaporant (which control dose and flux, respectively) the layering sequence of the desired structure can be customized. This technique has been used to control the layering of oxides on a unit cell level, allowing the preparation of single phase films of nearly energetically degenerate compounds, including cuprate superconductors.<sup>2,23-27</sup> A low growth temperature is frequently used to kinetically minimize subsequent bulk reordering and minimize the loss of the customized (and metastable) layered structures. A unique advantage of MBE is *in situ* characterization of the growing surface using RHEED, which allows the process to be closely monitored. The sensitivity of this grazing angle diffraction technique to surface structure is ideal for monitoring the evolution of growth from initial nucleation to the deposition of each subsequent layer. The formation of intermediate reaction products or impurity phases can be readily monitored and the growth conditions adjusted *during growth* accordingly. Epitaxial growth, a clean UHV deposition environment, *in situ* RHEED characterization during growth, AA composition control, and the notable absence of highly energetic species are distinct advantages of this MBE approach. These capabilities are key to the customized growth of metastable oxides.



**Fig. 7.** A highly schematic representation of the MBE growth of a  $\text{YBa}_2\text{Cu}_3\text{O}_{7-\delta}$  film on an  $\text{MgO}$  barrier layer on a GaAs substrate by reactive MBE.

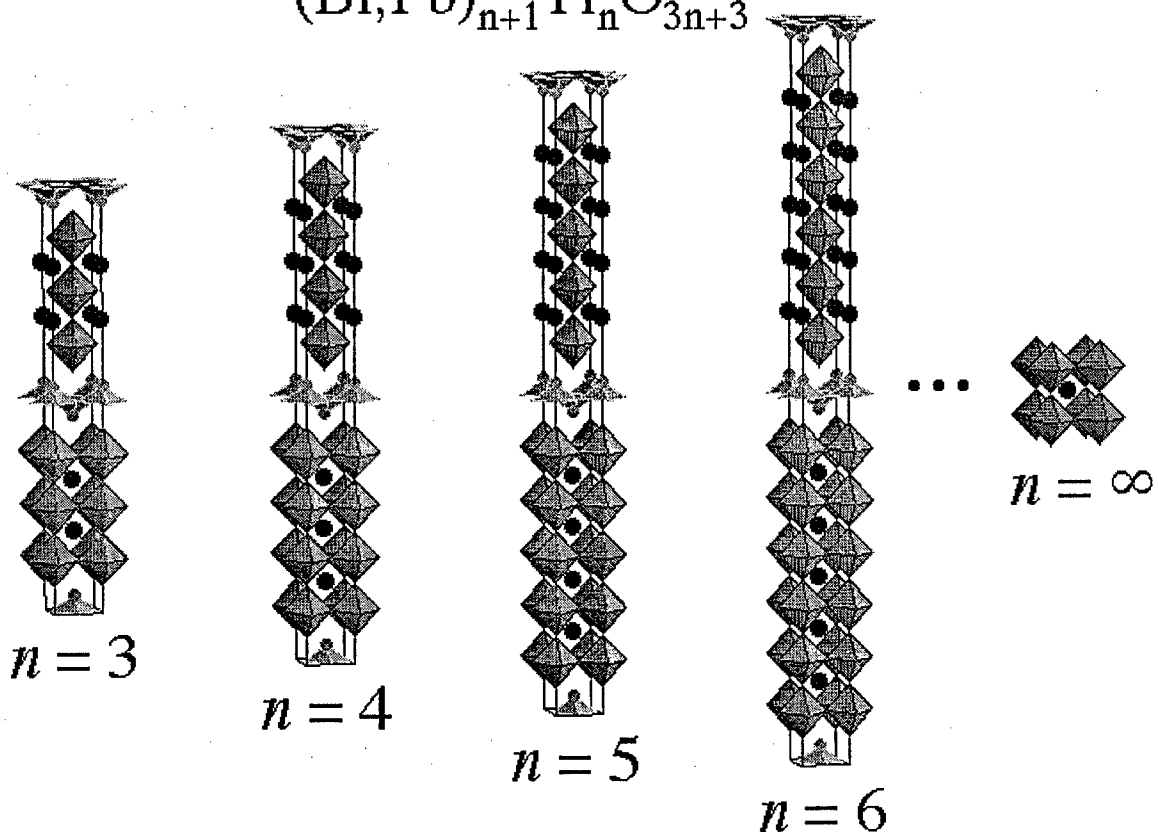
## EXAMPLES OF MBE-GROWN OXIDE HETEROSTRUCTURES

To date oxide MBE has been most widely applied to the growth of high  $T_c$  superconductors. For such oxide heterostructures, MBE has been extremely successful and demonstrated atomic-scale layering control that parallels its achievements for semiconductor growth. Several notable examples are: (1) the use of MBE to prepare single phase  $\text{Bi}_2\text{Sr}_2\text{Ca}_{n-1}\text{Cu}_n\text{O}_{2n+4}$  films, for  $n = 1$  to 11,<sup>24,28,29</sup> demonstrating the ability of this technique to select between nearly energetically-degenerate phases; (2) the synthesis of metastable superlattices, e.g.,  $[\text{Bi}_2\text{Sr}_2\text{CuO}_6 / \text{Bi}_2\text{Sr}_2\text{Ca}_2\text{Cu}_3\text{O}_{10}]_n$ ,<sup>23</sup> and metastable phases, e.g.,  $\text{Bi}_2\text{Sr}_2\text{SrCu}_2\text{O}_8$ ,<sup>23</sup> and (3) the synthesis of superconductor-insulator-superconductor (SIS) Josephson junctions by atomic-layer engineering of the barrier layer between two superconducting layers.<sup>30</sup>

Although first used for the growth of  $\text{LiNbO}_3$  over ten years ago,<sup>31,32</sup> the use of reactive MBE to grow oxide ferroelectric heterostructures has recently intensified.<sup>33,34</sup> Here we describe the growth of  $\text{PbTiO}_3$  and  $\text{Bi}_4\text{Ti}_3\text{O}_{12}$  by MBE. A more detailed description is given elsewhere.<sup>35</sup>

$\text{PbTiO}_3$  has the largest remanent polarization ( $75 \mu\text{C}/\text{cm}^2$ ) of any known ferroelectric.<sup>36,37</sup>  $\text{Bi}_4\text{Ti}_3\text{O}_{12}$  has lower remanent polarization ( $\sim 50 \mu\text{C}/\text{cm}^2$  of which the component along the  $c$ -axis is  $\sim 4 \mu\text{C}/\text{cm}^2$ ),<sup>38</sup> but can withstand far more polarization reversals before it fatigues.<sup>39</sup>  $\text{PbTiO}_3$  and  $\text{Bi}_4\text{Ti}_3\text{O}_{12}$  are both members of the  $(\text{Bi},\text{Pb})_{n+1}\text{Ti}_n\text{O}_{3n+3}$  Aurivillius homologous series<sup>40-44</sup> shown in Fig. 8.  $\text{PbTiO}_3$  is the  $n = \infty$  member of this series and contains a network of  $\text{TiO}_6$  octahedra connected in three dimensions.  $\text{Bi}_4\text{Ti}_3\text{O}_{12}$  lies at the other end of this homologous series,  $n = 3$ , and is highly layered with a two-dimensionally connected network of  $\text{TiO}_6$  octahedra. Its structure consists of  $\text{Bi}_2\text{O}_2$  layers separated by  $\text{Bi}_2\text{Ti}_3\text{O}_{10}$  perovskite sheets. The resistance to fatigue of  $\text{Bi}_4\text{Ti}_3\text{O}_{12}$  and other Aurivillius phases make these materials of interest for use in non-volatile ferroelectric random access memories (FRAMs).<sup>45</sup> On the other hand, the high  $P_r$  of  $\text{PbTiO}_3$  makes it of interest for superconducting field-effect transistors (SuFETs).<sup>46</sup> We are interested in the variation of properties that occur in the  $(\text{Bi},\text{Pb})_{n+1}\text{Ti}_n\text{O}_{3n+3}$  homologous series and describe below the preparation of the two end members of this series by adsorption-controlled MBE.

# Aurivillius Homologous Series

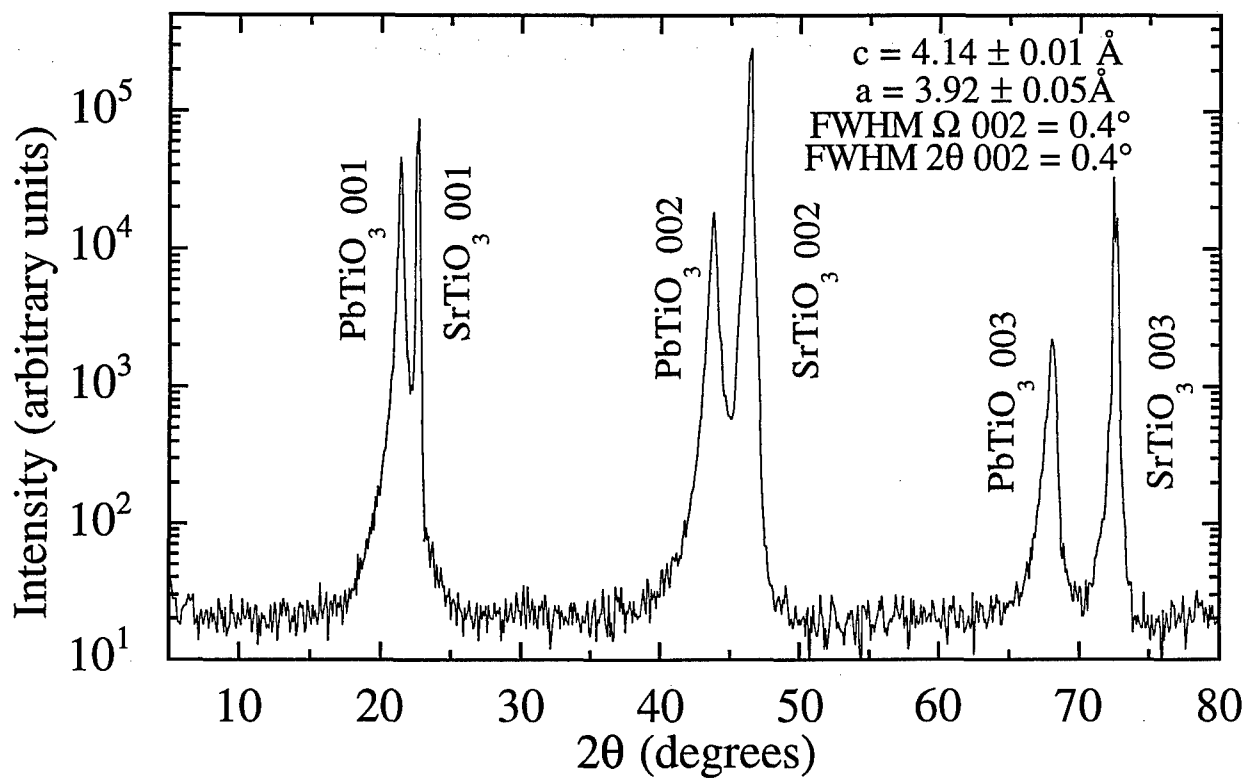
$$(Bi,Pb)_{n+1}Ti_nO_{3n+3}$$


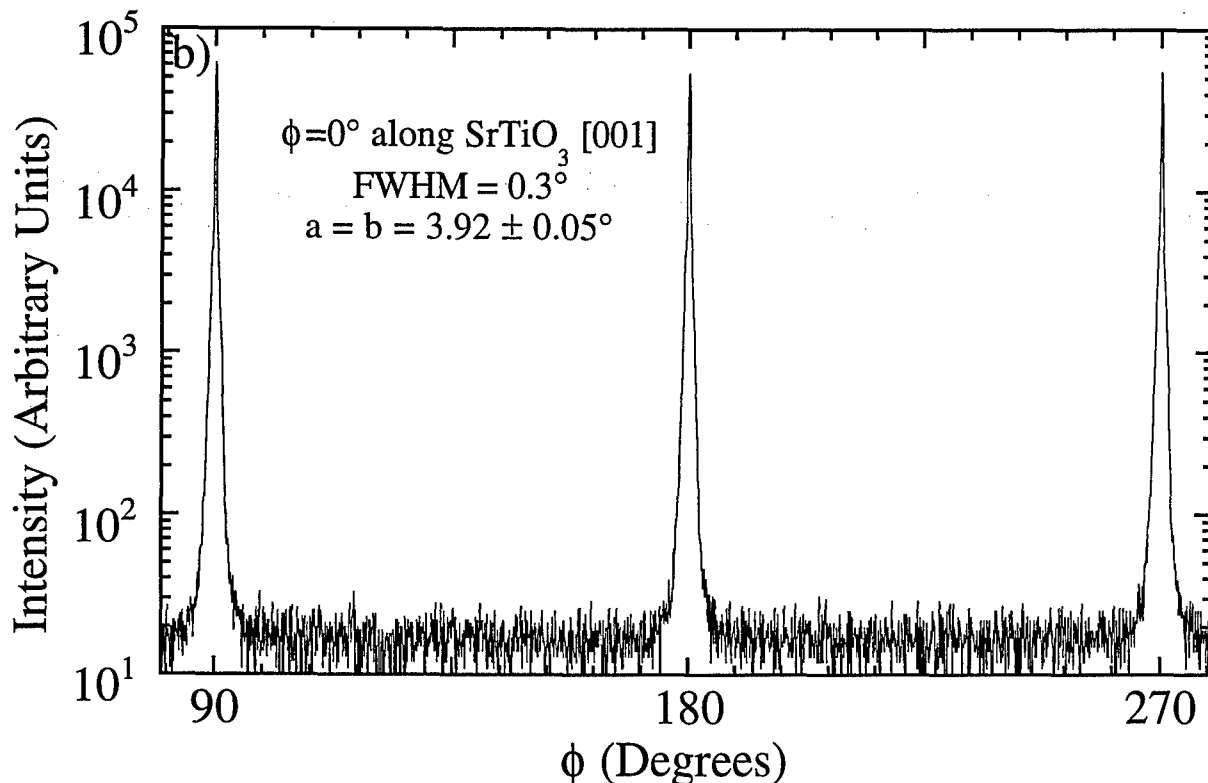
**Fig. 8.** The Aurivillius phases:  $n = 3$   $Bi_4Ti_3O_{12}$ ,  $n = 4$   $PbBi_4Ti_4O_{15}$ ,  $n = 5$   $Pb_2Bi_4Ti_5O_{18}$ ,  $n = 6$   $Pb_3Bi_4Ti_6O_{21}$ , and  $n = \infty$   $PbTiO_3$ .

$PbTiO_3$  and  $Bi_4Ti_3O_{12}$  are both grown under conditions where the titanium flux determines the growth rate, and ozone, lead, and bismuth are supplied in excess (2-100 times greater than the titanium flux). The excess ozone, lead, and bismuth desorb leading to the growth of  $PbTiO_3$  and  $Bi_4Ti_3O_{12}$  films that are stoichiometric within the measurement error of Rutherford backscattering spectrometry (RBS). A similar adsorption-controlled mechanism was shown to be operative by de Keijser and Dormans<sup>47</sup> for organometallic chemical vapor deposited  $Pb(Zr,Ti)O_3$  thin films. The growth of  $PbTiO_3$  and  $Bi_4Ti_3O_{12}$  by reactive MBE is thus quite similar to the MBE growth of III-V semiconductors where the group V species is supplied in overabundance and the group III species determines the growth rate.

4-circle x-ray diffraction scans indicate that these ferroelectric films are epitaxial and have bulk lattice constants. In Fig. 9 the  $\theta$ - $2\theta$  and  $\phi$ -scans of a 1000 Å thick film of  $PbTiO_3$  grown on (100)  $SrTiO_3$  are shown. Intense  $00\ell$  peaks indicate that the  $c$ -axis of the film is oriented perpendicular to the substrate ( $c$ -axis oriented); additional scans showed no evidence of  $a$ -axis

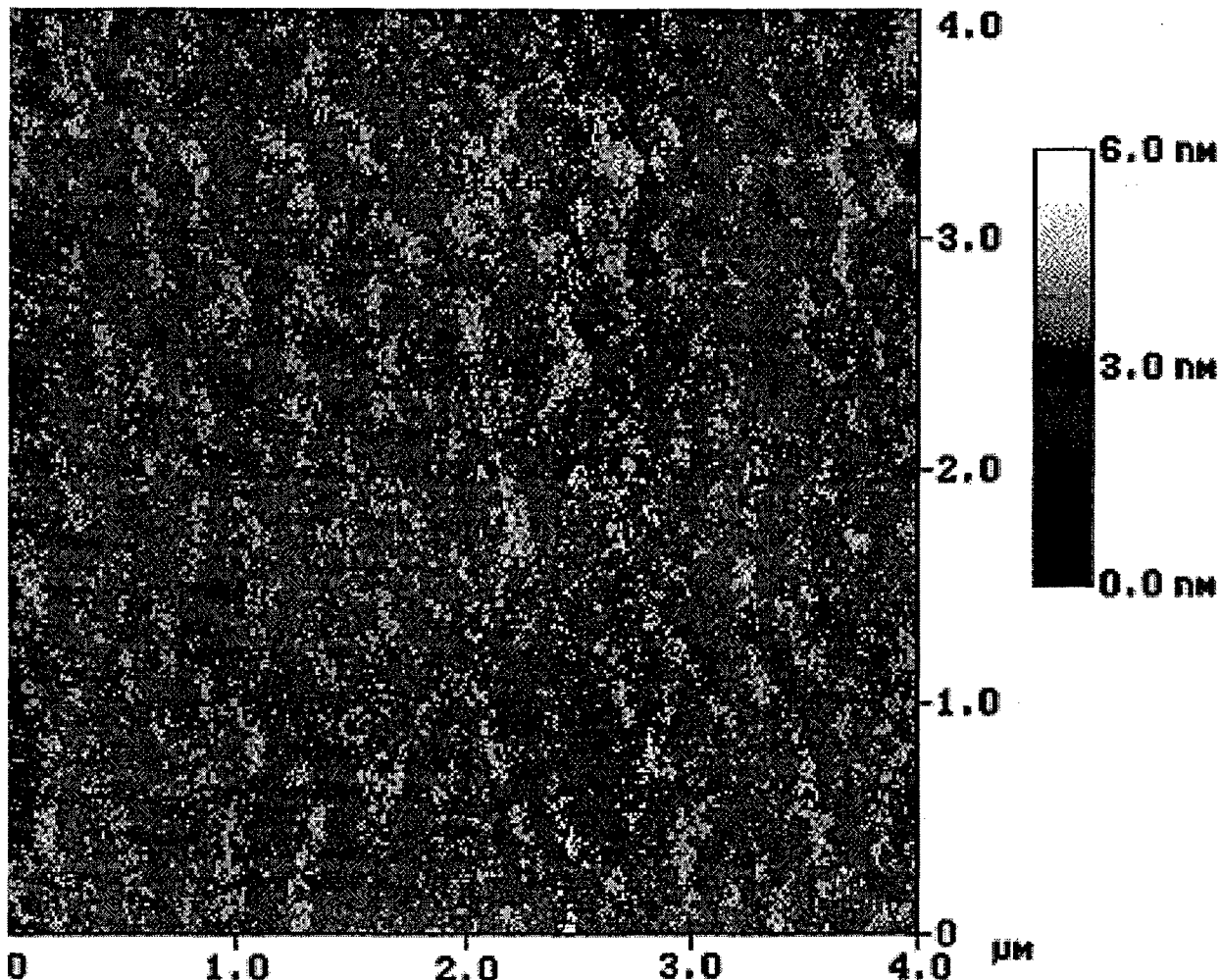
oriented domains. The  $\phi$ -scan demonstrates that the film is also oriented in the plane of the substrate, with a cube-on-cube epitaxial orientation relationship. The widths of the x-ray diffraction peaks are all approaching the instrumental resolution of our diffractometer.





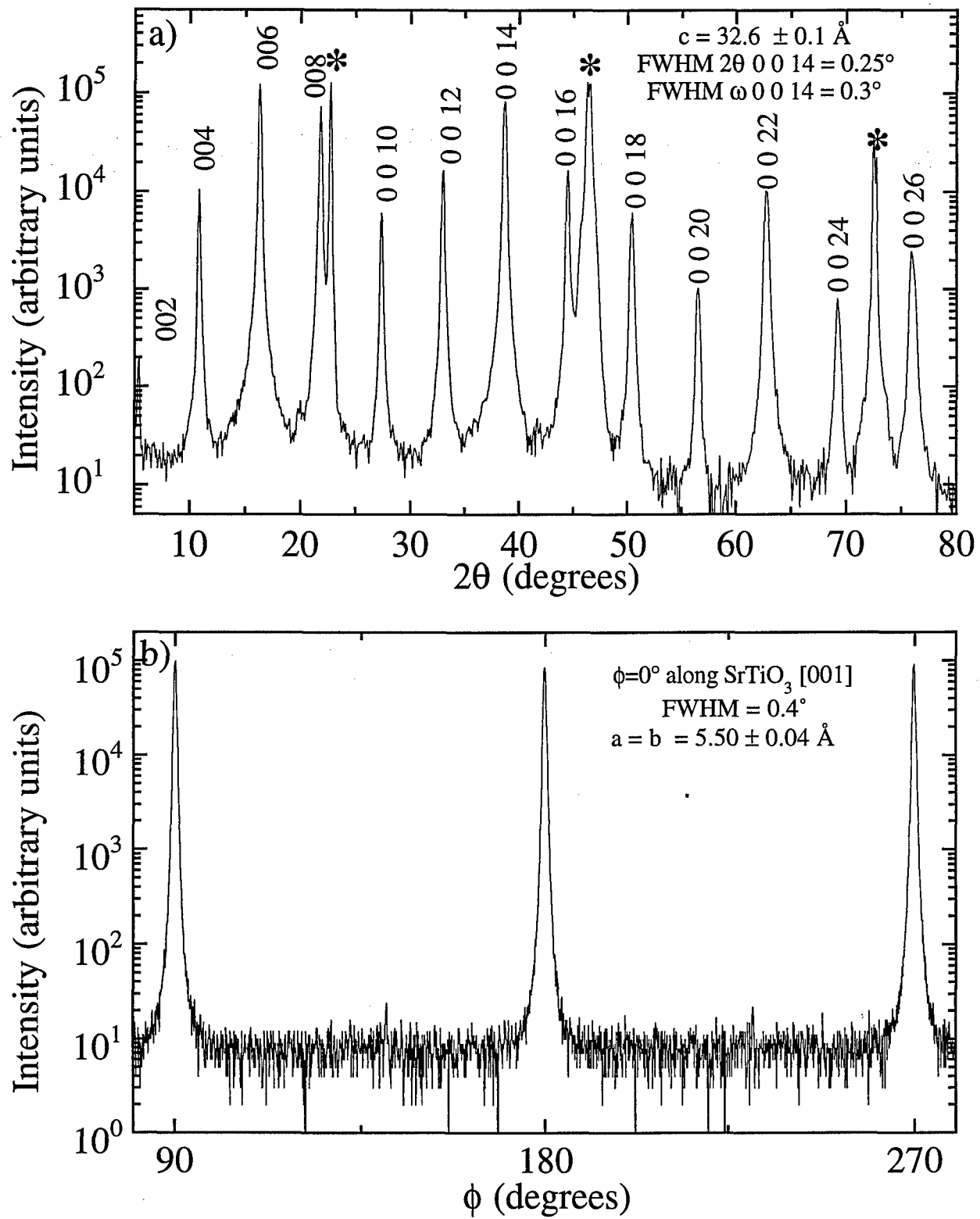
**Fig. 9.** (a)  $\theta$ - $2\theta$  scan and (b)  $\phi$ -scan of 101 reflections of a 1000 Å thick  $\text{PbTiO}_3$  film grown on a (100)  $\text{SrTiO}_3$  substrate (\* indicates substrate reflections).

Atomic force microscopy (AFM) images of the surface of this same  $\text{PbTiO}_3$  film, Fig. 10, show extremely smooth morphologies with a root mean square (RMS) roughness of < 5 Å. This surface structure is indicative of a layer-by-layer growth mechanism.



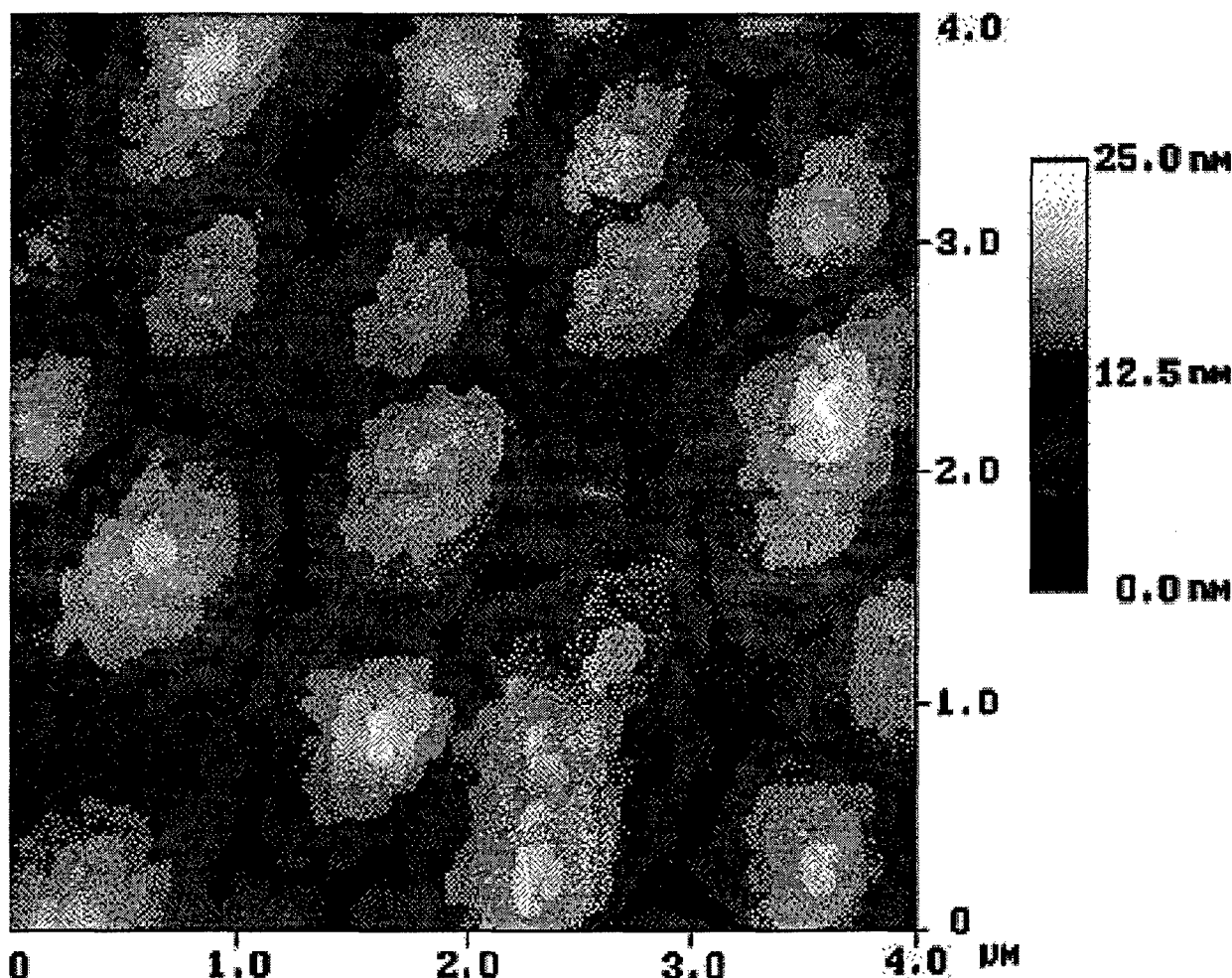
**Fig. 10.** AFM image of the surface of a 1000 Å thick  $\text{PbTiO}_3$  film grown on (100)  $\text{SrTiO}_3$ .

The  $\theta$ - $2\theta$  and  $\phi$ -scans of a 1000 Å thick film of  $\text{Bi}_4\text{Ti}_3\text{O}_{12}$  grown on (100)  $\text{SrTiO}_3$  are shown in Fig. 11. The intense  $00\ell$  peaks indicate that the film is entirely *c*-axis oriented. The  $\phi$ -scan demonstrates that the film is also oriented in the plane of the substrate, with a  $\text{Bi}_4\text{Ti}_3\text{O}_{12}$  [110] //  $\text{SrTiO}_3$  [010] orientation relationship. Again the peak widths are all comparable to the instrument resolution of our Picker 4-circle diffractometer. RBS channeling results for this film showed a minimum channeling yield ( $\chi_{\min}$ ) of 0.2, which is the lowest reported value for epitaxial  $\text{Bi}_4\text{Ti}_3\text{O}_{12}$ . Polarization-electric field hysteresis measurements indicate that these MBE-grown  $\text{Bi}_4\text{Ti}_3\text{O}_{12}$  films have a remanent polarization of about  $3 \mu\text{C}/\text{cm}^2$  along the *c*-axis, which again is the highest value reported in thin films and nearly equal to the value measured for bulk single crystals.<sup>35</sup>



**Fig. 11.** (a)  $\theta$ - $2\theta$  scan and (b)  $\phi$ -scan of 117 reflections of a  $1000 \text{ \AA}$  thick  $\text{Bi}_4\text{Ti}_3\text{O}_{12}$  film grown on a (100)  $\text{SrTiO}_3$  substrate (\* indicates substrate reflections).

In Fig. 12 an AFM image of the surface of this same  $\text{Bi}_4\text{Ti}_3\text{O}_{12}$  film is shown. Clearly visible on the surface are micron-sized islands that protrude  $\sim 100 - 200 \text{ \AA}$  above the film surface. The terraces making up these islands have step heights that are integral multiples of a half unit cell.<sup>†</sup> This surface morphology is reminiscent of that of layered perovskite superconductor films,<sup>48,49</sup> although it is unclear if oppositely-signed screw dislocations are present within each mound or if the mounds are free of screw dislocations and arise due to limited surface diffusion.



**Fig. 12.** AFM image of the surface of a  $1000 \text{ \AA}$  thick  $\text{Bi}_4\text{Ti}_3\text{O}_{12}$  film grown on (100)  $\text{SrTiO}_3$ .

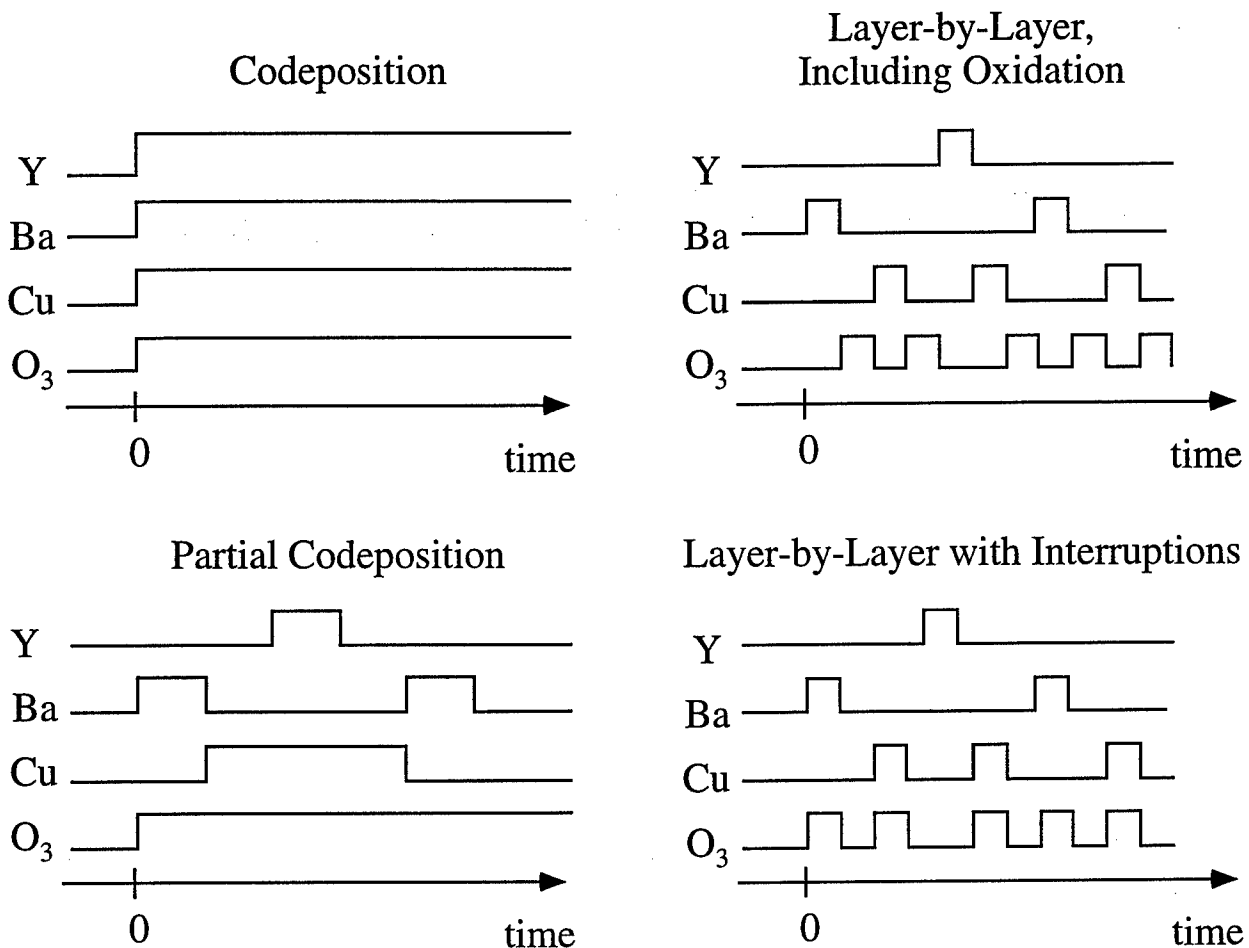
## CHALLENGES

There are three major challenges that must be overcome before reactive MBE is a useful technique for the growth of oxide heterostructures: (1) achieving sufficient oxidation of the growing film without compromising the long mean free path necessary for MBE, (2) achieving accurate composition control during growth, and (3) maintaining flat surfaces during growth. The

<sup>†</sup> A  $\text{Bi}_4\text{Ti}_3\text{O}_{12}$  formula unit is contained within each half unit cell as can be seen from Fig. 8.

pressure of oxidant needed to achieve sufficient oxidation depends on the phase being grown as well as the oxidant and growth temperature used. If the oxidant is restricted to molecular oxygen, the growth of most oxide superconductors would not be possible by MBE. The use of more reactive oxidants, e.g., ozone,  $\text{NO}_2$ , or the reactive species in an oxygen plasma, have been key to the realization of oxide superconductor films by MBE.<sup>2</sup> Composition control is also crucial; the inherent flexibility of the MBE technique is only advantageous when it is accompanied by adequate composition control. Without it, the user will be unable to control the formation of the desired custom-made structures and controllably dope them. For the growth of heterostructures containing oxide superconductors, composition control at or better than about  $\pm 1$  atomic percent is necessary to produce films with good transport properties.<sup>50,51</sup> Controlling each monolayer with 1% accuracy requires a resolution in whatever composition monitoring method is used of about  $7 \times 10^{12}$  atoms or about one nanogram for a typical perovskite (e.g., those oxides in Table I). For many elements AA has such sensitivity and has thus become the composition control method of choice for many oxide MBE groups. Finally, even if the growth environment provides sufficient oxidation and sufficient composition control, it is almost always desired to have flat interfaces in oxide heterostructures. To this end it is clearly important to begin with a flat and relatively defect-free substrate. Oxide substrate preparation for MBE growth is an important area of research.<sup>52,53</sup> *In situ* monitoring techniques like RHEED and spectroscopic ellipsometry can be quite helpful in monitoring surface roughness *in situ* and optimizing growth conditions so that flat surfaces are maintained during growth.<sup>54</sup>

Once these three major challenges are met, MBE offers an incredibly flexible growth environment with independent control of a large parameter space. For example, the deposition rate of each constituent, the order in which the constituent fluxes (including the oxidant) are sequentially or simultaneously supplied to the growth surface, the duration of dosing, the introduction of periodic growth interruptions, and the substrate temperature are all independently controllable in the MBE process. A timing diagram of a few significantly different ways in which  $\text{YBa}_2\text{Cu}_3\text{O}_{7-\delta}$  films could be deposited is shown in Fig. 13.



**Fig. 13.** A few examples of shutter timing diagrams for the growth of  $\text{YBa}_2\text{Cu}_3\text{O}_{7-\delta}$  by MBE.

However, this tremendous inherent flexibility of the MBE technique brings up a crucial challenge. *What is the best way of navigating this large parameter space to achieve the desired oxide heterostructure?* The improvements that oxide MBE can offer in our ability to customize the structure of oxides on an atomic-level challenges would be greatly enhanced if we had a better microscopic understanding of how oxides grow, e.g., what the diffusing species are and their rates as a function of oxidant pressure and temperature, how nucleation occurs on different substrates, which layer bonds to the substrate, which layer terminates the growing surface, surface reconstructions, the influence of vicinal substrates on growth, etc. With such knowledge, reactive MBE could be used to intelligently navigate this large parameter space to produce the desired phase or heterostructure in short order.

## CONCLUSIONS

The use of reactive MBE for the growth of oxide heterostructures is still in its infancy and many hurdles, in particular accurate composition control, remain to be overcome for this technique

to develop greater structural and doping control at the atomic layer level, as well as reproducibility. Nonetheless, reactive MBE has become established as the premiere synthesis technique for epitaxial oxide heterostructures when customized layering control is needed. As the complexity and metastability of desired oxide heterostructures increases, the requirement for a controlled synthesis environment capable of atomic layer engineering of new materials and device heterostructures will become all the more important. MBE appears to be the most likely technique to meet this challenge.

#### **ACKNOWLEDGMENTS**

We gratefully acknowledge fruitful interactions with G.W. Brown, B.J. Gibbons, C.J. Kraisinger, S. Trolier-McKinstry, and J. Yeh, and the financial support of the Office of Naval Research (ONR) through grants N00014-93-1-0512, N00014-94-1-0690, and N00014-94-1-0815.

## REFERENCES

- <sup>1</sup> R.D. Shannon, "Revised Effective Ionic Radii and Systematic Studies of Interatomic Distances in Halides and Chalcogenides," *Acta Cryst. A* **32** (1976) 751-767.
- <sup>2</sup> D.G. Schlom and J.S. Harris, Jr., "MBE Growth of High  $T_c$  Superconductors," in: *Molecular Beam Epitaxy: Applications to Key Materials*, edited by R.F.C. Farrow (Noyes, Park Ridge, 1995), pp. 505-622.
- <sup>3</sup> C.P. Flynn, "Strain-Assisted Epitaxial Growth of New Ordered Compounds," *Phys. Rev. Lett.* **57** (1986) 599-602.
- <sup>4</sup> See for example, *Molecular Beam Epitaxy: Applications to Key Materials*, edited by R.F.C. Farrow (Noyes, Park Ridge, 1995).
- <sup>5</sup> M.H. Yang and C.P. Flynn, "Growth of Alkali Halides from Molecular Beams: Global Growth Characteristics," *Phys. Rev. Lett.* **62** (1989) 2476-2479.
- <sup>6</sup> Y. Tokura and T. Arima, "New Classification Method for Layered Copper Oxide Compounds and Its Application to Design of New High  $T_c$  Superconductors," *Jpn. J. Appl. Phys.* **29** (1990) 2388-2402.
- <sup>7</sup> J.M. Tarascon, W.R. McKinnon, P. Barboux, D.M. Hwang, B.G. Bagley, L.H. Greene, G.W. Hull, Y. LePage, N. Stoffel, and M. Giroud, "Preparation, Structure, and Properties of the Superconducting Compound Series  $\text{Bi}_2\text{Sr}_2\text{Ca}_{n-1}\text{Cu}_n\text{O}_y$  with  $n = 1, 2$ , and 3," *Phys. Rev. B* **38** (1988) 8885-8892.
- <sup>8</sup> O. Eibl, "Crystal Defects in  $\text{Bi}_2\text{Sr}_2\text{Ca}_{n-1}\text{Cu}_n\text{O}_{4+2n+\delta}$  Ceramics," *Physica C* **168** (1990) 249-256.
- <sup>9</sup> See for example, B. Raveau, C. Michel, and M. Hervieu, "Crystal Chemistry of Superconductive Bismuth and Thallium Cuprates," in: *Advances in Superconductivity: Proceedings of the 1st International Symposium on Superconductivity (ISS '88)*, (K. Kitazawa and T. Ishiguro, eds.) pp. 151-157, Springer-Verlag, Tokyo (1989). In this work TEM analysis of samples produced by bulk synthesis methods yielding a majority of the  $n = 4$   $\text{Tl}_2\text{Ba}_2\text{Ca}_{n-1}\text{Cu}_n\text{O}_{2n+4}$  phase revealed numerous intergrowths up to  $n = 7$ .
- <sup>10</sup> M.A. Señaris-Rodríguez, A.M. Chippindale, A. Várez, E. Morán, and M.A. Alario-Franco, "A Novel '126' Phase of the Family of  $\text{Y}_2\text{Ba}_4\text{Cu}_{6+n}\text{O}_{14+n}$  High-Temperature Superconducting Materials," *Physica C* **172** (1991) 477-480.
- <sup>11</sup> R.J. Cava, T. Siegrist, B. Hessen, J.J. Krajewski, W.F. Peck, Jr., B. Batlogg, H. Takagi, J.V. Waszczak, L.F. Schneemeyer, and H.W. Zandbergen, "A New Homologous Series of Lanthanum Copper Oxides," *J. Solid State Chem.* **94** (1991) 170-184.
- <sup>12</sup> W.T. Fu, H.W. Zandbergen, Q. Xu, J.M. van Ruitenbeek, L.J. de Jongh, and G. van Tendeloo, "Structural and Transport Properties of the Triple-Layer Compounds  $\text{Ba}_4(\text{Pb}_{1-x}\text{Bi}_x)_3\text{O}_{10}$  ( $0 \leq x < 0.3$ )," *Solid State Comm.* **70** (1989) 1117-1121.

- 
- <sup>13</sup> B.G. Hyde and S. Andersson, *Inorganic Crystal Structures*, Wiley-Interscience, New York (1989).
- <sup>14</sup> M. Laguës, X.M. Xie, H. Tebbji, X.Z. Xu, V. Mairet, C. Hatterer, C.F. Beuran, and C. Deville-Cavellin, "Evidence Suggesting Superconductivity at 250 K in a Sequentially Deposited Cuprate Film," *Science* **262** (1993) 1850-1852.
- <sup>15</sup> I. Bozovic, J.N. Eckstein, and G.F. Virshup, "Superconducting Oxide Multilayers and Superlattices: Physics, Chemistry, and Nanoengineering," *Physica C* **235-240** (1994) 178-181.
- <sup>16</sup> K.R. Udayakumar and A.N. Cormack, "Structural Aspects of Phase Equilibria in the Strontium-Titanium-Oxygen System," *J. Am. Ceram. Soc.* **71** (1988) C-469 - C-471; K.R. Udayakumar and A.N. Cormack, "Non-Stoichiometry in Alkaline Earth Excess Alkaline Earth Titanates," *J. Phys. Chem. Solids* **50** (1989) 55-60.
- <sup>17</sup> R.J.D. Tilley, "An Electron Microscope Study of Perovskite-Related Oxides in the Sr-Ti-O System," *J. Solid State Chem.* **21** (1977) 293-301.
- <sup>18</sup> EPI 930. EPI, Chorus Corporation, St. Paul, MN.
- <sup>19</sup> C.D. Theis and D.G. Schlom, "Cheap and Stable Titanium Source for Use in Oxide Molecular Beam Epitaxy Systems," *J. Vac. Sci. Technol. A* **14** (1996) 2677-2679.
- <sup>20</sup> M.E. Klausmeier-Brown, J.N. Eckstein, I. Bozovic, and G.F. Virshup, "Accurate Measurement of Atomic Beam Flux by Pseudo-Double-Beam Atomic Absorption Spectroscopy for Growth of Thin-Film Oxide Superconductors," *Appl. Phys. Lett.* **60** (1992) 657-659.
- <sup>21</sup> ATOMICAS. Intelligent Sensor Technology, Mountain View, CA.
- <sup>22</sup> MicroCrystal. WeckTech Systems, Pleasanton, CA.
- <sup>23</sup> D.G. Schlom, A.F. Marshall, J.S. Harris, Jr., I. Bozovic, and J.N. Eckstein, "Growth of Metastable Phases and Superlattice Structures of Bi-Sr-Ca-Cu-O Compounds by an Atomic Layering MBE Technique," in: *Advances in Superconductivity III: Proceedings of the 3rd International Symposium on Superconductivity (ISS '90)*, edited by K. Kajimura and H. Hayakawa (Springer-Verlag, Tokyo, 1991), pp. 1011-1016.
- <sup>24</sup> D.G. Schlom, J.N. Eckstein, I. Bozovic, Z.J. Chen, A.F. Marshall, K.E. von Dessonneck, and J.S. Harris, Jr., "Molecular beam epitaxy—a path to novel high  $T_c$  superconductors?," in: *Growth of Semiconductor Structures and High- $T_c$  Thin Films on Semiconductors*, SPIE Vol. 1285 (SPIE, Bellingham, 1990), pp. 234-247 and in: *High  $T_c$  Superconductivity: Thin Films and Applications*, SPIE Vol. 1287 (SPIE, Bellingham, 1990), pp. 152-165.
- <sup>25</sup> J.N. Eckstein, I. Bozovic, M.E. Klausmeier-Brown, G.F. Virshup, and K.S. Ralls, "Control of Composition and Microstructure in High-Temperature Superconductors at the Atomic Level by Molecular Beam Epitaxy," *MRS Bulletin* **17** (August 1992) 27-33.

- 
- <sup>26</sup> I. Bozovic, J.N. Eckstein, G.F. Virshup, A. Chaiken, M. Wall, R. Howell, and M. Fluss, "Atomic-Layer Engineering of Cuprate Superconductors," *J. Supercond.* **7** (1994) 187-195.
- <sup>27</sup> J.N. Eckstein, I. Bozovic, and G.F. Virshup, "Atomic Layer-by-Layer Engineering of High  $T_c$  Materials and Heterostructure Devices," *MRS Bulletin* **19** (September 1994) 44-50.
- <sup>28</sup> M.E. Klausmeier-Brown, G.F. Virshup, I. Bozovic, and J.N. Eckstein, "Engineering of Ultrathin Barriers in High  $T_c$ , Trilayer Josephson Junctions," *Appl. Phys. Lett.* **60** (1992) 2806-2808.
- <sup>29</sup> A. Brazdeikis, A. Vailionis, and A.S. Flodström, "Layer-by-Layer Growth of  $\text{Bi}_2\text{Sr}_2\text{Ca}_{n-1}\text{Cu}_n\text{O}_x$  Films with  $n \geq 3$  by Molecular Beam Epitaxy," *Physica C* **235-240** (1994) 711-712.
- <sup>30</sup> I. Bozovic and J.N. Eckstein, "Atomic-Level Engineering of Cuprates and Manganites," *Appl. Surf. Sci.* (1997) (in press).
- <sup>31</sup> R.A. Betts and C.W. Pitt, "Growth of Thin-Film Lithium Niobate by Molecular Beam Epitaxy," *Electron. Lett.* **21** (1985) 960-962.
- <sup>32</sup> M. Petrucci, C.W. Pitt, and P.J. Dobson, "RHEED Studies on  $z$ -Cut  $\text{LiNbO}_3$ ," *Electron. Lett.* **22** (1986) 954-956.
- <sup>33</sup> R.A. McKee, F.J. Walker, J.R. Conner, E.D. Specht, and D.E. Zelmon, "Molecular Beam Epitaxy Growth of Epitaxial Barium Silicide, Barium Oxide, and Barium Titanate on Silicon," *Appl. Phys. Lett.* **59** (1991) 782-784.
- <sup>34</sup> C.D. Theis and D.G. Schlom, "Epitaxial Lead Titanate Grown by MBE," to be published in *J. Cryst. Growth*.
- <sup>35</sup> C.D. Theis, J. Yeh, G.W. Brown, M.E. Hawley, and D.G. Schlom, in preparation.
- <sup>36</sup> Landolt-Börnstein: *Numerical Data and Functional Relationships in Science and Technology*, New Series, Group III, Vol. 28a, edited by T. Mitsui and E. Nakamura (Springer-Verlag, Berlin, 1990), p. 76.
- <sup>37</sup> E. C. Subbarao, "Ferroelectric and Antiferroelectric Materials," *Ferroelectrics* **5** (1973) 267-280.
- <sup>38</sup> Landolt-Börnstein: *Numerical Data and Functional Relationships in Science and Technology*, New Series, Group III, Vol. 16a, edited by K.-H. Hellwege and A.M. Hellwege (Springer-Verlag, Berlin, 1981), p. 237.
- <sup>39</sup> C. A-Paz de Araujo, J.D. Cuchiaro, L.D. McMillan, M.C. Scott, and J.F. Scott, "Fatigue-Free Ferroelectric Capacitors with Platinum Electrodes," *Nature* **374** (1995) 627-629.
- <sup>40</sup> B. Aurivillius, "Mixed Bismuth Oxides with Layer Lattices I. The Structure Type of  $\text{CaNb}_2\text{Bi}_2\text{O}_9$ ," *Arkiv Kemi* **1** (1949) 463-480.
- <sup>41</sup> B. Aurivillius, "Mixed Bismuth Oxides with Layer Lattices II. Structure of  $\text{Bi}_4\text{Ti}_3\text{O}_{12}$ ," *Arkiv Kemi* **1** (1949) 499-512.

- 
- <sup>42</sup> B. Aurivillius, "Mixed Oxides with Layer Lattices III. Structure of BaBi<sub>4</sub>Ti<sub>4</sub>O<sub>15</sub>," *Arkiv Kemi* **2** (1950) 519-527.
- <sup>43</sup> B. Aurivillius, "The Structure of Bi<sub>2</sub>NbO<sub>5</sub>F and Isomorphous Compounds," *Arkiv Kemi* **5** (1952) 39-47.
- <sup>44</sup> B. Aurivillius and P.H. Fang, "Ferroelectricity in the Compound Ba<sub>2</sub>Bi<sub>4</sub>Ti<sub>5</sub>O<sub>18</sub>," *Phys. Rev.* **126** (1962) 893-896.
- <sup>45</sup> C.A. Paz de Araujo, J.D. Cuchiaro, M.C. Scott, and L.D. McMillan, "Layered Superlattice Material Applications," International Patent, publication no. WO 93/12542.
- <sup>46</sup> J. Mannhart, "High- $T_c$  Transistors," *Supercond. Sci. Technol.* **9** (1996) 49-67.
- <sup>47</sup> M. de Keijser and G.J.M. Dormans, "Chemical Vapor Deposition of Electroceramic Thin Films," *MRS Bulletin*, **21** (June, 1996) 37-43.
- <sup>48</sup> C. Gerber, D. Anselmetti, J.G. Bednorz, J. Mannhart, and D.G. Schlom, "Screw Dislocations in High- $T_c$  Films," *Nature* **350** (1991) 279-280.
- <sup>49</sup> M. Hawley, I. D. Raistrick, J. G. Beery, and R. J. Houlton, "Growth Mechanism of Sputtered Films of YBa<sub>2</sub>Cu<sub>3</sub>O<sub>7</sub> Studied by Scanning Tunneling Microscopy," *Science* **251** (1991) 1587-1589.
- <sup>50</sup> N.G. Chew, S.W. Goodyear, J.A. Edwards, J.S. Satchell, S.E. Blenkinsop, and R.G. Humphreys, "Effect of Small Changes in Composition on the Electrical and Structural Properties of YBa<sub>2</sub>Cu<sub>3</sub>O<sub>7</sub> Thin Films," *Appl. Phys. Lett.* **57** (1990) 2016-2018.
- <sup>51</sup> D.J. Carlson, M.P. Siegal, J.M. Phillips, T.H. Tiefel, and J.H. Marshall, "Stoichiometric Effects in Epitaxial Ba<sub>2-x</sub>Y<sub>1-y</sub>Cu<sub>3-z</sub>O<sub>7-δ</sub> Thin Films on LaAlO<sub>3</sub>(100)," *J. Mater. Res.* **5** (1990) 2797-2801.
- <sup>52</sup> M. Kawasaki, K. Takahashi, T. Maeda, R. Tsuchiya, M. Shinohara, O. Ishiyama, T. Yonezawa, M. Yoshimoto, and H. Koinuma, "Atomic Control of the SrTiO<sub>3</sub> Crystal Surface," *Science* **266**, (1994) 1540-1542.
- <sup>53</sup> M. Yoshimoto, T. Maeda, T. Ohnishi, H. Koinuma, O. Ishiyama, M. Shinohara, M. Kubo, R. Miura, and A. Miyamoto, "Atomic-Scale Formation of Ultrasmooth Surfaces on Sapphire Substrates for High-Quality Thin-Film Formation," *Appl. Phys. Lett.* **67** (1995) 2615-2617.
- <sup>54</sup> I. Bozovic and J.N. Eckstein, "Analysis of Growing Films of Complex Oxides by RHEED," *MRS Bulletin* **20** (May 1995) 32-38.

## Adsorption-Controlled Growth of $\text{Bi}_4\text{Ti}_3\text{O}_{12}$ by Reactive Molecular Beam Epitaxy

C. D. Theis, J. Yeh, and D. G. Schlom

*Department of Materials Science and Engineering, The Pennsylvania State University,  
University Park, PA 16802-5005*

M. E. Hawley and G. W. Brown

*Center for Materials Science, Los Alamos National Laboratory, Los Alamos, NM 87545*

(Received

### Abstract

Adsorption-controlled conditions have been identified and utilized to grow epitaxial bismuth titanate thin films by reactive molecular beam epitaxy (MBE). Growth of stoichiometric, phase pure, *c*-axis oriented, epitaxial films is achieved by supplying a large overabundance of bismuth and ozone continuously to the surface of the depositing film. Titanium is supplied to the film in the form of shuttered bursts each containing a three monolayer dose of titanium to grow one formula unit of  $\text{Bi}_4\text{Ti}_3\text{O}_{12}$ . It is seen from measured film thickness, Rutherford backscattering spectrometry (RBS) composition measurements, monitoring of reflection high-energy electron diffraction (RHEED) half-order intensity oscillations during growth, and *in situ* flux measurements using atomic absorption spectroscopy (AA) that at suitable temperature and ozone background pressure, the titanium sticking coefficient approaches one and the excess bismuth desorbs from the surface. Film growth proceeds by the formation of mounds whose step heights are predominantly integral multiples of a half-unit-cell.

$\text{Bi}_4\text{Ti}_3\text{O}_{12}$  is the  $n = 3$  member of the Aurivillius homologous series  $(\text{Bi}_2\text{O}_2)(\text{A}_{n-1}\text{B}_n\text{O}_{3n+1})$ .<sup>1</sup>

The structure consists of  $\text{Bi}_2\text{O}_2$  layers separated by  $\text{Bi}_2\text{Ti}_3\text{O}_{10}$  perovskite sheets. It is pseudo-orthorhombic<sup>2</sup> at room temperature with lattice constants  $a = 5.41$ ,  $b = 5.45$ , and  $c = 32.83 \text{ \AA}$ .<sup>3</sup> It is attractive as a ferroelectric material for use in non-volatile memories because of its demonstrated fatigue resistance.<sup>4</sup> Additionally, its highly layered perovskite structure makes it ideally suited for study using the atomic scale layering capabilities of molecular beam epitaxy (MBE). Epitaxial  $\text{Bi}_4\text{Ti}_3\text{O}_{12}$  has been successfully grown on various substrates by sputtering,<sup>5</sup> laser ablation,<sup>6</sup> and by laser-MBE.<sup>7</sup> It is often difficult, however, to control film stoichiometry because of the volatility of bismuth during film growth in high temperature, low pressure environments. Even by enriching targets with excess bismuth to counteract such losses, it is still difficult to achieve reproducibility from film to film because of the sensitivity of film composition to deposition parameters. We have used adsorption-controlled growth conditions to *accurately and reproducibly* grow stoichiometric films.

The EPI 930 MBE system<sup>8</sup> used for this study is described in detail elsewhere.<sup>9</sup> Bismuth is continuously supplied to the surface of the depositing film from a low-temperature effusion cell. Titanium is sublimated onto the film from a titanium sublimation pump. The Ti-Ball<sup>TM,10</sup> is powered by a low-noise DC power supply. The resulting titanium flux has a maximum peak-to-peak variation of  $\pm 2.5\%$  over 5 hours<sup>11</sup> (about five times longer than the time needed to grow a  $1000 \text{ \AA}$  thick  $\text{Bi}_4\text{Ti}_3\text{O}_{12}$  film). The fluxes of all depositing species are monitored simultaneously *in situ* using atomic absorption spectroscopy (AA).<sup>12</sup> Oxygen is supplied to the film in the form of ~80% pure distilled ozone.<sup>13</sup> Film growth is monitored continuously using reflection high-energy electron diffraction (RHEED). The substrate holder-block temperature is measured using an optical pyrometer. (001)  $\text{LaAlO}_3$ <sup>14</sup> and (001)  $\text{SrTiO}_3$  substrates are attached to wafer holders using silver paint. The  $\text{SrTiO}_3$  wafers are etched with a buffered-HF solution prior to growth<sup>15</sup> exposing the  $\text{TiO}_2$ -terminated surface.

During growth, bismuth and ozone are supplied to the surface of the film continuously while the substrate temperature is maintained at  $600 - 645 \text{ }^\circ\text{C}$ . The ozone background pressure

used during growth is  $2 \times 10^{-5}$  Torr, which represents an incident flux of ozone hundreds of times greater than the flux incorporated into the growing film. Similarly, bismuth is supplied at an incident flux 2 to 5 times greater than the average titanium incident flux. Titanium is supplied in shuttered doses each containing three monolayers of titania which make up the  $\text{Bi}_2\text{Ti}_3\text{O}_{10}$  perovskite sheets. Adsorption-controlled growth is achieved under these conditions. At slightly higher temperatures (665 °C) the film quality degrades as evidenced by broadened diffraction peak widths and degraded intensities in RHEED and 4-circle x-ray diffraction, presumably due to bismuth deficiency. At still higher temperatures (685 °C) the films contain only phase-pure anatase ( $\text{TiO}_2$ ).

Using the growth conditions described above it is possible to use a range of bismuth incident fluxes and substrate temperatures and still obtain phase-pure material. Results obtained from film thickness calculated from x-ray diffraction peak widths and thickness fringes of ultrathin films, Rutherford backscattering spectrometry (RBS) composition measurements, counting RHEED half-order intensity oscillations during growth, and *in situ* flux measurements using a quartz crystal thickness monitor and AA spectroscopy all indicate that the incident titanium flux determines the growth rate of the films. The excess bismuth and oxygen desorb from the surface. A similar adsorption-controlled growth mechanism was shown to be operative by de Keijser and Dormans<sup>16</sup> for  $\text{Pb}(\text{Zr},\text{Ti})\text{O}_3$  thin films grown by organometallic chemical vapor deposition (OMCVD). They found that by using a range of lead precursor partial pressures, it was possible to obtain stoichiometric films.<sup>16</sup>

Adsorption-controlled growth was first successfully utilized for the MBE synthesis of epitaxial GaAs thin films nearly 30 years ago.<sup>17</sup> Since that time, significant research efforts have been directed at understanding and quantifying the physical mechanisms involved during the growth process such as physisorption, surface migration, chemisorption, and surface evaporation.<sup>18</sup> This growth mechanism relies on the volatility of the group V component. In the case of GaAs, the equilibrium vapor pressure of gaseous  $\text{As}_{4,(g)}$  over pure, solid  $\text{As}_{(s)}$  is about ten orders of magnitude higher than the equilibrium vapor pressure of gaseous  $\text{As}_{2,(g)}$  over a gallium-

rich GaAs surface at 600 °C.<sup>19</sup> As a result, stoichiometric films are easily grown by supplying an excess of arsenic to the surface of the depositing film.

For the case of bismuth titanate, thermodynamic data are unavailable, but we have demonstrated the ability to synthesize stoichiometric films under adsorption-controlled conditions. At the incident bismuth flux and growth temperatures employed, elemental bismuth will not condense on the substrate surface<sup>20</sup> and must first be oxidized. Although  $\text{Bi}_2\text{O}_{3,(s)}$  does not evaporate congruently, the primary oxide species present in the vapor phase under growth conditions that we typically employ are  $\text{BiO}$ ,  $\text{Bi}_4\text{O}_6$ , and  $\text{Bi}_2\text{O}_3$ .<sup>21</sup> It is the volatility of these oxides that must be considered to take the place of the group V molecules during adsorption-controlled growth. Our achievement of adsorption-controlled growth indicates that the equilibrium vapor pressure of these bismuth oxide complexes over pure  $\text{Bi}_2\text{O}_{3,(s)}$  is much higher than over a pure, titania-rich  $\text{Bi}_4\text{Ti}_3\text{O}_{12,(s)}$  surface.

As described below, we find numerous similarities in the temporal evolution of the RHEED patterns between the MBE growth of III-V and II-VI compounds and perovskite oxides containing a volatile oxide species. Additionally, for the growth of  $\text{Bi}_4\text{Ti}_3\text{O}_{12}$  we have utilized changes in the surface symmetry as a means of controlling shutters during growth.

Prior to the initiation of growth, the continuous exposure of ozone and bismuth on the substrate surface is established. This aids in the cleaning of the substrate surface.<sup>20</sup> No change in the RHEED pattern is observed until the titanium flux is initiated. Even if the substrate is not exposed to a bismuth flux prior to the initiation of the titanium flux, the same evolution of the RHEED pattern described below is observed.

Figure 1(a) shows the RHEED pattern of the bare etched  $\text{SrTiO}_3$  substrate at ~ 640 °C during exposure to  $2 \times 10^{-5}$  Torr of ozone. Figure 1(b)-1(f) shows the evolution of the RHEED pattern during the deposition of one half-unit-cell of  $\text{Bi}_4\text{Ti}_3\text{O}_{12}$  oriented with its *c*-axis normal to the substrate surface (*c*-axis oriented). The half-order streaks present along the substrate [110] azimuth (Fig. 1(b)) are due to the epitaxial relationship between the cubic substrate and orthorhombic film where  $\text{Bi}_4\text{Ti}_3\text{O}_{12}$  [100] ||  $\text{SrTiO}_3$  [110]. With each opening of the titanium

shutter, the half-order streaks disappear after a period of time that corresponds to the deposition of 1.5 monolayers of titania as shown in Fig. 1(c). After the deposition of 3 monolayers of titania, the half order streaks again reappear as shown in Fig. 1(d). The disappearance of the half-order streaks halfway through the titanium burst of each formula unit could be due to the reduced distortion of the centermost layer of  $\text{TiO}_6$  octahedra in the  $\text{Bi}_4\text{Ti}_3\text{O}_{12}$  crystal structure. The octahedra in this central layer, unlike those on either side of the  $\text{Bi}_2\text{O}_2$  layers, are not rotated about the  $c$ -axis of  $\text{Bi}_4\text{Ti}_3\text{O}_{12}$ .<sup>2,22</sup> The square surface mesh of the central  $\text{TiO}_6$  layer has a perovskite lattice spacing ( $a_p$ ) like the substrate and thus produces no half-order streaks. However, due to the  $\sim 7^\circ$  anti-phase rotation of the  $\text{TiO}_6$  octahedra in the other two layers,<sup>2,22</sup> they have a lattice spacing of  $\sim \sqrt{2} a_p$  and a surface mesh that yields half-order streaks. It is the comparatively shorter Bi-O bond distance which causes the tilt and rotation of the  $\text{TiO}_6$  octahedra adjacent to it. The centermost  $\text{TiO}_6$  octahedra are the only ones in the  $\text{Bi}_4\text{Ti}_3\text{O}_{12}$  structure not adjacent to  $\text{Bi}_2\text{O}_2$  layers. They alone have a square, surface-net symmetry which can yield a RHEED pattern with no half-order streaks. After the reappearance of the half-order streaks, indicating the return of a surface with a lattice spacing of  $\sim \sqrt{2} a_p$ , the titanium shutter is closed. The  $\text{Bi}_2\text{O}_2$  layer then quickly forms. Figure 1(e) and 1(f) shows the disappearance and reappearance again of the half-order streaks during this time which could be due to the bismuth adatoms reordering on the surface during the formation of the  $\text{Bi}_2\text{O}_2$  planes.

If the titanium shutter is not closed following the initial reappearance of the half-order streaks (Fig. 1(d)), the film surface quickly roughens and the RHEED pattern becomes spotty. The spotty RHEED pattern observed is consistent with the formation of anatase ( $\text{TiO}_2$ ), which has been conclusively identified in subsequent 4-circle x-ray diffraction measurements. If titanium is never closed (i.e., codeposition), under the growth temperatures (600 - 645 °C) and ozone background pressure ( $2 \times 10^{-5}$  Torr) utilized, these bismuth double layers do not form and anatase crystallizes out of the near-surface transition layer while all bismuth desorbs from the surface. During the growth of GaAs it is not necessary to shutter the gallium source and codeposition

works well. In contrast, we are unable to grow phase-pure bismuth titanate under the temperature and pressure conditions given unless we shutter the titanium. This difference may be related to the necessity to oxidize bismuth before an adsorption-controlled growth regime can be achieved. We have previously shown that the activation energy barrier for oxidation is significantly higher for bismuth than for titanium in the MBE environment.<sup>13</sup> During codeposition, the presence of titanium may significantly reduce the reactivity of the bismuth so that the  $\text{Bi}_2\text{O}_2$  double layer cannot form.

Although we argue that the sticking coefficients of bismuth oxide complexes to pure  $\text{Bi}_{2\text{O}}_{3(\text{s})}$  are negligible under adsorption-controlled conditions, one  $\text{Bi}_2\text{O}_2$  double layer is incorporated with each  $\text{Bi}_2\text{Ti}_3\text{O}_{10}$  perovskite sheet to form  $\text{Bi}_4\text{Ti}_3\text{O}_{12}$  during growth. This behavior is consistent with maintaining charge neutrality—one  $(\text{Bi}_2\text{O}_2)^{2+}$  is incorporated to neutralize each  $(\text{Bi}_2\text{Ti}_3\text{O}_{10})^2$  sheet. Thermodynamically, phase pure  $\text{Bi}_{2\text{O}}_{3(\text{s})}$  is never formed, only two Bi-O layers in a square pyramidal configuration are present in the  $\text{Bi}_4\text{Ti}_3\text{O}_{12(\text{s})}$  phase. It is concluded that the equilibrium vapor pressure of bismuth oxide species over growing  $\text{Bi}_4\text{Ti}_3\text{O}_{12}$  is much lower than over a nucleated  $\text{Bi}_{2\text{O}}_{3(\text{s})}$  phase.

The adsorption-limited incorporation of bismuth was also recently demonstrated for the growth of the superconductor  $\text{Bi}_2\text{Sr}_2\text{CuO}_6$  by MBE.<sup>23</sup> Migita *et al.*<sup>23</sup> found that under adsorption-limited growth conditions that bismuth incorporation was limited to two BiO layers per formula unit of  $\text{Bi}_2\text{Sr}_2\text{CuO}_6$ , despite their flooding the film surface with excess bismuth. This observation is also consistent with our hypothesis of adsorption-limited incorporation to achieve charge neutrality.

In Fig. 2 the  $\theta$ - $2\theta$  4-circle x-ray diffraction scan (using  $\text{CuK}_\alpha$  radiation) of a 1000 Å thick  $\text{Bi}_4\text{Ti}_3\text{O}_{12}$  film grown on (001)  $\text{SrTiO}_3$  is shown. Intense  $00\ell$  peaks indicate that the film is pure *c*-axis oriented  $\text{Bi}_4\text{Ti}_3\text{O}_{12}$ . The rocking curve full width at half maximum (FWHM) of the  $\text{Bi}_4\text{Ti}_3\text{O}_{12}$   $00\bar{1}4$  reflection is measured to be  $0.3^\circ$  in  $\omega$  and  $0.25^\circ$  in  $2\theta$  showing minimal out-of-plane misalignment. Figure 3 shows the azimuthal scan ( $\phi$ -scan) of the 117 reflections of this

same film. The peaks indicate a  $\text{Bi}_4\text{Ti}_3\text{O}_{12}$  [110]  $\parallel$   $\text{SrTiO}_3$  [010] orientation relationship with a FWHM of  $0.4^\circ$  in  $\phi$ , indicating little variation in the in-plane alignment. These peak widths are all comparable to the instrumental resolution of our Picker 4-circle diffractometer. RBS channeling results for this film showed a minimum channeling yield ( $\chi_{\min}$ ) of 0.20 for the bismuth signal behind the surface peak, which is the lowest reported value for  $\text{Bi}_4\text{Ti}_3\text{O}_{12}$  thin films.

An atomic force microscopy (AFM) image of the surface of this same film is shown in Fig. 4. Clearly visible on the surface are micron-sized mounds that protrude approximately 100 - 200 Å out of the film. The terraces making up these mounds have step heights that are predominantly integral multiples of a half-unit-cell (the height of a  $\text{Bi}_4\text{Ti}_3\text{O}_{12}$  formula unit). The surface morphology revealed by AFM is reminiscent of that of layered perovskite superconductor films,<sup>24,25</sup> although it is unclear if oppositely-signed screw dislocations are present within each mound or if the mounds arise due to limited surface diffusion across Ehrlich-Schwoebel step-edge barriers.<sup>26,27</sup> The presence of the mounds shown in Fig. 4 is consistent with our RHEED observations. The films are epitaxial, well connected, and lack surface irregularities that would give rise to a transmission diffraction pattern (i.e., a spotty RHEED pattern).

In conclusion, we have grown epitaxial  $\text{Bi}_4\text{Ti}_3\text{O}_{12}$  films by reactive MBE under conditions of ozone background pressure and temperature where an adsorption-controlled growth mechanism dominates, i.e., the excess bismuth, bismuth oxides, and ozone desorb from the surface leaving behind a phase pure, stoichiometric crystal. AFM analysis indicates that films have micron-sized mounds that protrude ~100-200 Å out of the surface of the film. These morphologies are consistent with either a spiral-type growth mechanism where film growth normal to the substrate surface is mediated by oppositely-signed pairs of screw dislocations, or by step-edge barriers that limit interlayer surface diffusion.

We gratefully acknowledge the financial support of the Office of Naval Research through grant N00014-94-1-0690 and Dr. Larry McIntyre of the University of Arizona for the RBS analysis. CDT gratefully acknowledges the support of the IMAPS Educational Foundation.

REFERENCES

---

- <sup>1</sup> B. Aurivillius, Arkiv Kemi **1**, 463 (1949); B. Aurivillius, Arkiv Kemi **1**, 499 (1949);  
B. Aurivillius, Arkiv Kemi **2**, 519 (1950); B. Aurivillius, Arkiv Kemi **5**, 39 (1952);  
B. Aurivillius and P.H. Fang, Phys. Rev. **126**, 893 (1962).
- <sup>2</sup>  $\text{Bi}_4\text{Ti}_3\text{O}_{12}$  is monoclinic with space group  $B1\alpha 1$  as shown by A. D. Rae, J. G. Thompson, R. L. Withers, and A. C. Willis, Acta Cryst. **B46**, 474 (1990).
- <sup>3</sup> Landolt-Bornstein: *Numerical Data and Functional Relationships in Science and Technology*, New Series, Group III, Vol. 16a, edited by K.-H. Hellwege and A. M. Hellwege (Springer-Verlag, Berlin, 1981), p. 237.
- <sup>4</sup> C. A-Paz de Araujo, J. D. Cuchiaro, L. D. McMillan, M. C. Scott, and J. F. Scott, Nature **374**, 627 (1995).
- <sup>5</sup> Y. Ichikawa, H. Adachi, K. Setsune, and K. Wasa, Appl. Surf. Sci. **60/61**, 749 (1992).
- <sup>6</sup> R. Ramesh, A. Inam, W. K. Chan, B. Wilkens, K. Myers, K. Remschnig, D. L. Hart, and J. M. Tarascon, Science **252**, 944 (1991).
- <sup>7</sup> S. Choopun, T. Matsumoto, and T. Kawai, Appl. Phys. Lett. **67**, 1072 (1995).
- <sup>8</sup> EPI, Chorus Corporation, St. Paul, MN.
- <sup>9</sup> C. D. Theis and D. G. Schlom, J. Cryst. Growth. **174**, 473 (1997).
- <sup>10</sup> Varian Vacuum Products, Lexington, MA.
- <sup>11</sup> C. D. Theis and D. G. Schlom, J. Vac. Sci. Technol. A **14**, 2677 (1996).
- <sup>12</sup> Intelligent Sensor Technology, Mountain View, CA.
- <sup>13</sup> C. D. Theis and D. G. Schlom, to be published in Proc. Electrochem. Soc.
- <sup>14</sup> Pseudocubic indices. At the film growth temperature  $\text{LaAlO}_3$  is cubic. However, on cooling to room temperature it transforms to rhombohedral. The substrate orientation is (012) for the rhombohedral axes.
- <sup>15</sup> M. Kawasaki, K. Takahashi, T. Maeda, R. Tsuchiya, M. Shinohara, O. Ishiyama, T. Yonezawa, M. Yoshimoto, and H. Koinuma, Science **266**, 1540 (1994).

- <sup>16</sup> M. de Keijser and G. J. M. Dormans, MRS Bulletin **37**, (June, 1996).
- <sup>17</sup> J. R. Arthur, J. Appl. Phys. **39**, 4032 (1968).
- <sup>18</sup> M. A. Herman and H. Sitter, *Molecular Beam Epitaxy: Fundamentals and Current Status*, 2nd. ed. (Springer, New York, 1996).
- <sup>19</sup> I. Barin, *Thermochemical Data of Pure Substances*, 3rd. ed. (VCH Publishers, Inc., New York, 1995).
- <sup>20</sup> S. Watanabe, T. Hikita, and Maki Kawai, J. Vac. Sci. Technol. A **9**, 2394 (1991).
- <sup>21</sup> L. N. Sidorov, I. I. Minayeva, E. Z. Zasorin, I. D. Sorokin, and A. Ya. Borshchevskiy, High Temp. Sci. **12**, 175 (1980).
- <sup>22</sup> I. M. Reaney, M. Roulin, H. S. Shulman, and N. Setter, Ferroelectrics **165**, 295 (1995).
- <sup>23</sup> S. Migita, Y. Kasai, H. Ota, and S. Sakai, submitted to Appl. Phys. Lett.
- <sup>24</sup> C. Gerber, D. Anselmetti, J. G. Bednorz, J. Mannhart, and D. G. Schlom, Nature **350**, 279 (1991).
- <sup>25</sup> M. Hawley, I. D. Raistrick, J. G. Beery, and R. J. Houlton, Science **251**, 1587 (1991).
- <sup>26</sup> G. Ehrlich and F. G. Hudde, J. Chem. Phys. **44**, 1039 (1966).
- <sup>27</sup> R. L. Schwoebel and E. J. Shipsey, J. Appl. Phys. **37**, 3682 (1966).

FIGURE CAPTIONS

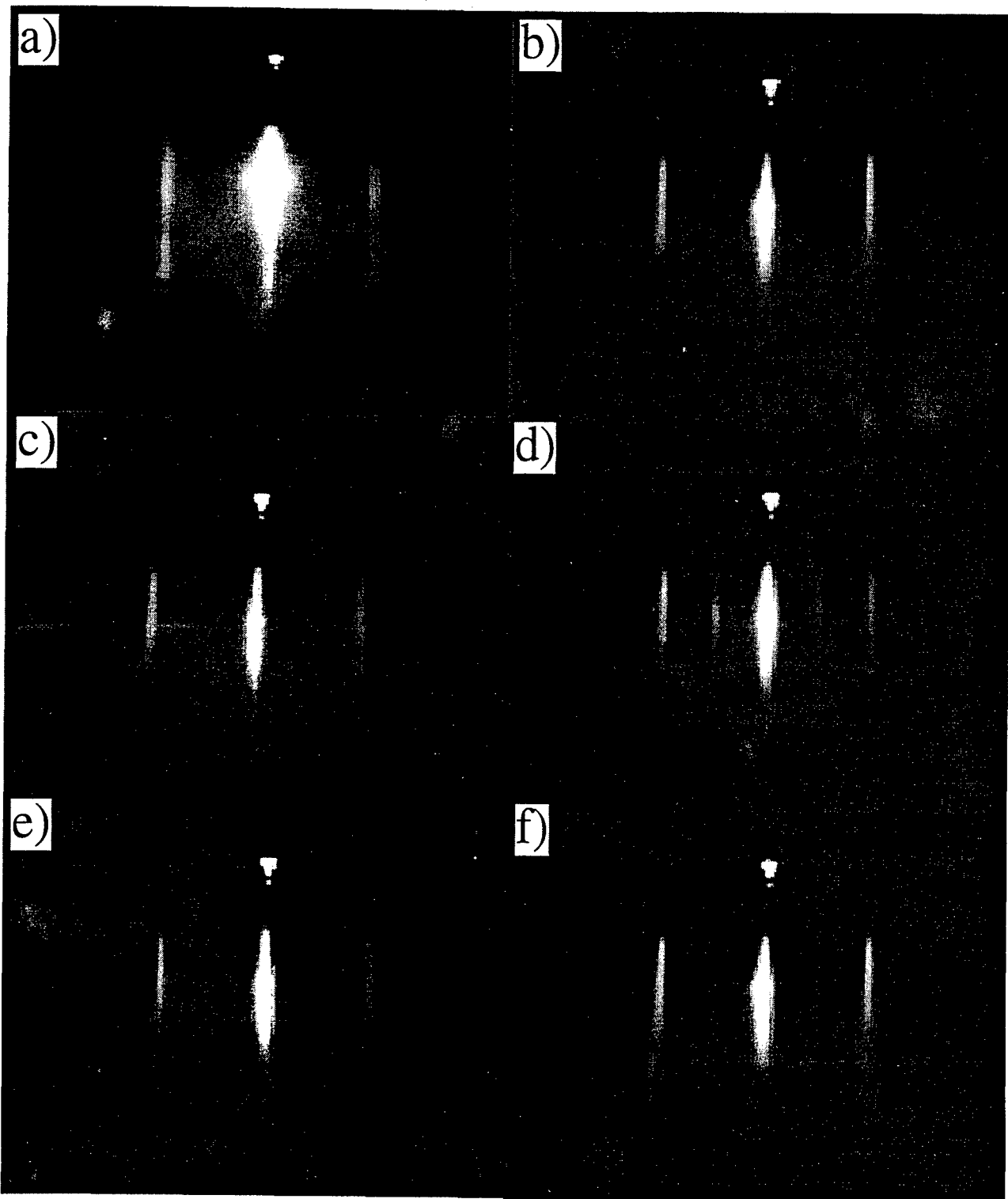
Fig. 1. RHEED patterns with the electron beam incident along the [110] azimuth of the (001) SrTiO<sub>3</sub> substrate for (a) the bare etched (001) SrTiO<sub>3</sub> substrate at ~ 640 °C during exposure to  $2 \times 10^{-5}$  Torr of ozone, (b-d) during deposition of the Bi<sub>2</sub>Ti<sub>3</sub>O<sub>10</sub> perovskite sheets showing the  $\sqrt{2} a_p$  to  $a_p$  to  $\sqrt{2} a_p$  transition in the surface periodicity (with concomitant disappearance of half-order streaks), and (e,f) during the deposition of the Bi<sub>2</sub>O<sub>2</sub> planes where the faded half order streaks (e) could result from bismuth adatoms reordering on the surface.

Fig. 2. θ-2θ 4-circle x-ray diffraction scan of a 1000 Å thick (001)-oriented Bi<sub>4</sub>Ti<sub>3</sub>O<sub>12</sub> film grown on (001) SrTiO<sub>3</sub>. This scan indicates that the *c*-axis of the film is  $32.6 \pm 0.1$  Å.

Fig. 3. Azimuthal scan ( $\phi$ -scan) of the 117 reflections of a 1000 Å thick Bi<sub>4</sub>Ti<sub>3</sub>O<sub>12</sub> film grown on (001) SrTiO<sub>3</sub>. This scan indicates that the in-plane lattice constants of the Bi<sub>4</sub>Ti<sub>3</sub>O<sub>12</sub> film are  $a \approx b \approx 5.50 \pm 0.04$  Å.

Fig. 4. An AFM image of the surface of a 1000 Å thick Bi<sub>4</sub>Ti<sub>3</sub>O<sub>12</sub> film grown on (001) SrTiO<sub>3</sub>. The surface is epitaxial and well connected with micron-sized mounds that protrude ~100 - 200 Å.

Fig. 1



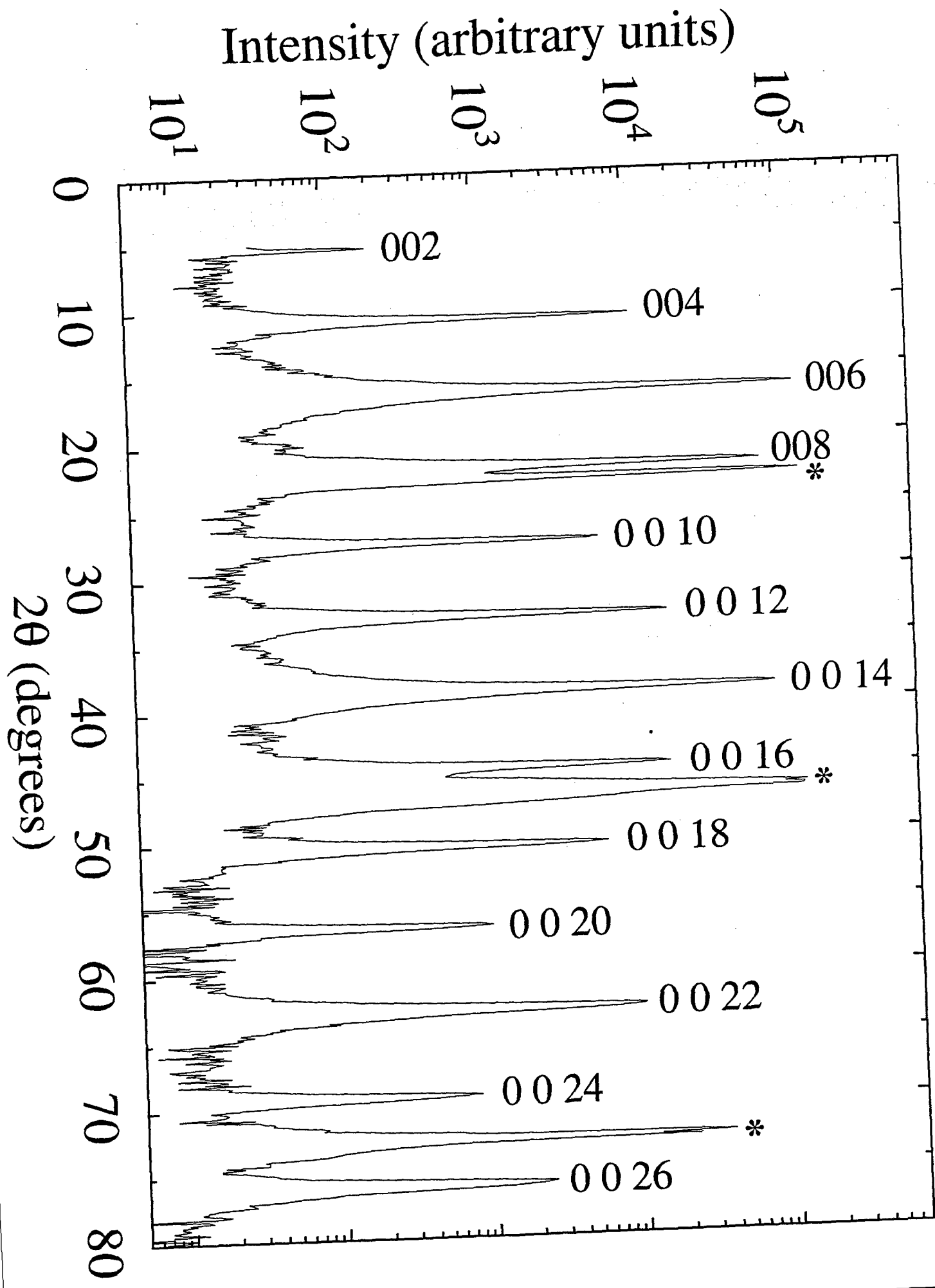


Fig.3

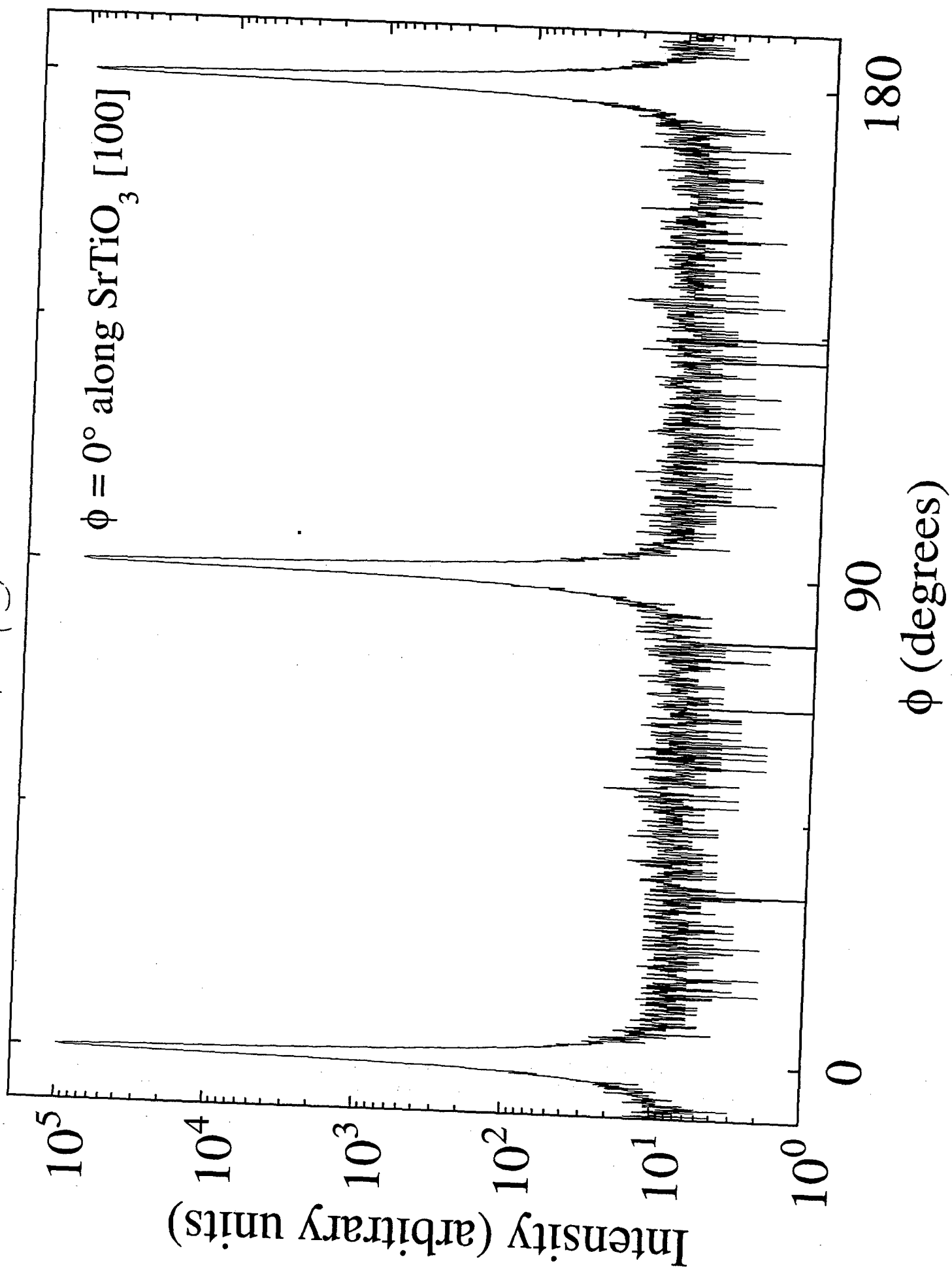
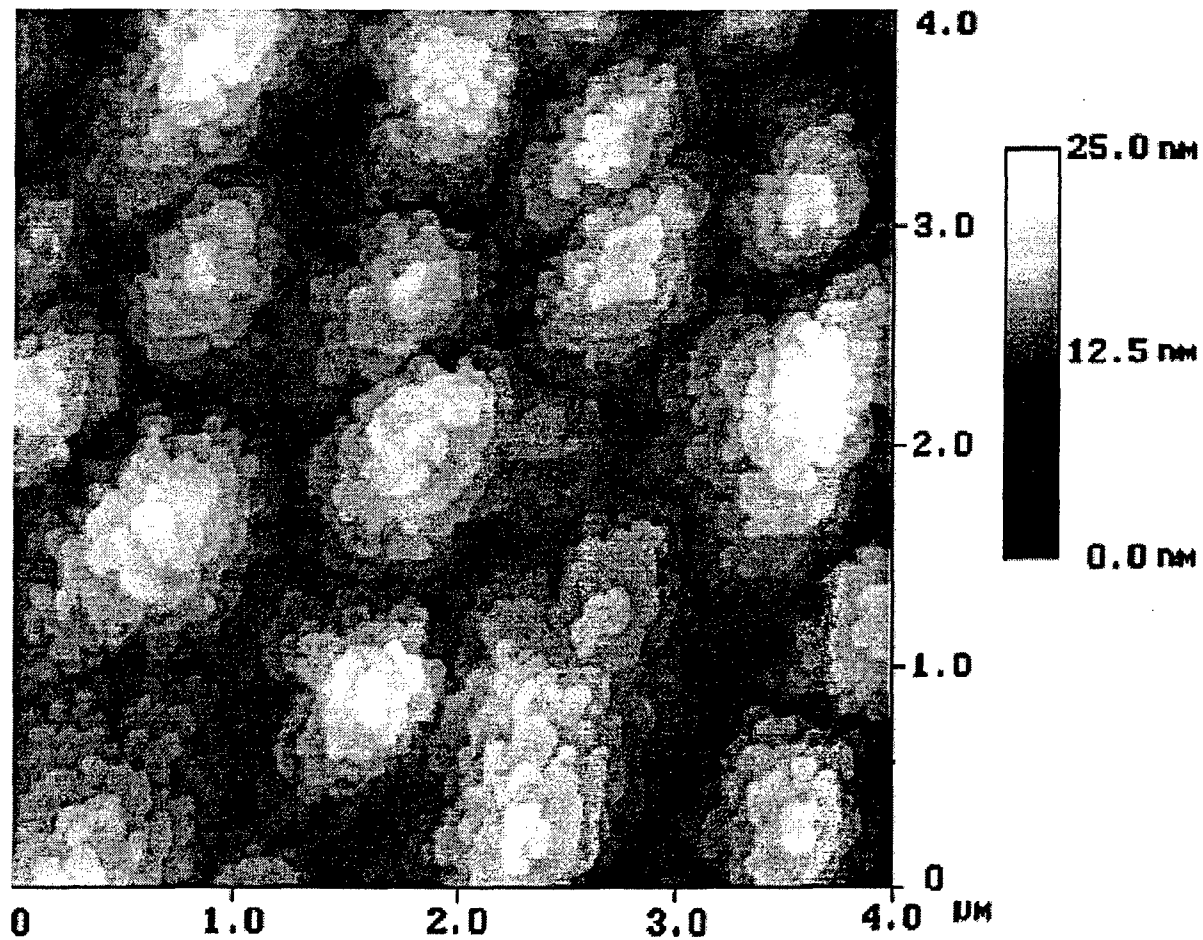


Fig. 4



## Adsorption-Controlled Growth of PbTiO<sub>3</sub> by Reactive Molecular Beam Epitaxy

C. D. Theis, J. Yeh, and D. G. Schlom

*Department of Materials Science and Engineering, The Pennsylvania State University,  
University Park, PA 16802-5005*

M. E. Hawley and G. W. Brown

*Center for Materials Science, Los Alamos National Laboratory, Los Alamos, NM 87545*

### **Abstract**

Epitaxial lead titanate films have been grown on (001) SrTiO<sub>3</sub> substrates by reactive molecular beam epitaxy (MBE). Growth of stoichiometric, phase pure, epitaxial PbTiO<sub>3</sub> films is achieved by supplying a continuous excess of lead and ozone to the surface of the depositing film. Results obtained from RBS composition analysis, measured film thicknesses, and flux measurements using atomic absorption spectroscopy (AA) indicate that the film growth rate is completely determined by the incident titanium flux supplied to the surface. Atomic force microscopy (AFM) results show that films grow smoothly in a layer-by-layer fashion with an RMS roughness of < 0.5 nm. The sticking coefficient of titanium is determined to be approximately unity while the excess lead, lead oxide, and ozone desorb. Lead and ozone beam equivalent pressures have been measured in the MBE environment. Thermodynamic analysis is used to help describe the processes that prevent the incorporation of PbO into films under adsorption-controlled growth conditions.

**Keywords:** PbTiO<sub>3</sub>, oxide MBE, adsorption-control, ozone, thin film, epitaxy

## 1. Introduction

Lead titanate has become one of the most extensively studied thin film ferroelectric materials in recent years. Because of its large remanent polarization ( $\sim 75 \mu\text{C}/\text{cm}^2$ ), the largest of any known ferroelectric, it remains a prime candidate for integration into superconducting/ferroelectric field effect transistors (SuFETs) because of the potential to electrically dope the superconducting layer with large numbers of charge carriers per unit area. High quality, epitaxial  $\text{PbTiO}_3$  films have been grown by metal organic chemical vapor deposition (MOCVD),<sup>1-11</sup> pulsed laser deposition (PLD),<sup>12-20</sup> sputtering,<sup>21-27</sup> and through the use of solution precursors.<sup>28,29</sup>

Some reports indicate that  $\text{PbTiO}_3$  films grown by PLD<sup>15</sup> and sputtering<sup>22-24</sup> have been hampered by the volatility of both lead and lead oxide. High energy plasmas and ablated species make the re-evaporation of excess lead from the substrate surface difficult to control. Films show a range of composition as a function of growth conditions from lead-rich to lead-poor. As a result it is difficult to accurately reproduce stoichiometric films. In contrast, some results obtained for bulk ceramics,<sup>30</sup> solution deposited thin films,<sup>28,29,31</sup> and lead-based films grown by MOCVD<sup>3,32</sup> indicate that the incorporation of lead can be self-limiting. That is, by providing a significant excess of lead during growth lead-deficient phases are avoided and excess lead is evaporated from the material leaving behind a stoichiometric product.

We have investigated the use of molecular beam epitaxy (MBE) to accurately and reproducibly control film stoichiometry via an adsorption-controlled growth mechanism. Adsorption-controlled growth was first successfully utilized for the MBE synthesis of epitaxial GaAs thin films nearly 30 years ago.<sup>33-36</sup> Since that time, significant research efforts have been directed at understanding and quantifying the molecular processes involved in GaAs growth such as physisorption, surface migration, chemisorption, and surface evaporation.<sup>37</sup> This growth mechanism relies on the volatility of the group V component. The use of adsorption-controlled growth has proven to be extremely effective for the MBE growth of lead titanate (described here),

bismuth titanate,<sup>38</sup>  $\text{Bi}_2\text{Sr}_2\text{CuO}_6$ ,<sup>39</sup> and to a lesser degree the growth of  $(\text{Rb},\text{Ba})\text{BiO}_3$ <sup>40</sup> by MBE. We anticipate that adsorption-controlled growth will be applicable to the synthesis of many other volatile metal—metal oxide systems by MBE.<sup>41</sup>

## 2. Experimental

The EPI 930 MBE system<sup>42</sup> used for this study is described in detail elsewhere.<sup>43</sup> Lead is continuously supplied to the surface of the depositing film from a low-temperature dual-filament effusion cell. Titanium is sublimated onto the film from a titanium sublimation pump. The Ti-Ball<sup>TM,44</sup> is powered by a low noise DC power supply. The resulting titanium flux has a maximum peak-to-peak variation of  $\pm 2.5\%$  over 5 hours<sup>45</sup> (about 5 times longer than the time needed to grow a 100 nm thick  $\text{PbTiO}_3$  film). The fluxes of all depositing species are monitored simultaneously *in situ* using atomic absorption spectroscopy (AA).<sup>46,47</sup> Oxygen is supplied to the film in the form of ~80% pure distilled ozone.<sup>48</sup> Film growth is monitored continuously using reflection high energy electron diffraction (RHEED). The substrate heater block temperature is measured using an optical pyrometer. (001)  $\text{SrTiO}_3$  substrates are attached to Haynes<sup>49</sup> alloy 214 heater blocks using silver paint. The  $\text{SrTiO}_3$  wafers are etched with a buffered  $\text{NH}_4\text{F-HF}$  solution prior to growth,<sup>50</sup> exposing the  $\text{TiO}_2$ -terminated surface.

During growth, lead and ozone are supplied to the surface of the film continuously while the substrate temperature is maintained at 600 - 630 °C. The ozone background pressure for a typical growth is  $2 \times 10^{-5}$  Torr ( $2.7 \times 10^{-3}$  Pa), which represents an incident flux of ozone hundreds of times greater than a stoichiometric incident flux (i.e., a  $\text{Pb}:\text{Ti}:\text{O}_3$  incident flux ratio of 1:1:3). Similarly, lead is supplied at an incident flux two to five times greater than the average titanium incident flux. Titanium is supplied in shuttered doses controlled by closed-loop direct feedback from the AA composition control system to the MBE shutters to deliver individual monolayers or submonolayers of titania.<sup>51</sup> At temperatures higher than 630 °C and/or ozone background

pressures lower than  $2 \times 10^{-5}$  Torr ( $2.7 \times 10^{-3}$  Pa), we detect  $\text{TiO}_2$  (anatase) as an impurity phase in the films.

Using these growth conditions it is possible to use the full range of lead incident fluxes stated above and still obtain phase-pure material. Rutherford backscattering spectrometry (RBS) measurements performed on films grown on  $\text{LaAlO}_3$  indicate that the  $\text{PbTiO}_3$  films are stoichiometric within the error of the measurement ( $\pm 3\%$ ). Figure 1 is a phase stability diagram showing regions of substrate temperature and ozone background pressures where  $\text{PbTiO}_3$  and  $\text{TiO}_2$  (anatase) are formed. All of the films in this figure were grown using a large lead overpressure. The collection of experimental points suggests that growth is dominated by thermodynamics at higher ozone pressures, but reaches a non-thermodynamic limit at lower ozone pressures. The relevant features of this plot will be discussed in detail in the discussion section.

### 3. Results

#### 3.1. Film Characterization

Figure 2(a) shows the RHEED pattern taken along the [110] azimuth of a bare (001)  $\text{SrTiO}_3$  substrate prior to growth. The exposure of the substrate surface to ozone often significantly improves the quality of the RHEED pattern, perhaps by removing any residual organics. Similarly, Fig. 2(b) shows the RHEED pattern along the same azimuth immediately following growth of a 100 nm thick (001)  $\text{PbTiO}_3$  film, indicating a smooth surface morphology with a cube-on-cube epitaxial relationship between substrate and film.

In Fig. 3(a) the  $\theta$ - $2\theta$  4-circle x-ray diffraction scan of a 70 nm thick  $\text{PbTiO}_3$  film grown on (001)  $\text{SrTiO}_3$  is shown. Intense  $00\ell$  peaks indicate that the film is *c*-axis oriented  $\text{PbTiO}_3$ . The film lattice constants, determined from the x-ray diffraction scans in Fig. 3, are  $c = 0.414 \pm 0.001$  nm and  $a = 0.392 \pm 0.005$  nm. Here the *c*-axis lattice parameter has been calculated using a Nelson-Riley<sup>52</sup> analysis of the  $00\ell$  reflections. The *a*-axis lattice parameter has

been calculated using a combination of the *c*-axis lattice parameter and the *d*-spacing of the PbTiO<sub>3</sub> 101 reflections (Fig. 3(c)). The error estimates are calculated using standard error propagation methods.<sup>53</sup> These values are equal (to within our experimental measurement accuracy) to the lattice constants measured for bulk PbTiO<sub>3</sub> and single crystals.<sup>54</sup> It is likely that a film of this thickness is not fully relaxed and any real deviation of the measured lattice constants from bulk single crystal values is a result of the film being clamped at the substrate-film interface.

Figure 3(b) shows the rocking curve of the SrTiO<sub>3</sub> 002 reflection over a sufficient range to detect 200 PbTiO<sub>3</sub> peaks (from PbTiO<sub>3</sub> *a*-domains) if they were present. Due to the large degree of tetragonality in PbTiO<sub>3</sub>, these domains will be tilted away from the crystallographic normal by ~3.5° and should appear at the same *d*-spacing as the SrTiO<sub>3</sub> lattice parameter within the error of our 4-circle diffractometer.<sup>55</sup> Because of the 4-fold rotational symmetry of the (001) SrTiO<sub>3</sub> substrate, *a*-oriented domains in the PbTiO<sub>3</sub> film will align along all four SrTiO<sub>3</sub> <100> directions.<sup>56</sup> Therefore, we have performed the rocking curve shown in Fig. 3(b) along a SrTiO<sub>3</sub> <100> crystallographic direction looking for *a*-oriented PbTiO<sub>3</sub> domains with a lattice parameter of ~0.390 nm. As seen in Fig. 3(b), films of this thickness (70 nm) show no evidence of *a*-axis oriented PbTiO<sub>3</sub> domains.

The rocking curve full width at half maximum (FWHM) of the PbTiO<sub>3</sub> 002 reflection is measured to be 0.4° showing minimal out-of-plane misalignment. The FWHM of the PbTiO<sub>3</sub> 002 peak is 0.4° in 2θ. Figure 3(c) shows the azimuthal scan ( $\phi$ -scan) of the 101 reflections of this same film. The peaks show a PbTiO<sub>3</sub> [100] || SrTiO<sub>3</sub> [100] orientation relationship with a FWHM of 0.3° in  $\phi$ , indicating little variation in the in-plane alignment. These peak widths are all comparable to the instrumental resolution of our Picker 4-circle x-ray diffractometer. An atomic force microscopy (AFM) image of the surface of this same film is shown in Fig. 4. The film shows an extremely smooth surface morphology with an RMS roughness of <0.5 nm. The surface structure is indicative of a layer-by-layer growth mechanism.

### 3.2. Titanium Sticking Coefficient

Figure 5 shows the  $\theta$ - $2\theta$  x-ray diffraction scan for a  $15.0 \pm 0.4$  nm thick  $\text{PbTiO}_3$  film grown on  $\text{SrTiO}_3$ . Clearly present are only  $00\ell$  reflections indicating the film is *c*-axis oriented perovskite lead titanate. Film thickness was calculated from the thickness fringes present near the  $00\ell$  reflections. From the film thickness and incident fluxes, we have calculated the titanium sticking coefficient to be approximately unity. Here the titanium sticking coefficient is defined as the total number of titanium atoms that are incorporated into the film during growth divided by the total number of titanium atoms that are incident onto the surface of the depositing film.

The *apparent* titanium sticking coefficient that we have measured during growth is less than unity. Here the apparent titanium sticking coefficient is defined as the total number of titanium atoms that are incorporated into the film during growth divided by the total number of titanium atoms deposited onto a quartz crystal monitor (QCM) placed near the position of the substrate at room temperature in vacuum. It is this flux that is measured with the QCM and used to calibrate the AA system, which in turn has been used to supply doses of titanium to the film.

To explain the difference between the apparent and true titanium sticking coefficients, we consider the film shown in Fig. 5. Titanium was supplied in shuttered bursts containing one monolayer each (according to the QCM) to deliver a total of 50 individual monolayers (which corresponds to a lead titanate film thickness of  $\sim 20.7$  nm) and lead was continuously supplied at an incident flux three times higher than the titanium incident flux. We divide the actual thickness of the film calculated from thickness fringes by the attempted film thickness of 20.7 nm to obtain an apparent titanium sticking coefficient of  $\sim 0.72 \pm 0.02$ . This value is consistent with the apparent titanium sticking coefficient calculated from RHEED intensity oscillations for pure  $\text{TiO}_2$  films grown on  $\text{LaAlO}_3$  which was measured to be  $\sim 0.70$ . This value is further confirmed by RBS which yielded a stoichiometric film thickness of  $67 \pm 3$  nm for a film grown to be 100 nm thick, which implies an apparent sticking coefficient of  $0.67 \pm 0.3$ .

The apparent titanium sticking coefficient is less than one for two reasons. First, at the high ozone growth pressures required for the synthesis of  $\text{PbTiO}_3$  at the substrate temperatures employed, there is some scattering of the impinging atomic fluxes. Measurements indicate that the equivalent pressure of ozone at the substrate position is about twenty times higher than the measured background pressure due to the directed ozone introduction geometry.<sup>48</sup> At the growth pressure used we have directly measured a decrease in the incident metals flux reaching the substrate due to scattering at high ozone pressures.<sup>48</sup> We find that other titanates grown at very low ozone background pressures (e.g.,  $\text{SrTiO}_3$  films grown at  $\sim 1 \times 10^{-6}$  Torr ( $1 \times 10^{-4}$  Pa)) have an apparent titanium sticking coefficient of  $\sim 0.80$ . Second, the actual position of the QCM in the chamber is slightly in front of the substrate making it closer to the titanium source material. Geometric calculations that take this difference into account indicate that the titanium flux at the substrate surface should be  $0.79 \pm 0.08$  of the flux measured at the QCM (i.e., a tooling factor). This implies that the *true* titanium sticking coefficient is close to unity. The tooling factor of the QCM reduces the apparent sticking coefficient of titanium from 1 to about 0.80, and the scattering of the titanium beam in the ozone pressures used during growth reduces this further to about 0.70. The film thickness and film composition is independent of the incident lead flux for the high excess Pb-flux conditions used to grow these films. These results indicate that the incident titanium flux determines the growth rate of the films; just as the incident Group III flux determines the growth rate of III-IV films by MBE. The excess of the volatile species present desorb from the surface.

#### 4. Discussion

A similar adsorption-controlled growth mechanism was shown to be operative by de Keijser and Dormans<sup>10</sup> for  $\text{Pb}(\text{Zr},\text{Ti})\text{O}_3$  thin films grown by MOCVD. They found that by using a range of lead precursor partial pressures, it was possible to obtain stoichiometric films.<sup>10</sup> Additionally, other researchers have alluded to the importance of the vaporization of  $\text{PbO}$  in a physical vapor deposition environment and its importance to the self-limiting incorporation of lead into  $\text{PbTiO}_3$ .<sup>16,29,57</sup> Below we extend this understanding using thermodynamic calculations as a

basis for a more complete physical picture. In the first-order thermodynamic analysis presented, we consider only specific reactions involving the dominant species present and ignore differences in free energy between the standard state compositions utilized in the calculations and the actual species present. We ignore these second order details in order to attain a rough but informative understanding of the adsorption-controlled mechanism.

In the low-pressure MBE environment, the depositing species in each molecular beam have thermal energies of less than 1 eV. This growth environment is free of plasmas or ablated species and it is possible to accurately convert beam fluxes into equivalent elemental gas pressures at the substrate surface using the kinetic theory of gases as is commonly done for the MBE growth of Group IV, III-V, and II-VI semiconductors. Additionally, we have accurately measured the ozone flux at the substrate surface and can relate it to the measured background pressure. We expect that in such an environment, that is free of many of the high energy species common to other physical vapor deposition processes, a thermodynamic evaluation of the reactions involved at the substrate surface should be more meaningful. Indeed, thermodynamics has been successfully applied to describe the growth of III-V compound semiconductors by MBE.<sup>58-61</sup> For the following calculations, we will consider a typical substrate temperature of 600 °C for the growth of PbTiO<sub>3</sub> by MBE.

#### 4.1. *Thermodynamic Evaluation*

Figure 6<sup>62</sup> shows a section of the equilibrium vaporization curve for elemental lead. We have converted our typical incident lead flux during growth into a lead gas pressure from:<sup>63</sup>

$$P_{pb} = \frac{\Phi_{Pb}}{\cos\theta} \sqrt{\frac{\pi m k_B T}{8}} \quad (1),$$

where  $P_{pb}$  is lead gas pressure (Pa),  $m$  is lead atomic mass (kg),  $k_B$  is Boltzmann's constant (J/K),  $T$  is temperature (K),  $\theta$  is the angle of the incident molecular beam, and  $\Phi$  is flux ( $\frac{\text{atoms}}{\text{m}^2 \text{s}}$ ) calculated using a QCM located near the position of the substrate and corrected to yield the flux at

the substrate by the geometrical tooling factor  $\sim 0.8$  (described in section 3.2). Our measured lead beam equivalent pressure is  $\sim 1 \times 10^{-6}$  Torr ( $1 \times 10^{-4}$  Pa) at the substrate surface. This incident lead pressure is far below the stability line for the vaporization of elemental lead shown in Fig. 6. It can be seen that this lead pressure is not high enough to condense lead onto the surface of the film at the growth temperatures that we employ (i.e., all the lead deposited will re-evaporate under our growth conditions unless it is oxidized as described below).

Next we consider the equilibrium  $O_2(g)$  pressure for the oxidation of lead (the upper reaction shown in Fig. 7).<sup>62</sup> The ozone pressure at the substrate surface ( $4 \times 10^{-4}$  Torr ( $5 \times 10^{-2}$  Pa)) during growth is also shown in Fig. 7. Thermodynamically, elemental lead should be fully oxidized to form  $PbO$  at the growth temperatures and pressures that we employ because the incident ozone flux lies far above the stability line for the reactions shown. The use of  $O_{3(g)}$  in our case drives the stability line further down so that condensed  $PbO$  is even more stable (lower curve in Fig. 7). We note that this reaction is for condensed-phase lead. The formation of  $PbO$  should also be dependent on the residence time of elemental lead on the surface of the film. As we have shown thermodynamically in Fig. 6, at  $600\text{ }^{\circ}\text{C}$  elemental lead will not condense on the surface of the depositing film, irrespective of its surface termination (i.e.,  $PbO$  or  $TiO_2$ ). Additionally, there are no favorable reactions ( $\Delta G < 0$ ) between  $Pb$  and  $TiO_2$  leading to oxidation of the lead and reduction of the titania when the lead reaches the film surface. We can infer, therefore, that at the  $O_{3(g)}$  incident flux that we employ for  $PbTiO_3$  film growth, lead must have sufficient residence time on the film surface to form a significant fraction of  $PbO$ . Although thermodynamically a similar result should be achievable using  $O_2$ , it has been shown that lower growth temperatures ( $450\text{ }^{\circ}\text{C}$ ) and higher oxidant pressures (10 mTorr (1.3 Pa)) are required to oxidize the incident lead.<sup>64</sup> This indicates that the formation of  $PbO$  is dependent on not only the residence time of lead on the film surface, but also on the kinetic barrier to oxidation (or statistically, the reaction probability per lead—oxidant collision, which is dependent on the oxidant employed). In addition to these factors, experiments performed with a mass spectrometer placed in the position of the substrate

indicate that a small fraction of the incident lead reacts with  $O_{3(g)}$  to form PbO in gas-phase collisions near the substrate surface. At typical growth pressures, this fraction is much smaller than the amount of PbO incorporated into the film. Our mass spectrometer experiments showed that PbO cannot be formed in the gas phase using  $O_{2(g)}$  at similar pressures. We conclude that the majority of PbO incorporated into the film is oxidized on the surface of the film by the directed ozone beam, and that the contributions to PbO present in the gas phase include a small fraction of lead oxidized by gas-phase collisions and the remainder by the vaporization of condensed PbO formed on the surface of the film.

Based on these arguments, we consider that the vaporization of condensed PbO should dominate the adsorption-controlled growth mechanism. Lamoreaux *et al.*<sup>65</sup> have calculated equilibrium vapor pressure curves of all  $Pb_xO_y$  species for the congruent vaporization of PbO. They show that at 600 °C congruent vaporization of PbO occurs for an  $O_2$  partial pressure of  $\sim 10^{-6}$  Torr ( $10^4$  Pa) and  $PbO_{(g)}$  is the primary species in the vapor phase. All other  $Pb_xO_y$  species do not have appreciable vapor pressures and therefore will not be considered in this first-order thermodynamic analysis. These authors have also shown that at higher  $O_2$  partial pressures up to atmospheric pressure,  $PbO_{(g)}$  remains the predominant species in the vapor phase over condensed PbO. During the MBE growth of  $PbTiO_3$ , the ozone pressure at the substrate surface is  $4 \times 10^{-4}$  Torr ( $5 \times 10^2$  Pa). We may therefore conclude that thermodynamically,  $PbO_{(g)}$  should be the primary species in the vapor phase during the MBE growth of  $PbTiO_3$ . Armed with this knowledge, we are now in a position to consider the reactions shown in Fig. 8.

#### 4.2. Adsorption-Control

In Fig. 8<sup>62</sup> we have used the thermodynamic stability of GaAs with respect to arsenic ( $As_{2(g)}$  and  $As_{4(g)}$ ), which is the classic example of adsorption-controlled MBE growth, as a comparison to the  $PbTiO_3$  system. Only the gaseous species are considered which have significant vapor pressures over the condensed phases in question, i.e.,  $As_{2(g)}$  and  $As_{4(g)}$ . The lower dashed curve shows the equilibrium vapor pressure of  $As_{2(g)}$  over a Ga-rich GaAs surface. For an arsenic

beam equivalent pressure above this line, arsenic will condense onto a Ga-terminated surface. The upper dashed curve shows the equilibrium vapor pressure of  $\text{As}_{4(g)}$  over pure condensed arsenic. For an arsenic beam equivalent pressure below this line, arsenic will not precipitate out of the gas phase onto the surface of the film and will desorb into the vacuum chamber. The arsenic gas pressure between these two dashed lines spans about 10 orders of magnitude at 600 °C. Phase-pure GaAs can easily be grown by MBE by ensuring that the appropriate arsenic beam equivalent pressure and substrate temperatures are utilized. To first order this adsorption-controlled region is the 10 orders of magnitude wide region between these two dashed lines.

In practice, the truly meaningful equilibrium is not between condensed and gaseous arsenic (as shown in the upper dashed curve of Fig. 8), but between an arsenic-rich GaAs surface and gaseous arsenic. In other words, the important equilibrium is between the second adsorbed monolayer of arsenic above an arsenic-terminated surface and gaseous arsenic. More involved thermodynamic analysis<sup>59</sup> and measurement<sup>66,67</sup> of this equilibrium shifts the upper dashed line in Fig. 8 down slightly (about 3-4 orders of magnitude at 600 °C). Despite this difference, the principal features that control the adsorption-limited incorporation of arsenic remain unchanged.

We now consider the case for  $\text{PbTiO}_3$  where we have shown that condensed and gaseous  $\text{PbO}$  should control the lead incorporation into the film. The lower solid curve (Fig. 8) is the equilibrium vapor pressure of  $\text{PbO}_{(g)}$  over a titania-rich  $\text{PbTiO}_3$  surface. For a  $\text{PbO}$  gas pressure above this line,  $\text{PbO}$  will condense onto a titania-terminated surface. The upper solid curve (Fig. 8) shows the equilibrium vapor pressure of  $\text{PbO}_{(g)}$  over pure condensed  $\text{PbO}$ . For a  $\text{PbO}$  gas pressure below this line,  $\text{PbO}$  will not precipitate out of the gas phase onto the surface of the film and will desorb into the vacuum chamber. The  $\text{PbO}$  gas pressure between these two lines spans about 3 orders of magnitude at 600 °C. Thermodynamically, phase-pure  $\text{PbTiO}_3$  can be grown by maintaining a  $\text{PbO}$  gas pressure between these two curves and supplying doses of titanium to the surface of the film. Additionally, the typical range of lead beam equivalent pressures used for growth by MBE are shown in Fig. 8. From this figure it is apparent that the experimental lead beam equivalent pressures that we use fall in the adsorption-controlled regime for

$\text{PbTiO}_3$ . As pointed out above, the actual  $\text{PbO}_{(g)}$  pressure over the surface of the films depends on the residence time of elemental lead on the film surface, the kinetic barrier to oxidation, and on the amount of  $\text{PbO}$  that is incorporated into the film itself (which cannot contribute to the desorbed  $\text{PbO}$  gas phase). These three effects decrease the actual  $\text{PbO}$  present in the gas phase (as compared to the lead beam equivalent pressure shown on Fig. 8) during growth, yet we remain in a thermodynamic region where adsorption-controlled growth is expected to dominate in accord with our experimental observations.

We consider again Fig. 1 showing the experimental phase stability diagram for the formation of  $\text{PbTiO}_3$  and  $\text{TiO}_2$  (anatase). Here the slanted line is positioned arbitrarily to separate the region of  $\text{PbTiO}_3$  phase stability from the region of  $\text{TiO}_2$  phase stability at higher background pressure. The slope is taken from the equilibrium vapor pressure of  $\text{PbO}_{(g)}$  over a titania-rich  $\text{PbTiO}_3$  surface. Thermodynamically, at the lower ozone pressures and substrate temperatures shown in Fig. 1,  $\text{PbTiO}_3$  should be the stable phase. However, anatase is formed below the horizontal line indicating insufficient lead oxidation. In this region, there is not a significant fraction of  $\text{PbO}$  formed on the substrate surface and all lead desorbs primarily in its elemental form. This is due to the decreased probability of lead—ozone collisions (for which the reaction probability per collision is less than unity<sup>48</sup>) at lower pressures.

The calculations above are simplified versions of reality. The presence of other species in the gas phase have not been accounted for and a considerable fraction of the reactions that could be occurring at the substrate surface have been ignored. More detailed modeling is possible by including the entire thermodynamic system if the desorbing species were experimentally measured with a mass spectrometer (as was done for the growth of GaAs).<sup>66,67</sup> Despite these simplifications, the agreement between experiment and calculation implies that the adsorption-controlled growth of  $\text{PbTiO}_3$  in an MBE environment is dominated by the vaporization of  $\text{PbO}$ . Additionally, we note that even simplified calculations that provide qualitative information about the processes controlling film growth at the substrate surface will enable us to make intelligent decisions in order to improve film quality. For example, a tremendous amount of research has been directed at understanding

and improving film growth in the III-V semiconductor community. This work provides us with a roadmap of ideas for the future such as utilizing migration enhanced epitaxy (MEE)<sup>68</sup> to increase atomic surface mobility and enhance film morphology at lower growth temperatures. Additionally, the thermodynamic calculations performed indicate that using a PbO molecular beam source (where the lead arrives at the substrate surface pre-oxidized) should allow for better control of film growth and the use of higher substrate temperatures.

## 5. Conclusions

In conclusion, we have grown epitaxial PbTiO<sub>3</sub> films by reactive MBE. AFM analysis indicates that the PbTiO<sub>3</sub> has a smooth surface morphology (RMS roughness < 0.5 nm) indicative of a two-dimensional growth mechanism. We have measured the titanium sticking coefficient during film growth to be close to unity. We have identified regions of ozone pressure, substrate temperature, and incident lead metal flux where an adsorption-controlled growth mechanism dominates; the excess of lead, lead oxide, and ozone desorb from the surface leaving behind a phase pure, stoichiometric crystal. Thermodynamic calculations indicate that the adsorption-controlled growth of PbTiO<sub>3</sub> is analogous to the adsorption-controlled growth of GaAs by MBE. During growth, it is the PbO component that serves the function of volatile arsenic and controls the adsorption-limited incorporation of lead into the film.

We gratefully acknowledge the financial support of the Office of Naval Research through grant N00014-94-1-0690, the Department of Energy through grant DE-FG02-97ER45638, Dr. Larry McIntyre of the University of Arizona for the RBS analysis, and Dr. Karl Spear for helpful thermodynamic discussions.

REFERENCES

- 
- <sup>1</sup> S. G. Yoon and H. G. Kim, *J. Mater. Sci.* **23**, 2059 (1988).
  - <sup>2</sup> Y. Gao, G. Bai, K. L. Merkle, Y. Shi, H. L. M. Chang, Z. Shen, and D. J. Lam, *J. Mater. Res.* **8**, 145 (1993).
  - <sup>3</sup> H. Funakubo, T. Hioki, M. Otsu, K. Shinozaki, and N. Mizutani, *Jpn. J. Appl. Phys.* **32**, 4175 (1993).
  - <sup>4</sup> G. R. Bai, H. L. M. Chang, C. M. Foster, Z. Shen, and D. J. Lam, *J. Mater. Res.* **9**, 156 (1994).
  - <sup>5</sup> Z. Li, C. Foster, D. Guo, H. Zhang, G. R. Bai, P. M. Baldo, and L. E. Rehn, *Appl. Phys. Lett.* **65**, 1106 (1994).
  - <sup>6</sup> C. M. Foster, Z. Li, M. Buckett, D. Miller, P. M. Baldo, L. E. Rehn, G. R. Bai, D. Guo, H. You, and K. L. Merkle, *J. Appl. Phys.* **78**, 2607 (1995).
  - <sup>7</sup> L. Shun, Y.-F. Chen, T. Yu, J.-X. Chen, and N.-B. Ming, *J. Phys.: Condens. Matter* **7**, 6537 (1995).
  - <sup>8</sup> Y.-F. Chen, T. Yu, J.-X. Chen, L. Shun, P. Li, and N.-B. Ming, *Appl. Phys. Lett.* **66**, 148 (1995).
  - <sup>9</sup> Y.-F. Chen, L. Sun, T. Yu, J.-X. Chen, Y.-Y. Zhu, N.-B. Ming, X.-Y. Chen, and Z.-G. Liu, *Thin Solid Films* **269**, 18 (1995).
  - <sup>10</sup> M. de Keijser, D. M. de Leeuw, P. J. van Veldhoven, A. E. M. De Veirman, D. G. Neerinck, and G. J. M. Dormans, *Thin Solid Films* **266**, 157 (1995).
  - <sup>11</sup> E. Ching-Prado, A. Reynes-Figueroa, R. S. Katiyar, S. B. Majumder, and D. C. Agrawal, *J. Appl. Phys.* **78**, 1920 (1995).
  - <sup>12</sup> H. Tabata, T. Kawai, S. Kawai, O. Murata, J. Fujioka, and S. Minakata, *Appl. Phys. Lett.* **59**, 2354 (1991).
  - <sup>13</sup> H. Tabata, O. Murata, T. Kawai, and M. Okuyama, *Jpn. J. Appl. Phys.* **31**, 2968 (1992).

- <sup>14</sup> H. Tabata, O. Murata, T. Kawai, S. Kawai, and M. Okuyama, *Appl. Phys. Lett.* **64**, 428 (1994).
- <sup>15</sup> W.-Y. Hsu, *Growth, Domain Structure, and Nonlinear Optical Properties of Ferroelectric Lead Titanate Thin Films*, Ph.D. thesis, Cornell University, 1994.
- <sup>16</sup> H. Tanaka, H. Tabata, T. Kawai, and S. Kawai, *Jpn. J. Appl. Phys.* **33**, 451 (1994).
- <sup>17</sup> W.-Y. Hsu and R. Raj, *Appl. Phys. Lett.* **67**, 792 (1995).
- <sup>18</sup> S. Stemmer, S. K. Streiffer, F. Ernst, M. Ruhle, W.-Y. Hsu, and R. Raj, *Solid State Ionics* **75**, 43 (1995).
- <sup>19</sup> S. Stemmer, S. K. Streiffer, W.-Y. Hsu, F. Ernst, R. Raj, and M. Ruhle, *J. Mater. Res.* **10**, 791 (1995).
- <sup>20</sup> C. D. Theis and D. G. Schlom, in *Epitaxial Oxide Thin Films II*, edited by D. K. Fork, J. S. Speck, R. M. Wolf, and T. Shiosaki (Mat. Res. Soc. Symp. Proc., Pittsburgh, 1996), Vol. **401**, pp. 171-176.
- <sup>21</sup> K. Iijima, Y. Tomita, R. Takayama, and I. Ueda, *J. Appl. Phys.* **60**, 361 (1986).
- <sup>22</sup> A. Pignolet, P. E. Schmid, L. Wang, and F. Levy, *J. Phys. D* **24**, 619 (1991).
- <sup>23</sup> K. Iijima, I. Ueda, and K. Kugimiya, *Jpn. J. Appl. Phys.* **30**, 2149 (1991).
- <sup>24</sup> T. Mihara, S. Mochizuki, S. Kimura, and R. Makabe, *Jpn. J. Appl. Phys.* **31**, 1872 (1992).
- <sup>25</sup> H. Maiwa, N. Ichinose, and K. Okazaki, *Jpn. J. Appl. Phys.* **31**, 3029 (1992).
- <sup>26</sup> K. Wasa, Y. Haneda, T. Satoh, H. Adachi, S. Hayashi, and K. Setune, *Jpn. J. Appl. Phys.* **34**, 5132 (1995).
- <sup>27</sup> S. Kim, Y. Kang, and S. Baik, *Thin Solid Films* **256**, 240 (1995).
- <sup>28</sup> A. Seifert, F. F. Lang, and J. S. Speck, *J. Mater. Res.* **10**, 680 (1995).
- <sup>29</sup> E. Sato, Y. Huang, M. Kosec, A. Bell, and N. Setter, *Appl. Phys. Lett.* **65**, 2678 (1994).
- <sup>30</sup> A. I. Kingon and J. B. Clark, *J. Amer. Ceram. Soc.* **66**, 253 (1983).
- <sup>31</sup> H. N. Al-Shareef, K. R. Bellur, O. Auciello, X. Chen, and A. I. Kingon, *Thin Solid Films* **252**, 38 (1994).

- <sup>32</sup> M. de Keijser and G. J. M. Dormans, MRS Bulletin **37**, (June, 1996).
- <sup>33</sup> J. R. Arthur, J. Appl. Phys. **39**, 4032 (1968).
- <sup>34</sup> A. Y. Cho, Surf. Sci. **17**, 494 (1969).
- <sup>35</sup> A. Y. Cho, J. Appl. Phys. **41**, 2780 (1970).
- <sup>36</sup> A. Y. Cho, J. Appl. Phys. **42**, 2074 (1971).
- <sup>37</sup> M. A. Herman and H. Sitter, *Molecular Beam Epitaxy: Fundamentals and Current Status*, 2nd. ed. (Springer, New York, 1996).
- <sup>38</sup> C. D. Theis, J. Yeh, D. G. Schlom, M. E. Hawley, and G. W. Brown, submitted to Appl. Phys. Lett.
- <sup>39</sup> S. Migita, Y. Kasai, H. Ota, and S. Sakai, Appl. Phys. Lett. **71**, 3712 (1997).
- <sup>40</sup> E. S. Hellman and E. H. Hartford, J. Vac. Sci. Technol. B **8**, 332 (1990).
- <sup>41</sup> Although the authors do not discuss this aspect, from the lithium-rich growth conditions reported, LiNbO<sub>3</sub> may be another example of adsorption-controlled oxide growth by MBE. See R. A. Betts and C. W. Pritt, Electron. Lett. **21**, 960 (1985).
- <sup>42</sup> EPI, Chorus Corporation, St. Paul, MN.
- <sup>43</sup> C. D. Theis and D. G. Schlom, J. Cryst. Growth. **174**, 473 (1997).
- <sup>44</sup> Varian Vacuum Products, Lexington, MA.
- <sup>45</sup> C. D. Theis and D. G. Schlom, J. Vac. Sci. Technol. A **14**, 2677 (1996).
- <sup>46</sup> Intelligent Sensor Technology, Mountain View, CA.
- <sup>47</sup> C. Lu and Y. Guan, J.Vac. Sci. Technol. A **13**, 1797 (1995).
- <sup>48</sup> C. D. Theis and D. G. Schlom, in *High Temperature Materials Chemistry IX*, edited by K. E. Spear (Electrochemical Society, New Jersey, 1997), vol. **97-39**, pp. 610-616.
- <sup>49</sup> Haynes is a registered trademark of Haynes International, Kokomo, Indiana.
- <sup>50</sup> M. Kawasaki, K. Takahashi, T. Maeda, R. Tsuchiya, M. Shinohara, O. Ishiyama, T. Yonezawa, M. Yoshimoto, and H. Koinuma, Science **266**, 1540 (1994).

- <sup>51</sup> If the titanium is deposited continuously to the substrate, we detect TiO<sub>2</sub> (anatase) as an impurity in the grown films.
- <sup>52</sup> J.B. Nelson and D.P. Riley, Proc. Phys. Soc. London **57**, 160 (1945).
- <sup>53</sup> P.R. Bevington, *Data Reduction and Error Analysis for the Physical Sciences* (McGraw-Hill, New York, 1969) pp. 56-65.
- <sup>54</sup> Landolt - Bornstein: *Numerical Data and Functional Relationships in Science and Technology*, New Series, edited by K.-H. Hellwege (Springer-Verlag, Berlin, 1975), series III, Vol. **7b1**, pp. 26-27.
- <sup>55</sup> C. M. Foster, Z. Li, M. Buckett, D. Miller, P. M. Baldo, L. E. Rehn, G. R. Bai, D. Guo, H. You, and K. L. Merkle, J. Appl. Phys. **78**, 2607 (1995).
- <sup>56</sup> C. D. Theis and D. G. Schlom, J. Mater. Res. **12**, 1297 (1997).
- <sup>57</sup> A. E. M de Veirman, J. Timmers, F. J. G. Hakkens, J. F. M. Cillessen, and R. M. Wolf, Phillips J. Res. **47**, 185 (1993).
- <sup>58</sup> R. Heckingbottom, G. J. Davies, and K. A. Prior, Surf. Sci. **132**, 375 (1983).
- <sup>59</sup> H. Seki and A. Koukitu, J. Cryst. Growth **74**, 172 (1986).
- <sup>60</sup> J. Y. Tsao, J. Cryst. Growth **110**, 595 (1991).
- <sup>61</sup> J. Y. Tsao, *Materials Fundamentals of Molecular Beam Epitaxy* (Academic Press, Boston, 1993) pp. 65-88.
- <sup>62</sup> Plots calculated from data taken from: I. Barin, *Thermochemical Data of Pure Substances*, 3rd ed. (VCH Publishers, Inc., New York, 1995).
- <sup>63</sup> *Molecular Beam Epitaxy, Applications to Key Materials*, edited by R. C. Farrow (Noyes, New Jersey, 1995) p. 544.
- <sup>64</sup> R. Bruchhaus, H. Huber, D. Pitzer, and W. Wersing, Integr. Ferroelectr. **2**, 157 (1992).
- <sup>65</sup> R. H. Lamoreaux, D. L. Hildenbrand, and L. Brewer, J. Phys. Chem. Ref. Data **16**, 419 (1987).
- <sup>66</sup> J.R. Arthur, J. Phys. Chem. Solids **28**, 2257 (1967).

- <sup>67</sup> C.T. Foxon, J.A. Harvey, and B.A. Joyce, *J. Phys. Chem. Solids* **34**, 1693 (1973).
- <sup>68</sup> Y. Horikoshi, M. Kawashima, and H. Yamaguchi, *Jpn. J. Appl. Phys.* **27**, 169 (1988).

## FIGURE CAPTIONS

Fig. 1 Phase stability diagram showing regions of ozone background pressure and substrate temperature where  $\text{PbTiO}_3$  (triangles) and  $\text{TiO}_2$  (circles) are formed using a large lead overpressure in all cases. At low ozone background pressures, there is insufficient ozone flux at the substrate surface to oxidize the depositing lead before it desorbs.

Fig. 2 RHEED pattern taken along the  $\text{SrTiO}_3$  [110] azimuth (a) of a bare (001)  $\text{SrTiO}_3$  substrate prior to growth and (b) immediately following growth of a 100 nm thick (001)  $\text{PbTiO}_3$  film.

Fig. 3(a)  $\theta$ - $2\theta$  4-circle x-ray diffraction scan of a 70 nm thick *c*-axis oriented  $\text{PbTiO}_3$  film grown on (001)  $\text{SrTiO}_3$ . The substrate peaks are marked by an asterisk (\*). (b)  $\omega$ -scan of the  $\text{PbTiO}_3$  200 reflections showing that there are no *a*-oriented  $\text{PbTiO}_3$  domains present in this film. (c) Azimuthal scan of the 101  $\text{PbTiO}_3$  reflections indicating that this film is epitaxial with [100]  $\text{SrTiO}_3$  || [100]  $\text{PbTiO}_3$ .  $\phi = 0$  is set parallel to the [100]  $\text{SrTiO}_3$  direction.

Fig. 4 AFM image of a 70 nm thick  $\text{PbTiO}_3$  film grown on (001)  $\text{SrTiO}_3$ . The RMS roughness is < 0.5 nm.

Fig. 5  $\theta$ - $2\theta$  4-circle x-ray diffraction scan of a 15 nm thick *c*-axis oriented  $\text{PbTiO}_3$  film grown on (001)  $\text{SrTiO}_3$ . The substrate peaks are marked by an asterisk (\*).

Fig. 6 Equilibrium vaporization curve for elemental lead. The incident lead beam equivalent pressure typically used for  $\text{PbTiO}_3$  growth by MBE is shown.

Fig. 7 Equilibrium oxidation curves for condensed lead with both  $O_{2(g)}$  and  $O_{3(g)}$ . The ozone pressure at the substrate surface utilized for  $PbTiO_3$  growth by MBE is shown.

Fig. 8 Equilibrium curves for two reactions governing adsorption-controlled growth of GaAs (dashed lines), and two reactions governing adsorption-controlled growth of  $PbTiO_3$  (solid lines).

Fig. 1

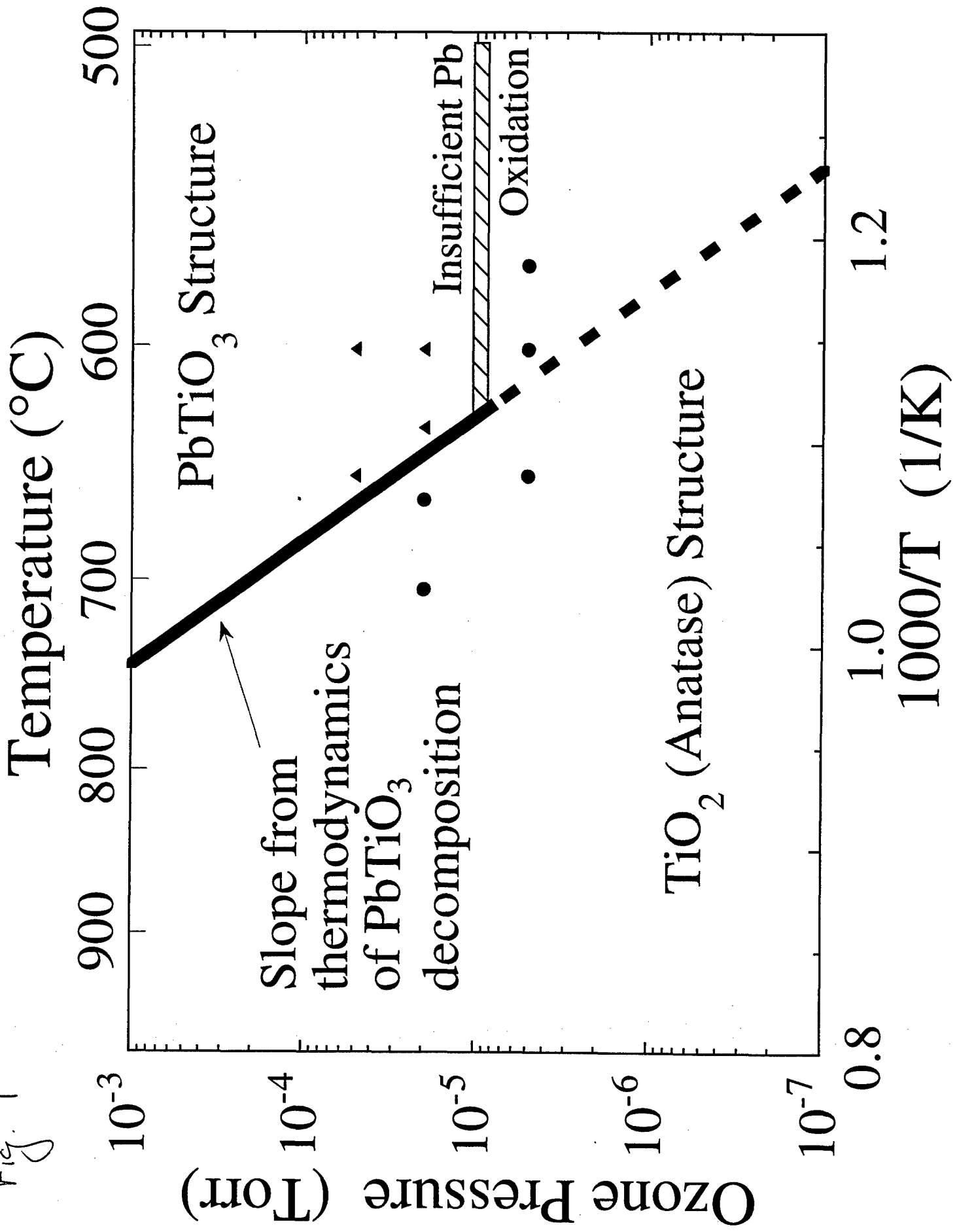


Fig. 2(a)

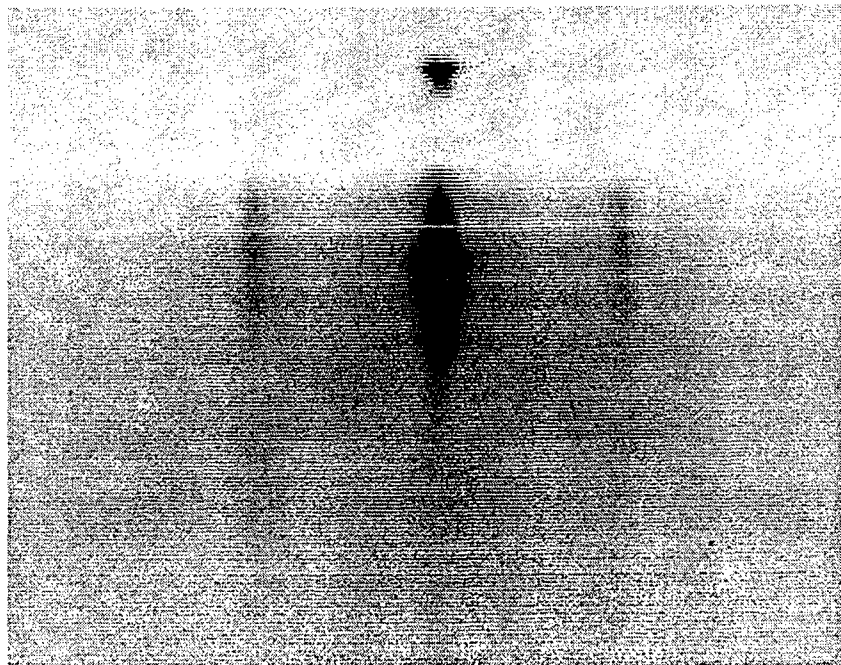
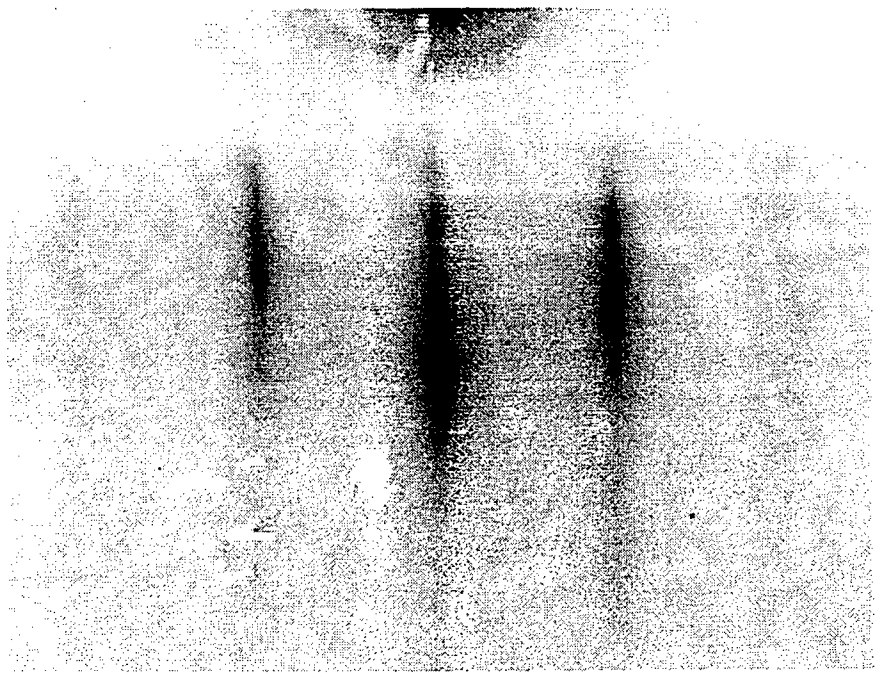


Fig 2(b)



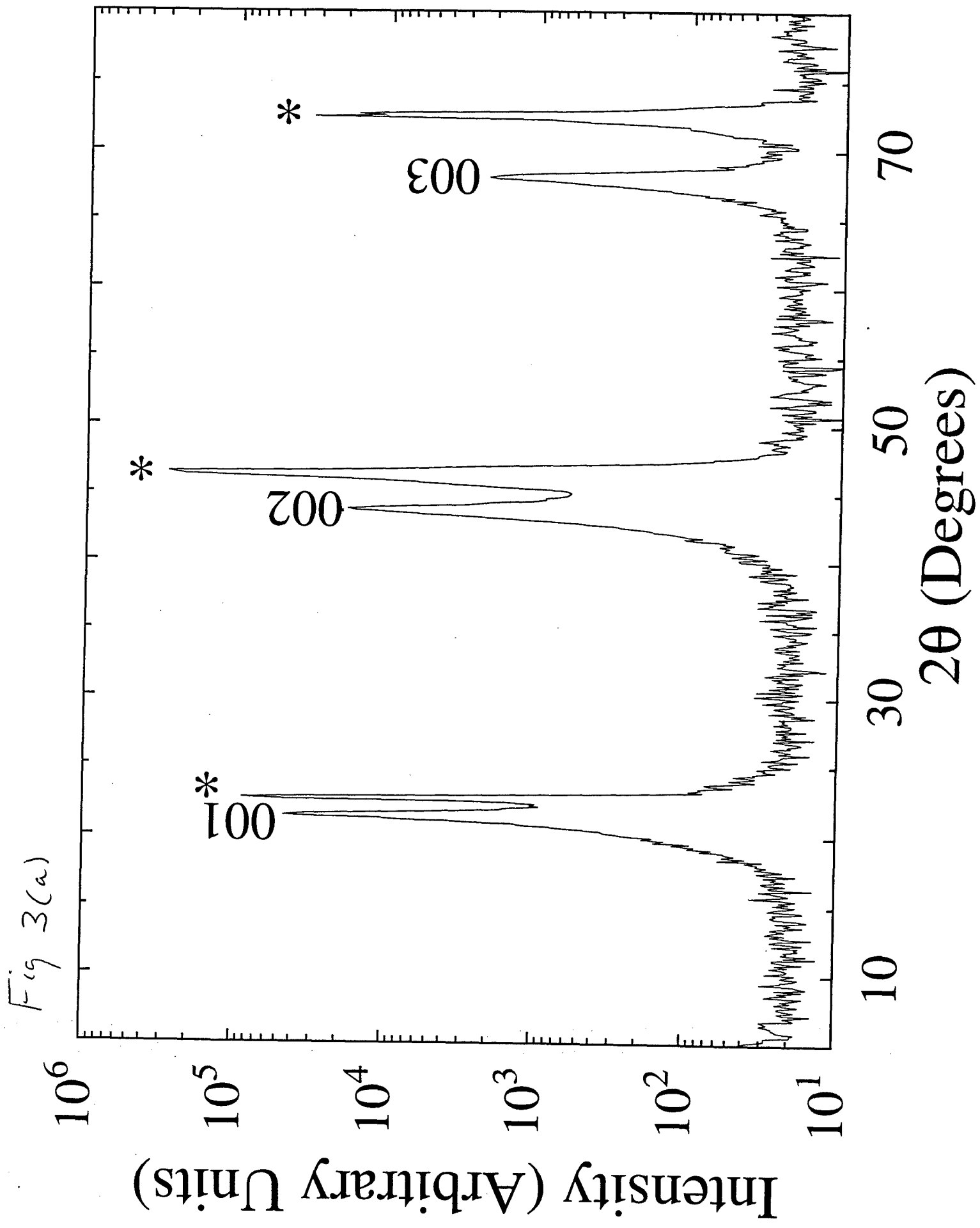


Fig. 3(b)

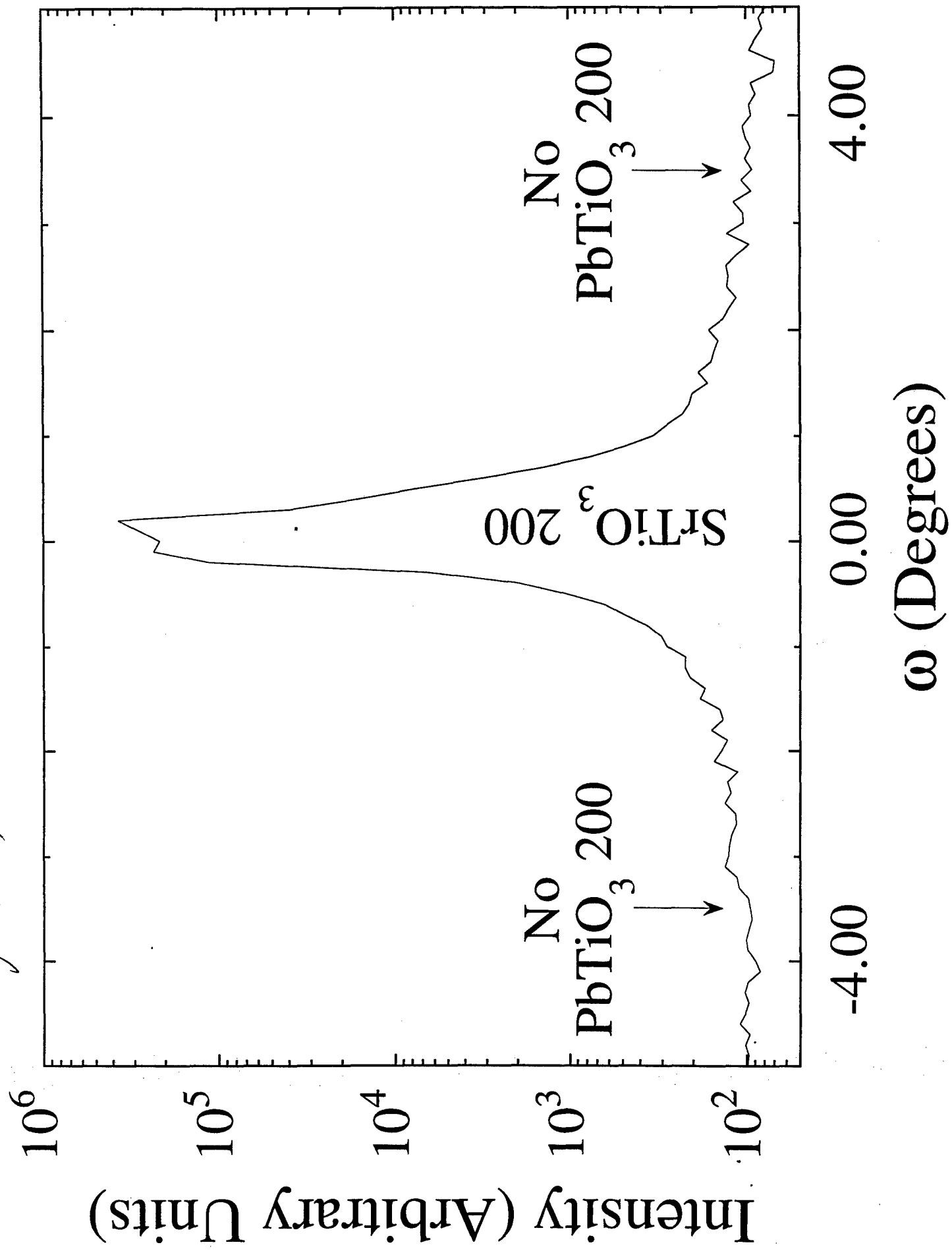


Fig. 3(c)

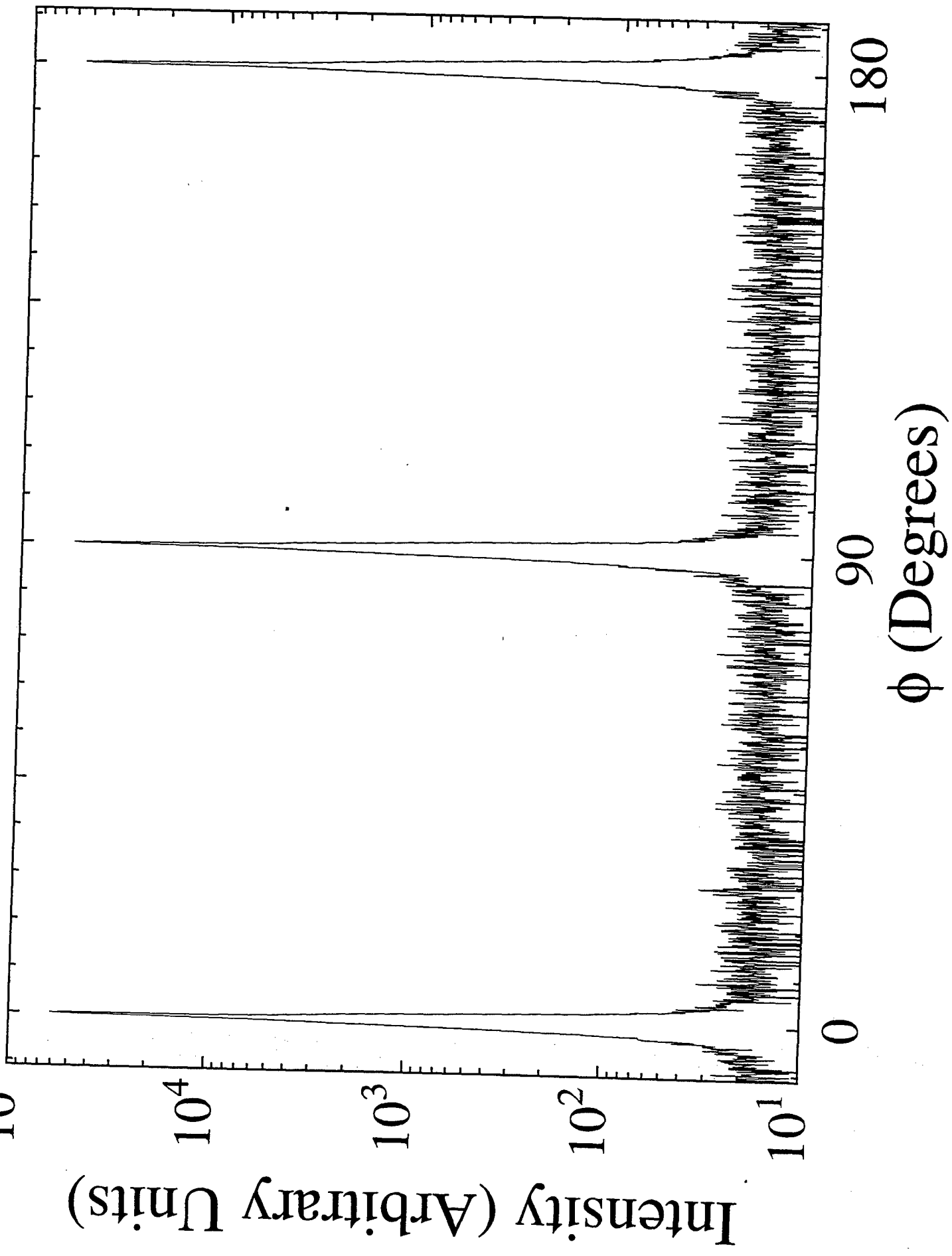


Fig 4/

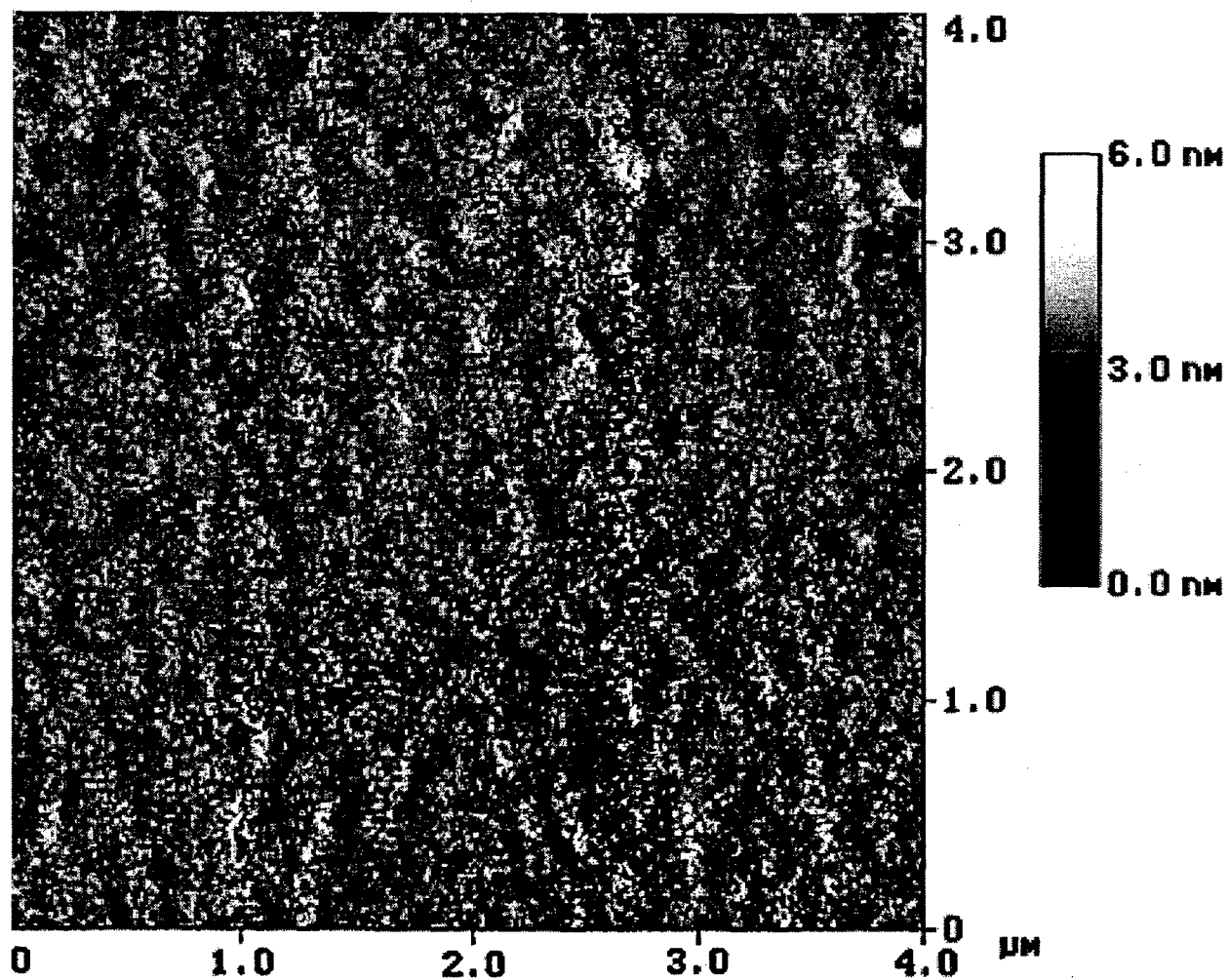


Fig. 5

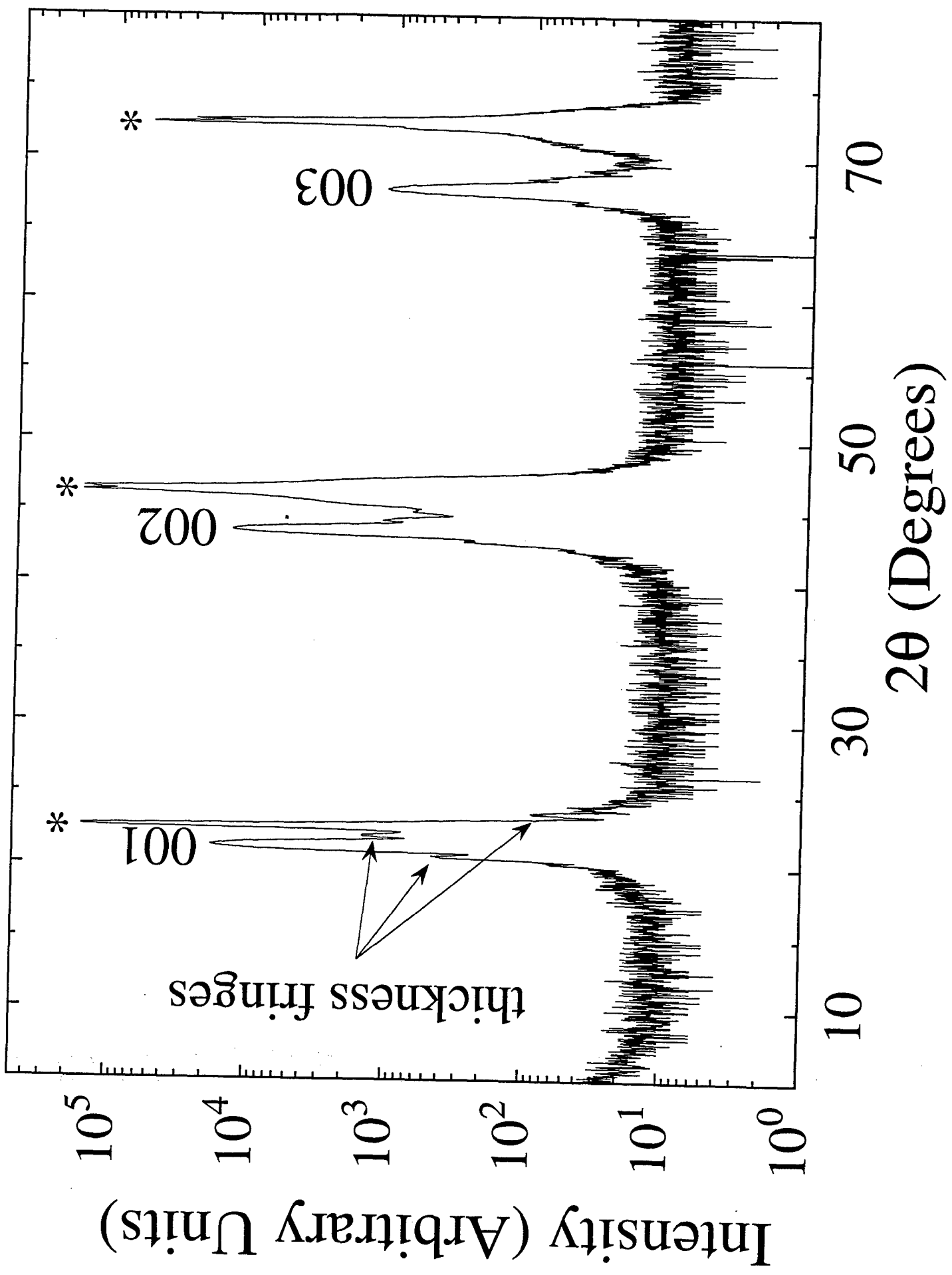


Fig. 6

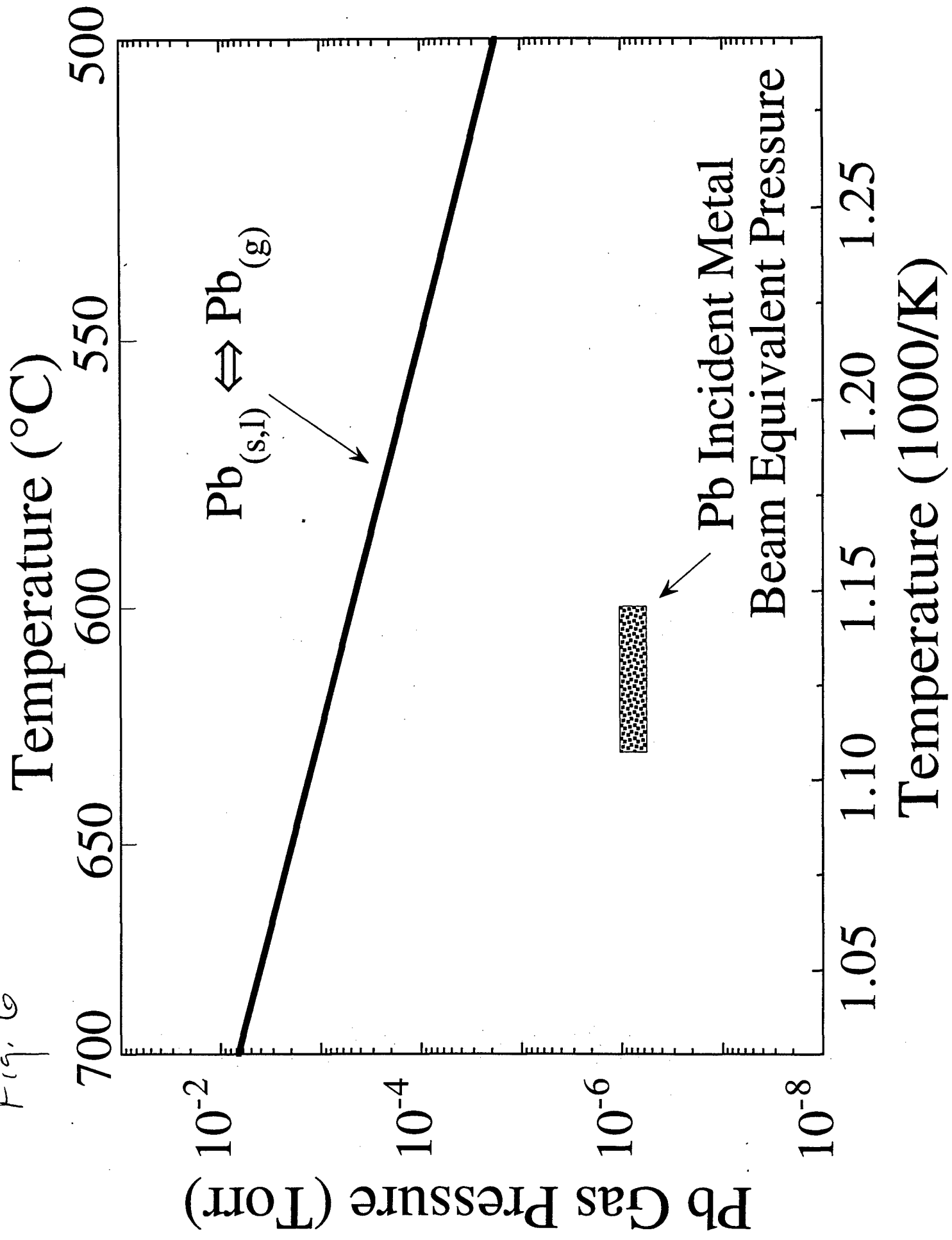


Fig. 7

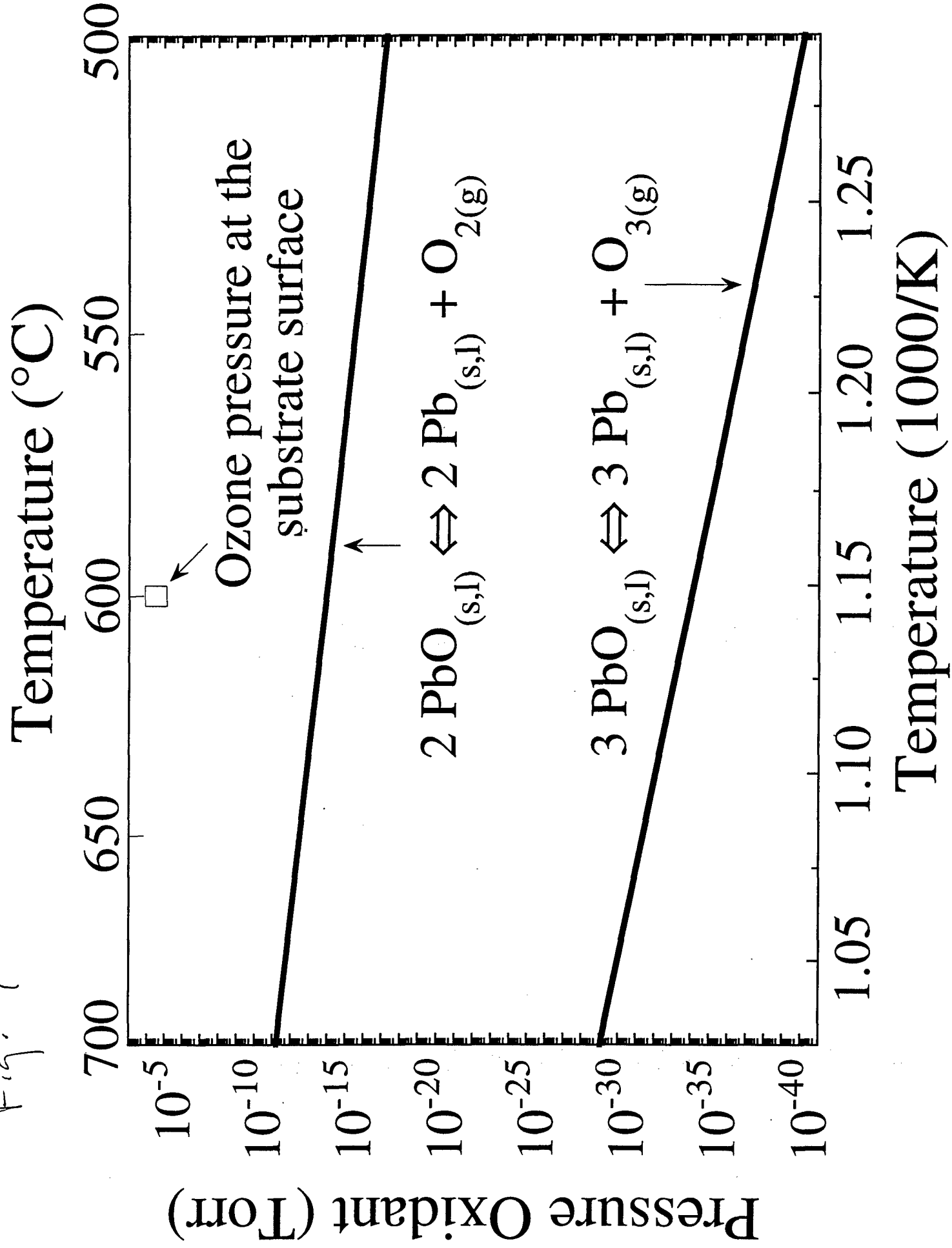
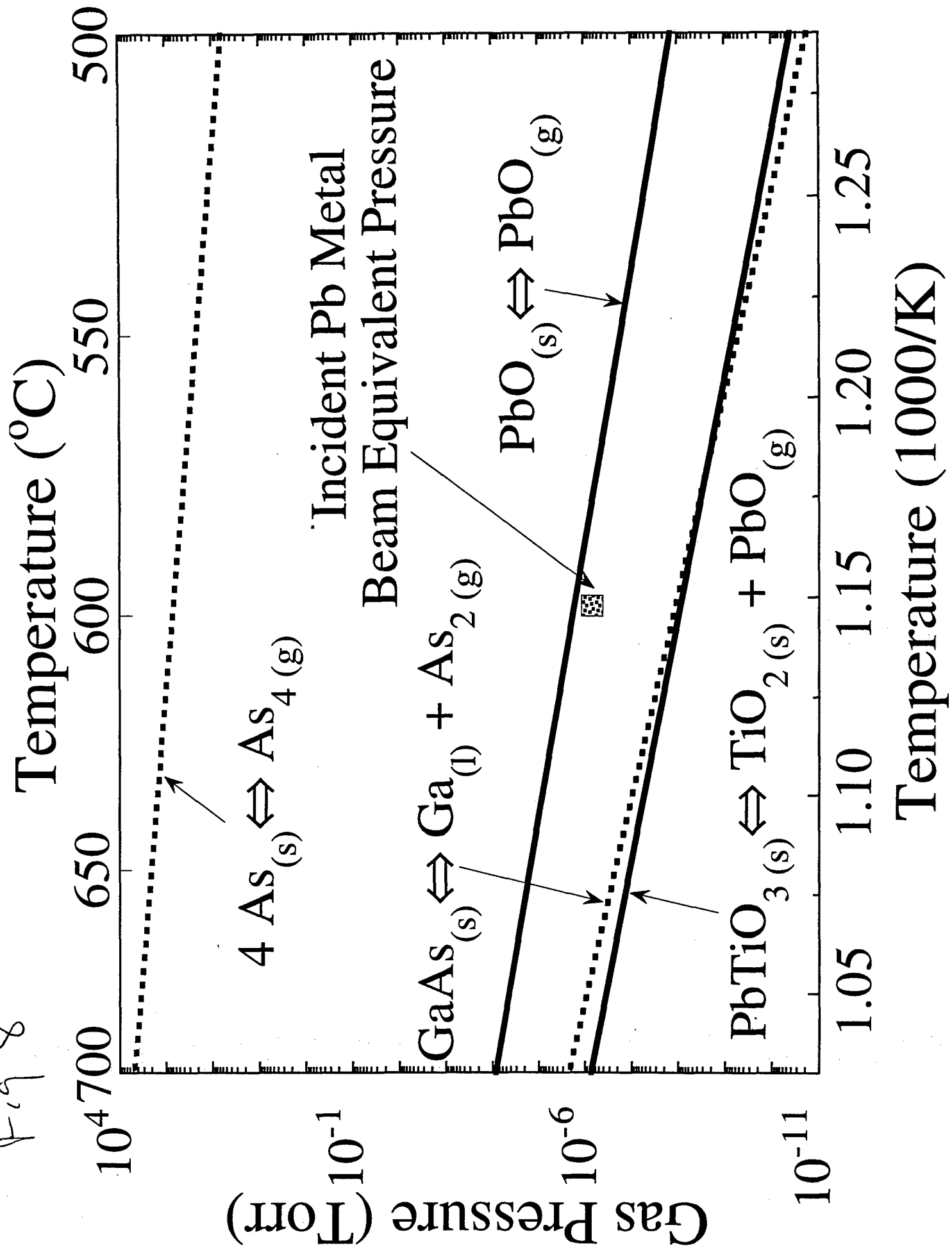


Fig 8



## **The Distribution of Gas Emitted by a Ring-Shaped Orifice in the Molecular Flow Regime**

C. J. Kraisinger and D. G. Schlom

Department of Materials Science and Engineering, The Pennsylvania State University, University Park, Pennsylvania, 16802-5005

(Received

The spatial distribution of gas emitted by a ring-shaped orifice was determined using a photoresist etching technique. The measured distributions were compared to gas flow simulations utilizing the equations developed by Knudsen, Clausing, and others, appropriate to the molecular flow regime. The measured spatial distribution agreed with the simulated results within experimental error and showed the expected change in gas distribution pattern through the same nozzle for two different flow rates, i.e., due to the change in effective nozzle length to diameter ratio that occurs as the flow rate is changed.

For the *in situ* growth of oxides, including superconductors, by reactive molecular beam epitaxy (MBE), it is desired to achieve as high a flux of oxidizing species as possible at the growth surface, and as little as possible elsewhere. A major challenge in using reactive MBE to synthesize cuprate superconductors requiring high oxygen pressures to form (e.g.,  $\text{YBa}_2\text{Cu}_3\text{O}_{7-\delta}$  or even more so for  $\text{Y}_2\text{Ba}_4\text{Cu}_8\text{O}_{16}$ ) lies in locally supplying an oxidizing species of sufficient reactivity to the growing film, in sufficient quantity, while keeping the chamber background pressure low enough so as to not disrupt the beam-like character of the depositing cation species.<sup>1</sup>

To achieve a high localized oxidant pressure in the region desired and minimize it elsewhere within a deposition system, optimized gas injection nozzles are beneficial. Gas flow distributions for simple orifices (e.g., single tubes with different length/diameter ratios) have been measured previously and found to agree well with theory.<sup>2</sup> However, more complicated nozzles, which may be thought of as being comprised of many such simple nozzles, may be more suited for an optimized deposition system. One such more complex geometry that has been widely studied (and utilized for masers) consists of a bundle of closely-packed parallel tubes of small diameter, i.e., a multichannel array.<sup>3-7</sup> Here we report the gas flow distribution through a ring-shaped source that has been optimized for a reactive MBE deposition geometry. The ring is located close to the substrate for efficient gas delivery and the hole in the ring allows the molecular beams coming from the effusion cells to also reach the substrate.

To simulate the gas flow distribution from more complex nozzles (e.g., rings and large tubes) the equations governing gas flow in the molecular flow regime derived by Knudsen,<sup>8</sup> Clausing,<sup>9-11</sup> and others have been implemented in the form of a computer algorithm. This algorithm calculates the superposition of the gas flowing through a combination of simple nozzles equivalent to the complex nozzle under consideration.<sup>12,13</sup> Utilizing such simulations, we optimized the design of a gas delivery nozzle compatible with MBE growth. For the particular chamber under consideration, it was determined that an orifice with its exit slit in the shape of an annulus was optimal. Here we describe measurements of the gas distribution from this ring-shaped nozzle at two different flow rates and compare the results to the simulations.

The inner and outer walls of the ring-shaped nozzle were inclined at 61° to the substrate normal, thus making the nozzle a portion of a truncated cone whose apex would be at the center of the substrate. The ring diameter at the exit end of the nozzle was 2.0 cm, and the width of the orifice slit was 0.76 mm. The gas flow simulations predicted that such a nozzle would achieve the highest possible gas flux efficiency compatible with MBE growth in our chamber geometry, where the efficiency is defined as the fraction of all gas molecules passed into the chamber which impacted the 1 cm<sup>2</sup> substrate area.

As shown in Fig. 1, the simulations predicted that for a gas throughput of 1.9 sccm, the nozzle efficiency was 19.5%. This represents a gain in the ratio of the equivalent gas pressure at the substrate surface to the chamber background pressure (as calculated for the experimental system used, for which the pumping speed was determined to be 340 liters/sec) of 17.8. Note that the emitted gas distribution, efficiency, and pressure gain ratio all have a dependence upon the gas throughput. For the experimental conditions discussed below, at the higher flow rate (which produced Figures 4 and 5(b)), the simulated delivery efficiency is only 19.5% as compared with a calculated efficiency of 20.5% for the lower flow rate (Figures 3 and 5(a)). The calculated pressure gain ratios varied in a similar manner and were 17.6 and 19.2, respectively. Higher flow rates require higher source pressures and result in higher pressures at every point between the entrance and exit ends of the nozzle. Therefore, at higher flow rates the point at which the gas pressure drops into the molecular flow regime (the regime in which the gas flow equations used apply) is closer to the exit end of the nozzle. This results in a lower ratio of the *effective* length (*L*) to diameter (*D*) ratio of the nozzle and therefore a somewhat lower collimating effect upon the gas distribution emitted. The effective length of the nozzle is that portion for which the mean free path of the gas molecules is equal to (or greater than) the remaining distance to the orifice opening.<sup>4</sup> The effective diameter of each simple nozzle making up the ring shaped nozzle was taken to be the width of the opening of the ring-shaped slit.

The method used to measure the spatial distribution of the gas reaching the substrate involves the etching of an initially uniform photoresist layer by an oxidant gas. A patterned photoresist grid

with initially uniform height is exposed to an oxidant (ozone). Measurement of the height of the photoresist grid after exposure to the oxidant reveals the flux distribution. Related methods have been used to measure oxidant gas flux but not its distribution. For example, Yamamoto *et al.*<sup>14</sup> used a photoresist-coated quartz crystal on a quartz crystal monitor (QCM) to determine the total flux of atomic oxygen reaching the QCM. Gregory *et al.*<sup>15</sup> measured the atomic oxygen flux incident upon a graphite surface in earth orbit by measuring the change in resistivity of the graphite as it was oxidized.

Standard photolithographic techniques were used to define a grid of  $200 \mu\text{m} \times 200 \mu\text{m}$  photoresist squares (Hoechst Celanese AZ1805) spaced 1 mm apart on 5 cm diameter silicon wafers. Each wafer was placed on the heating block in the experimental chamber (in the position normally occupied by the substrate) and heated to 600 °C. At 600 °C it was exposed for several minutes to a constant flow rate of ozone gas introduced via the nozzle. (Negligible reaction of the photoresist with ozone gas occurs at less than 400 °C.) After exposure, the heights of more than 900 of the photoresist elements on each wafer were measured using a profilometer.<sup>16</sup>

Figure 2 shows a plot of the gas distribution measured in this way when a flow rate of  $1.3 \times 10^{-2} \text{ Torr}\cdot\ell/\text{s}$  (1.0 sccm) was used, yielding an  $L/D$  quotient of 7.2. Here the image has been inverted to show the depth etched (the gas flux distribution) as a protrusion rather than as a recess. The large amount of noise in the measurement is mainly due to height variations that exist between photoresist elements after spinning, development, and baking. Profile measurements made on one wafer processed like the others (including heating in the chamber to 600 °C), but which was not exposed to ozone gas, revealed a random height variation even between adjacent  $200 \mu\text{m} \times 200 \mu\text{m}$  elements with a standard deviation in the height measurements of about 3.3 nm.

In order to average out some of the noise and enable a better comparison with the simulated gas profiles, the data were replotted after replacing each data point with the average height value of that point and the four nearest neighbor points. The data smoothed in this way are shown in

Figs. 3 and 4 for the low flow rate ( $L/D = 7.2$ ) and the high flow rate ( $9.6 \times 10^{-2}$  Torr·ℓ/s,  $L/D = 2.2$ ) trials, respectively.

Finally, in order to more directly compare the differences between the simulated and the measured gas flux distributions for each of the two flow rate conditions, cross-sectional plots of the radially symmetric simulated distributions were overlaid with a radial average of the measured data. Comparisons are shown in Fig. 5. As can be seen, the averaged cross-sectional profiles of the measured data match the simulated distributions within the experimental error (approximately 3.3 nm). Despite the significant noise in the raw data, the agreement with the predicted spatial distribution of the gas flux is excellent. Indeed this photoresist thickness measuring technique was able to discern the relatively small differences in the flux distributions due to a low flow rate and a flow rate a factor of about 8 higher. The seemingly anomalous points in the center of the experimental cross-sections are due to the fact that at the very center there is no radial averaging.

In summary, we have demonstrated that the distribution of gas emanating from a complex nozzle constructed on the basis of the gas flow equations applicable to the molecular flow regime agree with the expected distributions measured via the etching effect of ozone gas upon a photoresist material. The resolution of the technique is limited by the ability to produce a uniform thickness of the patterned photoresist layer. In the current study, thickness uniformity on the order of  $\pm 3.3$  nm was achieved.

This work was supported by the Office of Naval Research through contract N00014-93-1-0512.

## REFERENCES

- <sup>1</sup> D.G. Schlom and J.S. Harris, Jr., in *Molecular Beam Epitaxy: Applications to Key Materials*, edited by R.F.C. Farrow (Noyes Publications, Park Ridge, NJ, 1995), pp. 505-622.
- <sup>2</sup> H. Cook and E.A. Richley, *Measurements of Efflux Patterns and Flow Rates from Cylindrical Tubes in Free-Molecule and Slip Flows*, NASA Technical Note: NASA TN D-2480, (NASA, Washington, D.C., 1964).
- <sup>3</sup> J.A. Giordmaine and T.C. Wang, *J. Appl. Phys.* **31**, 463 (1960).
- <sup>4</sup> G.R. Hanes, *J. Appl. Phys.* **31**, 2171 (1960).
- <sup>5</sup> R.H. Jones, D.R. Olander, and V.R. Kruger, *J. Appl. Phys.* **40**, 4641 (1969).
- <sup>6</sup> H.C.W. Beijerinck and N.F. Verster, *J. Appl. Phys.* **46**, 2083 (1975).
- <sup>7</sup> L.Y.L. Shen, *J. Vac. Sci. Technol.* **15**, 10 (1978).
- <sup>8</sup> M. Knudsen, *Ann. Phys. (Leipzig)* **31**, 205 (1910).
- <sup>9</sup> P. Clausing, *Ann. Phys. (Leipzig)* **12**, 961 (1932); P. Clausing, *J. Vac. Sci. Technol.* **8**, 636 (1971).
- <sup>10</sup> P. Clausing, *Z. Phys.* **66**, 471 (1930).
- <sup>11</sup> B.B. Dayton, in *1956 National Symposium on Vacuum Technology Transactions*, edited by E.S. Perry and J.H. Durant (Pergamon, London, 1957), pp. 5-11; *Vakuum-Technik* **7**, 7 (1958).
- <sup>12</sup> C.J. Kraisinger, D.M. Fusina, and D.G. Schlom, in: *Epitaxial Oxide Thin Films II* edited by J.S. Speck, D.K. Fork, R.M. Wolf, and T. Shiosaki, Vol. 401 (Materials Research Society, Pittsburgh, 1996), pp. 387-392.
- <sup>13</sup> C.J. Kraisinger, M.S. thesis, The Pennsylvania State University, 1996.
- <sup>14</sup> K. Yamamoto, R.H. Hammond, and J.S. Harris, Jr., *J. Vac. Sci. Technol. A* **9**, 2587 (1991).

<sup>15</sup> J.C. Gregory, G.P. Miller, P.J. Pettigrew, G.N. Raikar, J.B. Cross, E. Lan, C.L. Renschler, and W.T. Sutherland, in *NASA Conference Publication 3275*, Part 3, (NASA, 1993) pp. 957-970.

<sup>16</sup> Alpha-Step 200, Tencor, Inc., Mountain View, CA.

## **FIGURE CAPTIONS**

Fig. 1. Calculated gas flux distribution for the ring-shaped nozzle for a throughput of 1.9 sccm yielding a delivery efficiency upon a  $1 \text{ cm}^2$  substrate of 19.5% and a pressure gain at the substrate of 17.8 over the background pressure.

Fig. 2. A plot of the measured gas flux distribution for a throughput of 1.0 sccm, resulting in  $L/D = 7.2$ .

Fig. 3. A smoothed plot of the measured gas flux distribution shown in Fig. 2 ( $L/D = 7.2$ ).

Fig. 4. A smoothed plot of the measured gas flux distribution for a throughput of 7.6 sccm, resulting in  $L/D = 2.2$ .

Fig. 5. Comparison of the simulated and radially-averaged measured cross-sectional gas distribution profiles (normalized flux units) for (a)  $L/D = 7.2$  (low flow rate); and (b)  $L/D = 2.2$  (high flow rate).

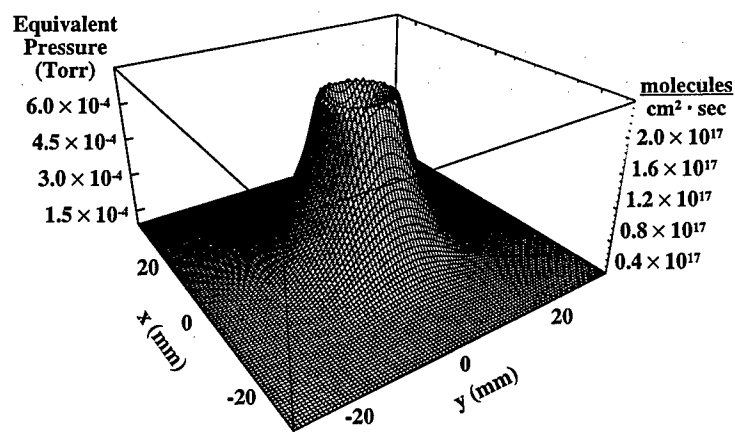


Figure 1

C.J. Kraisinger and D.G. Schлом  
*submitted to JVSTA*

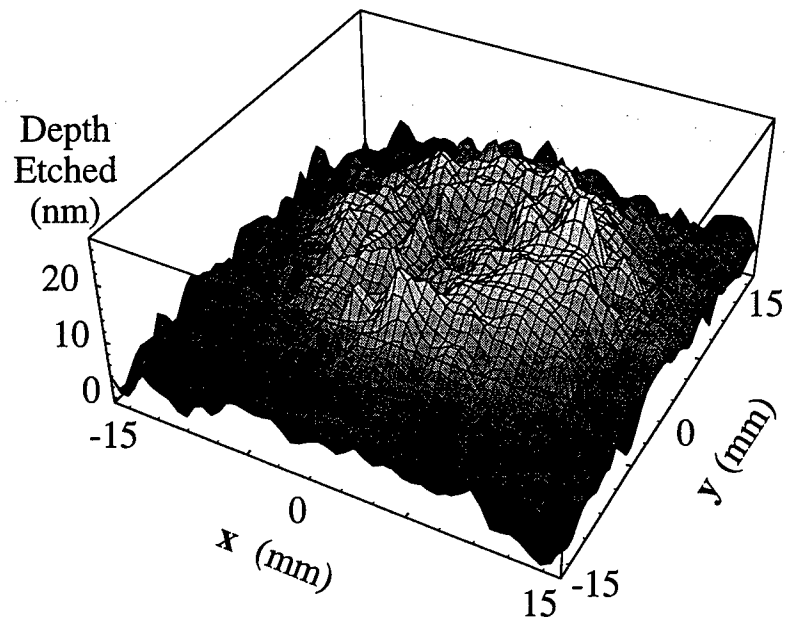


Figure 2

C.J. Kraisinger and D.G. Schlom  
*submitted to JVSTA*

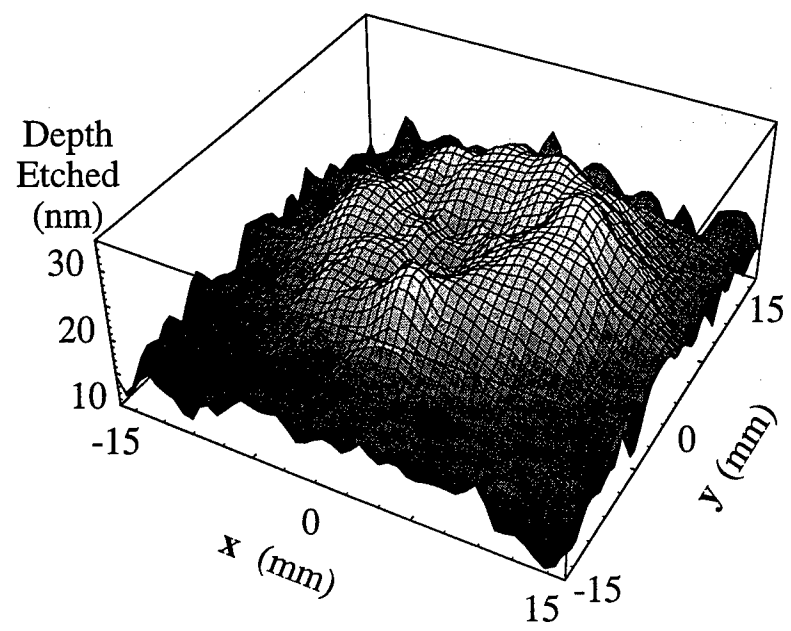


Figure 3

C.J. Kraisinger and D.G. Schlom  
*submitted to JVST A*

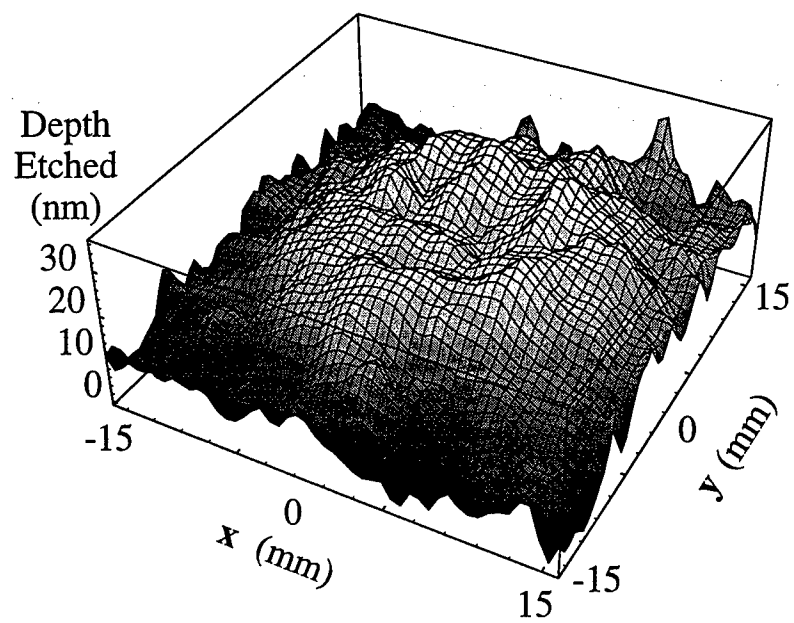


Figure 4

C.J. Kraisinger and D.G. Schlom  
*submitted to JVSTA*

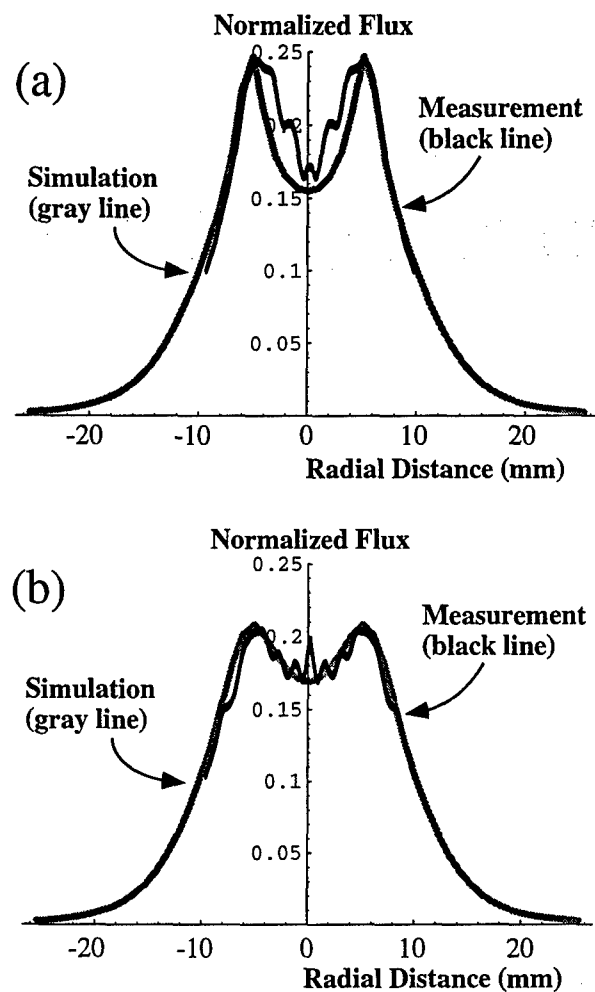


Figure 5

C.J. Kraisinger and D.G. Schlom  
submitted to JVST A

## DEFECT-MEDIATED GROWTH OF $\text{YBa}_2\text{Cu}_3\text{O}_{7-\delta}$ FILMS

D.G. SCHLOM,<sup>†\*</sup> D. ANSELMETTI,<sup>‡\*</sup> J.G. BEDNORZ,<sup>§</sup> CH. GERBER,<sup>§</sup> AND  
J. MANNHART<sup>§</sup>

<sup>†</sup>The Pennsylvania State University, Department of Materials Science and Engineering,  
University Park, PA 16802

<sup>‡</sup>University of Basel, Institute of Physics, Klingelbergstrasse 82, CH-4056 Basel, Switzerland

<sup>§</sup>IBM Research Division, Zurich Research Laboratory, CH-8803 Rüschlikon, Switzerland

### ABSTRACT

The evolution of the surface microstructure of sputtered *c*-axis oriented epitaxial  $\text{YBa}_2\text{Cu}_3\text{O}_{7-\delta}$  films has been monitored by scanning tunneling microscopy (STM). The results indicate that growth is dominated by the incorporation of depositing species at defect sites. These defect sites, which provide energetically favorable positions for accommodating the arriving species, are at ledges—either along growth spirals emanating from screw dislocations, or due to the closely spaced surface steps arising from the macroscopic tilt of the substrate. If the substrate is misoriented sufficiently, the depositing species may diffuse to and be accommodated by these surface steps, without the supersaturation on the terraces attaining a high enough level for two-dimensional nucleation to occur. Under these conditions, growth occurs by step propagation. Otherwise, a high density of screw dislocations ( $\approx 10^9 \text{ cm}^{-2}$ ) is nucleated during the initial stages of growth, which provides a continual supply of ledge incorporation sites in the vicinity of the depositing species. The surface evolution reported appears to be an intrinsic feature of *c*-axis oriented  $\text{YBa}_2\text{Cu}_3\text{O}_{7-\delta}$  films for a wide range of growth conditions, irrespective of the substrate material or vapor phase deposition method.

### INTRODUCTION

Vapor phase deposition techniques have achieved immense success in preparing epitaxial high temperature superconductor thin films with electrical properties superior to those made by bulk synthesis techniques. Such high quality films are produced routinely by a variety of vapor phase deposition methods. Interestingly, these films contain numerous defects, frequently including a high density of screw dislocations ( $10^8\text{-}10^{10} \text{ cm}^{-2}$ ), which have been observed in *c*-axis oriented  $\text{YBa}_2\text{Cu}_3\text{O}_{7-\delta}$  films grown by virtually all vapor deposition growth methods on all of the common substrate materials. For example, high densities of screw dislocations have been observed in films grown by sputtering [1-7], pulsed laser deposition [6-10], thermal evaporation [11], chemical vapor deposition (CVD) [7], and molecular beam epitaxy (MBE) [12,13] on  $\text{SrTiO}_3$  {100} [1,2,5-7,12,13],  $\text{MgO}$  {100} [2,3,6,7,11,13],  $\text{LaAlO}_3$  {100} [9], yttria-stabilized  $\text{ZrO}_2$  {100} [8],  $\text{NdGaO}_3$  {001} [4,13], and  $\text{Mg}_2\text{TiO}_4$  {100} [10]. These screw dislocations not only may be strong vortex pinning sites which enhance the critical current densities of the thin films [14], but also reveal the film growth mechanism [6,15]. Despite the widely varying growth conditions which accompany these different growth methods, the specific conditions used by different research groups, and the range of lattice match, crystal structure, substrate perfection, and surface preparation of these substrates, definite similarities exist in the observed film surface morphologies. These similarities may be readily explained by invoking a common growth mechanism, which will be briefly described here and accounts for the observed microstructure. The present discussion is limited to *c*-axis oriented  $\text{YBa}_2\text{Cu}_3\text{O}_{7-\delta}$  films in which the constituent species are co-deposited; detailed studies on films grown by sequential deposition methods are needed to ascertain how such growth conditions impact the film growth process. Efforts to understand the growth mechanism of oxide superconductor films have substantially profited from STM and AFM images of film surfaces; it was these techniques which first detected the presence of numerous screw dislocations in oxide superconductor films [1,2].

---

\* Work performed while at IBM Research Division, Zurich Research Laboratory, CH-8803 Rüschlikon, Switzerland.

## GROWTH MECHANISM

The presence of a high density of growth spirals emanating from screw dislocations in *c*-axis oriented  $\text{YBa}_2\text{Cu}_3\text{O}_{7-\delta}$  films [1-13,15] indicates that film growth takes place by accommodating species along the spiral shaped step which emanates from each screw dislocation. Surface steps are energetically favorable attachment sites [16]. As growth proceeds, the growth spirals rotate around the screw dislocations at their centers, ascending one layer higher with each rotation. In this manner screw dislocations produce self-perpetuating (spiral-shaped) surface steps. This well-known growth mechanism, first proposed by Frank [17], has been observed for the growth of other *c*-axis oriented layered micaeous materials, and for the growth of the basal plane of many hexagonal materials [18-22].

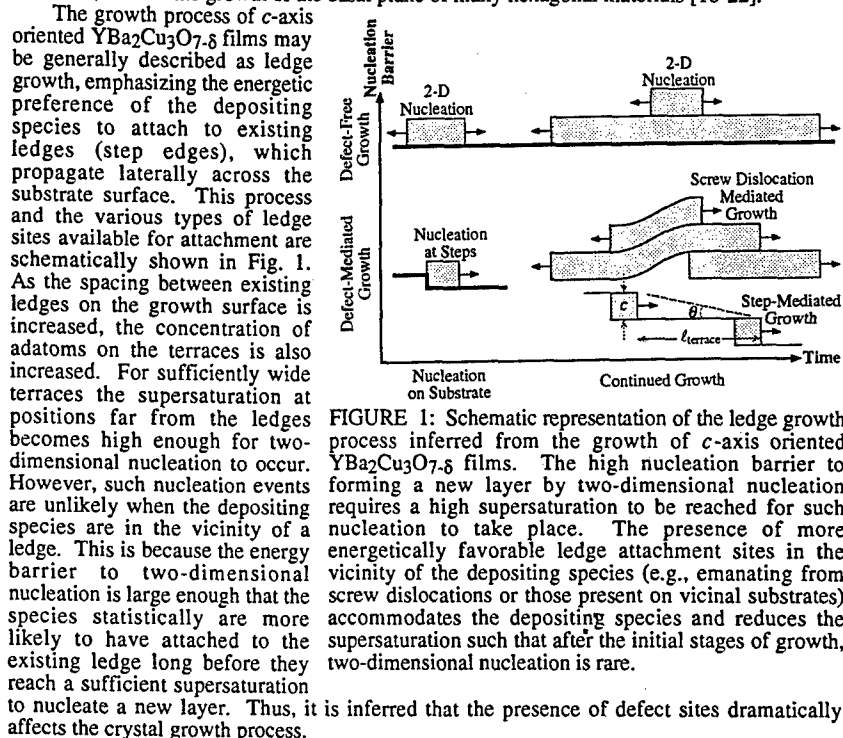


FIGURE 1: Schematic representation of the ledge growth process inferred from the growth of *c*-axis oriented  $\text{YBa}_2\text{Cu}_3\text{O}_{7-\delta}$  films. The high nucleation barrier to forming a new layer by two-dimensional nucleation requires a high supersaturation to be reached for such nucleation to take place. The presence of more energetically favorable ledge attachment sites in the vicinity of the depositing species (e.g., emanating from screw dislocations or those present on vicinal substrates) accommodates the depositing species and reduces the supersaturation such that after the initial stages of growth, two-dimensional nucleation is rare.

At the initiation of growth, the only available ledge sites on a perfect substrate are surface steps. Indeed TEM studies show that the initial nucleation occurs predominantly there [23]. If the substrate is sufficiently well oriented and the substrate temperature low enough that the supersaturation on the terrace can reach the level required for two-dimensional nucleation, growth will take place by the nucleation of new layers (two-dimensional nucleation) in regions far from ledges. However, if a sufficient density of screw dislocations were to be generated (possible mechanisms for which are described below), an endless supply of energetically favorable ledge attachment sites would be available to accommodate the depositing species. Since the observed surface morphologies indicate the presence of high densities of screw dislocations in  $\text{YBa}_2\text{Cu}_3\text{O}_{7-\delta}$  films grown on well oriented substrates, screw dislocation generation clearly has taken place. STM studies [1,6] have revealed the presence of a high density of screw dislocations in films as thin as  $\approx 120 \text{ \AA}$  thick, indicating that the screw dislocations are generated in the initial stages of film growth.

When slightly misoriented from (100), the microscopic surface structure of commonly used substrates consists of a sequence of steps separating (100) terraces. These surface steps are favorable sites for nucleation and subsequent growth [16]. Although the substrate step

height does not match the layer height of  $\text{YBa}_2\text{Cu}_3\text{O}_{7-\delta}$ , a sequence of steps develops, separating (001)  $\text{YBa}_2\text{Cu}_3\text{O}_{7-\delta}$  terraces and accommodating the macroscopic tilt of the substrate. As growth proceeds by the incorporation of the depositing species at these steps, the steps propagate across the film surface. The amount of substrate tilt necessary to achieve growth mainly by this step propagation growth mechanism is presumably that which causes the steps to be spaced sufficiently close together that the depositing species diffuse to and are accommodated by the existing ledges without reaching a supersaturation on the terrace sufficient for two-dimensional nucleation [24]. Experimentally, a cross-over from screw dislocation mediated growth to step propagation has been observed on vicinal  $\text{SrTiO}_3$  (100) surfaces, and the amount of tilt necessary decreases as the growth temperature is increased [6]. This cross-over is shown in Fig. 2 for the sputtered growth of  $\text{YBa}_2\text{Cu}_3\text{O}_{7-\delta}$  on  $\text{SrTiO}_3$  at a substrate block temperature of 750 °C [6]. Under these growth conditions, the transition occurs at about

$\theta_c = 2^\circ$ , which implies an average terrace spacing of about 30 nm. Growth on less vicinal substrates under the same growth conditions results in a comparable terrace spacing ( $\approx 20$  nm [6]) between turns of the growth spirals, as is to be expected for this analogous defect-mediated ledge growth process. With additional data (e.g., the surface free energy and the concentration of adatoms at the ledges) the surface diffusion coefficient may be calculated from this cross-over terrace spacing. However, this spacing alone is insufficient to make such a determination [24]. The influence of substrate orientation on the film growth mechanism explains the apparently disparate results of several studies (in which substrate misorientations were not reported) where nominally identical growth conditions yielded drastically different growth morphologies [3,5].

Reflection high energy electron diffraction (RHEED) intensity oscillations are not expected to occur for growth occurring by the addition of species to established growth spirals or to a propagating sequence of surface steps, since the surface step density is essentially time independent for these growth modes. Indeed, the observation of RHEED intensity oscillations has only been reported [25,26] to occur during the initial stages of growth (for thickness  $\leq 200$  Å for  $\text{YBa}_2\text{Cu}_3\text{O}_{7-\delta}$  films) on bare substrates, indicative of the time necessary for a steady state surface step density to become established. On thicker films, no RHEED intensity oscillations are seen, even if the growth is briefly interrupted [25,26].

### NUCLEATION OF SCREW DISLOCATIONS

An important but so far unresolved issue is the mechanism of nucleation of the screw dislocations. Two likely mechanisms, which have been documented for the growth of other layered micaeous materials [19-22], are (1) the coalescence of two separate growth fronts having vertically offset and inclined surfaces with respect to each other, and (2) the recombination of two branches of a single growth front which became offset in layer height from each other during growth. The ability of  $\text{YBa}_2\text{Cu}_3\text{O}_{7-\delta}$  to flow over irregularities [27] (which can lead to offsets in layer height between coalescing growth fronts and thus the nucleation of screw dislocations) is facilitated by the ledge growth mechanism. The first mechanism of screw dislocation nucleation is likely to occur during the coalescence of the initial nuclei that form on the substrate surface. Obstacles leading to the second mechanism of screw dislocation nucleation may include impurity particles or even steps on the substrate surface. For example, nanometer-size  $\text{Y}_2\text{O}_3$  precipitates with concentrations over two orders of magnitude higher than the surface screw dislocation density have been identified in  $\text{YBa}_2\text{Cu}_3\text{O}_{7-\delta}$  films [28]. These precipitates are of appropriate size and density to give rise to the "holes" observed in STM images [1,6] and to precipitates detected as hillocks in AFM

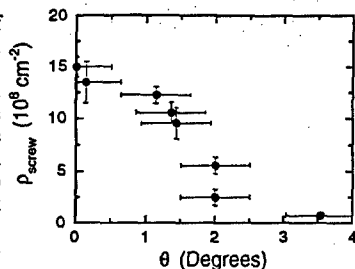


FIGURE 2: Screw dislocation density ( $\rho_{\text{screw}}$ ) as a function of substrate misorientation angle ( $\theta$ ) for sputtered 1000-1500 Å thick  $\text{YBa}_2\text{Cu}_3\text{O}_{7-\delta}$  films grown at  $T_{\text{sub}} = 750$  °C and a growth rate of 0.5-1.8 Å/sec on nominally (100) oriented  $\text{SrTiO}_3$  substrates [6].

studies [29], which have been observed at positions around which the growth fronts have developed branches. In-plane alignment of the coalescing nuclei is necessary for the first nucleation mechanism to occur, and this is made possible by the epitaxial alignment of the individual nuclei to the underlying substrate. TEM and STM images of ultra-thin  $\text{YBa}_2\text{Cu}_3\text{O}_{7-\delta}$  films contain features suggestive of screw dislocation nucleation, consistent with these two nucleation mechanisms [30,31].

## REFERENCES

- [1] Ch. Gerber, D. Anselmetti, J.G. Bednorz, J. Mannhart, and D.G. Schlom, *Nature* **350**, 279 (1991).
- [2] M. Hawley, I.D. Raistrick, J.G. Beery, R.J. Houlton, *Science* **251**, 1587 (1991).
- [3] J. Moreland, P. Rice, S.E. Russek, B. Jeanneret, A. Rosko, R.H. Ono, and D.A. Rudman, *Appl. Phys. Lett.* **59**, 3039 (1991).
- [4] M.E. Hawley, I.D. Raistrick, R.J. Houlton, F.H. Garzon, and M. Piza, *Ultramicroscopy* **42-44**, 705 (1992).
- [5] I. Maggio-Aprile, Å.D. Kent, Ph. Niedermann, Ch. Renner, L. Antognazza, L. Miéville, O. Brunner, J.-M. Triscone, and Ø. Fischer, *Ultramicroscopy* **42-44**, 728 (1992).
- [6] D.G. Schlom, D. Anselmetti, J.G. Bednorz, R.F. Broom, A. Catana, T. Frey, Ch. Gerber, H.-J. Güntherodt, H.P. Lang, and J. Mannhart, *Z. Phys. B* **86**, 163 (1992).
- [7] J. Burger, P. Bauer, M. Veith, and G. Saemann-Ischenko, *Ultramicroscopy* **42-44**, 721 (1992).
- [8] H. Olin, G. Brorsson, P. Davidsson, Z.G. Ivanov, P.-Å. Nilsson, and T. Claeson, *Ultramicroscopy* **42-44**, 734 (1992).
- [9] M. McElfresh, T.G. Miller, D.M. Schaefer, R. Reifenberger, R.E. Muenchhausen, M. Hawley, S.R. Folty, and X.D. Wu, *J. Appl. Phys.* **71**, 5099 (1992).
- [10] H. Haefke, H.P. Lang, R. Sum, H.-J. Güntherodt, L. Berthold, and D. Hesse, *Appl. Phys. Lett.* **61**, 2359 (1992).
- [11] F. Baudenbacher, K. Hirata, P. Berberich, H. Kinder, W. Assmann, and H.P. Lang, *Physica C* **185-189**, 2177 (1991).
- [12] N. Chandrasekhar, V. Agrawal, V.S. Achutharaman, and A.M. Goldman, *Appl. Phys. Lett.* **60**, 2424 (1992).
- [13] H.S. Wang, D. Eissler, W. Dietsche, A. Fischer, and K. Ploog, submitted to *J. Cryst. Growth*.
- [14] J. Mannhart, D. Anselmetti, J.G. Bednorz, A. Catana, Ch. Gerber, K.A. Müller, and D.G. Schlom, *Z. Phys. B* **86**, 177 (1992).
- [15] D.G. Schlom in *International Workshop on Superconductivity Co-Sponsored by ISTEC and MRS: Controlled Growth of Single- and Poly-Crystals of High Temperature Superconductors* (ISTEC/MRS, Honolulu, 1992), p. 34.
- [16] B.K. Chakraverty and G.M. Pound, *Acta Metall.* **12**, 851 (1964).
- [17] F.C. Frank, *Disc. Farad. Soc.* **5**, 48 (1949).
- [18] A.R. Verma, *Crystal Growth and Dislocations* (Butterworths, London, 1953).
- [19] G.G. Lemmllein and E.D. Dukova, *Sov. Phys. Crystallogr.* **1**, 269 (1956).
- [20] M.I. Kozlovskii, *Sov. Phys. Crystallogr.* **3**, 206 (1958).
- [21] M.I. Kozlovskii, *Sov. Phys. Crystallogr.* **3**, 236 (1958).
- [22] A. Baronnet, *J. Cryst. Growth* **19**, 193 (1973).
- [23] M.G. Norton and C.B. Carter, *J. Cryst. Growth* **110**, 641 (1991).
- [24] T. Nishinaga, T. Shitara, K. Mochizuki, and K.I. Cho, *J. Cryst. Growth* **99**, 482 (1990).
- [25] N. Chandrasekhar (private communication) for the growth of  $\text{YBa}_2\text{Cu}_3\text{O}_{7-\delta}$  by MBE.
- [26] T. Frey (private communication) for the growth of  $\text{YBa}_2\text{Cu}_3\text{O}_{7-\delta}$  by PLD.
- [27] See for example, S.K. Streiffer, B.M. Lairson, C.B. Eom, B.M. Clemens, J.C. Bravman, and T.H. Geballe, *Phys. Rev. B* **43**, 13007 (1991).
- [28] A. Catana, R.F. Broom, J.G. Bednorz, J. Mannhart, and D.G. Schlom, *Appl. Phys. Lett.* **60**, 1016 (1992).
- [29] A. Catana, J.G. Bednorz, Ch. Gerber, J. Mannhart, and D.G. Schlom, submitted to *Appl. Phys. Lett.*
- [30] S.K. Streiffer in *Proceedings of the 49th Annual Meeting of the Electron Microscopy Society of America*, edited by G.W. Bailey (EMSA, San Francisco, 1991) p. 1070.
- [31] I. Maggio-Aprile (private communication).

## THERMODYNAMIC STABILITY OF BINARY OXIDES IN CONTACT WITH SILICON

K. J. HUBBARD AND D. G. SCHLOM

The Pennsylvania State University, Department of Materials Science and Engineering,  
University Park, PA, 16802-5005

### ABSTRACT

Using tabulated thermodynamic data, a comprehensive investigation of the thermodynamic stability of binary oxides in contact with silicon at 1000 K was conducted. Reactions between silicon and each binary oxide at 1000 K, including those involving ternary phases, were considered. Sufficient thermodynamic data exists to conclude that all binary oxides except the following are unstable in contact with silicon at 1000 K: Li<sub>2</sub>O, the alkaline earth oxides (BeO, MgO, CaO, SrO, and BaO), the column IIIB oxides (Sc<sub>2</sub>O<sub>3</sub>, Y<sub>2</sub>O<sub>3</sub>, and *Re*<sub>2</sub>O<sub>3</sub> where *Re* is a rare earth), ThO<sub>2</sub>, ZrO<sub>2</sub>, HfO<sub>2</sub>, and Al<sub>2</sub>O<sub>3</sub>. Of these remaining oxides, sufficient thermodynamic data exists to conclude that MgO, CaO, and ZrO<sub>2</sub> are thermodynamically stable in contact with silicon at 1000 K.

### INTRODUCTION

The fabrication of oxide thin-film microstructures on silicon substrates offers tremendous opportunities for the future of microelectronic devices. Such microstructures would allow oxide layers to be fully integrated with silicon circuitry and the broad variety of optical, electronic, and magnetic properties of oxides to be utilized on-chip. If high dielectric constant ( $\epsilon_r$ ) oxides, ferroelectric oxides, high transition temperature ( $T_c$ ) superconducting oxides, or magnetic oxides could be combined with existing semiconductor technology, the materials properties available for use in microelectronics would be drastically enhanced, allowing improved functionality and performance to be realized. Unfortunately, direct growth of these oxides on silicon is frequently accompanied by extensive interdiffusion or chemical reactions that degrade the properties of the oxide, the underlying silicon, or both.<sup>1</sup> Consequently, the focus of a great deal of materials research has been devoted to identifying compatible buffer layers for use between silicon and the desired oxide layers.<sup>2</sup>

Several factors must be considered in selecting materials for use as buffer layers between silicon and a particular oxide: chemical reactions, interdiffusion, thermal expansion match, crystal structure and lattice match are some of the most important.<sup>2</sup> Extensive chemical reaction between the buffer layer material and silicon or between the buffer layer material and the overlying oxide can result in the formation of interfacial phases that often result in a loss of epitaxy. Interdiffusion between silicon, the buffer layer, and the overlying oxide can severely degrade the desired properties of these materials. For example, impurities diffusing into an oxide superconductor film can lower the  $T_c$ , reduce the temperature coefficient of resistivity, and increase the normal-state resistivity. Impurities diffusing into the silicon substrate, especially those that produce deep levels such as the yttrium, barium, and copper constituents of the  $YBa_2Cu_3O_{7-\delta}$  high  $T_c$  superconductor, dramatically alter carrier concentration profiles and lower carrier lifetimes in the silicon.<sup>1</sup> Thermal expansion mismatch must be minimized to prevent cracking due to thermally-induced strains upon cooling after growth, especially if these strains lead to a state of tension in the overgrown oxide films, which is typically the case due to the low thermal expansion coefficient of silicon. In addition, the crystal structure and lattice match between each of the layers must be considered when epitaxy is desired. Ideally a buffer layer for the growth of an oxide on silicon should provide a non-reactive diffusion barrier and a stable nucleation template for the epitaxial growth of the desired oxide.

This contribution addresses the issue of chemical reaction between silicon and binary oxide buffer layers. Specifically the thermodynamic stability of binary oxides in contact with silicon for

potential use as epitaxial buffer layers between silicon and oxide thin-films was examined at 1000 K, since this is a typical deposition temperature for the epitaxial growth of oxides. Most of the binary oxides considered in this comprehensive study were determined to be unstable in contact with silicon and consequently were eliminated. For a great deal of the remaining materials the calculations were unable to be completed due to the lack of thermodynamic data for silicides, ternary phases, or both. These materials could neither be eliminated nor determined to be stable. Existing experimental results indicate that many of these remaining materials are stable in contact with silicon; those that have not been reported warrant experimental investigation. Finally, sufficient data exists to conclude that  $MgO$ ,  $CaO$ , and  $ZrO_2$  are thermodynamically compatible with silicon.

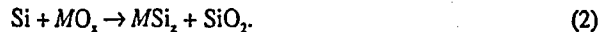
## METHOD

In order to narrow down the list of binary oxides that could be stable in contact with silicon at 1000 K, possible reactions between each binary oxide and silicon, for which thermodynamic data existed, were considered. Any reaction leading to a lowering of the Gibbs free energy of the system ( $\Delta G < 0$ ) allowed the binary oxide to be eliminated from further consideration. This is not to say that the reaction found was the most favorable of all possible reactions, but the identification of any reaction products more stable than silicon in contact with the binary oxide imply that the later interface is thermodynamically unstable. Identification of the most stable reaction products was not our goal, and in many cases cannot be accomplished due to insufficient thermodynamic data. The method employed is the same as that used by Beyers<sup>3</sup> to determine the  $M$ -Si-O phase diagrams for  $M = Ti$  and  $Zr$ . Here it is applied to all elements of the periodic table in order to identify prudent choices of silicon-compatible binary oxides for subsequent experimental studies.<sup>4</sup>

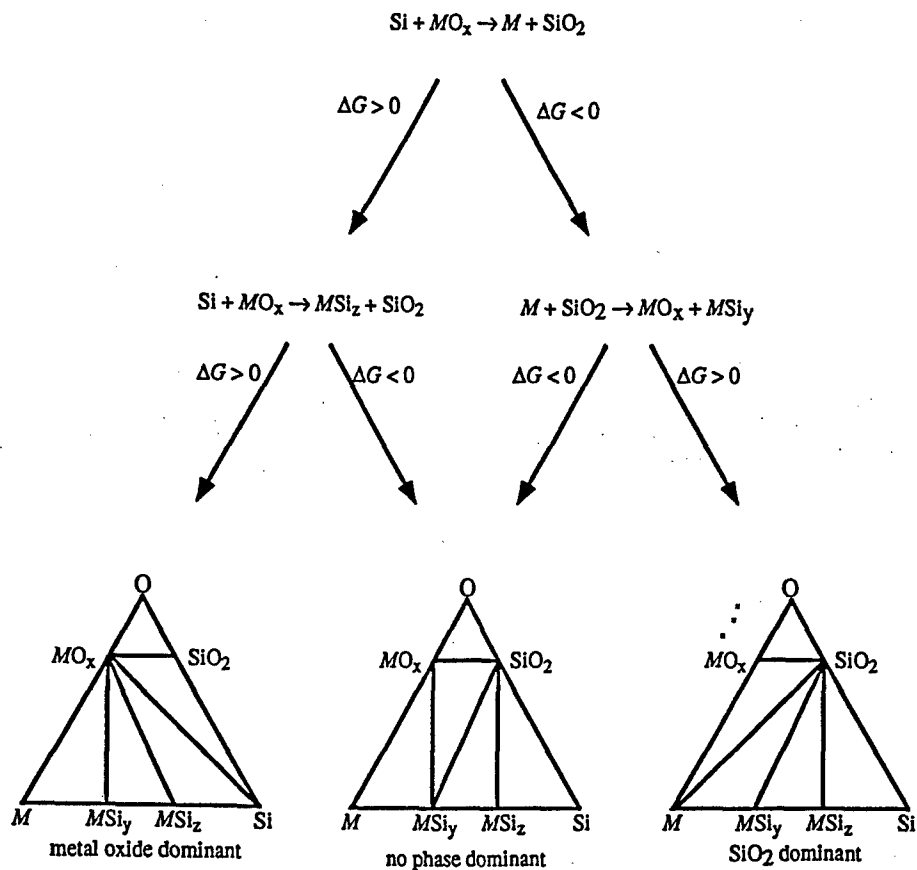
Although there are many possible reactions, several key reactions can be identified by considering the phase diagram of a  $M$ -Si-O system. This phase diagram contains silicon, the binary oxide under consideration,  $MO_x$ , and all the possible products of a reaction between silicon and the binary oxide. In general this phase diagram will contain ternary  $M$ -Si-O phases, but due to the lack of thermodynamic data for ternary phases we first consider the phase diagram of a  $M$ -Si-O system free of ternary phases, as shown at the bottom of Fig. 1.<sup>3</sup> Ti-Si-O is an example of such a system free of ternary phases. For the binary oxide to be stable in contact with silicon, a tie-line must exist between  $MO_x$  and silicon. The existence of such a stable tie-line constrains the rest of the phase diagram, since the crossing of tie-lines is forbidden (a consequence of the Gibbs phase rule). There are only three possible types of  $M$ -Si-O phase diagrams. These are shown at the bottom of Fig. 1 and referred to as "metal oxide dominant," " $SiO_2$  dominant," and "no phase dominant," following the work of Beyers.<sup>3</sup> Note that if the  $M$ -Si-O system contains more than one metal-silicide phase, there will be several phase diagram possibilities within the "no phase dominant" type. In this study we are interested only in the metal oxide dominant-type, since it is the only type having a tie-line between  $MO_x$  and silicon. Thermodynamic data may be used to determine which of these three types of phase diagrams a particular  $M$ -Si-O system belongs to. A reaction flowchart allowing this determination is given in Fig. 1. For the purposes of the present study, any system that fails a reaction along the path to the metal oxide dominant-type system can be eliminated from further consideration. The (unbalanced) reactions along this path are:



and



If an element has multiple silicides, the most silicon-rich silicide ( $MSi_x$ ) should be used in equation (2). Any system that fails ( $\Delta G < 0$ ) equation (1) can be eliminated from further consideration. Any system that passes equation (1), but fails ( $\Delta G < 0$ ) equation (2) can also be eliminated. This conclusion is true even if the  $M$ -Si-O system contains ternary phases, because failing equation (1) or (2) implies that silicon is unstable in contact with the binary oxide.



**Figure 1.** A reaction flowchart showing what two reactions (unbalanced as-shown) can be used to determine which of the three types of phase diagrams a particular  $M\text{-Si}\text{-O}$  system belongs to if the system contains no ternary phases ( $MSi_xO_y$ ).

If the  $M$ -Si-O system contains ternary phases, then after passing equations (1) and (2), further reactions involving ternary products must be tested. In general, the relevant reaction to test is that at the crossing of two potential tie-lines. For the case at hand, the relevant crossing is between the Si- $MO_x$  tie-line with one dictated by the location of the ternary phase(s). If a ternary phase ( $MSi_xO_y$ ) which exists at 1000 K, lies on the tie-line between silicon and the binary oxide ( $MO_x$ ), silicon will not be stable in contact with  $MO_x$  and the system can be eliminated from further consideration. No such examples were found. If all of the ternary phases existing at 1000 K are only on one side or the other of the Si- $MO_x$  tie-line, the relevant reactions depend on which side they occur as shown in Fig. 2. If all of the ternary phases lie above the Si- $MO_x$  tie-line (as shown in Fig. 2a), the relevant reactions are



and

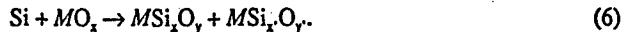


whereas if all of the ternary phases lie below the Si- $MO_x$  tie-line (as shown in Fig. 2b), the relevant reaction is



Equations (3) and (4) only need to be evaluated for those ternary oxides ( $MSi_xO_y$ ) that are positioned such that the triangle  $MSi_xO_y - MO_x - Si - MSi_xO_y$  does not contain any other ternary oxides. Those ternary oxides satisfying this condition are shown as solid dots in Fig. 2a. Equation (3) only needs to be evaluated for the most silicon-rich silicide ( $MSi_x$ ). Only if equations (3) and (4) are passed ( $\Delta G > 0$ ) by all such ternary oxides, can the Si- $MO_x$  tie-line be concluded to be thermodynamically stable. Similarly, equation (5) only needs to be evaluated for those ternary oxides ( $MSi_xO_y$ ) that are positioned such that the triangle  $MSi_xO_y - MO_x - Si - MSi_xO_y$  does not contain any other ternary oxides. The ternary oxides satisfying this condition are shown as solid dots in Fig. 2b. Only if equation (5) is passed ( $\Delta G > 0$ ) by all such ternary oxides, can the Si- $MO_x$  tie-line be concluded to be thermodynamically stable. In this study, no ternary phases of systems that passed equations (1) and (2) lay beneath the Si- $MO_x$  tie-line.

If the  $M$ -Si-O system contains ternary phases on both sides of the Si- $MO_x$  tie-line, the relevant reaction to test is



However, none of the systems that passed equations (1) and (2) were of this type.

## DISCUSSION

All naturally occurring elements ( $M$ ) that form binary oxides ( $MO_x$ ) listed in Ref. 5 were considered in this comprehensive study. Of these, only nonradioactive oxides that exist as solids at 1000 K were pertinent. The thermodynamic stability of each binary oxide in contact with silicon was evaluated using the method described in the previous section. The numerical results of these thermodynamic calculations are given in Ref. 4; here we summarize those results.

Many binary oxides were eliminated from consideration from what limited thermodynamic data exists. Sufficient data exists to conclude that  $MgO$ ,  $CaO$ ,  $ZrO_2$ , and  $SiO_2$  are thermodynamically stable in contact with silicon at 1000 K. There is no thermodynamic data available to show that  $Li_2O$ , the alkaline earth oxides ( $BeO$ ,  $MgO$ ,  $CaO$ ,  $SrO$ , and  $BaO$ ), the column IIIB oxides ( $Sc_2O_3$ ,  $Y_2O_3$ , and  $Re_2O_3$ , where  $Re$  is a rare earth),  $ThO_2$ ,  $ZrO_2$ ,  $HfO_2$ , and  $Al_2O_3$  are not stable in contact with silicon. The native oxide of silicon,  $SiO_2$ , is the trivial case of an oxide that is stable in contact with silicon.  $SiO_2$  might seem like the obvious choice for

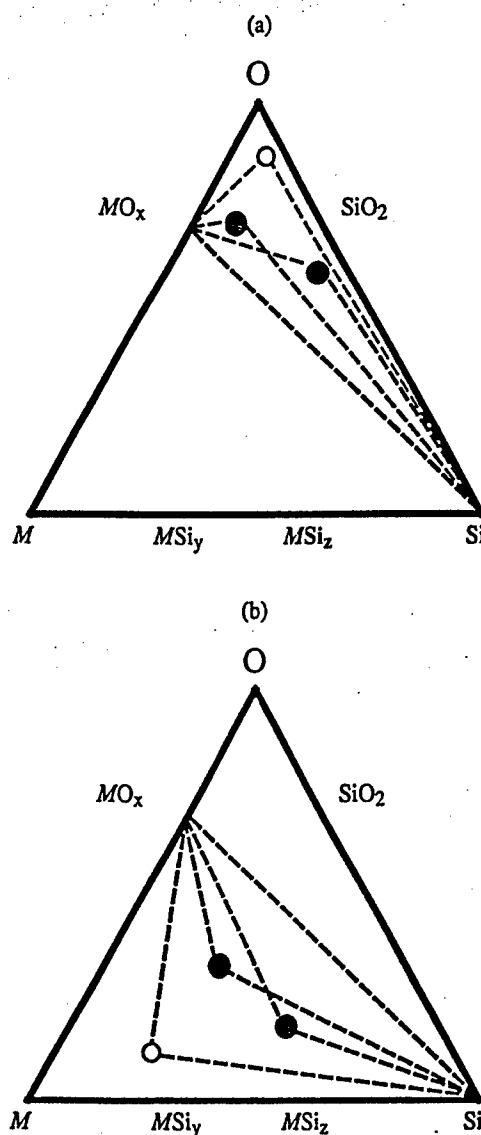


Figure 2.  $M\text{-Si}\text{-O}$  phase diagrams containing one or more ternary phases ( $MSi_xO_y$ , at position of dots) located (a) above the  $\text{Si}\text{-}MO_x$  tie-line and (b) beneath the  $\text{Si}\text{-}MO_x$  tie-line. For case (a) equation (3) should be used to test the stability of the  $\text{Si}\text{-}MO_x$  tie-line with the bold-faced silicide ( $MSi_2$ ) and those ternary phases ( $MSi_xO_y$ ) indicated by a solid dot. For case (b) equation (4) should be used with those ternary phases ( $MSi_xO_y$ ) indicated by a solid dot.

integration of silicon with oxide overlayers, however, the amorphous nature of overgrown  $\text{SiO}_2$  or  $\text{SiO}_2$  formed by the oxidation of silicon makes the growth of epitaxial oxide overlayers on  $\text{SiO}_2$  a formidable obstacle.

#### Comparison to Experimental Observations

The results of this study are remarkably consistent with experimental reports. With the possible exception of  $\text{CeO}_2$ ,  $\text{RuO}_2$ , and  $\text{In}_2\text{O}_3$ , the only binary oxides found to be free of reaction layers with silicon are all among the list of candidate materials identified in this study. A full comparison between the observed results and these thermodynamic calculations is reported elsewhere.<sup>4</sup> The  $\text{RuO}_2/\text{Si}$  interfaces and  $\text{In}_2\text{O}_3/\text{Si}$  interfaces need to be characterized in more detail (e.g., by cross-sectional TEM) before a meaningful comparison can be made. Although from a thermodynamic standpoint the calculations presented show that  $\text{CeO}_2$  is unstable in contact with silicon,  $\text{Ce}_2\text{O}_3$  is potentially stable in contact with silicon. This apparent discrepancy between experimental observation and the present thermodynamic calculations would be absent if at the silicon interface the  $\text{CeO}_2$  is locally reduced to  $\text{Ce}_2\text{O}_3$ , yielding a stable  $\text{Si}/\text{Ce}_2\text{O}_3/\text{CeO}_2$  interface. The integration of several of the candidate materials with silicon, i.e.,  $\text{Li}_2\text{O}$ ,  $\text{Sc}_2\text{O}_3$ , most of the  $\text{Re}_2\text{O}_3$  oxides, and  $\text{HfO}_2$ , has not been experimentally reported and warrants investigation.

#### CONCLUSIONS

Thermodynamic data indicates that  $\text{MgO}$ ,  $\text{CaO}$ , and  $\text{ZrO}_2$  are thermodynamically stable in contact with silicon at 1000 K. There is no thermodynamic data available to show that  $\text{Li}_2\text{O}$ , the alkaline earth oxides ( $\text{BeO}$ ,  $\text{MgO}$ ,  $\text{CaO}$ ,  $\text{SrO}$ , and  $\text{BaO}$ ), the column IIIB oxides ( $\text{Sc}_2\text{O}_3$ ,  $\text{Y}_2\text{O}_3$ , and  $\text{Re}_2\text{O}_3$  where  $\text{Re}$  is a rare earth),  $\text{ThO}_2$ ,  $\text{ZrO}_2$ ,  $\text{HfO}_2$ , and  $\text{Al}_2\text{O}_3$  are not stable in contact with silicon. Of these materials,  $\text{BeO}$ ,  $\text{MgO}$ ,  $\text{CaO}$ ,  $\text{SrO}$ ,  $\text{BaO}$ ,  $\text{Y}_2\text{O}_3$ ,  $\text{PrO}_2$ ,  $\text{Pr}_2\text{O}_3$ ,  $\text{ThO}_2$ ,  $\text{ZrO}_2$ , and  $\text{Al}_2\text{O}_3$  have been integrated with silicon and appear to be free of reaction layers. The remaining materials ( $\text{Li}_2\text{O}$ ,  $\text{Sc}_2\text{O}_3$ , most of the  $\text{Re}_2\text{O}_3$  oxides, and  $\text{HfO}_2$ ) are candidates for future experimental investigations. For the successful integration of oxide overayers (e.g., high  $T_c$  superconductors, ferroelectrics, etc.) on top of the binary oxides identified in this study as being stable or potentially stable in contact with silicon, compatibility between the overlayer and the binary oxide is also necessary. Although such stability was not the subject of this study, the limited number of binary oxides identified as being compatible or potentially compatible with silicon greatly limits the possibilities for a single binary oxide interlayer between the desired overlayer and a silicon substrate.

#### ACKNOWLEDGMENTS

We gratefully acknowledge stimulating discussions with Robby Beyers and the financial support of ONR through contracts N00014-93-1-0512 and N00014-94-1-0690.

#### REFERENCES

- 1 . A. Mogro-Campero, Supercond. Sci. Technol. 3, 155 (1990).
- 2 . E.J. Tarsa, K.L. McCormick, and J.S. Speck in *Epitaxial Oxide Thin Films and Heterostructures*, edited by D.K. Fork, J.M. Phillips, R. Ramesh, and R.M. Wolf (Mater. Res. Soc. Proc. 341, Pittsburgh, PA, 1994) pp. 73-85.
- 3 . R. Beyers, Ph. D. Thesis, Stanford University, 1989, pp. 38-76.
- 4 . K.J. Hubbard and D.G. Schlom, submitted to J. Mater. Res.
- 5 . CRC *Handbook of Chemistry and Physics*, 71st. ed. (CRC Press, Cleveland, 1990/91).

## THERMODYNAMIC STABILITY OF BINARY OXIDES IN CONTACT WITH SILICON

K.J. HUBBARD AND D.G. SCHLOM

The Pennsylvania State University, Department of Materials Science and Engineering,  
University Park, PA, 16802-5005, schlom@ems.psu.edu

### ABSTRACT

Using tabulated thermodynamic data, a comprehensive investigation of the thermodynamic stability of binary oxides in contact with silicon at 1000 K was conducted. Reactions between silicon and each binary oxide at 1000 K, including those involving ternary phases, were considered. Sufficient thermodynamic data exists to conclude that all binary oxides except the following are unstable in contact with silicon at 1000 K: Li<sub>2</sub>O, the alkaline earth oxides (BeO, MgO, CaO, SrO, and BaO), the column IIIB oxides (Sc<sub>2</sub>O<sub>3</sub>, Y<sub>2</sub>O<sub>3</sub>, and Re<sub>2</sub>O<sub>3</sub>, where Re is a rare earth), ThO<sub>2</sub>, UO<sub>2</sub>, ZrO<sub>2</sub>, HfO<sub>2</sub>, and Al<sub>2</sub>O<sub>3</sub>. Of these remaining oxides, sufficient thermodynamic data exists to conclude that BeO, MgO, CaO, and ZrO<sub>2</sub> are thermodynamically stable in contact with silicon at 1000 K. Our results are consistent with reported investigations of silicon/binary oxide interfaces and identify candidate materials for future investigations.

### INTRODUCTION

The fabrication of microstructures containing oxide thin films on silicon substrates offers tremendous opportunities for the future of microelectronic devices. Such microstructures would allow oxide layers to be fully integrated with silicon circuitry and the broad variety of optical, electronic, and magnetic properties of oxides to be utilized on-chip. Unfortunately, the direct growth of oxides on silicon is frequently accompanied by extensive interdiffusion or chemical reactions that degrade the properties of the oxide, the underlying silicon, or both.<sup>1</sup> Consequently, the focus of a great deal of materials research has been devoted to identifying compatible buffer layers for use between silicon and the desired oxide layers.<sup>1,2</sup>

Several factors must be considered in selecting materials for use as buffer layers between silicon and a particular oxide: chemical reactions, interdiffusion, and thermal expansion match are some of the most important.<sup>1-3</sup> In addition, when epitaxy is desired the crystal structure and lattice match between must also be considered.<sup>1-3</sup>

This contribution addresses the issue of chemical reaction between silicon and binary oxide buffer layers. Specifically the thermodynamic stability of binary oxides in contact with silicon for potential use as epitaxial buffer layers between silicon and oxide thin films was examined at 1000 K, since this is a typical deposition temperature for the epitaxial growth of oxides. Reactions involving gaseous species were not considered as it was desired to test the stability of the interface between two solids (silicon and the binary oxide) and there is thus no free volume in which a gas can exist. Most of the binary oxides considered in this comprehensive study were determined to be unstable in contact with silicon and consequently were eliminated. For many of the remaining materials the calculations were unable to be completed due to the lack of thermodynamic data for silicides, ternary phases, or both. These materials could neither be eliminated nor determined to be stable. Existing experimental results indicate that many of these remaining materials are stable in contact with silicon; those that have not been reported warrant experimental investigation. Finally, sufficient data exists to conclude that BeO, MgO, CaO, and ZrO<sub>2</sub> are thermodynamically stable in contact with silicon.

### METHOD

Details of the method employed may be found elsewhere.<sup>4,5</sup> In brief, to narrow down the list of binary oxides that could be stable in contact with silicon at 1000 K, possible reactions between each binary oxide and silicon, for which thermodynamic data existed, were considered. Any reaction leading to a lowering of the Gibbs free energy of the system ( $\Delta G < 0$ ) allowed the binary oxide to be eliminated from further consideration. This is not to say that the reaction found was the

most favorable of all possible reactions, but the identification of any reaction products more stable than silicon in contact with the binary oxide implies that the later interface is thermodynamically unstable. Identification of the most stable reaction products was not our goal, and in many cases cannot be accomplished due to insufficient thermodynamic data.

## RESULTS

All naturally occurring elements,  $M$  (of which there are a total of 90), that form binary oxides,  $MO_x$ , listed in the *CRC Handbook of Chemistry and Physics*<sup>6</sup> were considered in this comprehensive study. Of these, only nonradioactive oxides that exist as solids at 1000 K were pertinent. This constraint led to the elimination of *all* of the binary oxides of 34 elements. Two key (unbalanced) reactions led to the elimination of *all* of the binary oxides of 30 of the remaining 56 elements:

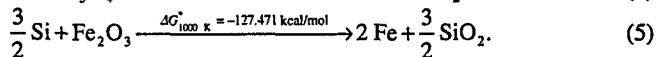
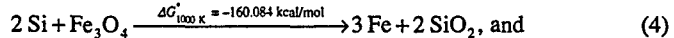
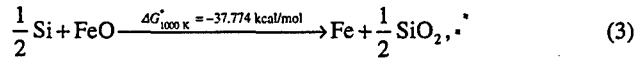


and

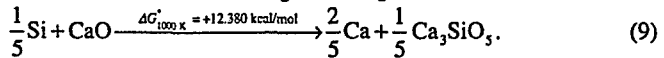
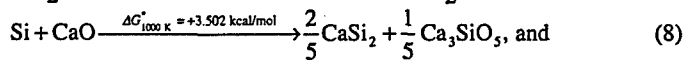
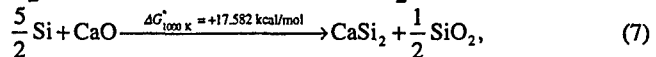
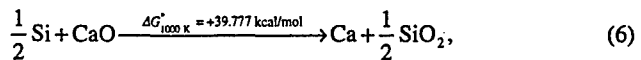


where  $MSi_x$  is the most silicon-rich silicide of the element  $M$ . In addition to these reactions, reactions involving multiple binary oxides and ternary phases were also considered. These led to the elimination of additional binary oxides (but not to the elimination of all the binary oxides of any additional elements) and allowed the stability of four binary oxides to be firmly established from thermodynamic data: BeO, MgO, CaO, and ZrO<sub>2</sub>. For the remaining binary oxides, there is insufficient thermodynamic data to complete the calculations.<sup>5</sup>

These results are graphically summarized on the periodic table shown in Fig. 1. Elements having no suitable or potentially suitable binary oxides are shaded and the reason for their elimination is given. An element is only shaded when *all* of its binary oxides have been eliminated. For example, iron has three binary oxides that are solid at 1000 K: FeO, Fe<sub>3</sub>O<sub>4</sub>, and Fe<sub>2</sub>O<sub>3</sub>.<sup>6</sup> But all of these fail ( $\Delta G < 0$ ) reaction (1) as shown by the following reactions:



This indicates that all of these binary oxides are thermodynamically unstable in contact with silicon and thus Fe appears shaded on the periodic table in Fig. 1. The specific binary oxides remaining after the completion of our thermodynamic analysis are shown in Table I. An example of a binary oxide for which there was sufficient thermodynamic data to complete our calculations and demonstrate its thermodynamic stability in contact with silicon is CaO, as shown below:



Numerical results of all of the thermodynamic calculations are given in Ref. 5.

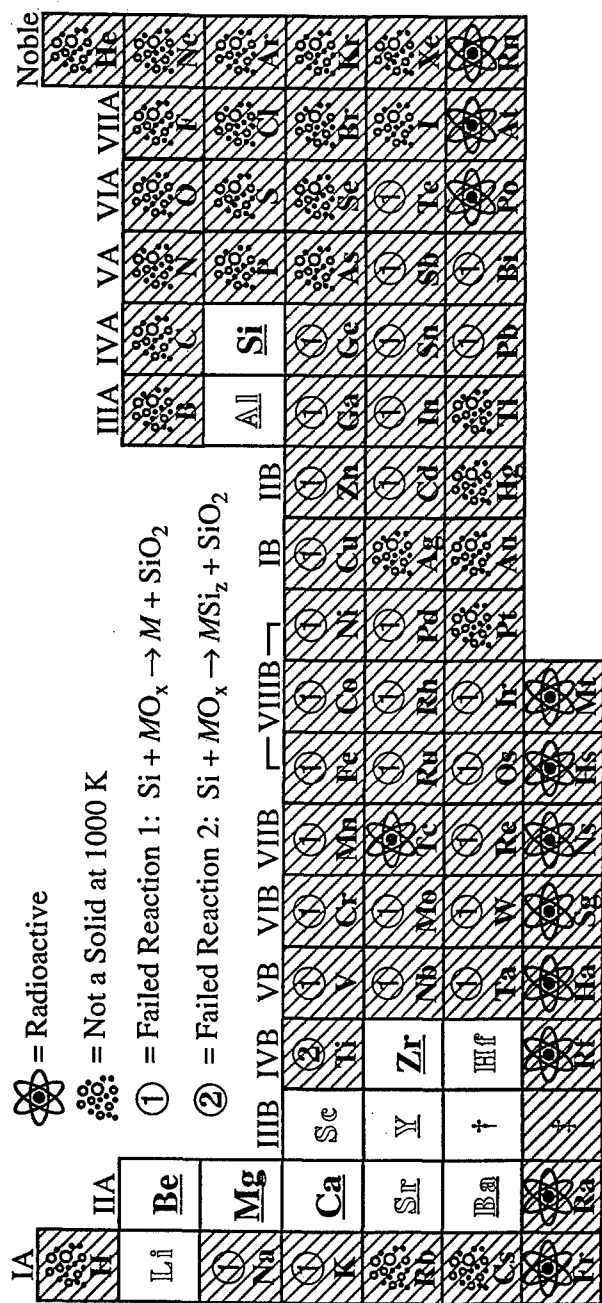


Figure 1: Summary of the results of the thermodynamic calculations.

Insufficient Thermodynamic Data to Complete Calculations

Experimentally Demonstrated

Table I: Summary of the remaining binary oxides that were not able to be eliminated on thermodynamic grounds. These are the only binary oxides that *may* be stable in contact with silicon. Due to the lack of free energy data for relevant silicides, ternary phases, or both, only for a limited number of binary oxides (shown in **bold**) could thermodynamic stability with silicon be concluded.

Oxide	$\Delta G_{1000}^{\circ}$ per $MO_x$ for Reaction 1 <sup>†</sup> (kcal/mol)	$\Delta G_{1000}^{\circ}$ per $MO_x$ for Reaction 2 <sup>‡</sup> (kcal/mol)	$\Delta G_{1000}^{\circ}$ per $MO_x$ for Reaction 8 <sup>§</sup> (kcal/mol)	$\Delta G_{1000}^{\circ}$ per $MO_x$ for Reaction 9 <sup>¶</sup> (kcal/mol)
$Li_2O$	+24.298	†	†	Positive <sup>¶</sup>
$BeO$	+32.365	‡	‡	+14.394 <sup>§</sup>
$MgO$	+30.582	+23.385	+7.951 <sup>§</sup>	+11.589 <sup>§</sup>
$CaO$	+39.777	+17.582	+3.502 <sup>§</sup>	+12.380 <sup>§</sup>
$SrO$	+33.531	†	†	Positive <sup>¶</sup>
$BaO$	+21.338	†	†	Positive <sup>¶</sup>
$Sc_2O_3$	+123.646	+91.297	§	§
$Y_2O_3$	+116.823	†	†§	§
$La_2O_3$	+91.206	+66.372	§	§
$Ce_2O_3$	+104.946	+17.896	§	§
$Pr_2O_3$	+105.768	†	†§	§
$Nd_2O_3$	+102.313	+76.974	§	§
$Sm_2O_3$	+103.941	†	†§	§
$EuO$	+33.238	†	†§	§
$Gd_2O_3$	+105.980	+88.582	§	§
$Tb_2O_3$	+114.762	†	†§	§
$Dy_2O_3$	+112.435	†	†§	§
$Ho_2O_3$	+118.450	†	†§	§
$Er_2O_3$	+122.030	†	†§	§
$Tm_2O_3$	+116.654	†	†§	§
$Yb_2O_3$	+103.830	†	†§	§
$Lu_2O_3$	+116.965	†	†§	§
$ThO_2$	+75.513	†	†§	§
$UO_2$	+43.670	+12.066	§	§
$ZrO_2$	+42.326	+5.914	+1.253 <sup>§</sup>	+19.459 <sup>§</sup>
$HfO_2$	+48.557	†	†§	§
$Al_2O_3$	+63.162	‡	‡	Positive <sup>¶</sup>

<sup>†</sup> Reactions (balanced appropriately)

- 1:  $Si + MO_x \rightarrow M + SiO_x$  at 1000 K
- 2:  $Si + MO_x \rightarrow MSi_x + SiO_x$  at 1000 K
- 8:  $Si + MO_x \rightarrow MSi_x + MSi_xO_y$  at 1000 K
- 9:  $Si + MO_x \rightarrow M + MSi_xO_y$  at 1000 K

<sup>‡</sup> Free energy data for the silicide(s) were unavailable.

<sup>§</sup> No known silicides.

<sup>¶</sup> Free energy data for the relevant ternary phase(s) were unavailable.

<sup>¤</sup> Free energy data for the relevant ternary phase(s) were not available. The free energy change at 1000 K ( $\Delta G_{1000}^{\circ}$ ) for each of the phases for which data were available was positive.

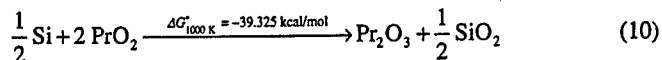
<sup>¤</sup> Free energy data for the relevant ternary phase(s) were available and reactions 8 and 9 were positive in all cases.

<sup>¤</sup> Radioactive, but still considered since thermodynamic data exist.

### Comparison to Experimental Observations

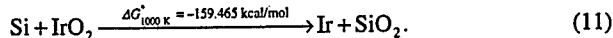
The results of this study are remarkably consistent with experimental reports. With the possible exception of  $\text{PrO}_2$  and  $\text{IrO}_2$ , for which detailed analysis of the interface with silicon is lacking as described below, the only binary oxides found to be free of reaction layers with silicon are all among the list of candidate materials identified in this study. Specifically, those that have been experimentally shown to be stable in contact with silicon are  $\text{BeO}$ ,  $\text{MgO}$ ,  $\text{CaO}$ ,  $\text{SrO}$ ,  $\text{BaO}$ ,  $\text{Y}_2\text{O}_3$ ,  $\text{Ce}_2\text{O}_3$ ,  $\text{Pr}_2\text{O}_3$ ,  $\text{Nd}_2\text{O}_3$ ,  $\text{ThO}_2$ ,  $\text{ZrO}_2$ ,  $\text{Al}_2\text{O}_3$ , and  $\text{SiO}_2$  (the trivial case of a binary oxide that is stable in contact with silicon).<sup>5</sup> The integration of several of the candidate materials with silicon, i.e.,  $\text{Li}_2\text{O}$ ,  $\text{Sc}_2\text{O}_3$ , most of the  $\text{Re}_2\text{O}_3$  oxides, and  $\text{HfO}_2$ , has not been experimentally reported and warrants investigation.

Based on the reaction



we concluded that  $\text{PrO}_2$  is thermodynamically unstable in contact with silicon at 1000 K. Yet Fork *et al.*<sup>7</sup> have grown epitaxial  $\text{PrO}_2$  on silicon at substrate temperatures between 823 K and 923 K. At these lower growth temperatures,  $\Delta G^\circ$  for equation (10) is still negative; in fact, it becomes even more negative than it is at 1000 K. The reported results would be in complete agreement with our thermodynamic analysis if during the initial stages of growth a stable  $\text{PrO}_2/\text{Pr}_2\text{O}_3/\text{Si}$  interface is formed; such a situation is analogous to the unstable  $\text{CeO}_2/\text{Si}$  interface at which<sup>8</sup> interfacial reaction occurs leading to the formation of a stable  $\text{CeO}_2/\text{CeO}_{2-x}$  (or  $\text{Ce}_2\text{O}_3$ )/ $\text{Si}$  interface.<sup>8</sup> Unfortunately, cross-sectional TEM studies of  $\text{PrO}_2/\text{Si}$  interfaces have not been reported.

Using secondary ion mass spectrometry (SIMS) and x-ray diffraction, Nakamura *et al.*<sup>9</sup> recently concluded that the interface between polycrystalline silicon and polycrystalline  $\text{IrO}_2$  is non-reactive at processing temperatures up to 1073 K. Our thermodynamic calculations lead to the opposite conclusion;  $\text{IrO}_2$  fails ( $\Delta G < 0$ ) equation (1) as shown below:



Unfortunately, in the SIMS analysis presented by Nakamura *et al.*,<sup>9</sup> the “ $\text{IrO}_2/\text{Si}$ ” interface occurred at about 0.6  $\mu\text{m}$  below the sample surface, lowering the resolution at which the interface was chemically profiled. Further experimental investigation, e.g., high-resolution TEM, is needed to resolve this discrepancy.

Relatively few examples of reactions of binary oxides with silicon have been reported. This may at first seem surprising considering that the vast majority of binary oxides are unstable in contact with silicon at 1000 K as indicated by Fig. 1, but a non-reactive barrier layer is clearly more newsworthy than a reactive one. What few reports exist, are often relegated to brief remarks or footnotes in the description of an otherwise successful experiment. With the possible exception of  $\text{Gd}_2\text{O}_3$ , all reported reactions (i.e.,  $\text{Gd}_2\text{O}_3$ ,  $\text{SnO}_2$ , and  $\text{PbO}$ ) are in accord with our thermodynamic calculations. Although we were unable to complete our thermodynamic calculations for  $\text{Gd}_2\text{O}_3$  due to the lack of thermodynamic data,  $\text{Gd}_2\text{O}_3$  passed ( $\Delta G > 0$ ) the two reactions for which sufficient data was available (equations (1) and (2)). Tarsa *et al.*<sup>2</sup> suggested that  $\text{Gd}_2\text{O}_3$  reacts with silicon to form  $\text{GdO}_2$ . Unfortunately, we were unable to assess if this reaction is thermodynamically favored due to the absence of thermodynamic data for  $\text{GdO}_2$ .

A thermodynamically equivalent means of showing that a  $M\text{O}/\text{Si}$  interface is unstable is to demonstrate the stability of another interface in the  $M\text{-Si-O}$  phase diagram that would necessarily cross the  $\text{Si}-M\text{O}$  tie-line. For example, a stable  $M/\text{SiO}_2$  interface in a given  $M\text{-Si-O}$  system implies that the  $M\text{O}/\text{Si}$  interface in that system must be unstable, since the crossing of tie-lines is forbidden (a consequence of the Gibbs phase rule). Experiments have shown that the metals Cr, Mo, W, Mn, Fe, Co, Ni, Pd, Pt, and Cu and the silicides  $\text{TiSi}$ ,  $\text{TiSi}_2$ ,  $\text{V}_3\text{Si}$ , and  $\text{TaSi}_2$  are all stable in contact with  $\text{SiO}_2$ . This signifies that the corresponding metal-oxides are all *unstable* in contact with silicon. These results are all in agreement with our thermodynamic calculations.

A full comparison between the observed results and these thermodynamic calculations is reported elsewhere.<sup>5</sup>

## CONCLUSIONS

Thermodynamic data indicates that BeO, MgO, CaO, and ZrO<sub>2</sub> are thermodynamically stable in contact with silicon at 1000 K. There is no thermodynamic data available to show that Li<sub>2</sub>O, the alkaline earth oxides (BeO, MgO, CaO, SrO, and BaO), the column IIIB oxides (Sc<sub>2</sub>O<sub>3</sub>, Y<sub>2</sub>O<sub>3</sub>, and Re<sub>2</sub>O<sub>3</sub> where Re is a rare earth), ThO<sub>2</sub>, UO<sub>2</sub>, ZrO<sub>2</sub>, HfO<sub>2</sub>, and Al<sub>2</sub>O<sub>3</sub> are not stable in contact with silicon. Of these materials, BeO, MgO, CaO, SrO, BaO, Y<sub>2</sub>O<sub>3</sub>, Pr<sub>2</sub>O<sub>3</sub>, Nd<sub>2</sub>O<sub>3</sub>, ThO<sub>2</sub>, ZrO<sub>2</sub>, and Al<sub>2</sub>O<sub>3</sub> have been integrated with silicon and appear to be free of reaction layers. The remaining materials (Li<sub>2</sub>O, Sc<sub>2</sub>O<sub>3</sub>, most of the Re<sub>2</sub>O<sub>3</sub> oxides, and HfO<sub>2</sub>) are candidates for future experimental investigations. An important practical result of our calculations is that *there are not any conducting binary oxides that are thermodynamically stable in contact with silicon at 1000 K.*

A rule of thumb for choosing potential ternary or higher multicomponent oxides for direct integration with silicon is to choose those made of combinations of binary oxides that are all thermodynamically compatible with silicon. Examples that follow this simple guide that have been experimentally demonstrated to be compatible with silicon are yttria-stabilized cubic zirconia (Y<sub>2</sub>O<sub>3</sub>—ZrO<sub>2</sub>), (Ba,Sr)O, LaAlO<sub>3</sub>, ZrSiO<sub>4</sub>, Al<sub>2</sub>BeO<sub>4</sub>, and MgAl<sub>2</sub>O<sub>4</sub>, whereas SrTiO<sub>3</sub> is not.<sup>5</sup>

## ACKNOWLEDGMENTS

We gratefully acknowledge stimulating discussions with Robby Beyers and the financial support of ONR through contracts N00014-93-1-0512 and N00014-94-1-0690.

## REFERENCES

1. D.K. Fork in *Pulsed Laser Deposition of Thin Films*, edited by D.B. Chrisey and G.K. Hubler (Wiley, New York, 1994), pp. 393-415.
2. E.J. Tarsa, K.L. McCormick, and J.S. Speck in *Epitaxial Oxide Thin Films and Heterostructures*, edited by D.K. Fork, J.M. Phillips, R. Ramesh, and R.M. Wolf (Mater. Res. Soc. Proc. 341, Pittsburgh, PA, 1994), pp. 73-85.
3. J.M. Phillips, MRS Bulletin 20, 35 (April 1995); J.M. Phillips, to be published in *Processing and Properties of High T<sub>c</sub> Superconductors, Volume 2: Thin Films*, edited by S. Jin and D.K. Christen (World Scientific).
4. K.J. Hubbard and D.G. Schlom in: *Structure and Properties of Interfaces in Ceramics*, edited by D.A. Bonnell, U. Chowdhry, and M. Rühle, (Mater. Res. Soc. Proc. 357, Pittsburgh, PA, 1995), pp. 331-336.
5. K.J. Hubbard and D.G. Schlom, to be published in J. Mater. Res.
6. *CRC Handbook of Chemistry and Physics*, 71st. ed. (CRC Press, Cleveland, Ohio, 1990/91).
7. D.K. Fork, D.B. Fenner, and T.H. Geballe, J. Appl. Phys. 68, 4316 (1990).
8. H. Nagata, M. Yoshimoto, T. Tsukahara, S. Gonda, and H. Koinuma in *Evolution of Thin-Film and Surface Microstructure*, edited by C.V. Thompson, J.Y. Tsao, and D.J. Srolovitz (Mater. Res. Soc. Proc. 202, Pittsburgh, PA, 1991), pp. 445-450.
9. T. Nakamura, Y. Nakao, A. Kamisawa, and H. Takasu, Appl. Phys. Lett. 65, 1522 (1994); T. Nakamura, Y. Nakao, A. Kamisawa, and H. Takasu, Jpn. J. Appl. Phys. 33, 5207 (1994).

## COMPUTER SIMULATION, DESIGN, AND CHARACTERIZATION OF A NOZZLE FOR MORE EFFECTIVE DELIVERY OF OXIDIZING GASES

C.J. KRAISINGER, D.M. FUSINA, AND D.G. SCHLOM

Department of Materials Science and Engineering, The Pennsylvania State University,  
University Park, PA 16802-5005, krais@pangaea.ems.psu.edu

### ABSTRACT

For the *in situ* growth of cuprate superconductors and related oxides by vacuum deposition methods it is desired to achieve as high a flux of oxidizing species as possible at the growing surface and as little as possible elsewhere within the reaction chamber. The well known gas flow equations derived by Knudsen, Clausing, and others which apply to the molecular flow regime were implemented in a computer algorithm to simulate the gas flow upon a substrate from hypothetical nozzles of several different geometries. The optimal design for a particular MBE chamber and substrate size was determined and such a nozzle was fabricated and characterized. A dysprosium-coated quartz crystal monitor was used to determine the oxidant flux. The measured result matches predictions of the computer model within a factor of three. The computer algorithm was also used to model the spatial distribution of ozone gas through a nozzle of another reported geometry, where measurements of the resulting flux had been made. The shape of the calculated flux distribution agrees to within a few percent and the absolute values of flux reported agree within a factor of two.

### INTRODUCTION

The goals of this study are three-fold: (1) to develop an accurate computer simulation allowing optimization of gas delivery in the MBE growth of oxides; (2) to design, using this computer simulation, the optimal nozzle for our MBE chamber; and (3) to measure the flux distribution and test the predictions of the computer simulation.

If there were no other constraints and it was simply desired that as large a percentage as possible of a gas introduced into a vacuum chamber fell upon a substrate of known size, then a tube with a cross-sectional area the same size as and nearly in contact with the substrate would achieve essentially 100% efficiency. However, subject to the condition that the gas delivery tube must lie outside of the line-of-sight path of a metal flux from an effusion cell (or other source), then 100% efficiency cannot be achieved. In order to obtain the maximum gas delivery efficiency it becomes necessary to use a directed, i.e., collimated, beam of oxidant gas, with the orifice and associated plumbing lying outside the path of the metal flux(es).

The equations governing gas fluences from circular orifices for which the gas pressure is sufficiently low that the gas molecules are far more likely to collide with the walls of the tubing and vacuum chamber than with each other (molecular flow), are well known and were derived by M. Knudsen<sup>1</sup> and P. Clausing.<sup>2</sup> In our computer algorithm we make use of Clausing's extension of the earlier work of Knudsen to include the collimating effect of the length to diameter ratio of a tube (for gas pressure in the molecular flow regime). Examples of the solutions to Clausing's equations for various length/diameter ratios are shown in Fig. 1. Note that this polar plot shows the flux at any angle normalized to that which is projected at 0° (i.e., straight ahead from the nozzle orifice.) Note also that the value of the length used for these calculations is not

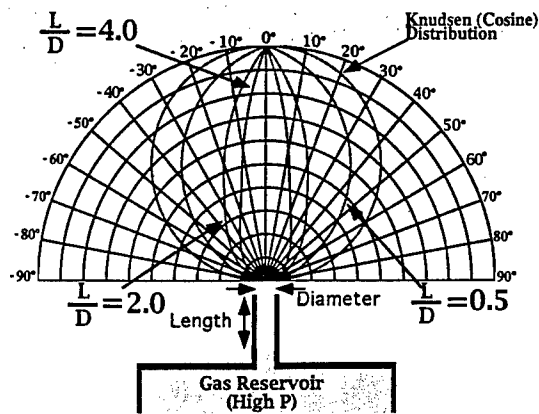


Figure 1. Polar plot showing solutions to Clausing's equations for various length/diameter ratios.

necessarily the total length of the tube, but only that portion of it for which the pressure is low enough that molecular flow prevails.

Three simple geometries of nozzle orifices were considered: a cylindrical tube with a circular orifice, a rectangular cross-section tube, and an annulus or ring-shaped tube. In each case fluences from various sizes of the tubes were simulated. Also varied were the locations of these hypothetical nozzles and especially the angle between the normal to the nozzle orifice and the substrate normal. The two constraints to the geometrical consideration of nozzle direction, shape, size, and placement were that they (1) must not shadow the metal flux flux from our effusion cell having a 3.8 cm diameter mouth located 12.9 cm away inclined  $7^\circ$  from the substrate normal, and (2) cannot be located any nearer than 6 mm from the plane of the substrate. The maximum effective length which determines the Clausing factor, i.e., the degree of collimation of any of the tubes, is given by where inside the tube the mean free path becomes longer than the remaining distance to exit the tube, and thus is a function of the throughput of the tube. All calculations done here are for a throughput of 1.9 sccm and a pumping speed of 1000 liters/second.

The calculation method involves discretizing both the nozzle orifice and the substrate surface into a large number of elements. The Clausing equations are then applied in succession from each nozzle element to each substrate element. The sum of the flux received by each substrate element from all the nozzle elements is determined, and the total flux upon the elements in the plane which make up a  $1 \text{ cm}^2$  substrate is computed. This value is then compared to the values found for hypothetical nozzles having other directions and locations until the maximum in the total flux reaching a  $1 \text{ cm}^2$  is determined. The geometry of the vector algebra definitions used in this algorithm are shown below in Fig. 2. The equations used to calculate the Clausing factor are given in the paper by B.B. Dayton.<sup>3</sup>

## RESULTS AND DISCUSSION

Figures 3 and 4 present the calculated maximum possible flux distributions for a simple cylindrical tube and a ring shaped orifice, respectively, given the aforementioned constraints.

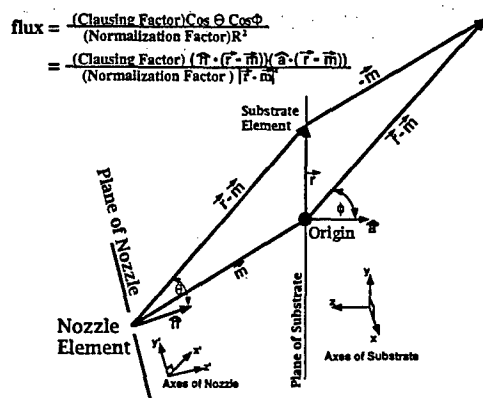


Figure 2. Vector algebra definitions used in the algorithm for flux calculations.

The maximum possible for a rectangular shaped orifice, was in all cases lower than that for a simple cylindrical tube (except when the cross-sectional dimensions are approximately equal in which case the result is little different from that of a tube with a circular cross-section). The vertical scale for both Figs. 3 and 4 are for a throughput of 1.9 sccm and a pumping speed of 1000 liters/sec. The nozzle efficiency, defined as the fraction of all gas molecules to fall upon a  $1 \text{ cm}^2$  region at the centers of Figs. 3 and 4, was calculated to be 12.5% for a simple cylindrical tube and 19.5% for a ring-shaped nozzle. The lowest flux reaching any part of the  $1 \text{ cm}^2$  substrate was calculated to be  $3.99 \times 10^{16} \text{ cm}^{-2} \text{ sec}^{-1}$  for the tube and  $1.13 \times 10^{17} \text{ cm}^{-2} \text{ sec}^{-1}$  for the ring. The ring-shaped nozzle used to generate Fig. 4 is really a portion of a cone with a  $29^\circ$  angle of inclination, such that each orifice element is focussed nearly to the center of the substrate. The overall diameter of the ring orifice is 2.0 cm and the center of the ring is 0.9 cm from the center of the substrate. As this result gives both the highest flux possible upon our substrate as well as a far more uniform distribution than that possible with a simple tube placed to one side of the substrate, a nozzle corresponding to this geometry was fabricated. A cross-sectional schematic of this ring-shaped nozzle is shown as Fig. 5.

The accuracy of the simulated flux distribution (Fig. 4) was tested for the ring-shaped nozzle constructed using a quartz crystal monitor (QCM) technique developed by Matijasevic *et al.*<sup>4</sup> Figure 6 shows the change in mass after introducing O<sub>2</sub> onto a QCM which had been freshly coated with dysprosium metal. The initial slope is about  $5.2 \times 10^{-8} \text{ g/sec}$  and is approximately 62% of the value expected to fall upon the exposed area of the QCM from our computer simulation. Because the position of the quartz crystal monitor in our chamber is not adjustable, it was only possible to measure the flux in this way at the center position in the plane of the substrate. Attempts will be made to measure the flux distribution over a larger area by another technique in the future. The reason for the difference between the simulated value and the value measured using the crystal monitor is not definitely known but may be largely due to the error introduced by the exothermic reaction of metal and oxidant. We have observed during other trials involving deposition of a metal with simultaneous exposure to an oxidizing gas, that more than one hour is often necessary to achieve steady state, i.e., temperature equilibrium, with significant observable (false) mass deviations until steady state is reached. Another limitation is the small time interval over which the "initial" rate of mass change is measured.

We also calculated the expected flux distribution for a simple cylindrical tube 6.3 cm from a substrate as had been constructed and characterized by Kucera *et al.*<sup>5</sup> Figure 7(a) shows the flux

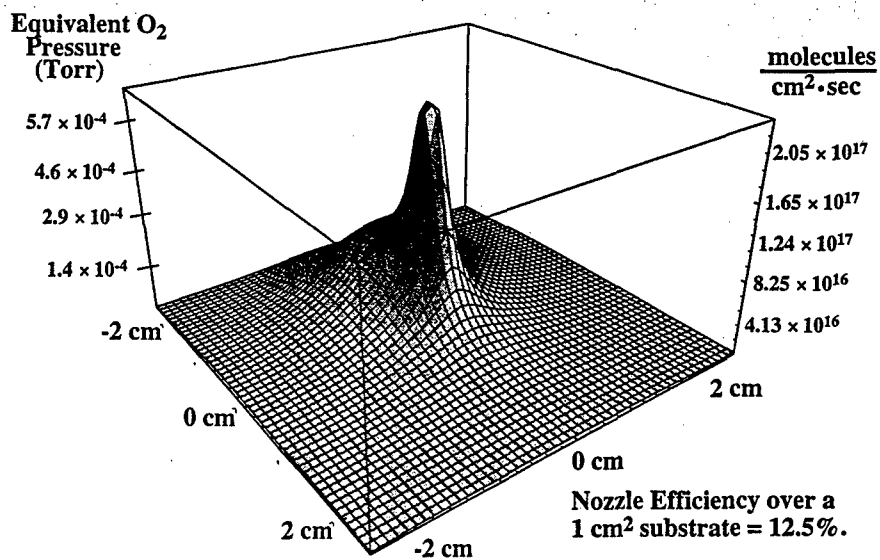


Figure 3. Maximum flux distribution possible from a cylindrical tube(as simulated).  
Vertical axes are based upon a throughput of 1.9 sccm.

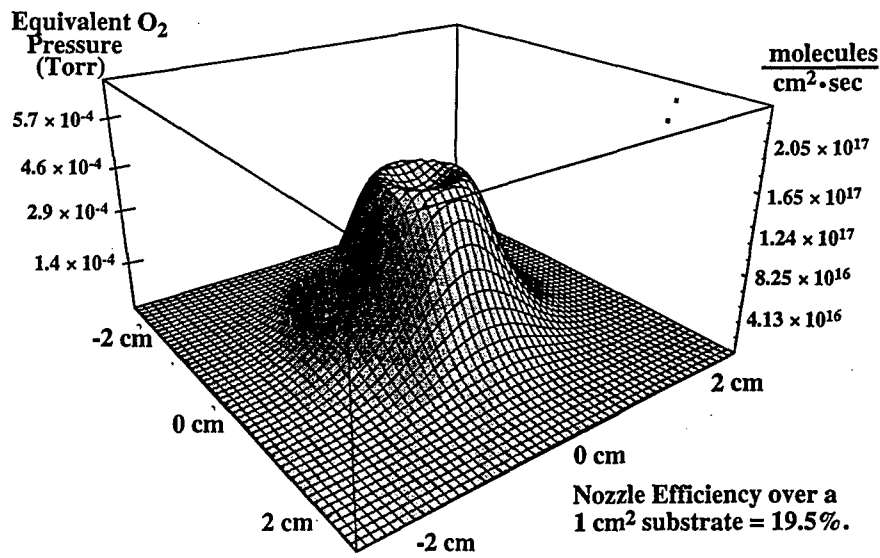


Figure 4. Maximum flux distribution from a ring-shaped nozzle (as simulated).  
Vertical axes based upon throughput of 1.9 sccm.

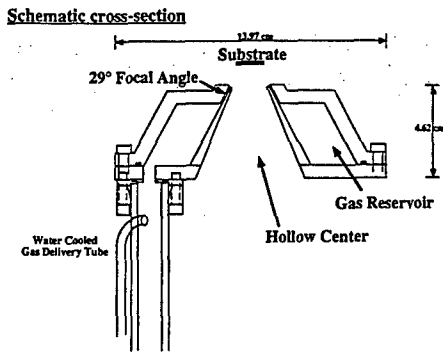


Figure 5. Schematic cross-section of the ring-shaped nozzle which was fabricated and tested based upon the optimized gas delivery simulation shown in Fig. 4.

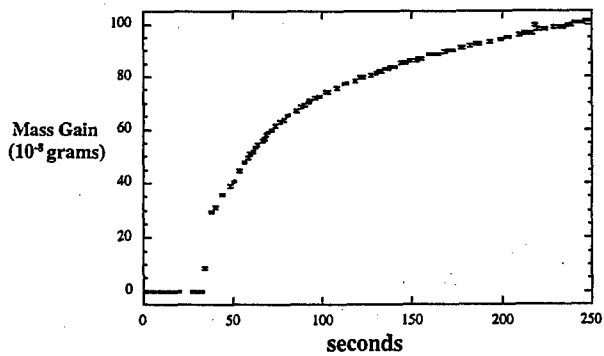


Figure 6. Mass gain recorded upon a QCM freshly coated with dysprosium metal. The oxidizing gas was introduced at  $t = 43$  seconds and the slope suggests a detection of about 62% of the expected gas flux.

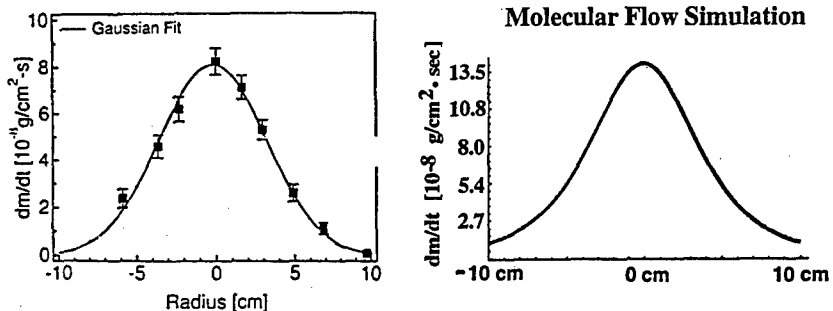


Figure 7(a). Data of Kucera *et al.* (Ref. 4) as measured for ozone upon a QCM from a cylindrical tube 6.3 cm from the plane of the measurement.

Figure 7(b). Simulated result from a tube of the same geometry. Note the vertical scale has been reduced 60% compared with Fig. 7(a).

of ozone at a throughput of 1.9 sccm as measured by Kucera *et al.*<sup>5</sup> upon a moveable QCM. Figure 7(b) alongside shows the corresponding flux distribution expected from our computer simulation. The agreement in shape is excellent, however, our calculation suggests that Kucera *et al.*<sup>5</sup> measured only about 60% of the flux expected at each point. The difference may be due, in part, to the detection efficiency of the QCM technique for measuring ozone and the purity of the ozone used. Kucera *et al.*<sup>5</sup>, reported that the area under the Gaussian curve drawn through their data points represents only 26% of the total throughput assuming the gas was 100% O<sub>3</sub>. The difference between our value (60%) and their reported value (26%) is partly due to their assumption of a Gaussian shape; the tails of our simulated distribution are not Gaussian.

Another factor that may have influenced their measured fluxes is the exothermic reaction of silver with ozone, leading to changes in the temperature and temperature gradient of the QCM. These changes alter the oscillation frequency of the QCM and make the initial mass change inaccurate. To overcome inaccuracies in initial-slope QCM measurements of oxidant flux arising from exothermic oxidation reactions, we will measure the oxidant flux using a steady state method in which the metal and oxidant are codeposited. We have confirmed that the metal flux from our effusion cell is sufficiently stable (stable to better than  $\pm 0.6\%$  per hour after the first two hours at temperature) to utilize this flux measurement method. This will enable us to more accurately determine the oxidant flux passing through our nozzle. In addition, once we establish the oxidant flux, we can pass ozone through this same nozzle to determine the purity of the delivered ozone.

## CONCLUSIONS

Using the gas flow equations applicable to the molecular flow regime, a ring shaped nozzle was calculated to have the greatest efficiency given the geometric constraints of our system. The optimized nozzle design was fabricated and the flux upon a QCM was measured to be within a factor of about two of the expected (simulated) value. The predictions of our gas flow simulations agree well with reported measurements both in magnitude and in shape.

## ACKNOWLEDGEMENTS

We gratefully acknowledge the support provided by the Office of Naval Research under contract N00014-93-1-0512. We also acknowledge the help of Messrs. Ken Biddle, Chris Miller, and Bob Patterson in fabrication of the nozzle, and Peter Rosenthal for the vector algebra algorithm (Fig. 2).

## REFERENCES

1. M. Knudsen, Ann. Physik **28**, 75 (1909).
2. P. Clausing, Ann. Physik **12**, 961 (1932).
3. B.B. Dayton, *1956 National Symposium on Vacuum Symposium Transactions*, Edited by E.S. Perry and J.H. Durant (Pergamon Press, New York, 1956) pp. 5 - 11.
4. V. Matijasevic, E.L. Garwin, and R.H. Hammond, Rev. Sci. Instrum. **61**, 1747, 1990
5. J.T. Kucera, J.D. Perkins, K. Uwai, J.M. Graybeal, and T.P. Orlando, Rev. Sci. Instrum. **62**, 1630, 1991

## EPINTAX OF $\text{PbTiO}_3$ ON (100) $\text{SrTiO}_3$ AND VICINAL (100) $\text{SrTiO}_3$ BY PULSED LASER DEPOSITION

C. D. THEIS AND D. G. SCHLOM

Department of Materials Science and Engineering, The Pennsylvania State University, University Park, PA 16802-5005, theis@ems.psu.edu

### ABSTRACT

Epitaxial  $\text{PbTiO}_3$  films have been grown on (100)  $\text{SrTiO}_3$  substrates by pulsed laser deposition. X-ray diffraction analysis indicates pure *c*-axis oriented  $\text{PbTiO}_3$  films with a rocking curve FWHM of 0.25° for the 002 reflection. Thicker films (~ 2000 Å) grown on 4° miscut  $\text{SrTiO}_3$  show mixed *a*-axis and *c*-axis  $\text{PbTiO}_3$  due to twinning along {011} planes. The [100] axis of the *a*-axis domains are misoriented by 3.4° - 3.8° toward <001> substrate directions with respect to the substrate normal. In contrast to growth on well-oriented (100)  $\text{SrTiO}_3$  surfaces where the four equivalent tilts of the [100] axis of the *a*-axis domains are equally likely, on vicinal  $\text{SrTiO}_3$  the *a*-axis domains are preferentially oriented (~ 90 vol. %) in an uphill direction with respect to the miscut substrate.

### INTRODUCTION

$\text{PbTiO}_3$  has become an extensively studied ferroelectric material. It has a variety of potential applications including ultrasonic sensors, infrared detectors, and ferroelectric random access memories.<sup>1</sup> Growth of  $\text{PbTiO}_3$  has been hampered by problems with lead volatility.<sup>2,3</sup> However, high quality films have been made by MOCVD,<sup>4</sup> laser ablation,<sup>5</sup> sputtering,<sup>6</sup> and through the use of solution precursors.<sup>2</sup> We have been able to grow  $\text{PbTiO}_3$  films with excellent phase purity and crystallinity by laser ablation using a lead-rich target. Paramount to the growth of well-oriented  $\text{PbTiO}_3$  has been careful control of the substrate temperature. The extreme volatility of lead has given us a small (< 20° C) window where stoichiometric  $\text{PbTiO}_3$  has been realized.<sup>6</sup> On the cold side of this window we see evidence of lead-rich phases ( $\text{PbO}$ , the litharge polymorph). On the other hand, lead-poor phases are present ( $\text{PbTi}_3\text{O}_7$  and  $\text{TiO}_2$ , the anatase polymorph) when a stoichiometric  $\text{PbTiO}_3$  target is employed.

### EXPERIMENTAL

$\text{PbTiO}_3$  targets (2.5 cm diameter) are synthesized in-house using a traditional ceramic synthesis route. Powders of  $\text{PbO}$  and  $\text{PbTiO}_3$  are ball milled in water for 36 hours using Darvan C as a dispersant. The mixture is then dried and pressed in a uniaxial press to 1500 psi (10 MPa) in order to achieve sufficient green strength to transport the pellet to a cold isostatic press. The pellet is then cold isostatic pressed to 40,000 psi (276 MPa). Sintering occurs in a lead-rich atmosphere (to prevent lead loss) at 770° C for 4 hours. Using this synthesis route we are able to achieve densities in excess of 98% of theoretical while minimizing lead loss (< 0.5% by weight).

Figure 1 shows a schematic of our film deposition system. The rotating target is ablated by a 248 nm KrF excimer laser. The substrate is radiatively heated by an alumina furnace with a Kanthal<sup>®</sup> A-1 heating element which surrounds the substrate and allows for easy switching between off-axis and on-axis geometries. Typical deposition temperatures for  $\text{PbTiO}_3$  are 630° C - 640° C using  $\text{SrTiO}_3$  (100) and vicinal (100)  $\text{SrTiO}_3$  single crystal substrates. In a typical growth, the substrate is located 6-7 cm from the target in an oxygen/ozone (~ 5%  $\text{O}_3$ ) ambient of 5-30 mTorr. The laser is focused to achieve an energy density of 2 J/cm<sup>2</sup> with a repetition frequency of 20-30 Hz.

The targets have a 60% to 40% molar ratio of  $\text{PbTiO}_3$  to  $\text{PbO}$ , respectively. This excess lead content enables us to grow stoichiometric  $\text{PbTiO}_3$  by adjusting the temperature to achieve a ~ 1:1 ratio of Pb to Ti in the depositing films.<sup>6</sup>

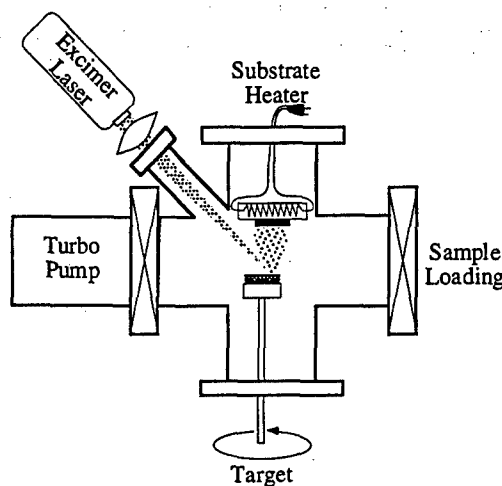


Fig. 1. A schematic of the laser ablation setup

## RESULTS AND DISCUSSION

The presence of  $\text{PbTiO}_3$  grains oriented with their  $a$ -axis perpendicular to the (100)  $\text{SrTiO}_3$  substrate ( $a$ -axis oriented  $\text{PbTiO}_3$ ) mixed with grains oriented with their  $c$ -axis perpendicular to the substrate ( $c$ -axis oriented  $\text{PbTiO}_3$ ) have been seen in films grown from solution precursors,<sup>2</sup> and grown by MOCVD<sup>8</sup> and laser ablation.<sup>9</sup> Seifert *et al.*<sup>2</sup> reported a relative tilt of  $3.5^\circ$  between the [100] axis of  $a$ -oriented  $\text{PbTiO}_3$  grains and the [001] axis of  $c$ -oriented  $\text{PbTiO}_3$  grains caused by twinning along {011} planes. Similarly, Li *et al.*<sup>8</sup> saw a  $3.0^\circ$  tilt of the  $a$ -axis of  $a$ -oriented  $\text{PbTiO}_3$  grains away from the substrate normal. They reported that below a thickness of 150 nm, the x-ray intensity associated with the  $a$ -axis oriented  $\text{PbTiO}_3$  domains disappears<sup>8</sup> indicating that thinner films are completely  $c$ -axis oriented. Films thicker than 150 nm grown on (100)  $\text{SrTiO}_3$  display mixed  $a$ -axis and  $c$ -axis orientation.<sup>8</sup> Hsu and Raj<sup>9</sup> report a relative tilt of  $2.65 \pm 0.5^\circ$  of the  $a$ -axis of  $a$ -oriented  $\text{PbTiO}_3$  grains away from the (100)  $\text{SrTiO}_3$  substrate normal. This tilt angle remains independent of thickness from 50 to 350 nm, and the volume fraction of  $a$ -oriented material increases continuously as a function of thickness.<sup>9</sup> Below a thickness of 37 nm they report that there are no longer  $a$ -oriented domains present based on x-ray diffraction analysis.<sup>9</sup> TEM studies of the  $\text{PbTiO}_3$ /substrate interface have shown that the domain boundaries begin at the interface and extend into the film.<sup>2,8,10,11</sup> The importance of this observation will be discussed in conjunction with the structure of thick  $\text{PbTiO}_3$  on vicinal ( $4^\circ$  miscut) (100)  $\text{SrTiO}_3$ .

Figure 2 shows the x-ray diffraction pattern of a 400 Å thick  $\text{PbTiO}_3$  film deposited on (100)  $\text{SrTiO}_3$  by  $90^\circ$  off-axis PLD. Intense  $00\ell$  peaks indicate that the film is pure  $c$ -axis oriented  $\text{PbTiO}_3$ ; additional scans show that no other orientations are present. The rocking curve FWHM of the  $\text{PbTiO}_3$  002 reflection is measured to be  $0.25^\circ$  showing excellent out-of-plane alignment. Figure 3 is an azimuthal scan ( $q$ -scan) of the 101 reflections of this same film. The peaks show a cube-on-cube orientation with a FWHM of  $0.4^\circ$  in  $\phi$ , indicating little variation in the in-plane alignment. These peak widths are all comparable to the instrument resolution of our Picker 4-circle diffractometer. This film contains no  $a$ -axis grains caused by {011} twin boundaries in agreement with the findings for epitaxial  $\text{PbTiO}_3$  films grown on (100)  $\text{SrTiO}_3$  by MOCVD.<sup>8</sup>

Figure 4(a) shows the x-ray scan of a 2000 Å thick film of  $\text{PbTiO}_3$  grown on a  $4^\circ$  miscut  $\text{SrTiO}_3$  substrate using on-axis PLD. The vicinal (100) substrate was misoriented by  $4^\circ$  toward [001]. The  $c$ -axis is slightly, but resolvably ( $0.1^\circ$ ), misoriented from the substrate normal. The scan shows good out-of-plane orientation with a rocking curve FWHM of  $0.35^\circ$  for the  $\text{PbTiO}_3$  002 reflection. The peaks at  $\omega = +3.4^\circ$  and  $\omega = -3.8^\circ$  in figure 4(b) show the presence of  $a$ -oriented

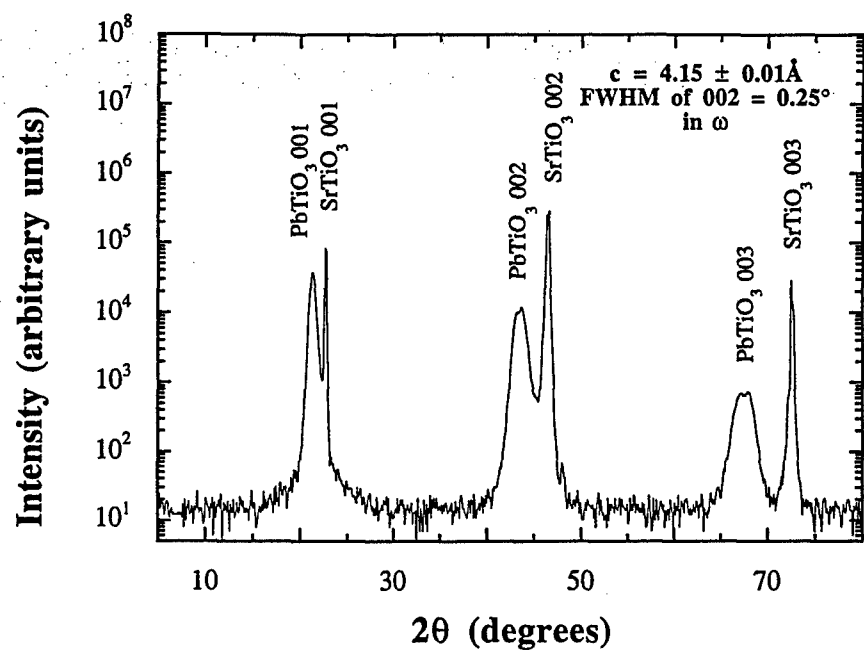


Fig 2.  $\theta$ - $2\theta$  scan of a 400  $\text{\AA}$  thick film of  $\text{PbTiO}_3$  on a (100)  $\text{SrTiO}_3$  substrate

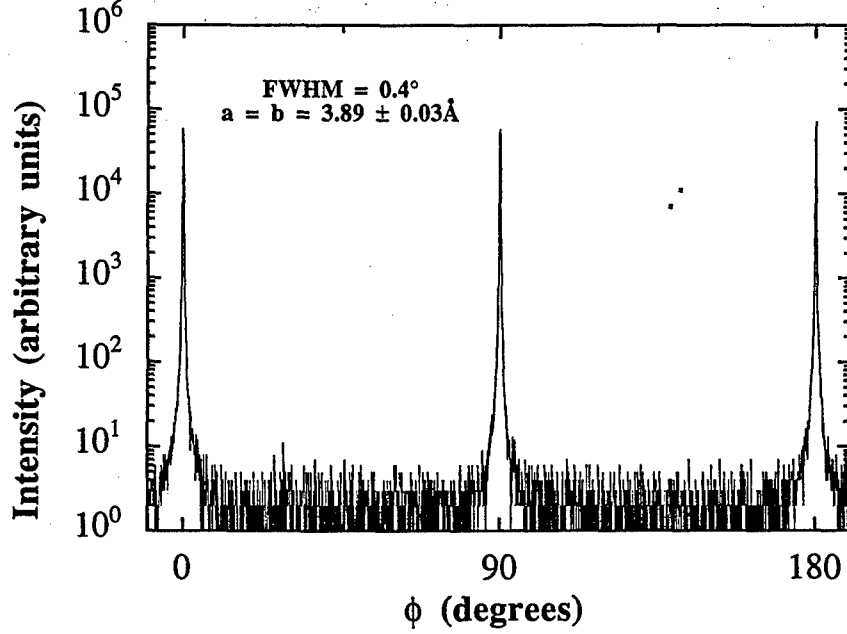


Fig. 3. Azimuthal scan of a 400  $\text{\AA}$  thick  $\text{PbTiO}_3$  film; 101  $\text{PbTiO}_3$  reflections

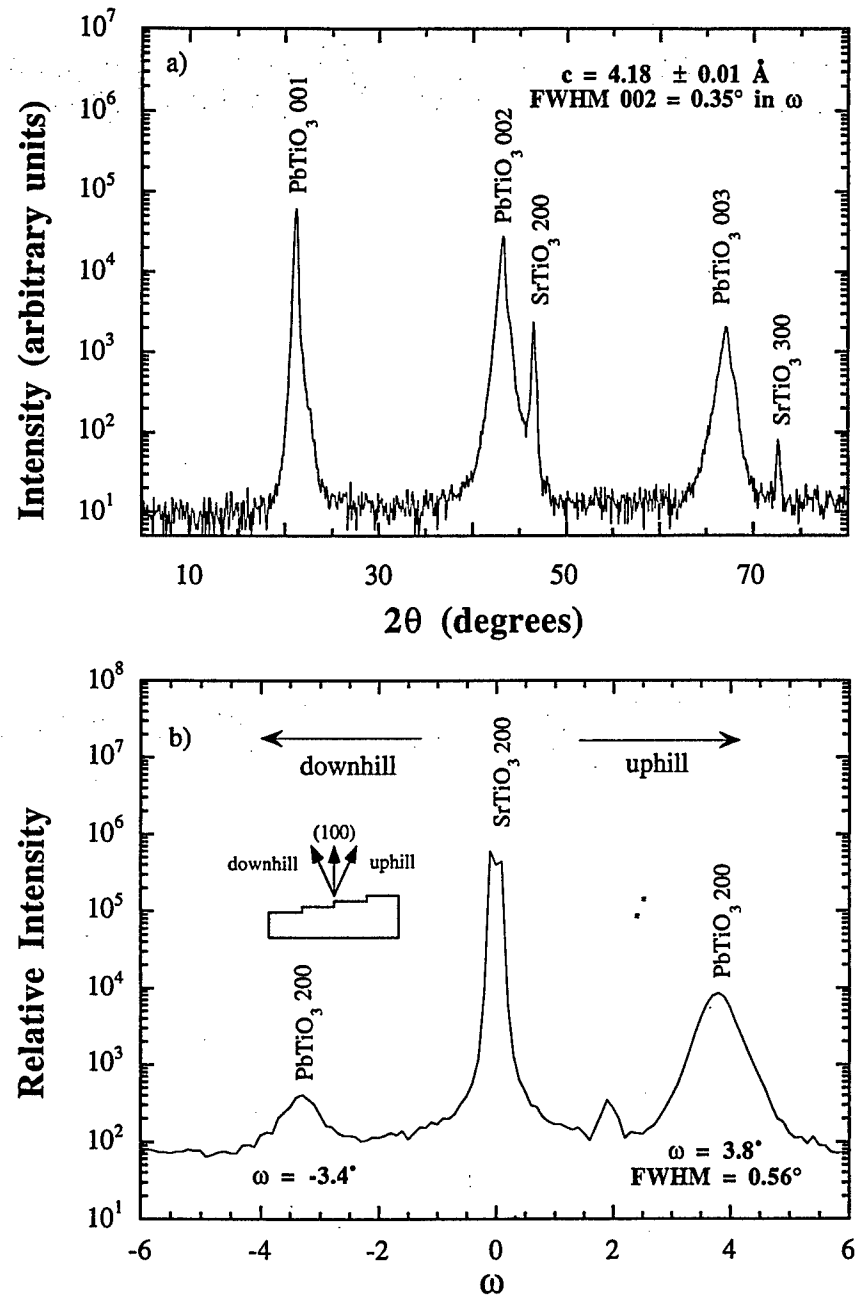


Fig. 4: (a)  $\theta$  -  $2\theta$  scan of a 2000 Å thick film of  $\text{PbTiO}_3$  on vicinal (mis cut  $4^\circ$  from (100))  $\text{SrTiO}_3$ , (b) Rocking curve of the  $\text{SrTiO}_3$  200 reflection showing  $a$ -axis  $\text{PbTiO}_3$  preferentially oriented "uphill"

$\text{PbTiO}_3$  grains. The offset in  $\omega$  is caused by  $\sim 90^\circ$  domain boundaries along  $\{011\}$  planes.<sup>2,8</sup> From the integrated x-ray intensity it is evident that the  $a$ -axis  $\text{PbTiO}_3$  domains have a smaller volume fraction than the  $c$ -axis domains. The  $a$ -axis is preferentially tilted "uphill," as defined by the macroscopic tilt of the substrate surface with respect to the  $(100)$   $\text{SrTiO}_3$  plane and schematically indicated in Fig. 4(b). The tilt of the  $a$ -axis grains has been previously described as a geometrical consequence of the large  $\sim 1.06 c/a$  ratio in  $\text{PbTiO}_3$ .<sup>2,8</sup> Because  $\text{SrTiO}_3$  has 4-fold rotational symmetry, we see four directions of  $a$ -axis tilt following the four equivalent  $\{011\}$  twin planes. Based on x-ray diffraction integrated intensity, 90 volume percent of the  $a$ -axis material is tilted uphill, 4% tilts downhill, and 3% is tilted toward each of the non-tilted directions of the substrate (toward  $[010]$  and  $[0\bar{1}0]$ ). This is in contrast to the equally likely (i.e., four peaks of equal intensity)  $\{011\}$  twin boundaries previously reported in  $\text{PbTiO}_3$  films grown on well-oriented  $(100)$   $\text{SrTiO}_3$  substrates.<sup>2,8</sup>

The preferential orientation of the  $a$ -axis  $\text{PbTiO}_3$  domains can be explained by lattice matching considerations. As the film growth temperature is well above the Curie temperature ( $490^\circ \text{C}$  for bulk  $\text{PbTiO}_3$ ), twinning of the  $\text{PbTiO}_3$  must occur during cooling following film growth. The  $\langle 100 \rangle$  directions of the  $\text{SrTiO}_3$  substrate — both the in-plane directions of the  $(100)$   $\text{SrTiO}_3$  surface as well as those of the integral-unit cell high step edges — are much better lattice matched to the  $a$ -axes of  $\text{PbTiO}_3$  than to its  $c$ -axis. Consequently, as schematically depicted in figure 5, it is energetically favorable for the regions of the  $\text{PbTiO}_3$  film in contact with the  $\{100\}$   $\text{SrTiO}_3$  surfaces to be  $\{001\}$   $\text{PbTiO}_3$  surfaces. Such an orientational relationship provides excellent lattice matching between the in-plane  $\langle 100 \rangle$   $\text{SrTiO}_3$  directions and the in-plane  $[100]$  and  $[010]$   $\text{PbTiO}_3$  directions.

## PbTiO<sub>3</sub> film

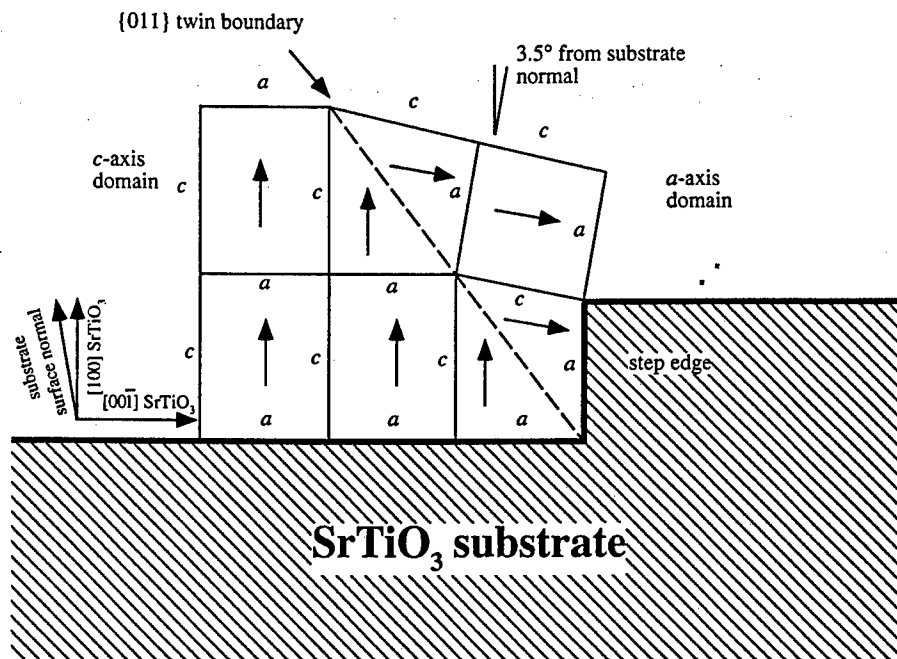


Fig. 5. Schematic showing how the presence of step edges on a vicinal  $(100)$   $\text{SrTiO}_3$  substrate may lead to the preferred nucleation of a  $\{011\}$  twin boundary. The arrows indicate the direction in which the  $c$ -axis lies. The tetragonality of  $\text{PbTiO}_3$  has been exaggerated for clarity.

An interesting situation arises at the step edge. Here, the favorable lattice match of (001) PbTiO<sub>3</sub> to *both* the SrTiO<sub>3</sub> terrace and to the SrTiO<sub>3</sub> step edge results in a (101) twin boundary. Other workers have shown that the introduction of domain boundaries in PbTiO<sub>3</sub> films grown on SrTiO<sub>3</sub> is favored to reduce strains that arise from the PbTiO<sub>3</sub> phase transition and differences in thermal expansion between the film and substrate upon cooling.<sup>12,13</sup> Step edges are an energetically favorable place for these twin boundaries to intersect the substrate.

On well-oriented (100) SrTiO<sub>3</sub> surfaces there is not a dominance of any step edge, and all four types of {011} twin boundaries occur with equal likelihood. However, the vicinal (100) SrTiO<sub>3</sub> surface contains a dominant step edge direction and the corresponding (101) twin boundary dominates as is schematically shown in figure 5. The tetragonality of PbTiO<sub>3</sub> has been exaggerated in this figure to clearly illustrate the geometrical cause of the 3.5° tilt of the *a*-axis of PbTiO<sub>3</sub> with respect to the crystallographic normal. This explanation is consistent with our observation that a preferred orientation of *a*-domains is found *only* on vicinal substrates. This indicates that the phenomenon is related to a dominance in the direction of the steps on the SrTiO<sub>3</sub> substrate.

## CONCLUSIONS

We have grown high quality epitaxial PbTiO<sub>3</sub> films on (100) SrTiO<sub>3</sub> and vicinal (100) SrTiO<sub>3</sub> by pulsed laser deposition. A lead-rich target was employed to eliminate problems with lead volatility. By locating a narrow temperature window where there exists a ~ 1:1 Pb to Ti ratio in as-deposited films, we have grown thin (< 500 Å) PbTiO<sub>3</sub> films that are completely *c*-axis oriented and have narrow rocking curve widths. Similarly, high quality thick films (~ 2000 Å) have been grown on vicinal (4° miscut) (100) SrTiO<sub>3</sub> substrates with *a*-axis and *c*-axis PbTiO<sub>3</sub> domains present. The *a*-axis PbTiO<sub>3</sub> domains are preferentially oriented in an uphill direction with respect to the miscut substrate.

## ACKNOWLEDGMENTS

We gratefully acknowledge Y. Hou at AT&T Bell Laboratories for the RBS composition analysis and the financial support of the Office of Naval Research through grant N00014-94-1-0690.

## REFERENCES

1. J. F. Scott and D. A. Paz de Araujo, *Science* **246**, 1400 (1989).
2. A. Seifert, F. F. Lange, and J. S. Speck, *J. Mater. Res.* **10**, (1995).
3. K. Iijima, I. Ueda, and K. Kugimiya, *Jpn. J. Appl. Phys.* **30**, 2149 (1991).
4. Y.-F. Chen, T. Yu, J.-X. Chen, L. Shun, P. Li, and N.-B. Ming, *Appl. Phys. Lett.* **66**, 148 (1995).
5. H. Tabata, O. Murata, T. Kawai, S. Kawai, and M. Okuyama, *Appl. Phys. Lett.* **64**, 428 (1994).
6. Although 4-circle x-ray diffraction indicates that these films are phase-pure PbTiO<sub>3</sub>, composition analysis by Rutherford backscattering spectrometry (RBS) indicates that even such single-phase films have a Pb/Ti ratio of 1.10 to 1.15.
7. Kanthal is a registered trademark of Kanthal AB, Sweden.
8. Z. Li, C. M. Foster, D. Guo, H. Zhang, G. R. Bai, P. M. Baldo, and L. E. Rehn, *Appl. Phys. Lett.* **65**, 1106 (1994).
9. W.-Y. Hsu and R. Raj, *Appl. Phys. Lett.* **67**, 792 (1995).
10. S. Stemmer, S. K. Streiffer, F. Ernst, M. Ruhle, W.-Y. Hsu, and R. Raj, *Solid State Ionics* **75**, 43 (1995).
11. S. Stemmer, S. K. Streiffer, W.-Y. Hsu, F. Ernst, R. Raj, and M. Ruhle, *J. Mater. Res.* **10**, 791 (1995).
12. J. S. Speck and W. Pompe, *J. Appl. Phys.* **76**, 466 (1994).
13. W. Pompe, X. Gong, Z. Suo, and J. S. Speck, *J. Appl. Phys.* **74**, 6012 (1993).

## SIZE EFFECTS AND DOMAINS IN FERROELECTRIC THIN FILM ACTUATORS

S. TROLIER-MCKINSTRY, C. A. RANDALL, J. P. MARIA, C. THEIS, D. G. SCHLOM, J. SHEPARD Jr., and K. YAMAKAWA

Department of Materials Science and Engineering and Intercollege Materials Research Laboratory, Pennsylvania State University, University Park, PA 16802

### Abstract

Ferroelectric thin films typically differ from bulk ceramics in terms of both the average grain size and the degree of stress imposed on the film by the substrate. Studies on bulk ceramics have demonstrated that the number of domain variants within grains depends on the grain size for sizes  $<\sim 1\mu\text{m}$ . This can diminish the poling efficiency of the material. Since most thin films show primary grain sizes well below a micron, similar effects should be observed in films. In addition, since the perovskite ferroelectrics contain ferroelastic as well as ferroelectric domains, it seems clear that stress in thin films may markedly alter the degree to which domain walls contribute to the observed properties. In this paper, the relative importance of these factors are discussed for several types of ferroelectric thin films. Films have been prepared by pulsed laser deposition, magnetron sputtering, and by sol-gel processing. It has been found that epitaxial  $\text{BaTiO}_3$  films are ferroelectric at 77K down to thicknesses as low as  $\sim 60\text{nm}$ . Data on the low and high field electrical properties are reported as a function of temperature, the film crystallinity, and film thickness for representative perovskite films.

### INTRODUCTION

This paper discusses the role that size effects and domains have in contributing to the properties of ferroelectric thin films. Here, size effect will be used to describe any change on the properties of the ferroelectric associated with a decrease in dimension. The paper will be broken down into 5 sections: 1) a review of size effects in bulk PZT materials, 2) a description of size effects in laser-ablated  $\text{BaTiO}_3$  thin films, 3) a description of domains in  $\text{PbTiO}_3$  on miscut substrates, 4) an introduction to the effect of in-plane stress on polycrystalline thin films, and finally, 5) a review of phase switching  $\text{PbZrO}_3$  films which may be useful in high strain actuators.

### SIZE EFFECTS IN LEAD ZIRCONATE TITANATE CERAMICS

In considering the role that size plays in controlling the properties of thin films, it is important to examine what is known regarding the role of size in bulk ceramic materials. In polycrystalline  $\text{Pb}(\text{Zr}_{1-x}\text{Ti}_x)\text{O}_3$  (PZT) ceramics, it is well known that in addition to the intrinsic response of the material which would be expected for a single domain specimen, there is a significant contribution to the observed dielectric constant,  $\epsilon_r$ , due to domain wall motion. As described by Zhang et al.,<sup>1</sup> soft PZT compositions show a significant enhancement in the room temperature dielectric constant due to mobile domain walls, over either hard PZTs or the phenomenological prediction of properties (which includes no domain wall contributions). As the temperature is decreased to 0K, the domain wall motion is frozen out, and the properties of all the PZTs converge. Similar behavior was shown for the piezoelectric coefficients,<sup>1</sup> where non 180° twin walls were shown to contribute roughly one-half of the room temperature piezoelectric properties of soft PZTs. Thus, in describing size effects in ferroelectrics, it is important to consider the roles of both intrinsic and domain wall contributions to the properties.

An excellent example of this is discussed in the work of Kim *et al.* on grain size effects in PZT ceramics.<sup>2</sup> In that work, fine-grained Nb-doped PZT ceramics were prepared by a reactive calcination route combined with hot pressing. This resulted in ceramics with clean grain boundaries and sharp phase transitions. With decreasing particle size, these materials showed a decrease in the poled dielectric constant measured at 300K for grain sizes  $<\sim 1\mu\text{m}$ , while  $\tan\delta$  rose. On the other hand, much less size dependence was observed at 10K, where domain wall contributions are largely frozen out. Thus, it appears that as grain size is decreased in PZT

ceramics, there is less domain wall contributions to the properties than is observed in larger grained ceramics of the same composition. Two factors were investigated to account for this. Fig. 1 shows the changes in the lattice parameters of tetragonal PZT ceramics with grain size. It is clear that both the unit cell volume and the tetragonality decrease at grain size below  $\sim 1 \mu\text{m}$ . Similar behavior was observed in rhombohedral compositions. In contrast, fine powders with the same particle sizes show no decrease in the spontaneous strain, implying that the three-dimensional residual stresses in the polycrystalline ceramic are responsible for the size dependent changes. Since the spontaneous polarization is tied to the distortion in the unit cell, this should result in some size dependent properties.

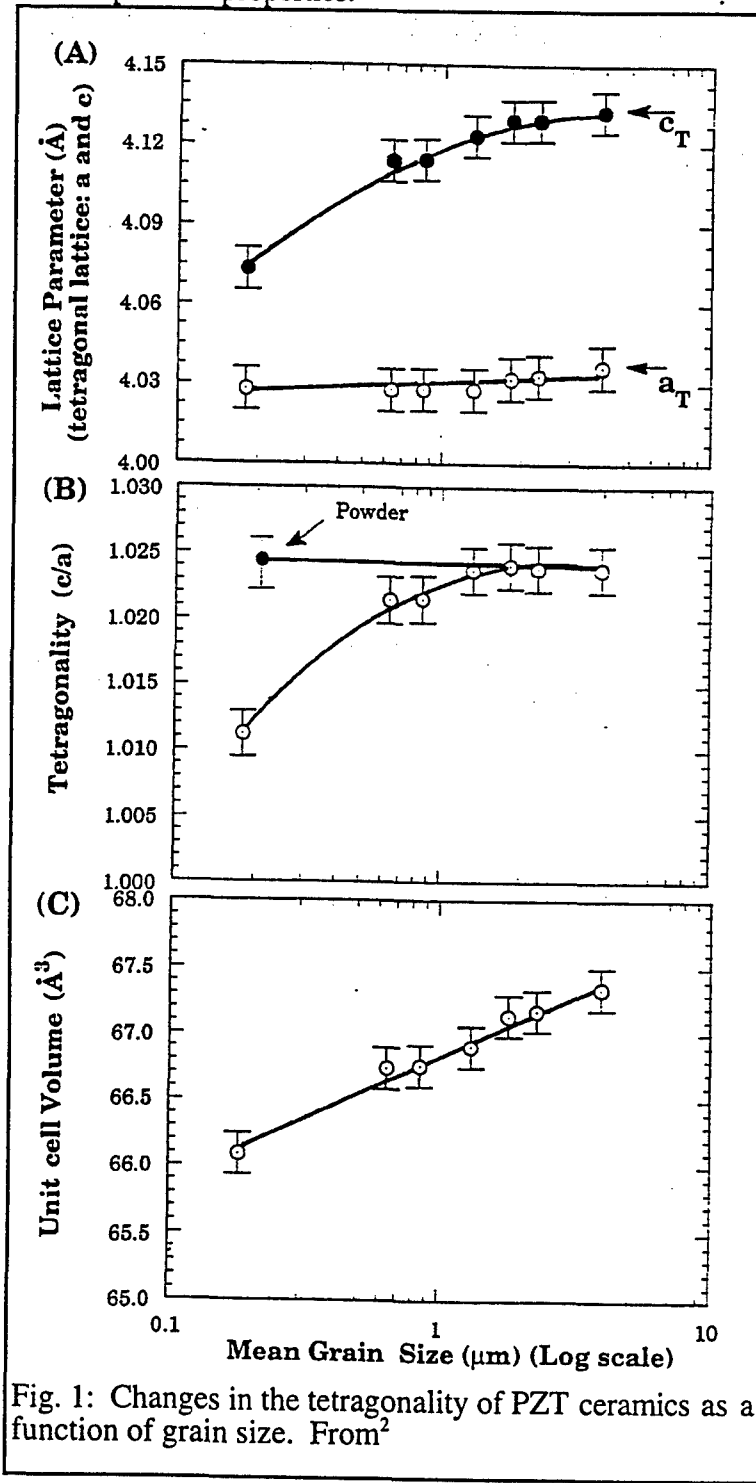


Fig. 1: Changes in the tetragonality of PZT ceramics as a function of grain size. From<sup>2</sup>

Augmenting this behavior is a simultaneous change in the domain structure. As has been demonstrated by Randall,<sup>3</sup> the size of twin domains in PZT ceramics depends on the grain size so that as the grain size is reduced, the domain size drops as  $(\text{grain size})^{1/2}$  over the size range of 0.2 to 10  $\mu\text{m}$ . At sizes below  $\sim 0.2 \mu\text{m}$ , the domain size drops even more quickly. In addition to the change in domain density, Randall noted that with decreasing size, the number of domain variants per grain drops as well. The latter point appears to have profound consequences in terms of properties. As shown schematically in Fig. 2, it has been observed that in many cases, twin walls are often related across grain boundaries. As a consequence, poling of the material entails coupled motion of domain walls in adjacent grains. Because the number of domain variants drops for small-grained PZT ceramics, this may inhibit the efficiency of poling in these materials. This was shown for ceramic PZT by Kim et al.,<sup>2</sup> where a drop in both the saturation and the remanent polarizations were noted as a function of decreasing grain size. This was attributed to a decrease in domain wall mobility in the fine-grained materials probably associated with elastic constraints. (Note that for these data on Nb-doped PZT, the grain boundaries were shown to be clean, so that the size-induced changes were not determined by dilution with a non-ferroelectric grain boundary phase.). As a consequence of the decrease in the remanent polarization, the piezoelectric coefficients  $d_{33}$  and  $d_{31}$  for these ceramics also dropped for grain sizes  $< 1 \mu\text{m}$ . Given these

data and the fact that thin films typically have grain sizes  $< 0.5 \mu\text{m}$ , it becomes a significant question as to whether it will be possible to generate appreciable domain wall contributions to dielectric or piezoelectric properties in thin films.

A second significant difference between ceramics and thin films is the stress state of the materials. In bulk ceramics, the average stress on each particle is approximately hydrostatic, whereas in thin films, the stress is largely biaxial. Since many ferroelectrics are ferroelastic as well as ferroelectric, stresses should strongly influence the film properties (particularly through domain wall mobilities). Consequently, size effects may be considerably different for ferroelectrics experiencing different elastic or electrical boundary conditions.

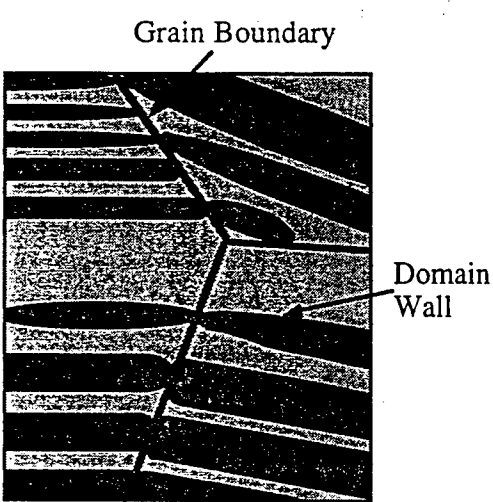


Fig. 2: Schematic representation of twin walls showing coupling across grain boundaries in PZT ceramics, after reference<sup>3</sup>.

## SIZE EFFECTS IN BaTiO<sub>3</sub> THIN FILMS

In order to investigate intrinsic size effects in ferroelectrics, epitaxial (001) BaTiO<sub>3</sub> thin films were grown on a variety of substrates by pulsed laser deposition (PLD).<sup>4</sup> BaTiO<sub>3</sub> has been shown previously to be susceptible to size effects in powder, ceramic, and single crystal forms.<sup>5,6,7,8,9,10,11</sup> A sintered BaTiO<sub>3</sub> target was ablated using a KrF excimer laser. All films were grown in a 10% ozone/oxygen ambient to improve the oxygen stoichiometry. Typical background gas pressures during deposition were  $\sim 100$  mtorr. Substrates were conductively heated to between 600 and 700°C during deposition to enable epitaxial growth.

Depositing in the off-axis geometry resulted in very little energetic bombardment of the film during growth. As a result, the films were quite close to stoichiometry (as measured by Rutherford backscattering (RBS)), but multiple in-plane orientations were always seen in  $\phi$ -scans taken with

the 4-circle X-ray diffractometer. On the other hand, epitaxy was easily achieved when films were grown in the on-axis geometry, where the films experienced more bombardment by high energy species during growth. The surface morphology of on and off-axis films followed predictions from the structure zone model for growth under high and low adatom mobility conditions, respectively.

It was found that excessive bombardment during growth resulted in anomalously large lattice parameters, peak splitting, and Ba deficient films (See Fig. 3). These factors resulted in poor film properties. Once the bombardment levels were reduced, BaTiO<sub>3</sub> films with lattice parameters close to the bulk material could be deposited. Similar behavior was observed in the epitaxial SrRuO<sub>3</sub> films used as bottom electrodes.

Using appropriate deposition conditions, epitaxial BaTiO<sub>3</sub> films between 60 and 200 nm in thickness were deposited on ablated SrRuO<sub>3</sub> electrodes on polished LaAlO<sub>3</sub> and SrTiO<sub>3</sub> substrates. Gold electrodes were then sputtered onto the top surface of the film through a shadow mask so that through-the-thickness electrical property measurements could be made. Concentrated HF was used to remove the BaTiO<sub>3</sub> in one region of the film to permit electrical contact to the bottom electrode. The dielectric properties were measured as a function of temperature at 10 kHz using an HP 4276A LCR meter and a convection oven with a range of -175°C to 270°C. Hysteresis measurements were made at both room temperature and 77K using an RT66A. Epitaxy was confirmed using a Picker 4-circle X-ray diffractometer which had angular resolutions of 0.15°, 0.24°, 0.35°, and 1.8° in the  $2\theta$ ,  $\omega$ ,  $\phi$ , and  $\chi$  circles, respectively.

As expected on the basis of the lattice mismatch, the BaTiO<sub>3</sub> films in BaTiO<sub>3</sub>/SrRuO<sub>3</sub>/SrTiO<sub>3</sub> (BSS) heterostructures showed lower full width half max (FWHM) values in all circles than did films of the same thickness, deposited under identical conditions, prepared on LaAlO<sub>3</sub> substrates (BSL series). This was reflected in a larger coherent diffraction region

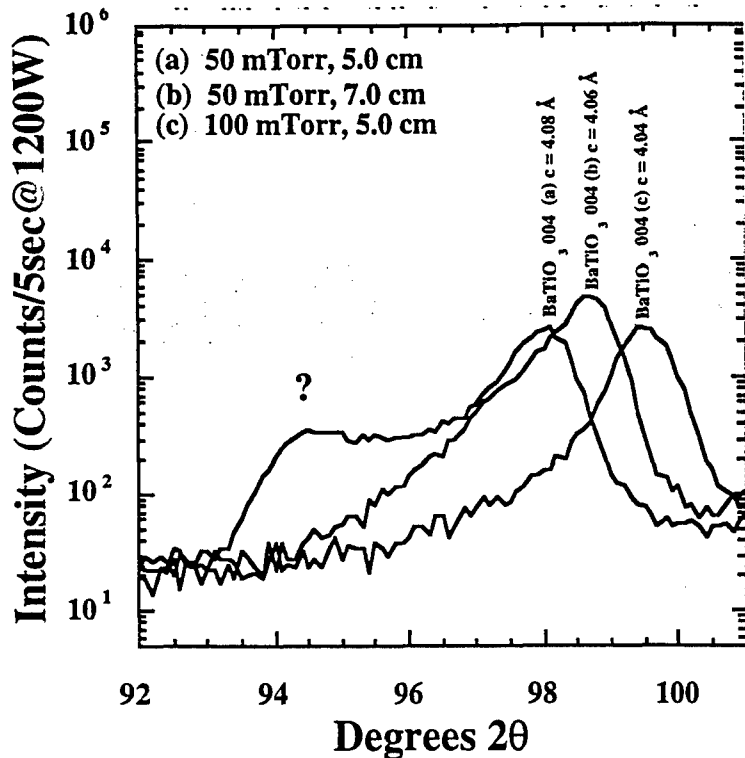


Fig. 3:  $\theta - 2\theta$  X-ray diffraction patterns of the  $\text{BaTiO}_3$  004 peak for epitaxial  $\text{BaTiO}_3$  films as a function of the bombardment during growth. All films were grown in the on-axis geometry. The background pressure and the film-substrate distance are given in the legend. The degree of bombardment decreases from (a) to (b) to (c).

Table 1: Crystallinity of PLD  $\text{BaTiO}_3$  Films

Sample	002 peak FWHM ( $^{\circ}2\theta$ )	Coherence length calculated from $00\ell$ reflections	Lattice parameters at 25°
BSS-12	0.3	79 nm	$c = 4.03\text{\AA}$ $a = 4.00\text{\AA}$
BSL-18	0.6	33 nm	$a = c = 4.01\text{\AA}$

calculated from the 001, 002, 003, and 004 peaks using the Hall-Williamson method<sup>12</sup> for the film on  $\text{SrTiO}_3$  (See Table 1). In addition, the BSS film showed room temperature tetragonality, implying the stabilization of the ferroelectric phase, while the film on  $\text{LaAlO}_3$  was cubic, within the resolution of our diffractometer. Both films were  $\sim 3 \pm 5\%$  Ba-deficient as measured by RBS and dc plasma emission spectroscopy. It is important to note, however, that no second phases were observed by X-ray diffraction, even though Ba-deficient bulk materials show phase separation at small nonstoichiometries. Thus, it appears that in these films, a composition outside of the normal solubility limits was stabilized by the epitaxial arrangement between the film and the substrate.

When the electrical properties of these two films were measured (see Fig. 4) it was clear that the transition temperature depended on the film crystallinity, with the more perfect film showing higher transition temperatures. Stress effects associated with the difference in thermal expansion coefficients between the film and the substrate from the growth temperature to room temperature cannot account for the observed transition temperature shifts.<sup>13</sup> Moreover, when the high field properties of these films were measured, it was found that BSS-12 showed hysteresis in the polarization at room temperature, where BSL-18 did not. This is consistent with the X-ray measurements. Both films, when cooled down to 77K showed clear hysteresis loops with  $P_c$  values of  $\sim 3 \mu\text{C}/\text{cm}^2$  and  $\sim 2 \mu\text{C}/\text{cm}^2$ , respectively.

It was also noted that the decrease in the transition temperature was not as severe in off-axis deposited films, perhaps as a result of those films being closer to the correct Ba/Ti stoichiometric ratio. This is seen in Fig. 5, where data for the permittivity as a function of temperature is shown

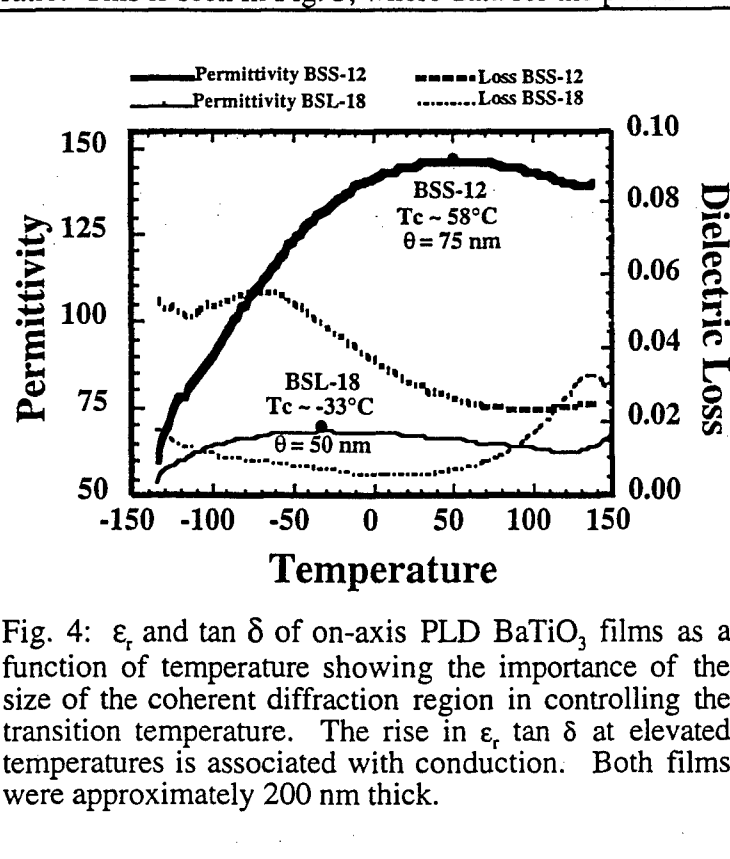


Fig. 4:  $\epsilon_r$  and  $\tan \delta$  of on-axis PLD  $\text{BaTiO}_3$  films as a function of temperature showing the importance of the size of the coherent diffraction region in controlling the transition temperature. The rise in  $\epsilon_r$ ,  $\tan \delta$  at elevated temperatures is associated with conduction. Both films were approximately 200 nm thick.

for a 60 nm thick  $\text{BaTiO}_3$  film (Note that as explained earlier, this film showed extra in-plane orientations). In this film, as in the off-axis films, the dielectric maxima showed a diffuse phase transition. The low dielectric loss values above 100°C shown by this film permitted a Curie-Weiss analysis of the data. It was found that the Curie constant for this film was approximately an order of magnitude below that of bulk  $\text{BaTiO}_3$  ceramics ( $1.6 \times 10^5/\text{K}$ ). The origin of this behavior is currently under investigation. This film showed a well-developed hysteresis loop at 77K ( $P_r \sim 5 \mu\text{C}/\text{cm}^2$ ) as well as breakdown strength  $> 3 \text{ MV}/\text{cm}$  at 77K.

From this data, it is clear that transition temperature in ferroelectric thin films is affected by the size of the coherent diffraction region, even in epitaxial films, where presumably the "grain" - to - "grain" coupling should be quite good.

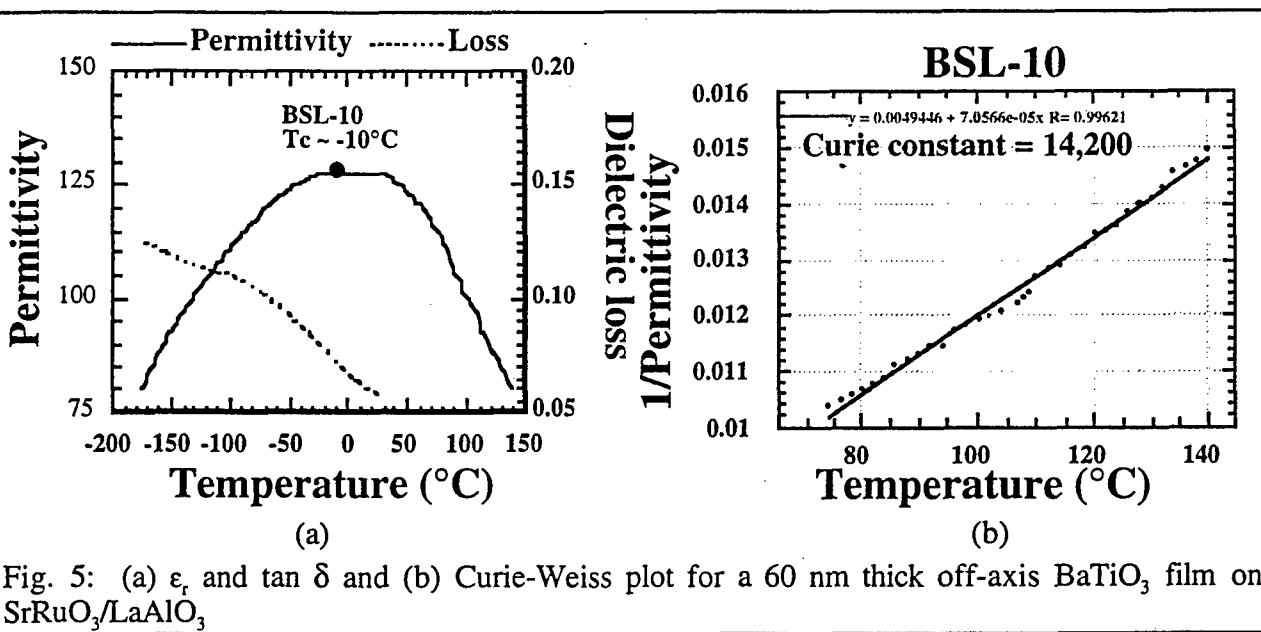


Fig. 5: (a)  $\epsilon_r$  and  $\tan \delta$  and (b) Curie-Weiss plot for a 60 nm thick off-axis  $\text{BaTiO}_3$  film on  $\text{SrRuO}_3/\text{LaAlO}_3$

## DOMAINS IN EPITAXIAL $\text{PbTiO}_3$ on $\text{SrTiO}_3$

Because domain walls can make such a considerable contribution to the properties of ferroelectric thin films, it is also important to examine the way in which domains behave in epitaxial films. Some recent work in this area was recently carried out by Theis and Schlom of Penn State for epitaxial  $\text{PbTiO}_3$  on  $\text{SrTiO}_3$ .<sup>14,15</sup> As has been described by Pompe *et al.*,<sup>16</sup> when

$\text{PbTiO}_3$  epitaxial films are cooled from the growth temperature, it is common for the films to show primarily  $c$ -axis orientation, with some  $a$  domains which appear tilted from the  $\text{PbTiO}_3$   $c$ -axis in each of four equivalent directions. To investigate some of the factors controlling the stability of domain walls in this system, Theis and Schlom grew epitaxial  $\text{PbTiO}_3$  films on well-oriented and vicinal (001)  $\text{SrTiO}_3$  substrates by PLD. As expected, films grown on normal cut  $\text{SrTiO}_3$  showed the expected four  $a$  domain orientations. However, as shown in Fig. 6, films grown on misoriented  $\text{SrTiO}_3$  showed that the  $a$  domains were preferentially oriented in the uphill direction. That is, the presence of aligned steps on the  $\text{SrTiO}_3$  substrate led to preferential orientation in the observed domain patterns for the films. The degree of preferential alignment of the  $a$  domains increased as the miscut angle of the substrate increased. It was also observed that on miscut substrates, the  $c$  axis of the  $\text{PbTiO}_3$  film was tilted a small, but measurable, angle away from the [001]  $\text{SrTiO}_3$ .

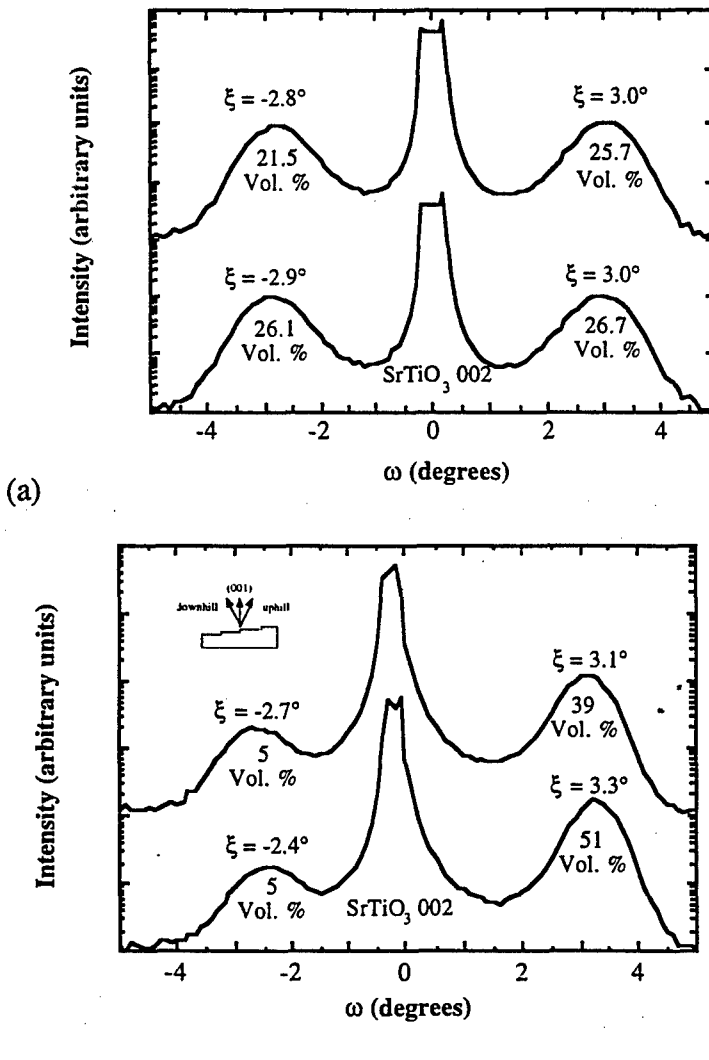


Fig. 6: Rocking curve of the  $\text{SrTiO}_3$  002 reflection for  $\text{PbTiO}_3$  films on (a) normal cut and (b) miscut (001)  $\text{SrTiO}_3$  substrates. The satellite peaks correspond to  $\text{PbTiO}_3$  200 reflections. It is clear from the log scale involved that misoriented substrates can lead to significant levels of preferred orientation in the  $a$  domains.

This behavior was modeled as shown in Fig. 7. Since the  $a$  lattice parameter of  $\text{PbTiO}_3$  has a much better lattice match to the  $\text{SrTiO}_3$   $a$  axis than is the  $\text{PbTiO}_3$   $c$ -axis, when the film is cooled from the growth temperature through the Curie temperature, it is reasonable to believe that at step edges, the  $a$  lattice parameter will be elastically constrained by the substrate on both faces of the step. This in turn, could force the nucleation of  $a$  domains in the film. Since in a miscut substrate,

the steps are faceted with {100} surfaces and are arranged to accommodate the macroscopic tilt of the substrate (i.e. the steps are preferentially oriented in specific directions), this would explain the observed partiality for a single  $a$  domain orientation.

Given this model, one of the key questions to consider is the mobility of such elastically constrained domain walls. If in fact, the wall is pinned by the substrate, then it is not clear that under reasonable applied fields that the twin wall will be mobile. That is, not only may it be impossible to remove the 90° twins, it may also be difficult to generate appreciable lateral motion of the domain wall. As a result, it is possible that such domain walls will not contribute in any significant way to either the dielectric or the electromechanical properties of these ferroelectric films. Since, as described above, twin wall motion accounts for ~ one half of the observed piezoelectric coefficients of soft PZT ceramics, loss of twin wall mobility may significantly limit the electromechanical response which can be generated in thin films. (Note that 180° domain walls, which may be mobile, do not contribute to the piezoelectric response). This clearly has significant consequences for the microelectromechanical systems (MEMS) community, where large displacement thin film actuators are desired. It remains to be seen whether the ability to prepare highly oriented or epitaxial PZT films will increase the piezoelectric coefficients enough over the randomly oriented polycrystalline case to make up for much of this loss.

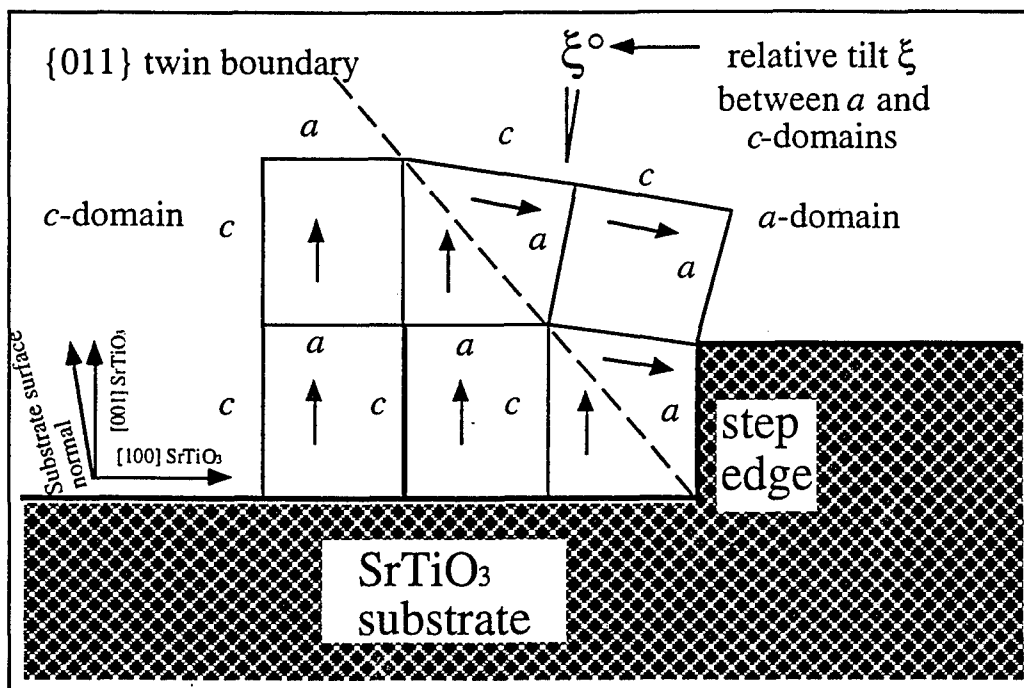


Fig. 7: Schematic representation of the origin of preferred domain orientations for PbTiO<sub>3</sub> films on miscut (001) SrTiO<sub>3</sub> substrates. The tetragonality distortion of PbTiO<sub>3</sub> has been exaggerated.

## CONTROLLED IN-PLANE STRESS EXPERIMENTS IN PZT THIN FILMS

In order to begin to examine the mobility of domain walls in PZT thin films, a series of experiments has been initiated where the properties of the PZT films were measured while the film was maintained in a state of controlled biaxial stress. This was done using a fixture which supported the substrate at three equidistant points while pressing down on the top at the center. Both load and displacement were monitored throughout the measurements.

The sol-gel PZT 52/48 films used were prepared using a methoxyethanol solvent following a modification of the Budd, Dey, and Payne procedure.<sup>17</sup> Multiple coatings of the solution were spun onto Pt/Ti/SiO<sub>x</sub>/Si substrates, with an intermediate pyrolysis step between each layer. The film was then crystallized using a rapid thermal annealer. Typically, these film had primary grain sizes on the order of 50-100 nm. A corner of the bottom electrode was exposed by etching the PZT with dilute HF solution. Sputtered gold top electrodes 1.5 mm in diameter were

used as top contacts. The low and high field electrical properties were then measured at fixed biaxial stress levels using an HP 4192A impedance analyzer and an RT66A ferroelectrics tester, respectively.

Prior to exerting a controlled in-plane stress on the film, the initial stress state of both the electrode and the PZT were measured using wafer curvature. As received, the sputtered Pt/Ti electrode was in a state of compressive stress. However, as has been reported elsewhere, following exposure to the PZT crystallization procedure, the room temperature stress was strongly tensile. The final PZT stress state following crystallization was between 70 and 110 MPa tensile for a  $0.38\mu\text{m}$  thick film. Similar stress states following heating were observed in electron beam evaporated electrodes.

Several of these films were then exposed to additional tensile stress by flexing the substrate. As can be seen in Fig. 8, the result was a drop in the capacitance; the dielectric loss of the film remained unchanged. Similar results were reported by Garino and Harrington.<sup>18</sup> This change was coupled with a decrease in the remanent and saturation polarization values for films under tensile loading conditions (See Fig. 9).

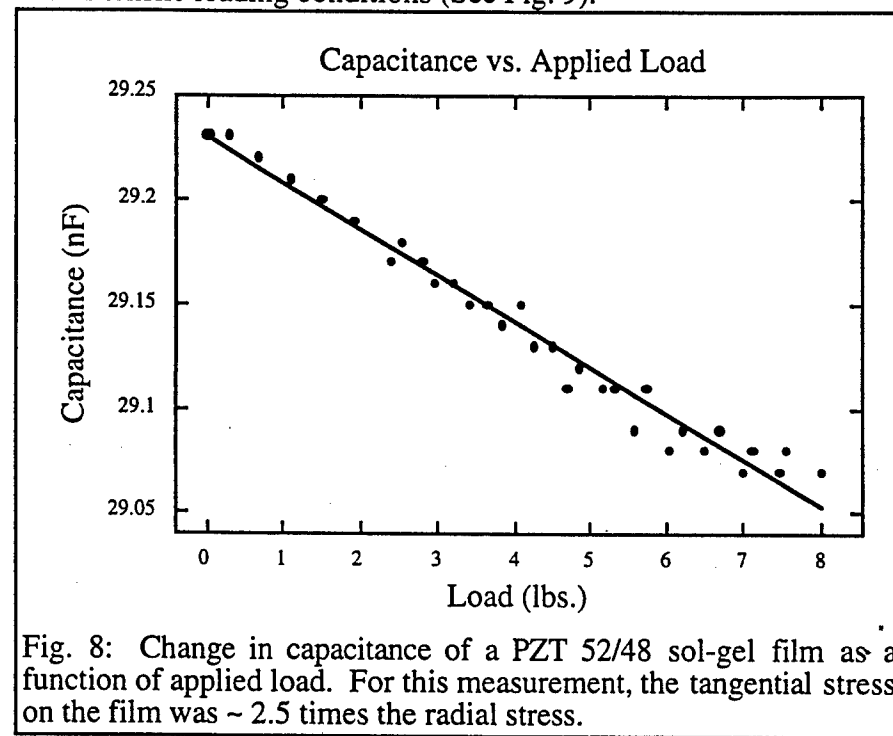


Fig. 8: Change in capacitance of a PZT 52/48 sol-gel film as a function of applied load. For this measurement, the tangential stress on the film was  $\sim 2.5$  times the radial stress.

On unloading, the hysteresis remanent polarization was recovered to its initial value. That is, the change on loading and unloading was reversible (See Fig. 10). Experiments are underway to measure the piezo-electric response of the films as a function of the in-plane stress level. This should be quite useful in describing the properties of PZT films in MEMS applications, particularly in structures where it may not be possible to design a low stress level into the PZT. This work should also help determine if it will be possible to generate significant domain wall

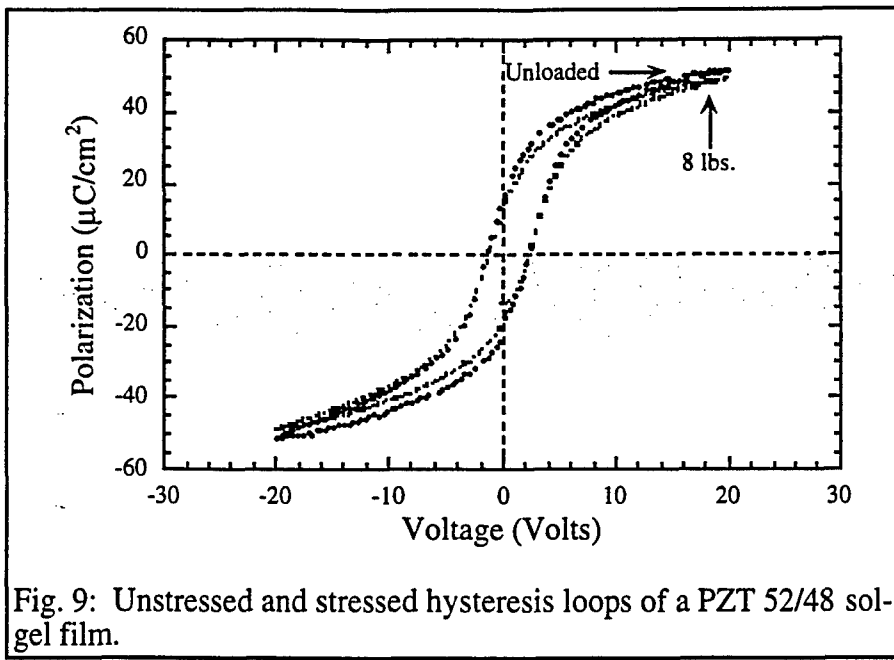


Fig. 9: Unstressed and stressed hysteresis loops of a PZT 52/48 sol-gel film.

motion at any stress level in thin films. (i.e. whether it will be possible to prepare a truly soft PZT thin film).

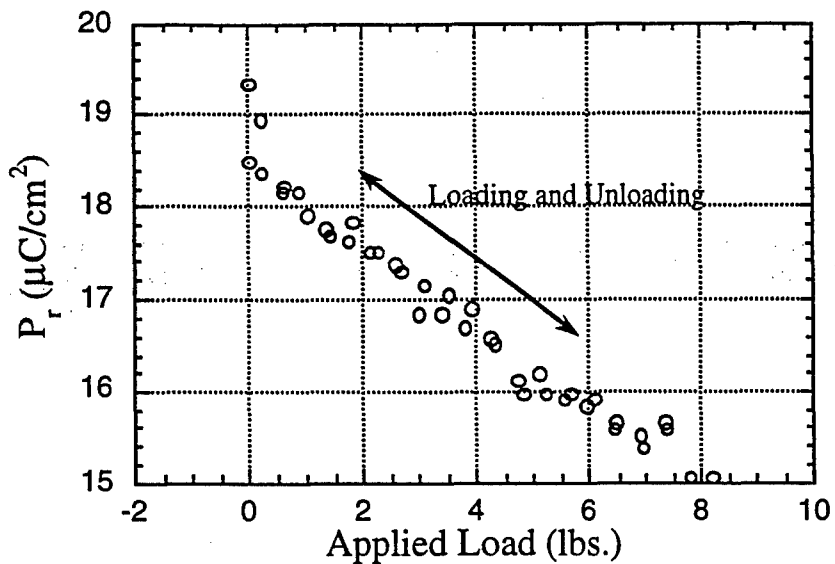


Fig. 10: Variation in the remanent polarization of a sol-gel PZT film on loading and unloading in biaxial flexure.

#### ANTIFERROELECTRIC PbZrO<sub>3</sub> THIN FILMS

Because it is not clear whether or not it will be possible to generate appreciable domain wall contributions to the electromechanical properties of ferroelectric (FE) thin film actuators, one of the important questions for MEMS applications is how to develop high displacement actuators. To address this need, highly (111) oriented (indexed on the cubic unit cell) dc magnetron sputtered PbZrO<sub>3</sub> thin films have been prepared.<sup>19,20</sup> Films were deposited at room temperature onto a Pt/Ti/SiO<sub>2</sub>/Si target. In order to maintain reproducible film composition, the Pb target was current controlled, while the Zr target was power controlled. Typical deposition conditions were 52 mA to the Pb target, 250 W to Zr target, and a background gas pressure of 10 mtorr (90%Ar/10%O<sub>2</sub>). Crystallization was performed using a rapid thermal annealer using annealing times of 700°C for 30 seconds.

These films show clear double hysteresis loops associated with the field-forced antiferroelectric (AFE) phase transition (See Fig. 11). The field levels required to generate the ferroelectric phase were on the order of 290 kV/cm, while the reverse transition occurred at 180 kV/cm. Saturation polarizations up to 70 μC/cm<sup>2</sup> were obtained at room temperature. This is considerably larger than the 40 μC/cm<sup>2</sup> that can be generated in polycrystalline ceramics due to the high degree of orientation. In the low field properties, the PbZrO<sub>3</sub> films showed a broadened phase transition with a transition temperature of 248°C, ~20°C higher than the transition in bulk crystals, probably because of the stress in the film. On cooling to liquid nitrogen temperature, the films showed an antiferroelectric-ferroelectric phase transition the first time the electric field was applied. On releasing the field, the film developed a metastable ferroelectric phase and a ferroelectric-ferroelectric phase transition on subsequent traverses of the hysteresis loop. The stable ferroelectric phase could be restored by heating the film to room temperature. This behavior is comparable to that observed in PbZrO<sub>3</sub> single crystals,<sup>21</sup> but is rarely observed in polycrystalline ceramics.

The strain accompanying the antiferroelectric-ferroelectric phase transition in these films was measured using a double beam interferometer with a displacement resolution of 10<sup>-2</sup> Å. In this arrangement, light is reflected from both the front and back surface of the film, thus errors associated with flexure of the substrate are minimized. For electrical contact, 1.5mm gold electrodes were sputtered onto the front surface of the films through a shadow mask. Again, a portion of the film was etched away to expose the bottom electrode. For these measurements, a dc bias of 6.5 V was applied in order to put the film near the phase switching point. A 10 Hz alternating field was then superimposed to force the phase transition. As shown in Fig. 12, these films show appreciable electrically-induced strain, up to 0.25%. The onset of the strain is rather

gradual, possibly due to variations in the antiferroelectric-ferroelectric transition field level. Because the breakdown strength of the films was quite high, it should be possible to use these films as large strain actuators.

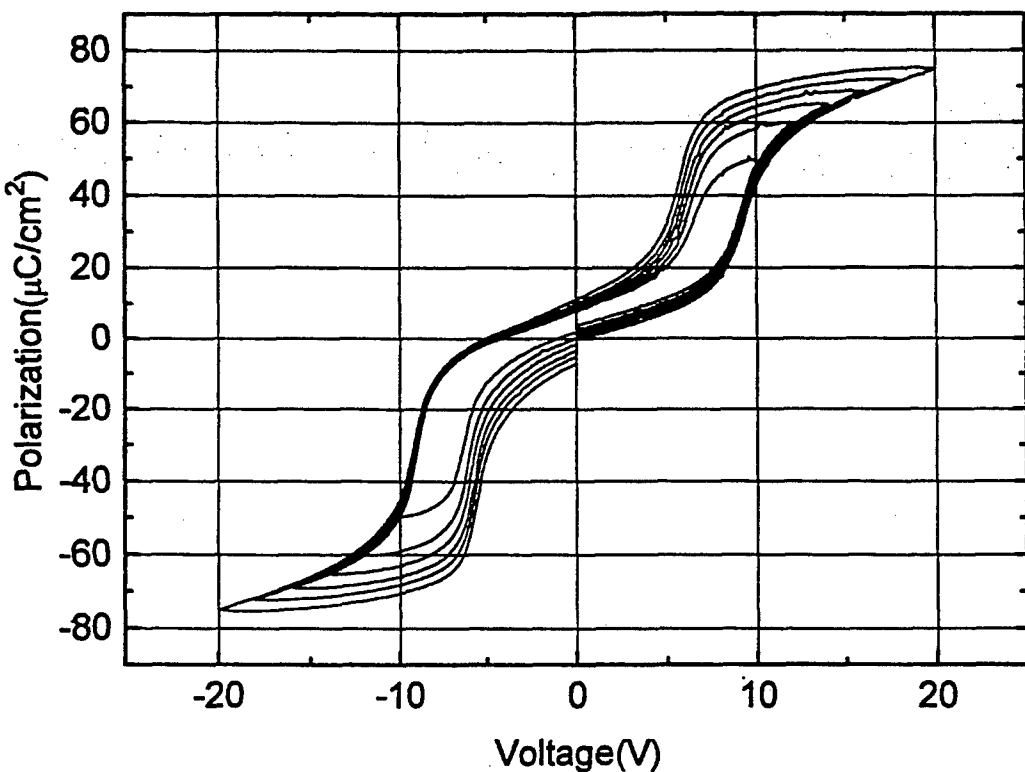


Fig. 11: Polarization-electric field hysteresis loop for an oriented  $\text{PbZrO}_3$  film showing the antiferroelectric to ferroelectric transition

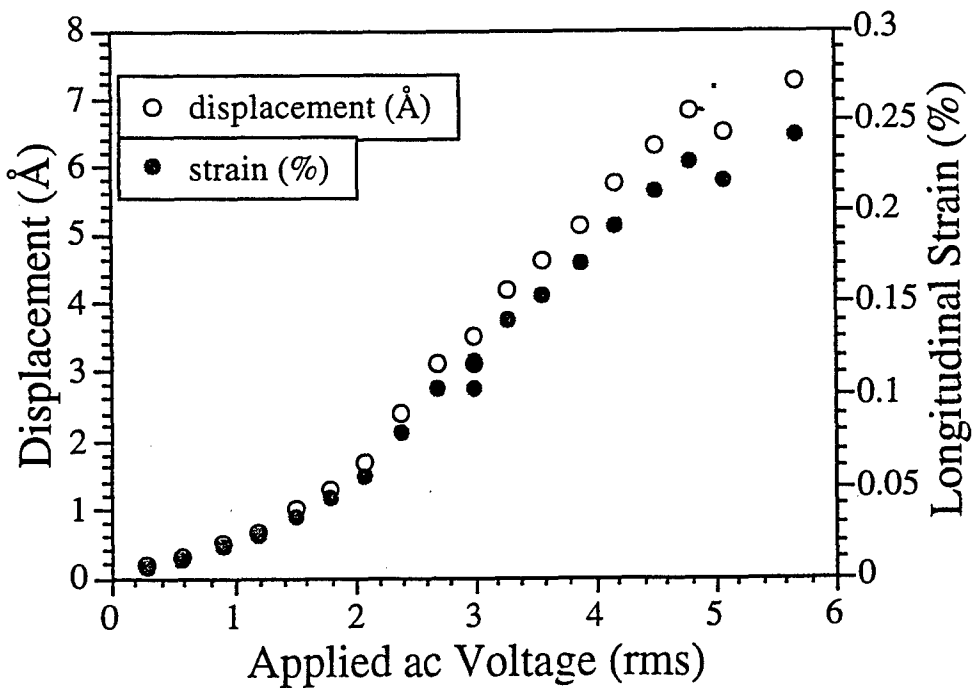


Fig. 12: Displacement and strain in an antiferroelectric  $\text{PbZrO}_3$  film prepared by dc magnetron sputtering

## CONCLUSIONS

This paper has tried to address some of the issues pertinent to size effects in ferroelectric thin films. In describing size effects, it is important to consider both intrinsic changes in the properties as well as changes to the extrinsic contributions (such as domain wall mobility) as the physical dimension is changed. It is clear from the work on bulk PZT ceramics that some decrease in both the intrinsic and extrinsic contributions to the properties should be expected for materials where the grain size falls below 0.5  $\mu\text{m}$ . Most thin films fall in to this category. In epitaxial films, size effects can be strongly influenced by the film stress state, the stabilization of off-stoichiometry structures, the size of the coherent diffraction region, and the substrate step density. It remains an open question as to how much domain walls contribute to the dielectric and electromechanical properties of ferroelectric thin films and to what extent properties can be recovered by the deposition of oriented films. Although it is not clear whether or not piezoelectrically soft PZT films can be generated, it has been demonstrated that  $\text{PbZrO}_3$  phase switching compositions are an alternative for thin film actuator in large strain applications.

## ACKNOWLEDGMENTS

This work supported by NSF grants DMR-9223847 and DMR-9502431 and by ARPA through grant DABT63-95-C-0053. Dan Chen is gratefully acknowledged as the source of the interferometry data.

---

## REFERENCES

1. X. L. Zhang, Z. X. Chen, L. E. Cross, and W. A. Schulze, *J. Mat. Sci.* **18**, 968 (1983).
2. Namchul Kim, PhD Thesis, The Pennsylvania State University, 1994.
3. W. Cao and C. Randall, accepted *J. Phys. Chem., Sol.* (1996).
4. Jon-Paul Maria, MS Thesis, The Pennsylvania State University, 1996.
5. G. Arlt, D. Hennings, and G. de With, *J. Appl. Phys.* **54**, 1619 (1985).
6. K. Kinoshita and A. Yamaji, *J. Appl. Phys.* **47**, 371 (1975).
7. S. B. Desu, *J. Electrochem. Soc.* **140**, 2981 (1993).
8. K. Abe and S. Komatsu in *Ferroelectric Thin Films IV*, edited by B. A. Tuttle et al. (Mater. Res. Soc. Proc. 243, Pittsburgh, PA, 1994).
9. V. P. Dudkevich, V. M. Mukhortov, Y. I. Golovko, Y. G. Sindeev, and E. G. Fesenko, *Sov. Phys. Sol. State* **65** 463 (1981).
10. M. H. Frey and D. A. Payne, *Appl. Phys. Lett.* **63**, 2735 (1993).
11. H. Terauchi, Y. Watanabe, H. Kasatane, K. Kamagaki, Y. Yano, T. Terashima, and Y. Bando, *J. Phys. Soc. Jpn.* **61**, 2194 (1992).
12. G. K. Williamson and W. H. Hall, *Acta Met.* **1** 22 (1953).
13. P. W. Forsbergh, Jr. *Phys. Rev.* **93** 686 (1954).
14. C. D. Theis and D. G. Schlom, *MRS Proc.* **401** 171 (1996).

- 
15. C. Theis, M.S. Thesis, The Pennsylvania State University 1996.
  16. W. Pompe, X. Gong, Z. Suo, and J. S. Speck, *J. Appl. Phys.* **74** 6012 (1993).
  17. J. Chen, K. R. Udayakumar, K. G. Brooks, and L. E. Cross, *J. Appl. Phys.* **71** 4465 (1992).
  18. T. J. Garino and M. Harrington in Ferroelectric Thin Films II, ed. A. I. Kingon, E. R. Myers, and B. Tuttle, (*Mater. Res. Soc. Proc.* **243**, Pittsburgh, PA (1992) pp. 341.
  19. K. Yamakawa, S. Trolier-McKinstry, J. P. Dougherty, and S. B. Krupanidhi, *Appl. Phys. Lett.* **67** 2014 (1995).
  20. K. Yamakawa, K. Wa Gachigi, S. Trolier-McKinstry, and J. P. Dougherty, *Ferr. Lett.* **20** 149 (1996).
  21. O. E. Fesenko, R. V. Kolesova, and Yu. G. Sindeyev, *Ferroelectrics* **20** 177 (1978).

# Domain Structure of $\text{PbTiO}_3$ Films Grown on Vicinal (001) $\text{SrTiO}_3$

C. D. Theis and D. G. Schlom

Department of Materials Science and Engineering  
The Pennsylvania State University  
University Park, PA 16802 USA

**Abstract**—Epitaxial  $\text{PbTiO}_3$  films have been grown on vicinal (001)  $\text{SrTiO}_3$  substrates by pulsed laser deposition. Vicinal  $\text{SrTiO}_3$  substrates with misorientations up to  $9^\circ$  from (001) were used and the influence of the direction of misorientation on the resulting domain structure was studied. 4-circle x-ray diffraction analysis indicates that thin (40 nm)  $\text{PbTiO}_3$  films are completely *c*-axis oriented (rocking curve FWHM of  $0.25^\circ$  for the  $002$  reflection) and that thicker films ( $\sim 200$  nm) contain mixed *a*-axis and *c*-axis  $\text{PbTiO}_3$  domains due to twinning along  $\{011\}$  planes. The [100] axis of the *a*-axis domains are misoriented by  $2.1^\circ$  to  $3.3^\circ$  toward  $\langle 100 \rangle$  substrate directions with respect to the [001] axis of the *c*-axis domains. In contrast to growth on well-oriented (001)  $\text{SrTiO}_3$  surfaces where the four equivalent tilts of the [100] axis of the *a*-axis domains are equally likely, on vicinal  $\text{SrTiO}_3$ , the *a*-axis domains are preferentially oriented in an uphill direction with respect to the crystallographic miscut.

## I. INTRODUCTION

Lead titanate has become an extensively studied ferroelectric material. It has a variety of potential applications including ultrasonic sensors, infrared detectors, and ferroelectric random access memories [1]. Growth of  $\text{PbTiO}_3$  has been hampered by problems with lead volatility [2,3]. However, high quality films have been made by metal-organic chemical vapor deposition (MOCVD) [4,5], pulsed laser deposition

(PLD) [6,7], sputtering [3], and through the use of solution precursors [2]. Because of the anisotropic nature of lead titanate, many of its properties, including remanent polarization, pyroelectric coefficient, and coefficient of second harmonic generation, are dependent on its crystallographic orientation. For most of these applications it is desirable to have a single-domain film with the  $\text{PbTiO}_3$  *c*-axis normal to the substrate surface. To date, the growth of relatively thick films  $\geq (50\text{-}150)$  nm [5,7] of pure *c*-axis oriented epitaxial lead titanate has been hampered by the formation of  $\{011\}$  domain boundaries resulting in mixed *c* and *a*-domain films [2,4,7,8]. Researchers have shown that the introduction of domain boundaries in  $\text{PbTiO}_3$  films grown on  $\text{SrTiO}_3$  is favored to reduce strains that arise from the  $\text{PbTiO}_3$  phase transition, lattice mismatch, and differences in thermal expansion between the film and substrate upon cooling [9]. In order to more fully understand the mechanisms that contribute to the ultimate population and orientation of these *a*-domains we have grown epitaxial lead titanate films on vicinal (001)  $\text{SrTiO}_3$  substrates [10].

## II. BACKGROUND

Prior TEM and STM studies of vicinal (001)  $\text{SrTiO}_3$  surfaces have established that the edges of the steps on vicinal (001)  $\text{SrTiO}_3$  surfaces are primarily faceted along  $\langle 100 \rangle$  directions (i.e., the step edges run along  $\langle 100 \rangle$  directions) and that the height of the steps are integral multiples of the unit cell height of  $\text{SrTiO}_3$  as depicted schematically in Fig. 1. Additionally, TEM studies of the  $\text{PbTiO}_3$ /substrate interface

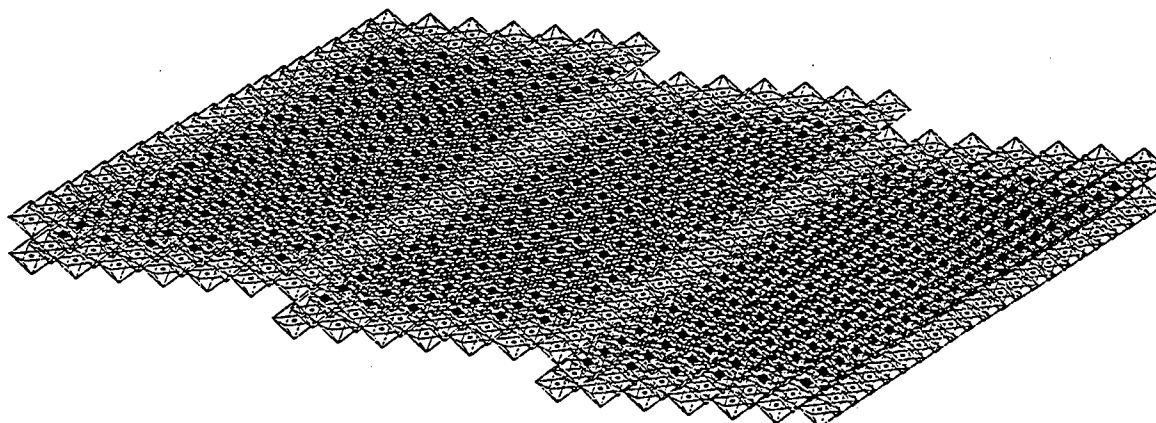


Fig. 1 Schematic of the surface of a vicinal  $\text{SrTiO}_3$  substrate;  $\text{SrTiO}_3$  facets along  $\langle 100 \rangle$  directions.

have shown that the {011} domain boundaries begin at the interface and extend into the film [2,8]. The importance of these observations, and an explanation of the apparent discrepancies in the reported tilt angle of  $\alpha$ -oriented  $\text{PbTiO}_3$ /({001})  $\text{SrTiO}_3$  will be discussed in conjunction with the structure of thick epitaxial  $\text{PbTiO}_3$  films grown on vicinal ({001})  $\text{SrTiO}_3$  substrates.

To date, the use of vicinal substrates for the growth of  $\text{PbTiO}_3$  has been limited. Kim *et al.* [11] report the use of vicinal ( $5.5^\circ$  miscut)  $\text{MgO}$  substrates for the growth of  $\text{PbTiO}_3$  by rf sputtering. They note that the  $c$ -domains are misoriented by  $1.0^\circ$  away from the  $\text{MgO}$  (001), and the  $\alpha$ -domains are misoriented by  $0.5^\circ$  from the  $\text{MgO}$  (001). Both the  $\alpha$  and  $c$  domains are reported to be tilted toward the macroscopic surface normal, or equivalently downhill as defined by the macroscopic tilt of the substrate surface with respect to the (001)  $\text{MgO}$  plane (see inset to Fig. 2). Additionally, Kim *et al.* [11] note that the presence of  $\text{MgO}$  step edges has no influence on the in-plane orientation of the  $\alpha$ -oriented domains. That is, equal volume fractions of  $\alpha$ -domains were measured with the  $c$ -axis parallel to and perpendicular to the  $\text{MgO}$  step edges [11]. As will be described below, the domain structure of  $\text{PbTiO}_3$  films grown on vicinal ({001})  $\text{SrTiO}_3$  surfaces is much different than those results for growth on vicinal ({001})  $\text{MgO}$  surfaces.

Kim *et al.* [11] found that the  $\text{PbTiO}_3$  film crystalline quality improved dramatically using vicinal  $\text{MgO}$  substrates. They reported an improvement in the FWHM of the  $\text{PbTiO}_3$  (001) rocking curve width from  $2.28^\circ$  to  $1.64^\circ$  for growth on nominal and vicinal ( $5.5^\circ$  miscut)  $\text{MgO}$  substrates, respectively [11].

Similarly, Wasa *et al.* [12] deposited  $\text{PbTiO}_3$  films on vicinal ( $1.7^\circ$  miscut) (001)  $\text{SrTiO}_3$  using rf sputtering. The substrates were miscut toward the [100]  $\text{SrTiO}_3$  axis. These films were found to have extremely smooth surfaces, less than 3 nm for a film thickness of 100 nm [12].

### III. EXPERIMENTAL

Films were synthesized by PLD using a KrF excimer laser. A detailed description of our target synthesis and deposition system is given elsewhere [10]. Typical deposition temperatures for  $\text{PbTiO}_3$  are  $\sim 775^\circ\text{C}$  using  $\text{SrTiO}_3$  (001) and vicinal (001)  $\text{SrTiO}_3$  single crystal substrates. The substrate is located 6-7 cm from the target in an oxygen/ozone ( $\sim 5\%$   $\text{O}_3$ ) ambient of 5-30 mTorr. The laser is focused to achieve an energy density of  $2 \text{ J/cm}^2$  with a repetition frequency of 20-30 Hz.

### IV. RESULTS AND DISCUSSION

#### A. 4-Circle X-Ray Diffraction Analysis

In order to more fully understand the factors that influence the formation of domain boundaries in thicker films,

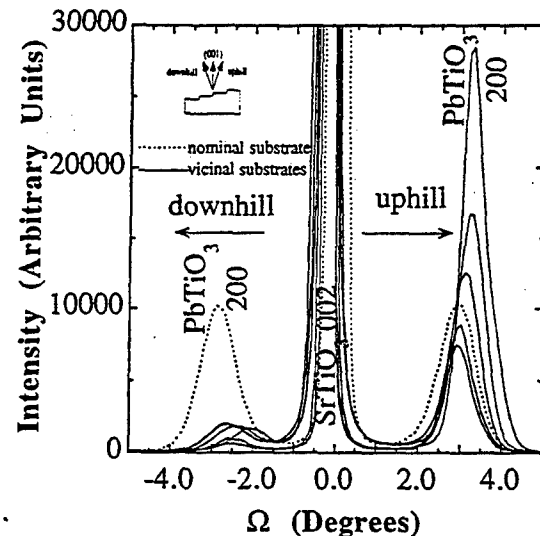


Fig. 2 Overlay of several rocking curves for the  $\text{PbTiO}_3$  200 reflections showing the asymmetry in domain populations on vicinal (100)  $\text{SrTiO}_3$  substrates.

numerous samples having thicknesses of  $\sim 200$  nm were grown under identical conditions with similar cooling rates ( $\sim 10^\circ\text{C/min}$ ) on vicinal (001)  $\text{SrTiO}_3$ . Vicinal (001)  $\text{SrTiO}_3$  substrates miscut toward the [100] or [110] were utilized, and the degree of miscut was varied from less than  $1^\circ$  to more than  $9^\circ$ . The rocking curves of the  $\text{PbTiO}_3$  200 reflections shown in Fig. 2 indicate the presence of  $\alpha$ -oriented  $\text{PbTiO}_3$  grains, where  $\xi$  is the angle of tilt between the  $c$ -axis of the  $c$ -domains and the  $\alpha$ -axis of the  $\alpha$ -domains. The diffraction patterns in Fig. 2 are measured along  $\text{SrTiO}_3$  [100] and [010] directions. The  $\alpha$ -axis domains are preferentially tilted uphill, as defined by the macroscopic tilt of the substrate surface with respect to the (001)  $\text{SrTiO}_3$  plane and schematically indicated in the inset within Fig. 2. This is in contrast to the equally likely (i.e., four peaks of equal intensity) {011} twin boundaries previously reported in  $\text{PbTiO}_3$  films grown on well-oriented (001)  $\text{SrTiO}_3$  substrates [2,5,7]. Note that the direction of tilt of the  $\alpha$ -domains is opposite to that observed in the growth of  $\text{PbTiO}_3$  films on vicinal (001)  $\text{MgO}$  surfaces [11]. In addition the influence of the volume fraction of  $\alpha$ -domains present in a specific orientation on the magnitude of the tilt angle  $\xi$  can be seen from Fig. 2. As the relative volume fraction of  $\alpha$ -oriented material tilted in a certain direction increases, the tilt between that  $\alpha$ -domain and the  $c$ -domain increases (higher  $\xi$ ). Similarly, as the relative volume fraction of  $\alpha$ -oriented material tilted in a certain direction decreases, the tilt between that  $\alpha$ -domain and the  $c$ -domain decreases (lower  $\xi$ ).

#### B. Model of Preferred $\alpha$ -domain orientations

The preferential orientation of the  $\alpha$ -axis  $\text{PbTiO}_3$  domains can be explained by lattice matching considerations. As the

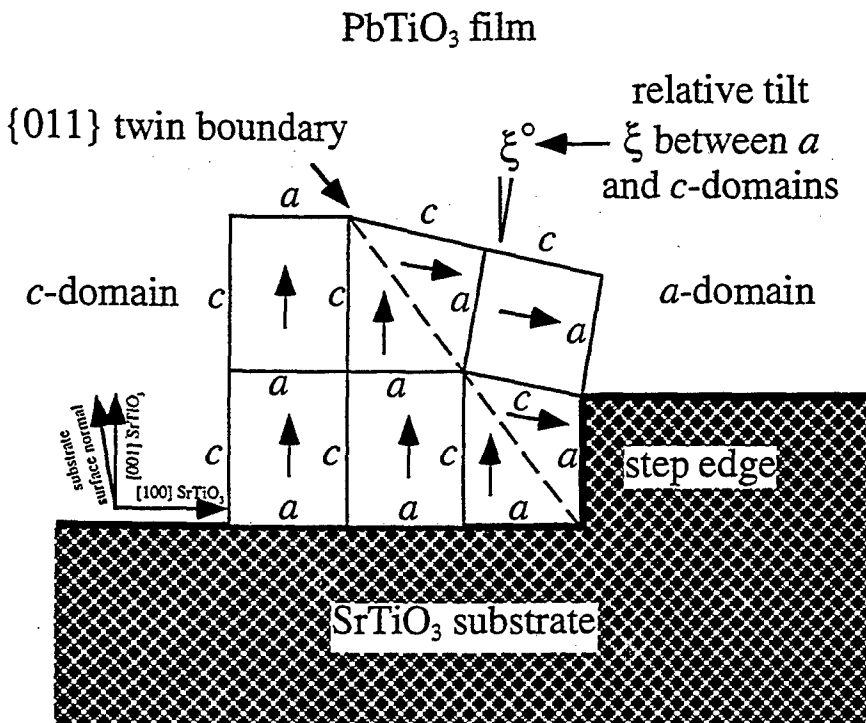


Fig. 3 Schematic showing how the presence of step edges on a vicinal  $\text{SrTiO}_3$  substrate may lead to the preferred nucleation of a  $\text{PbTiO}_3$  (011) twin boundary. The arrows indicate the direction in which the  $c$ -axis lies. The tetragonality has been exaggerated for clarity.

film growth temperature is well above the Curie temperature (490 °C for bulk  $\text{PbTiO}_3$ ), twinning of the  $\text{PbTiO}_3$  must occur during cooling following film growth. The  $\langle 100 \rangle$  directions of the  $\text{SrTiO}_3$  substrate — both the in-plane directions of the (001)  $\text{SrTiO}_3$  surface as well as those of the integral-unit cell high step edges — are much better lattice matched to the  $a$ -axis of  $\text{PbTiO}_3$  than to its  $c$ -axis. Consequently, as schematically depicted in Fig. 3, it is energetically favorable for the regions of the  $\text{PbTiO}_3$  film in contact with the {100}  $\text{SrTiO}_3$  surfaces to be (001)  $\text{PbTiO}_3$  surfaces.

On well-oriented (001)  $\text{SrTiO}_3$  surfaces there is not a dominance of any step edge, and all four types of {011} twin boundaries occur with equal likelihood. However, the vicinal (001)  $\text{SrTiO}_3$  surface contains a dominant step edge direction, and the corresponding (011) twin boundary dominates as is schematically shown in Fig. 3. The tetragonality of  $\text{PbTiO}_3$  has been exaggerated in this figure to clearly illustrate the geometrical cause of the tilt of the  $a$ -oriented material of  $\text{PbTiO}_3$  with respect to the crystallographic normal. This explanation is consistent with our observation that a preferred orientation of  $a$ -domains is found *only* on vicinal substrates. This indicates that the phenomenon is related to a dominance in the direction of the steps on the  $\text{SrTiO}_3$  substrate.

The lattice matching arguments presented above and depicted in Fig. 3 imply that the  $c$ -axis of all  $a$ -domains will lie parallel to the projection of the [100] axis of the  $a$ -domain

onto the  $\text{SrTiO}_3$  (001) surface and not perpendicular to this projection. Indeed, only this expected orientation of  $a$ -domains is observed by 4-circle x-ray diffraction. Unlike the orientation of  $a$ -domains on vicinal (100)  $\text{MgO}$ , where equal volume fractions were measured with their  $c$ -axis parallel and perpendicular to the  $\text{MgO}$  step edges [11], on vicinal (100)  $\text{SrTiO}_3$  the  $c$ -axis of  $a$ -domains lies solely perpendicular to the step edge.

In thick ( $\geq 50$ -150 nm [5,7])  $\text{PbTiO}_3$  films the ability to nucleate a preferred domain wall orientation could be useful for increasing the optical transmission along a specific crystallographic direction. An obvious advantage to such films would be the reduction in optical scattering perpendicular to the preferred domain wall orientation as compared to a film containing randomly oriented walls for use in devices such as infrared sensors or optical switches. For a more detailed discussion on the origins of the preferred orientation we refer the reader to [10].

#### C. Influence of Terrace Length on Tilt Angle $\xi$

The effect of these  $\text{SrTiO}_3$  step edges can be further understood if we consider the ratio of the volume fraction of material tilted uphill/downhill for a given crystallographic [100] or [010] direction as a function of the average distance between steps in that direction (Fig. 4). An uphill/downhill

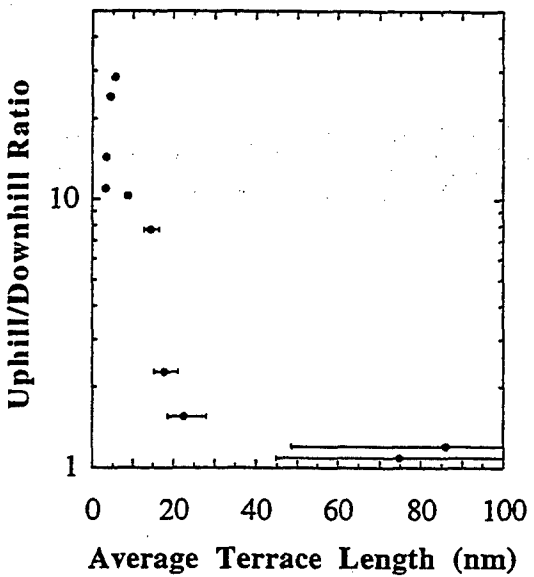


Fig. 4 Graph of the ratio of uphill/downhill a-axis volume fractions along a specific [100] or [010] crystallographic orientation as a function of the average terrace length in that direction.

ratio of 1 (seen at low misorientations) indicates that the  $a$ -axis domains are equally populated. As the substrate misorientation increases beyond  $\sim 1^\circ$ , the dominance of the uphill  $a$ -domain clearly emerges. This threshold corresponds to an average terrace length between steps of about 20 nm. Here the average distance between steps,  $d_{avg}$ , is calculated as

$$d_{avg} = \left[ \frac{a_{SrTiO_3}}{\tan(\theta_m)} \right], \text{ where } a_{SrTiO_3} \text{ is the lattice constant of SrTiO}_3 \text{, and } \theta_m \text{ is the component of the misorientation angle of the substrate toward [100].}$$

Other researchers have seen and measured the average width of  $a$ -domains in epitaxial PbTiO<sub>3</sub> on SrTiO<sub>3</sub> by TEM analysis [2,8] to be approximately 20 nm. In Fig. 4 it is clear that as the average distance between step edges becomes large compared to the average  $a$ -domain width measured for the PbTiO<sub>3</sub>/SrTiO<sub>3</sub> system, the ratio of the volume fraction of  $a$ -oriented material tilted uphill/downhill approaches unity (i.e., the measured ratio for PbTiO<sub>3</sub> films on nominal (001) SrTiO<sub>3</sub> substrates). The effect of vicinal substrates causing a preferred orientation in  $a$ -domain abundance appears to become significant when the average terrace length approaches the average  $a$ -domain width previously measured [8]. The points illustrated in Fig. 4 are only meant to show a trend as the error induced can be very large when measuring downhill volume fractions of less than  $\sim 5\%$  (i.e., at uphill/downhill ratios  $\geq 10$ ). The influence of terrace length on domain population is discussed in more detail elsewhere [10].

## V. CONCLUSIONS

We have grown high quality thin films (40 nm) of PbTiO<sub>3</sub> on SrTiO<sub>3</sub> with good epitaxial alignment that are free of

$a$ -axis domains. Thicker films ( $\sim 200$  nm) grown on vicinal (up to  $9^\circ$  miscut) (001) SrTiO<sub>3</sub> substrates contain both  $a$ -axis and  $c$ -axis PbTiO<sub>3</sub> domains. The  $a$ -domains have a preferred orientation in an uphill direction with respect to the macroscopic substrate surface. The excellent lattice matching of the PbTiO<sub>3</sub> (001) planes to the SrTiO<sub>3</sub> {100} planes on both the substrate surface, and at the SrTiO<sub>3</sub> step edges make this an ideal location for the formation of PbTiO<sub>3</sub> {011} domain boundaries. The predicted tilt angle of the  $a$ -domains,  $90^\circ - 2 \tan^{-1} \left( \frac{a}{c} \right)$ , is not achieved [10]. In our films where there is only one  $c$ -axis orientation, there appears to be a compromise between the  $c$ -domain orientation and the four equivalent  $a$ -domain orientations based on the respective volume fractions of  $a$ -domains present.

The effect of step edges in causing a preferred orientation in  $a$ -domain abundance exists, but only becomes significant when the average distance between these steps is on the order of or less than the average  $a$ -domain width.

## ACKNOWLEDGMENTS

We gratefully acknowledge the financial support of the Office of Naval Research through grant N00014-94-1-0690.

## REFERENCES

- [1] J. F. Scott and D. A. Paz de Araujo, "Ferroelectric memories," *Science*, vol. 246, p. 1400, December 1989.
- [2] A. Seifert, F. F. Lang, and J. S. Speck, "Epitaxial growth of PbTiO<sub>3</sub> thin films on (001) SrTiO<sub>3</sub> from solution precursors," *J. Mater. Res.*, vol. 10, p. 680, March 1995.
- [3] K. Iijima, I. Ueda, and K. Kugimiya, "Preparation and properties of lead zirconate-titanate thin films," *Jpn. J. Appl. Phys.*, vol. 30, p. 2149, September 1991.
- [4] G. R. Bai, H. L. M. Chang, C. M. Foster, Z. Shen, and D. J. Lam, "The relationship between the MOCVD parameters and the crystallinity, epitaxy, and domain structure of PbTiO<sub>3</sub> films," *J. Mater. Res.*, vol. 9, p. 156, January 1994.
- [5] C. M. Foster, Z. Li, M. Buckett, D. Miller, P. M. Baldo, L. E. Rehn, G. R. Bai, D. Guo, H. You, and K. L. Merkle, "Substrate effects on the surface of epitaxial PbTiO<sub>3</sub> thin films prepared on MgO, LaAlO<sub>3</sub>, and SrTiO<sub>3</sub> by metalorganic chemical vapor deposition," *J. Appl. Phys.*, vol. 78, p. 2607 August 1995.
- [6] H. Tabata, "Electric and pyroelectric behaviors of PbTiO<sub>3</sub> thin films formed by an excimer laser ablation technique," *Jpn. J. Appl. Phys.*, vol. 32, p. 5611, December 1993.
- [7] W.-Y. Hsu and R. Raj, "X-ray characterization of the domain structure of epitaxial lead titanate thin films on (001) strontium titanate," *Appl. Phys. Lett.*, vol. 67, p. 792, August 1995.
- [8] S. Stemmer, S. K. Streiffer, R. Raj, "Domain configurations in ferroelectric PbTiO<sub>3</sub> thin films: The influence of substrate and film thickness," *Solid State Ion.*, vol. 75, p. 43, January 1995.
- [9] J. S. Speck and W. Pompe, "Domain configuration due to multiple misfit relaxation mechanisms in epitaxial ferroelectric thin films. I. Theory," *J. Appl. Phys.*, vol. 76, p. 466, July 1994.
- [10] C. D. Theis and D. G. Schliom, "Domain structure of epitaxial PbTiO<sub>3</sub> films grown on vicinal (001) SrTiO<sub>3</sub>", unpublished.
- [11] S. Kim, Y. Kang, and S. Baik, "Growth of PbTiO<sub>3</sub> thin films by r.f. sputtering on vicinal MgO(100) substrates," *Thin Solid Films*, vol. 256, p. 240, February 1995.
- [12] K. Wasa, Y. Haneda, T. Satoh, H. Adachi, S. Hayashi, and K. Setsune, "Structural control of epitaxially grown sputtered PbTiO<sub>3</sub> thin films," *Jpn. J. Appl. Phys.*, vol. 34, p. 5132, September 1995.

## ADSORPTION-CONTROLLED GROWTH OF FERROELECTRIC PbTiO<sub>3</sub> AND Bi<sub>4</sub>Ti<sub>3</sub>O<sub>12</sub> FILMS FOR NONVOLATILE MEMORY APPLICATIONS BY MBE

C. D. THEIS\*, J. YEH\*, M. E. HAWLEY\*\*, G. W. BROWN\*\*, and D. G. SCHLOM\*

\*Department of Materials Science and Engineering, The Pennsylvania State University, University Park, PA 16802-5005, theis@ems.psu.edu

\*\*Center for Materials Science, Los Alamos National Laboratory, Los Alamos, NM 87545

### ABSTRACT

Epitaxial PbTiO<sub>3</sub> and Bi<sub>4</sub>Ti<sub>3</sub>O<sub>12</sub> thin films have been grown on (100) SrTiO<sub>3</sub> and (100) LaAlO<sub>3</sub> substrates by reactive molecular beam epitaxy (MBE). Titanium is supplied to the film in the form of shuttered bursts each containing a one monolayer dose of titanium atoms for the growth of PbTiO<sub>3</sub> and three monolayers for the growth of Bi<sub>4</sub>Ti<sub>3</sub>O<sub>12</sub>. Lead, bismuth, and ozone are continuously supplied to the surface of the depositing film. Growth of phase pure, *c*-axis oriented epitaxial films with bulk lattice constants is achieved using an overpressure of these volatile species. With the proper choice of substrate temperature (600 - 650 °C) and ozone background pressure ( $P_{O_3} = 2 \times 10^{-5}$  Torr), the excess of the volatile metals and ozone desorb from the surface of the depositing film leaving a phase-pure stoichiometric crystal. The smooth PbTiO<sub>3</sub> surface morphology revealed by atomic force microscopy (AFM) suggests that the PbTiO<sub>3</sub> films grow in a layer-by-layer fashion. In contrast the Bi<sub>4</sub>Ti<sub>3</sub>O<sub>12</sub> films contain islands which evolve either continuously or around screw dislocations via a spiral-type growth mechanism.

### INTRODUCTION

PbTiO<sub>3</sub> and Bi<sub>4</sub>Ti<sub>3</sub>O<sub>12</sub> are well known ferroelectric oxides and are both members of the (Bi,Pb)<sub>n+1</sub>Ti<sub>n</sub>O<sub>3n+3</sub> Aurivillius homologous series [1]. PbTiO<sub>3</sub> is the  $n = \infty$  member of this series and has the largest remanent polarization (80 μC/cm<sup>2</sup>) of any known ferroelectric [2]. PbTiO<sub>3</sub> has a tetragonal unit cell at room temperature with  $a = b = 3.90$  Å and  $c = 4.15$  Å [3]. At the other end of this homologous series,  $n = 3$ , lies the highly layered compound Bi<sub>4</sub>Ti<sub>3</sub>O<sub>12</sub> which has lower remanent polarization (~50 μC/cm<sup>2</sup> of which the component along the *c*-axis is ~4 μC/cm<sup>2</sup> [3]), but can withstand far more polarization reversals before it fatigues [4]. The structure consists of Bi<sub>2</sub>O<sub>3</sub> layers separated by Bi<sub>2</sub>Ti<sub>3</sub>O<sub>10</sub> perovskite sheets. It is orthorhombic at room temperature with lattice constants  $a = 5.41$ ,  $b = 5.45$  and  $c = 32.83$  Å [3]. The resistance to fatigue of Bi<sub>4</sub>Ti<sub>3</sub>O<sub>12</sub> and other Aurivillius phases make these materials of interest for use in non-volatile ferroelectric random access memories (FRAMs). On the other hand the high  $P_c$  of PbTiO<sub>3</sub> makes it of interest for superconducting field effect transistors (SuFETs) [5]. We are interested in the variation of properties that occur in the (Bi,Pb)<sub>n+1</sub>Ti<sub>n</sub>O<sub>3n+3</sub> homologous series and describe below the preparation of the two end members of this series by MBE.

### EXPERIMENTAL

Bismuth and lead titanate are grown using reactive MBE. The system used for this study is described in detail elsewhere [6]. Lead and bismuth are continuously supplied to the surface of the depositing film from low-temperature effusion cells. Titanium is sublimated onto the film from a titanium sublimation pump. The Ti-Ball™ [7] is powered by a low noise DC power supply. The resulting titanium flux has a maximum peak-to-peak variation of ±2.5% over 5 hours [8] (about five times longer than the time needed to grow a 1000 Å thick PbTiO<sub>3</sub> or Bi<sub>4</sub>Ti<sub>3</sub>O<sub>12</sub> film).

The fluxes of all depositing species are monitored *in situ* using atomic absorption spectroscopy (AA). Oxygen is supplied to the film in the form of ~80% pure distilled ozone. Film growth is monitored continuously using reflection high energy electron diffraction (RHEED). The substrate heater-block temperature is measured by an optical pyrometer. (100) LaAlO<sub>3</sub> and (100) SrTiO<sub>3</sub> substrates are used. The SrTiO<sub>3</sub> wafers are etched with a buffered-HF solution prior to growth [9]. The substrates are attached to heater blocks using silver paint.

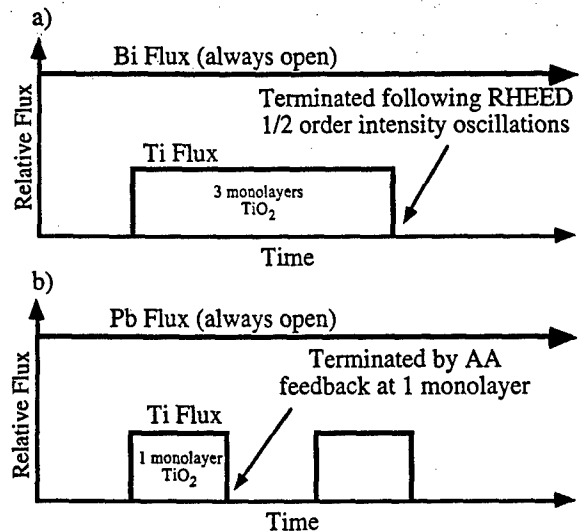


Fig. 1. Flux vs. time for a typical MBE growth of (a)  $\text{Bi}_4\text{Ti}_3\text{O}_{12}$  or (b)  $\text{PbTiO}_3$ . Ozone is supplied continuously to the surface of the depositing film.

Figure 1(a) shows the depositing flux as a function of time used for the  $\text{Bi}_4\text{Ti}_3\text{O}_{12}$  growths. Bismuth and ozone are supplied to the surface of the film continuously while the substrate temperature is maintained at  $\sim 640^\circ\text{C}$ . The ozone background pressure for a typical growth is  $2 \times 10^{-5}$  Torr which represents an incident flux of ozone hundreds of times greater than required for a stoichiometric crystal. Similarly, bismuth is supplied at an incident flux  $\sim 2 - 5$  times greater than the average titanium incident flux. Titanium is supplied in shuttered doses each containing three monolayers of titania which make up the  $\text{Bi}_4\text{Ti}_3\text{O}_{10}$  perovskite sheets. The titanium dose is terminated by the evolution of RHEED half-order streaks present along the substrate [110] azimuth. The oscillating half-order streaks, which are not damped throughout film growth, are due to the epitaxial relationship between the cubic substrate and orthorhombic film where  $\text{Bi}_4\text{Ti}_3\text{O}_{12}$  [100] //  $\text{SrTiO}_3$  [110]. The disappearance of these oscillating half-order streaks could be a manifestation of the higher symmetry of the centermost  $\text{TiO}_6$  octahedra which are not tilted with respect to *c*-axis or rotated with respect to the *a*-*b* plane of  $\text{Bi}_4\text{Ti}_3\text{O}_{12}$  [10]. As the film growth proceeds in the *c*-axis direction, the tilt and rotation of the  $\text{TiO}_6$  octahedra on either side of the  $\text{Bi}_2\text{O}_2$  layers, which yields the orthorhombic symmetry of the unit cell, could result in the reappearance of the half-order streaks.

Figure 1(b) shows the depositing flux as a function of time for a typical  $\text{PbTiO}_3$  growth. The typical substrate temperature is  $\sim 630^\circ\text{C}$ . Again, lead and ozone are supplied to the surface of the film continuously, while the ozone background pressure is maintained at  $2 \times 10^{-5}$  Torr. The lead flux is maintained at a rate of incidence  $2 - 5$  times greater than the titanium flux. The titanium is shuttered to deliver individual  $\text{TiO}_2$  monolayers using direct feedback from the AA signal.

#### RESULTS AND DISCUSSION

Using the growth conditions described above it is possible to use a range of lead and bismuth incident fluxes and still obtain phase pure material. Rutherford backscattering spectrometry (RBS) measurements indicate that the  $\text{Bi}_4\text{Ti}_3\text{O}_{12}$  and  $\text{PbTiO}_3$  films are stoichiometric within the error of the measurement. A similar mechanism was shown to be operative by de Keijser and Dormans [11] for

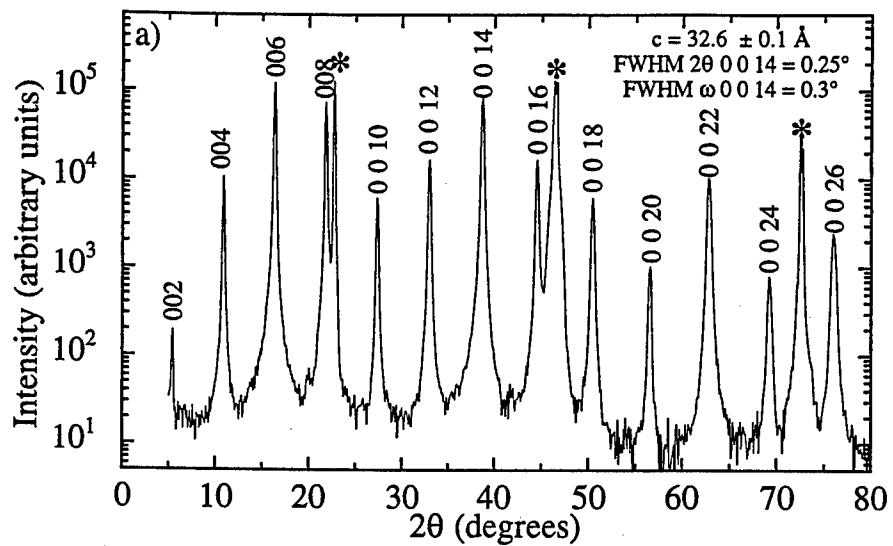


Fig. 2(a)  $\theta$ - $2\theta$  scan of a 1000 Å thick film of  $\text{Bi}_4\text{Ti}_3\text{O}_{12}$  on a (100)  $\text{SrTiO}_3$  substrate (\* indicates substrate reflections).

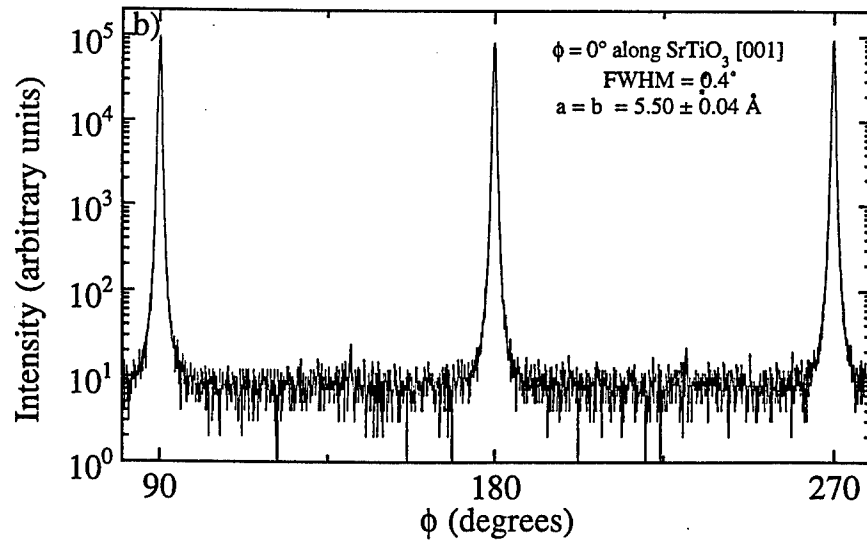


Fig. 2(b) Azimuthal  $\phi$ -scan of a 1000 Å thick  $\text{Bi}_4\text{Ti}_3\text{O}_{12}$  film; 117  $\text{Bi}_4\text{Ti}_3\text{O}_{12}$  reflections.

organometallic chemical vapor deposited PZT thin films. They found that by using a range of lead precursor partial pressures, it was possible to obtain stoichiometric films [11]. This adsorption controlled growth mechanism is reliant on the presence of a volatile metal — metal-oxide system. We attribute this adsorption-controlled mechanism, under the proper choice of background pressure and substrate temperature, to conditions where the sticking coefficient of lead or bismuth to the  $\text{TiO}_2$  layer approaches unity while the sticking coefficient of lead or bismuth to the  $\text{PbO}$  or  $\text{BiO}$  surface is negligible. The near unity sticking coefficient of titania is substantiated by the film thickness calculated from the x-ray diffraction peak widths and thickness fringes of ultrathin  $\text{Bi}_4\text{Ti}_3\text{O}_{12}$  films, RBS composition measurements, counting RHEED half-order intensity oscillations during growth, and *in situ* flux measurements using a quartz crystal thickness monitor and AA spectroscopy. All of these indicate that the incident titanium flux determines the growth rate of the titanate films. The excess of the volatile cations and the excess ozone present desorb from the surface. Similar to the MBE growth of GaAs films where arsenic is supplied in massive overabundance, the adsorption-controlled growth mechanism generates phase pure single crystal films eliminating many of the difficulties associated with accurate composition control.

Figure 2(a) is a  $\theta$ - $2\theta$  4-circle x-ray diffraction scan of 1000 Å thick  $\text{Bi}_4\text{Ti}_3\text{O}_{12}$  film grown on (100)  $\text{SrTiO}_3$ . Intense  $00l$  peaks indicate that the film is pure c-axis oriented  $\text{Bi}_4\text{Ti}_3\text{O}_{12}$ . The rocking curve full width at half maximum (FWHM) of the  $\text{Bi}_4\text{Ti}_3\text{O}_{12}$   $0014$  reflection is measured to be  $0.3^\circ$  showing minimal out-of-plane misalignment. Figure 2(b) is an azimuthal scan ( $\phi$ -scan) of the 117 reflections of this same film. The peaks show a  $\text{Bi}_4\text{Ti}_3\text{O}_{12}$  [110] //  $\text{SrTiO}_3$  [010] orientation with a FWHM of  $0.4^\circ$  in  $\phi$ , indicating little variation in the in-plane alignment. These peak widths are all comparable to the instrument resolution of our Picker 4-circle diffractometer. RBS channeling results for this film showed a minimum channeling yield ( $\chi_{\min}$ ) of 0.2, which is the lowest reported value for epitaxial  $\text{Bi}_4\text{Ti}_3\text{O}_{12}$ . Figure 3 is an AFM image of the surface of this same film. Clearly visible on the surface are micron size islands that protrude  $\sim 100$  -  $200$  Å out of the film. The terraces making up these islands have step heights that are integral multiples of a half

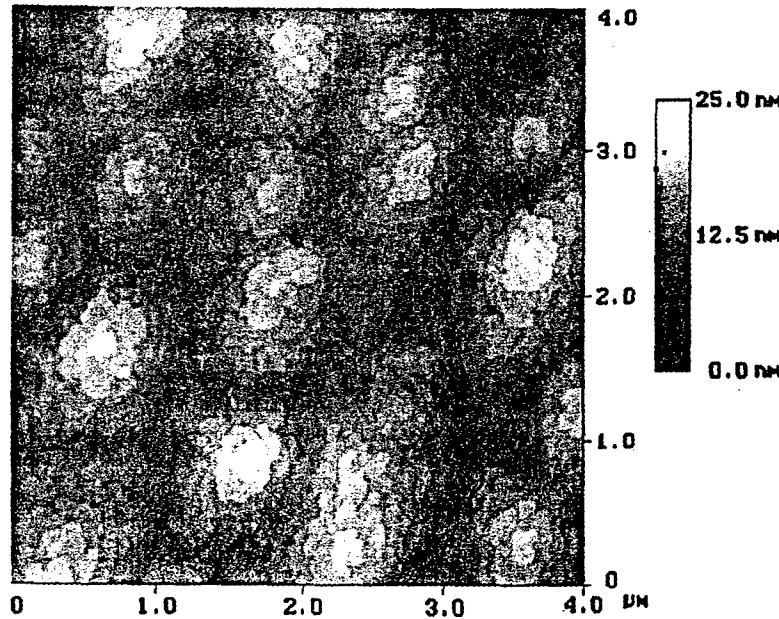


Fig. 3 AFM image of the surface of 1000 Å thick  $\text{Bi}_4\text{Ti}_3\text{O}_{12}$  film grown on  $\text{SrTiO}_3$ .

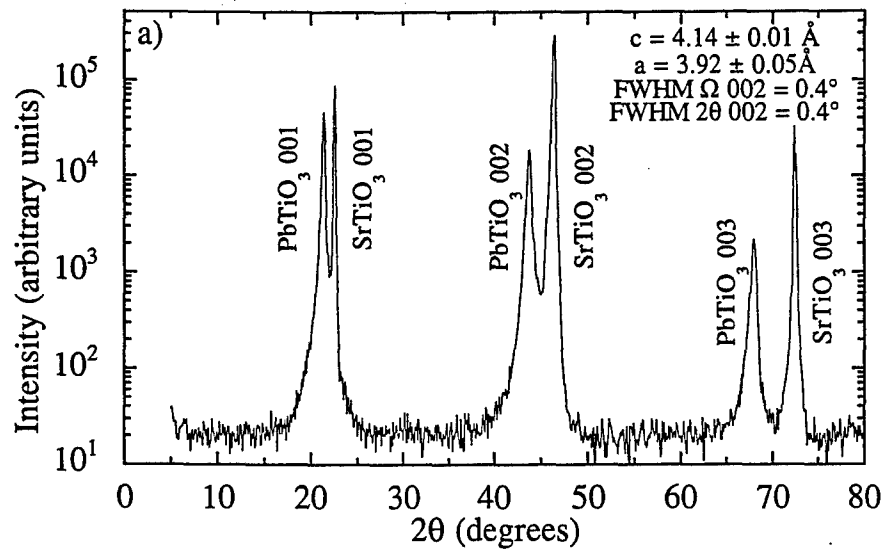


Fig. 4(a)  $\theta$ - $2\theta$  scan of a 1000  $\text{\AA}$  thick film of  $\text{PbTiO}_3$  on a (100)  $\text{SrTiO}_3$  substrate.

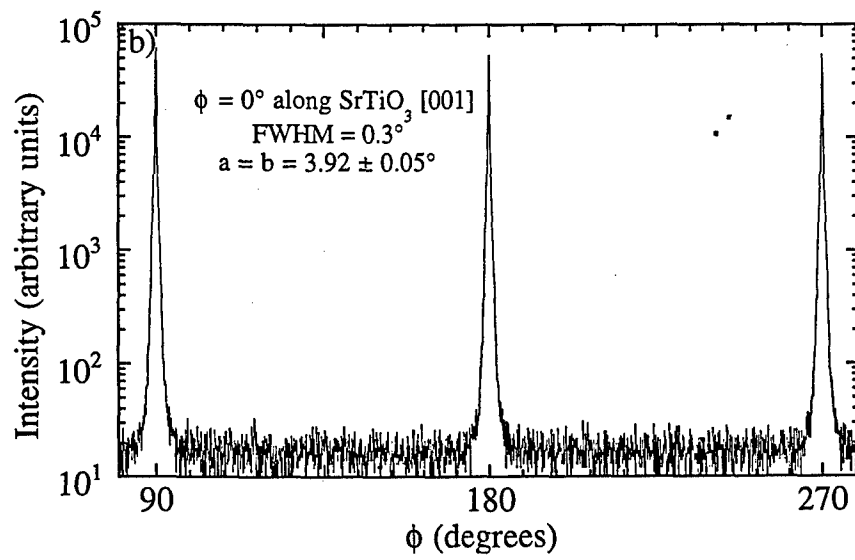


Fig. 4(b) Azimuthal  $\phi$ -scan of a 1000  $\text{\AA}$  thick  $\text{PbTiO}_3$  film; 101  $\text{PbTiO}_3$  reflections.

unit cell. The surface morphology revealed by AFM is reminiscent of that of layered perovskite superconductor films [12,13], although it is unclear if oppositely-signed screw dislocations are present within each mound or if the mounds are screw dislocation-free islands that arise due to limited surface diffusion.

In Fig. 4(a) a  $\theta$ -2 $\theta$  4-circle x-ray diffraction scan of a 1000 Å thick film of  $\text{PbTiO}_3$  grown on (100)  $\text{SrTiO}_3$  is shown. Intense  $00\ell$  peaks indicate that the film is pure *c*-axis oriented  $\text{PbTiO}_3$ ; additional scans showed no evidence of *a*-axis oriented domains. The  $\phi$ -scan in Fig. 4(b) demonstrates that the film is epitaxial with a cube-on-cube orientational relationship between film and substrate and a FWHM in  $\phi$  of 0.3°. AFM images of the  $\text{PbTiO}_3$  film surface show extremely smooth morphologies with a root mean square (RMS) roughness of < 5 Å. This surface structure is indicative of a layer-by-layer growth mechanism.

## CONCLUSIONS

We have grown epitaxial  $\text{PbTiO}_3$  and  $\text{Bi}_4\text{Ti}_3\text{O}_{12}$  films by reactive MBE. Under conditions of ozone background pressure and temperature where an adsorption-controlled growth mechanism dominates, we believe that the sticking coefficient of the volatile metal cations is close to one on  $\text{TiO}_2$  surfaces and negligible on other adsorbed species. The excess of lead, bismuth, and ozone desorb from the surface leaving behind a phase pure, stoichiometric crystal. AFM analysis indicates that the  $\text{PbTiO}_3$  has a smooth surface morphology (RMS roughness < 5 Å).  $\text{Bi}_4\text{Ti}_3\text{O}_{12}$  films have micron sized islands present at the surface that span 100 - 200 Å from top to bottom. These morphologies are consistent with either a spiral-type growth mechanism where film growth normal to the substrate surface is mediated by screw dislocations or an island-type growth mechanism.

## ACKNOWLEDGMENTS

We gratefully acknowledge the financial support of the Office of Naval Research through grant N00014-94-1-0690.

## REFERENCES

1. B. Aurivillius, *Arkiv Kemi* **1**, 463 (1949); B. Aurivillius, *Arkiv Kemi* **1**, 499 (1949); B. Aurivillius, *Arkiv Kemi* **2**, 519 (1950); B. Aurivillius, *Arkiv Kemi* **5**, 39 (1952); B. Aurivillius and P.H. Fang, *Phys. Rev.* **126**, 893 (1962).
2. E. C. Subbarao, *Ferroelectrics* **5**, 267 (1973).
3. Landolt-Bornstein: *Numerical Data and Functional Relationships in Science and Technology*, New Series, Group III, Vol. 16a, edited by K.-H. Hellwege (Springer-Verlag, Berlin, 1981), pp. 77, 237.
4. C. A-Paz de Araujo, J. D. Cuchiaro, L. D. McMillan, M. C. Scott, and J. F. Scott, *Nature* **374**, 627 (1995).
5. J. Mannhart, *Supercond. Sci. Technol.* **9**, 49 (1996).
6. C. D. Theis and D. G. Schlom, to be published in *J. Cryst. Growth*.
7. Varian Vacuum Products, Lexington, MA.
8. C. D. Theis and D. G. Schlom, *J. Vac. Sci. Technol. A* **14**, 2677 (1996).
9. M. Kawasaki, K. Takahashi, T. Maeda, R. Tsuchiya, M. Shinohara, O. Ishiyama, T. Yonezawa, M. Yoshimoto, and H. Koinuma, *Science* **266**, 1540 (1994).
10. I. M. Reaney, M. Roulin, H. S. Shulman, and N. Setter, *Ferroelectrics* **165**, 295 (1995).
11. M. de Keijser and G. J. M. Dormans, *MRS Bulletin*, 37 (June, 1996).
12. C. Gerber, D. Anselmetti, J. G. Bednorz, J. Mannhart, and D. G. Schlom, *Nature* **350**, 279 (1991).
13. M. Hawley, I. D. Raistrick, J. G. Beery, and R. J. Houlton, *Science* **251**, 1587 (1991).

## THE CONTROLLED GROWTH OF PEROVSKITE THIN FILMS: OPPORTUNITIES, CHALLENGES, AND SYNTHESIS

Darrell G. Schlom  
Department of Materials Science and Engineering  
Penn State University  
103 Steidle Building  
University Park, PA 16802-5005

Chris D. Theis  
Department of Materials Science and Engineering  
Penn State University  
106 Materials Research Institute Building  
University Park, PA 16802

Marilyn E. Hawley  
Center for Materials Science  
MS K765  
Los Alamos National Laboratory  
Los Alamos, NM 87545

### ABSTRACT

The broad spectrum of electronic and optical properties exhibited by perovskites offers tremendous opportunities for microelectronic devices, especially when a combination of properties in a single device is desired. Molecular beam epitaxy (MBE) has achieved unparalleled control in the integration of semiconductors at the monolayer-level; its use for the integration of perovskites with similar nanoscale customization appears promising. Composition control and oxidation are often significant challenges to the growth of perovskites by MBE, but we show that these can be met through the use of purified ozone as an oxidant and real-time atomic absorption composition control. The opportunities, challenges, and synthesis of oxide heterostructures by reactive MBE are described, with examples taken from the growth of oxide superconductors and oxide ferroelectrics.

### INTRODUCTION

Oxides exhibit the full spectrum of electronic, optical, and magnetic behavior; insulating, semiconducting, metallic, high temperature superconducting, pyroelectric, piezoelectric, ferroelectric, ferromagnetic, and non-linear optical effects are all contained within structurally-compatible oxides (particularly perovskites). Examples are given in Table I and some of their crystal structures are shown in Fig. 1. The electroceramics industry, a more than \$20 billion/year industry, utilizes these electrical properties generally in single devices made primarily by bulk synthesis methods for capacitors, sensors, actuators, night vision and other applications. However, a significant opportunity exists to combine these properties together in oxide heterostructures where multiple properties can be utilized to yield a functional integrated device. Integration of

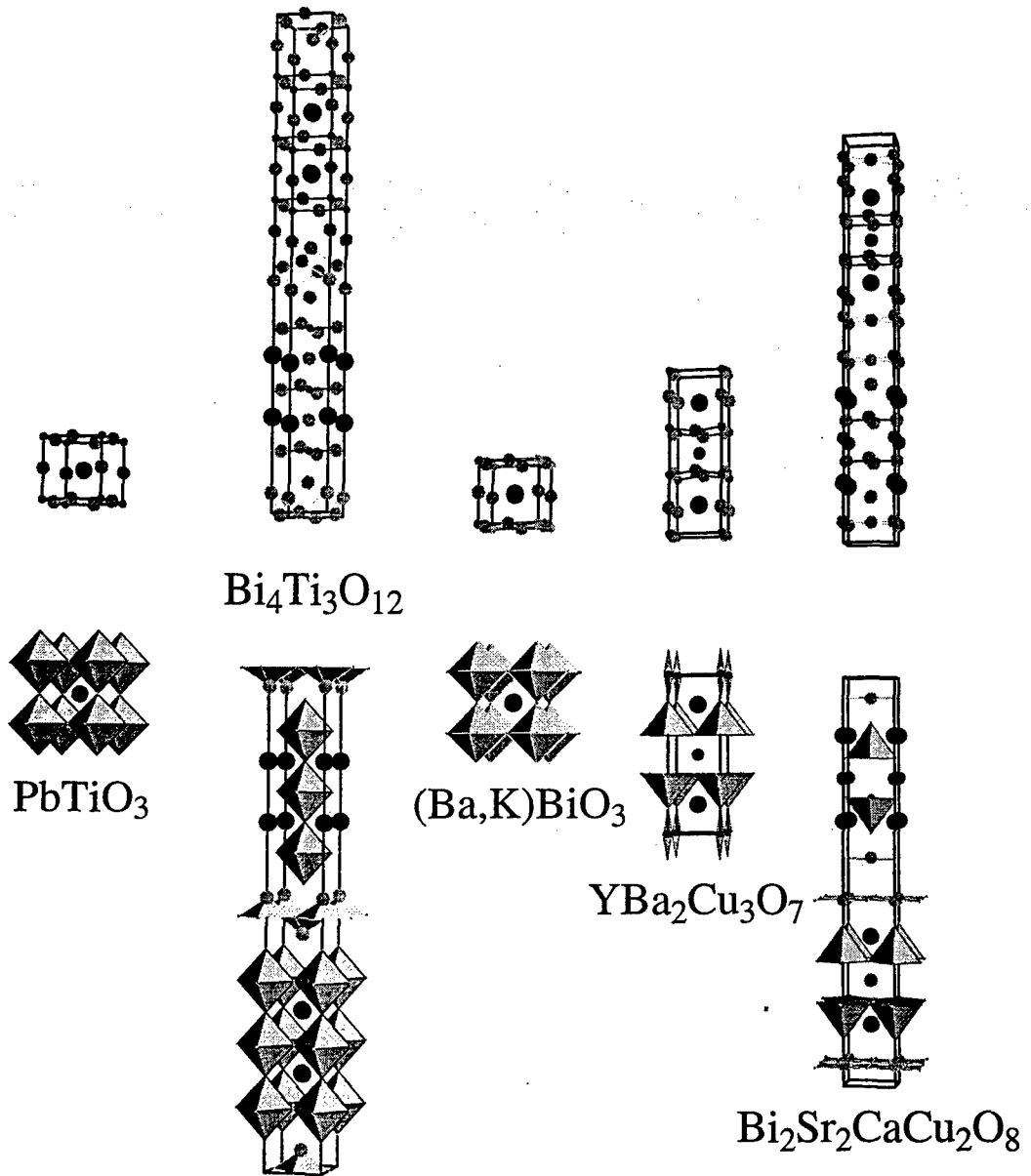


Fig. 1. The crystal structure of some perovskite-related structures exhibiting the properties described in Table I. Two equivalent representations of these crystal structures are shown: the atomic positions (above) and the coordination polyhedra (below). The oxygen atoms occupy the vertices of the coordination polyhedra. The tetragonal subcells of the  $\text{Bi}_4\text{Ti}_3\text{O}_{12}$  and  $\text{Bi}_2\text{Sr}_2\text{CaCu}_2\text{O}_{8+8}$  structures are shown for clarity and to illustrate the similarities between these perovskite-related phases. The relative sizes of the atoms reflect their relative ionic radii as given by Ref. 1.

Table I: Examples of the properties of compatible (perovskite) oxides.

Property	Value	Oxide Material
High $\epsilon_r$ Insulators	$\rho \approx 1 \times 10^{11} \Omega \cdot m$ $\epsilon_r = 20000$ (4 K)	$\text{SrTiO}_3$
Low $\epsilon_r$ Insulators	$\epsilon_r = 16$ (77 K)	$\text{LaAlO}_3$
Conductors	$\rho \approx 1 \times 10^{-7} \Omega \cdot m$ (77 K)	$\text{Sr}_2\text{RuO}_4$
Superconductors	$\rho \approx 0$	$\text{YBa}_2\text{Cu}_3\text{O}_{7-\delta}$
Ferroelectrics	$P_r = 0.75 \text{ C/m}^2$	$\text{PbTiO}_3$
Pyroelectrics	$p_3 = 500 \frac{\mu\text{C}}{\text{m}^2 \text{K}}$	$(\text{Ba},\text{Sr})\text{TiO}_3$
Piezoelectrics	$d_{15} = 600 \text{ pC/N}$	$\text{BaTiO}_3$
Ferromagnets	$M_s = 1.4 \mu_B$	$\text{SrRuO}_3$
Colossal Magnetoresistance	$\Delta R/R_H > 10^4$ (6 T)	$(\text{La},\text{Sr})\text{MnO}_3$

epitaxial stacks of these oxide crystals is motivated by the similarity in crystal structure (the perovskite oxides listed in Table I all have perovskite subcell dimensions in the 3.8 Å to 4.0 Å range), the chemical compatibility that exists between many oxides, and the enhanced properties that these materials exhibit in single crystal form. The increase in performance can be by many orders of magnitude for the critical current density ( $J_c$ ) of a superconductor or the magnetoresistance effect. In addition to synthesizing oxide heterostructures that integrate relatively thick layers of different oxides together, in principle, new oxides can be engineered if structural control can be achieved at the atomic-layer level. Although now commonplace in the growth of semiconductors (i.e., by MBE), such an ability would be new to oxides and would likely result in the discovery/engineering of higher performance materials and possibly the exploitation of new electrical phenomena. Numerous attempts by conventional solid-state techniques to synthesize oxide structures believed to be of significant scientific and technological importance have failed.

Just as MBE made possible the bandgap engineering of semiconductor heterostructures, reactive MBE shows great promise for the growth of oxide heterostructures with control down to the atomic layer level, i.e., atomic layer engineering of oxides.<sup>2</sup> Using MBE to integrate perovskite heterostructures and even to engineer new perovskites with nanometer control is particularly attractive. The perovskite structure can accommodate the majority of the periodic table, as shown in Fig. 2. Such a malleable structural host offers an opportunity to customize electronic, magnetic, and optical properties in thin films far beyond that possible with conventional semiconductors.

Structure-property relations have been studied for a great many oxides using solid-state synthesis methods. Many cases have been found where the property of a structurally-related family of oxides (i.e., a homologous series) changes drastically from one end to the other of the series. Examples include the

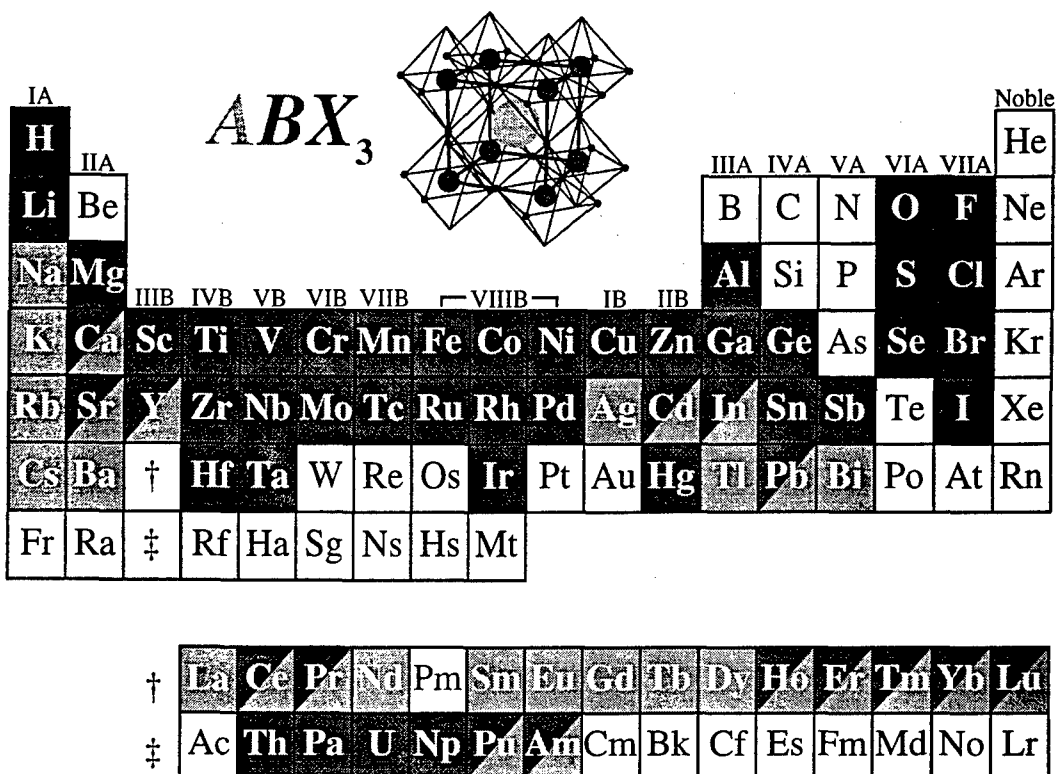


Fig. 2. A compilation of which elements of the periodic table can occupy the three sites (*A*, *B*, and *X*) of the perovskite crystal structure (based on the data in Ref. 3).

$\text{Sr}_{n+1}\text{Ru}_n\text{O}_{3n+1}$  Ruddlesden-Popper homologous series shown in Fig. 3. The  $n = 1$  ( $\text{Sr}_2\text{RuO}_4$ ) member of the series is paramagnetic and superconducting whereas the  $n = \infty$  ( $\text{SrRuO}_3$ ) member of the series is ferromagnetic. Many other equally fascinating homologous series exist in perovskite-related oxide structures showing interesting variation in ferromagnetic, ferroelectric, superconducting, or metal-insulator behavior. However, when the goal is to study the property variation with changing  $n$  in detail, solid-state synthesis methods fall short. Invariably researchers have only been able to find conditions of temperature and pressure yielding single-phase products for low values of  $n$  and for  $n = \infty$ . Attempts to make intermediate  $n$  values result in uncontrolled intergrowths.<sup>4-11</sup> Calculation of the energy of formation of several homologous series of layered oxide phases indicates the reason for this difficulty—differences in formation energy become smaller and smaller as more building layers are inserted into the parent structure

(i.e., with increasing  $n$ ).<sup>\*12</sup> Thus, apart from theoretical calculations, little is known about how the properties of a series of structures vary with  $n$  as the dimensionality of the structure changes. A key advantage of the use of MBE for the preparation of oxide heterostructures is that single-phase epitaxial films with intermediate  $n$  values can often be synthesized even though nearby phases have similar formation energies.<sup>2</sup> This is made possible by the ability to supply incident species in any desired sequence with submonolayer composition control. A particular phase can often be grown by supplying the constituents in an ordered sequence corresponding to the atomic arrangement of these constituents in the desired phase.

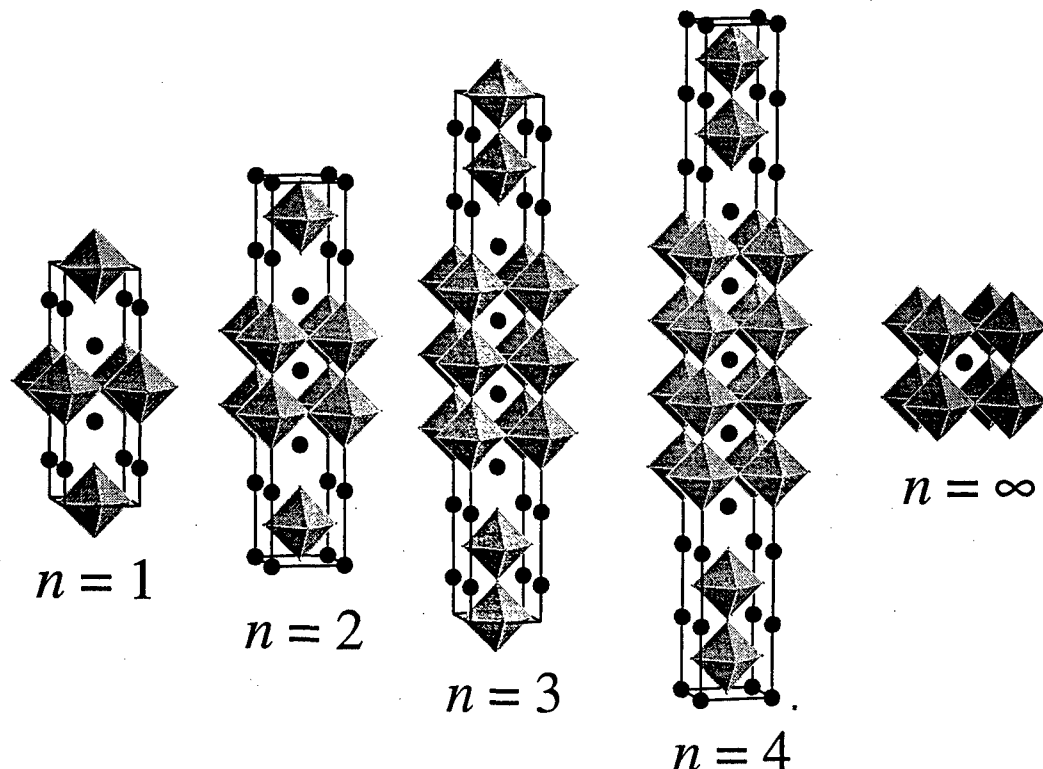


Fig. 3.  $n = 1 (\text{Sr}_2\text{RuO}_4)$ ,  $n = 2 (\text{Sr}_3\text{Ru}_2\text{O}_7)$ ,  $n = 3 (\text{Sr}_4\text{Ru}_3\text{O}_{10})$ ,  $n = 4 (\text{Sr}_5\text{Ru}_4\text{O}_{13})$ , and  $n = \infty (\text{SrRuO}_3)$  members of the homologous Ruddlesden-Popper series of compounds  $\text{Sr}_{n+1}\text{Ru}_n\text{O}_{3n+1}$ .

\* For example, in the  $\text{Sr}_{n+1}\text{Ti}_n\text{O}_{3n+1}$  homologous series of compounds (another perovskite-related series of compounds), calculations indicate that the formation enthalpy remains essentially constant for  $n > 2$ .<sup>12</sup> Since there is insufficient enthalpic driving force for forming a low entropy phase-pure compound, disordered intergrowths are to be expected in the synthesis of these compounds by bulk methods. Indeed, TEM images of these  $\text{Sr}_{n+1}\text{Ti}_n\text{O}_{3n+1}$  phases<sup>5</sup> show disordered syntactic intergrowths where  $n$  ranges from 2 to 8, as would be expected for the bulk preparation of essentially energetically degenerate phases.

MBE even allows metastable phases to be formed by utilizing interfacial strain energies to favor the desired metastable phase over the equilibrium phase (epitaxial stabilization).<sup>13</sup> In contrast to bulk synthesis, in epitaxial growth, interfacial energies play a significant role. Specifically, strain energies due to interfacial mismatch are often sufficient to shift the energetics of which phase is most stable. In cases where the equilibrium structure has significantly different lattice spacing than a desired metastable structure, the formation of the metastable structure may be made favorable by selecting a substrate that is lattice matched to it rather than to the equilibrium structure. Numerous examples of epitaxially-stabilized phases exist in semiconductor, metal, and alkali halide systems.<sup>13-15</sup> Many of these examples have been grown by MBE.

Below the road to the controlled synthesis of oxide heterostructures is first described, followed by examples indicating the promise and current capabilities of reactive MBE. The low growth temperature and atomic layering capability of MBE, widely utilized for the growth of metastable layered semiconductor superlattices, have enabled the *controlled* customized layering of high  $T_c$  phases whose phase-pure growth is unattainable by bulk synthesis methods.<sup>2</sup> These results demonstrate the capability of MBE to grow customized layered structures and metastable phases within *oxide* systems.

#### MBE GROWTH APPARATUS

MBE machines for the growth of semiconductors (e.g., IV-IV, III-V, and II-VI materials systems) are present in many laboratories and the technique has enjoyed significant success in the preparation of semiconductor microstructures with nanoscale thickness control and exceptional device characteristics. The use of MBE for the controlled growth of multi-component oxides is relatively new.<sup>2</sup>

A schematic diagram of the growth chamber of the MBE machine<sup>16</sup> used by the authors is shown in Fig. 4. Eight independent shutters, controlled by a computer, supply elemental fluxes to the substrate either at the same time (codeposition) or separately (sequential deposition), as described below. Purified ozone is used to provide sufficient oxidation, while maintaining the long mean free path necessary for MBE.<sup>2</sup> A titanium sublimation pump, powered by a precision current supply, is used as a stable (flux variation of less than 1% per hour)<sup>17</sup> and economical titanium source.

The lack of adequate composition control has been a major problem for previous oxide MBE work.<sup>2</sup> The use of atomic absorption spectroscopy (AA) for oxide MBE composition control has allowed flux stability of better than 1% to be achieved.<sup>18</sup> The MBE system also contains a retractable quartz crystal microbalance to provide an absolute *in situ* flux measurement at the position of the wafer (prior to growth) for calibration of the AA signals. The depositing fluxes of *all* the sources (up to eight different elements simultaneously) are monitored during growth by AA.<sup>19</sup> The measured AA signal is fed into the MBE computer control system, which integrates the AA fluxes and closes the appropriate shutters after the desired dose has been delivered to the substrate.<sup>20</sup> In addition, the system also contains the standard features found in MBE systems: *in situ* reflection high energy electron diffraction (RHEED), a mass spectrometer, computer-controlled shutters and furnaces for eight elemental sources, and a load-locked wafer introduction chamber.

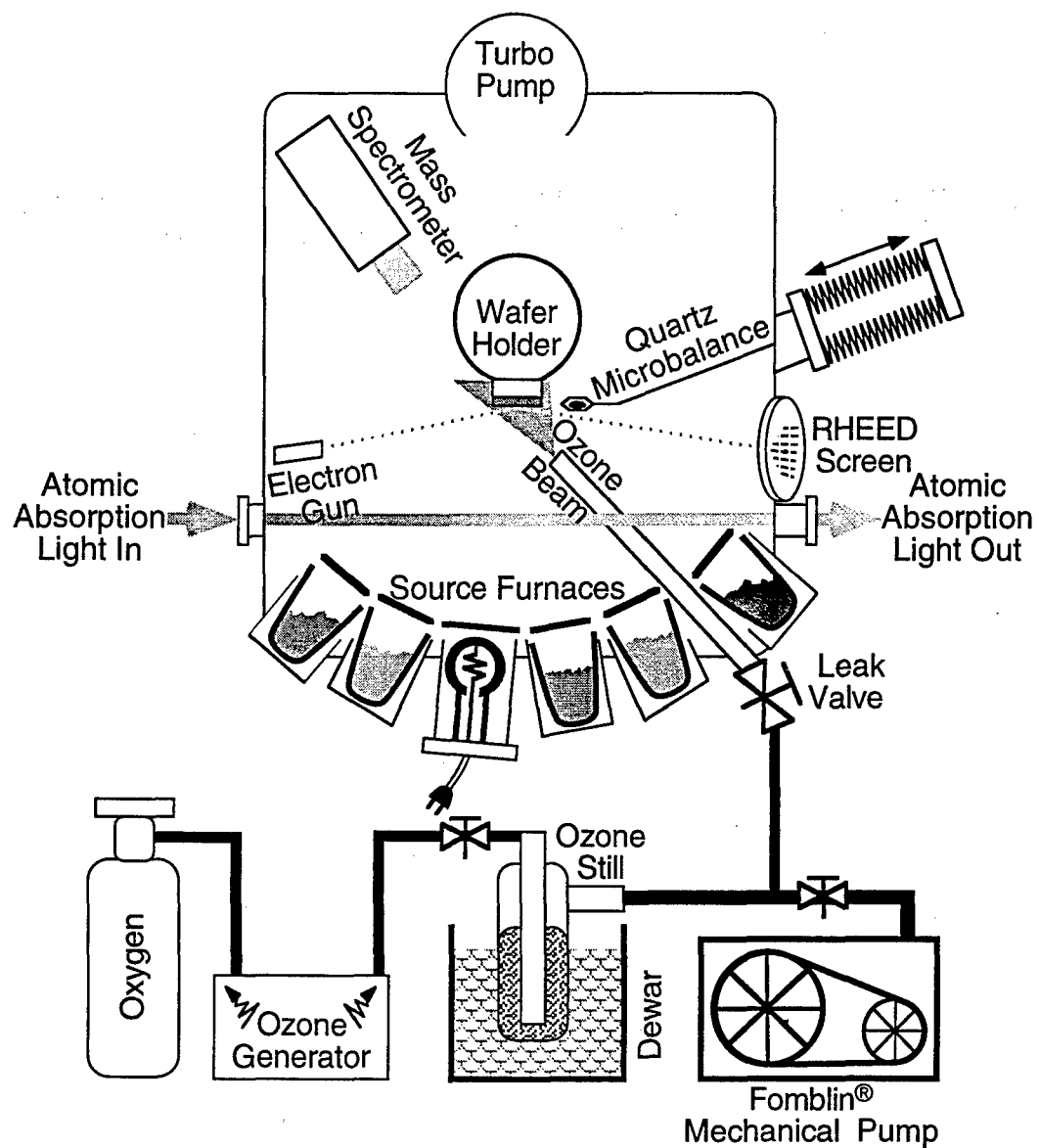


Fig. 4: A schematic diagram of the growth chamber of an MBE system dedicated to the controlled synthesis of oxide heterostructures.

The MBE method of thin film growth may be thought of as atomic spray painting, as shown in Fig. 5 in which an oxide heterostructure consisting of the superconductor  $\text{Bi}_2\text{Sr}_2\text{CaCu}_2\text{O}_8$  is schematically assembled layer-by-layer. The flux of spray from each atomic or molecular beam is controlled by the temperature (and thus vapor pressure) of the effusion cell in which each species is contained. The duration of spray is individually controlled for each beam by shutters, which control not only the open time (and thus dose), but also the sequence in which species reach the growth surface. By controlling the shutters

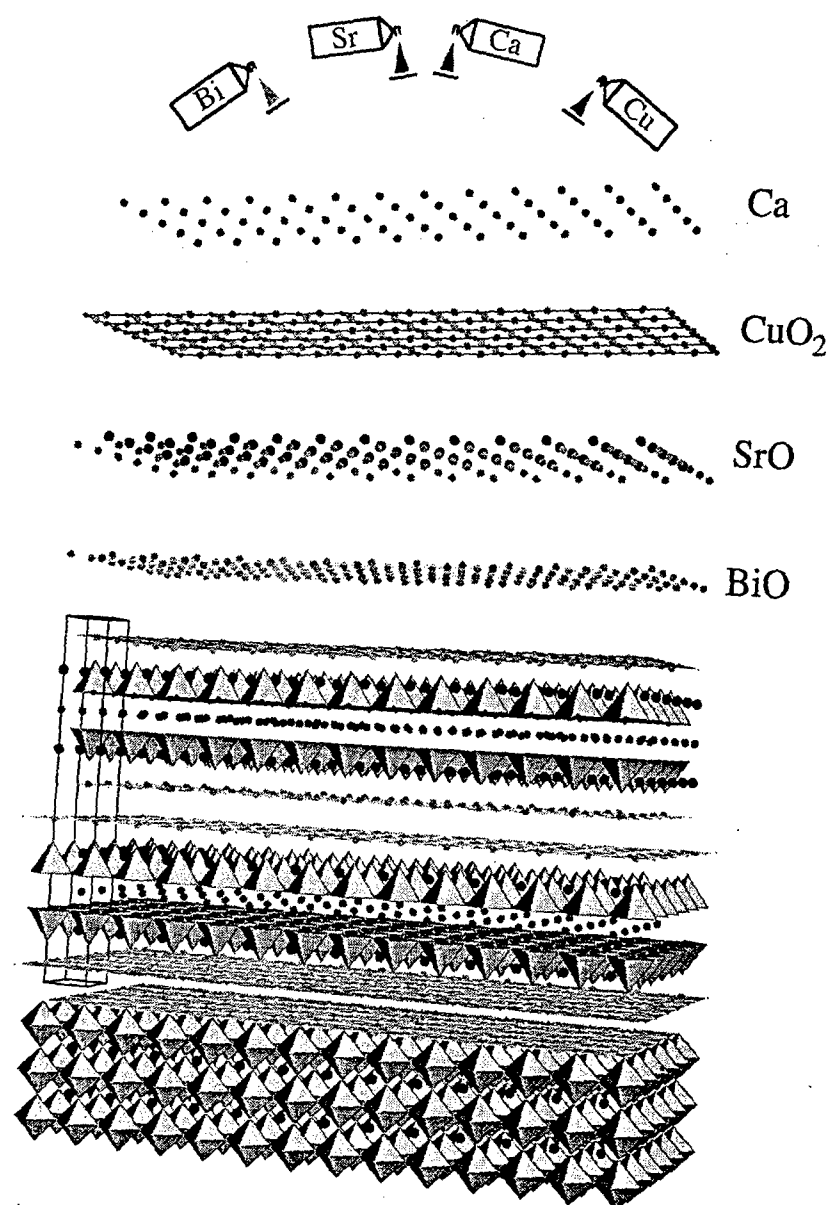


Fig. 5. A highly schematic representation of the MBE growth of a  $\text{Bi}_2\text{Sr}_2\text{Ca}\text{Cu}_2\text{O}_8$  film on a  $\text{SrTiO}_3$  substrate by reactive MBE.

and temperature of the evaporant (which control dose and flux, respectively) the layering sequence of the desired structure can be customized. This technique has been used to control the layering of oxides on a unit cell level, allowing the preparation of single phase films of nearly energetically degenerate compounds, including cuprate superconductors.<sup>2,21-25</sup> A low growth temperature is frequently used to kinetically minimize subsequent bulk reordering and minimize the loss of the customized (and metastable) layered structures. A unique advantage of MBE

is *in situ* characterization of the growing surface using RHEED, which allows the process to be closely monitored. The sensitivity of this grazing angle diffraction technique to surface structure is ideal for monitoring the evolution of growth from initial nucleation to the deposition of each subsequent layer. The formation of intermediate reaction products or impurity phases can be readily monitored and the growth conditions adjusted *during growth* accordingly. Epitaxial growth, a clean UHV deposition environment, *in situ* RHEED characterization during growth, AA composition control, and the notable absence of highly energetic species are distinct advantages of this MBE approach. These capabilities are key to the customized growth of metastable oxides.

### EXAMPLES OF MBE-GROWN OXIDE HETEROSTRUCTURES

To date oxide MBE has been most widely applied to the growth of high  $T_c$  superconductors. For such oxide heterostructures, MBE has been extremely successful and demonstrated atomic-scale layering control that parallels its achievements for semiconductor growth. Several notable examples are: (1) the use of MBE to prepare single phase  $\text{Bi}_2\text{Sr}_2\text{Ca}_{n-1}\text{Cu}_n\text{O}_{2n+4}$  films, for  $n = 1$  to 11,<sup>22,26,27</sup> demonstrating the ability of this technique to select between nearly energetically-degenerate phases; (2) the synthesis of metastable superlattices, e.g.,  $[\text{Bi}_2\text{Sr}_2\text{CuO}_6 / \text{Bi}_2\text{Sr}_2\text{Ca}_2\text{Cu}_3\text{O}_{10}]_n$ ,<sup>21</sup> and metastable phases, e.g.,  $\text{Bi}_2\text{Sr}_2\text{SrCu}_2\text{O}_8$ ;<sup>21</sup> and (3) the synthesis of superconductor-insulator-superconductor (SIS) Josephson junctions by atomic-layer engineering of the barrier layer between two superconducting layers.<sup>28</sup>

Although first used for the growth of  $\text{LiNbO}_3$  over ten years ago,<sup>29,30</sup> the use of reactive MBE to grow oxide ferroelectric heterostructures has recently intensified.<sup>31,32</sup> Here we describe the growth of  $\text{PbTiO}_3$  and  $\text{Bi}_4\text{Ti}_3\text{O}_{12}$  by MBE. A more detailed description is given elsewhere.<sup>33</sup>

$\text{PbTiO}_3$  has the largest remanent polarization ( $75 \mu\text{C}/\text{cm}^2$ ) of any known ferroelectric.<sup>34,35</sup>  $\text{Bi}_4\text{Ti}_3\text{O}_{12}$  has lower remanent polarization ( $\sim 50 \mu\text{C}/\text{cm}^2$  of which the component along the  $c$ -axis is  $\sim 4 \mu\text{C}/\text{cm}^2$ ),<sup>36</sup> but can withstand far more polarization reversals before it fatigues.<sup>37</sup>  $\text{PbTiO}_3$  and  $\text{Bi}_4\text{Ti}_3\text{O}_{12}$  are both members of the  $(\text{Bi},\text{Pb})_{n+1}\text{Ti}_n\text{O}_{3n+3}$  Aurivillius homologous series<sup>38-42</sup> shown in Fig. 6.  $\text{PbTiO}_3$  is the  $n = \infty$  member of this series and contains a network of  $\text{TiO}_6$  octahedra connected in three dimensions.  $\text{Bi}_4\text{Ti}_3\text{O}_{12}$  lies at the other end of this homologous series,  $n = 3$ , and is highly layered with a two-dimensionally connected network of  $\text{TiO}_6$  octahedra. Its structure consists of  $\text{Bi}_2\text{O}_2$  layers separated by  $\text{Bi}_2\text{Ti}_3\text{O}_{10}$  perovskite sheets. The resistance to fatigue of  $\text{Bi}_4\text{Ti}_3\text{O}_{12}$  and other Aurivillius phases make these materials of interest for use in non-volatile ferroelectric random access memories (FRAMs).<sup>43</sup> On the other hand, the high  $P_c$  of  $\text{PbTiO}_3$  makes it of interest for superconducting field-effect transistors (SuFETs).<sup>44</sup> We are interested in the variation of properties that occur in the  $(\text{Bi},\text{Pb})_{n+1}\text{Ti}_n\text{O}_{3n+3}$  homologous series and describe below the preparation of the two end members of this series by adsorption-controlled MBE.

$\text{PbTiO}_3$  and  $\text{Bi}_4\text{Ti}_3\text{O}_{12}$  are both grown under conditions where the titanium flux determines the growth rate, and ozone, lead, and bismuth are supplied in excess (2-100 times greater than the titanium flux). The excess ozone, lead, and

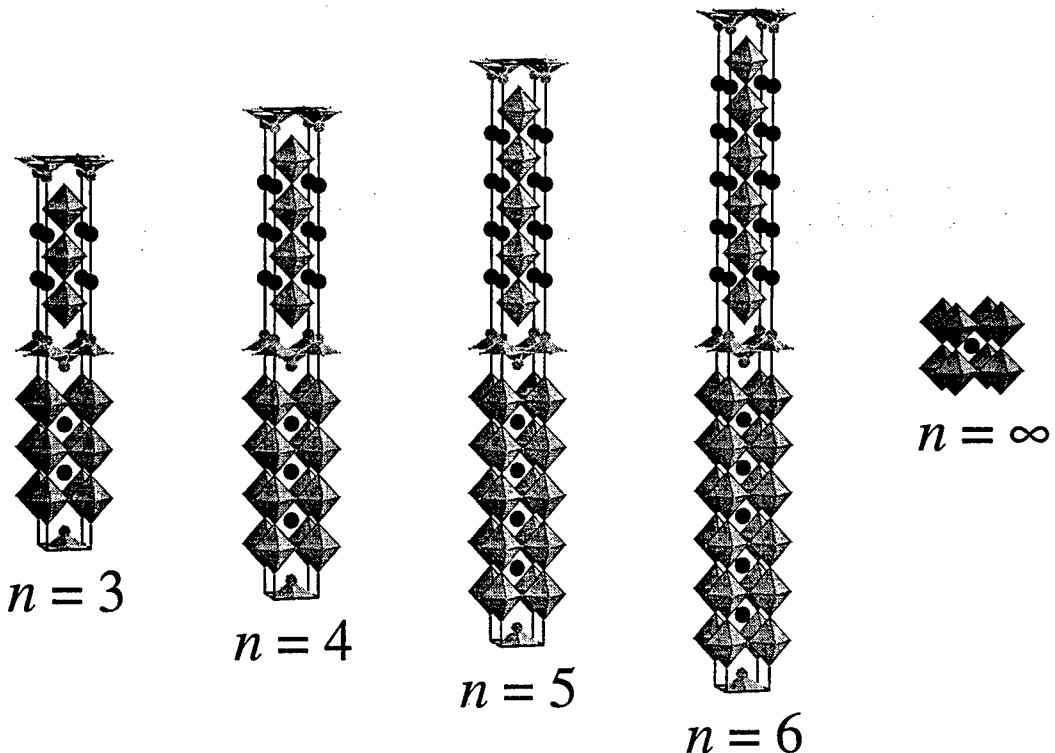


Fig. 6. The Aurivillius phases:  $n = 3$   $\text{Bi}_4\text{Ti}_3\text{O}_{12}$ ,  $n = 4$   $\text{PbBi}_4\text{Ti}_4\text{O}_{15}$ ,  $n = 5$   $\text{Pb}_2\text{Bi}_4\text{Ti}_5\text{O}_{18}$ ,  $n = 6$   $\text{Pb}_3\text{Bi}_4\text{Ti}_6\text{O}_{21}$ , and  $n = \infty$   $\text{PbTiO}_3$ .

bismuth desorb leading to the growth of  $\text{PbTiO}_3$  and  $\text{Bi}_4\text{Ti}_3\text{O}_{12}$  films that are stoichiometric within the measurement error of Rutherford backscattering spectrometry (RBS). A similar adsorption-controlled mechanism was shown to be operative by de Keijser and Dormans<sup>45</sup> for organometallic chemical vapor deposited  $\text{Pb}(\text{Zr},\text{Ti})\text{O}_3$  thin films. The growth of  $\text{PbTiO}_3$  and  $\text{Bi}_4\text{Ti}_3\text{O}_{12}$  by reactive MBE is thus quite similar to the MBE growth of III-V semiconductors where the group V species is supplied in overabundance and the group III species determines the growth rate.

Four-circle x-ray diffraction scans indicate that these ferroelectric films are epitaxial and have bulk lattice constants. In Fig. 7 the  $\theta$ - $2\theta$  and  $\phi$ -scans of a 1000 Å thick film of  $\text{PbTiO}_3$ , grown on (100)  $\text{SrTiO}_3$ , are shown. Intense  $00\ell$  peaks indicate that the  $c$ -axis of the film is oriented perpendicular to the substrate ( $c$ -axis oriented); additional scans showed no evidence of  $a$ -axis oriented domains. The  $\phi$ -scan demonstrates that the film is also oriented in the plane of the substrate, with a cube-on-cube epitaxial orientation relationship. The widths of the x-ray diffraction peaks are all approaching the instrumental resolution of our diffractometer.

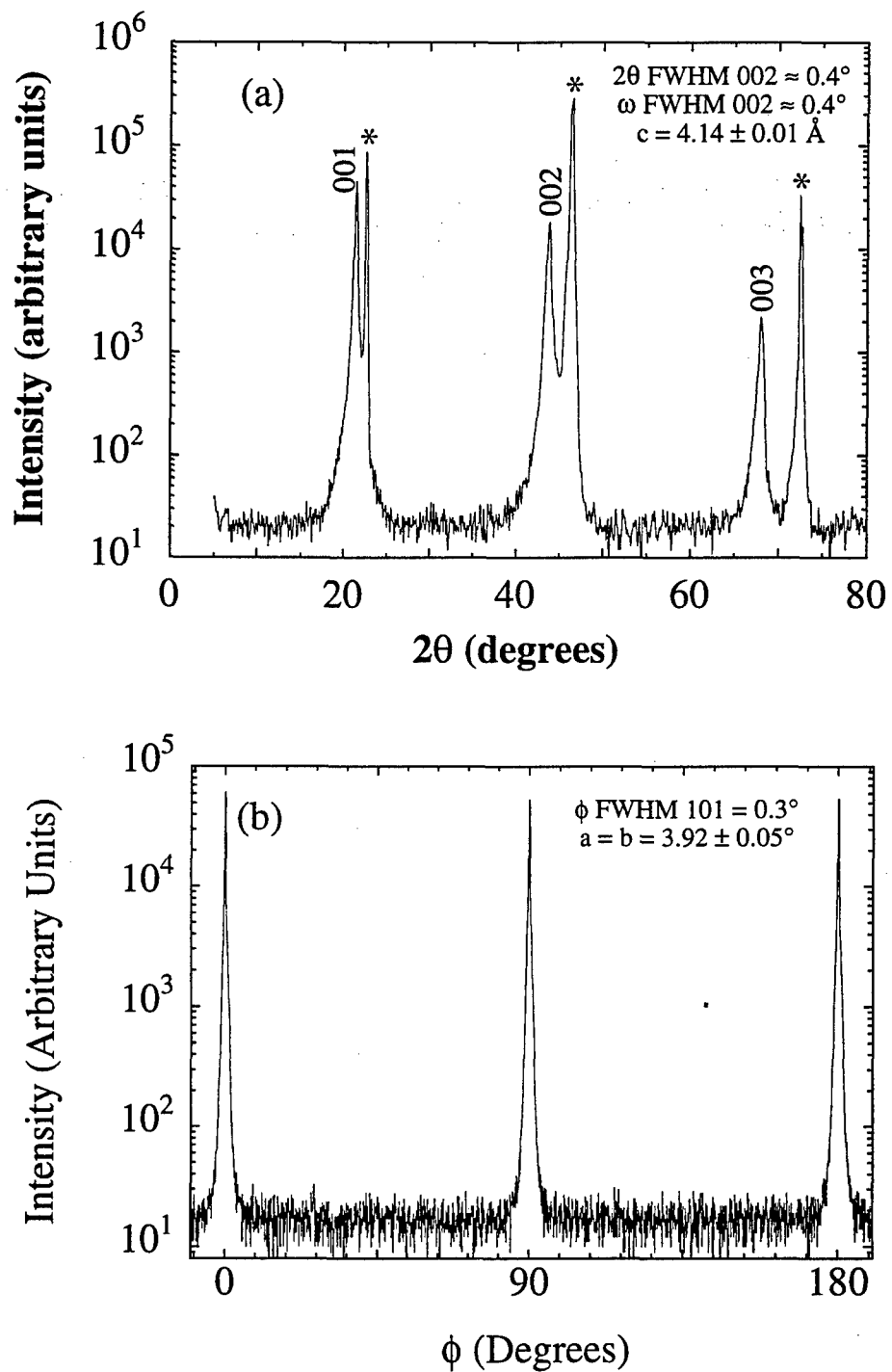


Fig. 7. (a)  $\theta$ - $2\theta$  scan and (b)  $\phi$ -scan of 101 reflections of a 1000  $\text{\AA}$  thick  $\text{PbTiO}_3$  film grown on a (100)  $\text{SrTiO}_3$  substrate (\* indicates substrate reflections).

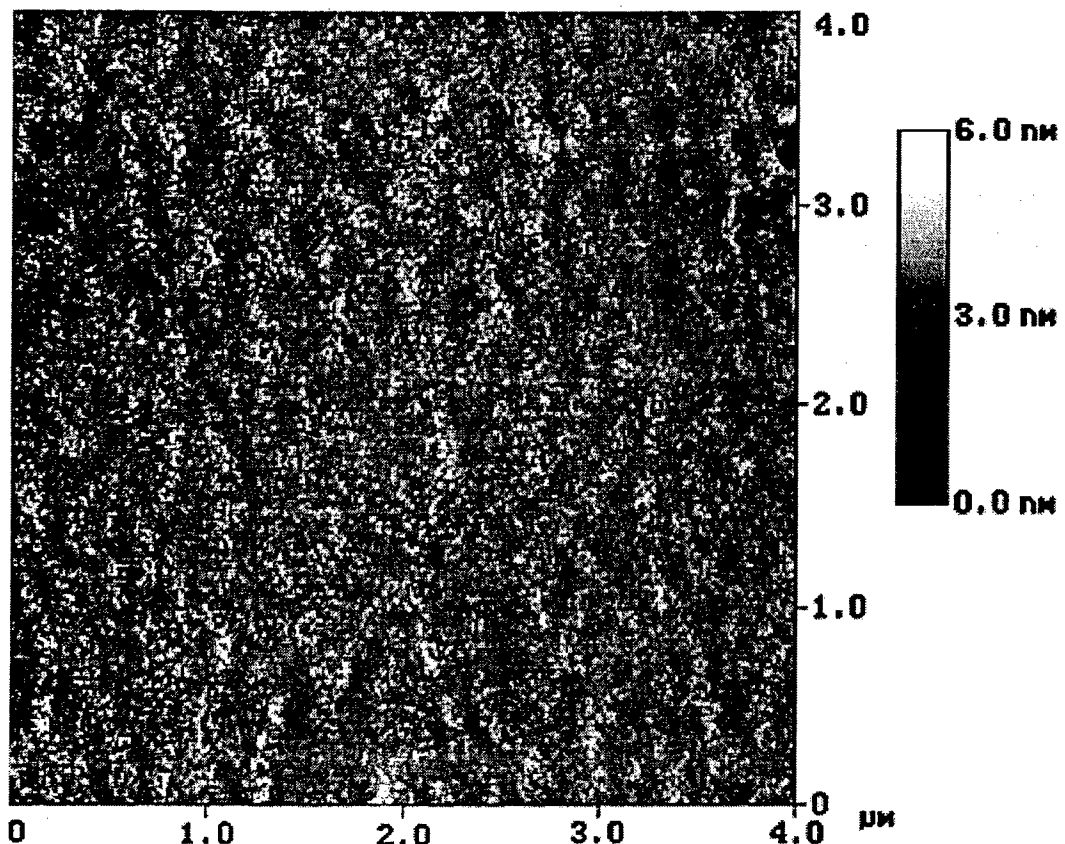


Fig. 8. AFM image of the surface of a 1000 Å thick PbTiO<sub>3</sub> film grown on (100) SrTiO<sub>3</sub>.

Atomic force microscopy (AFM) images of the surface of this same PbTiO<sub>3</sub> film, Fig. 8, show extremely smooth morphologies with a root mean square (RMS) roughness of < 5 Å. This surface structure is indicative of a layer-by-layer growth mechanism.

The θ-2θ and φ-scans of a 1000 Å thick film of Bi<sub>4</sub>Ti<sub>3</sub>O<sub>12</sub> grown on (100) SrTiO<sub>3</sub> are shown in Fig. 9. The intense 00l peaks indicate that the film is entirely c-axis oriented. The φ-scan demonstrates that the film is also oriented in the plane of the substrate, with a Bi<sub>4</sub>Ti<sub>3</sub>O<sub>12</sub> [110] || SrTiO<sub>3</sub> [010] orientation relationship. Again the peak widths are all comparable to the instrument resolution of our Picker 4-circle diffractometer. RBS channeling results for this film showed a minimum channeling yield ( $\chi_{\min}$ ) of 0.2, which is the lowest reported value for epitaxial Bi<sub>4</sub>Ti<sub>3</sub>O<sub>12</sub>.

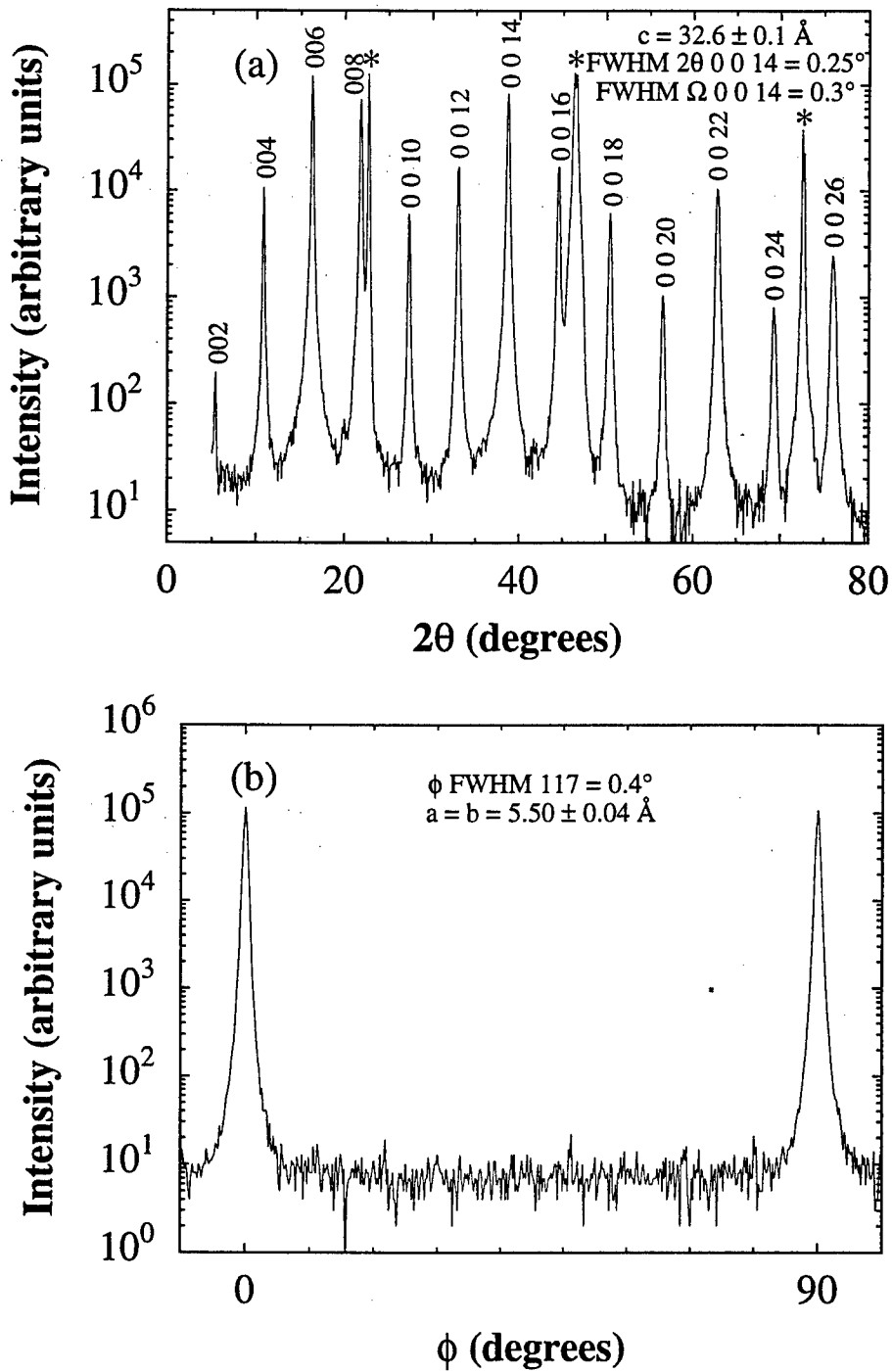


Fig. 9. (a)  $\theta$ - $2\theta$  scan and (b)  $\phi$ -scan of 117 reflections of a 1000  $\text{\AA}$  thick  $\text{Bi}_4\text{Ti}_3\text{O}_{12}$  film grown on a (100)  $\text{SrTiO}_3$  substrate (\* indicates substrate reflections).

In Fig. 10 an AFM image of the surface of this same  $\text{Bi}_4\text{Ti}_3\text{O}_{12}$  film is shown. Clearly visible on the surface are micron-sized islands that protrude  $\sim 100 - 200 \text{ \AA}$  above the film surface. The terraces making up these islands have step heights that are integral multiples of a half unit cell.\* This surface morphology is reminiscent of that of layered perovskite superconductor films,<sup>46,47</sup> although it is unclear if oppositely-signed screw dislocations are present within each mound or if the mounds are free of screw dislocations and arise due to limited surface diffusion.

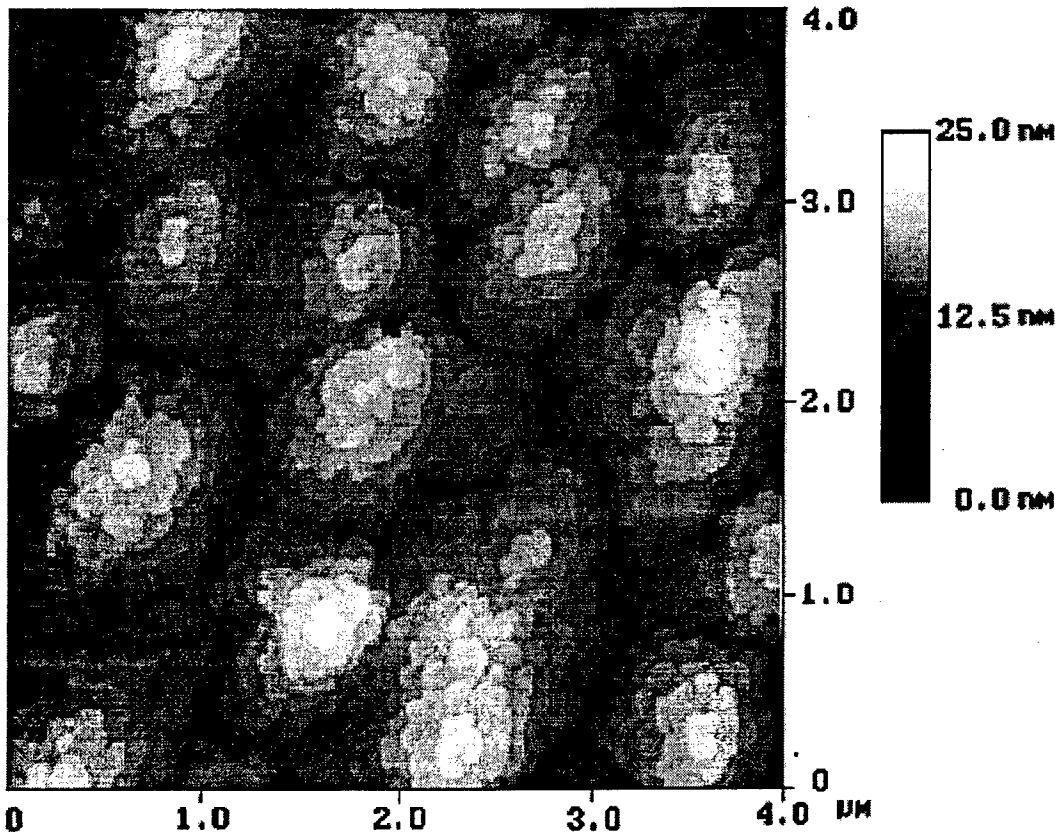


Fig. 10. AFM image of the surface of a  $1000 \text{ \AA}$  thick  $\text{Bi}_4\text{Ti}_3\text{O}_{12}$  film grown on (100)  $\text{SrTiO}_3$ .

### CHALLENGES

There are three major challenges that must be overcome before reactive MBE is a useful technique for the growth of oxide heterostructures: (1) achieving sufficient oxidation of the growing film without compromising the long mean free path necessary for MBE, (2) achieving accurate composition control during

\* A  $\text{Bi}_4\text{Ti}_3\text{O}_{12}$  formula unit is contained within each half unit cell as can be seen from Fig. 6.

growth, and (3) maintaining flat surfaces during growth. The pressure of oxidant needed to achieve sufficient oxidation depends on the phase being grown as well as the oxidant and growth temperature used. If the oxidant is restricted to molecular oxygen, the growth of most oxide superconductors would not be possible by MBE. The use of more reactive oxidants, e.g., ozone, NO<sub>2</sub>, or the reactive species in an oxygen plasma, have been key to the realization of oxide superconductor films by MBE.<sup>2</sup> Composition control is also crucial; the inherent flexibility of the MBE technique is only advantageous when it is accompanied by adequate composition control. Without it, the user will be unable to control the formation of the desired custom-made structures and controllably dope them. For the growth of heterostructures containing oxide superconductors, composition control at or better than about  $\pm 1$  atomic percent is necessary to produce films with good transport properties.<sup>48,49</sup> Controlling each monolayer with 1% accuracy requires a resolution in whatever composition monitoring method is used of about  $7 \times 10^{12}$  atoms or about one nanogram for a typical perovskite (e.g., those oxides in Table I). For many elements AA has such sensitivity and has thus become the composition control method of choice for many oxide MBE groups. Finally, even if the growth environment provides sufficient oxidation and sufficient composition control, it is almost always desired to have flat interfaces in oxide heterostructures. To this end it is clearly important to begin with a flat and relatively defect-free substrate. Oxide substrate preparation for MBE growth is an important area of research.<sup>50,51</sup> *In situ* monitoring techniques like RHEED and spectroscopic ellipsometry can be quite helpful in monitoring surface roughness *in situ* and optimizing growth conditions so that flat surfaces are maintained during growth.<sup>52</sup>

Once these three major challenges are met, MBE offers an incredibly flexible growth environment with independent control of a large parameter space. For example, the deposition rate of each constituent, the order in which the constituent fluxes (including the oxidant) are sequentially or simultaneously supplied to the growth surface, the duration of dosing, the introduction of periodic growth interruptions, and the substrate temperature are all independently controllable in the MBE process. A timing diagram of a few significantly different ways in which YBa<sub>2</sub>Cu<sub>3</sub>O<sub>7-8</sub> films could be deposited is shown in Fig. 11. However, this tremendous inherent flexibility of the MBE technique brings up a crucial challenge. *What is the best way of navigating this large parameter space to achieve the desired oxide heterostructure?* The improvements that oxide MBE can offer in our ability to customize the structure of oxides on an atomic-level challenges would be greatly enhanced if we had a better microscopic understanding of how oxides grow, e.g., what the diffusing species are and their rates as a function of oxidant pressure and temperature, how nucleation occurs on different substrates, which layer bonds to the substrate, which layer terminates the growing surface, surface reconstructions, the influence of vicinal substrates on growth, etc. With such knowledge, reactive MBE could be used to intelligently navigate this large parameter space to produce the desired phase or heterostructure in short order.

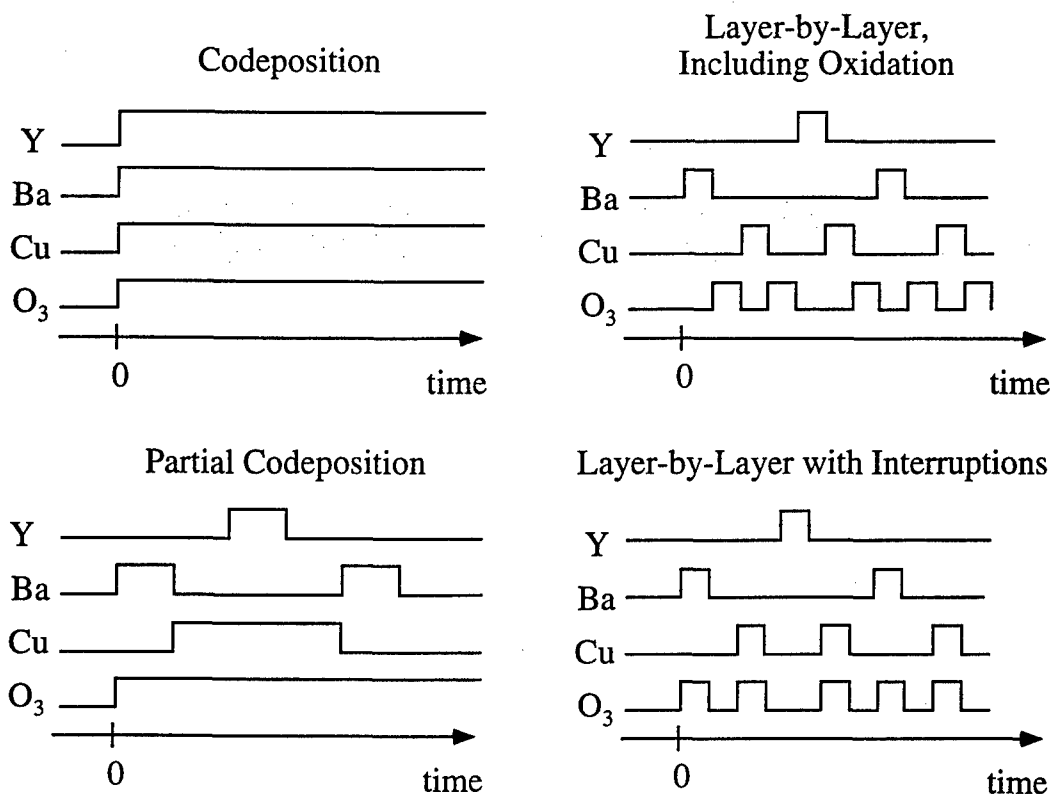


Fig. 11. A few examples of shutter timing diagrams for the growth of  $\text{YBa}_2\text{Cu}_3\text{O}_{7-\delta}$  by MBE.

## CONCLUSIONS

The use of reactive MBE for the growth of oxide heterostructures is still in its infancy and many hurdles, in particular accurate composition control, remain to be overcome for this technique to develop greater structural and doping control at the atomic layer level, as well as reproducibility. Nonetheless, reactive MBE has become established as the premiere synthesis technique for epitaxial oxide heterostructures when customized layering control is needed. As the complexity and metastability of desired oxide heterostructures increases, the requirement for a controlled synthesis environment capable of atomic layer engineering of new materials and device heterostructures will become all the more important. MBE appears to be the most likely technique to meet this challenge.

## ACKNOWLEDGMENTS

We gratefully acknowledge fruitful interactions with G.W. Brown, B.J. Gibbons, C.J. Kraisinger, S. Trolier-M'Kinstry, and J. Yeh, and the financial support of the Office of Naval Research (ONR) through grants N00014-93-1-0512, N00014-94-1-0690, and N00014-94-1-0815.

## REFERENCES

- <sup>1</sup> R.D. Shannon, "Revised Effective Ionic Radii and Systematic Studies of Interatomic Distances in Halides and Chalcogenides," *Acta Cryst. A* **32** (1976) 751-767.
- <sup>2</sup> D.G. Schlom and J.S. Harris, Jr., "MBE Growth of High  $T_c$  Superconductors," in: *Molecular Beam Epitaxy: Applications to Key Materials*, edited by R.F.C. Farrow (Noyes, Park Ridge, 1995), pp. 505-622.
- <sup>3</sup> K.-H. Hellwege and A.M. Hellwege, *Landolt-Börnstein: Numerical Data and Functional Relationships in Science and Technology*, Group III, Vol. 12a (Springer-Verlag, Berlin, 1978), pp. 126-206.
- <sup>4</sup> B.G. Hyde and S. Andersson, *Inorganic Crystal Structures*, Wiley-Interscience, New York (1989).
- <sup>5</sup> R.J.D. Tilley, "An Electron Microscope Study of Perovskite-Related Oxides in the Sr-Ti-O System," *J. Solid State Chem.* **21** (1977) 293-301.
- <sup>6</sup> J.M. Tarascon, W.R. McKinnon, P. Barboux, D.M. Hwang, B.G. Bagley, L.H. Greene, G.W. Hull, Y. LePage, N. Stoffel, and M. Giroud, "Preparation, Structure, and Properties of the Superconducting Compound Series  $\text{Bi}_2\text{Sr}_2\text{Ca}_{n-1}\text{Cu}_n\text{O}_y$  with  $n = 1, 2$ , and  $3$ ," *Phys. Rev. B* **38** (1988) 8885-8892.
- <sup>7</sup> O. Eibl, "Crystal Defects in  $\text{Bi}_2\text{Sr}_2\text{Ca}_{n-1}\text{Cu}_n\text{O}_{4+2n+\delta}$  Ceramics," *Physica C* **168** (1990) 249-256.
- <sup>8</sup> B. Raveau, C. Michel, and M. Hervieu, "Crystal Chemistry of Superconductive Bismuth and Thallium Cuprates," in: *Advances in Superconductivity: Proceedings of the 1st International Symposium on Superconductivity (ISS '88)*, (K. Kitazawa and T. Ishiguro, eds.) pp. 151-157, Springer-Verlag, Tokyo (1989).
- <sup>9</sup> M.A. Señaris-Rodríguez, A.M. Chippindale, A. Várez, E. Morán, and M.A. Alario-Franco, "A Novel '126' Phase of the Family of  $\text{Y}_2\text{Ba}_4\text{Cu}_{6n}\text{O}_{14n}$  High-Temperature Superconducting Materials," *Physica C* **172** (1991) 477-480.
- <sup>10</sup> R.J. Cava, T. Siegrist, B. Hessen, J.J. Krajewski, W.F. Peck, Jr., B. Batlogg, H. Takagi, J.V. Waszczak, L.F. Schneemeyer, and H.W. Zandbergen, "A New Homologous Series of Lanthanum Copper Oxides," *J. Solid State Chem.* **94** (1991) 170-184.
- <sup>11</sup> W.T. Fu, H.W. Zandbergen, Q. Xu, J.M. van Ruitenbeek, L.J. de Jongh, and G. van Tendeloo, "Structural and Transport Properties of the Triple-Layer Compounds  $\text{Ba}_4(\text{Pb}_{1-x}\text{Bi}_x)_3\text{O}_{10}$  ( $0 \leq x < 0.3$ )," *Solid State Comm.* **70** (1989) 1117-1121.
- <sup>12</sup> K.R. Udayakumar and A.N. Cormack, "Structural Aspects of Phase Equilibria in the Strontium-Titanium-Oxygen System," *J. Am. Ceram. Soc.* **71** (1988) C-469 - C-471; K.R. Udayakumar and A.N. Cormack, "Non-Stoichiometry in Alkaline Earth Excess Alkaline Earth Titanates," *J. Phys. Chem. Solids* **50** (1989) 55-60.
- <sup>13</sup> C.P. Flynn, "Strain-Assisted Epitaxial Growth of New Ordered Compounds," *Phys. Rev. Lett.* **57** (1986) 599-602.
- <sup>14</sup> See for example, *Molecular Beam Epitaxy: Applications to Key Materials*, edited by R.F.C. Farrow (Noyes, Park Ridge, 1995).

- <sup>15</sup> M.H. Yang and C.P. Flynn, "Growth of Alkali Halides from Molecular Beams: Global Growth Characteristics," *Phys. Rev. Lett.* **62** (1989) 2476-2479.
- <sup>16</sup> EPI 930. EPI, Chorus Corporation, St. Paul, MN.
- <sup>17</sup> C.D. Theis and D.G. Schlom, "Cheap and Stable Titanium Source for Use in Oxide Molecular Beam Epitaxy Systems," *J. Vac. Sci. Technol. A* **14** (1996) 2677-2679.
- <sup>18</sup> M.E. Klausmeier-Brown, J.N. Eckstein, I. Bozovic, and G.F. Virshup, "Accurate Measurement of Atomic Beam Flux by Pseudo-Double-Beam Atomic Absorption Spectroscopy for Growth of Thin-Film Oxide Superconductors," *Appl. Phys. Lett.* **60** (1992) 657-659.
- <sup>19</sup> ATOMICAS. Intelligent Sensor Technology, Mountain View, CA.
- <sup>20</sup> MicroCrystal. WeckTech Systems, Pleasanton, CA.
- <sup>21</sup> D.G. Schlom, A.F. Marshall, J.S. Harris, Jr., I. Bozovic, and J.N. Eckstein, "Growth of Metastable Phases and Superlattice Structures of Bi-Sr-Ca-Cu-O Compounds by an Atomic Layering MBE Technique," in: *Advances in Superconductivity III: Proceedings of the 3rd International Symposium on Superconductivity (ISS '90)*, edited by K. Kajimura and H. Hayakawa (Springer-Verlag, Tokyo, 1991), pp. 1011-1016.
- <sup>22</sup> D.G. Schlom, J.N. Eckstein, I. Bozovic, Z.J. Chen, A.F. Marshall, K.E. von Dessonneck, and J.S. Harris, Jr., "Molecular beam epitaxy—a path to novel high  $T_c$  superconductors?," in: *Growth of Semiconductor Structures and High- $T_c$  Thin Films on Semiconductors*, SPIE Vol. 1285 (SPIE, Bellingham, 1990), pp. 234-247 and in: *High  $T_c$  Superconductivity: Thin Films and Applications*, SPIE Vol. 1287 (SPIE, Bellingham, 1990), pp. 152-165.
- <sup>23</sup> J.N. Eckstein, I. Bozovic, M.E. Klausmeier-Brown, G.F. Virshup, and K.S. Ralls, "Control of Composition and Microstructure in High-Temperature Superconductors at the Atomic Level by Molecular Beam Epitaxy," *MRS Bulletin* **17** (August 1992) 27-33.
- <sup>24</sup> I. Bozovic, J.N. Eckstein, G.F. Virshup, A. Chaiken, M. Wall, R. Howell, and M. Fluss, "Atomic-Layer Engineering of Cuprate Superconductors," *J. Supercond.* **7** (1994) 187-195.
- <sup>25</sup> J.N. Eckstein, I. Bozovic, and G.F. Virshup, "Atomic Layer-by-Layer Engineering of High  $T_c$  Materials and Heterostructure Devices," *MRS Bulletin* **19** (September 1994) 44-50.
- <sup>26</sup> M.E. Klausmeier-Brown, G.F. Virshup, I. Bozovic, and J.N. Eckstein, "Engineering of Ultrathin Barriers in High  $T_c$ , Trilayer Josephson Junctions," *Appl. Phys. Lett.* **60** (1992) 2806-2808.
- <sup>27</sup> A. Brazdeikis, A. Vailionis, and A.S. Flodström, "Layer-by-Layer Growth of  $\text{Bi}_2\text{Sr}_2\text{Ca}_{n-1}\text{Cu}_n\text{O}_x$  Films with  $n \geq 3$  by Molecular Beam Epitaxy," *Physica C* **235-240** (1994) 711-712.
- <sup>28</sup> I. Bozovic and J.N. Eckstein, "Atomic-Level Engineering of Cuprates and Manganites," *Appl. Surf. Sci.* (1997) (in press).
- <sup>29</sup> R.A. Betts and C.W. Pitt, "Growth of Thin-Film Lithium Niobate by Molecular Beam Epitaxy," *Electron. Lett.* **21** (1985) 960-962.
- <sup>30</sup> M. Petrucci, C.W. Pitt, and P.J. Dobson, "RHEED Studies on  $\text{z}$ -Cut  $\text{LiNbO}_3$ ," *Electron. Lett.* **22** (1986) 954-956.

- <sup>31</sup> R.A. McKee, F.J. Walker, J.R. Conner, E.D. Specht, and D.E. Zelmon, "Molecular Beam Epitaxy Growth of Epitaxial Barium Silicide, Barium Oxide, and Barium Titanate on Silicon," *Appl. Phys. Lett.* **59** (1991) 782-784.
- <sup>32</sup> C.D. Theis and D.G. Schlom, "Epitaxial Lead Titanate Grown by MBE," to be published in *J. Cryst. Growth*.
- <sup>33</sup> C.D. Theis, J. Yeh, D.G. Schlom, M.E. Hawley, and G.W. Brown, submitted to *Appl. Phys. Lett.*
- <sup>34</sup> Landolt-Börnstein: *Numerical Data and Functional Relationships in Science and Technology*, New Series, Group III, Vol. 28a, edited by T. Mitsui and E. Nakamura (Springer-Verlag, Berlin, 1990), p. 76.
- <sup>35</sup> E. C. Subbarao, "Ferroelectric and Antiferroelectric Materials," *Ferroelectrics* **5** (1973) 267-280.
- <sup>36</sup> Landolt-Börnstein: *Numerical Data and Functional Relationships in Science and Technology*, New Series, Group III, Vol. 16a, edited by K.-H. Hellwege and A.M. Hellwege (Springer-Verlag, Berlin, 1981), p. 237.
- <sup>37</sup> C. A-Paz de Araujo, J.D. Cuchiaro, L.D. McMillan, M.C. Scott, and J.F. Scott, "Fatigue-Free Ferroelectric Capacitors with Platinum Electrodes," *Nature* **374** (1995) 627-629.
- <sup>38</sup> B. Aurivillius, "Mixed Bismuth Oxides with Layer Lattices I. The Structure Type of  $\text{CaNb}_2\text{Bi}_2\text{O}_9$ ," *Arkiv Kemi* **1** (1949) 463-480.
- <sup>39</sup> B. Aurivillius, "Mixed Bismuth Oxides with Layer Lattices II. Structure of  $\text{Bi}_4\text{Ti}_3\text{O}_{12}$ ," *Arkiv Kemi* **1** (1949) 499-512.
- <sup>40</sup> B. Aurivillius, "Mixed Oxides with Layer Lattices III. Structure of  $\text{BaBi}_4\text{Ti}_4\text{O}_{15}$ ," *Arkiv Kemi* **2** (1950) 519-527.
- <sup>41</sup> B. Aurivillius, "The Structure of  $\text{Bi}_2\text{NbO}_5\text{F}$  and Isomorphous Compounds," *Arkiv Kemi* **5** (1952) 39-47.
- <sup>42</sup> B. Aurivillius and P.H. Fang, "Ferroelectricity in the Compound  $\text{Ba}_2\text{Bi}_4\text{Ti}_5\text{O}_{18}$ ," *Phys. Rev.* **126** (1962) 893-896.
- <sup>43</sup> C.A. Paz de Araujo, J.D. Cuchiaro, M.C. Scott, and L.D. McMillan, "Layered Superlattice Material Applications," International Patent, publication no. WO 93/12542.
- <sup>44</sup> J. Mannhart, "High- $T_c$  Transistors," *Supercond. Sci. Technol.* **9** (1996) 49-67.
- <sup>45</sup> M. de Keijser and G.J.M. Dormans, "Chemical Vapor Deposition of Electroceramic Thin Films," *MRS Bulletin*, **21** (June, 1996) 37-43.
- <sup>46</sup> C. Gerber, D. Anselmetti, J.G. Bednorz, J. Mannhart, and D.G. Schlom, "Screw Dislocations in High- $T_c$  Films," *Nature* **350** (1991) 279-280.
- <sup>47</sup> M. Hawley, I. D. Raistrick, J. G. Beery, and R. J. Houlton, "Growth Mechanism of Sputtered Films of  $\text{YBa}_2\text{Cu}_3\text{O}_7$  Studied by Scanning Tunneling Microscopy," *Science* **251** (1991) 1587-1589.
- <sup>48</sup> N.G. Chew, S.W. Goodyear, J.A. Edwards, J.S. Satchell, S.E. Blenkinsop, and R.G. Humphreys, "Effect of Small Changes in Composition on the Electrical and Structural Properties of  $\text{YBa}_2\text{Cu}_3\text{O}_7$  Thin Films," *Appl. Phys. Lett.* **57** (1990) 2016-2018.
- <sup>49</sup> D.J. Carlson, M.P. Siegal, J.M. Phillips, T.H. Tiefel, and J.H. Marshall, "Stoichiometric Effects in Epitaxial  $\text{Ba}_{2-x}\text{Y}_{1-y}\text{Cu}_{3-z}\text{O}_{7-\delta}$  Thin Films on  $\text{LaAlO}_3(100)$ ," *J. Mater. Res.* **5** (1990) 2797-2801.

- <sup>50</sup> M. Kawasaki, K. Takahashi, T. Maeda, R. Tsuchiya, M. Shinohara, O. Ishiyama, T. Yonezawa, M. Yoshimoto, and H. Koinuma, "Atomic Control of the SrTiO<sub>3</sub> Crystal Surface," *Science* **266**, (1994) 1540-1542.
- <sup>51</sup> M. Yoshimoto, T. Maeda, T. Ohnishi, H. Koinuma, O. Ishiyama, M. Shinohara, M. Kubo, R. Miura, and A. Miyamoto, "Atomic-Scale Formation of Ultrasmooth Surfaces on Sapphire Substrates for High-Quality Thin-Film Formation," *Appl. Phys. Lett.* **67** (1995) 2615-2617.
- <sup>52</sup> I. Bozovic and J.N. Eckstein, "Analysis of Growing Films of Complex Oxides by RHEED," *MRS Bulletin* **20** (May 1995) 32-38.

# THE REACTIVITY OF OZONE INCIDENT ONTO THE SURFACE OF PEROVSKITE THIN FILMS GROWN BY MBE

C. D. Theis and D. G. Schlom  
Department of Materials Science and Engineering  
The Pennsylvania State University  
University Park, PA 16802-5005 USA

Methods for measuring key parameters in the growth of oxide film by MBE have been established. Using a directed gas inlet nozzle to supply ozone to the surface of the depositing film, we have determined the ozone partial pressure (or rate of incidence) at the substrate surface. Additionally, the purity of ozone reaching the substrate, as well as the sticking coefficient or reactivity of ozone with various constituent elements are given.

## INTRODUCTION

Superconductivity, colossal magnetoresistivity, conductivity, dielectricity, and ferroelectricity are a small number of the electrical and magnetic properties exhibited by perovskite-based oxides. Electronic thin film devices composed of these materials has become an area of intense research in recent years. The ability to integrate oxides in the form of epitaxial thin film heterostructures is essential to understanding and optimizing device performance.

Molecular beam epitaxy (MBE) is a powerful tool for investigating oxide heterostructures because of the ability to control film structure on an atomic level in a layer-by-layer fashion. One of the key challenges in the growth of oxides by MBE is the oxidation of metal cations in the high temperature, low pressure MBE growth environment. We have demonstrated the ability to grow phase pure materials using purified ozone in conjunction with real-time atomic absorption spectroscopy (AA) composition control and feedback from electron diffraction intensity oscillations of the growth surface.

## EXPERIMENTAL SETUP

Figure 1 is a schematic of our MBE system. It is the first commercial MBE system containing ports for atomic absorption spectroscopy (AA) (1), allowing real-time monitoring of all the depositing fluxes simultaneously. It also contains a retractable quartz crystal microbalance (QCM) to provide an absolute *in situ* flux measurement at the position of the wafer (prior to growth) for calibration of the AA signals. The depositing fluxes of all the sources (up to eight different elements simultaneously) are monitored during growth by AA (2). The measured AA signal is fed into the MBE computer control system (3), which integrates the AA fluxes and closes the appropriate shutters after the desired dose has been delivered to the substrate. Purified ozone is used to provide sufficient oxidation, while maintaining the long mean free path necessary for MBE (4). The system also contains the standard features found in MBE systems: *in situ* reflection high energy electron diffraction (RHEED), a mass spectrometer, computer-controlled shutters and furnaces for 8 elemental sources, and a load-locked wafer introduction chamber. For the growth of titanates, a titanium sublimation pump is employed as a titanium source. The Ti-Ball™ (5) is available commercially from Varian Vacuum Products, and has proven to be a comparatively cheap and stable source of titanium. The stability and suitability of the Ti-

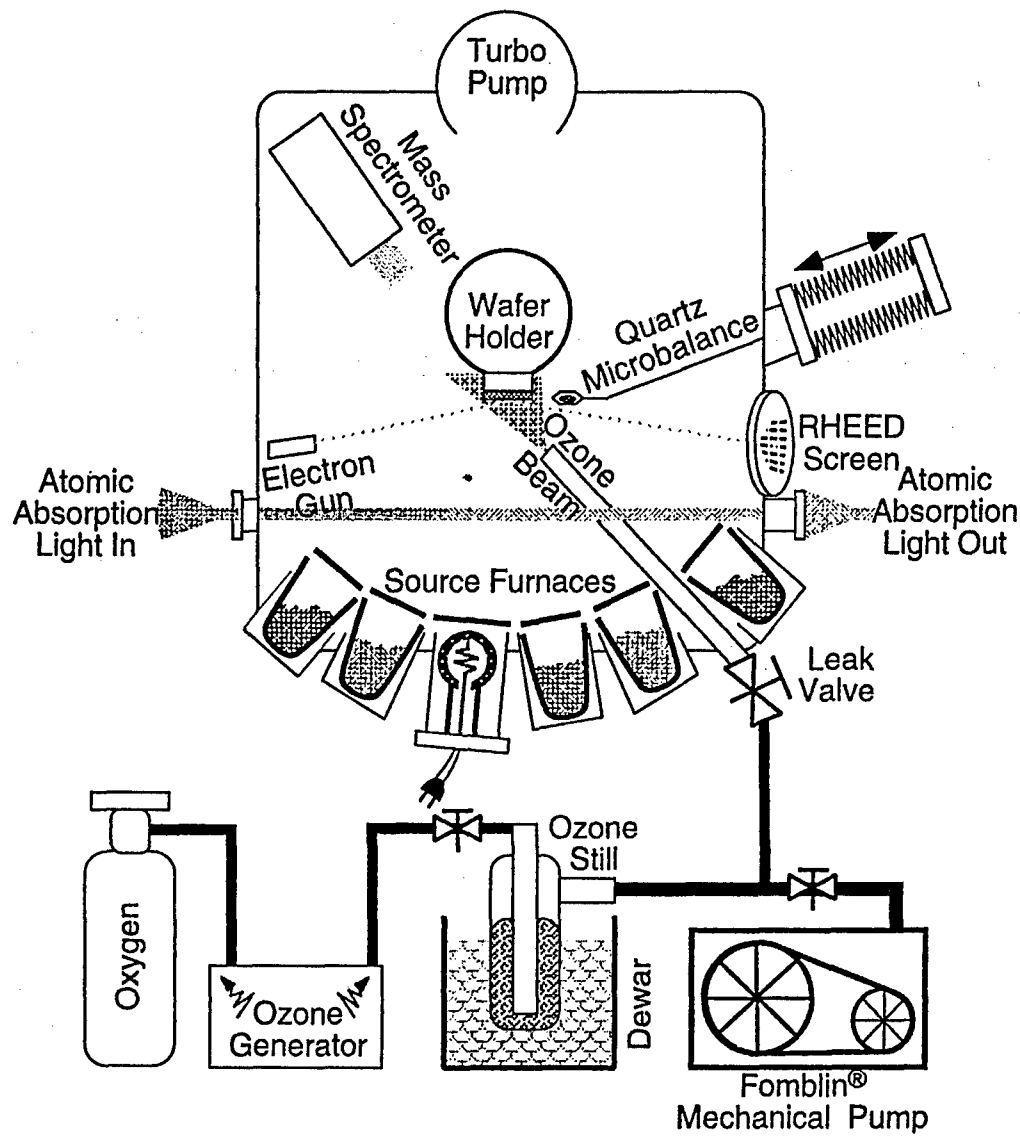


Figure 1. Schematic representation of the MBE system used for thin film growth equipped with *in situ* atomic absorption composition control and a quartz microbalance.

Ball™ as an MBE source, as well as its compatibility with an oxidizing environment is described in more detail elsewhere (6).

Measurements of key growth parameters—the ozone partial pressure at the substrate surface, the purity of ozone reaching the substrate, and the sticking coefficient of ozone with various elements—were made in the MBE itself. Ozone was purified using an ozone distillation apparatus (4) shown in Fig. 1. A 10% ozone / oxygen mixture was obtained by flowing molecular oxygen through a PCI Ozone Corporation model G-1L ozone generator (7). The ozone / oxygen mixture was then flowed into a liquid nitrogen cooled still. All gases were allowed to adsorb onto the surface of a silica gel located inside the still which was maintained at a temperature of ~ - 100 °C during collection. After about

0.75 hours, ozone / oxygen collection was terminated and the still was evacuated. Because the equilibrium vapor pressure of oxygen is much higher than the equilibrium vapor pressure of ozone at the temperatures maintained in the still, oxygen adsorbed onto the silica gel was quickly evaporated leaving behind purified ozone. After distillation, ozone was supplied to the surface of the quartz microbalance through the water cooled, directed gas inlet tube as shown while the metal cation being studied was evaporated/sublimated from an effusion cell. The mass accumulation on the surface of the microbalance was monitored as a function of time and ozone background pressure.

## RESULTS AND DISCUSSION

### Ozone Purity

Ozone purity is determined using a suitable metal that does not oxidize at room temperature in the presence of molecular oxygen. Lead is one such suitable metal. Figure 2 shows the lead flux measured as a function of time in the presence of molecular oxygen. Clearly there is no increase in mass accumulation rate at the quartz crystal monitor as the background pressures of oxygen is increased to as high as  $2 \times 10^{-5}$  Torr. Actually, there is a slight decrease in flux at the QCM at the highest pressures. This is caused by the scattering of lead out of its molecular beam at the relatively high pressures. This shows that lead is not oxidized at room temperature by molecular oxygen under MBE conditions, as well as directly indicating the extent of the pressure regime where lead exists as a molecular beam and MBE can take place.

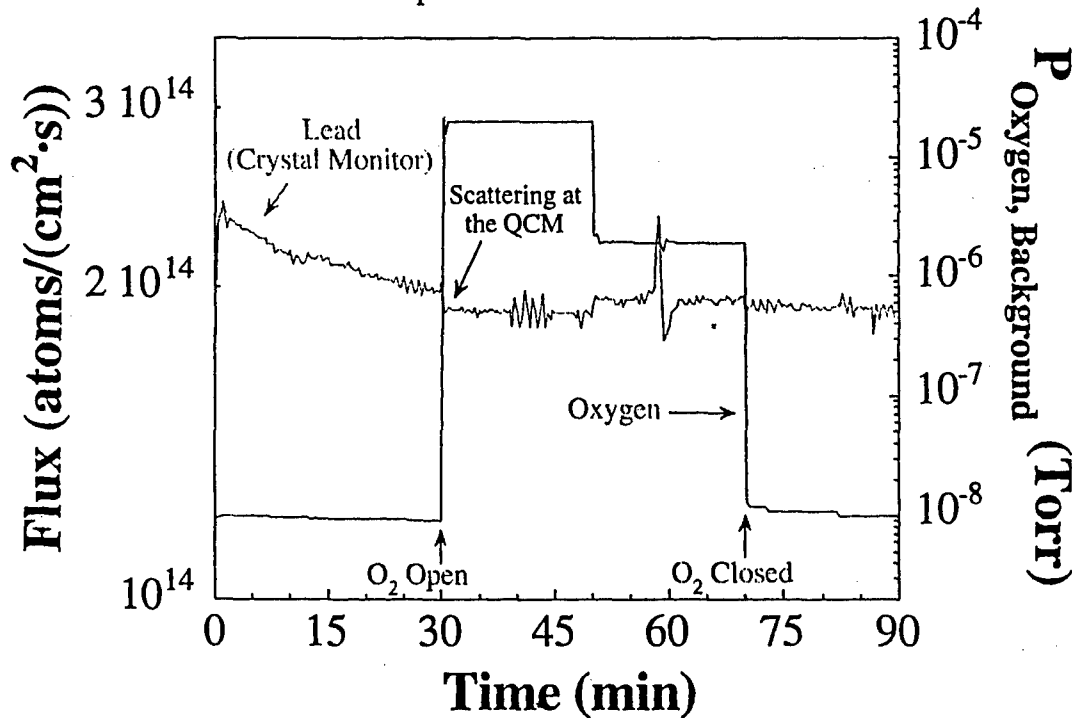


Figure 2. Graph showing the effect of oxygen pressure (right side) on the mass accumulation rate of lead on a quartz crystal monitor (converted to a flux, left side). At room temperature and low pressure, lead is not oxidized by molecular oxygen ( $O_2$ ).

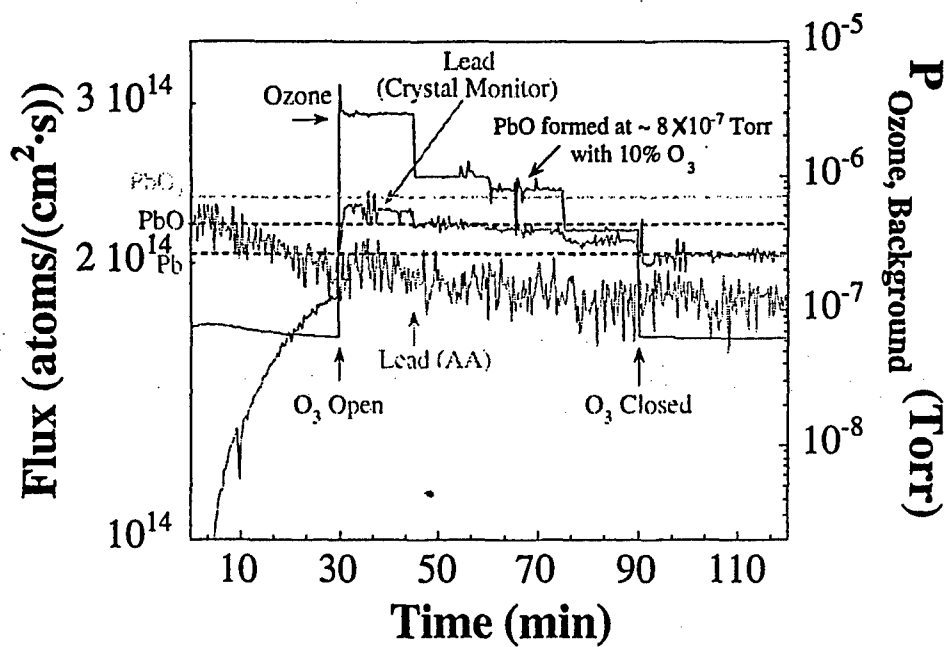


Figure 3. Graph showing the ozone background pressure required to form PbO with an ozone/oxygen mixture of known purity (10% O<sub>3</sub>). At a pressure of  $8 \times 10^{-7}$  Torr every incident lead cation reacts, on average, with one oxygen atom.

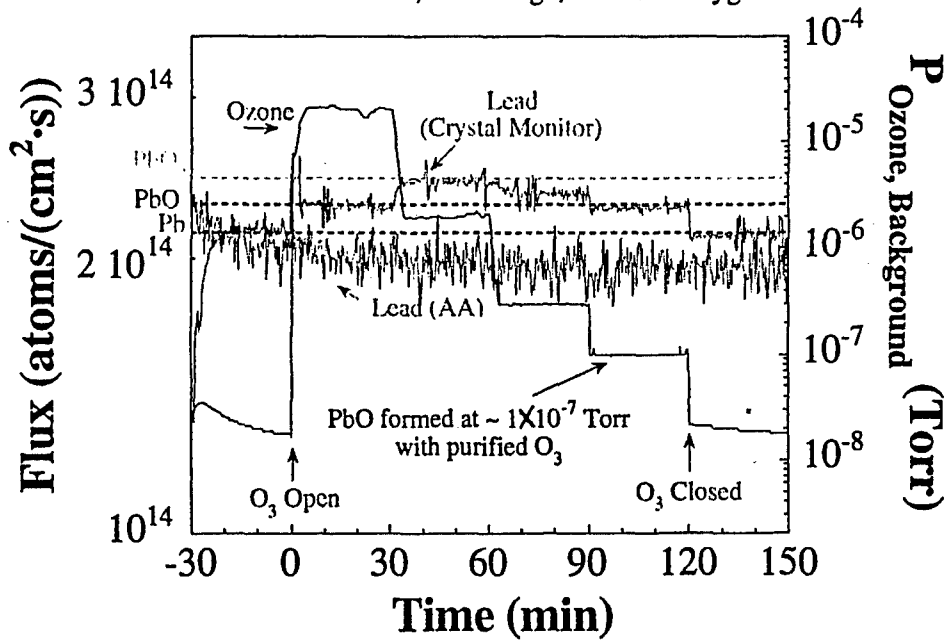


Figure 4. Graph showing the purified ozone background pressure required to form PbO at the same incident lead flux as used in the experiment shown in Fig. 3. At a pressure of  $1 \times 10^{-7}$  Torr every incident lead cation reacts, on average, with one oxygen atom.

In contrast to molecular oxygen, ozone is capable of oxidizing lead at room temperature and low MBE-compatible pressures. Using a lead molecular beam it is possible to measure the purity of our ozone flux. First the background pressure of purified ozone required to oxidize a certain fraction of an incident lead flux at room temperature is measured. This pressure is compared to the background pressure of an ozone/oxygen mixture of known purity required to oxidize the same fraction of the same lead flux. Our known consisted of a measured 10% ozone / 90% oxygen mixture plumbed directly from the output of our ozone generator. The purity of the undistilled output was measured using a PCI Ozone meter. Figure 3 shows the incident lead flux measured as a function of time in the presence of the 10% ozone/ 90% oxygen mixture. As seen in the figure, the apparent flux increases upon introduction of oxygen/ozone which corresponds to the oxidation of the incident lead, the oxidation of some underlying lead, and frequency shifts of the QCM due to temperature changes and thermal gradients resulting from the exothermic oxidation reaction. These later factors which influence the oscillation frequency of the QCM and thus its inferred mass accumulation rate are absent under steady-state deposition conditions. Sufficient times were monitored at each oxidant pressure to determine the true mass accumulation rate free of these complicating factors. All results are based on the steady-state mass accumulation rates. By converting the flux values to an absolute mass and knowing from simultaneous measurements of the incident lead flux by AA (shown in Fig. 3 and 4) that the lead flux remains constant, it is possible to determine the oxygen to lead ratio on the QCM as a function of the ozone/oxygen background pressure. As shown in Fig. 3, as the background pressure of ozone/oxygen is increased or decreased, the oxygen to lead ratio on the QCM increases or decreases. In Fig. 3 we have marked the background pressure of  $\sim 8 \times 10^{-7}$  Torr where the oxygen to lead ratio is approximately 1:1.

Similarly, Fig. 4 shows the same incident lead flux as shown in Fig. 3 measured as a function of time in the presence of purified ozone. At relatively high ozone background pressures  $PbO_2$  is formed. In this figure we have again identified the ozone background pressure required to lower the oxygen to lead ratio at the QCM to 1:1. This background pressure is  $\sim 1 \times 10^{-7}$  Torr. Knowing that the ozone rate of incidence at the substrate surface is directly proportional to the ozone partial pressure at the surface and that lead is not oxidized under these conditions by molecular oxygen, we conclude that the distilled ozone has a purity of  $\sim 80\%$  by equating the ozone partial pressure of the 10% ozone,  $P_{O_3} = (10\%)(8 \times 10^{-7} \text{ Torr}) = 8 \times 10^{-8} \text{ Torr}$ , with that of the purified ozone,  $P_{O_3} = (8 \times 10^{-8} \text{ Torr}) = (\text{purity})(1 \times 10^{-7} \text{ Torr}) \Rightarrow \text{purity} = 80\%$ . Note that this result does not depend on the sticking coefficient of ozone to a lead surface since the same element (lead) was oxidized by ozone under identical conditions except for the purity of the incident ozone/oxygen mixture.

#### Ozone Rate of Incidence and Sticking Coefficient

To improve our understanding of and ability to grow oxides by MBE, in addition to accurately knowing and controlling the incident flux of each metal species, it is important to know the ozone flux reaching the substrate surface. As the ozone gas inlet nozzle is directed toward the substrate surface, the pressure at the substrate is much higher than the chamber background pressure. Once the amount of ozone incident onto the surface is known, it is necessary to determine how much stays on the surface (or how reactive the ozone is with various elements). Using oxidation studies, it is impossible to determine this pressure(or flux) exactly because there is no metal that will react with 100% of the incident gas. In order to determine these parameters as accurately as possible, we use strontium

metal as a standard because of its extreme reactivity with even molecular oxygen at room temperature. In essence, a fraction of the incident strontium flux is oxidized using a very low background pressure of molecular oxygen. It is assumed that every oxygen molecule reacts with exactly two strontium atoms (i.e., each oxygen molecule contributes two O's) and there is no activation barrier to reaction. Since the fraction of the incident strontium flux oxidized is measured directly using the QCM, the oxygen flux ( $\Phi_{O_2}$ ) and oxidized strontium fluxes ( $\Phi_{Sr, Oxidized}$ ) may be simply related:

$$\Phi_{O_2} = 1/2 \Phi_{Sr, Oxidized} \quad [1]$$

This oxygen flux *at the substrate surface* may now be related to an oxygen pressure using the kinetic theory of gases:

$$\Phi_{O_2} = \frac{P_{O_2}}{\sqrt{2\pi mkT}} \quad [2]$$

We have calculated the oxygen pressure at the substrate surface using this method and compared it to the chamber background pressure. We have determined that the pressure at the substrate surface upon which the incident gas is directed by a nozzle is ~ 20 times higher than the measured background pressure in the chamber.

In order to calculate ozone sticking coefficients to various metals, the incident ozone flux is related to the chamber background pressure by a constant  $K_{Sr}$  which is calculated from Eqn. 2:

$$\Phi_{O_3} = K_{Sr} \cdot P_{O_2} \quad [3]$$

Here it is assumed that the functional relationship between the chamber background pressure and the incident ozone gas flux is linear and independent of the higher molecular weight of ozone as compared to oxygen (this assumption is made because it is unclear if the ion pressure gauge is measuring the actual ozone background pressure or if the hot filament in the ion gauge causes the ozone to decompose into molecular oxygen and is measuring its pressure).

The ozone background pressure required to oxidize high fractions (between 64% and 77%) and low fractions (between 42% and 67%) of various metals (Ti, Pb, Bi, Cu) has been measured and converted into an incident ozone flux using Eqn. 3. The fraction of metal flux oxidized by the ozone has also been converted into an incident ozone flux using Eqn. 1 (without the factor of 1/2 because it is assumed that each  $O_3$  molecule contributes one O to the reaction). These metals are not oxidized by molecular oxygen at room temperature at pressures in the MBE regime. By comparing the ozone flux calculated from the background pressure to the ozone flux calculated from the fraction of the incident metal flux oxidized, it is possible to determine the sticking coefficient/reactivity of ozone with each metal measured. The results are summarized in Table I.

Table I Ozone Sticking Coefficients to Various Metals at Room Temperature

	Ozone Sticking Coefficient (high fraction oxidized (~ 75%))	Ozone Sticking Coefficient (low fraction oxidized (~ 50%))	Average Value
Titanium	56%	91%	74%
Lead	4%	10%	7%
Bismuth	11%	—	11%
Copper	9%	11%	10%

### CONCLUSIONS

We have established methods for measuring key parameters in the growth of oxide films by MBE. The purity of the distilled ozone reaching the substrate surface was measured to be ~ 80%. Using a directed gas inlet nozzle, the pressure at the substrate surface was calculated to be ~ 20 times higher than the measured chamber background pressure. Ozone sticking coefficients to various metal cations were measured at room temperature. The sticking coefficients are significantly different for different elements and decrease as the element is further oxidized.

### REFERENCES

1. C. Lu and Y. Guan, *J. Vac. Sci. Technol. A* **13**, 1797 (1995).
2. Intelligent Sensor Technology, Mountain View, CA.
3. WeckTech Systems, Pleasanton, CA.
4. D. G. Schlom and J. S. Harris, Jr., "MBE Growth of High T<sub>c</sub> Superconductors," in *Molecular Beam Epitaxy: Applications to Key Materials*, R. F. C. Farrow, Editor, Noyes, Park Ridge (1995).
5. Ti-Ball is a registered trademark of Varian Vacuum Products, Lexington, MA.
6. C. D. Theis and D. G. Schlom, *J. Vac. Sci. Technol. A* **14**, 2677 (1996).
- 7 PCI Ozone Corporation, West Caldwell, NJ.

## HIGH- $T_c$ THIN FILMS. GROWTH MODES – STRUCTURE – APPLICATIONS

J. MANNHART, J.G. BEDNORZ, A. CATANA\*, Ch. GERBER and

D.G. SCHLOM\*\*

*IBM Research Division,*

*Zurich Research Laboratory,*

*8803 Rüschlikon, Switzerland*

**ABSTRACT.** Using microscopic investigations, a basic understanding of the growth mode of high- $T_c$  films has been obtained in the past couple of years. In this presentation a brief overview of the growth mechanism of  $\text{YBa}_2\text{Cu}_3\text{O}_{7-\delta}$  films will be given, and the morphology of the films as well as their potential applications will be addressed.

### 1. Introduction

Thin solid films are the basis of countless electronic and optical devices and play a vital role in most fields of solid-state physics, including research in superconductivity.

Accordingly, soon after the discovery of high- $T_c$  superconductivity many groups embarked on the fabrication of high-quality films of the new superconductors. However, epitaxial growth of high- $T_c$  compounds was found to be a challenge, because the high- $T_c$  materials have characteristic properties which require growth conditions and growth techniques different from those used to deposit films of classical superconductors like Nb or Al or for films of semiconductors like Si or GaAs. Compared to these materials, the high- $T_c$  compounds have a far more complex unit cell, which involves at least four different types of atoms, and require growth temperatures of 600–900 °C which is 0.7 to 0.85 times the melting temperature. Nevertheless, substantial progress has been made over the past few years in solving the problems associated with the epitaxial growth of the high- $T_c$  compounds [1], and excellent high- $T_c$  films are now fabricated on a routine basis, notably by laser-ablation, sputter deposition, molecular beam epitaxy (MBE) and chemical vapor deposition (CVD). After film deposition was mastered, an important question remained: How does the growth of high- $T_c$  films proceed under such unusual conditions?

In the first part of this lecture this question will be discussed, based on microstructural investigations of high- $T_c$  films with scanning tunneling microscopy (STM), atomic force microscopy (AFM), and transmission electron microscopy (TEM), as these techniques proved

\* Present address: EPFL, Prospective and Research, 1015 Lausanne, Switzerland

\*\* Present address: Department of Materials Science and Engineering, The Pennsylvania State University, University Park, PA 16802-5005, USA

to be sources of valuable information about film growth. To limit the scope of the discussion, we restrict ourselves to the growth properties of films for which epitaxial growth occurred at the time of deposition, rather than during a subsequent high-temperature annealing step.

The growth mechanism has a direct influence on a film's microstructure, which, in turn, controls the film's superconducting properties. For the high- $T_c$  materials the superconducting characteristics are particularly sensitive to the microstructure, a consequence of their extremely short coherence lengths of only a few angstroms. Hence, due to its importance, the microstructure of the films will be discussed in some detail in the second chapter, with special attention given to growth-induced defects. In the third chapter we discuss the potential of epitaxial high- $T_c$  films with respect to applications.

As the fields to be addressed are rather broad, the discussions will be centered on epitaxial  $\text{YBa}_2\text{Cu}_3\text{O}_{7-\delta}$  films, which have been investigated in great detail and can serve to some extent as an example for the other high- $T_c$  systems, too.

The discussions given are valid for films with a thickness below a critical value of, say,  $0.5 \mu\text{m}$ , beyond which epitaxy becomes poor. We name these films "thin" to distinguish them from films that are much thicker than one micron, which are mostly polycrystalline and are at present intensively being studied as a substitute for bulk materials for current transport applications.

The purpose of this lecture is to give a brief introduction to the physics and materials science of high- $T_c$  films; for a more extensive or a more complete understanding of the field, the reader is referred to the reference list.

## 2. Growth Modes

Most information about the growth mechanism of high- $T_c$  films stems from investigations of the films' surfaces by AFM/STM and TEM, from cross-sectional TEM studies and from the observation of intensity oscillations of reflective high energy electron diffraction (RHEED) patterns in the early stages of film growth [2,3]. One of the prominent features in the AFM/STM images of the (001) surface of  $\text{YBa}_2\text{Cu}_3\text{O}_{7-\delta}$  films is a rather high density ( $5 \times 10^4 \text{ cm}^{-1}$  in Fig. 1 and  $5 \times 10^5 \text{ cm}^{-1}$  in Fig. 2) of steps one unit cell high. If the films are grown on well-oriented substrates, growth spirals emanating from screw dislocations with a dislocation core oriented parallel to the  $c$ -axis provide the surface steps (Fig. 1). If the substrates are oriented a few degrees away from (100), the steps run basically

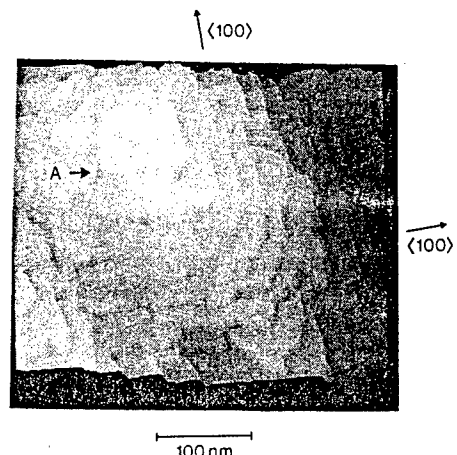


Figure 1: STM image of a  $\text{YBa}_2\text{Cu}_3\text{O}_{7-\delta}$  film sputtered on a  $\text{SrTiO}_3$  substrate at a substrate holder temperature of  $\approx 755^\circ\text{C}$ . The image shows a growth spiral with a step height of one unit cell ( $\approx 11 \text{ \AA}$ ). The small dark spots such as the one pointed to by arrow A are holes or insulating regions. Clumps of material with irregular shape, for example at arrow B, are present at the step edges (from [19]).

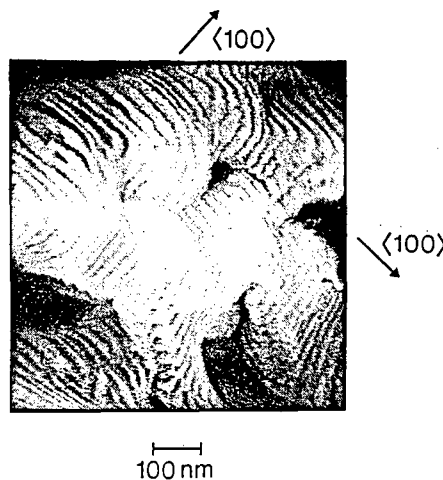


Figure 2: STM image of a  $\text{YBa}_2\text{Cu}_3\text{O}_{7-\delta}$  film sputtered on a vicinal  $\text{SrTiO}_3$  substrate at a substrate holder temperature of  $\approx 780^\circ\text{C}$ . The micrograph shows a surface structure dominated by growth steps originating from the substrate tilt (from [19]).

perpendicular to the substrate tilt (Fig. 2). These surface steps give clear evidence that the films grow by accommodating adatoms at growth steps, which are energetically favorable attachment sites.

If growth spirals are present, arriving species at the spiral ledges cause the spiral to rotate around the screw dislocation at its center. Thereby the spirals ascend one layer with each rotation, leading to self-perpetuating, spiral shaped surface steps, as illustrated in Fig. 3. This screw dislocation-mediated growth mechanism is well known from many different materials including  $\text{NaCl}$  [4],  $\text{Ag}$  [5],  $\text{SiC}$  [6] or organic materials such as paraffin [7] and  $\beta$ -methylnaphtalene [8] and was proposed by Frank as early as 1949 [9]. Of course, when this growth mechanism is dominant, a high density of screw dislocations ( $\geq 10^7 - 10^8 \text{ cm}^{-2}$ ) is present in the films, which leads to the question of the screw dislocation nucleation process. This issue is currently unsettled, but AFM investigations of the early stages of film growth support mechanisms based on the coalescence of

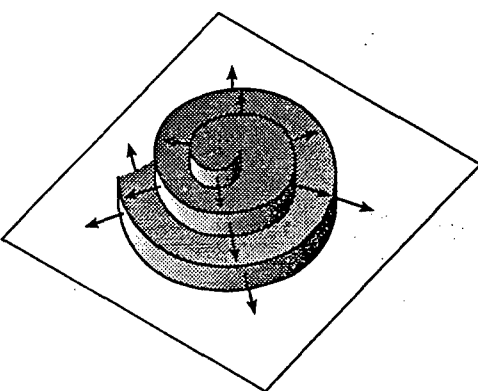


Figure 3: Illustration of the screw dislocation-mediated growth mechanism.

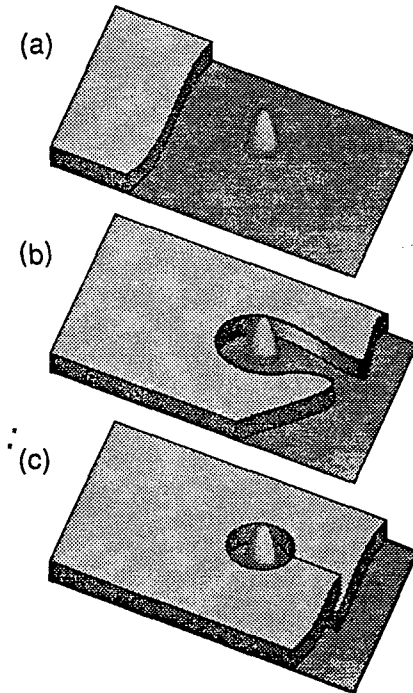


Figure 4: Illustration of screw dislocation nucleation by the incoherent joining of growth fronts.

growth fronts which are vertically offset and inclined with respect to each other. These growth fronts may consist either of two separate fronts or of two branches of a single growth front which became separated and offset during growth, for example by flowing around obstacles (see Fig. 4), [8, 10–12] such as defects or substrate imperfections. Such defects have been observed by TEM, for example in ultrathin films deposited on MgO [13], and AFM images of early stages of the growth of sputtered  $\text{YBa}_2\text{Cu}_3\text{O}_{7-\delta}$  films onto  $\text{SrTiO}_3$  substrates suggest that screw dislocations are indeed nucleated by these mechanisms [14]. Screw dislocations may also arise, at least to some extent, from the inheritance of substrate dislocations. But as screw dislocation densities of  $10^8 - 10^{10} \text{ cm}^{-2}$  have been found for  $\text{YBa}_2\text{Cu}_3\text{O}_{7-\delta}$  films grown on virtually all available substrate materials ( $\text{SrTiO}_3$  [15–25]  $\text{MgO}$  [16, 17, 19, 20, 24–30]  $\text{LaAlO}_3$  [17, 31, 32],  $\text{ZrO}_2$  (Y) [33],  $\text{NdGaO}_3$  [25, 34],  $\text{Mg}_2\text{TiO}_4$  [35]) which have dissimilar microstructural properties and low screw dislocation densities, it is unlikely that this nucleation mechanism is the dominant one.

When tilted a few degrees away from  $<100>$ , the microscopic surface structure of the substrate consists of a sequence of steps separating (100) terraces. These surface steps are energetically favorable sites for film nucleation and subsequent [19, 36, 37] growth. As growth proceeds by the incorporation of the arriving adatoms at the steps, the steps propagate laterally across the film surface (Fig. 5). The substrate tilt necessary to achieve growth by this step propagating growth mechanism is presumably that which causes the steps to be spaced sufficiently close together that the depositing species diffuse to and are accommodated by the existing ledges without reaching a supersaturation on the terrace for two-dimensional nucleation to occur [38]. Indeed, a crossover from screw dislocation-mediated growth to growth by step propagation has been observed experimentally on vicinal  $\text{SrTiO}_3$  (100) surfaces, and the amount of tilt necessary was seen to decrease as the growth temperature was increased [19]. As the substrate steps guide the propagation of the growth fronts in a direction parallel to the substrate tilt and thereby reduce the chance for incoherent encounter between growth fronts, one may expect the screw dislocation density to decrease with increasing substrate misorientation. This was indeed observed as shown in Fig. 6, where the

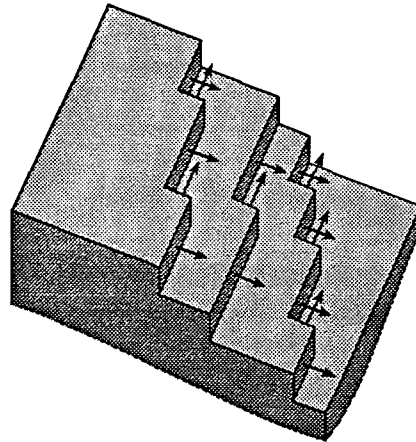


Figure 5: Illustration of film growth by the propagation of growth steps caused by substrate tilt.

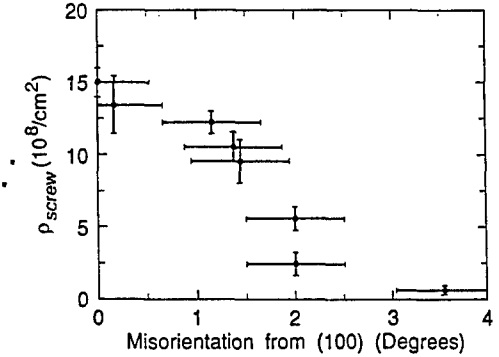


Figure 6: Screw dislocation density as a function of substrate misorientation angle for  $\text{YBa}_2\text{Cu}_3\text{O}_{7-\delta}$  films sputter-deposited onto  $\text{SrTiO}_3$  substrates. The films were grown at a substrate holder temperature of  $\approx 750^\circ\text{C}$  to a thickness of  $1000 - 1500 \text{ \AA}$ .

screw dislocation density is plotted as a function of misorientation of a  $\text{SrTiO}_3$  substrate away from (100). The crossover from screw dislocation-mediated growth to growth by step propagation is illustrated by Fig. 7, which shows an AFM image of an  $\text{YBa}_2\text{Cu}_3\text{O}_{7-\delta}$  film grown on a  $\text{SrTiO}_3$  substrate misoriented  $\approx 3^\circ$  from (100). The surface of this film is clearly dominated by surface steps reflecting the substrate misorientation. However, as a secondary feature, screw dislocations are also observed on several terraces. But because of the finite substrate tilt, the screw dislocations could no longer give rise to well-developed growth spirals.

In the case where screw dislocations are lacking and growth occurs by step propagation, situations can arise in which the supersaturation on a terrace becomes high enough for two-dimensional nucleation to occur. For instance, the width of the top terrace of a vicinal film tends to increase steadily as growth proceeds. But once a terrace has attained a critical width, the supersaturation far from the terrace steps becomes large enough for two-dimensional nucleation to take place (Fig. 8). Thereby new ledges are created which serve as attachment sites and reduce the supersaturation again.

Frequently, the observation of RHEED intensity oscillations during film growth has been taken as evidence that the films grow in a layer-by-layer mode, in the sense that the majority of one growth layer is completed before the next layer is nucleated. Such a growth mode would be highly interesting as it bears the intriguing possibility of growing truly flat films. Unfortunately, layer-by-layer growth does not appear to be reconcilable with the AFM/STM results described above. For film growth by ledge propagation, RHEED intensity oscillations are not expected, since the surface step density is essentially time-independent. Indeed, the observation of RHEED intensity oscillations has only been reported [39, 40] to occur during the initial stage of growth on bare substrates, indicative for the time necessary for a steady-state surface step density to become established.

Bauer [41] introduced three classifications for film growth: island growth (Volmer-Weber), layer-by-layer growth (Frank-van der Merwe) and initial layer growth followed by island growth (Stranski-Krastanov). These classifications are based only on the relative

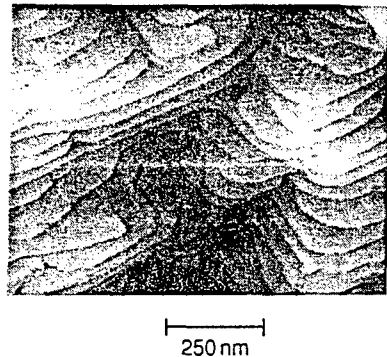


Figure 7: STM image of a  $\text{YBa}_2\text{Cu}_3\text{O}_{7-\delta}$  film sputtered on a vicinal  $\text{SrTiO}_3$  substrate at a substrate holder temperature of  $\approx 750^\circ\text{C}$  with a surface morphology characterized by growth steps originating from the substrate tilt and from screw dislocations.

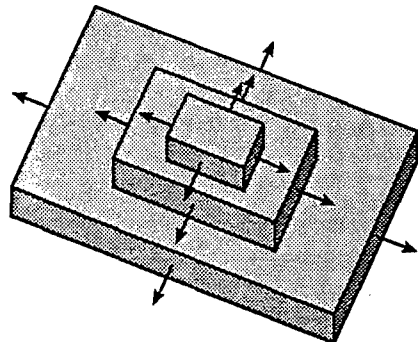


Figure 8: Illustration of the two-dimensional nucleation of growth fronts.

surface energies of the substrate and the overlayer, and on the strain energy in the overlayer. One of these growth modes should characterize a particular substrate/overlayer system in the absence of substrate surface defect sites. In the case of high- $T_c$  films, however, as elaborated above, defect sites such as screw dislocations or step edges impact the crystal growth process greatly by supplying low-energy attachment sites for adatom incorporation. Since the observed STM/AFM or AFM images of the  $\text{YBa}_2\text{Cu}_3\text{O}_{7-\delta}$  films do not indicate which of these classical growth modes would be operative in the *absence* of defects, we find it appropriate to use the term "ledge growth" [2, 13] rather than "island growth" or "layer-by-layer growth" to describe the growth mechanism leading to the observed microstructure.

In summary, the growth process of *c*-axis oriented  $\text{YBa}_2\text{Cu}_3\text{O}_{7-\delta}$  films may be generally described as ledge growth, emphasizing the energetic preference of the depositing species to be incorporated at step edges which propagate laterally across the film surface. The ledges can be provided by two-dimensional nucleation, but more favorably – and more frequently – by screw dislocations and by substrate steps.

### 3. Microstructure

Compared to bulk single crystals, high- $T_c$  films are grown at lower temperatures and in much shorter times. Therefore one expects high- $T_c$  films to be rich in growth defects. Indeed, it has been found that all high- $T_c$  films are abundant in defects of various types.

Many defects are already induced in the early stages of film growth by the substrates. For example, due to the finite lattice mismatch between substrate and film, the films are exposed to substantial elastic strain which, for films with a thickness exceeding a critical value of 100 – 200 Å, is accommodated by the formation of misfit dislocations. By HREM [36, 42–45], interface dislocations have been observed directly, with densities as high as  $8 \times 10^5 \text{ cm}^{-1}$ . In another study, for  $\text{YBa}_2\text{Cu}_3\text{O}_{7-\delta}$  films grown on  $\text{LaAlO}_3$ , interface dislocations were found only near surface steps [46]. In addition, due to the high growth temperature, interdiffusion between the substrate and the film is often non-negligible. Interdiffusion leads to substitutional or interstitial point defects in the vicinity of the interface, which can destroy superconductivity if substrate materials like Si or GaAs are used.

Moreover, numerous types of defects are introduced during growth and thus are not substrate-related. Oxygen vacancies are point defects that are expected to be abundant in high- $T_c$  films, with densities of the order of  $10^{21} \text{ cm}^{-3}$ , depending on the film's oxygen concentration. Unfortunately, due to the lack of instrumental resolution, point defects have not been directly observed yet.

Stacking faults are common defects in high- $T_c$  films, too. They are usually caused by small deviations of the film's stoichiometry, and, for  $\text{YBa}_2\text{Cu}_3\text{O}_{7-\delta}$ , have been reported to consist frequently of extra Cu-O planes [44, 47]. Among the Bi- and Tl-based superconductors, stacking faults are particularly abundant. Frequently, the stacking faults form superconducting phases which are members of the same family of superconductors as the matrix material, i.e. for  $\text{Bi}_2\text{Sr}_2\text{CaCu}_2\text{O}_{8+\delta}$ , stacking faults consist of the  $\text{Bi}_2\text{Sr}_2\text{CuO}_{6+\delta}$  and the  $\text{Bi}_2\text{Sr}_2\text{Ca}_2\text{Cu}_3\text{O}_{10+\delta}$  phase.

Precipitates, like stacking faults, are frequently observed and are caused by deviations of the film stoichiometry. An entire zoo of precipitates has been observed both in the bulk and at the film surface, depending on growth conditions and stoichiometry. For instance, for

$\text{YBa}_2\text{Cu}_3\text{O}_{7-\delta}$  films, precipitates consisting of the following phases have been reported:  $\text{CuO}$  [44, 48, 49],  $\text{Y}_2\text{O}_3$  [44, 50, 51],  $\text{YCuO}_2$  [49, 52],  $\text{BaCu}_2\text{O}_2$  [44],  $\text{Y}_2\text{Cu}_2\text{O}_5$  [44],  $\text{Y}_2\text{BaCuO}_{5-x}$  [44, 48], where the precipitates consist either of single-phase material or are an agglomeration of phases. Precipitate morphology is a fascinating field of study, as intriguing growth phenomena result from the interaction between the precipitates and the film matrix as shall be demonstrated with the examples given in Figures 9-11, which are micrographs of precipitates in sputtered  $\text{YBa}_2\text{Cu}_3\text{O}_{7-\delta}$  films.

Figure 9 shows a cross-sectional HREM micrograph of a  $\text{Y}_2\text{O}_3$  surface precipitate where the [110] planes of the  $\text{Y}_2\text{O}_3$  lie parallel to the (001)  $\text{YBa}_2\text{Cu}_3\text{O}_{7-\delta}$  planes. The precipitate separates *c*-axis from *a,b*-axis oriented  $\text{YBa}_2\text{Cu}_3\text{O}_{7-\delta}$  regions, a configuration which has frequently been observed [43, 49, 53] and is favored owing to good lattice matching between (001)  $\text{Y}_2\text{O}_3$  and (001)  $\text{YBa}_2\text{Cu}_3\text{O}_{7-\delta}$ . The presence of *a*-axis oriented  $\text{YBa}_2\text{Cu}_3\text{O}_{7-\delta}$  grains promotes the nucleation and enhances the growth rate of  $\text{Y}_2\text{O}_3$  with this particular orientation.

Precipitates may also be incorporated epitaxially into the film matrix, an example of which is given in Fig. 10. Once more, this figure shows a  $\text{Y}_2\text{O}_3$  precipitate with (001)  $\text{Y}_2\text{O}_3$  parallel to (001)  $\text{YBa}_2\text{Cu}_3\text{O}_{7-\delta}$ , but this time within a *c*-axis oriented  $\text{YBa}_2\text{Cu}_3\text{O}_{7-\delta}$  grain. With this orientation, epitaxial overgrowth by  $\text{YBa}_2\text{Cu}_3\text{O}_{7-\delta}$  occurs. However, the lattice mismatch between these materials is 3% when parallel to the (001)  $\text{YBa}_2\text{Cu}_3\text{O}_{7-\delta}$  planes, but 9% when perpendicular to it, as can be seen by looking at Fig. 10 at a grazing angle. As suggested by this micrograph, if overgrowth occurs in an imperfect manner, or if the lattice mismatch is significant, precipitates can be a source of additional lattice defects, such as stacking faults or edge and screw dislocations.

Conversely, precipitate formation is promoted by existing defects within the  $\text{YBa}_2\text{Cu}_3\text{O}_{7-\delta}$  matrix, an example of which is given in Fig. 11. This figure shows an AFM image of the (001) surface of a  $\text{YBa}_2\text{Cu}_3\text{O}_{7-\delta}$  film with various types of surface outgrowths (I:  $\text{Y}_2\text{O}_3$ , II:  $\text{Y}_2\text{O}_3\text{CuYO}_2$ , III:  $\text{YBa}_2\text{Cu}_3\text{O}_{7-\delta} / \text{Y}_2\text{O}_3 / \text{CuO}$ ). It is pointed out that one out-

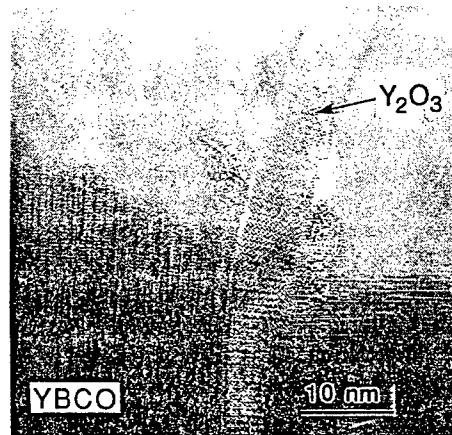


Figure 9: Cross-sectional TEM micrograph of an epitaxial  $\text{Y}_2\text{O}_3$  outgrowth at an *a,b*-axis  $\text{YBa}_2\text{Cu}_3\text{O}_{7-\delta}$  / *c*-axis  $\text{YBa}_2\text{Cu}_3\text{O}_{7-\delta}$  domain boundary in a sputtered film (from [50]).

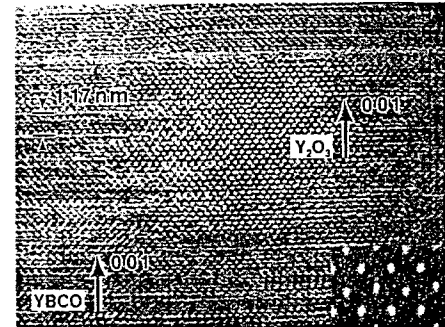


Figure 10: Cross-sectional TEM micrograph of a  $\text{Y}_2\text{O}_3$  inclusion in a sputtered  $\text{YBa}_2\text{Cu}_3\text{O}_{7-\delta}$  film. The (001)  $\text{Y}_2\text{O}_3$  planes are parallel to the (001)  $\text{YBa}_2\text{Cu}_3\text{O}_{7-\delta}$  planes (from [50]).

growth, which is labelled B in Fig. 11, is located at the center of a growth spiral. This interesting configuration can presumably be accounted for by high interfacial energies and internal stresses between the non-epitaxial precipitates and the  $\text{YBa}_2\text{Cu}_3\text{O}_{7-\delta}$  matrix. This stress provides a driving force for the transport of the impurity species to energetically more favorable attachment sites, for example to locations where defects such as dislocations or grain boundaries intersect the film surface. Surface outgrowths induced by compressive stress are known to occur in thin films; these stresses are relieved by the transport of material along easy diffusion paths, such as dislocation cores or grain boundaries (compare also with Fig. 9) [49].

Thus we have shown that, during growth, precipitates frequently interact with other lattice defects. On the one hand, precipitate formation is fostered by existing defects, and on the other hand, precipitates promote the nucleation of additional lattice imperfections.

Grain boundaries are prominent defects that have already been mentioned several times. Low-angle grain boundaries, which for (001) oriented films consist in most cases of arrays of edge dislocations with cores parallel to [001] [54], are frequently caused by the coalescence of crystallites during the initial stages of growth on a substrate not perfectly lattice-matched, due to rotational or translational misalignment of the coalescing crystallites. For example,  $10^{11}$  dislocations/cm<sup>2</sup> were observed to be generated in the coalescence of  $\text{YBa}_2\text{Cu}_3\text{O}_{7-\delta}$  crystallites on MgO substrates [13]. Analogously, during screw dislocation-mediated growth, low-angle grain boundaries are formed if neighboring growth spirals are misaligned. Another source of low-angle grain boundaries is the substrate's mosaic structure, which reflects a network of subgrain boundaries inherited by the film during growth. As a consequence, higher critical current densities have been reported for films grown on substrates with smaller mosaic spread [55] because then the misorientation angle of the subgrain boundaries is lower and low-angle grain boundaries have higher critical current densities [56].

An example for substrate defects that cause high-angle grain boundaries is provided by substrate surface steps, as they can serve not only as nucleation sites for second phases [36]

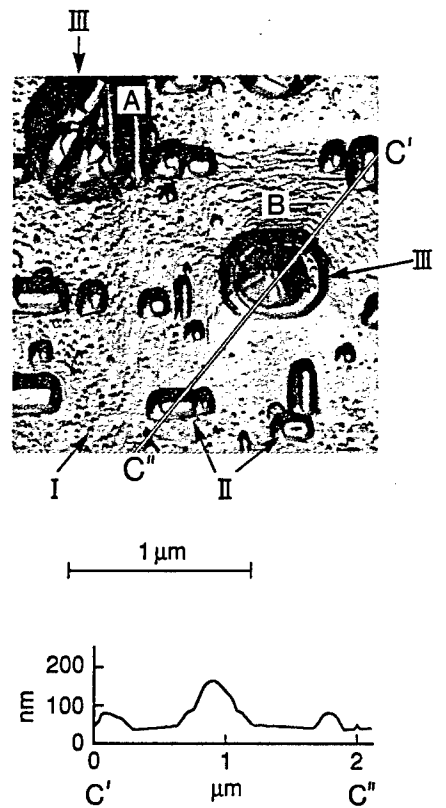


Figure 11: AFM image of the (001) surface of a sputtered  $\text{YBa}_2\text{Cu}_3\text{O}_{7-\delta}$  film showing densely distributed outgrowths of three different types (I-III). A refers to a type III precipitate which is located at the center of a growth spiral. At the bottom a height profile along the line C'-C'' is shown (from [49]).

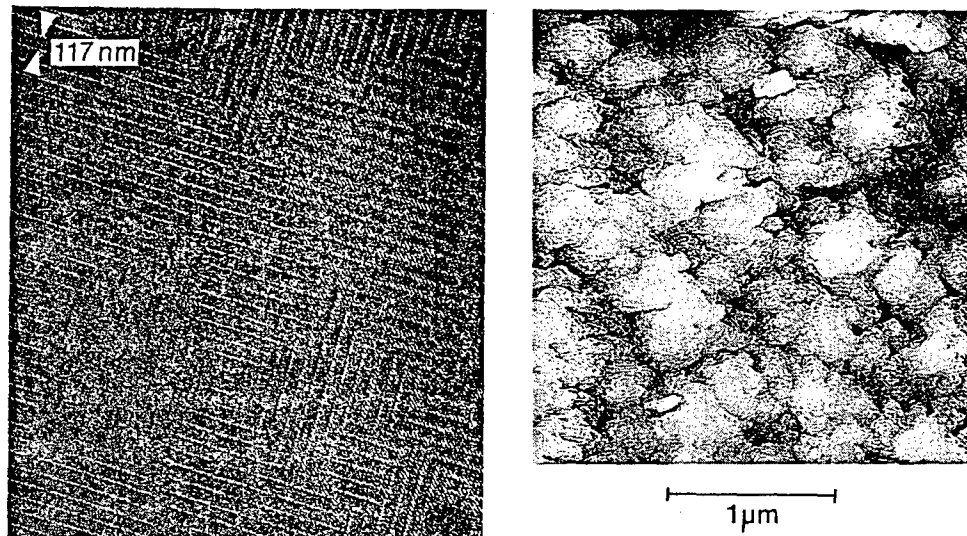


Figure 12: Planar TEM image of an *a*-axis oriented  $\text{YBa}_2\text{Cu}_3\text{O}_{7-\delta}$  film grown by sputter deposition. Small *a*-axis grains and various grain boundaries are shown (from [60]. © 1990 by the AAAS).

but also for  $90^\circ$  misoriented grains. For instance, *c*-axis oriented grains have been observed to nucleate at substrate steps within *a,b*-axis oriented films [36], and *a,b*-axis oriented grains within *c*-axis oriented films [57, 58]. The corresponding grain boundaries act as Josephson junctions, which is exploited in the step edge junction technology to fabricate Josephson junctions within epitaxial  $\text{YBa}_2\text{Cu}_3\text{O}_{7-\delta}$  films by growing the films on substrates with surface steps [59].

Other well-known high-angle grain boundaries are the twin planes along [110] in (001)-oriented  $\text{YBa}_2\text{Cu}_3\text{O}_{7-\delta}$  films and, for *a*-axis oriented  $\text{YBa}_2\text{Cu}_3\text{O}_{7-\delta}$  films, the boundaries between grains with the *c*-axis parallel to the substrate [100] and [010], respectively (see Fig. 12) [60]. If not purposely avoided, for example by breaking the substrate symmetry between  $\langle 100 \rangle$  and  $\langle 010 \rangle$  with applied stress, twin planes occur with a density as high as  $4 \times 10^5 \text{ cm}^{-2}$  [61]. As shown in Fig. 12, the density of the  $90^\circ$  grain boundaries in the *a*-axis oriented films can be even higher, as the grains have side lengths of some 10 nm.

Defects that appear at astonishingly high densities are dislocations. Edge dislocations with densities between  $10^9$  and  $10^{11} \text{ cm}^{-2}$  have been observed with TEM by a number of groups working with excellent films [13, 44]. Screw dislocation densities can be as high as  $10^{10} \text{ cm}^{-2}$  so that in some films they completely dominate the surface morphology, as illustrated by Fig. 13.

Figure 13: STM image of a *c*-axis oriented, 1200 Å thick  $\text{YBa}_2\text{Cu}_3\text{O}_{7-\delta}$  film grown by sputter deposition, showing left- and right-hand growth spirals emanating from screw dislocations.

Dislocations are not only important for the growth process, they directly influence the superconducting properties of the films, too [62]. This is because the dislocations are line defects, which are excellent pinning sites for magnetic flux lines if these are oriented parallel to the dislocation core.

The morphology of the film surface is of prime importance for many electronic applications of high- $T_c$  films. For rf devices, for example, the surface is required to have excellent superconducting properties; for other applications, like for planar tunnel junctions, a very flat surface is needed in addition. Both are tough requirements to meet with  $\text{YBa}_2\text{Cu}_3\text{O}_{7-\delta}$  films.

Because the coherence length of the high- $T_c$  compounds is so short, surface superconductivity is highly dependent on the quality of the top layers. Unfortunately, surface layers with excellent superconducting properties are difficult to obtain, because the film surface is chemically reactive and degrades quickly as soon as the films are removed from the deposition chamber. In addition, the surface relaxes by surface reconstruction processes, as recently shown for  $\text{GdBa}_2\text{Cu}_3\text{O}_{7-\delta}$  films with HREM [63].

As demonstrated in the previous figures, surface outgrowths and growth steps govern the surface morphology. Surface outgrowths can be minimized by adjusting the film's composition to the exact stoichiometric values, or by limiting diffusion by lowering the growth temperature or by enhancing the growth rate, so that off-stoichiometric species are not able to agglomerate as surface precipitates. Relatively smooth films can be grown between the precipitates by adjusting growth rate and deposition temperature. Also it is observed that  $\text{YBa}_2\text{Cu}_3\text{O}_{7-\delta}$  films grown on buffer layers of  $\text{PrBa}_2\text{Cu}_3\text{O}_{7-\delta}$  have a reduced surface roughness. However, no way has yet been found to grow films that are free of growth steps over areas of several square millimeters, which is the size desired for applications or for studies which involve single unit cells of high- $T_c$  materials.

Surface defects in *c*-axis oriented films, which appear as small dark spots such as the ones labelled "A" in Fig. 1, have been observed by many groups in STM investigations, but are not yet sufficiently understood. These spots measure about 5-10 nm in diameter and can appear at rather high densities of the order of  $10^{10} \text{ cm}^{-2}$  [15, 19]. They are most likely holes which are more than 2 nm deep, but may also consist of insulating regions. The growth fronts frequently envelop these spots, as though these spots impeded the crystal growth process. This observation implies that the spots are holes present during growth and are not due to tip-induced damage during STM imaging. Concerning the spots' origin, two explanations seem reasonable: First, the dots may be associated with *c*-axis oriented cores of edge dislocations. The dislocation cores could be hollow or filled with insulating material. Second, the spots may be caused by small ( $\text{Y}_2\text{O}_3$ ) precipitates buried underneath. Disturbed overgrowth can lead to insulating regions at the film surface or even to holes. As the STM tip is not observed to touch the film surface during imaging of the spots, although it is moved  $\approx 2$  nm towards the film (which is more than its flying height), it is concluded that the spots are most likely caused by holes rather than by insulating regions.

In summary, high- $T_c$  films have the tendency to be rich in defects. If the films are to be optimized with respect to applications, control of defect type, size, orientation and density is required. For some applications the defect density should simply be minimized: when the defects degrade the pertinent sample qualities for a particular application. For example, the surface microwave resistance of epitaxial films is increased by grain boundaries and precipitates. For other applications, such as planar tunnel junctions or devices which involve

ultrathin films, the surface roughness is to be minimized. Thus, in this case, precipitates are deleterious and even surface steps have to be avoided.

On the other hand, defects such as dislocations, point defects or precipitates act as pinning sites for magnetic flux lines. Therefore, if a high critical current density is to be achieved, films are desired that contain a spectrum of defects optimized for vortex pinning.

#### 4. Applications

When thinking of applications of high- $T_c$  films, applications in electronic circuitry usually come to mind. But high- $T_c$  films are also applied in various fields of research as model systems for bulk materials, as will be described in the first part of this chapter.

##### 4.1 MODEL SYSTEMS

High- $T_c$  films are grown under different conditions than for the growth of bulk materials. For films, growth occurs at higher supersaturations, so that they crystallize under conditions further from equilibrium. Thus it is possible to obtain phases in the films that cannot be achieved with bulk compounds. Further, finite lattice mismatch between the substrate and the film easily results in significant stress and strain; to achieve comparable stress in bulk materials requires the application of substantial pressure.

For example, bulk synthesis of the infinite layer compound  $\text{SrCuO}_2$  requires the application of high pressures [64], whereas  $\text{Sr}_x\text{CuO}_2$  films can be grown by alternate deposition of  $\text{SrO}_x$  and  $\text{CuO}_x$  layers in a low-pressure atmosphere of  $\text{NO}_2$  [65]. Moreover, using multiple source deposition systems with adequate rate control, the film stoichiometry can be varied during growth to modulate the film composition at a scale of one unit cell or even below. This technique allows the growth of films with stacking sequences not attainable in bulk materials. For instance, by using shuttered molecular beam epitaxy, superconducting  $\text{BiSrCaCuO}$  films have been grown that are composed of 61 bilayers, each consisting of a half unit cell of  $\text{Bi}_2\text{Sr}_2\text{CuO}_{6+\delta}$  followed by a half unit cell of  $\text{Bi}_2\text{Sr}_2\text{Ca}_2\text{Cu}_3\text{O}_{10+\delta}$  [66].

Superlattices with longer modulation lengths, consisting of layers of a high- $T_c$  compound (one or several unit cells thick) alternating with non-superconducting layers (e.g.  $\text{YBa}_2\text{Cu}_3\text{O}_{7-\delta}$ ) alternating with

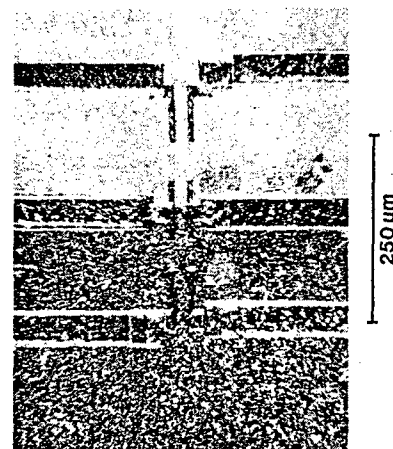


Figure 14: Photograph of an excimer-laser patterned  $\text{YBa}_2\text{Cu}_3\text{O}_{7-\delta}$  film showing three superconducting bridges: two bridges within adjacent grains and one bridge straddling the grain boundary. By using an oblique-incidence illumination technique, the two adjacent grains are clearly distinguishable as dark and light regions (from [56]).

$\text{PrBa}_2\text{Cu}_3\text{O}_{7-\delta}$ ) [67] have been utilized to study the importance of *c*-axis coupling between CuO layers or to investigate whether a minimal thickness is required for high- $T_c$  layers to be superconducting.

However, there are even more aspects of bulk materials that can be investigated by utilizing high- $T_c$  films as model systems. For example, by using large grained  $\text{YBa}_2\text{Cu}_3\text{O}_{7-\delta}$  films, it has been proved that the critical current densities in bulk high- $T_c$  materials are limited by grain boundaries. This has been achieved by directly measuring the critical current of superconducting bridges straddling single grain boundaries as illustrated in Fig. 14 [68]. The value of the critical current across the grain boundary was always found to be lower than that within the adjacent grains (see Fig. 14). The grain boundary critical current can be easily depressed with applied magnetic fields, giving evidence for weak superconducting coupling across grain boundaries. Using a bicrystal technique, it is even possible to measure the grain boundary critical current as a function of a misorientation of the adjacent grains [56]. Clearly, such experiments are much more difficult to perform with bulk materials than with thin films; the latter may be utilized as convenient model systems to understand the critical current limitations of bulk materials [69]. Notably, the bicrystal experiments described have directly led to the development of bicrystalline high- $T_c$  Squids [68, 70], with the possibility of selecting the critical current density of the Squids by adjusting the grain boundary misorientation.

#### 4.2 ELECTRONIC APPLICATIONS

Electronic applications of high- $T_c$  films can be divided into two groups: passive and active devices, respectively. The former usually consist of plain films, whereas the latter rely on heterostructures and/or weak links to be incorporated into the films.

##### 4.2.1 Passive Devices

**4.2.1.1 Interconnects.** Epitaxial high- $T_c$  films are of interest for interchip connects in digital applications and for general wiring purposes in (analog) rf devices. For these applications, superconductors offer numerous advantages over conventional conductors, such as signal transmission with low dispersion and low loss, high current densities (which permits a high wiring density) and negligible electromigration. Of course, these advantages have to outweigh the efforts required to integrate high- $T_c$  films into the device fabrication process and the need for cryogenic operating temperatures. In general, however, superconducting interconnects for data transfer become more attractive with increasing frequency and with increasing line length. For example, for interconnection lengths of more than 1 cm, superconducting lines seem to have a clear edge over conventional ones for frequencies above 100 GHz [71]. But as clock frequencies of present computers are well below this value, there is no motivation at present or in the near future to incorporate high- $T_c$  transmission lines into standard computers, which would otherwise be operated at room temperature.

For other high-frequency signal processing devices, high- $T_c$  transmission lines offer advantages that are already clear. The potential of operating GaAs MESFETs or HEMTs at 77 K with high- $T_c$  interconnects has been demonstrated recently by a number of groups [72, 73] by fabricating rf amplifiers and oscillators. Given present progress in the development of cryocoolers, the cooling of superconducting devices is not generally considered to be a

major disadvantage, in particular as cooling provides additional benefits, such as the possibility to reduce noise or to enhance the performance of semiconducting devices.

**4.2.1.2 Microwave Devices.** Superconducting microwave devices benefit from the low surface resistance of superconducting materials, which allows the fabrication of devices with large quality factors (Q-values). For example, at 77 K and at 10 GHz the surface resistance of Cu is  $R_S = 13 \text{ m}\Omega$ , whereas for  $\text{Tl}_2\text{Ba}_2\text{CaCu}_2\text{O}_8$  on  $\text{LaAlO}_3$  a value of  $R_S = 130 \mu\Omega$  has been reported [74]. We should point out in this context that the surface resistance of superconductors rises (theoretically) with the square of the operating frequency, compared to a square root increase for conventional conductors. They thus outperform superconductors beyond a certain crossover frequency. For example, at 77 K the surface resistance of  $\text{YBa}_2\text{Cu}_3\text{O}_{7-\delta}$  exceeds that of Cu above  $\approx 230$  GHz. Low surface resistance not only reduces losses, it also offers the possibility of reducing the size and the weight of the respective microwave component drastically, which is an important issue for avionic and space applications. As the advantages of high- $T_c$  microwave devices are obvious and their fabrication is comparatively simple, their development has already reached a relatively mature state. Devices under investigation, some of which are already on the market, encompass a broad spectrum including resonators, filters, antennas, delay lines, mixers, phase shifters and other signal processing units including convolvers, correlators and Fourier transformers. For an overview of the present status of this field, the reader is referred to [75].

**4.2.1.3 Bolometers.** High- $T_c$  films can be used as efficient bolometers by operating them right at the superconducting transition temperature and by recording their resistance increase due to heating caused by the IR irradiation to be detected. These bolometers are of particular interest for the wavelength region  $> 20 \mu\text{m}$  for which no semiconducting detectors are available at present [76]. The responsiveness of high- $T_c$  bolometers has been measured to be above 1000 V/W, and response times have been optimized to be as short as a few microseconds [77]. For high-quality films, noise equivalent powers of  $(1 - 20) \times 10^{-12} \text{ W/Hz}^{-1/2}$  have been predicted [76], which compare favorably to the noise data of conventional 77 K pyroelectric detectors.

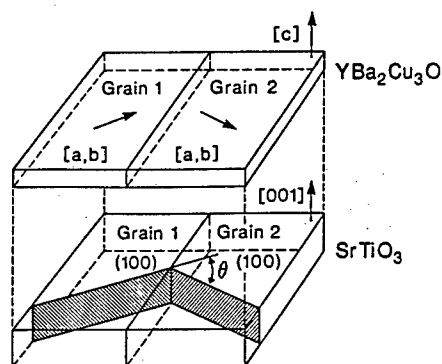
#### 4.2.2 Active Devices

**4.2.2.1 Two-Terminal Devices.** All active, two-terminal high- $T_c$  devices rely on some type of weak link, which is preferably a Josephson junction. There are numerous viable high- $T_c$  thin film Josephson junctions available, a selection of which is sketched in Fig. 15.

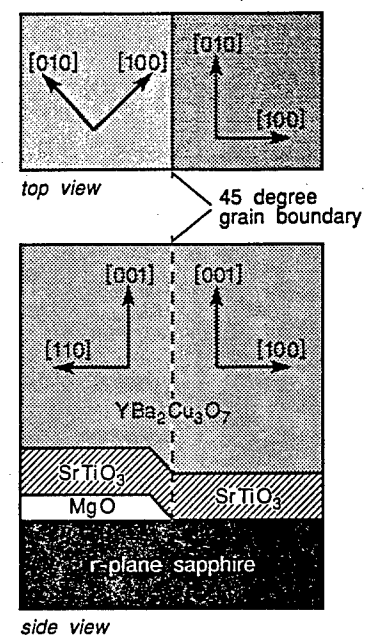
As high-angle grain boundaries have been shown to act as Josephson junctions [56], one road to viable high- $T_c$  junctions consists of adding grain boundaries to high- $T_c$  films. The objective is to use single grain boundary junctions [68, 70], as each grain boundary is a source of noise. There are several ways to achieve this goal, one is to fabricate bicrystalline films by deposition on bicrystalline substrates [56], another is to use seed layers to change the film orientation on part of the substrate [78]. Grain boundaries can also be induced by taking advantage of 90° misoriented grains which nucleate at surface steps, as illustrated in Fig. 15 [59].

In another family of high- $T_c$  junctions, the weak link, is caused by a thin layer of non-high- $T_c$  material separating two superconducting electrodes (preferably in the  $a,b$ -direc-

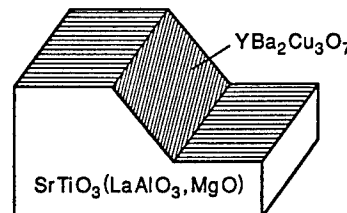
## Bicrystalline junctions



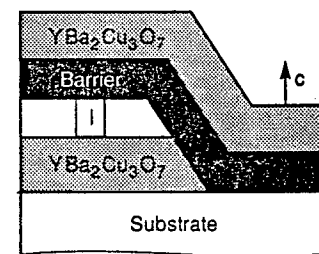
## Biepitaxial junctions



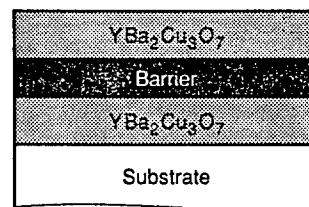
## Step-edge junctions



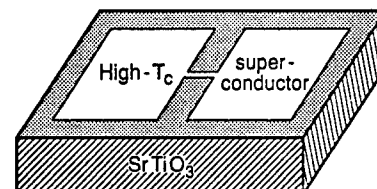
## Ramp-type junctions



## Planar junctions



## Microbridge

Figure 15: Sketches of various types of high- $T_c$  Josephson junctions.

tion) like in the ramp-type junctions [79, 80] or in the more conventional planar junctions [81].

Finally, microbridges, which are narrow constrictions structured into the films, can be used as Josephson junctions.

These junctions are the basis of applications within digital electronics, but also of Squid-based sensors. Although the high- $T_c$  Squids can be improved further, especially with respect to  $1/f$  noise and the reproducible fabrication of low-noise Squids, the noise data of available high- $T_c$  thin film Squids are quite appealing. For dc-Squids based on step-edge junctions, energy sensitivities of  $2 \times 10^{-29} \text{ J/Hz}$  at 1 Hz have been achieved [82], which compare favorably to the resolution of commercial rf Squids operated at 4.2 K. If the Squids are to be used as magnetometers, the magnetic field sensitivity is the figure of merit, because it also reflects the quality of the flux transformer and the magnetic coupling of the transformer to the Squid loop. Although the integration of low-noise flux transformers into the Squids is still in its infancy, magnetic field sensitivities of  $170 \text{ fT Hz}^{-1/2}$  have been reported at 77 K for frequencies exceeding 1 Hz [83], which is sufficient to monitor the human heartbeat magnetically.

**4.2.2.2 Three-Terminal Devices.** Various concepts for true high- $T_c$  transistors are being investigated at present (see Fig. 16). In these devices a supercurrent flowing in the drain-source channels is controlled either by applying magnetic fields (superconducting flux flow transistor) [84], by electric fields (superconducting field effect transistor [85], or by injection of quasiparticles (direct current injection transistor [86]). In another approach, normal currents flowing between  $\text{YBa}_2\text{Cu}_3\text{O}_{7-\delta}$  contacts on the surface of a  $\text{SrTiO}_3$  substrate are controlled by means of an electric field (dielectric base transistor) [87].

Compared to the high- $T_c$  Josephson junctions, these three-terminal devices are in an early stage of development, and at present it is far from clear whether these approaches will lead to viable transistors. But much exciting progress has been made within a relatively short

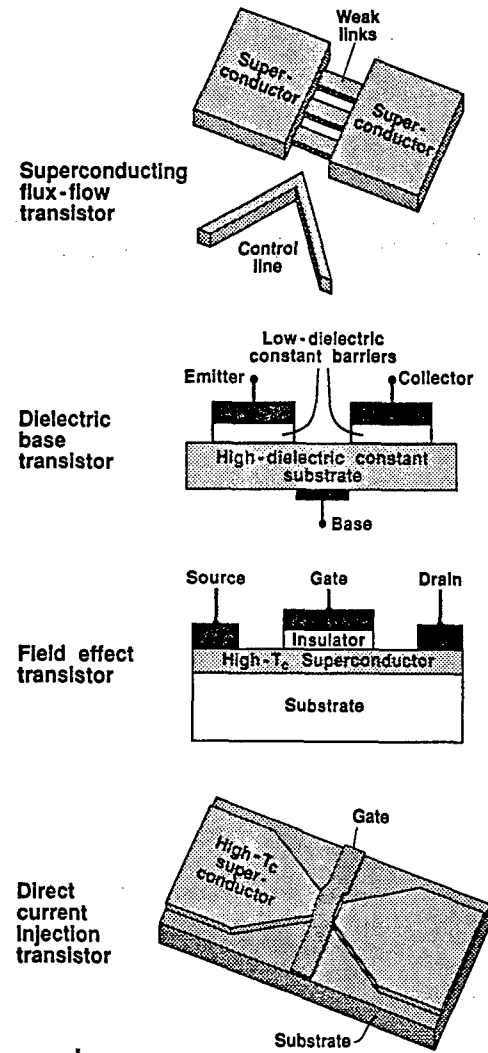


Figure 16: Sketches of various sample structures used to investigate high- $T_c$  three-terminal devices.

time in this dynamic field, as demonstrated in Fig. 17 for a field effect sample. The curve shows the resistance vs. temperature characteristic of a weakly linked  $\text{YBa}_2\text{Cu}_3\text{O}_{7-\delta}$  channel; the parameter is an applied electric field. As shown, by applying the electric field, the critical temperature of the  $\text{YBa}_2\text{Cu}_3\text{O}_{7-\delta}$  film can be suppressed by more than 10 K [88] which is quite an interesting number for device applications.

**Acknowledgment.** Many thanks to the American Association for the Advancement of Science for permission to reprint Figure 12.

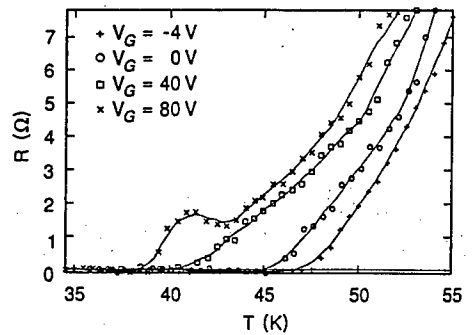


Figure 17:  $R(T)$  curve of a weakly linked  $\text{YBa}_2\text{Cu}_3\text{O}_{7-\delta}$  film of an electric field effect structure as shown in Fig. 16 with four different gate voltages  $V_G$  applied. The  $\text{YBa}_2\text{Cu}_3\text{O}_{7-\delta}$  film was  $\approx 80 \text{ \AA}$  thick.

## 5. REFERENCES

1. P. Chaudhari, R.H. Koch, R.B. Laibowitz, T.R. McGuire, and R.J. Gambino, Phys. Rev. Lett. **58**, 2684 (1987).
2. D.G. Schlom, D. Anselmetti, J.G. Bednorz, Ch. Gerber, and J. Mannhart, "Defect-Mediated Growth of  $\text{YBa}_2\text{Cu}_3\text{O}_{7-\delta}$  Films," Proc. MRS Fall Meeting, Boston, MA, (1992) in press.
3. D.G. Schlom, "Epitaxial Growth of High Temperature Superconductors from the Gas Phase," in Int'l Workshop on Superconductivity, Co-sponsored by ISTEC and MRS: Controlled Growth of Single- and Polycrystals of High-Temperature Superconductors (ISTEC/MRS, Honolulu, 1992) p. 34.
4. B. Mutaftschiev, "Crystal Growth and Dislocations" in *Dislocations in Solids*, F.R.N. Nabarro, ed. (North Holland, Amsterdam, 1980).
5. T. Suzuki, J. Cryst. Growth **20**, 202 (1973).
6. W. Dekeyser and S. Amelinckx, "Les Dislocations et la Croissance des Cristaux," Masson, Paris (1955).
7. C.M. Heck, Phys. Rev. **51**, 690 (1937).
8. M.I. Kozlovskii, Sov. Phys. Crystallogr. **3**, 236 (1958).
9. F.C. Frank, Disc. Farad. Soc. **5**, 48 (1949).
10. G.G. Lemmlein and E.D. Dukova, Sov. Phys. Crystallogr. **1**, 269 (1956).
11. M.I. Kozlovskii, Sov. Phys. Crystallogr. **3**, 206 (1958).
12. A. Baronnet, J. Cryst. Growth **19**, 193 (1973).
13. S.K. Streiffer, B.M. Lairson, C.B. Eom, B.M. Clemens, J.C. Bravman and T.H. Geballe, Phys. Rev. **B43**, 13007 (1991).
14. J. Burger, PhD thesis, University of Erlangen (1992), (in German).
15. Ch. Gerber, D. Anselmetti, J.G. Bednorz, J. Mannhart, and D.G. Schlom, Nature **350**, 279 (1991).
16. M. Hawley, I.D. Raistrick, J.G. Beery, R.J. Houlton, Science **251**, 1587 (1991).
17. I.D. Raistrick, M. Hawley, J.G. Beery, F.H. Garzon, and R.J. Houlton, Appl. Phys. Lett. **59**, 3177 (1991).
18. I. Maggio-Aprile, A.D. Kent, Ph. Niedermann, Ch. Renner, L. Antognazza, L. Mieville, O. Brunner, J.M. Triscone and O. Fischer, Ultramicroscopy **42-44**, 728 (1992).
19. D.G. Schlom, D. Anselmetti, J.G. Bednorz, R.F. Broom, A. Catana, T. Frey, Ch. Gerber, H.-J. Güntherodt, H.P. Lang, and J. Mannhart, Z. Phys. B **86**, 163 (1992).
20. J. Burger, P. Bauer, M. Veith, and G. Saemann-Ischenko, Ultramicroscopy **42-44**, 721 (1992).
21. N. Chandrasekhar, V. Agrawal, V.S. Achutharaman, and A.M. Goldman, Appl. Phys. Lett. **60**, 2424 (1992).
22. M. Kawasaki, J.P. Gong, M. Nantoh, T. Hasegawa, K. Kitazawa, M. Kumagai, K. Hirai, K. Horiguchi, M. Yoshimoto, and H. Koinuma, to be published in Jpn. J. Appl. Phys.

23. L. Luo, M.E. Hawley, C.J. Maggiore, R.C. Dye, R.E. Muenchhausen, L. Chen, B. Schmidt, and A.E. Kaloyeros, *Appl. Phys. Lett.* **62**, 99 (1993).
24. X.-Y. Zeng, D.H. Lowndes, S. Zhu, J.D. Budai, and R.J. Warmack, *Phys. Rev. B* **45**, 7584 (1992).
25. H.S. Wang, D. Eissler, W. Dietsche, A. Fischer, and K. Ploog, *J. Cryst. Growth* **126**, 565 (1993).
26. J. Moreland, P. Rice, S.E. Russek, B. Jeanneret, A. Roshko, R.H. Ono, and D.A. Rudman, *Appl. Phys. Lett.* **59**, 3039 (1991).
27. H.P. Lang, T. Frey, H.-J. Güntherodt, *Europhys. Lett.* **15**, 667 (1991).
28. H.U. Krebs, Ch. Krauns, X. Yang, and U. Geyer, *Appl. Phys. Lett.* **59**, 2180 (1991).
29. F. Baudenbacher, K. Hirata, P. Berberich, H. Kinder, W. Assmann, and H.P. Lang, *Physica C* **185-189**, 2177 (1991).
30. J.R. Sheats and P. Merchant, *Appl. Phys. Lett.* **62**, 99 (1993).
31. H.P. Lang, H. Haefke, G. Leemann, and H.-J. Güntherodt, *Physica C* **194**, 81 (1992).
32. M. McElfresh, T.G. Miller, D.M. Schaefer, R. Reifenberger, R.E. Muenchhausen, M. Hawley, S.R. Foltyn, and X.D. Wu, *J. Appl. Phys.* **71**, 5099 (1992).
33. H. Olin, G. Brorsson, P. Davidsson, Z.G. Ivanov, P.A. Nilsson, and T. Claesson, *Ultramicroscopy* **42-44**, 734 (1992).
34. M.E. Hawley, I.D. Raistrick, R.J. Houlton, F.H. Garzon, and M. Piza, *Ultramicroscopy*, **42-44**, 705 (1992).
35. H. Haefke, H.P. Lang, R. Sum, H.-J. Güntherodt, L. Berthold, and D. Hesse, *Appl. Phys. Lett.* **61**, 2359 (1992).
36. R. Ramesh, A. Inam, D.M. Hwang, T.S. Ravi, T.D. Sands, X.X. Xi, X.D. Wu, Q. Li, T. Venkatesan, and R. Kilaas, *J. Mater. Res.* **6**, 2264 (1991).
37. M.G. Norton and C.B. Carter, *J. Cryst. Growth* **110**, 641 (1991).
38. T. Nishinaga, T. Shitara, K. Mochizuki, and K.I. Cho, *J. Cryst. Growth* **99**, 482 (1990).
39. T. Frey (private communications) for the growth of  $\text{YBa}_2\text{Cu}_3\text{O}_{7-\delta}$  by PLD.
40. N. Chandrasekhar (private communications) for the growth of  $\text{YBa}_2\text{Cu}_3\text{O}_{7-\delta}$  by MBE.
41. E. Bauer, Z. Kristallogr. **110**, 372 (1958).
42. M.G. Norton and C.B. Carter, "Growth of  $\text{YBa}_2\text{Cu}_3\text{O}_{7-\delta}$  Thin Films – Nucleation, Heteroepitaxy and Interfaces," submitted to Scanning Microscopy.
43. R. Ramesh, A. Inam, D.M. Hwang, T.D. Sands, C.C. Chang, and D.L. Hart, *Appl. Phys. Lett.* **58**, 1557 (1991).
44. O. Eibl and B. Roas, *J. Mater. Res.* **5**, 2620 (1990).
45. S.N. Basu, A.H. Carim, and T.E. Mitchell, *J. Mater. Res.* **6**, 1823 (1991).
46. J.G. Wen, C. Traeholt, and H.W. Zandbergen, *Physica C* **205**, 354 (1993).
47. T.E. Mitchell, "Microstructure of Epitaxial  $\text{YBa}_2\text{Cu}_3\text{O}_{7-\delta}$  Films," in *Ceramic Superconductors*, 2nd Int'l Conf. Ceramic Science and Technol., Orlando, FL, November 12-15, 1990, (American Ceramic Society).
48. M.J. Casanove, A. Alimoussa, C. Roucau, C. Escribe-Filippini, P.L. Reydet, and P. Marcus, *Physica C* **175**, 285 (1991).
49. A. Catana, J.G. Bednorz, Ch. Gerber, J. Mannhart, and D.G. Schlom, "Surface Outgrowths on Sputtered  $\text{YBa}_2\text{Cu}_3\text{O}_{7-\delta}$  Films: A Combined Atomic Force Microscopy and Transmission Electron Microscopy Study," submitted to *Appl. Phys. Lett.*
50. A. Catana, R.F. Broom, J.G. Bednorz, J. Mannhart, and D.G. Schlom, *Appl. Phys. Lett.* **60**, 1016 (1992).
51. T.I. Selinder, U. Helmersson, Z. Han, J.E. Sundgren, H. Sjöström, and L.R. Wallenberg, *Physica C* **202**, 69 (1992).
52. A.F. Marshall, V. Matijasevic, P. Roesenthal, K. Shinohara, R.H. Hammond, and M.R. Beasley, *Appl. Phys. Lett.* **57**, 1158 (1990).
53. A. Catana, D.G. Schlom, J. Mannhart and J.G. Bednorz, *Appl. Phys. Lett.* **61**, 720 (1992).
54. Y. Gao, K.L. Merkle, G. Bai, H.L.M. Chang, and D.J. Lam, *Physica C* **174**, 1 (1991).
55. W. Schauer, X.X. Xi, V. Windte, O. Meyer, G. Linker, Q. Li, and J. Geerk, *Cryogenics* **30**, 586 (1990).
56. D. Dimos, P. Chaudhari, J. Mannhart, and F.K. LeGoues, *Phys. Rev. Lett.* **61**, 219 (1988).
57. T.E. Mitchell, S.N. Basu, M. Nastasi, and T. Roy, *MRS Symp. Proc.* **183**, 357 (1990).
58. H. Takahashi, Y. Aoki, T. Usui, R. Fromknecht, T. Morishita, and S. Tanaka, *Physica C* **175**, 381 (1991).
59. K.P. Daly, W.D. Dozier, J.F. Burch, S.B. Coons, R. Hu, C.E. Platt, and R.W. Simon, *Appl. Phys. Lett.* **58**, 543 (1991).

60. C.B. Eom, A.F. Marshall, S.S. Laderman, R.D. Jacobowitz, and T.H. Geballe, *Science*, **249**, 1549 (1990).
61. D.H. Kim, D.J. Miller, J.C. Smith, R.A. Holoboff, J.H. Kang, and J. Talvacchio, *Phys. Rev. B* **44**, 7607 (1991).
62. J. Mannhart, D. Anselmetti, J.G. Bednorz, A. Catana, Ch. Gerber, K.A. Müller, and D.G. Schlom, *Z. Phys. B* **86**, 177 (1992).
63. H.W. Zandbergen, "Reconstruction and Relaxation of the Surface of (001) Cleaved  $\text{GdBa}_2\text{Cu}_3\text{O}_{7-\delta}$ ," in Proc. 1992 TCSUH Workshop on HTS Materials, Bulk Processing and Bulk Applications, Houston, Texas, Feb. 27-18, 1992 (World Scientific, Singapore).
64. M. Takano, Y. Takeda, H. Okada, M. Miyamoto, and T. Kusada, *Physica C* **159**, 375 (1989).
65. X. Li, M. Kanai, T. Kawai, and S. Kawai, *Jpn. J. Appl. Phys.* **31**, 217 (1992).
66. D.G. Schlom, A.F. Marshall, J.S. Harris, I. Bozovic, and J.N. Eckstein, "Growth of Metastable Phase and Superlattice Structures of Bi-Sr-Ca-Cu-O Compounds by an Atomic Layering MBE Technique," Proc. 3rd Int'l Symp. on Superconductivity, Sendai, Japan, Nov. 6-9, 1990.
67. J.M. Triscone, M.G. Karkut, L. Antognazza, O. Brunner, and O. Fischer, *Phys. Rev. Lett.* **63**, 1016 (1989); U. Poppe, P. Prieto, J. Schubert, H. Soltner, K. Urban, and Ch. Buchal, *Sol. State Comm.* **71**, 569 (1989).
68. P. Chaudhari, J. Mannhart, D. Dimos, C.C. Tsuei, J. Chi, M.M. Oprysko, and M. Scheuermann, *Phys. Rev. Lett.* **60**, 1653 (1988).
69. J. Mannhart and C.C. Tsuei, *Z. Phys. B* **77**, 53 (1989).
70. C.C. Tsuei, J. Mannhart, and D. Dimos, "Limitations on Critical Currents in High-Temperature Superconductors," Proc. Topical Conf. on High- $T_c$  Superconducting Thin Films, Devices and Applications, Atlanta, GA, 1988, G. Maraitondo, R. Joint, and M. Onellion, eds. (American Institute of Physics, New York, 1989) pp. 194-207.
71. S.K. Tewksbury, L.A. Hornak, and M. Hatamian, "High- $T_c$  Superconductors for Digital System Interconnections," preprint.
72. J.W. Smuk, M.G. Stubbs and J.S. Wight, "Hybrid Semiconductive/High Temperature Superconductive Ku-Band Oscillator and Amplifier MICs," Proc. IEEE MTT Symposium, Albuquerque, NM, June 1992, in press.
73. N.J. Rohrer, M.A. Richard, G.J. Valco, and K.B. Bhasin, "A 10 GHz YBCO/GaAs Hybrid Oscillator Proximity Coupled to a Circular Microstrip Patch Antenna," *IEEE Transactions on Applied Superconductivity*, March 1993.
74. W.L. Holstein, L.A. Parisi, C. Wilker, and R.B. Flippin, *Appl. Phys. Lett.* **60**, 2014 (1992).
75. M. Nisenoff, J.C. Ritter, G. Price, and S.A. Wolf, "High Temperature Superconductivity Space Experiment: HTSSE I - Components and HTSSE II - Subsystems and Advanced Devices," Proc. ASC '92.
76. P.L. Richards, J. Clarke, R. Leoni, Ph. Lerch, S. Verghese, M.R. Beasley, T.H. Geballe, R.H. Hammond, P. Rosenthal, and S.R. Spielman, *Appl. Phys. Lett.* **54**, 283 (1989).
77. K. Li, J.E. Johnson, and B.W. Aker, *J. Appl. Phys.* **73**, 1531 (1993).
78. K. Char, M.S. Colclough, S.M. Garrison, N. Newman, and G. Zaharchuck, *Appl. Phys. Lett.* **59**, 733 (1991).
79. M.S. Dilorio, S. Yoshizumi, M. Maung, K.Y. Yang, J. Zhang, and N.Q. Fan, *Nature* **354**, 513 (1991).
80. Yu.M. Boguslavskij, J. Gao, A.J.H.M. Rijnders, D. Terpstra, G.J. Gerritsma, and H. Rogalla, *Physica C* **194**, 268 (1992).
81. G.F. Virshup, M.E. Klausmeier-Brown, I. Bosovic, and J.N. Eckstein, *Appl. Phys. Lett.* **60**, 2288 (1992).
82. G. Friedl, M. Vildic, B. Roas, D. Uhl, F. Bömmel, M. Römhild, B. Hillenbrand, B. Stritzker, and G. Daalmans, *Appl. Phys. Lett.* **60**, 3048 (1992).
83. A.I. Braginski, *Cryogenics* **32**, ICEC Supplement 562 (1992); for this device, a superconducting washer was used instead of a flux transformer for flux focusing.
84. J.S. Martens, G.K.G. Hohenwarter, J.B. Beyer, and J.E. Nordman, *J. Appl. Phys.* **65**, 4057 (1989).
85. J. Mannhart, J.G. Bednorz, K.A. Müller, and D.G. Schlom, *Z. Phys. B* **83**, 307 (1991).
86. H. Higashino, K. Setsune, and K. Wasa, "Three Terminal Devices of High Temperature Superconductors," preprint.
87. H. Tamura, A. Yoshida, and S. Hasua, *Appl. Phys. Lett.* **59**, 298 (1991).
88. J. Mannhart, J. Ströbel, J.G. Bednorz, and Ch. Gerber, *Appl. Phys. Lett.* **62**, 630 (1993).

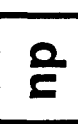
# **MOLECULAR BEAM EPITAXY**

## **Applications to Key Materials**

Edited by

**Robin F. C. Farrow**

*IBM Almaden Research Center  
San Jose, California*



**NOYES PUBLICATIONS**  
Park Ridge, New Jersey, U.S.A.

(c) 1995

119. Rowell, N. L., Noel, J. P., Houghton, D. C., and Buchanan, M., *Appl. Phys. Lett.*, 58(9):957-958 (1991)
120. *Mat. Res. Soc. Symp. Proc.*, (S. S. Iyer, R. T. Collins, and L. T. Canham, eds.), vol. 256 (1992)
121. Kesan, V. P., Bassous, E., Munguia, P., Pesarick, S. F., Freeman, M., Iyer, S. S., and Halbout, J. -M., *J. Vac. Sci. Technol. A*, 11(4):1736-1738 (1993)
122. Splett, A., Schmidchen, J., Schuppert, B., Petermann, K., Kasper, E., and Kibbel, H., *Elect. Lett.*, 27:1486-1488 (1991)
123. Pesarick, S. F., Treyz, G. V., Iyer, S. S., and Halbout, J. -M., *Elect. Lett.*, 28:159-160 (1992)
124. Lin, T. L., George, T., Jones, E. W., Ksendzov, A., and Huberman, M. L., *Appl. Phys. Lett.*, 60:380-382 (1992)
125. Tsaur, B. Y., Chen, C. K., and Marino, S. A., *IEEE Elect. Dev. Lett.*, 12:293-295 (1991)
126. Karunasiri, R. P. G., Park, J. S., Wang, K. I., *Appl. Phys. Lett.*, 61(20):2434-2436 (1992)
127. Gibbons, J. F., King, C. A., Hoyt, J. L., Noble, D. B., Gronet, C. M., Scott, M. P., Rosner, S. J., Reid, G., Laderman, S., Nauka, K., Turner, J., and Kaminis, T. I., *Int'l Elect. Dev. Mtg. (IEDM) Tech. Dig.*, pp. 566-569 (Dec 1988)

## 1.0 INTRODUCTION

The discovery by Bednorz and Müller<sup>[1]</sup> of a class of layered crystalline materials which exhibit superconductivity at unprecedentedly high transition temperatures (high  $T_c$ )<sup>\*</sup> opened new possibilities for future electronic devices. Because of the layered nature of these materials, MBE is a natural method to explore their growth. However, in contrast to the relatively fixed group V stoichiometry of III-V compounds grown by MBE, small variations in oxygen or cation composition change these materials from superconductors to semiconductors to insulators, thus requiring a deposition technique with very precise control of stoichiometry. While troublesome for deposition of superconducting films, this dramatic variation in conductivity, together with the existence of chemically and structurally compatible ferroelectric and piezoelectric,[3]-[6] ferrimagnetic,[7] and metallic[8]-[10] oxides provide exciting possibilities for new electronic devices, as the spectrum of physical properties exhibited by these oxides is unparalleled by any other materials system. Many new device concepts will likely employ alternately layered structures with dimensions as thin as

\* The relative term "high  $T_c$ " is used here to signify superconductors with  $T_c$  significantly greater than those compounds which until 1986 were known as "low  $T_c$ " (i.e., the A15 compounds with  $T_c$  up to 23 K for  $Nb_3Ge$ , which have since become known as "low  $T_c$ "). These new compounds, with the exception of the recently discovered fullerenes (e.g.,  $A_3C_{60}$  where A is an alkaline earth), are oxides and are distinguishable from other superconductors by an anomalously high  $T_c$  for their density of states at the Fermi level.[2] The growth of fullerenes is not discussed in this chapter.

the superconducting coherence length,  $\xi$ , which ranges from a few angstroms to a few tens of angstroms in high  $T_c$  materials. The earliest superconducting results were achieved with polycrystalline bulk forms of these materials which had very low critical current densities, making them unsuitable for electronic applications. Since the current carrying capability of high  $T_c$  superconductors is known to be degraded by grain boundaries,<sup>[11]</sup> the ideal form of these materials for most electronic applications is likely to be that of epitaxial films, prepared in such a way that composition and structure can be controlled at the level of single atomic layers.

The first epitaxial films of a high  $T_c$  superconductor were prepared by sputtering.<sup>[12]</sup> The discovery of additional high  $T_c$  superconductors, each in previously unmapped regions of composition (i.e., an absence of relevant phase diagram information), provided a challenging task for those attempting to prepare thin films of these materials. The first epitaxial films with  $T_c$ 's exceeding the vaporization temperature of nitrogen, 77 K, were synthesized using electron beam (e-beam) evaporation to codeposit the constituent elements.<sup>[13][14]</sup> This was followed by a high temperature ex-situ oxygen anneal, during which the high  $T_c$  phase formed by solid phase epitaxy. Other thin film deposition methods soon followed, including sputtering,<sup>[15][16]</sup> molecular beam deposition,<sup>[17][18]</sup> and a relatively new technique known as laser ablation or pulsed laser deposition (PLD).<sup>[19][20]</sup> These methods produced epitaxial films with drastically improved critical current densities compared to their polycrystalline bulk counterparts; however, the high temperature (800–900°C) ex-situ annealing step involved in all these methods was not compatible with the controlled synthesis of layered heterostructures.

The main obstacle to the in-situ growth of high  $T_c$  phases by traditional thin film methods was the necessity for high oxygen pressure during growth, as discussed in detail in Sec. 2.3. For diode and magnetron sputtering, negative ion bombardment was also a significant problem.<sup>[21][22]</sup> The use of relatively high oxygen pressures in e-beam evaporation (reactive evaporation),<sup>[23][24]</sup> PLD,<sup>[25][26]</sup> ion beam sputtering,<sup>[31]</sup> and off-axis<sup>[27][32]</sup> and hollow cylinder<sup>[28]</sup> reactive sputtering geometries, or with total pressures of several hundred mtorr to mitigate negative ion bombardment in the conventional planar sputtering geometry,<sup>[25]</sup> led to the in-situ formation of epitaxial high  $T_c$  superconductor films with excellent electrical transport properties. These in-situ techniques are now routinely used for the preparation of layered heterostructures, both for device structures<sup>[33]</sup> and for investigating the physics of high  $T_c$  superconductivity.<sup>[34][38]</sup>

The advantages of these other techniques over MBE are primarily cost and, in the case of PLD and off-axis sputtering, the nearly faithful composition transfer from target to substrate, which allows a single multi-component target with the same composition as the desired film to be used.<sup>[20][27]</sup> alleviating the need for accurate composition control, a critical component of MBE. MBE, on the other hand, is free from the micron-sized "boulders" common to PLD films<sup>[20]</sup> as well as the energetic species present in sputtering, which can lead to interlayer mixing due to ion bombardment effects.<sup>[39][40]</sup> The multi-element deposition control, growth flexibility, and in-situ monitoring advantages of MBE are well suited to the growth of high  $T_c$  phases which cannot be produced in single phase form by bulk techniques, including the customized growth of new metastable materials, and heterostructures containing these phases. Other deposition techniques, in particular PLD and off-axis sputtering, are, from an economic and process simplicity perspective, generally better suited than MBE to the synthesis of heterostructures made up of phases, each of which can be produced by bulk techniques in single phase form (i.e., the formation energy of each phase is sufficiently favored over other phases that could accommodate its composition).

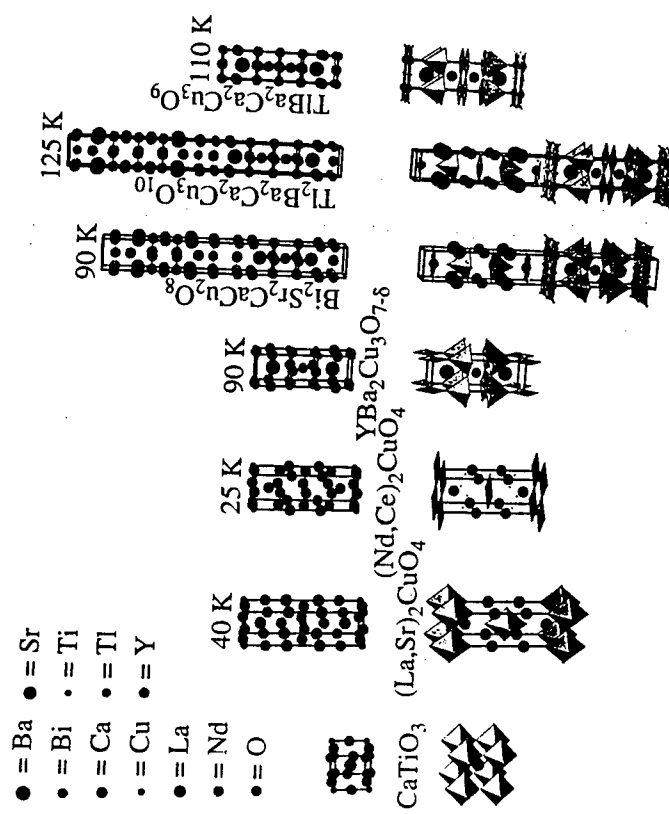
Interestingly, most, if not all, high  $T_c$  materials are metastable at room temperature and below.<sup>[41]</sup> Although no firm theoretical connection has been made between metastability and increasing  $T_c$ , from what is known about the existing high  $T_c$  phases, it appears that techniques capable of synthesizing metastable structures will be required to achieve superconducting materials with ever greater  $T_c$ 's.<sup>[41]</sup> Bulk chemical synthesis routes have led to the vast majority of high  $T_c$  materials discovered to date, but considering the increasing difficulty and complexity of the synthesis routes needed to form these metastable materials, a synthesis method with atomic-scale layering control, in-situ process and crystalline structure monitoring, and a low growth temperature to kinetically limit the decomposition of the deposited structures offers significant advantages over conventional solid state reaction methods as well as other thin film synthesis methods. MBE is an excellent synthesis technique not only for meeting the materials synthesis challenge of current and future high  $T_c$  materials, but also for incorporating these high  $T_c$  layers into device microstructures.

Motivated by the potential of creating high  $T_c$  microstructures with customized atomic layering, together with the ability of MBE to control composition and layering with atomic scale precision and compatibility

with vacuum in-situ characterization techniques, researchers developed MBE techniques for the controlled in-situ growth of high  $T_c$  superconductors.<sup>[42]-[45]</sup> In contrast to the relative simplicity of the other materials systems to which MBE has been successfully applied,<sup>[47]</sup> the growth of fully oxidized multi-element high  $T_c$  materials by MBE involves significant challenges. A powerful oxidant is necessary to oxidize the constituent elements sufficiently during growth to form the desired structure at a pressure low enough to preserve the long mean free path necessary for MBE. In addition, composition control is crucial in order to provide the proper mix of constituent species to form the desired multi-component phase and controllably dope it, while avoiding the formation of unwanted impurity phases. Finally, to realize layered metastable structures, a low temperature in-situ growth method is required.

After discussing the relevant physical properties of high  $T_c$  superconductors, this chapter describes the challenges, experimental methods, current status, and outlook of the growth of high  $T_c$  superconductors and related oxides by MBE. This new branch of MBE has already demonstrated many promising capabilities which are unmatched by other growth techniques. Custom-layered oxide heterostructures, including high  $T_c$  Josephson junctions and metastable structures, are currently being made by MBE with unit cell layering precision. In addition, MBE offers an ideal environment for the use of vacuum in-situ characterization methods, allowing the growth process itself to be studied. Such advantages make MBE a promising growth technique for the *controlled* preparation of high  $T_c$  superconductors. As the MBE technique is further perfected for the growth of high  $T_c$  oxide heterostructures, it is expected that this growth technique will be particularly useful for device fabrication. In addition, it will offer an excellent technique to fabricate unique metastable structures or superlattices to test high  $T_c$  theories, which may lead to the growth of even higher  $T_c$  materials.

construction of existing and potentially new high  $T_c$  structures.<sup>[50]</sup> All high  $T_c$  structures can be assembled from a relatively small number of more fundamental layer types. These 2-dimensional sheets shall be referred to as *building layers* in analogy to 0-dimensional building blocks. Just as building blocks are assembled in three dimensions, building layers are stacked in one dimension (the c-axis and the direction of MBE growth) to assemble high  $T_c$  structures.

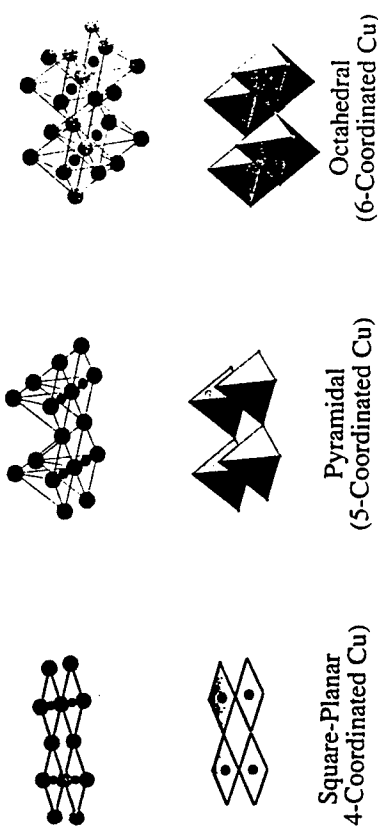


### 1.1 Crystal Structures and Types of Building Layers

Many structurally-related superconducting oxide phases have been identified, all of which have perovskite-related structures.<sup>[48]</sup> The crystal structure of perovskite ( $\text{CaTiO}_3$ ) and some of the better known structurally-related high  $T_c$  superconductors are shown in Fig. 1. High  $T_c$  structures may be viewed as a superlattice comprised of more fundamental layers, where the direction of layering is along the c-axis (the vertical direction in Fig. 1). Such a perspective provides a framework for the generalized

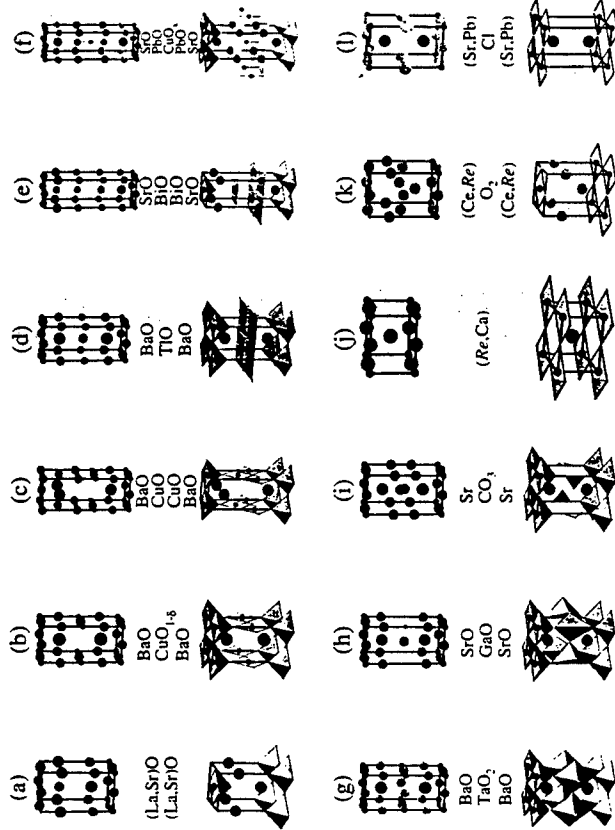
**Figure 1.** The crystal structure of perovskite ( $\text{CaTiO}_3$ ) and some of the better known high  $T_c$  superconductors ( $\text{CaTiO}_3$ ,  $(\text{La},\text{Sr})_2\text{CuO}_4$ ,  $\text{YBa}_2\text{Cu}_3\text{O}_{7-\delta}$ ,  $\text{Bi}_2\text{Sr}_2\text{Ca}\text{Cu}_2\text{O}_8$ ,  $\text{Tl}_2\text{Ba}_2\text{Ca}_2\text{Cu}_3\text{O}_{10}$ , and  $\text{TlBa}_2\text{Ca}_2\text{Cu}_3\text{O}_9$ ). Two equivalent representations of these crystal structures are shown: the atomic positions (above) and the copper coordination polyhedra (below). The oxygen atoms occupy the vertices of the copper coordination polyhedra. The tetragonal subcells of the  $(\text{La},\text{Sr})_2\text{CuO}_4$  and  $\text{Bi}_2\text{Sr}_2\text{Ca}\text{Cu}_2\text{O}_{8-\delta}$  structures are shown for clarity and to illustrate the similarities between these perovskite-related phases. The relative sizes of the atoms reflect their relative ionic radii as given by Ref. 49. The atomic shading given here is used throughout this chapter. The approximate superconducting transition temperatures are also shown.

A common feature of the crystal structures of all known copper-containing high  $T_c$  superconductors is the presence of  $\text{CuO}_2$  layers. These  $\text{CuO}_2$  layers, which are often slightly puckered, consist of an array of corner-sharing  $\text{CuO}_4$  squares, as shown in Fig. 2. The  $\text{CuO}_2$  layers are separated from one another along the  $c$ -axis of the crystal structure by various intervening layers, the known types of which are shown in Fig. 3. Depending on the presence of and positions of oxygen atoms in the intervening layers, the copper coordination polyhedra of the  $\text{CuO}_2$  layers are square-planar (4-coordinated Cu), pyramidal (5-coordinated Cu), or octahedral (6-coordinated Cu), as shown in Fig. 2. The superconducting charge carriers flow in these  $\text{CuO}_2$  layers. High  $T_c$  superconductivity with electrons as the charge carriers (n-type superconductivity) has been attained only in square-planar coordinated  $\text{CuO}_2$  layers, whereas superconductivity with holes as the charge carriers (p-type superconductivity) has been achieved only in pyramidal and octahedral coordinated  $\text{CuO}_2$  layers.<sup>[50]</sup>



**Figure 2.** The atomic structure of a  $\text{CuO}_2$  layer, the common structural component of all known superconductors with  $T_c$  exceeding the boiling point of liquid nitrogen. Depending on the surrounding layers, oxygen atoms may be present at apical positions, changing the copper coordination from 4 to 6. (After Ref. 50.)

There is only one known high  $T_c$  superconductor which does not contain  $\text{CuO}_2$  layers:<sup>[51]</sup>  $(\text{Ba}, \text{K})\text{BiO}_3$ , which has a  $T_c$  of about 30 K. Like the structurally-related solid solution<sup>[52]</sup>  $\text{Ba}(\text{Pb}, \text{Bi})\text{O}_3$  with  $T_c$  of approximately 13 K, it has a simple cubic perovskite structure, shown in Fig. 1, with Bi occupying the octahedrally coordinated Ti position and Ba and K occupying the larger Ca site. From a building layer standpoint,  $(\text{Ba}, \text{K})\text{BiO}_3$  consists of alternating  $\text{BiO}_2$  and  $(\text{Ba}, \text{K})\text{O}$  building layers.



**Figure 3.** The building layers of all known layered  $\text{CuO}_2$  structures: (a)  $[\text{La}, \text{Sr}] \text{O}$  ( $\text{La}, \text{Sr}$ )O or  $[(\text{Sr}, \text{Ca})(\text{Br}, \text{Cl})] \cdot (\text{Sr}, \text{Ca})(\text{Br}, \text{Cl})^+$ ; (b)  $[\text{BaO}-\text{CuO}-\text{CuO}-\text{BaO}]$ ; (c)  $[\text{BaO}-\text{TiO}-\text{BaO}]$  or  $[\text{BaO}-\text{HgO}_x-\text{BaO}]$  or  $[\text{SrO}-(\text{Bi}, \text{Cu})\text{O}_x-\text{SrO}]$  or  $[\text{SrO}-(\text{Bi}, \text{Cd})\text{O}-\text{SrO}]$  or  $[\text{SrO}-(\text{Pb}, \text{Sr})\text{O}-\text{SrO}]$  or  $[\text{SrO}-(\text{Pb}, \text{Cd})\text{O}-\text{SrO}]$  or  $[\text{SrO}-(\text{Ce}, \text{Cd})\text{O}-\text{SrO}]^*$  or  $[\text{SrO}-(\text{Ce}, \text{Cd})\text{O}-\text{SrO}]$ ; (d)  $[\text{BaO}-\text{TiO}-\text{BaO}]$  or  $[\text{BaO}-\text{HgO}_x-\text{HgO}_x-\text{BaO}]$  or  $[\text{SrO}-\text{BiO}-\text{BiO}-\text{SrO}]$  or  $[(\text{Ba}, \text{Sr})-\text{Pb}(\text{Cu})\text{O}_x-(\text{Pb}, \text{Cu})\text{O}_x-(\text{Ba}, \text{Sr})]\text{O}$ ; (e)  $[\text{SrO}-\text{PbO}-\text{CuO}_x-\text{PbO}-\text{SrO}]$ ; (f)  $[\text{LaO}-\text{SnO}_2-\text{LaO}]^*$  or  $[\text{BaO}-\text{TaO}_2-\text{BaO}]^*$  or  $[\text{SrO}-\text{AlO}-\text{SrO}]^*$ ; (g)  $[\text{SrO}-\text{Gao}-\text{SrO}]$  or  $[\text{SrO}-\text{CoO}-\text{SrO}]^*$  or  $[\text{SrO}-\text{CO}_3-\text{Sr}]$ ; (h)  $[(\text{Re}, \text{Ba})-\text{BO}_3-(\text{Re}, \text{Ba})]$ ; (i)  $[(\text{Re}, \text{Ca})]$ ; (k)  $[(\text{Ce}, \text{Re})-\text{O}_2(\text{Ce}, \text{Re})]$ ; and (l)  $[(\text{Sr}, \text{Pb})-\text{Cl}-(\text{Sr}, \text{Pb})]^*$ . The tetragonal subcell of each building layer is outlined.  $\text{CuO}_2$  layers are shown above and below each building layer to illustrate their attachment positions. Partial substitution for the constituents of these basic building layers is frequently possible and may be used for doping purposes (e.g.,  $\text{Bi} \leftrightarrow \text{Pb}$ ,  $\text{Ti} \leftrightarrow \text{Pb}$ ,  $\text{Sr} \leftrightarrow \text{La}$ ,  $\text{Ca} \leftrightarrow \text{Re}$ ). Most of these building layers are constituents of the copper-containing high  $T_c$  superconductors discovered to date. Those intervening layers known to occur between  $\text{CuO}_2$  layers, but so far not constituents of superconducting structures, are marked with an asterisk (\*). (After Ref. 50.)

Although high  $T_c$  phases are commonly referred to by formulae implying that they are stoichiometric, e.g.,  $\text{Bi}_2\text{Sr}_2\text{CaCu}_2\text{O}_8$ , this is an oversimplification. In reality, significant cation mixing, anion vacancies, or cation vacancies often occur within the building layers, with several percent mixing quite common in some layers, although not within the

$\text{CuO}_2$  layers. For example, site-sensitive structural refinement of a single crystal of the high  $T_c$  superconductor  $\text{Bi}_2\text{Sr}_2\text{Ca}\text{Cu}_2\text{O}_8$  determined that its overall composition was  $\text{Bi}_{2.15}\text{Sr}_{1.92}\text{Ca}_{0.75}\text{Cu}_2\text{O}_{8.1}$  with the Ca-site occupied by 75% Ca, 19% Sr, and 6% Bi.<sup>[53][54]</sup> Other sites in the crystal structure also showed cation mixing, although to a lesser extent. Non-stoichiometry is an important aspect of high  $T_c$  superconductors. For some phases, the adjustable non-stoichiometry (solid solution) within a particular building layer is explicitly stated, e.g.,  $(\text{La}, \text{Sr})_2\text{CuO}_4$ ,  $(\text{Nd}, \text{Ce})_2\text{CuO}_4$ ,  $\text{YBa}_2\text{Cu}_3\text{O}_{7-\delta}$ , and  $(\text{Ba}, \text{K})\text{BiO}_3$ . As described in the next section, non-stoichiometry in the building layers provides charge carriers via chemical doping. Pure  $\text{Bi}_{2.15}\text{Sr}_2\text{Ca}\text{Cu}_2\text{O}_8$  would not be superconducting, since the average oxidation state of Cu would be exactly +2 and there would be no charge carriers,<sup>[41]</sup> whereas  $\text{Bi}_{2.15}\text{Sr}_{1.92}\text{Ca}_{0.75}\text{Cu}_2\text{O}_{8.1}$  is superconducting and the average oxidation state of Cu is +2.21.

## 1.2 Chemical Doping

In addition to structural control, realizing the optimal carrier concentration in the  $\text{CuO}_2$  layers is a crucial part of the synthesis of high  $T_c$  materials. The building layers surrounding the  $\text{CuO}_2$  layers serve as charge reservoirs to dope the  $\text{CuO}_2$  layers by chemical means.<sup>[55]</sup> Doping the  $\text{CuO}_2$  layers with holes or electrons is a necessary, although not sufficient, condition for achieving superconductivity in these materials. A convenient method for charge counting to assess chemical doping is through the use of oxidation states.<sup>†</sup> In order to quantify the doping of the  $\text{CuO}_2$  layers it is sufficient to know the oxidation state of Cu, since that of O is defined to be -2. Cu has multiple oxidation states, ranging from +1 to +3. The average oxidation state of Cu is determined from the phase composition, the standard oxidation states of the remaining ions (e.g.,  $\text{O}^{2-}$ ,  $\text{Sr}^{2+}$ ,  $\text{La}^{3+}$ , etc.), and the condition of charge neutrality.<sup>‡</sup> For example, the average oxidation state of Cu is  $+2+x$  in  $\text{La}_{2-x}\text{Sr}_x\text{CuO}_4$  and  $+2-x$  in  $\text{Nd}_{2-x}\text{Ce}_x\text{CuO}_4$  (where Ce<sup>4+</sup> is present). In the parent compounds,  $\text{La}_2\text{CuO}_4$  and  $\text{Nd}_2\text{CuO}_4$ , where no chemical doping is present ( $x=0$ ), the oxidation state of Cu is +2 and the compounds are not superconducting. As  $x$  increases and the parent compounds are doped, carriers enter the  $\text{CuO}_2$  layers and the average oxidation state of Cu deviates from +2.

<sup>†</sup> Note that the oxidation state of an ion is not the same as the true charge on the ion.<sup>[56]</sup>

<sup>‡</sup> In compounds containing elements which, in addition to Cu, may assume a variety of oxidation states (e.g., Bi, Pb, Ti, Hg) or compounds with non-equivalent Cu sites (e.g., the  $\text{CuO}_x$  "chains" in Fig. 3b), additional information is necessary to ascertain the oxidation state of Cu in the  $\text{CuO}_2$  layers.<sup>[57]</sup> Non-integral average oxidation states may also be described as a mixed oxidation state. For example, an average Cu oxidation state of +2.2 corresponds to a mixture of 80% Cu<sup>2+</sup> and 20% Cu<sup>3+</sup>.

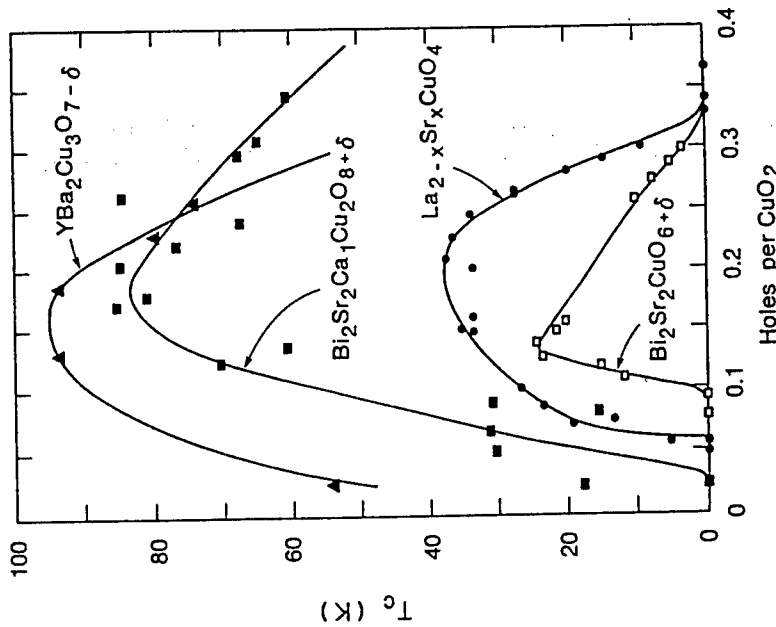


Figure 4.  $T_c$  as a function of hole concentration,  $n_h$ , per  $\text{CuO}_2$  unit for various high  $T_c$  superconductors as determined by chemical titration. (From Ref. 62.)

### 1.3 Phase Diagrams

The multicomponent phase diagrams spanning the compositional space in which a given high  $T_c$  phase is found invariably contain a multitude of phases, including many for which the structural details remain unresolved. A precise mapping of the equilibrium phase relationships in many high  $T_c$  systems is hampered by the large number of elemental components, a large number of previously unknown compounds, slow reaction kinetics at the growth temperatures of interest, and the presence of impurities (e.g., carbonates or fluxing agents). High  $T_c$  systems contain at least four components, and some important ones have as many as six. For example, lead is commonly added to  $\text{Bi}_2\text{Sr}_2\text{Ca}_2\text{Cu}_3\text{O}_{10}$  in order to synthesize this 110 K superconductor in single phase form by bulk techniques, making it a 6-component system. The significant variance of the phase relationships as functions of oxygen pressure and temperature further complicates this mapping.

Interestingly, no high  $T_c$  materials are known that are thermodynamically stable at room temperature or below, however, the kinetics of the decomposition of high  $T_c$  superconductors are so sluggish at low temperatures that this fact does not deter their utility.<sup>[63]</sup> While some high  $T_c$  superconductors are thermodynamically stable at high temperatures and may be quenched to avoid decomposition, others (e.g.,  $\text{YBa}_2\text{Cu}_3\text{O}_7$ ) are not stable at any temperature or pressure.<sup>[41][64]</sup> Their synthesis is commonly achieved by first forming a thermodynamically stable parent structure (e.g.,  $\text{YBa}_2\text{Cu}_3\text{O}_6$ ) and subsequently altering its composition after the sample has been cooled to a temperature where the parent structure is kinetically prevented from decomposing. The metastability of possibly all high  $T_c$  superconductors has led researchers to propose that these materials will continue to become more and more metastable as  $T_c$  increases.<sup>[41]</sup> Although all high  $T_c$  materials allow a finite range of atomic substitution for at least one component, which allows their carrier concentration to be altered by chemical doping, these solid solutions are far narrower than the solid solutions present in common semiconductor systems. The limited range of compositions over which the high  $T_c$  materials are stable poses significant composition control constraints for growing films free of second phases, as can be seen from the phase diagrams.

The pseudo-ternary phase diagram of the  $\text{YO}_{1.5}\text{BaO-CuO}$  system at 900°C in 1 atmosphere of oxygen is shown in Fig. 5.<sup>[65]</sup> This diagram represents a section through the full Y-Ba-Cu-O quaternary phase diagram

tetrahedron. As the oxygen pressure is lowered at a fixed temperature (e.g.,  $T = 850^\circ\text{C}$ ), the phases and tie-lines in contact with the high  $T_c$  compound  $\text{YBa}_2\text{Cu}_3\text{O}_{7-\delta}$  change considerably, as shown in Fig. 6.<sup>[66]</sup> Below an oxygen partial pressure,  $P_{\text{O}_2}$ , of 0.30 torr, the  $\text{YBa}_2\text{Cu}_3\text{O}_{7-\delta}$  phase is no longer thermodynamically stable at  $T = 850^\circ\text{C}$ . The temperature dependence of the various reactions is indicated in Fig. 7.<sup>[67]</sup> The minimum  $P_{\text{O}_2}$  at which a desired high  $T_c$  structure is thermodynamically stable has obvious significance for its MBE synthesis under vacuum conditions. The competing constraints of a high oxygen pressure for phase stability and a low oxygen pressure to maintain the long mean free path necessary for MBE have necessitated the use of activated oxygen species for MBE growth, as discussed in Sec. 2.

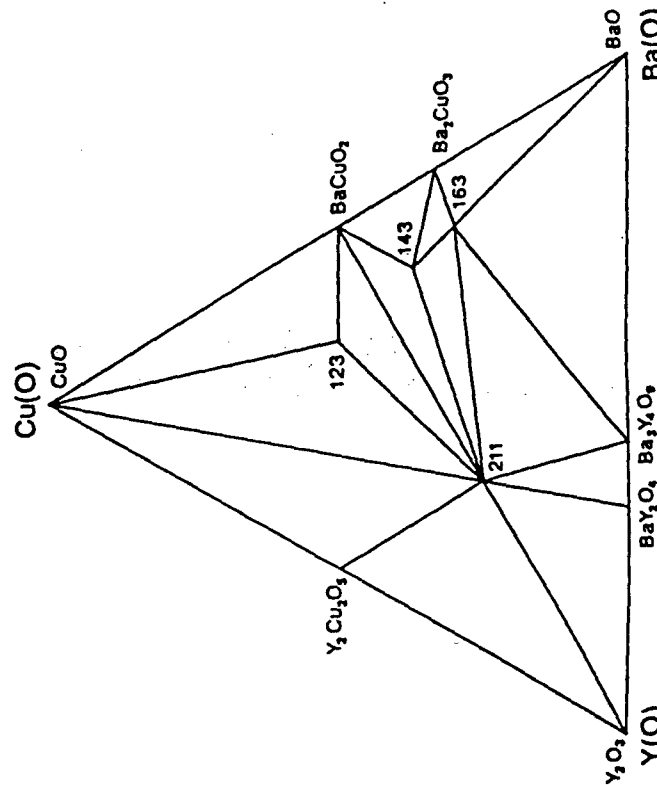
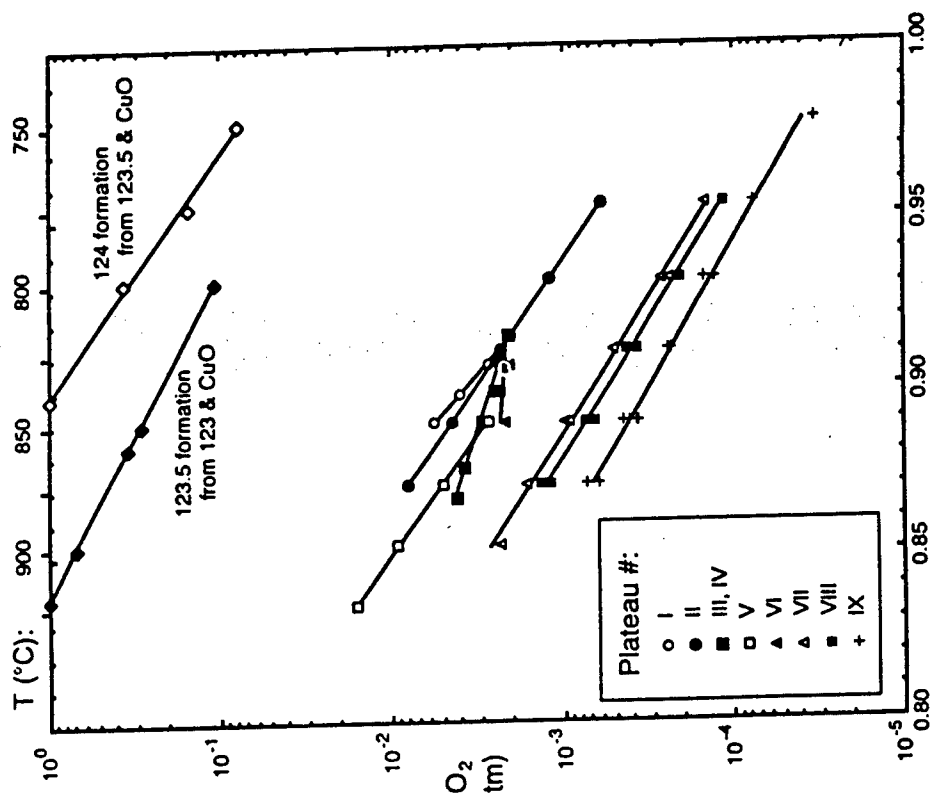
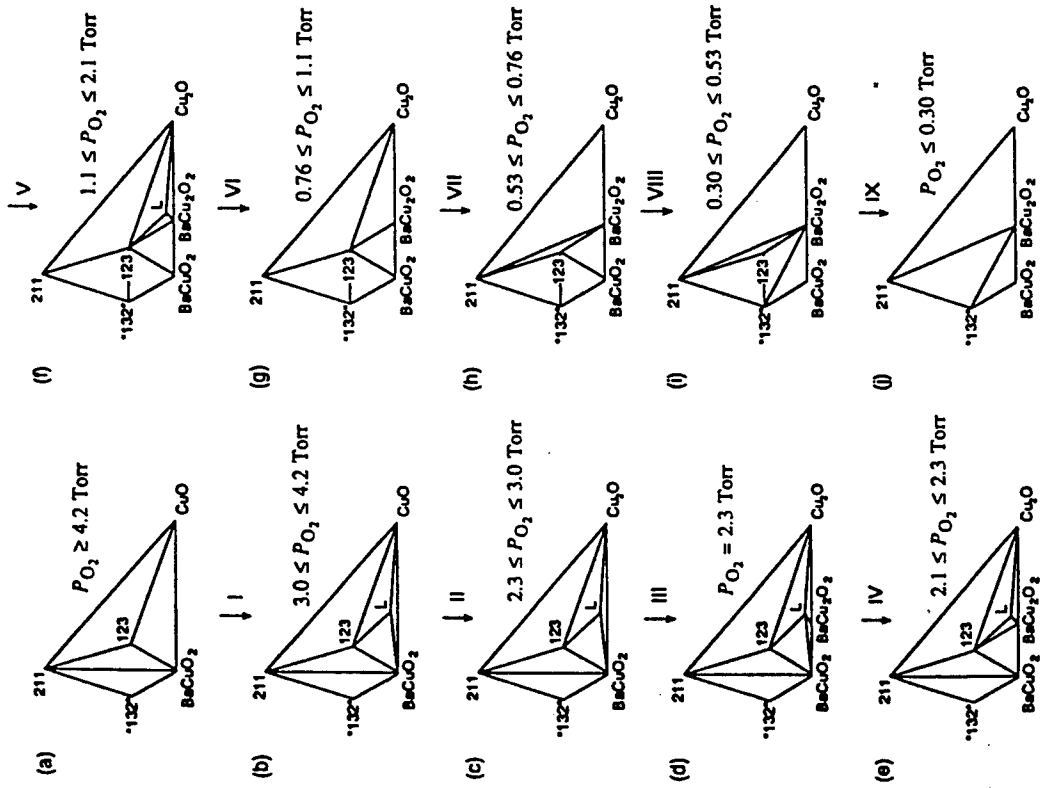


Figure 5. The subsolidus pseudo-ternary  $\text{YO}_{1.5}\text{BaO-CuO}$  phase diagram at  $T = 900^\circ\text{C}$  in 1 atm. oxygen. The numbers 123, 143, 163, and 211 represent the compounds  $\text{YBa}_2\text{Cu}_3\text{O}_{7-\delta}$ ,  $\text{YBa}_4\text{Cu}_5\text{O}_{8+\delta}$ ,  $\text{YBa}_6\text{Cu}_9\text{O}_{10+\delta}$ , and  $\text{Y}_2\text{BaCuO}_5$ , respectively. (From Ref. 65.)



**Figure 7.** The temperature dependence of the Y-Ba-Cu-O decomposition reactions shown in Fig. 6 (from Ref. 67).  
 The 5-component Bi-Sr-Ca-Cu-O system has an even richer phase diagram. The four pseudo-ternary faces of the pseudo-quaternary  $\text{BiO}_{1.5}\text{-SrO-CaO-CuO}$  tetrahedron are shown in Fig. 8 for  $T = 850^\circ\text{C}$  in one atmosphere of air. [68] The minimum  $P_{\text{O}_2}$  at which the  $\text{Bi}_2\text{Si}_2\text{CaCu}_2\text{O}_8$  and  $\text{Bi}_2\text{Sr}_2\text{Ca}_2\text{Cu}_3\text{O}_{10}$  phases are stable is shown in Fig. 9. [70]



**Figure 6.** The effect of oxygen pressure on the pseudo-ternary Y-Ba-Cu-O phase diagram at  $T = 850^\circ\text{C}$ . The oxygen partial pressure ( $P_{\text{O}_2}$ ) range for each diagram is indicated (from Ref. 66).

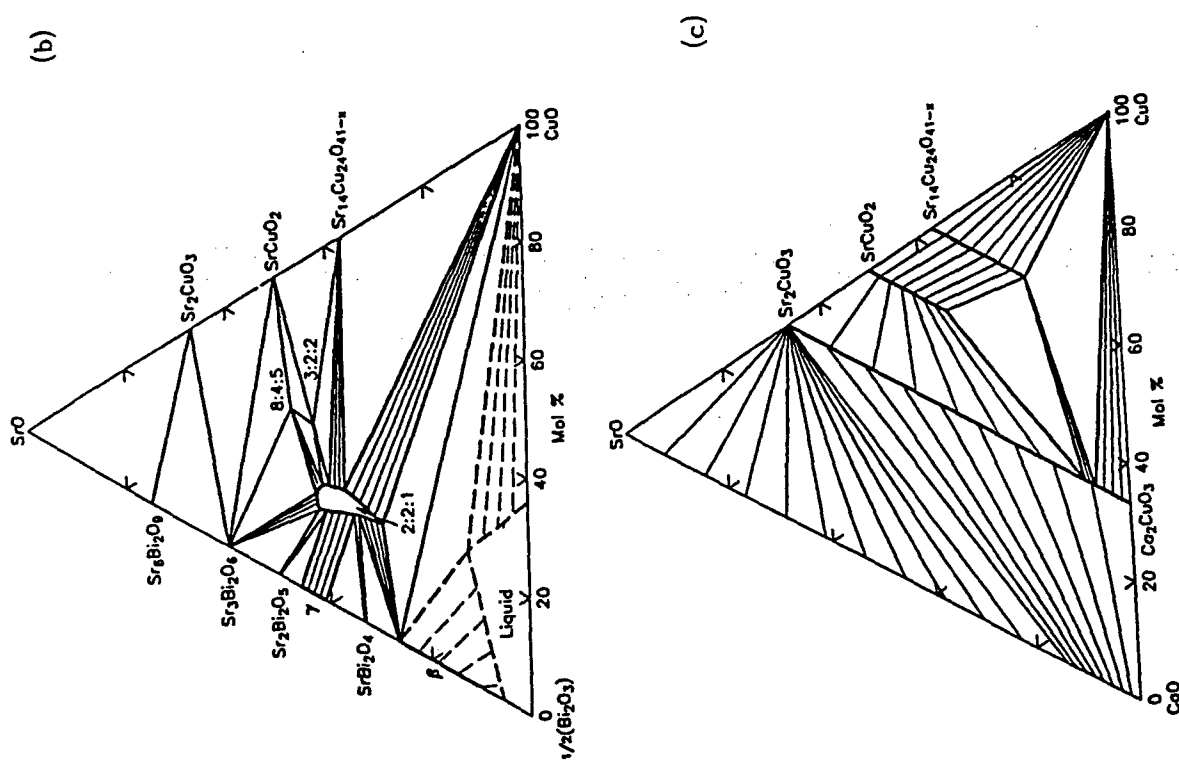


Figure 8. (Cont'd)

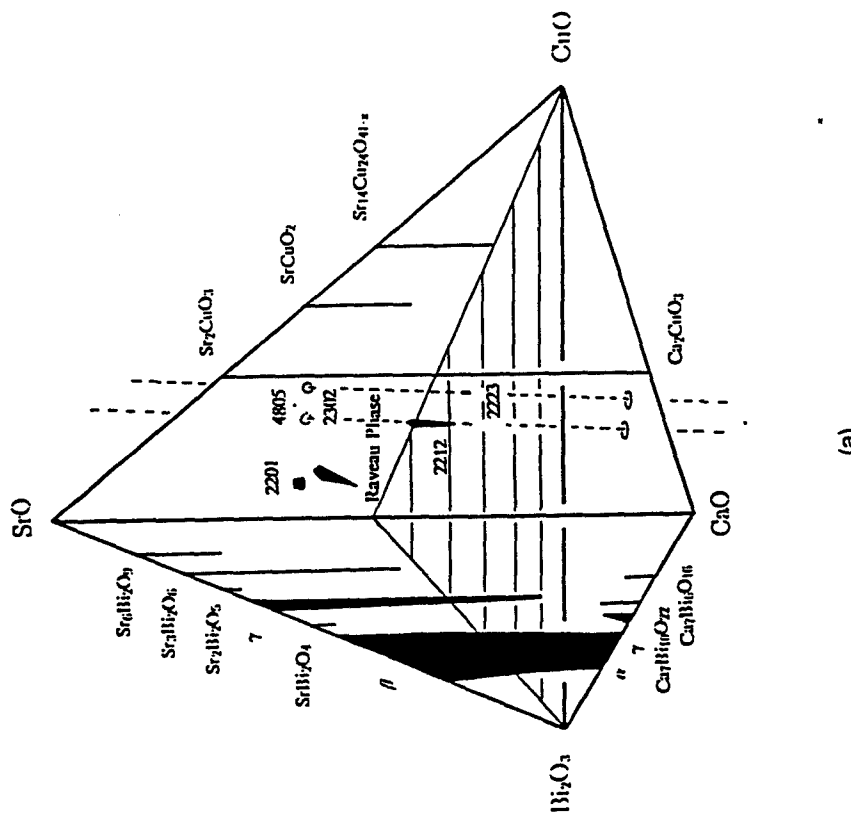
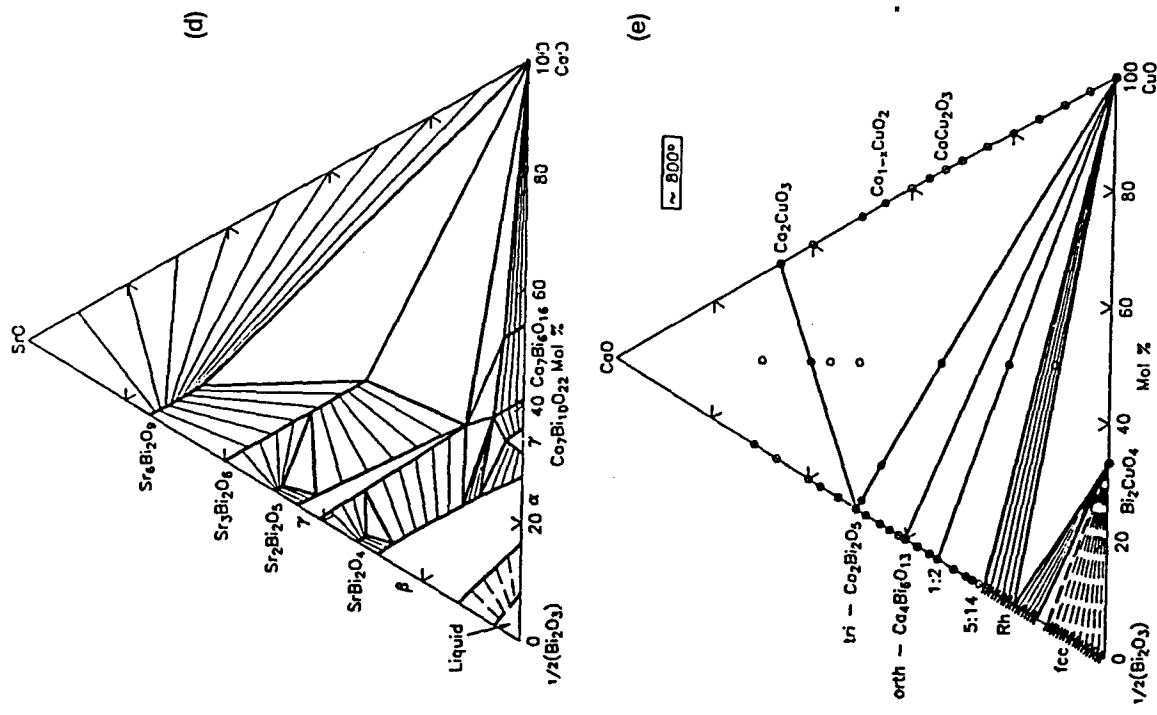
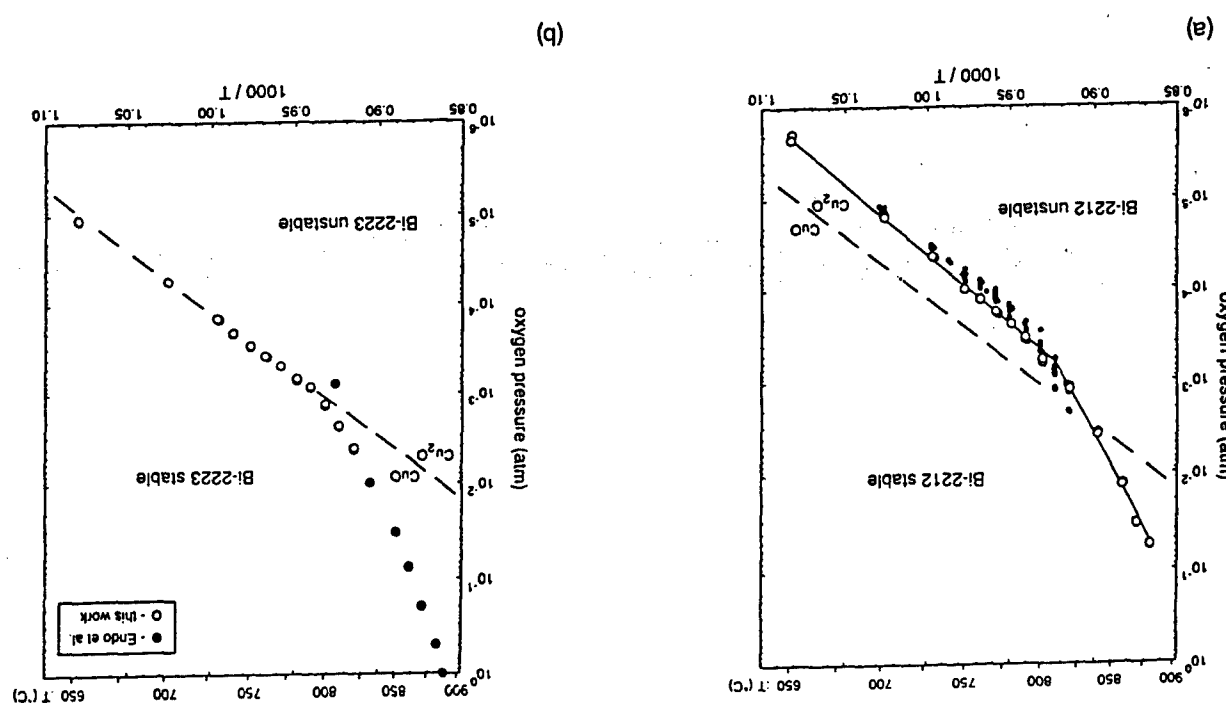


Figure 8. (a) The pseudo-quaternary BiO<sub>1.5</sub>-SrO-CaO-CuO phase diagram at T = 850 °C in air (from Ref. 68), along with the four pseudo-ternary phase diagrams that form the faces of the pseudo-quaternary BiO<sub>1.5</sub>-SrO-CaO-CuO tetrahedron: (b) the pseudo-ternary BiO<sub>1.5</sub>-SrO-CuO phase diagram at T = 850°C in air (from Ref. 69), (c) the pseudo-ternary SrO-CaO-CuO phase diagram at T = 850°C in air (from Ref. 69), (d) the pseudo-ternary BiO<sub>1.5</sub>-SrO-CaO phase diagram at T = 850°C in air (from Ref. 69), (e) the pseudo-ternary BiO<sub>1.5</sub>-CaO-CuO phase diagram at T = 800°C (from Ref. 69).

(Cont'd next page.)

Figure 9. The equilibrium oxygen decom-



**Figure 8.** (Cont'd)

#### 1.4 Uncontrolled Intergrowths Inherent in Bulk Methods

By using  $\text{CuO}_2$  layers and the layers in Fig. 3 as alternate building layers, not only can the crystal structures of all known layered  $\text{CuO}_2$ -containing compounds (including all of the known copper-containing high  $T_c$  superconductors) be constructed,[59] but a great many additional structures may be imagined. The realization of additional high  $T_c$  structures by bulk synthesis techniques (e.g., mixing powders with a mortar and pestle followed by solid state reaction) has been an active area of research. However, bulk synthesis of such structures can be quite elusive, especially for structures with unit cells comprised of a large number of repeated building layers.

The crystal structures of the  $\text{Bi}_2\text{Sr}_2\text{Ca}_{n-1}\text{Cu}_n\text{O}_{2n+4}$  phases that have been synthesized in pure single phase form by bulk methods ( $n = 1$  to 3) are shown in Fig. 10 along with their approximate superconducting transition temperatures ( $T_c$ ). The synthesized structures are the first three members of a homologous series of phases. The members of such a series are related to each other by the addition or subtraction of a simple structural element, which in this case is comprised of a  $[\text{CuO}_2]$  and a  $[\text{Ca}]$  building layer. The next two members of this series are also shown in Fig. 10. The striking empirical trend of increasing  $T_c$  with the number of  $\text{CuO}_2$  layers in the unit cell of these structures (a similar trend exists for  $\text{TlBa}_2\text{Ca}_{n-1}\text{Cu}_n\text{O}_{2n+3}$ ,  $\text{Tl}_2\text{Ba}_2\text{Ca}_{n-1}\text{Cu}_n\text{O}_{2n+4}$ , and  $\text{HgBa}_2\text{Ca}_{n-1}\text{Cu}_n\text{O}_{2n+2}$  phases) led many researchers to attempt to prepare higher order members by bulk methods. However, as the number of  $(\text{CuO}_2)_n\text{Ca}_{n-1}$  layers in these structures become greater, pure single phase specimens become progressively more difficult to synthesize in bulk form, presumably because the differences between the free energies of formation of these phases become smaller and smaller.[71] Indeed, TEM studies of bulk samples reveal uncontrolled syntactic intergrowths of  $\text{Bi}_2\text{Sr}_2\text{Ca}_{n-1}\text{Cu}_n\text{O}_{2n+4}$  phases when the bulk synthesis of  $n > 2$  is attempted as shown in Fig. 11,[72] and of  $\text{Tl}_2\text{Ba}_2\text{Ca}_{n-1}\text{Cu}_n\text{O}_{2n+4}$  phases for  $n > 3$ .[73] Analogous examples of uncontrolled intergrowths abound for the bulk synthesis of other high  $T_c$  related homologous series, including the  $\text{Y}_2\text{Ba}_4\text{Cu}_{n+5}\text{O}_{n+13}$  phases, whose structures are shown in Fig. 12, for  $n > 3$ ,[74]  $\text{La}_{4n+4}\text{Cu}_{2n+8}\text{O}_{8n+14}$  for  $n > 3$ ,[75] and  $\text{Ba}_{n+1}(\text{Pb},\text{Bi})_n\text{O}_{3n+1}$  for  $n > 2$ .[76] Uncontrolled intergrowths also occur in the  $\text{Tl}_{1+x}\text{Ba}_2\text{Ca}_{n-1}\text{Cu}_n\text{O}_{2n+3+x}$  system (a random mixture of  $\text{TlBa}_2\text{Ca}_{n-1}\text{Cu}_n\text{O}_{2n+3}$  and  $\text{Tl}_2\text{Ba}_2\text{Ca}_{n-1}\text{Cu}_n\text{O}_{2n+4}$  phases) for  $0 < x < 1$ .[77] The disordered nature of intergrowths is not limited to high  $T_c$  systems; rather numerous examples have been documented for other homologous series of layered oxides.[78]

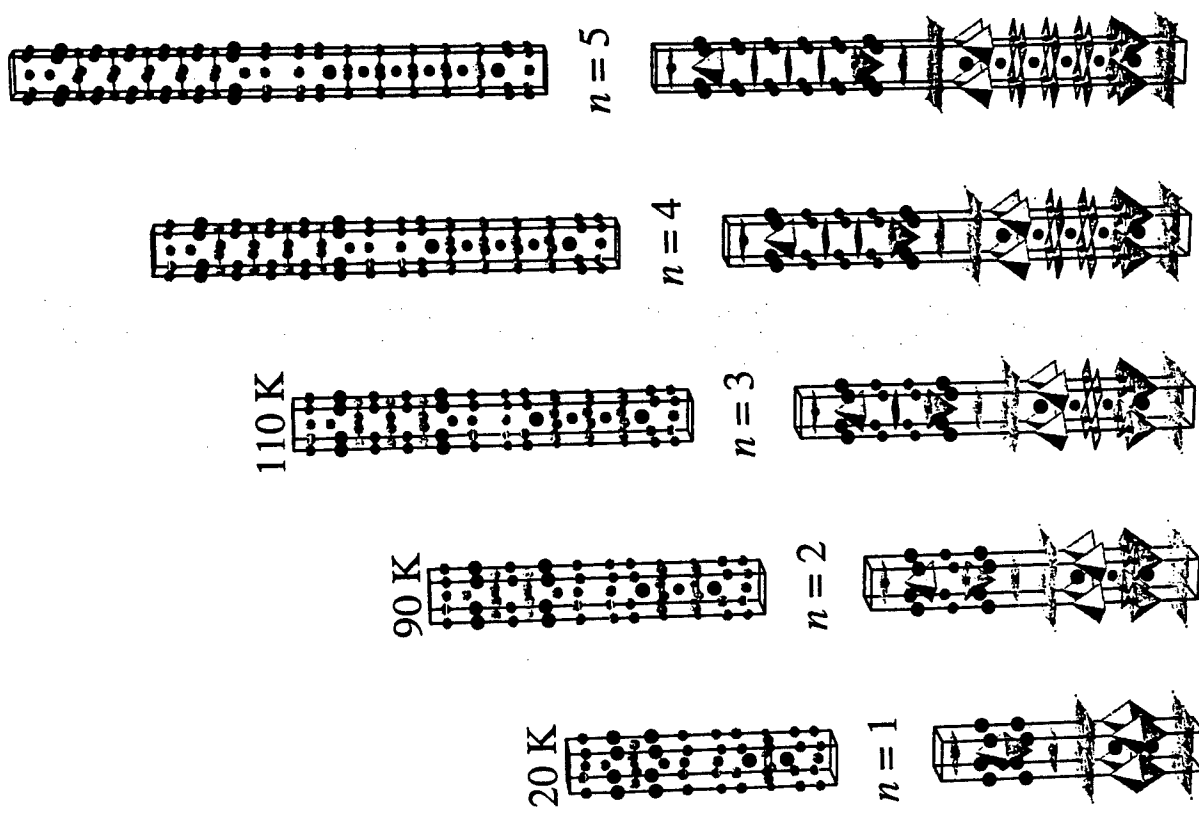


Figure 10. The crystal structures of the  $\text{Bi}_2\text{Sr}_2\text{Ca}_{n-1}\text{Cu}_n\text{O}_{2n+4}$  phases for  $n = 1$  to 5. The tetragonal subcells are shown for clarity. The approximate superconducting transition temperatures of the phases that have been prepared by bulk methods are also shown.

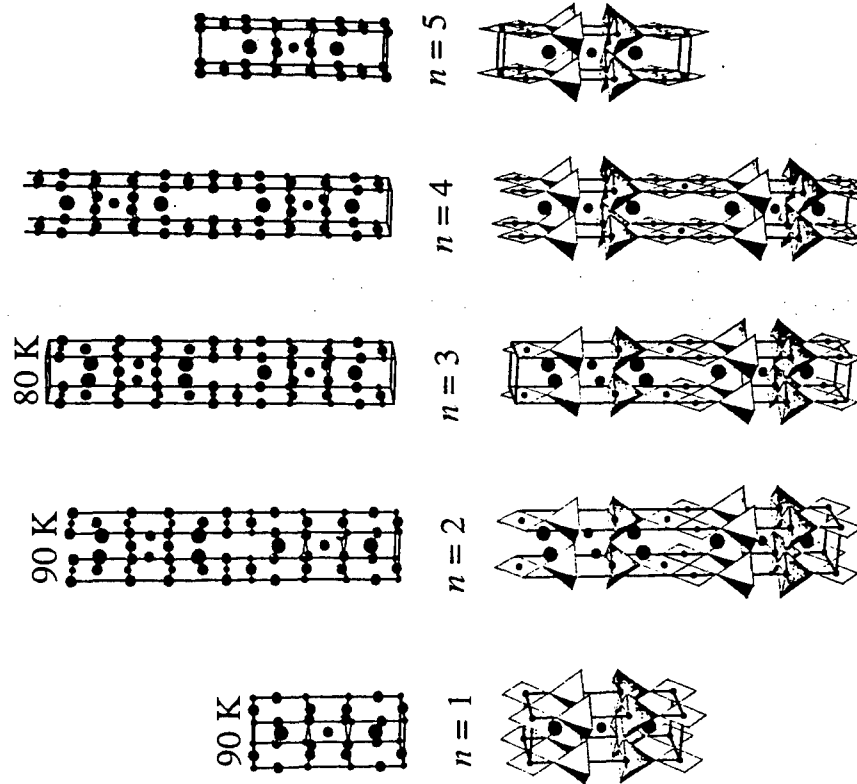


Figure 11. A high resolution TEM image showing the structural disorder present in a bulk synthesis attempt of the  $\text{Bi}_2\text{Sr}_2\text{Ca}_3\text{O}_{10}$  phase. However, high resolution TEM indicates that  $\text{Bi}_2\text{Sr}_2\text{Ca}_2\text{Cu}_3\text{O}_{10}$ , the  $n = 3$   $\text{Bi}_2\text{Sr}_2\text{Ca}_{n-1}\text{Cu}_n\text{O}_{2n+4}$  phase, is the majority phase (from Ref. 72). X-ray diffraction indicates that  $\text{Bi}_2\text{Sr}_2\text{Ca}_2\text{Cu}_3\text{O}_{10}$ , the  $n = 3$   $\text{Bi}_2\text{Sr}_2\text{Ca}_{n-1}\text{Cu}_n\text{O}_{2n+4}$  phase, is the majority phase. However, high resolution TEM images of the microstructure reveal the presence of many uncontrollable intergrowths, where  $n$  is seen to vary from 1 to 7.

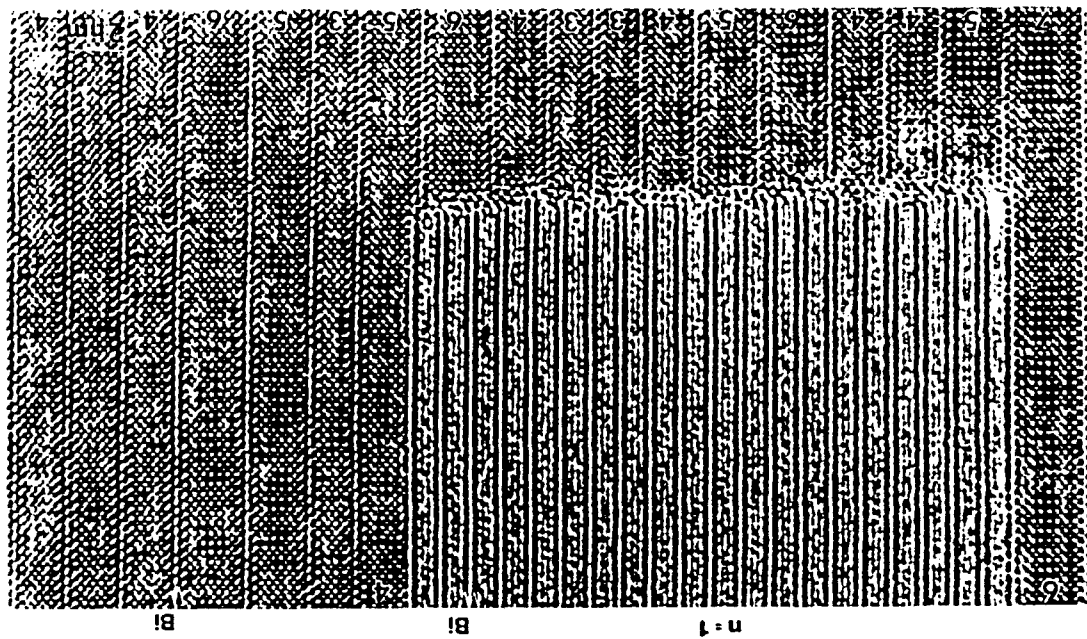
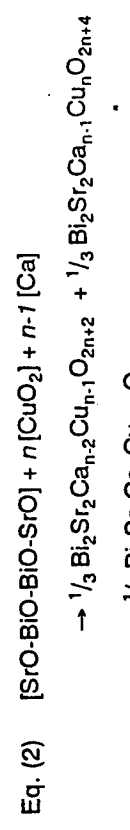
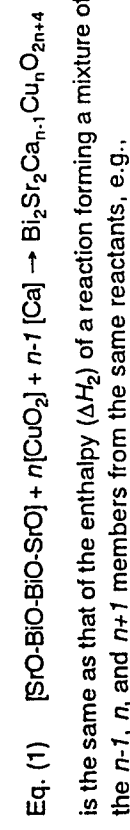


Figure 12. The crystal structures of the  $\text{Y}_2\text{Ba}_4\text{Cu}_{n+5}\text{O}_{13}$  phases for  $n = 1$  to 5. The approximate superconducting transition temperatures of the phases that have been prepared by bulk methods are also shown. For clarity, only unit cells of the  $n = 2$  and  $n = 4$  phases are shown.

Uncontrolled intergrowths appear to be a general feature and fundamental limitation of using bulk synthesis methods to prepare complex layered perovskite structures. Bulk techniques rely on the existence of sufficiently deep reaction free energy minima to transform the starting materials into a single phase at a particular temperature and pressure. If

the formation energies of other phases comprised of the same building layers (and therefore the same in-plane lattice constants) are nearly the same as the desired phase, the sample will contain uncontrolled syntactic intergrowths of these structurally related, but nearly energetically degenerate, phases. The increase in entropy of a syntactically intergrown phase, compared to a single phase sample, provides the free energy driving force for such intergrowths. This driving force increases with temperature and as the numerous examples cited above show, causes significant syntactic mixing at the high synthesis temperatures used in bulk synthesis methods. The overall sample composition is insufficient to determine the microscopic layering order when numerous syntactic members have nearly the same free energies; homologous series members containing fewer of the relevant structural building layers will be balanced out by those containing more in a randomly ordered syntactic mixture of these phases. For example, the  $\text{Bi}_2\text{Sr}_2\text{Ca}_{n-1}\text{Cu}_n\text{O}_{2n+4}$  phases are comprised of  $[\text{SrO-BiO-BiO-SrO}]$ ,  $[\text{CuO}_2]$ , and  $[\text{Ca}]$  building layers. If there is no energetic preference for the formation of the  $n$  member of this series over the  $n-1$  or  $n+1$  members (i.e.,  $\Delta H_f$  of  $\text{Bi}_2\text{Sr}_2\text{Ca}_{n-2}\text{Cu}_{n-1}\text{O}_{2n+2}$ ,  $\text{Bi}_2\text{Sr}_2\text{Ca}_{n-1}\text{Cu}_n\text{O}_{2n+4}$ , and  $\text{Bi}_2\text{Sr}_2\text{Ca}_n\text{Cu}_{n+1}\text{O}_{2n+6}$  are identical), then the enthalpy ( $\Delta H_1$ ) of the formation reaction of the  $n$  member,



Note that the free energy of the latter reaction ( $\Delta G_2$ ) will be lower than that of the former ( $\Delta G_1$ ) because of the increased entropy of the randomly layered mixture of the  $n-1$ ,  $n$ , and  $n+1$  members. Of course, Eq. (2) represents just one example of a random mixture composition that is energetically favored over the pure  $n$  member phase. In general, all of the members of the homologous series may participate and their fractions are free to vary such that the overall equation is balanced. As long as the enthalpies of formation of participating members are sufficiently equivalent, the free energy of the mixture will always be lower than that of the pure phase.

Calculation of the energy of formation of several homologous series of perovskite related phases indicates that the differences in formation energy become smaller and smaller as more building layers are inserted into the parent structure (i.e., with increasing  $n$ ).<sup>[79],†</sup>

The low growth temperature and atomic layering capability of MBE, widely utilized for the growth of metastable layered semiconductor superlattices, have enabled the *controlled* customized layering of high  $T_c$  phases whose phase-pure growth is unattainable by bulk synthesis methods. These results demonstrate the capability to grow customized layered structures and metastable phases within oxide systems encompassing the high  $T_c$  superconductors. The broad spectrum of electrical and optical properties possessed by oxides suggests that engineering these materials at the unit cell level will yield device heterostructures with significantly enhanced properties.

### 1.5 Layer-by-Layer MBE Growth

The intriguing connection between high  $T_c$  superconductivity and metastability is a major motivation for developing an MBE technique with atomic-level layering control for the growth of these oxides. By choosing growth conditions which kinetically limit decomposition of the deposited layers, MBE may be used to directly synthesize metastable structures which lie at local energy minima, provided that the activation energy needed to surmount the barriers separating the desired metastable phase from more energetically favored phases (including the equilibrium phases) are sufficiently high. The energy minimum of a desired metastable phase may frequently be made deeper and the energy minima of the undesired non-lattice matched phases raised by utilizing a substrate with a suitable template for the epitaxial growth of the desired phase. The second law of thermodynamics requires that the free energy of the entire thermodynamic system must be lowered in order for the products to form from the reactants. However, the relatively high free energies of the constituent elements used as reactants in MBE compared to the free energy of the equilibrium products allows, in principle, significantly metastable phases to be formed which lower the free energy of the entire system. The

<sup>†</sup> For example, in the  $\text{Sr}_{n-1}\text{Ti}_n\text{O}_{3n+1}$  homologous series of compounds (another perovskite-related series of compounds), calculations indicate that the formation enthalpy remains essentially constant for  $n > 2$ .<sup>[79]</sup> Since there is insufficient enthalpic driving force for forming a low entropy phase-pure compound, disordered intergrowths are to be expected in the synthesis of these compounds by bulk methods. Indeed, TEM images of these  $\text{Sr}_{n-1}\text{Ti}_n\text{O}_{3n+1}$  phases<sup>[80]</sup> show disordered syntactic intergrowths when  $n$  ranges from 2 to 8, as would be expected for the bulk preparation of essentially energetically degenerate phases.

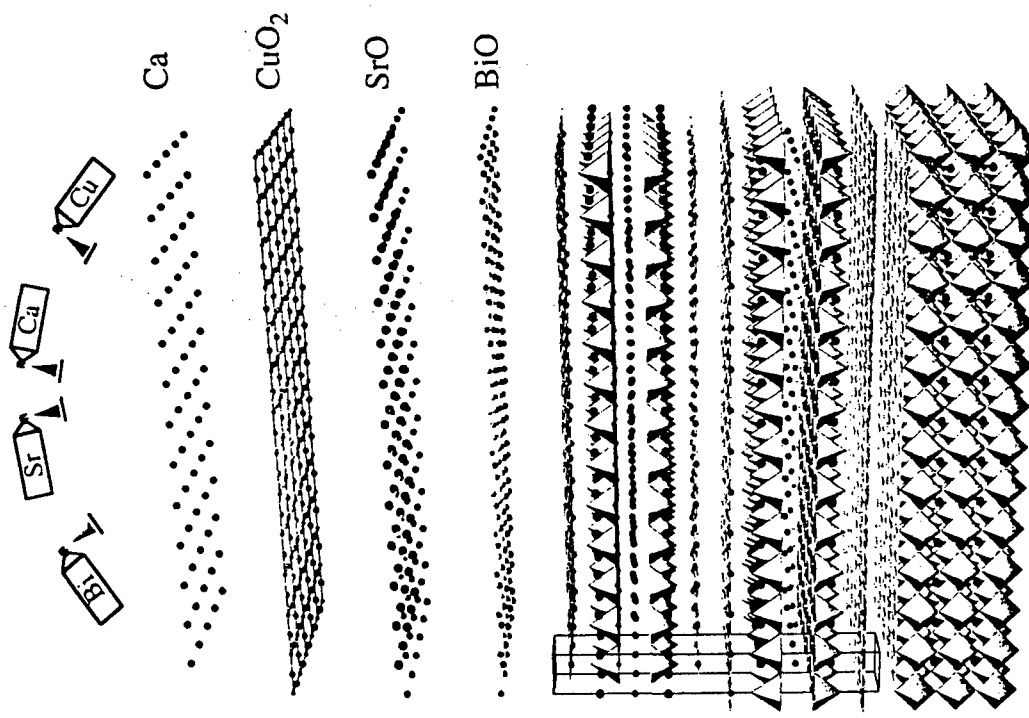
development of a theoretical understanding of the mechanism of high  $T_c$  superconductivity or at least a framework for predicting which structures should have higher  $T_c$ 's, will allow the customized layering capability of MBE to be most effectively focused on this task.

Several factors distinguish MBE for the synthesis of custom-layered high  $T_c$  superconductors. Because of the desired nanoscale layering control, the layers must be deposited in a state which does not require any subsequent high temperature processing which could result in intermixing of the layers or which would decompose metastable layer orderings. In addition, low growth temperatures are desired to minimize undesired bulk diffusion between the layers or between the substrate and film. These considerations require a synthesis method in which the deposited layers are crystallized in-situ during growth. In-situ growth exploits the significantly higher surface diffusion coefficients of the depositing species compared to bulk diffusion coefficients, resulting in lower synthesis temperatures and thus less bulk diffusion. Of course, abrupt interfaces and nanoscale layering control are also requirements of a suitable technique for the customized growth of high  $T_c$  superconductors. From the standpoint of MBE growth, the layering along the c-axis of these structures represents a superlattice of the constituent building layers; semiconductor superlattices of comparable dimensions are routinely grown by MBE.[81][82] MBE is capable of synthesizing new custom-made structures (even metastable ones), provided the growth can be achieved through the deposition of complete, flat, monolayers of the constituent building layers. An idealized view of the desired MBE growth process is shown in Fig. 13.

## 2.0 OXIDE MBE SYSTEMS

### 2.1 MBE System Configuration

The configuration of an MBE system for the growth of high  $T_c$  superconductors differs in several important ways from today's more conventional MBE systems designed for the growth of semiconductors. The major differences are the requirements to introduce an activated oxidant species, to provide more accurate composition control, and to have adequate pumping to handle the oxidant gas load. A schematic diagram of the growth chamber of an MBE system which contains most of the features commonly used in the growth of high  $T_c$  superconductors is shown in Fig. 14.



**Figure 13.** A schematic representation of the MBE growth of  $\text{Bi}_2\text{Sr}_2\text{Ca}\text{Cu}_2\text{O}_8$  on  $\text{SrTiO}_3$ . The sprayed beams are individually controlled by shutters which control the sequence and quantity of species reaching the growth surface. Note that this figure is highly schematic; the growth unit and growth mechanism of sequentially deposited oxide structures by MBE is not well understood.

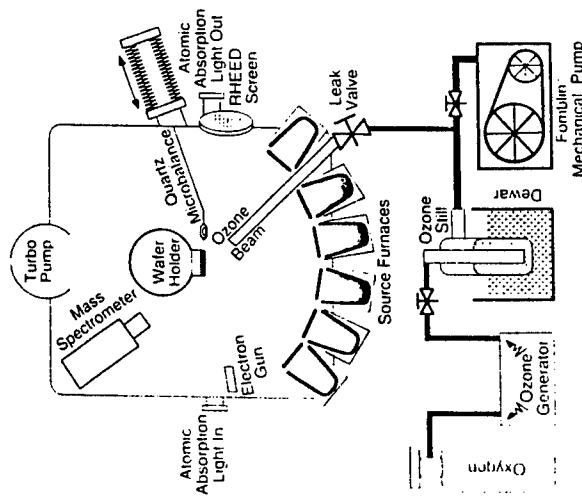


Figure 14. A schematic diagram of an MBE growth chamber for the growth of high  $T_c$  superconductors. The growth chamber shown contains most of the features commonly used: elemental source beams, shutters, activated oxidant introduction, RHEED, and in-situ composition monitors.

The introduction of a reactive oxidizing agent may involve its metered introduction and delivery from an external vessel (e.g., the ozone distillation and delivery system shown) or the generation of the activated oxygen species within the MBE chamber, e.g., utilizing an electron cyclotron resonant (ECR) plasma source. The materials that come into contact with the reactive oxidizing agent before reaching the substrate must be carefully chosen in order to minimize decomposition of the oxidant. The temperature of potential decomposition surfaces should also be considered, as radiant heat emanating from the substrate heater, effusion cells, ion gauges, etc., may heat the surfaces of oxidant delivery materials to temperatures where significant decomposition of the oxidant occurs, even though at room temperature these materials are quite compatible with the oxidant.

The amount of pumping necessary to maintain the long mean free path necessary for MBE growth depends on the oxidant used, the material

grown, the growth temperature and growth rate, and how efficiently the oxidant is introduced at the substrate. More than 500 l/s of pumping is common; some systems have as much as 4680 l/s.<sup>[83]</sup> Getter-pumping of oxygen by the rare-earth and alkaline earth species on the chamber walls often increases the pumping rate well beyond the active pump capacity during growth. Because of the high pumping speeds involved, turbomolecular and cryogenic pumps are most commonly used. When working with potentially explosive oxidants such as ozone, the use of cryogenic pumps is a serious hazard, since the adsorbed ozone may detonate when the pump is warmed during regeneration.<sup>[84]</sup>

Minor differences between the configuration of an MBE system for the growth of high  $T_c$  superconductors and a conventional MBE system for the growth of semiconductors include the selection of materials for high temperature components (heater filaments, crucibles, substrate holders, etc.) which do not react or decompose on exposure to the oxidant, and confining the oxidizing species to the substrate region through the use of differential pumping. Fluxes of the constituent metals are generated by resistively heating the constituent elements in effusion cells or by heating them with e-beam sources. When effusion cells are used, it is preferable to use designs which minimize condensation of the evaporating species at the effusion cell orifice, since this gradually reduces the orifice area and thus the flux. This problem can be quite severe for copper, but occurs more gradually for alkaline-earth sources. Just as dual-filament effusion cells have proven effective for reducing gallium droplets which condense at the crucible orifice in III-V growth,<sup>[85]</sup> they have also been successfully utilized to solve the crucible-lip condensation problem in the growth of high  $T_c$  superconductor materials.<sup>[86]</sup>

Although the use of molybdenum for parts that reach high temperatures is common in semiconductor MBE machines, the high volatility of  $\text{MoO}_3$ <sup>[87]</sup> makes the use of molybdenum in oxide MBE systems imprudent. High levels of molybdenum contamination have been found by many MBE researchers in samples grown on conventional molybdenum MBE substrate blocks<sup>[88]-[92]</sup> or when molybdenum clips were used to secure the substrates to the substrate block.<sup>[93]</sup> The presence of molybdenum in films of high  $T_c$  materials has been revealed by Rutherford backscattering spectrometry (RBS),<sup>[88]</sup> secondary ion mass spectrometry (SIMS),<sup>[94]</sup> inductively coupled plasma emission spectroscopy (ICP),<sup>[91]</sup> electron probe microanalysis (EPMA),<sup>[91][93]</sup> and even x-ray diffraction ( $\text{Mo}_2\text{O}_{28}$ ).<sup>[88]</sup> In extreme cases, the molybdenum content has amounted to several atomic

Naturally, the occurrence of such high molybdenum impurity concentrations adversely effects the superconducting properties of high  $T_c$  films. The conventional titanium-molybdenum alloy filaments utilized in Ti-sublimation pumps have been replaced with pure titanium to avoid molybdenum contamination from this source as well.<sup>[90]</sup> † Hot tungsten has also been reported to be a problem in high  $T_c$  MBE systems, again due to the volatility of tungsten oxides when tungsten was used as a crucible material (for copper).<sup>[96]</sup> It is thus important to choose either materials compatible with an oxidizing ambient throughout the MBE machine, or to confine the oxidizing species to the region of these compatible materials. This is particularly crucial for hot parts that are in the line-of-sight of the substrate, since volatilization from such parts can lead to unwanted contaminants in the deposited films. Stainless steel<sup>[97]</sup> (e.g., 304,<sup>[98]</sup> Haynes<sup>[99]</sup> alloy #214,<sup>[94]</sup> or Inconel<sup>[99]</sup>) substrate holders are commonly used since these materials, as opposed to molybdenum, are compatible with the strong oxidizing ambient which is inevitably present at the substrate position. Platinum has also been successfully employed as a substrate holder.<sup>[92]</sup>

## 2.2 In-situ Analyses

The high vacuum growth environment of MBE permits the simultaneous use of vacuum surface analytical tools. Reflection high energy electron diffraction (RHEED), low energy electron diffraction (LEED), Auger electron spectroscopy (AES), ultra-violet and x-ray photoemission spectroscopy (XPS), scanning electron microscopy (SEM), scanning tunneling microscopy (STM), and other vacuum characterization techniques can be readily applied to the as-grown surfaces of films. Several of these techniques can be used during growth to gather crucial information on the nucleation and growth mechanisms in real time, rather than relying on "pathology" after the growth. RHEED is particularly useful in this context. The sensitivity of grazing angle diffraction to surface structure is ideal for monitoring the evolution of film accumulation from initial nucleation to the

deposition of each subsequent building layer. The formation of intermediate reaction products or impurity phases can be readily monitored and the growth conditions adjusted during growth. Due to the many phases and phase transitions in these multicomponent oxide systems, such in-situ analytical tools are key to the achievement of atomic layer oxide engineering.

The fact that the building layers of the copper-containing high  $T_c$  superconductors shown in Fig. 3 are not electrically neutral is likely to influence the degree to which the layering can be customized, i.e., the minimum growth units are likely charge neutral.<sup>[50][101]</sup> The growth unit is well established for the growth of copper-containing high  $T_c$  superconductors and other perovskites when all of the constituent species are supplied simultaneously to the substrate in a continuous manner. For such codeposition growth conditions, the intensity of the RHEED pattern oscillates as shown in Fig. 15. The period of these RHEED oscillations corresponds to a deposited thickness of an electrically neutral formula unit of each compound.<sup>[102]</sup> For the growth of high  $T_c$  superconductor films with their c-axis aligned normal to the plane of the substrate, this amounts to one c-axis unit cell thickness for  $\text{YBa}_2\text{Cu}_3\text{O}_{7-\delta}$  and other high  $T_c$  materials (e.g.,  $(\text{Ba},\text{K})\text{BiO}_3$  and  $\text{TlBa}_2\text{Ca}_{n-1}\text{Cu}_n\text{O}_{2n+3}$ ) whose unit cells contain one formula unit, and one half the c-axis unit cell thickness for doped  $\text{La}_2\text{CuO}_4$  and other high  $T_c$  materials (e.g.,  $\text{Bi}_2\text{Sr}_2\text{Ca}_{n-1}\text{Cu}_n\text{O}_{2n+4}$  and  $\text{Tl}_2\text{Ba}_2\text{Ca}_{n-1}\text{Cu}_n\text{O}_{2n+4}$ ) whose unit cells contain two formula units. This minimum growth unit determined by RHEED oscillations is consistent with the step heights that have been observed by STM observations on the surfaces of high  $T_c$  superconductor films<sup>[103][104]</sup> and single crystals.<sup>[105][106]</sup>

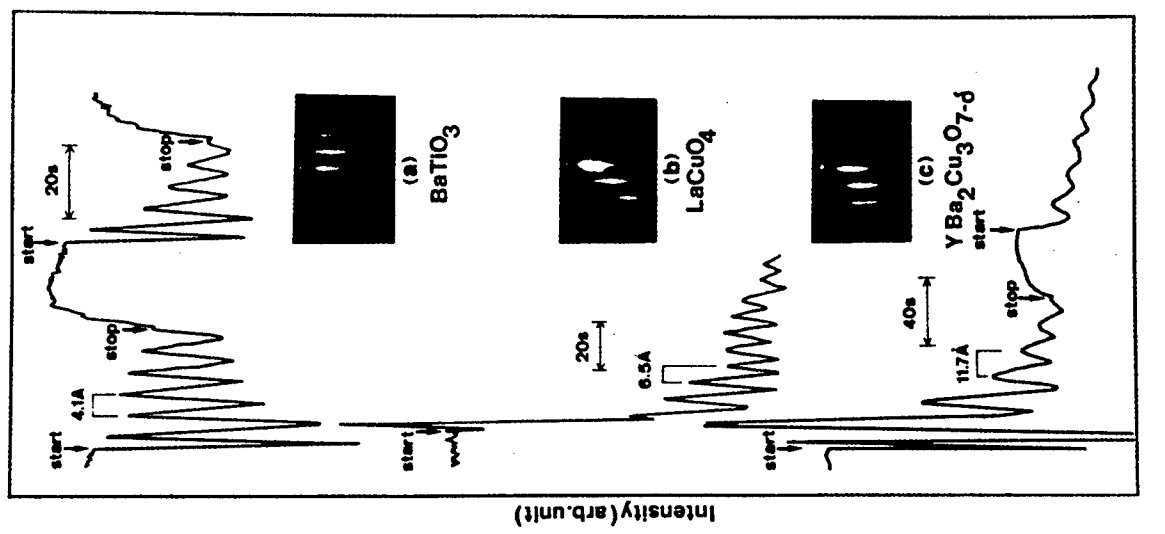
On the other hand, the growth unit of copper-containing high  $T_c$  superconductors formed by sequential deposition is more difficult to assess. Existing data indicate that the sequential deposition growth unit is at least as small as that of continuous deposition, but determination of the minimum attainable growth unit from RHEED data is complicated by the sequential growth process itself and its determination remains an active area of study. For example, although the intensity of the RHEED pattern oscillates as the incident species are modulated during sequential deposition,<sup>[104][105][107]</sup> the period of these oscillations does not necessarily correspond to the growth unit. The modulation of the incident fluxes itself causes corresponding oscillations in the RHEED intensity due to the differing scattering factors of the species being supplied in a discontinuous manner to the surface, as well as modulation of the surface reconstruction that may be induced by the changing surface species. Oscillations at the

<sup>†</sup> The low mechanical strength of pure titanium at temperatures where its sublimation rate is sufficient to achieve significant pumping speeds should be considered when substituting pure titanium filaments.<sup>[95]</sup> If unsupported, the pumping speed achievable with pure titanium filaments will be drastically reduced.<sup>[95]</sup> Molybdenum is present in the titanium-molybdenum alloy (85% Ti, 15% Mo by weight) of conventional filaments to provide sufficient hot strength.<sup>[95]</sup> Its presence allows titanium-molybdenum filaments to be operated (unsupported) at temperatures considerably higher than the melting temperature of pure titanium.<sup>[95]</sup>

shuttering frequency occur during migration enhanced epitaxial (MEE) growth of III-V materials,<sup>[108]</sup> a process which is completely analogous to the sequential deposition technique used for high  $T_c$  materials. In MEE growth, oscillations occur at the shuttering frequency even when the number of species being deposited does not correspond to a complete monolayer.<sup>[108]</sup> In such cases, a beat frequency caused by periodic layer completion, and indicating that an incomplete monolayer is being deposited in each flux burst, may accompany the first several MEE oscillations, but the presence of such beating has been shown to depend strongly on the growth conditions (e.g., it is absent at low growth temperatures) for III-V materials<sup>[108]</sup> and has not been studied for oxides.

Indirect evidence indicates that the growth unit during sequential deposition is at least as small as that of continuous deposition. As described in Sec. 3, shuttered MBE has achieved atomic substitution at particular sites within the smallest electrically neutral formula unit (the minimum growth unit for continuous growth), enabling the growth of metastable phases and site-specific doping. Like the minimum growth unit for continuous growth, the minimum growth unit for shuttered growth is also likely to be electrically neutral.<sup>[50][101]</sup> Whether these electrically neutral building blocks are an electrically neutral combination of building layers<sup>[50]</sup> or electrical neutrality is attained by varying the oxygen stoichiometry (e.g., CuO instead of CuO<sub>2</sub>, BiO<sub>1.5</sub> instead of BiO, etc.) of the building layers as they are deposited, with subsequent oxygen reordering upon deposition of a complete unit cell, is an unknown but fundamentally important aspect since the minimum building block size will limit the degree to which the layering of high  $T_c$  superconductors may be customized by MBE.

The sequential MBE growth process used to customize the layering of high  $T_c$  structures (illustrated in Fig. 13) uses physical means to influence the layering order of the constituent building layers. The MBE shutters are opened and closed to provide bursts of the depositing species in a sequence corresponding to the building layer order of the desired material. However, even with perfect control of the quantity of species in a burst, the depositing species may agglomerate into islands on the substrate surface, rather than forming the desired flat layer as shown schematically in Fig. 16. In-situ RHEED can be used to monitor this occurrence, and should islanding occur, the growth conditions may be altered in order to search for conditions conducive to layer-by-layer growth.



**Figure 15.** RHEED oscillations observed during the continuous codeposition of (a) BaTiO<sub>3</sub>, (b) La<sub>2</sub>CuO<sub>4</sub>, and (c) YBa<sub>2</sub>Cu<sub>3</sub>O<sub>7-d</sub>. (From Ref. 102).

Although the utility of RHEED during growth is a distinct advantage of MBE over other thin film growth techniques, several important aspects of RHEED must be kept in mind when interpreting RHEED data. The observation of RHEED streaks does not necessarily imply an atomically smooth surface. One-dimensional disorder in the growth direction will also give rise to RHEED streaks.<sup>[10]</sup> X-ray diffraction can be used to determine the extent of order in the growth direction, so that the RHEED streaks may be properly interpreted. Secondly, an ideally flat well-ordered surface will appear spotty, rather than streaky, due to the finite curvature of the Ewald sphere. These spots, which appear on arcs delineating the Laue zones, are readily distinguished from the 2-dimensional array of spots that results from the transmission diffraction pattern of a rough surface. Finally, even a surface which appears to be quite flat by RHEED may in reality contain deep pits; as long as the thickness of the flat regions is greater than the electron penetration depth, no transmission diffraction spots will be seen.<sup>[10]</sup>

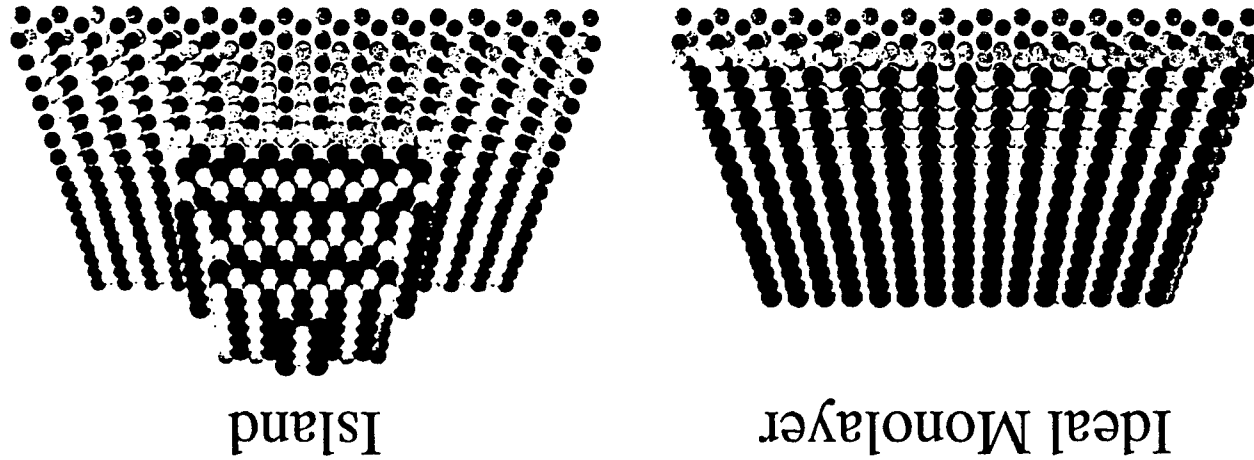
As described in Sec. 2.7, composition control is a crucial aspect of the successful growth of high  $T_c$  superconductors by MBE, especially when sequential deposition is used. Although the freezing-in of metastable layerings at the low growth temperatures employed can be a distinct advantage of the MBE technique, without adequate composition control (on a burst-by-burst level for sequential deposition), the lack of layering control results in uncontrolled layering disorder.<sup>[8]</sup> Customized cation substitution within a chosen building layer (e.g., chemical doping) is possible by sequential deposition MBE, but again this also requires excellent composition control.

### 2.3 Minimum O<sub>2</sub> Necessary to Form Structure

A major obstacle to the growth of high  $T_c$  superconductors by MBE is to provide sufficient oxygen to form the desired structure, while at the same time maintaining a long mean free path. In order to select appropriate growth conditions, it is desirable to know the lowest oxygen pressure at which the desired high  $T_c$  superconductor structure may be formed.

The thermodynamic stability limits of several high  $T_c$  superconductor structures have been measured as a function of oxygen pressure and temperature. As Figs. 6 and 7 show, the minimum oxygen pressure necessary to sustain  $\text{YBa}_2\text{Cu}_3\text{O}_{7-\delta}$  ( $\delta \approx 1$ ) as an equilibrium phase depends on temperature and sample composition. The lowest oxygen pressures at which the  $\text{YBa}_2\text{Cu}_3\text{O}_{7-\delta}$  phase was found to be thermodynamically stable

Figure 16. A schematic representation of how physically limiting the deposited number of atoms to exactly equal the amount in one monolayer does not imply perfect monolayer coverage. A complete SrO monolayer is shown on the left and a SrO island on the right.



as a function of temperature, reaction IX in Fig. 7, were obtained for samples with a stoichiometric 1:2:3 cation ratio. The temperature dependence of the minimum oxygen pressure necessary to sustain  $\text{Bi}_2\text{Sr}_2\text{Ca}_{n-1}\text{Cu}_n\text{O}_{2n+4}$  as equilibrium phases has only been measured at two compositions:  $\text{Bi}_2\text{Sr}_2\text{CaCu}_2\text{O}_{8+\delta}$  and  $\text{Bi}_2\text{Sr}_2\text{Ca}_2\text{Cu}_3\text{O}_{10+\delta}$  ( $\delta \sim 0$ ), and is shown in Fig. 9.

It may seem strange to be concerned with thermodynamic stability constraints for a process whose goal is to enable customized layering and the synthesis of metastable phases. The ability of MBE to provide customized layering arises from the low bulk diffusion coefficients at the growth temperatures used, which kinetically limit decomposition of the deposited layers. On the other hand, the growth temperatures must be high enough that the depositing species have sufficient mobility, at the film surface, to crystallize in a highly ordered manner. Since reactions, including oxidation, between the species reaching the substrate from the various molecular beams occur at the film surface, where surface diffusion is high and kinetic barriers are minimal, thermodynamic constraints are important. Thus, while the formation of each surface layer is significantly dependent on thermodynamics, it is the aim of the sequential deposition MBE process to preserve the customized layering order by limiting bulk diffusion.

The measurements of the minimum oxygen pressure necessary to stabilize the high  $T_c$  superconductors  $\text{YBa}_2\text{Cu}_3\text{O}_{7-\delta}$ ,  $\text{Bi}_2\text{Sr}_2\text{CaCu}_2\text{O}_{8+\delta}$ , and  $\text{Bi}_2\text{Sr}_2\text{Ca}_2\text{Cu}_3\text{O}_{10+\delta}$  have been made under conditions where the transformation kinetics of the bulk samples studied were sufficiently rapid that the thermodynamic stability limits of these phases could be determined.<sup>[65][67][70][11]</sup> Note, however, that these experiments were performed at pressures considerably higher than the MBE regime. Only a few measurements have been made at lower pressures, some of which extend into the MBE pressure range,<sup>[65][12][113]</sup> but with significantly decreased measurement precision. Thus, estimating the equilibrium stability limits under MBE conditions from currently available data involves extrapolating the higher pressure results to lower pressure or fitting thermodynamic functions to the many phases present in these systems which are consistent with the experimental data obtained at higher pressures, and calculating the phase relationships at reduced pressure, as has been performed by Degterov and Voronin.<sup>[64][114]</sup> The minimum oxygen pressures necessary to thermodynamically stabilize  $\text{YBa}_2\text{Cu}_3\text{O}_{7-\delta}$ ,  $\text{Bi}_2\text{Sr}_2\text{CaCu}_2\text{O}_{8+\delta}$ , and  $\text{Bi}_2\text{Sr}_2\text{Ca}_2\text{Cu}_3\text{O}_{10+\delta}$  as a function of temperature, extrapolated into the

MBE regime, are shown in Fig. 17. Although there is some scatter among the different copper-containing high  $T_c$  superconductors, as well as discrepancies between researchers investigating a particular phase, the data indicate that high oxygen pressures (by MBE standards) are required to stabilize the structures of copper-containing high  $T_c$  superconductors at relevant growth temperatures.

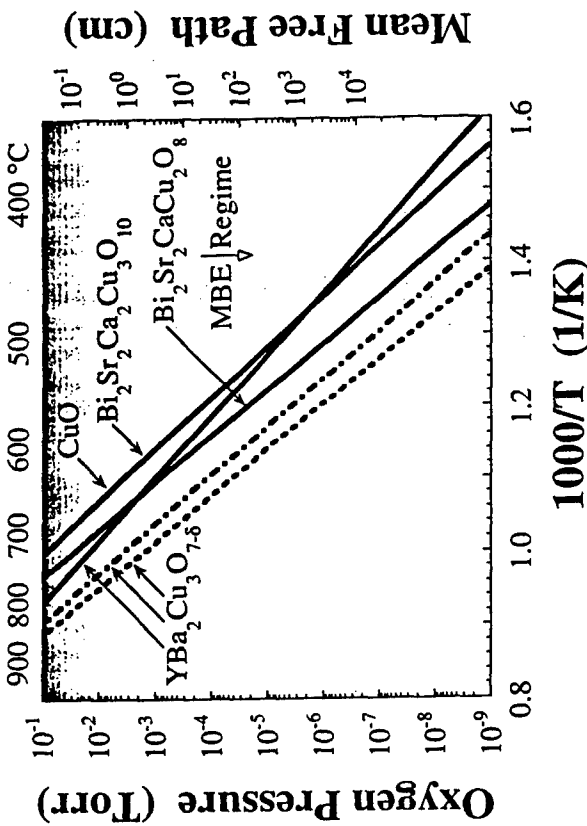


Figure 17. The thermodynamic stability lines extrapolated into the MBE regime from Figs. 7 and 9 showing the minimum molecular oxygen pressure necessary to sustain the structures of  $\text{YBa}_2\text{Cu}_3\text{O}_{7-\delta}$ ,  $\text{Bi}_2\text{Sr}_2\text{Ca}_2\text{Cu}_3\text{O}_{10}$ , and  $\text{CuO}$  (as equilibrium phases) as a function of temperature. The mean free path of Ba in molecular oxygen, from Fig. 18, is also shown to indicate the regime of MBE-compatible pressures. The minimum molecular oxygen pressure stability lines extrapolated into the MBE regime from Refs. 111 (dashed) and 114 (dot-dashed) for  $\text{YBa}_2\text{Cu}_3\text{O}_{7-\delta}$  are also shown.

The thermodynamic oxygen stability limit of the only copper-free high  $T_c$  superconductor,  $(\text{Ba}, \text{K})\text{BiO}_3$ , has not been measured. However, MBE growth studies have shown that molecular oxygen pressures at the limit of

the MBE regime (this limit is discussed in Sec. 2.4) result in an extremely low bismuth sticking coefficient, even at the low ( $345^\circ\text{C}$ ) substrate temperatures used.<sup>[115]</sup> Activated oxygen species are a common feature of the low-pressure growth methods successfully employed for the growth of  $(\text{Ba}, \text{K})\text{BiO}_3$  films.<sup>[116][117]</sup>

From these considerations, it is not surprising that the utilization of more reactive oxidant species is a crucial aspect in the successful growth by MBE of high  $T_c$  superconductors with respectable transport properties.

#### 2.4 Maximum O<sub>2</sub> Satisfying MBE Mean Free Path Constraint

As the thermodynamic considerations in the previous section show, significant oxygen pressures are necessary to make high  $T_c$  superconductor structures stable. On the other hand, in order to grow these materials by MBE, low oxygen pressures must be used. A necessary condition for MBE is maintaining a mean free path for each depositing species which is longer than the source to substrate distance. This distance is about 20 centimeters in a typical MBE machine. While it is possible to grow high  $T_c$  superconductors by physical vapor deposition at oxygen pressures exceeding these limits,<sup>[29][29][112][120][127]</sup><sup>f</sup> these high pressures can significantly complicate composition control<sup>[92][97][112][126]</sup>, and in-situ RHEED characterization. For example, due to frequent gas phase collisions at high pressures, as the evaporating species make their way toward the substrate, the flux of each constituent species actually reaching the substrate is strongly dependent on the oxygen pressure, which not only varies considerably with position, but also depends on the fluxes of any oxygen gettering species which are being simultaneously evaporated. The differing cross-sections and momenta of the evaporated species cause the fluxes of the constituent species reaching the substrate to be attenuated unequally, causing a shift in the relative mixture of arriving species, which results in a strong interrelationship between the oxygen flow rate, the individual fluxes, and the depositing composition. Growth at MBE-compatible pressures removes the interdependencies in this composition control problem.

Figure 18 shows the variation of the mean free path of many of the constituent species of high  $T_c$  superconductors, calculated for a random gas mixture of one such species with molecular oxygen. The appropriate formula for this calculation<sup>[128]</sup> has been corrected for the one diatomic species which was used (oxygen) and is given by the equation:<sup>f</sup>

$$\text{Eq. (3)} \quad L_i^{-1} = (\pi F_i d_i^2) \sqrt{\frac{2m_i}{3k_B T_i}} + \frac{\pi P_{O_2}}{k_B T_{O_2}} \left( \frac{d_i + d_{O_2}}{2} \right)^2 \sqrt{1 + \frac{5}{3} \left( \frac{T_{O_2}}{T_i} \right) \left( \frac{m_i}{m_{O_2}} \right)}$$

where  $L$  is mean free path,  $F$  is depositing flux,  $d$  is diameter,  $m$  is mass,  $k_B$  is Boltzman's constant,  $P$  is pressure, and  $T$  is absolute temperature. The subscript  $i$  refers to the beam species, and the subscript  $O_2$  to molecular oxygen. The parameters used in this calculation are given in Table 1. The shortest mean free paths are those of Rb, Hg, and Ba, while Cu has the longest. The variation between the mean free paths of the various high  $T_c$  superconductor constituents is about a factor of three in the region where their mean free paths are limited by scattering with  $O_2$ . Of the species with the shortest mean free paths, Ba is the most commonly used and for this reason the maximum oxygen pressure defining the MBE regime in Figs. 17 and 19 is for a depositing Ba flux. For the MBE growth of high  $T_c$  superconductors containing Rb (e.g.,  $(\text{Ba}, \text{Rb})\text{BiO}_3$ ) or Hg (e.g.,  $\text{HgBa}_2\text{Ca}_2\text{Cu}_3\text{O}_{8+x}$ , currently the highest  $T_c$  superconductor with  $T_c \approx 133$  K),<sup>[137]</sup> the MBE regime extends only to about  $1 \times 10^{-4}$  torr of oxygen. As the oxygen pressure decreases, the mean free paths increase ( $L^{-1} \propto P_{O_2}$ ) until the mean free paths become limited by scattering between the species themselves (this is the reason for the change in slope of the mean free paths in Fig. 18 at low  $P_{O_2}$ ).

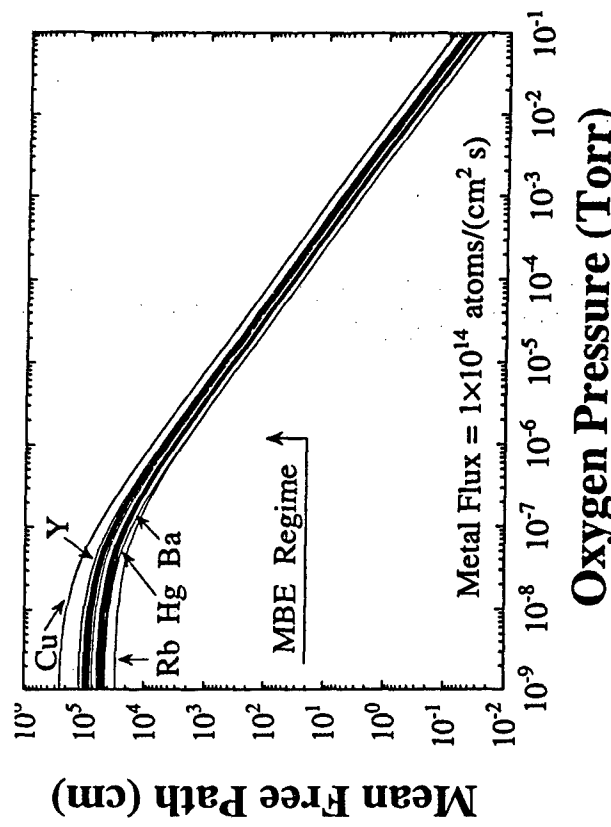
The minimum molecular oxygen pressure necessary to sustain the structure of several copper-containing high  $T_c$  superconductors and CuO (the thermodynamic stability lines from Sec. 2.3), is shown in Fig. 17 as a function of temperature, together with the mean free path of Ba in molecular oxygen. In order to have a mean free path  $\geq 20$  cm (the typical source to substrate distance in an MBE machine), the maximum  $O_2$  operating pressure is about  $2 \times 10^{-4}$  torr. In order to be above the CuO line, the

<sup>f</sup> By definition,<sup>[118]</sup> such a deposition process is no longer MBE, since well-defined thermal molecular beams are no longer present at the high pressures used. Deposition under such conditions is commonly referred to as "reactive evaporation." Only synthesis methods resulting in the epitaxial growth of a material from the reaction of well-defined thermal molecular beams with a crystalline surface (MBE<sup>1.8</sup> or reactive MBE<sup>1.9</sup>) are described in this chapter.

<sup>f</sup> The beam nature of the depositing species was ignored. A depositing flux of  $10^{14}$  atoms  $\text{cm}^{-2}\text{s}^{-1}$  (which corresponds to a growth rate of 0.15 metal-oxide monolayers per second or about 0.3 Å/s for  $\text{YBa}_2\text{Cu}_3\text{O}_{7-\delta}$  or  $\text{Bi}_2\text{Sr}_2\text{CaCu}_2\text{O}_8$ ), the atomic diameters from Ref. 134, the  $O_2$  diameter from Ref. 135, and typical furnace temperatures (listed in Table 1) for each species and room temperature for oxygen were used in the calculation. Only atomic depositing species were considered ( $\text{Bi}_2$ , which accounts for about 40% of the species in the bismuth molecular beam), was disregarded.

**Table 1.** Parameters Used in Mean Free Path Calculation

Source	$T_i$ (K)	$d_i$ ( $\text{\AA}$ )	$m_i$ (a.m.u.)	$P_i$ (Torr) at which $L_i = 20 \text{ cm}$
O <sub>2</sub>	3000	3.59	32	
Ba	9000	4.48	1.3734	$1.6 \times 10^{-4}$
Bi	9000	3.64	208.98	$1.8 \times 10^{-4}$
Ca	8500	3.93	40.08	$2.7 \times 10^{-4}$
Cc	19500	3.64	140.12	$2.6 \times 10^{-4}$
Cu	14500	2.55	63.54	$4.0 \times 10^{-4}$
Dy	13500	3.54	162.50	$2.3 \times 10^{-4}$
Er	14500	3.50	167.26	$2.3 \times 10^{-4}$
Eu	8500	4.08	151.96	$1.7 \times 10^{-4}$
Gd	18000	3.59	157.25	$2.5 \times 10^{-4}$
Hf	3000	3.10	200.59	$1.3 \times 10^{-4}$
Ho	14000	3.52	164.930	$2.3 \times 10^{-4}$
K	450	4.76	39.102	$1.8 \times 10^{-4}$
La	19500	3.741	138.91	$2.5 \times 10^{-4}$
Lu	18500	3.47	174.97	$2.5 \times 10^{-4}$
Nd	15500	3.63	144.24	$2.4 \times 10^{-4}$
Pb	950	3.49	207.19	$1.9 \times 10^{-4}$
Pr	17000	3.65	140.907	$2.5 \times 10^{-4}$
Rb	400	5.02	85.47	$1.3 \times 10^{-4}$
Sr	800	4.29	87.62	$1.9 \times 10^{-4}$
Tb	17500	3.54	158.924	$2.5 \times 10^{-4}$
Tl	850	3.42	204.37	$1.8 \times 10^{-4}$
Tm	11000	3.48	168.934	$2.1 \times 10^{-4}$
Y	1850	3.62	88.905	$2.9 \times 10^{-4}$
Yb	700	3.87	173.04	$1.6 \times 10^{-4}$



**Figure 18.** The mean free path of atomic fluxes of the constituent species of high  $T_c$  superconductors as a function of oxygen pressure. Calculated using Eq. (3) and the parameters in Table 1.

## 2.5 Alternative Oxidants

From thermodynamic considerations, potential alternative oxidants have been identified.<sup>[88][138][139]</sup> However, thermodynamic calculations assume equilibrium between all possible species and are not directly applicable to the deposition conditions used in this reactive MBE approach for the growth of high  $T_c$  superconductor films, where an enhanced, non-equilibrium concentration of an alternative oxidant is utilized to enable growth under MBE-compatible vacuum conditions. An indication of the inefficiency of  $O_2$  as an oxidant for these materials is provided by considering an ideal oxidant: one having high activity and no kinetic barriers to oxidation. Since even the most powerful oxidant must deliver an oxygen flux at least as great as the oxygen content of the crystal structure to be formed, the required minimum flux (and equivalent pressure<sup>†</sup>) may be calculated assuming complete incorporation of the oxidizing species for the desired growth rate of a given high  $T_c$  superconductor phase. For example, the minimum flux necessary to form  $YBa_2Cu_3O_6$  at a growth rate of 1 Å/s for an oxidant that provides one oxygen atom per oxidant molecule is  $3 \times 10^{14} \text{ cm}^{-2}\text{s}^{-1}$ , which corresponds to a pressure of about  $3 \times 10^{-7}$  torr. This minimum flux is more than three orders of magnitude lower than the minimum  $O_2$  flux (or pressure) necessary to stabilize the growth of  $YBa_2Cu_3O_6$  at typical growth temperatures which yield good transport characteristics (i.e.,  $T \geq 600^\circ\text{C}$ ). As Fig. 17 shows, the minimum amount of oxygen required to thermodynamically stabilize the high  $T_c$  structures rises rapidly with temperature. By  $750^\circ\text{C}$ , the performance advantage of an ideal oxidant over molecular oxygen is about five orders of magnitude in pressure. The inefficiency of molecular oxygen leaves considerable room for oxidant pressure reduction well into the MBE range by the use of more reactive oxidants.

An estimate of the increased oxidizing power of various alternative oxidants for copper-containing high  $T_c$  superconductors has been investigated by measuring the minimum oxidant flux needed to form CuO

<sup>†</sup> Because of the beam nature of the incident fluxes, the pressure at the plane of the substrate corresponding to the incident flux is given by

$$P_i = \frac{F_i}{\cos \theta} \sqrt{\frac{\pi m k_B T_i}{8}}$$

where  $\theta$  is the angle between the incident beam and the substrate normal, and  $P_i$ ,  $F_i$ ,  $m$ ,  $k_B$ , and  $T_i$  were defined previously (see Eq. 3).<sup>[140][141]</sup> This differs by a factor of  $4\cos\theta$  from the commonly used formula  $P_i = F_i \sqrt{\frac{2\pi m K_B T_i}{8}}$ , which is appropriate for a gas having completely random motion.<sup>[142]</sup>

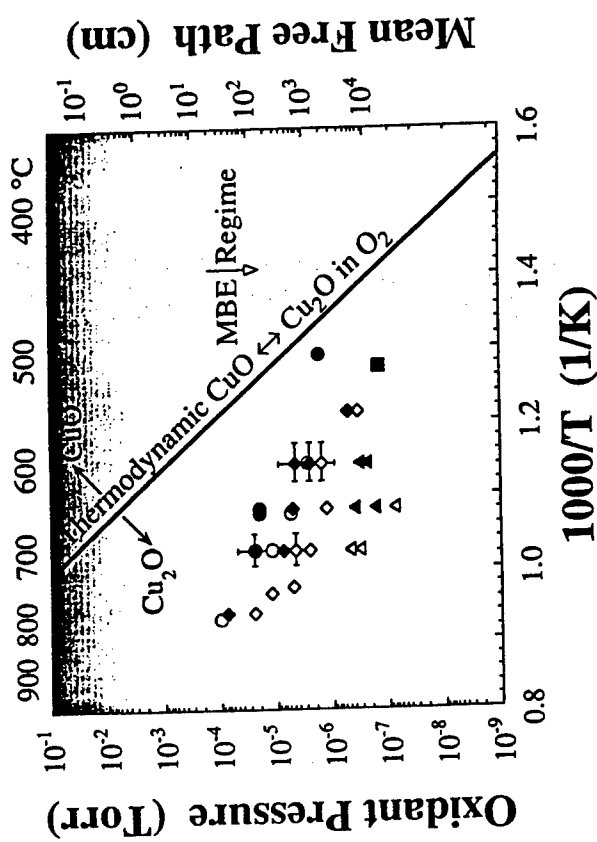
compared to the minimum  $O_2$  requirement. Of the binary oxide constituents of copper-containing high  $T_c$  superconductors, CuO requires the highest molecular oxygen pressure to be thermodynamically stable,<sup>[88]</sup> whereas rare-earth and alkaline earth constituents are readily oxidized by molecular oxygen at MBE-compatible pressures.<sup>[17][143][146]</sup> Studying the ability of alternative oxidants to oxidize Cu to CuO and comparing it to the ability of  $O_2$  to do so has several advantages over studying their ability to sufficiently oxidize specific copper-containing high  $T_c$  superconductors. First of all, forming CuO is free from the composition control problems which accompany the synthesis of multi-component copper-containing high  $T_c$  superconductors. Note from Fig. 6 that the minimum  $P_{O_2}$  necessary to thermodynamically stabilize a sample with composition Y:Ba:Cu = 1:2:3 (i.e.,  $YBa_2Cu_3O_8$ ) is significantly different from the  $P_{O_2}$  requirement for a slightly copper-rich composition, e.g., Y:Ba:Cu = 1:2:3.5. At  $850^\circ\text{C}$  the former is thermodynamically stable down to  $P_{O_2} = 300$  mtorr, while the latter will decompose below  $P_{O_2} = 760$  mtorr.<sup>[88]</sup> Secondly, forming CuO also gives a more definitive measure of the enhanced oxidation ability of the oxidant, since the minimum oxygen requirements of CuO are thermodynamically well established, while there remains considerable disagreement about the precise minimum  $O_2$  stability lines for the copper-containing high  $T_c$  superconductors at low pressures (e.g.,  $YBa_2Cu_3O_{7-\delta}$ <sup>[87][11][14][147]</sup> and  $Ba_2Sr_2CaCu_2O_{8+\delta}$ <sup>[70][148]</sup>).

In order to compare the ability of alternative oxidants to form cupric compounds, it is necessary to (i) produce a pure beam of a specific oxidant or of the oxidant diluted in  $O_2$ , since the oxidation behavior of  $O_2$  is understood, and (ii) know the flux (or pressure) of the oxidant at the substrate position itself. Although researchers have extensively utilized plasmas to enhance oxidation, relatively few studies have produced oxidant beams of the requisite purity to investigate the activity of specific oxidant species and quantified their flux at the position where oxidation occurs. Such studies, although over a rather limited range of experimental conditions, have been performed for atomic oxygen ( $O$ ),  $O^+$ , ozone ( $O_3$ ), and  $NO_2$ . In these studies, the ability of atomic oxygen ( $O$ ),  $O^+$ , ozone ( $O_3$ ), and  $NO_2$  to oxidize copper has been measured by depositing copper onto a substrate in the presence of one of these oxidants.<sup>[83][129][132]</sup> The formation of CuO (or Cu<sub>2</sub>O or Cu) has been monitored by in-situ RHEED,<sup>[83][129]</sup> in-situ optical reflectance,<sup>[129]</sup> in-situ x-ray photoelectron spectroscopy (XPS),<sup>[83][129][132]</sup> and ex-situ x-ray diffraction.<sup>[83][94][129]</sup> When the formation of CuO is tested by ex-situ methods or after the samples have

been cooled, the atmosphere in which the samples are cooled must be carefully considered.<sup>†</sup>

The limited data in the literature that meet these criteria are shown in Fig. 19. In these experiments, a heated MgO substrate was simultaneously exposed to an oxidant beam and a copper beam.<sup>[83][129][132]</sup> Growth conditions yielding CuO are shown as solid points and those resulting in Cu<sub>2</sub>O are shown as hollow points for the various oxidants. In addition to the data for atomic oxygen, O<sup>+</sup>, ozone, and NO<sub>2</sub> plotted in Fig. 19, the thermodynamic equilibrium line denoting the thermodynamic limit to CuO formation with molecular oxygen is also shown. All of these oxidants are significantly better than molecular oxygen, and allow the growth of cupric compounds to be achieved at MBE-compatible pressures. The flux needed to form CuO with O<sup>+</sup> is over one order of magnitude lower than the thermodynamic O<sub>2</sub> requirement at 510°C.<sup>[83]</sup> The flux of NO<sub>2</sub> used to produce CuO is about two orders of magnitude lower than the thermodynamic O<sub>2</sub> requirement at 650°C.<sup>[131][132]</sup> The pressure needed to form CuO with purified ozone is over two orders of magnitude lower at 600°C and over three orders of magnitude lower at 700°C compared to the equilibrium line for O<sub>2</sub>.<sup>[130][131]</sup> The required pressure for atomic oxygen is over four orders of magnitude lower at 650°C.<sup>[129]</sup>

This limited experimental data is insufficient to conclude which of these oxidants is the most effective. In all cases, the minimum oxidant fluxes found capable of producing CuO in these experiments approached the minimum amount, based on purely kinetic grounds, that an ideal oxidant would require for the copper fluxes used in these experiments. Thus, these powerful oxidants are nearly ideal oxidants. Side-by-side comparisons of NO<sub>2</sub> with ozone led Ogihara et al.<sup>[131]</sup> and Nonaka et al.<sup>[132]</sup> to conclude that NO<sub>2</sub> is slightly less reactive than O<sub>3</sub>. Ogihara et al.<sup>[131]</sup> found that the minimum oxidant pressure needed to form CuO was about five times lower for ozone than for NO<sub>2</sub>.<sup>[131]</sup> Nonaka et al.<sup>[132]</sup> attributed the decreased reactivity of NO<sub>2</sub> to the known reaction in which



**Figure 19.** A comparison of the enhanced ability of atomic oxygen (triangles), O<sup>+</sup> (squares), ozone (diamonds), and NO<sub>2</sub> (circles) to form cupric oxide compared to molecular oxygen. A copper flux was oxidized to CuO (solid points) and Cu<sub>2</sub>O (hollow points) by simultaneous exposure to the indicated pressure (flux) of these oxidants. The O<sub>2</sub> line indicates the thermodynamic line of coexistence of CuO with Cu<sub>2</sub>O as a function of molecular oxygen pressure. Above the line, CuO is the equilibrium phase, while below the line, Cu<sub>2</sub>O is the stable phase. The right hand axis shows the variation of the mean free path of Ba as the oxygen pressure is varied. Experimental data from Refs. 83, 129–132. Thermodynamic line calculated from Ref. 133.

one of the decomposition products of NO<sub>2</sub>, NO, reacts with CuO and reduces it:<sup>‡</sup>



The minimum flux (or pressure) of oxidant depends on the growth rate used since, by conservation of mass, at least one oxygen atom is required per

<sup>†</sup> NO<sub>2</sub> begins to decompose into NO and O at temperatures above 150°C.<sup>[132]</sup>

<sup>‡</sup> The cooling of a sample in the same oxidant flux in which it was grown (a horizontal cooling path in Fig. 19) results in an increasing driving force toward oxidation. For example, an as-grown Cu<sub>2</sub>O sample cooled at the same oxidant flux in which it was grown will eventually cross the Cu<sub>2</sub>O/CuO stability line. When this occurs, unless the kinetics of the Cu<sub>2</sub>O → CuO transformation are sluggish, the sample will transform into CuO and the ex-situ determination of the minimum oxidant pressure necessary to form CuO will be in error. In-situ x-ray diffraction analysis has shown that this transformation becomes kinetically limited at temperatures below about 550°C.<sup>[149]</sup> Thus, when determining the CuO/Cu<sub>2</sub>O stability line by ex-situ methods, it is preferable to cool the samples in vacuum rather than to cool them in the same oxidant pressure in which they were grown. This provides a lower-bound of the oxidation enhancement provided by the oxidant.

deposited copper atom. The increase in required oxidant flux at higher temperatures may reflect the oxygen loss rate from the film surface. For CuO films, XPS studies have found that the onset for oxygen loss at the sample surface is about 650°C.<sup>[129]</sup> At higher temperatures, the oxidant flux must not only provide sufficient oxygen to oxidize the incident copper, but must also supply sufficient oxygen to make up for that lost by vaporization.

Practical issues also affect the choice of oxidant. Although several oxidants are suitable for forming high  $T_c$  structures under MBE conditions, only in the cases of NO<sub>2</sub>, O<sup>+</sup>, and ozone have relatively pure beams of the oxidants been achieved. A disadvantage of plasma sources to produce active oxygen species for the MBE growth of high  $T_c$  compounds is the high pressure of molecular oxygen which accompanies the desired oxidant. This unwanted O<sub>2</sub>, which typically amounts to 90% or more of the gas flux,<sup>[45][112][150][152]</sup> increases the gas load and decreases the mean free path. High purity, mass separated, low energy O<sup>+</sup> ion beams have been achieved and their extreme activity has led to the formation of new oxide structures.<sup>[153]</sup> However, the O<sup>+</sup> fluxes are relatively low (typically  $3 \times 10^{14} \text{ O}^+ \text{ cm}^{-2} \text{ s}^{-1}$ ),<sup>[153]</sup> and the capital investment necessary is relatively high, compared to the use of NO<sub>2</sub> or purified ozone beams. The purity of the latter is estimated to be between 26% and 70% ozone, the remainder being O<sub>2</sub>.<sup>[154][157]</sup> An additional advantage of NO<sub>2</sub> and ozone is that they may be supplied from a vessel outside of the MBE chamber, and delivered in a very pure form to the substrate region using conventional ultra-high vacuum (UHV) materials like stainless steel,<sup>[156][159]</sup> whereas atomic oxygen and oxygen plasma species are much more sensitive to recombination. Note that XPS studies do not indicate the incorporation of nitrogen into CuO, NdBa<sub>2</sub>Cu<sub>3</sub>O<sub>6</sub>, or Bi<sub>2</sub>Sr<sub>2</sub>CuO<sub>6</sub> films when NO<sub>2</sub> is used as the oxidant at the growth temperatures employed.<sup>[132][161]</sup> †

Even when copper is deposited onto a substrate at room temperature, simultaneous MBE-compatible fluxes of atomic oxygen, O<sup>+</sup>, ozone, and NO<sub>2</sub> are capable of oxidizing the depositing copper into CuO.<sup>[83][129][160][162]</sup> indicating the absence of kinetic barriers to Cu oxidation for these reactive oxidants at temperatures above room temperature. This behavior is distinct from that of molecular oxygen. Kinetic barriers to the oxidation of copper by molecular oxygen exist, as was demonstrated by the inability of O<sub>2</sub> to oxidize copper at MBE-compatible fluxes at temperatures below 450°C.<sup>[94][139][157][162][163]</sup> even though these

† Nitrogen incorporation, via the formation of Sr(NO<sub>2</sub>)<sub>2</sub>, was detected by XPS in Bi<sub>2</sub>Sn<sub>2</sub>CuO<sub>6</sub> layers deposited at room temperature.<sup>[160]</sup> however, after heating to 300°C the films were free of nitrogen.<sup>[161]</sup>

fluxes are, from a thermodynamic standpoint (Fig. 19), sufficient to form CuO. This kinetic barrier to the oxidation of copper using molecular oxygen is absent by 550°C.<sup>[96][112]</sup> but by that point, the pressures of molecular oxygen required to thermodynamically stabilize cupric compounds are quite close to the limit of MBE-compatible pressures, as discussed above. Kinetic barriers also exist to the oxidation of bismuth by molecular oxygen.<sup>[164]</sup> Since all of the known high  $T_c$  superconductors contain copper or bismuth, the use of an activated oxygen source for the MBE growth of these materials is seen to be a necessity.

Although the oxidation sources considered and used to date for the MBE growth of high  $T_c$  superconductors are gaseous, solid source oxidants (e.g., Sb<sub>2</sub>O<sub>3</sub> and As<sub>2</sub>O<sub>3</sub>) have been used to grow other oxides at very low pressures,<sup>[165]</sup> well within the MBE regime. This chemical method of oxidation has the advantage of not requiring an expensive oxygen plasma source or the collection of potentially explosive purified ozone. However, the surface chemistry of growth is complicated by the presence of additional species that must be desorbed in order to grow oxide films free from the unwanted components of the particular molecular oxidant used.

Early in the development of the MBE technique for the growth of high  $T_c$  materials, it was recognized that more reactive oxidants, such as ozone, were desirable.<sup>[113]</sup> The ability of ozone to grow YBa<sub>2</sub>Cu<sub>3</sub>O<sub>7-δ</sub> and Bi<sub>2</sub>Sr<sub>2</sub>CaCu<sub>2</sub>O<sub>8</sub> under entirely MBE conditions (including substrate cooling after growth) was subsequently demonstrated.<sup>[166][167]</sup> For the reasons outlined above, ozone has become the dominant oxidant of choice for the MBE growth of high  $T_c$  materials; high quality films of YBa<sub>2</sub>Cu<sub>3</sub>O<sub>7-δ</sub>,<sup>[92][132][158]</sup> DyBa<sub>2</sub>Cu<sub>3</sub>O<sub>7-δ</sub>,<sup>[189][90][159]</sup> SmBa<sub>2</sub>Cu<sub>3</sub>O<sub>7-δ</sub>,<sup>[169]</sup> and Bi<sub>2</sub>Sr<sub>2</sub>Ca<sub>n-1</sub>Cu<sub>n</sub>O<sub>2n+4</sub><sup>[171][172]</sup> are now routinely grown with ozone.

NO<sub>2</sub> has not only been used to grow YBa<sub>2</sub>Cu<sub>3</sub>O<sub>7-δ</sub>, NdBa<sub>2</sub>Cu<sub>3</sub>O<sub>7-δ</sub>, and Bi<sub>2</sub>Sn<sub>2</sub>CaCu<sub>2</sub>O<sub>8</sub> films at typical substrate temperatures used for the growth of copper-containing high  $T_c$  superconductors,  $T_{\text{sub}} \sim 700^\circ\text{C}$ ,<sup>[133][173][174]</sup> but has also enabled the growth of superconducting DyBa<sub>2</sub>Cu<sub>3</sub>O<sub>7-δ</sub> films at temperatures as low as 420°C.<sup>[158]</sup> Epitaxial growth of the Bi<sub>2</sub>Si<sub>2</sub>Ca<sub>n-1</sub>Cu<sub>n</sub>O<sub>2n+4</sub> phases ( $n = 1$  and 2) has been achieved using NO<sub>2</sub> at temperatures as low as 300°C.<sup>[160][161][175]</sup> These are the lowest growth temperatures at which the successful epitaxial growth of copper-containing high  $T_c$  materials has been reported. An important aspect of this low temperature achievement was the sequential supply of the depositing species (the metallic elemental constituents, as well as the oxidant) on a monolayer basis by shuttered MBE to the growth surface.

## 2.6 Ozone System

As discussed in Sec. 2.5, more powerful oxidants than molecular oxygen are necessary to grow high  $T_c$  superconductors under MBE conditions, and ozone is a particularly effective and technologically convenient choice. In order to achieve growth conditions having the longest possible mean free path, it is desirable to deliver a pure beam of a strong oxidant to the growing surface. Less oxidizing species (i.e., molecular oxygen) result in a decreased mean free path without providing significant additional oxidation. Commercial ozone generators produce only a few percent ozone in the oxygen gas that passes through them. Since the vapor pressure of oxygen is much greater than that of ozone, it is possible to purify ozone by distillation.<sup>[176]-[178]</sup> A typical ozone collection, distillation, and delivery system is shown in Fig. 20.<sup>[94]</sup>

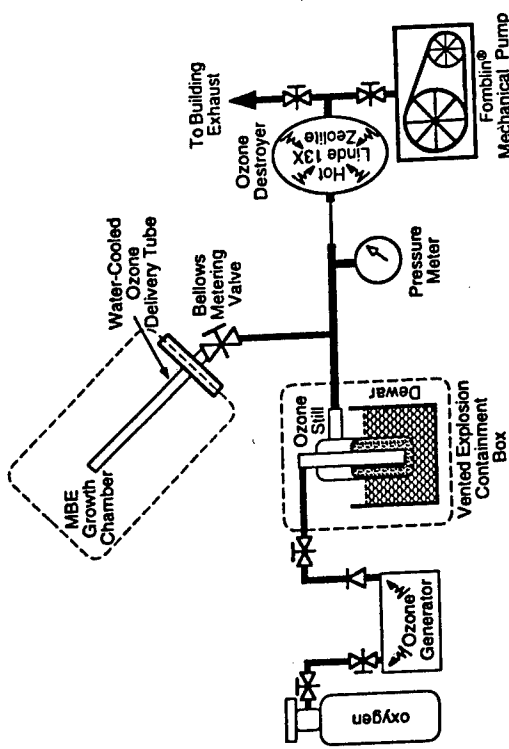


Figure 20. A schematic diagram of an ozone distillation and delivery system (after Ref. 94).

The heart of the system is the ozone trap which stores the ozone. A cross-sectional diagram of one example of such a trap is shown in Fig. 21.<sup>[94]</sup> Ozone is trapped in a silica gel containing silica gel in the design

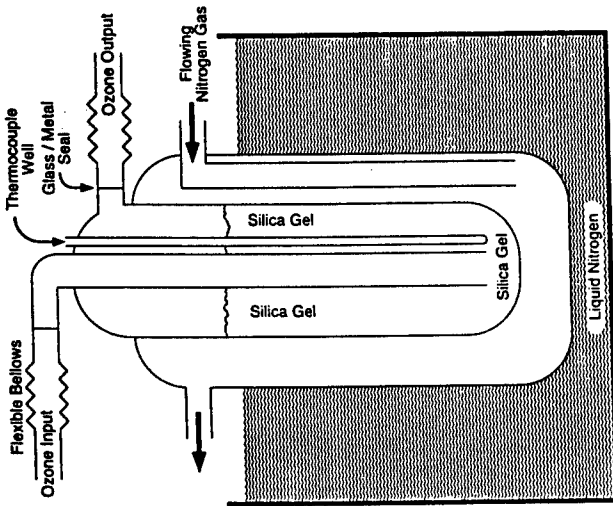


Figure 21. A schematic diagram of the glassware containing silica gel used to store ozone (from Ref. 94).

shown; other designs collect the ozone as a liquid.<sup>[84][91][92][162][166]</sup> The use of a silica gel to contain ozone has safety advantages over the collection of liquid ozone. Liquid ozone is far more sensitive to changes in temperature, pressure, vibration, etc. than ozone adsorbed in a silica gel.<sup>[176]</sup> When using a silica gel, ozone can easily be collected at temperatures higher than the liquefaction temperature of ozone. Indeed, this should always be done in order to prevent the accumulation of liquid ozone.<sup>[84][121]</sup> This can be conveniently accomplished by using dry ice (solid CO<sub>2</sub>) as a coolant for the ozone trap, since the sublimation point of CO<sub>2</sub>, 195 K (as opposed to the boiling point of nitrogen, 77 K), is well above the liquefaction temperature of ozone (161 K).<sup>[121]</sup> Although the rate of ozone decomposition increases with temperature, at 195 K the half-life of ozone stored in a stainless steel vessel is more than a week (and if the stainless steel is phosphated, the half-life exceeds four months).<sup>[179]</sup> indicating that the rate of ozone decomposition is negligible from a practical standpoint. To minimize decomposition, the ozone should only

be allowed to come into contact with compatible materials, e.g., silica gel,[176] glass, Teflon<sup>®</sup>[180] (and the related material Kel-F<sup>®</sup>[181]), stainless steel, aluminum, and alumina.[159] All parts should be thoroughly cleaned in order to eliminate organic residues that could later trigger an explosion.[178][182] Although at room temperature the materials listed above may be used to deliver a reasonably pure ozone flux to the substrate, at higher temperatures significant decomposition of the ozone may occur. Radiant heat from the hot filaments inside the MBE can lead to a significant temperature rise of the ozone-ducting within the MBE. For example, the orifice of a stainless steel ozone delivery tube reached  $\approx 130^\circ\text{C}$  during MBE growth when the tube was not cooled with water.[131] It is for this reason that the stainless steel tubing used to introduce ozone is water-cooled in the high  $T_c$  MBE systems that have demonstrated the most effective oxidation at the minimum ozone pressures.[90][130][131]

## 2.7 Composition Control

Achieving accurate composition control is a crucial aspect for the controlled growth of high  $T_c$  superconductors by MBE. Compared to the growth of conventional semiconductor materials by MBE, the growth of four and five element superconducting compounds requires far more stringent incident flux control. For example, stoichiometric GaAs grows relatively easily over a substantial substrate temperature range and As<sub>4</sub>:Ga flux ratio range where gallium has a near unity sticking coefficient and excess arsenic does not stick. In the growth of high  $T_c$  superconductors, the three or four metal components typically all have significant sticking coefficients. Thus, deposition uniformity across the substrate and shutter-induced source temperature transients affect both the stoichiometry of the growing film as well as the uniformity of film thickness. Experimental data on the effect of composition deviation on the superconducting properties of thin films,[152][183] as well as statistical considerations of the effect of composition errors on the chemical doping of high  $T_c$  superconductors (Fig. 4),[84] indicate that cation composition control at or better than about  $\pm 1$  atomic percent is necessary to produce quality films of high  $T_c$  superconductors. Off-axis sputtering and PLD have a distinct advantage over MBE in that accurate and reproducible composition control is built into these single-target deposition techniques. The inherent flexibility of the MBE technique is only advantageous when it is accompanied by adequate composition control; without it, the user will be unable to control the formation of the desired custom-made structures and controllably dope them. The relatively late arrival of MBE-grown high  $T_c$  superconductor

films with respectable and reproducible transport properties is in large part due to the inadequacy of the composition control used in the initial work, and the time that it took to develop and implement more precise composition control systems. When shuttered MBE growth is employed, *relative* control of the depositing species to  $\pm 1\%$  is no longer sufficient: the total number of atoms incorporated in each flux burst must be an integral number of monolayers, making absolute composition control a necessity. Reproducibly achieving such a level of composition control by MBE is a considerable challenge, which is only beginning to be met.

Several forms of flux measurement are applicable. Ion gauges,[171][154][184] quartz crystal microbalances,[28][43][86][124][125][152][160][166][167][174][185][189] mass spectrometry,[180][92][126][127][152][180][181][182] electron impact emission spectroscopy (EIES),[188][183][185] cold cathode emission spectroscopy (CCES),[186][197] and atomic absorption spectroscopy (AA)[12][198][202], are widely used techniques for thin film composition control, and all of them have been used for composition control for the *in-situ* growth of high  $T_c$  superconductors by evaporative means. Unfortunately, the techniques utilizing hot filaments, i.e., ion gauges, chopped ion gauges,[141][203] mass spectrometry, and EIES are difficult to implement during deposition due to the highly oxidizing conditions necessary for the growth of high  $T_c$  superconductors. For oxygen pressures above about  $10^{-5}$  to  $10^{-4}$  torr, composition control using these hot filament techniques becomes unsatisfactory.[92][12][189][191][194] Although the time-constant of fluctuation of resistively-heated MBE effusion cells is quite long, an advantage for precise composition control, deviations of the flux by 10% or more are not uncommon over the several hour duration of a typical growth.[86][94][204] Even larger changes in the fluxes (e.g., for alkaline earth sources) can occur after they are exposed to the high oxidant pressures that accompany growth, due to oxidation of the source materials and the consequent changes in source emissivity.[205] Thus, precise composition control methods that are able to monitor the fluxes during growth are desirable for the MBE growth of high  $T_c$  superconductors. Recently, CCES was used to control yttrium, barium, and copper during growth at oxygen pressures up to  $10^{-4}$  torr.[197] Atomic fluorescence[206] might also prove useful for accurate flux control during growth. An advantage of the use of quartz crystal microbalances is their ability to measure the active oxygen flux (atomic oxygen or ozone) when they are coated with silver[155][207] or copper.[139][208].

Even the most promising methods, e.g., AA and cross-beam quadrupole mass spectrometry, which have achieved better than  $\pm 1\%$  composition

control in the MBE growth of high  $T_c$  superconductors,[90][152][201][202] require an absolute composition measurement to calibrate the AA or mass spectrometer signal for the growth conditions used. This is often accomplished by growing calibration films whose absolute composition (atoms of each cation/cm<sup>2</sup>) is measured by an ex-situ method, e.g., RBS, ICP, or direct coupled plasma emission spectroscopy (DCP). However, the measurement error of these common composition analysis techniques typically is in excess of the  $\pm 1\%$  absolute composition control typically needed for the reproducible growth of high  $T_c$  superconductors with excellent electrical properties. The error of EPMA is about  $\pm 5\%$ ,[209][210] and can be significantly greater for films thinner than about 0.3  $\mu\text{m}$ , at which point the substrate becomes part of the excitation volume and the assumption that EPMA is probing a homogeneous composition is no longer satisfied.[211][112] Computational routines for heterogeneous samples which allow the presence of the underlying substrate to be included in EPMA composition analyses do exist,[212] but have yet to be widely implemented in commercially-available EPMA systems. In addition to the comparatively high error of EPMA composition analyses, it is insufficient for calibrating the MBE growth of high  $T_c$  superconductors by sequential deposition since it measures only the relative sample composition and not the absolute quantity of species present.

Ideally, absolute composition measurements can be performed in-situ, eliminating the need for, and delays involved with, the growth of calibration films and ex-situ analyses. The quartz crystal microbalance is capable of absolute in-situ flux measurements. Although there are several limitations to its use, particularly in an oxidizing environment where the oxidation state and thus the mass of the depositing species is uncertain, its sensitivity and ability to make absolute flux measurements contribute to its widespread use in MBE systems for the growth of high  $T_c$  superconductors. Even when another composition control method is used during growth, a quartz crystal microbalance that can be moved into the substrate position (thus avoiding any tooling factors which might change with time) is frequently used to calibrate the composition control system. In MBE systems where no flux monitoring is performed during growth, calibration with a quartz crystal microbalance is often performed prior to and following each growth. The main disadvantages of quartz crystal microbalances are the uncertainty in the oxidation state (and thus uncertainty in the flux) of species deposited in an oxidizing ambient, its sensitivity to temperature changes, the uncertainty in the acoustic impedance of the various layers

deposited on the crystal, and its low bandwidth as a flux monitor. The low bandwidth is not a problem for effusion cells, but is a concern for e-beam sources.

Accurate composition control is important not only for attaining optimal carrier concentration in the CuO<sub>2</sub> layers during coevaporated growth, but is also crucial for the controlled substitution and doping of cation sites when shuttered MBE growth is used. For example, the layering control of MBE may not only be exploited to make metastable layering sequences of nominally pure building layers, but also may be used to control the site substitution (cation mixing) and doping with sub-unit-cell precision. The ability to customize cation mixing within high  $T_c$  structures would be a powerful synthesis tool for probing the interrelationship between site doping and superconductivity in these materials. Bulk Bi<sub>2</sub>Sr<sub>2</sub>CaCu<sub>2</sub>O<sub>8</sub> crystals typically have a (Sr+Ca)/Bi ratio of 1.3 rather than the idealized Bi<sub>2</sub>Sr<sub>2</sub>CaCu<sub>2</sub>O<sub>8</sub> formula value of 1.5 and significant mixing of the cations between the various sites.[53][54] The best Bi<sub>2</sub>Sr<sub>2</sub>CaCu<sub>2</sub>O<sub>8</sub> films have also been produced by shuttered MBE with a (Sr+Ca)/Bi ratio significantly less than 1.5.[213] Depositing pure as well as doped building layers by sequential MBE growth requires accurate absolute composition control. Less stringent composition control is readily tolerated in the growth of equilibrium structures where phase separation may be used advantageously to produce a connected path of the equilibrium phase. Composition control, rather than oxidation, is the major remaining challenge to be overcome in order for the controlled growth of high  $T_c$  superconductors and related phases to become a more controlled and reproducible synthesis tool.

## 2.8 Crucibles

If the oxidizing environment necessary for the MBE growth of high  $T_c$  superconductor materials is not adequately confined to the region of the substrate, it may affect the performance of susceptible MBE components. In addition to hot filaments, the performance of pyrolytic boron nitride (pBN) crucibles can degrade. This degradation is particularly important when a molten species is contained in a pBN crucible. Oxidizing species react with hot pBN to form N<sub>2</sub> and B<sub>2</sub>O<sub>3</sub>.[94][95] The formation of B<sub>2</sub>O<sub>3</sub> was established based on studies in which a mass spectrometer was positioned in a line-of-sight position with a copper charge contained in a pBN crucible.[94][95] After oxygen exposure (e.g.,  $P_{\text{O}_2} = 2 \times 10^{-4}$  torr), not only

was there a significant decrease in the copper flux (as much as a factor of three lower), but the mass spectrometer detected masses consistent with the sporadic evaporation, or "spitting," of  $B_2O_3$  when it was exposed to the copper beam.<sup>[24]</sup> Several studies have found that elemental copper is compatible with BN,<sup>[214]-[216]</sup> the incompatibility is solely due to the oxidizing environment. The low density of  $B_2O_3$  compared to copper (and other liquid metal sources) results in the  $B_2O_3$  rising to the surface of the liquid source and forming an encapsulant much like that used for the liquid encapsulated Czochralski (LEC) growth of GaAs. The resultant  $B_2O_3$  encapsulating layer not only leads to boron contamination of films, but also greatly diminishes the flux of the desired evaporant. Even though significant boron contamination exists in films, its presence may not only go unnoticed by routine EPMA or RBS composition analysis, because boron is a light element, but may also escape detection by x-ray diffraction via the formation of amorphous boron phases or by boron substitution for copper in the high  $T_c$  phase being grown. For example, a solid solution between boron and copper in  $Y(Sr,Ba)_2Cu_3O_7$  exists allowing up to 90% of the copper in the CuO chain layer to be replaced by boron (note the similarity between building layer (b) and (i) in Fig. 3), which results in a concomitant decrease in  $T_c$ .<sup>[217]</sup> Several superconducting and non-superconducting structural analogs of high  $T_c$  materials containing borate layers have recently been discovered, e.g.,  $ReBaCuO_2BO_3$ , where  $Re$  is a rare earth ion.<sup>[217]-[218]</sup> Of course, oxides present in the source materials themselves may also react with pBN. For this reason, even if the oxidant pressure is adequately confined away from the effusion source in order that pBN crucibles may be used, it is advantageous to use vacuum-cast copper rather than air-cast copper and to etch the copper source material before loading to remove the copper oxide on its surface and thus avoid its reaction with the pBN crucibles.

Alumina ( $Al_2O_3$ ) crucibles are a viable alternative to pBN for containing both copper<sup>[239]-[241]-[219]-[220]</sup> and bismuth.<sup>[241]-[219]-[220]</sup> The contact angle between copper and alumina in vacuum at 1200°C is 138°.<sup>[221]</sup> This high angle indicates that alumina is not wetted by copper, making alumina a good crucible choice. Sintered alumina is known to contain many volatile impurities which could limit the obtainable purity in an MBE process.<sup>[222]</sup> However, the doping of superconductors does not appear to be nearly as sensitive to impurities as the doping of semiconductors, where impurity species often form undesirable deep levels. If purity should become a limit in the future, single crystal sapphire crucibles with drastically lower impurity concentrations are available and have been used in MBE.<sup>[85]-[223]</sup>

Although the thermal decomposition of  $Al_2O_3$  itself at the temperatures and vacuum conditions typically employed in MBE to contain bismuth and copper is not a concern,<sup>[224]</sup> care should be taken to avoid contacting the alumina with materials (e.g., tantalum<sup>[225]</sup>), that react with alumina and, at typical operation temperatures, can lead to significant fluxes of volatile components (e.g.,  $Al_2O$ <sup>[225]</sup>) and film contamination.

## 2.9 Common Substrates

Since large area single crystal substrates of high  $T_c$  superconductors such as  $YBa_2Cu_3O_{7-\delta}$  or  $Bi_2Sr_2CaCu_2O_{8+\delta}$  necessary for homoepitaxial growth, are not commercially available, other substrate materials must be selected for the heteroepitaxial growth of high  $T_c$  superconductors. The ideal substrate is one which is both chemically and structurally compatible with the epilayer. Other factors, including commercial availability, cost, the potential for integration with other device technologies, thermal expansion coefficient, dielectric constant, and the dielectric loss tangent at microwave frequencies (for high frequency operation of superconducting circuits) must also be considered. Table 2 lists some common substrate materials utilized for the growth of high  $T_c$  superconductors and their properties, including the room temperature lattice constants, the lattice mismatch<sup>[264]</sup> between these substrates and a (001) oriented  $YBa_2Cu_3O_{7-\delta}$  film,  $(a_{\text{sub}} - a_{\text{film}})/a_{\text{film}}$  at room temperature, the epitaxial relationship, and the approximate thermal expansion coefficient of the substrate between room temperature and 700°C,  $(a_{700^\circ\text{C}} - a_{25^\circ\text{C}})/(a_{25^\circ\text{C}}$  (700 - 25)), where available. Critical current densities at or in excess of  $10^6$  A/cm<sup>2</sup> at 77 K (in self-field) have been achieved in  $YBa_2Cu_3O_{7-\delta}$  films grown on all of the substrates<sup>[103]-[245]-[265]-[267]</sup> and substrate/barrier layer combinations<sup>[260]-[268]-[273]</sup> listed.

Unlike the heteroepitaxial growth of semiconductors, where it is imperative to choose a well lattice-matched substrate in order to avoid undesired dislocations in the grown structures, dislocations in superconductors<sup>[274]</sup> and especially in high  $T_c$  superconductors,<sup>[275]-[276]</sup> are believed to act as effective vortex pinning sites and lead to significantly higher critical current densities. Much higher critical current densities are observed in high  $T_c$  films<sup>[276]</sup> or multilayers<sup>[277]</sup> than in high  $T_c$  single crystals. For example, critical current densities as high as  $8 \times 10^6$  A/cm<sup>2</sup> at

<sup>†</sup> At temperatures less than 1300°C in UHV, the equilibrium vapor pressure of the main decomposition product of  $Al_2O_3$ ,  $Al$ , is less than  $10^{-9}$  torr.<sup>[224]</sup> Higher oxidant pressures stabilize  $Al_2O_3$  from decomposition, allowing it to be employed at even higher temperatures.

77 K (in self-field) have been achieved in  $\text{YBa}_2\text{Cu}_3\text{O}_{7-\delta}$  films[103][27][27] (1.1  $\times 10^7 \text{ A/cm}^2$  in  $\text{YBa}_2\text{Cu}_3\text{O}_{7-\delta}/(\text{Nd,Ce})_2\text{CuO}_4$  superlattices[27]), which is more than an order of magnitude higher than the highest critical current densities measured in  $\text{YBa}_2\text{Cu}_3\text{O}_{7-\delta}$  single crystals.[28] The significantly higher concentration of defects present in films, including in excess of  $10^9$  and perhaps as many as  $10^{11}$  dislocations per  $\text{cm}^2$ , are believed responsible for their improved transport properties.[103][104][27][27] Thus, the relatively large lattice mismatch between high  $T_c$  superconductors and the substrates listed in Table 2 is insufficient reason to dismiss many of them from implementation. Thermal expansion mismatches on the other hand, particularly those that lead to the film being in state of tension upon cooling (i.e., substrates with smaller thermal expansion coefficients), can be a significant problem for these brittle oxide materials and lead to film cracking.

The substrates listed satisfy varying aspects of the above criteria.  $\text{SrTiO}_3$ ,  $\text{LaAlO}_3$ , and  $\text{NdGaO}_3$  have good structural and chemical match to the copper-containing high  $T_c$  superconductors (this is not surprising, since these substrates and the high  $T_c$  superconductors all have perovskite-related structures). The excellent structural and chemical match of  $\text{SrTiO}_3$  to the copper-containing high  $T_c$  superconductors immediately made it the substrate of choice for epitaxial growth and DC transport measurements, and it remains the reference substrate to which growth on other substrates is compared. However, the high dielectric constant and high loss tangent of  $\text{SrTiO}_3$  make it useless for high frequency applications.[239][241][244]. Of the common perovskite substrate materials,  $\text{NdGaO}_3$  has the best lattice match to  $\text{YBa}_2\text{Cu}_3\text{O}_{7-\delta}$ , but the relatively high loss tangent of  $\text{NdGaO}_3$  (an order of magnitude higher than that of  $\text{LaAlO}_3$ ) precludes its use in many microwave applications.[244]  $\text{PrGaO}_3$  has an even better lattice match than  $\text{NdGaO}_3$  to  $\text{YBa}_2\text{Cu}_3\text{O}_{7-\delta}$ , [281] but crack-free and twin-free  $\text{PrGaO}_3$  crystals have only been grown with small diameters (5 mm or less)[282], and the critical current densities of  $\text{YBa}_2\text{Cu}_3\text{O}_{7-\delta}$  films grown on these substrates as well as the low temperature dielectric properties of this substrate have not been reported.  $\text{LaAlO}_3$  has the lowest loss tangent of these perovskite substrates and is currently available in diameters as large as 75 mm.[283] 100 mm diameter  $\text{LaAlO}_3$  wafers will soon be available.[284] These factors make  $\text{LaAlO}_3$  the substrate of choice for high frequency applications of the copper-containing high  $T_c$  superconductors, although a compatible substrate with a significantly lower loss tangent than  $\text{LaAlO}_3$  could significantly improve the performance of high  $T_c$  superconductor films used for high frequency, high Q (highly resonant) applications.[239][244]

Table 2(a). Properties of Common High  $T_c$  Superconductors

High $T_c$ Material	Lattice Constant(s) $\text{\AA}$	Theoretical Expansion (10 $^{-6}/\text{C}$ )	References
(La,Sr) $_2\text{CuO}_4$	$a = 3.779$ $c = 13.23$	11 (a)	226-229
(Nd,Ce) $_2\text{CuO}_4$	$a = 3.95$	14 (c)	60,226
YBa <sub>2</sub> Cu <sub>3</sub> O <sub>7-δ</sub> (123)	$a = 3.820$ $b = 3.885$ $c = 11.68$	11 (a) 13 (b) 11 (c)	230,231
YBa <sub>2</sub> Cu <sub>3</sub> O <sub>7-δ</sub> (123)	$a = 3.857$ $b = 3.857$ $c = 11.82$	10 (a) 10 (b) 21 (c)	230,231
Bi <sub>2</sub> Sr <sub>2</sub> Ca <sub>n-1</sub> Cu <sub>n</sub> O <sub>2n+4</sub>	$\frac{a}{2}$ and $\frac{b}{2}$ $\sqrt{2}$ and $\sqrt{2}$	14 (a and b) 20 (c or n=2) 25 (c or n=3)	56,71,226,232
Tl <sub>2</sub> Ba <sub>2</sub> Ca <sub>n-1</sub> Cu <sub>n</sub> O <sub>2n+4</sub>	$a = 3.83$ to 3.87 $c = 9.64 + n - 13.15$	56,226,230	
(Ba,K) $\text{BiO}_3$	$a = 4.287$	10	233,234

Table 2(b). Properties of Common Substrates for the Growth of High  $T_c$  Superconductors

Substrate Material and Lattice-Matched Constant(s) (hkl)	Lattice Expansion(s) at 25°C	Tilacria Coefficient (10 <sup>-6</sup> /°C)	$\tan \delta$ at 77 K	$E$ at 77 K	In-Plane Orientation Mismatch to $YBa_2Cu_3O_7$	for c-axis Growth $YBa_2Cu_3O_7$	References
STO(001)	$a = 3.905$	11	$1900$	$6 \times 10^{-2}$	1.4 %	$YBa_2Cu_3O_7$ [100] I	13.235-239
LAO(001)	$a = 3.791$	11	16	$8.3 \times 10^{-5}$	-1.6 %	$YBa_2Cu_3O_7$ [100] I	237.239-241
NDGO(001)	$a = 5.427$	12 (a) 6.6 (b)	22 $\varnothing$	$3 \times 10^{-4}$	0.3 %	$YBa_2Cu_3O_7$ [100] I	242.245
NDGO(110)	$a = 5.427$	12 (a) 6.6 (b)	22 $\varnothing$	$3 \times 10^{-4}$	0.9 % (a) 0.6 % (b)	$YBa_2Cu_3O_7$ [110] I NdGaO <sub>3</sub> [001]	242.245
NDGO(110)	$a = 5.427$	12 (a) 6.6 (b)	22 $\varnothing$	$3 \times 10^{-4}$	0.9 % (a) 0.6 % (b)	$YBa_2Cu_3O_7$ [110] I NdGaO <sub>3</sub> [001]	242.245
LaAlO <sub>3</sub> (001)	$a = 5.427$	12 (a) 6.6 (b)	16	$8.3 \times 10^{-5}$	-1.6 %	$YBa_2Cu_3O_7$ [100] I	237.239-241
NDGO(001)	$a = 5.427$	12 (a) 6.6 (b)	22 $\varnothing$	$3 \times 10^{-4}$	0.3 %	$YBa_2Cu_3O_7$ [100] I	242.245
NDGO(001)	$a = 5.427$	12 (a) 6.6 (b)	22 $\varnothing$	$3 \times 10^{-4}$	0.3 %	$YBa_2Cu_3O_7$ [110] I	242.245
Y <sub>2</sub> O <sub>3</sub> -ZrO <sub>2</sub> (001)	$a = 5.138$ (9 mol % Y <sub>2</sub> O <sub>3</sub> ) 10	11	25.4	$7.5 \times 10^{-3}$	-5.7 % 10 -3.5 %	$YBa_2Cu_3O_7$ [110] I $Y_2O_3$ -ZrO <sub>2</sub> [110] I	239.246-248
Y <sub>2</sub> O <sub>3</sub> -ZrO <sub>2</sub> (001)	$a = 5.260$ (60 mol % Y <sub>2</sub> O <sub>3</sub> ) 10	11	25.4	$7.5 \times 10^{-3}$	-4.3 % 10 -2.4 %	$YBa_2Cu_3O_7$ [110] I $Y_2O_3$ -ZrO <sub>2</sub> [100] I	239.246-248
MgO(001)	$a = 4.212$	13	9.6	$4 \times 10^{-5}$	9.3 %	$YBa_2Cu_3O_7$ [100] I	239.248-251

Table 2 (c). Properties of Common Substrate/Barrier-Layer Combinations for the Growth of High  $T_c$  Superconductors

The aromatic hydrocarbons with the lowest boiling points are benzene and toluene. The aromatic hydrocarbons with the highest boiling points are naphthalene and anthracene. The aromatic hydrocarbons with intermediate boiling points are xylene, m-xylene, p-xylene, ethylbenzene, propylbenzene, and isopropylbenzene.

Yttria-stabilized cubic zirconia ( $Y_2O_3-ZrO_2$ ) and  $MgO$  are more economical substrate materials and are widely utilized.  $Y_2O_3-ZrO_2$  reacts with  $YBa_2Cu_3O_{7-\delta}$  to form a thin epitaxial interfacial barrier layer of  $BaZrO_3$ ,<sup>[249][265]</sup> which effectively limits further reaction and degradation of the  $YBa_2Cu_3O_{7-\delta}$  overlayer. However, the high loss tangent of  $Y_2O_3-ZrO_2$  makes it unsuitable for high frequency applications.<sup>[250]</sup>  $MgO$  has reasonable dielectric properties for high frequency applications, but the multiple in-plane epitaxial orientations that often exist in films grown on  $MgO$  and  $Y_2O_3-ZrO_2$ , likely due to the poor lattice match of these substrates with the copper-containing high  $T_c$  superconductors, causes undesirable high angle grain boundaries in the films.<sup>[285][288]</sup> While these grain boundaries are in general undesirable, their controlled introduction has been utilized to prepare Josephson junctions at specific locations for superconducting microelectronics.<sup>[254][289][290]</sup> Note that  $MgO$  is quite well suited to the growth of the high  $T_c$  superconductor  $(Ba,K)BiO_3$ ,<sup>[291][292]</sup> in part due to the significantly larger lattice constants of  $(Ba,K)BiO_3$  compared to the copper-containing high  $T_c$  superconductors.

The favorable dielectric properties of sapphire ( $Al_2O_3$ ) make it the material of choice for high frequency applications, especially when a device structure with a high  $Q$  is desired.<sup>[239]</sup> However, direct growth of high  $T_c$  superconductors on sapphire is plagued by chemical reactions. Several barrier layers, including  $SiTiO_3$ ,<sup>[270]</sup>  $CaTiO_3$ ,<sup>[293]</sup>  $MgO$ ,<sup>[253][268][269]</sup>  $Y_2O_3-ZrO_2$ ,<sup>[255]</sup> and  $CeO_2$ ,<sup>[256][272]</sup> have been successfully implemented to circumvent this reaction. However, the in-plane alignment of high  $T_c$  superconductor films grown on these hybrid substrates is often poor, which is probably a consequence of the poor lattice match between the high  $T_c$  superconductor, the barrier layer, and sapphire. Frequently, several in-plane orientations or a comparatively large mosaic spread in the in-plane orientation is observed.<sup>[270][293]</sup> This results in higher surface resistances<sup>[289]</sup> and lower critical currents.<sup>[285]</sup>  $CeO_2$  and  $CaTiO_3$  barrier layers on sapphire appear to be the most promising, having demonstrated the best in-plane orientation and lowest surface resistance among these barrier layers. The surface resistance at microwave frequencies of  $YBa_2Cu_3O_{7-\delta}$  films grown on these latter barrier layers on sapphire is comparable to the best values obtained on any other substrate (i.e.,  $MgO$  and  $LaAlO_3$ ).<sup>[256][293]</sup>

## 2.10 Integration with Semiconductors

The integration of high  $T_c$  layers with Si {100} is clearly desirable considering that silicon is the workhorse of modern semiconductor technology, is available as large area wafers of unequalled perfection, and is inexpensive. However, despite its relatively good lattice match with the copper-containing high  $T_c$  superconductors, its successful use as a substrate remains elusive. The growth of copper-containing high  $T_c$  superconductors directly on silicon results in an interface reaction and significant diffusion tails into both materials,<sup>[290][295]</sup> even when moderate ( $T \leq 650^\circ C$ ) growth or annealing temperatures are used.<sup>[125][296][298]</sup> Although these materials are chemically incompatible, making direct integration impossible, suitable barrier layers have been found. The large amount of previous work on silicon-on-insulator technology,<sup>[299][300]</sup> coupled with the excellent lattice match between the copper-containing high  $T_c$  superconductors and Si {100}, simplifies the search for suitable barrier layers. For example, Si {100} has been found to grow epitaxially on  $Al_2O_3$  (1102),<sup>[301]</sup>  $MgAl_2O_4$  {100},<sup>[302]</sup> and  $Y_2O_3-ZrO_2$  {100}.<sup>[303]</sup> Additionally, the technology has been developed to grow these oxides on silicon,<sup>[259][304]-[309]</sup> making it, in principle, possible to move back and forth between silicon and epitaxial high  $T_c$  superconductors in heterostructures. The use of buffer layers between silicon and  $YBa_2Cu_3O_{7-\delta}$ , and in particular the use of  $Y_2O_3-ZrO_2$ ,<sup>[260]</sup> has allowed the fabrication of epitaxial  $YBa_2Cu_3O_{7-\delta}$  films with high critical current densities to be fabricated on silicon. Other buffer layers including  $MgO$ ,<sup>[6]</sup>  $MgAl_2O_4$ ,<sup>[310]</sup> and  $CeO_2$ ,<sup>[311]-[313]</sup> are significant improvements over the direct growth of high  $T_c$  superconductors on silicon substrates, but only  $Y_2O_3-ZrO_2$  buffer layers have allowed critical current densities in excess of  $10^6$  A/cm<sup>2</sup> at 77 K to be achieved in high  $T_c$  superconductor films. However, the large difference in thermal expansion coefficient between silicon and the copper-containing high  $T_c$  superconductors remains a significant problem. This thermal expansion problem is not nearly as severe for epitaxial high  $T_c$  superconductor films grown on silicon-on-sapphire, where crack-free  $YBa_2Cu_3O_{7-\delta}$  films more than eight times thicker than the onset of cracking for such films on silicon substrates ( $\sim 500 \text{ \AA}$ )<sup>[280]</sup> have been grown and have excellent critical current densities ( $4.6 \times 10^6$  A/cm<sup>2</sup> at 77 K for a 1300 Å thick film).<sup>[314]</sup> In light of the desirable high frequency properties of sapphire substrates and the progress that has been made in integrating them with high  $T_c$  superconductors, sapphire substrates may be the best substrate choice for monolithic superconductor-

semiconductor electronics. A significant step in this direction is the recent demonstration that functional silicon-based semiconductor circuitry and high  $T_c$  superconductor electronics can be fabricated on the same sapphire substrate.<sup>[315]</sup>

The integration of high  $T_c$  superconductor layers with GaAs and III-V materials is also highly desirable from a hybrid monolithic microwave integrated circuit (MMIC) standpoint. An MgO barrier layer has been found to work well for GaAs.<sup>[263]</sup> Not only are the properties of the superconductors grown on such barrier layers quite encouraging, but experiments have shown only minor degradation of III-V heterostructures (e.g., a two-dimensional electron gas 1200 Å below the MgO interface) after the growth of high  $T_c$  layers on top of these heterostructures.<sup>[316]</sup> Critical current densities as high as  $1.2 \times 10^6$  A/cm<sup>2</sup> at 77 K have been achieved with YBa<sub>2</sub>Cu<sub>3</sub>O<sub>7- $\delta$</sub> /MgO/GaAs films.<sup>[273]</sup> Because of the higher thermal expansion coefficient of GaAs compared to silicon, crack-free YBa<sub>2</sub>Cu<sub>3</sub>O<sub>7- $\delta$</sub>  films may be prepared up to a thickness about five times greater ( $\approx 2500$  Å)<sup>[317]</sup> than on silicon substrates.

### 3.0 SPECIFIC HIGH $T_c$ MATERIALS AND DEMONSTRATED SYNTHESIS CAPABILITIES

Despite significant improvements in the capabilities of the MBE technique for the growth of high  $T_c$  superconductor films, it must be noted that the films exhibiting the best transport properties have *not* been produced by MBE. Rather, the films with the highest transition temperatures and highest critical currents have been produced by PLD and sputtering.<sup>[103][277][279]</sup> Nor has MBE led to the discovery of new higher  $T_c$  superconductor materials; indeed it is bulk synthesis techniques which continue to provide such advances. The strength of the MBE technique is, in the opinion of the authors, not to duplicate what can be made by bulk techniques nor single target thin film synthesis methods, which are free from the multiple source composition control issues of MBE, but instead to provide a customized layering capability with control at the atomic layer level for the synthesis of metastable structures and device heterostructures. This is not to say that high  $T_c$  superconductor phases that may be readily produced by single target techniques, e.g., YBa<sub>2</sub>Cu<sub>3</sub>O<sub>7- $\delta$</sub> , are of poor quality when synthesized by MBE, but rather that for such a simple structure (a thick film of YBa<sub>2</sub>Cu<sub>3</sub>O<sub>7- $\delta$</sub> ) the capabilities of MBE are not

needed and that other (more economical) synthesis techniques would be more appropriate. For example, the highest critical current densities ( $J_c$ ) observed in ReBa<sub>2</sub>Cu<sub>3</sub>O<sub>7- $\delta$</sub>  films (where Re is Y or a rare earth) prepared by MBE are  $4 \times 10^6$  A/cm<sup>2</sup> at 77 K,<sup>[90][318]</sup> compared to  $8 \times 10^6$  A/cm<sup>2</sup> at 77 K which has been obtained in films grown by PLD and sputtering.<sup>[103][278][279]</sup> Just as a thick semiconductor layer requiring high mobility and excellent optical properties would be better grown by LPE, for example, than by MBE, only certain high  $T_c$  structures are appropriate for and warrant the use of MBE. MBE is best suited to structures requiring its layering control and in-situ diagnostic capabilities, and structures for which such layering control would yield a significant improvement in device performance or theoretical understanding. In the examples described below, we highlight the progress of the MBE technique toward customized growth. It is hoped that with continued advances, particularly in composition control, that the customized layering capability of MBE may be adequately exploited to allow the physics and device potentials of new layered structures that cannot be produced by bulk methods, including higher  $T_c$  superconductors, to be explored.

#### 3.1 ReBa<sub>2</sub>Cu<sub>3</sub>O<sub>7- $\delta$</sub>

ReBa<sub>2</sub>Cu<sub>3</sub>O<sub>7- $\delta$</sub>  superconducting films, where Re is Y,<sup>[45][92][97][132][165][188]</sup> Nd,<sup>[173]</sup> Sm,<sup>[170]</sup> and Dy<sup>[90][169]</sup> with acceptable transport properties have been grown by numerous groups using MBE. Notable among this research is the synthesis of DyBa<sub>2</sub>Cu<sub>3</sub>O<sub>7- $\delta$</sub>  films with  $T_c$ 's as high as 92 K and  $J_c$ 's (77 K, self-field) as high as  $4 \times 10^6$  A/cm<sup>2</sup> with a pressure at the substrate surface of about  $4 \times 10^{-6}$  torr, using ozone.<sup>[90]</sup> YBa<sub>2</sub>Cu<sub>3</sub>O<sub>7- $\delta$</sub>  films of similar quality have been produced by MBE using an atomic oxygen source with a pressure at the substrate surface of about  $1.5 \times 10^{-4}$  torr using an oxygen plasma source.<sup>[152]</sup>

In-situ RHEED analysis and RHEED oscillations have been used extensively during the MBE growth of these materials, allowing the thickness of the growth unit to be measured<sup>[90][168][173][191][320]</sup> as well as the in-plane orientation relationship.<sup>[18][42][46][90][94][174][204][321]</sup> lattice constant relaxation process,<sup>[45]</sup> and the formation of impurity phases<sup>[94][204]</sup> to be monitored. During the growth of ReBa<sub>2</sub>Cu<sub>3</sub>O<sub>7- $\delta$</sub>  film by codeposition, the periodicity of the RHEED oscillations corresponds to a layer thickness equal to the *c*-axis dimension of the unit cell for films oriented with their *c*-axis normal to the plane of the substrate<sup>[90][168][173][319]</sup> (confirming the

result that was first observed using RHEED oscillations during reactive evaporation<sup>[102]</sup> and a layer thickness equal to the  $a$ -axis dimension of the unit cell for films oriented with their  $a$ -axis perpendicular to the plane of the substrate.<sup>[320]</sup> The pristine surfaces prepared by MBE have been analyzed in-situ by low-energy ion scattering spectroscopy (LEISS) to establish that the surfaces of codeposited  $\text{YBa}_2\text{Cu}_3\text{O}_{7-\delta}$  films are terminated by the CuO chain layer.<sup>[321]</sup> This, together with the RHEED oscillation results, implies that the minimum growth unit during codeposition of  $\text{ReBa}_2\text{Cu}_3\text{O}_{7-\delta}$  phases is ( $\text{BaO}\text{-CuO}_2\text{-Re-CuO}_2\text{-BaO}$ ), with CuO at the film surface, or in terms of building layers, ( $\text{-BaO}\text{-}[\text{CuO}_2]\text{-}[\text{Re}\text{-}[\text{CuO}_2]\text{-}[\text{BaO}\text{-CuO}]$ ), where the ( $\text{BaO}\text{-CuO}\text{-BaO}$ ) building layer is split after the CuO chain layer. The step heights revealed by STM measurements on surfaces of MBE-grown  $\text{DyBa}_2\text{Cu}_3\text{O}_{7-\delta}$  films correspond to the periodicity of the RHEED oscillations (the minimum growth unit) and also indicate the presence of a high density ( $\sim 10^9 \text{ cm}^{-2}$ ) of screw dislocations.<sup>[90][319]</sup> Such densities have been seen in MBE films grown on  $\text{SrTiO}_3$  {100}, {100}[319]  $\text{MgO}$  {100}, [90] and  $\text{NdGaO}_3$  {100}.<sup>[90]</sup> These defect sites are not specific to MBE-grown films, but have also been reported in  $\text{ReBa}_2\text{Cu}_3\text{O}_{7-\delta}$  films grown by sputtering,<sup>[103][104][322]</sup> PLD,<sup>[322][323]</sup> reactive evaporation,<sup>[324]</sup> and CVD.<sup>[325]</sup> The presence of such a high density of screw dislocations is a common feature of the growth of  $\text{ReBa}_2\text{Cu}_3\text{O}_{7-\delta}$  films by gas phase codeposition methods on oriented substrates.<sup>[326]</sup> The resulting well-known spiral growth mechanism, first proposed by Frank,<sup>[327]</sup> occurs quite frequently in the growth of layered materials.<sup>[328][329]</sup> A consequence of this growth mechanism is that the film surfaces are not atomically flat; instead, the surfaces consist of mounds, each about 300 nm in diameter and each containing a screw dislocation at its center. The surface roughness depends on growth conditions, but height variations of 50–100 Å from the top of each mound to its intersection with the neighboring mound are fairly typical in MBE films.<sup>[90]</sup> Studies by other gas phase codeposition techniques (sputtering<sup>[322]</sup> and PLD<sup>[330]</sup>) have shown that, if the substrate is misoriented sufficiently (typically a few degrees for the growth of  $\text{YBa}_2\text{Cu}_3\text{O}_{7-\delta}$  films), a high density of screw dislocations is not nucleated, and instead growth occurs by step propagation of the terraces, which accommodate the tilt of the substrate and are energetically favorable incorporation sites. Detailed studies on the surface morphology of films grown by sequential/ deposition methods are needed to ascertain how such growth conditions impact the minimum growth unit compared to the more widespread use of codeposition.

Device structures utilizing MBE-grown  $\text{ReBa}_2\text{Cu}_3\text{O}_{7-\delta}$  superconductors have been made, but such structures have made use of lateral (in-plane) boundaries (edge junctions),<sup>[331][332]</sup> which rely on differences in epitaxy at a patterned edge, rather than making use of the layering capability of MBE. Similar device structures can be (and have been) made equally well by other thin film deposition techniques, and will not be discussed here. Attempts to grow vertical Josephson junctions using the layering capability of MBE have met with limited success, presumably due to pinholes in the thin insulator layer.<sup>[1][3]</sup>

In general, the layering capability of MBE has not been extensively utilized in the growth of high  $T_c$  structures containing  $\text{ReBa}_2\text{Cu}_3\text{O}_{7-\delta}$  phases. However, one notable example demonstrates the significant difference that shuttered MBE can have on the growth of  $\text{ReBa}_2\text{Cu}_3\text{O}_{7-\delta}$  superconductor phases, and has allowed them to be synthesized at much lower temperatures than can be achieved by other techniques. Utilizing sequential deposition, superconducting  $\text{DyBa}_2\text{Cu}_3\text{O}_{7-\delta}$  films with their  $c$ -axis normal to the plane of the substrate ( $c$ -axis oriented) have been prepared by MBE at substrate temperatures as low as 420°C.<sup>[158]</sup> Codeposition of the constituent species under the same conditions results in an amorphous film,<sup>[334]</sup> whereas shuttering the incident fluxes in the same order as the  $c$ -axis order of the building layers produces a  $c$ -axis oriented film.<sup>[158]</sup> It is well established from a variety of gas phase synthesis techniques that in order to attain  $c$ -axis oriented  $\text{ReBa}_2\text{Cu}_3\text{O}_{7-\delta}$  films by codeposition, high temperatures (typically exceeding about 650°C) are needed.<sup>[31][335][336]</sup> Lower temperatures result in films with their  $a$ -axis normal to the plane of the substrate<sup>[3][335][337]</sup> ( $a$ -axis oriented), until below about 500°C, where crystallization of the  $\text{ReBa}_2\text{Cu}_3\text{O}_{7-\delta}$  phase is no longer observed.<sup>[338]</sup> This is just one example of the layering (and in this case orientation) control achievable using shuttered MBE.

### 3.2 $\text{Bi}_2\text{Sr}_2\text{Ca}_{n-1}\text{Cu}_n\text{O}_{2n+4}$

In contrast to the MBE growth of  $\text{ReBa}_2\text{Cu}_3\text{O}_{7-\delta}$  high  $T_c$  superconductor phases, where little use has been made of shuttering, shuttering has been extensively used in the growth of  $\text{Bi}_2\text{Sr}_2\text{Ca}_{n-1}\text{Cu}_n\text{O}_{2n+4}$  phases.<sup>[88][91][130][154][160][161][171][172][175][339][348]</sup> As described in Sec. 1.4, bulk methods have only been capable of synthesizing  $\text{Bi}_2\text{Sr}_2\text{Ca}_{n-1}\text{Cu}_n\text{O}_{2n+4}$  phases in single phase form for  $n = 1$  to 3, presumably due to the nearly degenerate formation energies of higher  $n$  members of this homologous

series. Using shuttered MBE growth, single phase  $\text{Bi}_2\text{Sr}_2\text{Ca}_{n-1}\text{Cu}_n\text{O}_{2n+4}$  films, for  $n = 1$  to 11, have been grown, [130][34] demonstrating the ability of this technique to select between nearly energetically degenerate phases. In Fig. 22, 0-20° x-ray diffraction scans of as-grown,  $c$ -axis oriented, epitaxial  $\text{Bi}_2\text{Sr}_2\text{Ca}_{n-1}\text{Cu}_n\text{O}_{2n+4}$  films are shown for  $n = 1$  to 5.[130] The corresponding  $\text{Bi}_2\text{Sr}_2\text{Ca}_{n-1}\text{Cu}_n\text{O}_{2n+4}$  structures are shown in Fig. 10. Cross-sectional TEM has confirmed the layered nature of these films, shown  $b$ -axis superstructure, and revealed the presence of stacking faults in the films.[89][339] Atomic force microscopy (AFM) scans over  $0.5 \mu\text{m} \times 0.5 \mu\text{m}$  regions of the film surface have revealed a surface roughness of less than  $10 \text{ \AA}$ .[349] Superconducting films with as-grown zero resistance temperatures as high as  $90 \text{ K}$  [172] and  $J_c$ 's ( $4.2 \text{ K}$ , self-field) exceeding  $2 \times 10^7 \text{ A/cm}^2$  have been grown by shuttered MBE.[172] The success of the MBE growth of  $\text{Bi}_2\text{Sr}_2\text{Ca}_{n-1}\text{Cu}_n\text{O}_{2n+4}$  phases with sub-unit-cell layering precision has allowed the growth of metastable phases, ordered superlattices, and device heterostructures, which are described in Secs. 3.5, 3.6, and 3.7.

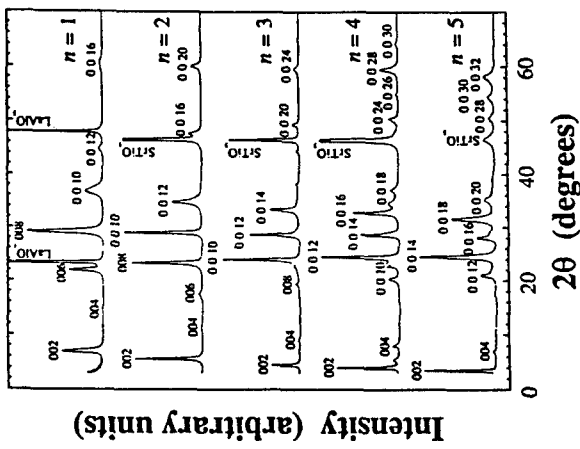


Figure 22. 0-20° x-ray diffraction scans of as-grown, single phase,  $c$ -axis oriented, epitaxial  $\text{Bi}_2\text{Sr}_2\text{Ca}_{n-1}\text{Cu}_n\text{O}_{2n+4}$  films (after Ref. 130) with  $n = 1$  to 5.

In-situ RHEED provides direct monitoring of the effect that supplying the constituent elements in different ways to the substrate during the growth of  $\text{Bi}_2\text{Sr}_2\text{Ca}_{n-1}\text{Cu}_n\text{O}_{2n+4}$  phases has on surface structure. A sequence of RHEED patterns is shown in Fig. 23 from the shuttered growth of a  $\text{Bi}_2\text{Sr}_2\text{CaCu}_2\text{O}_8$  film, where the cation fluxes were supplied individually in the same order as the building layers making up the structure (i.e.,  $\text{Bi-Sr-Cu-Ca-Cu-Sr-Bi, ...}$ ) and ozone was supplied continuously.[130] Figure 23(a) shows the bare  $\text{MgO}$  {100} substrate before growth. Figures 23(b) to 23(f) show the RHEED patterns during the growth of a half unit cell of  $\text{Bi}_2\text{Sr}_2\text{CaCu}_2\text{O}_8$  (from the bismuth layer completing the 28<sup>th</sup> half unit cell to that completing the 29<sup>th</sup> half unit cell). The streaked patterns observed after the deposition of the bismuth atoms [Fig. 23(b) and Fig. 23(f)] and the presence of spots in the other photos indicate that the surface is smoothest after the bismuth layers which complete each half unit cell, and that, within the growth of each half unit cell, islands (as schematically indicated in Fig. 16) are present. The pattern of spots in the RHEED pattern is consistent with the oriented presence of islands of the  $\text{Sr}_6\text{Bi}_2\text{O}_9$  phase.[350][351] Since only the  $\text{Bi}_2\text{Sr}_2\text{CaCu}_2\text{O}_8$  phase was observed by x-ray diffraction after growth, and SEM images of the surface did not indicate the presence of a second phase after growth, it was concluded that the  $\text{Sr}_6\text{Bi}_2\text{O}_9$  phase was only temporarily formed during the shuttered growth process; with the completion of each half unit cell, it is transformed into  $\text{Bi}_2\text{Sr}_2\text{CaCu}_2\text{O}_8$ .[130] The temporary formation of the  $\text{Sr}_6\text{Bi}_2\text{O}_9$  phase is believed to be the way that the surface adjusts to becoming strontium rich after the deposition of each strontium burst,[130] since  $\text{Sr}_6\text{Bi}_2\text{O}_9$  is the most strontium-rich  $\text{Bi-Sr-O}$  phase (see Fig. 8).[68][351] The streaked pattern observed after the completion of each half unit cell indicates that shuttered MBE is effective in layering on a half unit cell by half unit cell basis. The islanding of other phases on a temporary basis during the shuttered growth of  $\text{Bi}_2\text{Sr}_2\text{Ca}_{n-1}\text{Cu}_n\text{O}_{2n+4}$  phases, including  $\text{SrO}$  and  $\text{CaO}$ ,[172] has also been seen. As one might expect, the interplay between growth conditions and surface structure is significant, and a distinct advantage of MBE is the ability to explore this interplay in a controlled manner, since the growth conditions (substrate temperature, depositing fluxes, and flux sequence) may be controlled independently.

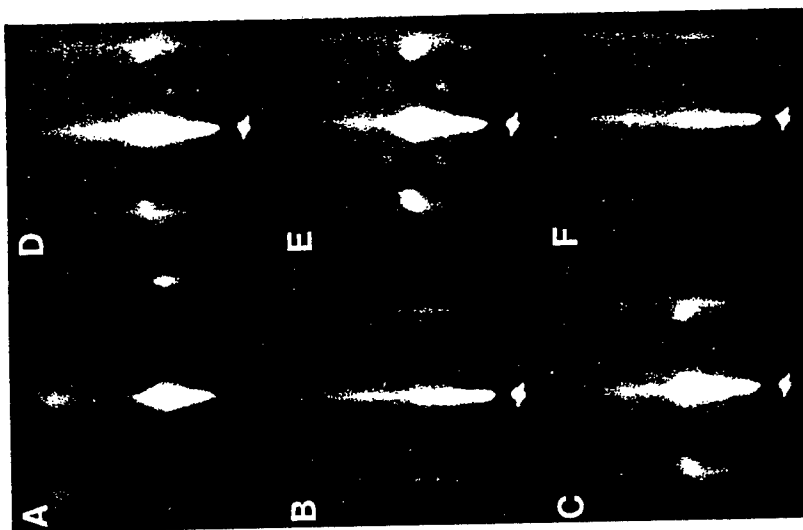
In order to achieve layering control on a finer scale than a half unit cell, it is necessary to find growth conditions which maintain a smooth surface at all times during the deposition of the building layers. This is easily studied in-situ using RHEED, or even more sensitively, using a

recently developed technique called difference RHEED,<sup>[345]</sup> in which a digitally stored RHEED image is subtracted from the current RHEED image in order to discern more sensitively the effects that the species deposited in the time between the two RHEED images have had on the surface structure.<sup>[345]</sup> This technique has been applied in real time to the growth of  $\text{Bi}_2\text{Sr}_2\text{Ca}_{n-1}\text{Cu}_n\text{O}_{2n+4}$  phases in order to monitor their smoothness.<sup>[345]</sup>

Growth conditions that discourage the temporary formation of islands during the growth of  $\text{Bi}_2\text{Sr}_2\text{Ca}_{n-1}\text{Cu}_n\text{O}_{2n+4}$  phases have been found. One method is to shutter the oxidant in addition to the cation species.<sup>[94][339]</sup> Decreasing the ozone pressure during the strontium flux burst was found to result in a streaked RHEED pattern throughout the shuttered growth of  $\text{Bi}_2\text{Sr}_2\text{CuO}_6$  films. This effect has been attributed to interplay between the incident oxidant flux and the surface mobility of the adatoms on the substrate surface.<sup>[94][339]</sup> When considered individually, the oxidation requirements of the constituent monolayers are significantly different,<sup>[108]</sup> so it is not surprising that modulation of the oxidant flux during growth may be beneficial. Shuttering the oxidant during the MBE growth of high  $T_c$  superconductors is quite analogous to the MEE growth of III-V compound semiconductors,<sup>[108]</sup> where the group III species are deposited in the absence of the group V species, resulting in a drastic increase in the surface mobility of the group III species.<sup>[108]</sup> Modulation of the oxidant flux, in addition to the cation fluxes, has been explored by several groups for the growth of  $\text{Bi}_2\text{Sr}_2\text{Ca}_{n-1}\text{Cu}_n\text{O}_{2n+4}$  phases.<sup>[94][160][161][175][339][346]</sup> In some cases, the substrate temperature has also been modulated,<sup>[160][161][175][346]</sup> demonstrating the extreme flexibility and range of growth conditions accessible with the MBE technique, and allowing  $\text{Bi}_2\text{Sr}_2\text{Ca}_{n-1}\text{Cu}_n\text{O}_{2n+4}$  phases to be formed at substrate temperatures as low as 300°C.<sup>[160][161][175]</sup> Avoiding the temporary formation of islands by modulating the ozone flux has allowed a superconducting metastable  $\text{Bi}_2\text{Sr}_3\text{Cu}_2\text{O}_8$  high  $T_c$  superconductor phase to be prepared by MBE, which is described in Sec. 3.7.

Another method of deterring the formation of islands during shuttered growth is to codeposit several of the constituent monolayers. For example, codepositing the calcium and copper fluxes has been used to eliminate the temporary formation of islands during the shuttered growth of  $\text{Bi}_2\text{Sr}_2\text{Ca}_{n-1}\text{Cu}_n\text{O}_{2n+4}$  phases, in which the other cation fluxes are individually supplied under a continuous flux of ozone.<sup>[172][341]</sup> However, as more of the constituent species are codeposited, the layering control of the MBE process is diminished and eventually reaches the half unit cell level when all of the  $\text{Bi}_2\text{Sr}_2\text{Ca}_{n-1}\text{Cu}_n\text{O}_{2n+4}$  constituents are codeposited, as has been established by RHEED oscillation measurements during codeposition.<sup>[352][353]</sup>

**Figure 23.** RHEED patterns observed along the  $\text{MgO} <100>$  azimuth during the growth of a  $\text{Bi}_2\text{Sr}_2\text{CaCu}_2\text{O}_8$  ( $n=2$ ) film on  $\text{MgO}$  {100} at  $T_{\text{sub}} \approx 650^\circ\text{C}$  (after Ref. 130). The shuttering sequence for each half unit cell was Sr-Cu-Ca-Cu-Sr-Bi, with ozone on continuously. (a) Bare  $\text{MgO}$  {100} substrate before growth. (b) After the  $\text{Bi}$  layer completing the 28<sup>th</sup> half unit cell. (c) After the first  $\text{Sr}$  layer of the 29<sup>th</sup> half unit cell. (d) After a  $\text{Cu}$  layer of the 29<sup>th</sup> half unit cell. (e) After the second  $\text{Sr}$  layer of the 29<sup>th</sup> half unit cell. (f) After the  $\text{Bi}$  layer completing the 29<sup>th</sup> half unit cell.



### 3.3 $\text{Ti}_2\text{Ba}_2\text{Ca}_{n-1}\text{Cu}_n\text{O}_{2n+4}$

Largely because of their toxicity, thin film research on the  $\text{TiBa}_2\text{Ca}_{n-1}\text{Cu}_n\text{O}_{2n+3}$  and  $\text{Ti}_2\text{Ba}_2\text{Ca}_{n-1}\text{Cu}_n\text{O}_{2n+4}$  phases has been relatively limited.

These materials have not been grown by MBE and only recently has their in-situ preparation been realized.<sup>[354]-[356]</sup> The pressures,  $\approx 200$  mtorr,<sup>[355]</sup> used in their in-situ growth by a combination of PLD<sup>[355]</sup> or sputtering<sup>[356]</sup> of Ba-Ca-Cu-O with simultaneous thermal evaporation of  $Tl_2O$  are well above the MBE regime, but the minimum oxygen pressure needed to stabilize these phases has not been measured. However, the oxygen pressure at which  $Tl_2Ba_2Ca_2Cu_3O_{10}$  decomposes into  $Tl_2Ba_2CaCu_2O_8$  has been measured as a function of temperature and oxygen pressure,<sup>[357]</sup> providing some hope that it may be possible to synthesize  $Tl_2Ba_2Ca_2Cu_3O_{10}$  under MBE conditions using an effective oxidant.

### 3.4 (Ba,K)BiO<sub>3</sub>

The growth of (Ba,K)BiO<sub>3</sub> and (Ba,Rb)BiO<sub>3</sub> have been extensively studied by MBE.<sup>[115]-[117][189][291][292]</sup> The simple cubic perovskite structure, comparatively long coherence length (longest of the high  $T_c$  superconductors), low number of constituents, and extremely low growth temperatures (typically 300°C) make this an obvious model system for study. In addition, MBE growth conditions in which the K (or Rb) and O incorporation are adsorption-controlled have been found.<sup>[115]</sup> This greatly simplifies the composition control requirements, since it becomes only necessary to control the barium and bismuth fluxes. Despite its comparatively low  $T_c$ , the excellent demonstrated properties of (Ba,K)BiO<sub>3</sub> and (Ba,Rb)BiO<sub>3</sub> Josephson junctions make this materials system a serious contender for future applications of high  $T_c$  superconductors in microelectronics, particularly for superconductor-insulator-superconductor (SIS) mixers. Metal-base transistors utilizing (Ba,Rb)BiO<sub>3</sub> as the metallic base layer have also been made by MBE.<sup>[358]</sup> Initial results indicate a common-base current gain,  $\alpha$ , near unity for these structures, which is a significant improvement over metal-base transistors made from conventional metals and semiconductors.<sup>[258]</sup>

Since it is the only 3-dimensional high  $T_c$  superconductor, it is of fundamental interest to study the effect of dimensional confinement on the superconducting properties of (Ba,K)BiO<sub>3</sub>. One method of accomplishing this would be to use the unit cell layering precision of MBE to intersperse barrier layers into (Ba,K)BiO<sub>3</sub> at controlled intervals. Dimensionality issues have been widely studied for several of the 2-dimensional copper-containing high  $T_c$  superconductors through the use of superlattices, in which non-superconducting layers separate the superconducting ones.<sup>[341]-[342]</sup> However, such studies by controlled thin film methods have not been performed on the 3-dimensional (Ba,K)BiO<sub>3</sub> superconductor. Bulk synthesis methods have been used to investigate the effect of reduced dimensionality on these materials through the synthesis of (Ba,K)<sub>n+1</sub>(Pb,Bi)<sub>n</sub>O<sub>3n+1</sub> phases.<sup>[76][359]-[361]</sup> These are layered structures in which (Ba,K)O layers occur between every  $n$  perovskite layers. However, the scope of these bulk studies has been severely limited both because of the presence of uncontrolled intergrowths for higher  $n$  and the restricted range of solid solution between the constituents.<sup>[76][359]-[361]</sup> Only the  $n=1$ ,  $n=2$ , and  $n=\infty$  members of this homologous series of compounds have been prepared in single phase form;<sup>[359]-[361]</sup> the  $n=3$  structure has been observed locally by TEM, intergrown with higher  $n$  compounds in an uncontrolled manner.<sup>[76]</sup> The layering control and site-selective doping capabilities of MBE are probably well suited to studying these materials.

### 3.5 Superlattices

Both ordered and disordered superlattices have been prepared by shuttered MBE,<sup>[94][130]</sup> although the latter were not deliberately prepared, but resulted from inadequate composition control.<sup>[88][94]</sup> An example of each will be discussed since other thin film techniques have also attempted to make ordered  $Bi_2Sr_2Ca_{n-1}Cu_nO_{2n+4}$  superlattices, thus providing an opportunity to compare the custom-layering capability of MBE with other techniques.

In order to interpret the x-ray diffraction patterns from  $Bi_2Sr_2Ca_{n-1}Cu_nO_{2n+4}$  superlattices, it is useful to compare the observed patterns to two limiting case simulations: an ideal superlattice (perfect building layer ordering) and completely disordered layering consisting of a random stacking sequence of the constituent building layers. These limiting cases are shown schematically in Fig. 24.

The x-ray diffraction theory necessary to perform these simulations is well established. The perfectly ordered superlattice can be simulated by standard kinematic diffraction theory,<sup>[362]</sup> where the diffracted intensity due to all of the cations in the ideal superlattice is appropriately summed,

<sup>†</sup> These devices are operated at temperatures above  $T_c$ , and thus do not utilize the superconducting properties of these oxides, but rather utilize their low carrier concentrations (typically  $5 \times 10^{21} cm^{-3}$  for high  $T_c$  superconductors), which are more than an order of magnitude lower than those of conventional metals.<sup>[358]</sup>

$\text{SrO}$ ] without oxygen, where the distance between these identical layers takes on distinct values, but for which the sequence of the spacings is random. For example, a randomly layered mixture of  $\text{Bi}_2\text{Sr}_2\text{CaCu}_2\text{O}_8$  and  $\text{Bi}_2\text{Sr}_2\text{Ca}_3\text{O}_{10}$  layers contains two distinct interlayer distances: half the  $c$ -axis length of  $\text{Bi}_2\text{Sr}_2\text{CaCu}_2\text{O}_8$  and half the  $c$ -axis length of  $\text{Bi}_2\text{Sr}_2\text{Ca}_2\text{Cu}_3\text{O}_{10}$ .<sup>[94]</sup>

Several groups have reported unusual x-ray patterns from  $\text{Bi-Sr-Ca-Cu-O}$  films grown by sputtering,<sup>[365][366]</sup> shuttered ion beam sputtering,<sup>[366]</sup> laser ablation,<sup>[367][368]</sup> and shuttered MBE.<sup>[88]</sup> The growth of superlattices was not attempted in these growths, so the strange x-ray patterns observed were at first not understood. Although their  $c$ -axis lengths and peak intensity distributions are similar to  $\text{Bi}_2\text{Sr}_2\text{Ca}_{n-1}\text{Cu}_n\text{O}_{2n+4}$  phases, the diffraction patterns do not correspond to any of the known  $\text{Bi}_2\text{Sr}_2\text{Ca}_{n-1}\text{Cu}_n\text{O}_{2n+4}$  phases. A least squares estimate of the  $c$ -axis length based on the peak positions results in values in between those of the known  $\text{Bi}_2\text{Sr}_2\text{Ca}_{n-1}\text{Cu}_n\text{O}_{2n+4}$  phases. Further, indexing the peaks to these intermediate lattice constants requires the use of both even and odd  $00\ell$  peaks. Due to the glide plane half way up the unit cell of all known  $\text{Bi}_2\text{Sr}_2\text{Ca}_{n-1}\text{Cu}_n\text{O}_{2n+4}$  structures, destructive interference results in the absence of all odd  $00\ell$  peaks, making the observed x-ray patterns quite unusual.

The repeated layering of a half unit cell of  $\text{Bi}_2\text{Sr}_2\text{CaCu}_2\text{O}_8$  followed by a half unit cell of  $\text{Bi}_2\text{Sr}_2\text{Ca}_2\text{Cu}_3\text{O}_{10}$  results in a new unit cell with  $c$ -axis length halfway between that of  $\text{Bi}_2\text{Sr}_2\text{CaCu}_2\text{O}_8$  and  $\text{Bi}_2\text{Sr}_2\text{Ca}_2\text{Cu}_3\text{O}_{10}$ . Since this ordered layering no longer contains a glide plane halfway up the unit cell, both even and odd  $00\ell$  x-ray diffraction peaks would be allowed. So one possibility is that the unusual x-ray patterns observed are due to an ordered superstructure of  $\text{Bi}_2\text{Sr}_2\text{Ca}_{n-1}\text{Cu}_n\text{O}_{2n+4}$  phases.

To test this explanation, the x-ray diffraction pattern of a hypothetical  $c$ -axis oriented  $\text{Bi}_4\text{Sr}_4\text{Ca}_3\text{Cu}_5\text{O}_{18}$  phase film ( $\text{Bi}_2\text{Sr}_2\text{CaCu}_2\text{O}_8 + \text{Bi}_2\text{Sr}_2\text{Ca}_2\text{Cu}_3\text{O}_{10}$ ) was calculated. Another possibility is that a random mixture of  $\text{Bi}_2\text{Sr}_2\text{CaCu}_2\text{O}_8$  and  $\text{Bi}_2\text{Sr}_2\text{Ca}_3\text{O}_{10}$  layers is present in such samples and so the x-ray patterns of  $c$ -axis oriented random mixtures of  $\text{Bi}_2\text{Sr}_2\text{CaCu}_2\text{O}_8$  and  $\text{Bi}_2\text{Sr}_2\text{Ca}_2\text{Cu}_3\text{O}_{10}$  layers in various proportions were also simulated. The simulated diffraction patterns are shown in Fig. 25 and Fig. 26. The most intense peaks of both the ordered and disordered layer lattice simulations lie at similar 20 positions. Comparison to the observed x-ray diffraction patterns requires consideration of more subtle aspects of the simulated patterns. The ordered superlattice contains more peaks, while the randomly layered mixture exhibits periodic broadening

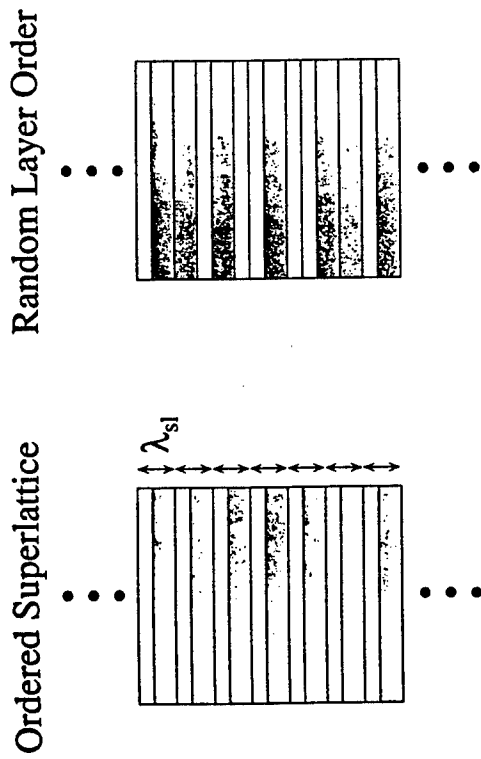


Figure 24. A schematic representation of the layering sequences of two limiting-case x-ray diffraction simulations. The perfectly ordered superlattice has regular repeat periodicity  $\lambda_{SL}$ , while the random layering sequence does not.

including the isotropic temperature factors and the Lorentz polarization factor.<sup>[94]</sup> For simplicity, flat idealized building layers free of vacancies, cation substitution, and incommensurate superstructure are assumed, and the oxygen atoms in these structures as well as x-ray absorption effects are disregarded. These simplifying assumptions allow qualitative comparisons to the observed x-ray diffraction patterns to be readily made, whereas accurate quantitative modeling of the patterns requires far more knowledge of the structure, strain, and site substitution actually present in these films, as opposed to their bulk counterparts. The completely disordered superlattice can be simulated using the theory of Hendricks and Teller<sup>[363]</sup> which applies to an infinitely thick, one-dimensional layer lattice with a random stacking sequence. For simplicity, scattering from the light atoms in these structures (oxygen, copper, and calcium) is disregarded. Since the atomic scattering factor,  $f_i$ , increases with atomic number, this is not a bad approximation since most of the scattering is due to the bismuth and strontium atoms in  $\text{Bi}_2\text{Sr}_2\text{Ca}_{n-1}\text{Cu}_n\text{O}_{2n+4}$  phases. The problem then reduces to scattering from only one type of building layer, [SrO-BiO-

and narrowing of the peak width as a function of diffraction vector. The observed patterns do not contain the extra peaks which should be present for an ordered sequence of the layers. Further, low-angle x-ray diffraction studies do not reveal the 001 or 003 peaks expected from the ordered layer simulation.<sup>[94]</sup> Thus, the x-ray diffraction data indicate an absence of layering order in these structures, which is not surprising since no attempt to attain a superlattice was made in these growths. The lack of repeated layering order has also been confirmed by cross-sectional TEM.<sup>[88]</sup> However, as discussed below, regularly alternating ordered superlattices including  $\text{Bi}_4\text{Sr}_4\text{Ca}_3\text{Cu}_5\text{O}_{18}$  ( $\text{Bi}_2\text{Sr}_2\text{Ca}_2\text{O}_8 + \text{Bi}_2\text{Sr}_2\text{Ca}_2\text{Cu}_3\text{O}_{10}$ ) and  $\text{Bi}_4\text{Sr}_4\text{Ca}_2\text{Cu}_2\text{O}_{16}$  ( $\text{Bi}_2\text{Sr}_2\text{Cu}_2\text{O}_6 + \text{Bi}_2\text{Sr}_2\text{Ca}_2\text{Cu}_3\text{O}_{10}$ ), can be grown by shuttered MBE by using a shuttering sequence corresponding to the desired ordered superlattice.<sup>[94]</sup>

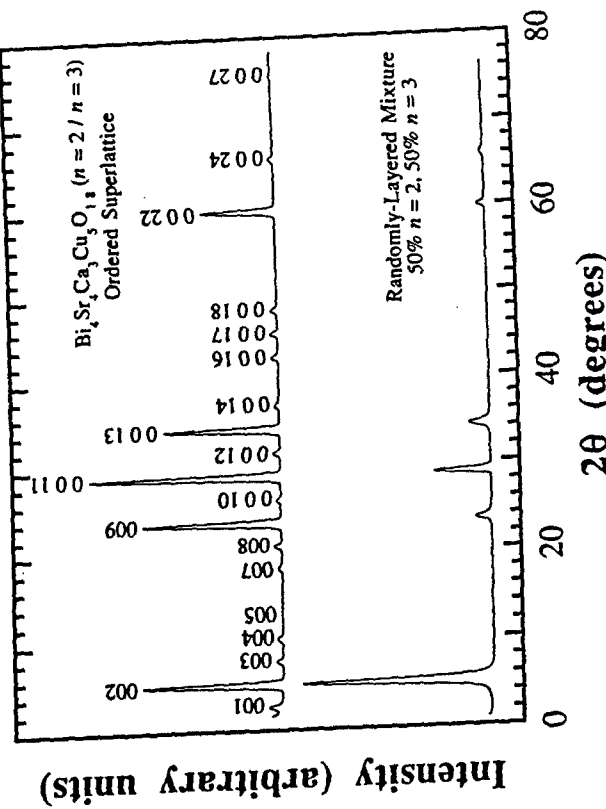


Figure 25. Calculated 0-20 x-ray diffraction intensity patterns for a perfectly ordered  $\text{Bi}_4\text{Sr}_4\text{Ca}_3\text{Cu}_5\text{O}_{18}$  phase (alternate half-unit-cells of  $\text{Bi}_2\text{Sr}_2\text{Ca}_2\text{Cu}_2\text{O}_8$  and  $\text{Bi}_2\text{Sr}_2\text{Ca}_2\text{Cu}_3\text{O}_{10}$ ) and an infinitely thick, layered, random mixture of 50%  $\text{Bi}_2\text{Sr}_2\text{Ca}_2\text{O}_8$  ( $n=2$ ) and 50%  $\text{Bi}_2\text{Sr}_2\text{Ca}_2\text{Cu}_2\text{O}_{10}$  ( $n=3$ ) layers. A Gaussian instrumental broadening of 0.5° was used in these calculations.

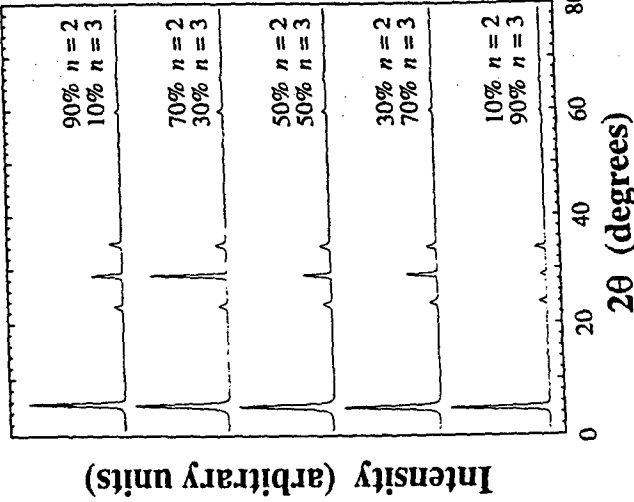
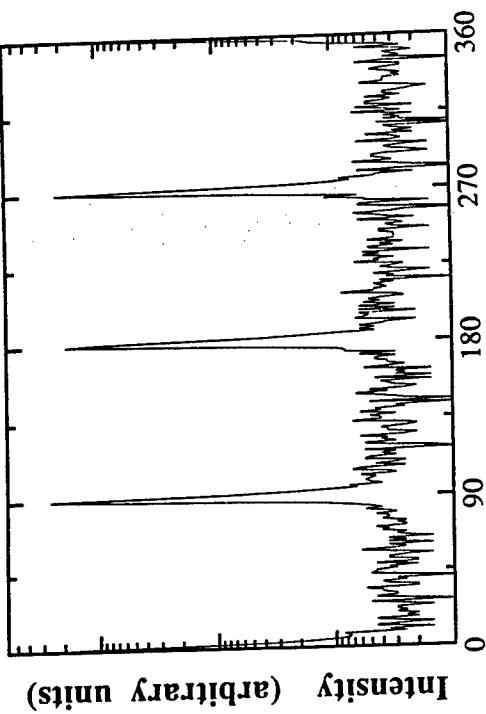


Figure 26. Calculated 0-20 x-ray diffraction intensity patterns for an infinitely thick, layered, random mixture of  $\text{Bi}_2\text{Sr}_2\text{Ca}_2\text{Cu}_2\text{O}_8$  ( $n=2$ ) and  $\text{Bi}_2\text{Sr}_2\text{Ca}_2\text{Cu}_3\text{O}_{10}$  ( $n=3$ ) layers in various proportions. A Gaussian instrumental broadening of 0.5° was used in these calculations.

Although in-situ RHEED patterns observed during the growth of  $\text{Bi}_2\text{Sr}_2\text{Ca}_{n-1}\text{Cu}_n\text{O}_{2n+4}$  phases, e.g., those shown in Fig. 23, indicate that shuttered MBE is capable of layering on a half unit cell basis, this has been directly tested by growing superlattices consisting of alternate half unit cells of  $\text{Bi}_2\text{Sr}_2\text{Ca}_{n-1}\text{Cu}_n\text{O}_{2n+4}$  phases.<sup>[94]</sup> For example, a shuttering sequence corresponding to the deposition of a half-unit-cell of  $\text{Bi}_2\text{Sr}_2\text{Cu}_3\text{O}_6$  followed by a half unit cell of  $\text{Bi}_2\text{Sr}_2\text{Ca}_2\text{Cu}_2\text{O}_8$  was repeated 61 times,<sup>f</sup>

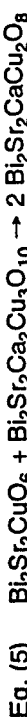
<sup>f</sup> This particular example is chosen because it clearly demonstrates the ability of MBE to control the layering order. Microscopic studies of bulk<sup>[38]</sup> and thin film<sup>[35]</sup> samples have shown the existence of a slight energetic preference for the alternate arrangement of  $\text{Bi}_2\text{Sr}_2\text{Ca}_{n-1}\text{Cu}_n\text{O}_{2n+4}$  and  $\text{Bi}_2\text{Sr}_2\text{Ca}_n\text{Cu}_{n-1}\text{O}_{2n+8}$  half-unit-cells in samples of intermediate composition. Fully ordered superlattices, i.e., phases, have not been seen in preparation methods not involving half unit cell layering control, but there does appear to be a slight driving force toward alternating stacking over a few repeat distances. For the superlattice example discussed, the average composition is  $\text{Bi}_2\text{Sr}_2\text{Ca}_2\text{O}_8$  (see Eq. 5). Since bulk techniques are capable of preparing the  $\text{Bi}_2\text{Sr}_2\text{Ca}_2\text{O}_8$  in single phase form, we know that energetically this phase is preferred over an alternating half-unit-cell superlattice of  $\text{Bi}_2\text{Sr}_2\text{Cu}_2\text{O}_8$  and  $\text{Bi}_2\text{Sr}_2\text{Ca}_2\text{Cu}_3\text{O}_{10}$  layers, making this a good test for the layering ability of MBE; the superlattice discussed is metastable with respect to the  $\text{Bi}_2\text{Sr}_2\text{Ca}_2\text{O}_8$  phase.

The x-ray diffraction pattern of the grown film is shown in Fig. 27. The  $\theta$ - $2\theta$  scan contains both even and odd  $00\ell$  peaks. The measured c-axis length ( $30.75 \pm 0.1$  Å) is about halfway between that of  $\text{Bi}_2\text{Sr}_2\text{CuO}_6$  and  $\text{Bi}_2\text{Sr}_2\text{Ca}_2\text{Cu}_3\text{O}_{10}$ . Rocking off the substrate (see Fig. 27) results in a reduction of the x-ray intensity to the noise level, indicating a highly oriented c-axis oriented sample. The epitaxial alignment between the superlattice and the underlying substrate has been confirmed by an x-ray  $\phi$ -scan of an inclined film reflection. The four peaks in Fig. 28 indicate that the superlattice is epitaxially oriented with respect to the  $\text{SrTiO}_3$  substrate with the same in-plane orientation relationship as observed for  $\text{Bi}_2\text{Sr}_2\text{Ca}_{n-1}\text{Cu}_n\text{O}_{2n+4}$  films.



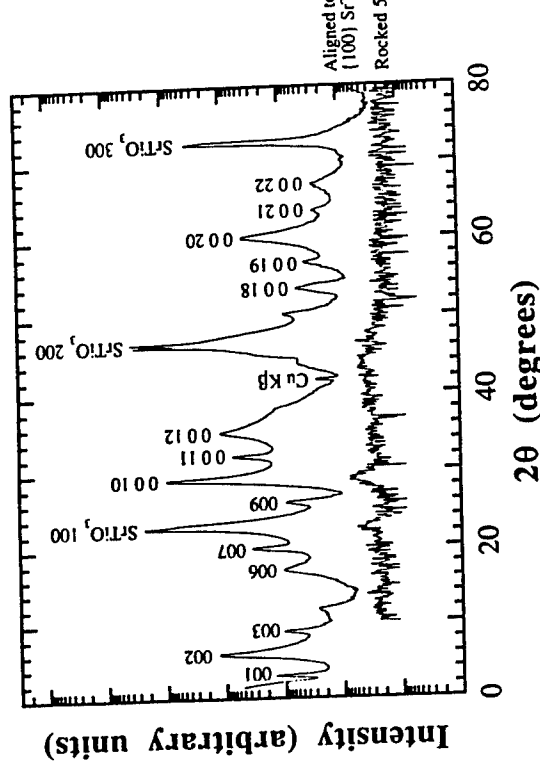
**Figure 28.** An x-ray diffraction  $\phi$ -scan of the 1115 peaks of an as-grown superlattice of alternating half unit cells of  $\text{Bi}_2\text{Sr}_2\text{CuO}_6$  ( $n=1$ ) and  $\text{Bi}_2\text{Sr}_2\text{Ca}_2\text{Cu}_3\text{O}_{10}$  ( $n=3$ ).  $\phi = 0$  was set parallel to  $\text{SrTiO}_3 <100>$ . This scan shows that the in-plane alignment between the film and substrate is with the  $a$  and  $b$  superlattice film axes parallel to  $\text{SrTiO}_3 <110>$  (from Ref. 130).

One possible atom rearrangement which could occur during the attempted growth of a superlattice consisting of alternating  $\text{Bi}_2\text{Sr}_2\text{CuO}_6$  and  $\text{Bi}_2\text{Sr}_2\text{Ca}_2\text{Cu}_3\text{O}_{10}$  layers, distinct from the formation of a randomly ordered mixture of these two phases, is the formation of single phase  $\text{Bi}_2\text{Sr}_2\text{CaCu}_2\text{O}_8$  by the reaction:



However, since the presence of a glide plane halfway up the unit cell of  $\text{Bi}_2\text{Sr}_2\text{CaCu}_2\text{O}_8$  (and all  $\text{Bi}_2\text{Sr}_2\text{Ca}_{n-1}\text{Cu}_n\text{O}_{2n+4}$  phases) leads to only even  $00\ell$  diffraction peaks, the presence of odd  $00\ell$  diffraction peaks in Fig. 27 rules out this possibility.

Comparison of the x-ray diffraction patterns of this superlattice to the two limiting case x-ray diffraction simulations confirms its layered nature and demonstrates that shuttered MBE is able to layer  $\text{Bi}_2\text{Sr}_2\text{Ca}_{n-1}\text{Cu}_n\text{O}_{2n+4}$  phases on a half unit cell basis. The simulated diffraction patterns are less



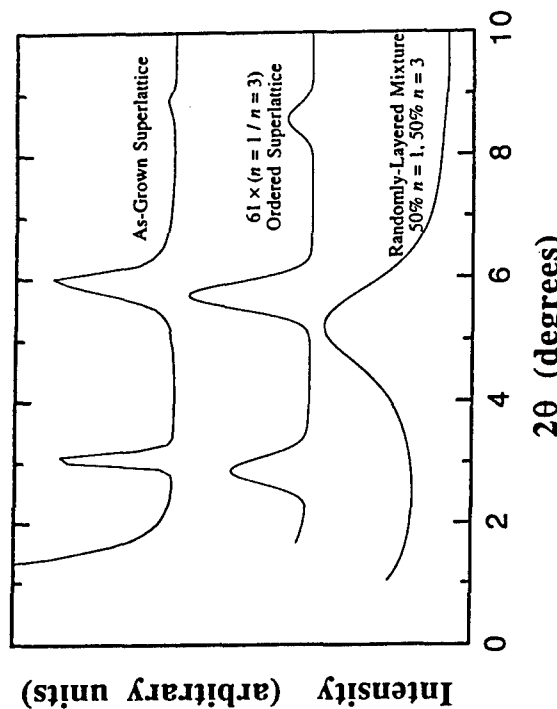
**Figure 27.** The 0-20 x-ray diffraction scans of an as-grown superlattice of alternating half-unit-cells of  $\text{Bi}_2\text{Sr}_2\text{CuO}_6$  ( $n=1$ ) and  $\text{Bi}_2\text{Sr}_2\text{Ca}_2\text{Cu}_3\text{O}_{10}$  ( $n=3$ ). Note the log intensity scale. The 0-20 scans aligned to the  $\text{SrTiO}_3 \{100\}$  substrate and rocked 5° in omega off alignment to the  $\text{SrTiO}_3 \{100\}$  substrate are shown (from Ref. 130).

sensitive to errors in the assumed structural parameters (which are extrapolated from the structure of bulk  $\text{Bi}_2\text{Sr}_2\text{Ca}_{n-1}\text{Cu}_n\text{O}_{2n+4}$  phases) at low 2θ angles than at high 2θ angles. In Fig. 29, a comparison between the observed x-ray diffraction pattern of the superlattice and the two limiting case x-ray diffraction simulations is shown for low 2θ values. The 001 peak (at  $2\theta = 3.1^\circ$ ), which would be absent for random layering, is quite evident in the observed diffraction pattern, indicating the presence of repeated ordered layering in this MBE-grown superlattice. The regularity of this and other MBE-prepared superlattices,[94][341][342] as revealed by x-ray diffraction and a comparison to these two limiting-case simulations, compares favorably to attempts to synthesize superlattices of  $\text{Bi}_2\text{Sr}_2\text{Ca}_{n-1}\text{Cu}_n\text{O}_{2n+4}$  phases by all other reported techniques.[40][370]-[372]

### 3.6 Josephson Junctions

Because of the extremely short coherence lengths,  $\xi$ , in high  $T_c$  superconductors, the fabrication of Josephson junctions, where two superconducting regions need to be separated by a pinhole-free non-superconducting barrier layer of a thickness comparable to  $\xi$ , is a considerable challenge. The length,  $\xi$ , ranges from a few angstroms to a few tens of angstroms in these materials, making the precise layering-control of MBE a necessity for the controlled synthesis of sandwich-type Josephson junctions. The MBE growth of sandwich-type Josephson junctions consisting of  $\text{Bi}_2\text{Sr}_2\text{Ca}_{n-1}\text{Cu}_n\text{O}_{2n+4}$  phases has been particularly successful and has yielded both hysteretic and non-hysteretic Josephson junctions.[343][344]

which are important for superconducting electronics. The junctions are formed by the MBE growth of a superconducting  $\text{Bi}_2\text{Sr}_2\text{CaCu}_2\text{O}_8$  film into which a single half unit cell thick barrier layer of  $\text{Bi}_2\text{Sr}_2\text{Ca}_{n-1}\text{Cu}_n\text{O}_{2n+4}$  (with  $n = 5$  to 11) is interspersed.[343][344] Using the site-selective doping capability of shuttered MBE, the central calcium monolayers of the  $\text{Bi}_2\text{Sr}_2\text{Ca}_{n-1}\text{Cu}_n\text{O}_{2n+4}$  barrier have been doped with bismuth, strontium, and dysprosium, causing significant changes in the conductivity of the barrier and allowing the junction critical current,  $I_c$ , of these sandwich-type Josephson junctions to be tuned over four orders of magnitude, while maintaining a nearly constant  $I_c R_n$  product of about 0.5 mV, where  $R_n$  is the junction normal state resistance.[343][344] The quality of the resulting junctions indicates that the half unit cell thick barrier layers (a thickness of 25 Å to 44 Å) are free of pinholes over the  $30 \mu\text{m} \times 30 \mu\text{m}$  areas of the sandwich junctions.[343][344] Subsequent work using Dy-doped  $\text{BiSr}_2\text{Ca}_7\text{Cu}_8\text{O}_{19}$  barriers has yielded  $I_c R_n$  products in excess of 5 mV.[172] MBE has also been used to prepare  $(\text{Ba},\text{K})\text{BiO}_3$  Josephson junctions.[373][376] The comparatively long coherence length ( $\approx 50 \text{ \AA}$ ) and isotropic cubic symmetry of  $(\text{Ba},\text{K})\text{BiO}_3$  are characteristics which distinguish  $(\text{Ba},\text{K})\text{BiO}_3$  from the rest of the high  $T_c$  superconductors and are technological advantages for the fabrication of Josephson junctions. Indeed,  $(\text{Ba},\text{K})\text{BiO}_3$  (and the related compound  $(\text{Ba},\text{Rb})\text{BiO}_3$ ) are the only high  $T_c$  materials from which Josephson junctions with nearly ideal BCS-like tunnel junction behavior have been fabricated.[373] Sandwich-type Josephson tunnel junctions have been fabricated using the layering capability of MBE to intersperse a non-superconducting  $\text{BaBi}_2\text{O}_y$  barrier layer between two superconducting  $(\text{Ba},\text{K})\text{BiO}_3$  layers.[374]  $\text{KNbO}_3$  has been found to work even better as a barrier layer, presumably because of the presence of potassium in all of the layers of the heterostructure; with it nearly ideal sandwich-type SIS Josephson junctions have been fabricated.[375]



**Figure 29.** The observed low angle 0-2θ x-ray scan of an as-grown superlattice of alternating half unit cells of  $\text{Bi}_2\text{Sr}_2\text{CuO}_6$  ( $n=1$ ) and  $\text{Bi}_2\text{Sr}_2\text{Ca}_2\text{Cu}_3\text{O}_{10}$  ( $n=3$ ), calculated 0-2θ x-ray intensity pattern for a perfectly ordered 61-period superlattice, and calculated 0-2θ diffracted x-ray intensity pattern for an infinitely thick layered random mixture of 50%  $\text{Bi}_2\text{Sr}_2\text{CuO}_6$  ( $n=1$ ) and 50%  $\text{Bi}_2\text{Sr}_2\text{Ca}_2\text{Cu}_3\text{O}_{10}$  ( $n=3$ ). A Gaussian instrumental broadening of  $0.5^\circ$  was used in the x-ray calculations.

Excellent SIS Josephson junctions have also been fabricated by creating a controlled grain boundary (the SIS junction) by growing (Ba,K)BiO<sub>3</sub> films on bicrystalline substrates.<sup>[376]</sup>

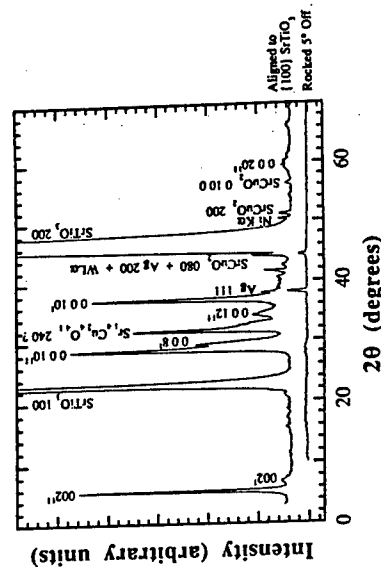
### 3.7 Formation of Metastable Structures

As described in Sec. 3.2, the ability to avoid the temporary formation of islands is a crucial aspect of achieving layering control on a finer scale than the unit cell or half unit cell level which is accessible through codeposition methods. By shuttering the oxidant flux in addition to the cation fluxes, islanding during the shuttered MBE growth of Bi<sub>2</sub>Sr<sub>2</sub>CuO<sub>6</sub> can be avoided, as evidenced by the RHEED pattern remaining streaked throughout the growth of Bi<sub>2</sub>Sr<sub>2</sub>CuO<sub>6</sub> films.<sup>[94][339]</sup> Using such growth conditions, the shuttered growth of a Bi<sub>2</sub>Sr<sub>2</sub>CaCu<sub>2</sub>O<sub>8</sub>-like structure in which the calcium monolayer is completely replaced by strontium has been attempted.<sup>[94][339]</sup> This hypothetical crystal structure is shown in Fig. 30. Such a composition may be written as Bi<sub>2</sub>Sr<sub>2</sub>SrCu<sub>2</sub>O<sub>8</sub> or simply Bi<sub>2</sub>Sr<sub>3</sub>Cu<sub>2</sub>O<sub>8</sub>. Bi<sub>2</sub>Sr<sub>3</sub>Cu<sub>2</sub>O<sub>8</sub> exists as an equilibrium phase, but does not have a Bi<sub>2</sub>Sr<sub>2</sub>CaCu<sub>2</sub>O<sub>8</sub>-like structure.<sup>[350][351]</sup> In the Bi-Sr-Ca-Cu-O phase diagram shown in Fig. 8(a), Bi<sub>2</sub>Sr<sub>3</sub>Cu<sub>2</sub>O<sub>8</sub> is denoted as 2302. It is also present in the Bi-Sr-Cu-O phase diagram in Fig. 8(b) and denoted as 3:2:2. Attempts to synthesize a fully Sr-for-Ca-substituted Bi<sub>2</sub>Sr<sub>2</sub>CaCu<sub>2</sub>O<sub>8</sub>-like structure by bulk techniques have failed.<sup>[351]</sup> Thus, the MBE synthesis of such a phase is a direct test of the ability of shuttered MBE to form metastable materials and customize layering on a finer scale than a half unit cell level.

The x-ray diffraction pattern of this as-grown Bi<sub>2</sub>Si<sub>3</sub>Cu<sub>2</sub>O<sub>8</sub> film is shown in Fig. 31.<sup>[94][339]</sup> Other than the intense SrTiO<sub>3</sub> {100} substrate peaks present, the most intense peaks are due to a *c*-axis oriented Bi<sub>2</sub>Sr<sub>2</sub>CaCu<sub>2</sub>O<sub>8</sub>-like structure with *c*-axis length of  $31.3 \pm 0.3$  Å. Some of the other peaks present could be due to the equilibrium polymorph of Bi<sub>2</sub>Si<sub>3</sub>Cu<sub>2</sub>O<sub>8</sub>, or due to Bi<sub>2</sub>Si<sub>2</sub>CuO<sub>6</sub> (a Bi<sub>2</sub>Si<sub>2</sub>CuO<sub>6</sub> buffer layer was grown underneath the Bi<sub>2</sub>Sr<sub>3</sub>Cu<sub>2</sub>O<sub>8</sub> film). X-ray diffraction scans of inclined film planes indicated that the *a*- and *b*-axes of the metastable Bi<sub>2</sub>Sr<sub>2</sub>CaCu<sub>2</sub>O<sub>8</sub>-like structure were aligned parallel to the SrTiO<sub>3</sub> <110> directions in the plane of the substrate.<sup>[94]</sup> This sample exhibited zero resistance at 15 K.<sup>[339]</sup> These experimental results indicate the ability of shuttered MBE to customize layering on a monolayer level. This metastable Bi<sub>2</sub>Sr<sub>2</sub>CuO<sub>6</sub> phase with a Bi<sub>2</sub>Sr<sub>2</sub>CaCu<sub>2</sub>O<sub>8</sub>-like structure has also been synthesized by sputtering.<sup>[377]</sup>



**Figure 30.** The crystal structure of a hypothetical Bi<sub>2</sub>Sr<sub>2</sub>CaCu<sub>2</sub>O<sub>8</sub>-related metastable phase containing no calcium. The tetragonal subcell of the Bi<sub>2</sub>Sr<sub>2</sub>CaCu<sub>2</sub>O<sub>8</sub> phase is shown with complete strontium substitution for the atoms at the calcium site.



**Figure 31.** The 0-2θ x-ray diffraction scans of an as-grown film containing a metastable Bi<sub>2</sub>Sr<sub>2</sub>CaCu<sub>2</sub>O<sub>8</sub>-like Bi<sub>2</sub>Sr<sub>2</sub>SrCu<sub>2</sub>O<sub>x</sub> phase (from Ref. 339). For clarity, the intensity of the scan aligned to the SrTiO<sub>3</sub> {100} substrate in omega is offset from the scan rocked 5° in omega off alignment to the SrTiO<sub>3</sub> substrate. The 002 peaks due to a Bi<sub>2</sub>Sr<sub>2</sub>CaCu<sub>2</sub>O<sub>8</sub>-related metastable phase are labeled (I) in addition to those due to other phases (II).

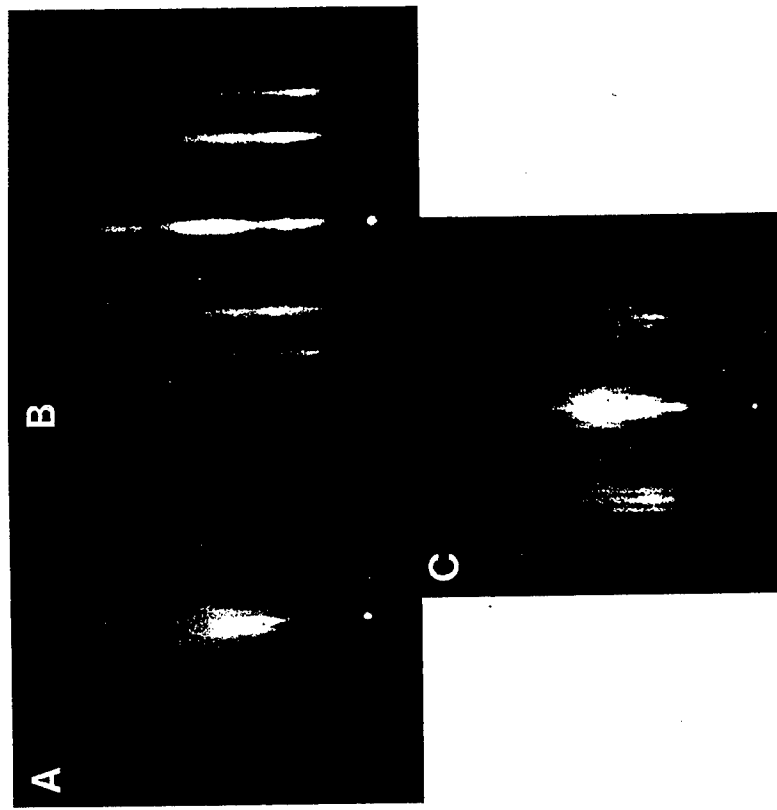
### 3.8 Twin-Free Growth

So far in this chapter, all the high  $T_c$  superconductor layers discussed have been oriented epitaxial layers. Although the crystallographic directions in the film have been strongly influenced by the crystallographic form of the substrate (epitaxy), the epitaxial films of high  $T_c$  superconductor materials having lower than tetragonal symmetry (e.g.,  $\text{YBa}_2\text{Cu}_3\text{O}_{7-\delta}$  and  $\text{Bi}_2\text{Sr}_2\text{Ca}_{n-1}\text{Cu}_n\text{O}_{2n+4}$ ) discussed so far contain many twin boundaries. In addition to the reflection twins common to  $\text{YBa}_2\text{Cu}_3\text{O}_{7-\delta}$ , 90° rotation twins<sup>[56]</sup> abound in these materials. Considering the square surface net of the common substrate materials employed with equivalent  $a$ - and  $b$ -axes, it is not surprising that both possible epitaxial alignments (related by a 90° rotation twin) of the non-equivalent  $a$ - and  $b$ -axes of the lower symmetry high  $T_c$  structures with the substrate axes occur.

Just as growth of GaAs or SiC on slightly misoriented silicon substrates has proven effective in eliminating anti-phase boundaries,<sup>[378][379]</sup> growth of high  $T_c$  superconductors on vicinal surfaces can significantly reduce the concentration of twin boundaries in  $\text{YBa}_2\text{Cu}_3\text{O}_{7-\delta}$  films,<sup>[380]</sup> and virtually eliminate them in  $\text{Bi}_2\text{Sr}_2\text{Ca}_{n-1}\text{Cu}_n\text{O}_{2n+4}$  and  $(\text{La},\text{Sr})_2\text{CuO}_4$  films.<sup>[340][381]-[389]</sup> Twin-free high  $T_c$  films were first reported for the  $\text{Bi}_2\text{Sr}_2\text{Ca}_{n-1}\text{Cu}_n\text{O}_{2n+4}$  system for (001) oriented films grown on slightly misoriented  $\text{SrTiO}_3$  substrates.<sup>[340]</sup> Twin-free growth in the  $\text{Bi}_2\text{Sr}_2\text{Ca}_{n-1}\text{Cu}_n\text{O}_{2n+4}$  system is easily discerned from RHEED patterns, due to the long ( $\sim 26 \text{ \AA}$ ) incommensurate superstructure which exists along the  $b$ -axis of these structures, but is absent along the  $a$ -axis.<sup>[531][390]-[392]</sup> Note that the lattice constants of the  $a$ - and  $b$ -axes of the  $\text{Bi}_2\text{Sr}_2\text{Ca}_{n-1}\text{Cu}_n\text{O}_{2n+4}$  phases themselves are very close in length (e.g.,  $a = 5.414 \text{ \AA}$  and  $b = 5.418 \text{ \AA}$  for the orthorhombic subcell of  $\text{Bi}_2\text{Sr}_2\text{CaCu}_2\text{O}_8$ ).<sup>[390]</sup> The incommensurate superstructure along the  $b$ -axis results in closely spaced satellite streaks (or spots) in RHEED patterns, which are easily discerned from the other RHEED streaks because of their very close spacing.

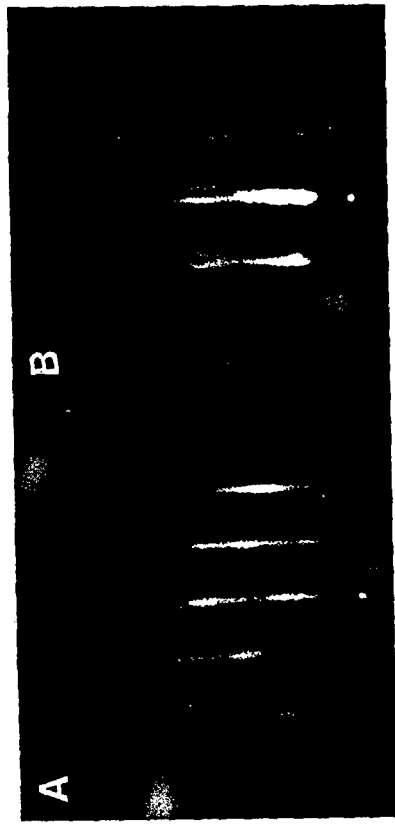
The RHEED patterns for the growth of  $\text{Bi}_2\text{Sr}_2\text{Ca}_{n-1}\text{Cu}_n\text{O}_{2n+4}$  (001) films on vicinal and well oriented perovskite substrates are shown in Fig. 32. For growth on a vicinal  $\text{SrTiO}_3$  (001) substrate, which is misoriented about  $4^\circ \rightarrow [1\bar{1}0]$ , the RHEED patterns observed along the  $\text{SrTiO}_3 <110>$  azimuths are clearly different from each other. The closely spaced satellite streaks observed along the  $\text{SrTiO}_3 [1\bar{1}0]$  azimuth indicate the lateral presence of the  $b$ -axis and its incommensurate superstructure, while the streaks observed along the  $\text{SrTiO}_3 [110]$  azimuth indicate the lateral presence of the  $a$ -axis. Note that in films grown on well oriented

(001) surfaces viewed along the corresponding RHEED azimuths, a superposition of these two patterns is observed along both perovskite  $<110>$  azimuths, as shown in Fig. 32(c). The RHEED patterns observed along the [100] perovskite azimuths for  $\text{Bi}_2\text{Sr}_2\text{Ca}_{n-1}\text{Cu}_n\text{O}_{2n+4}$  (001) films grown on vicinal and well oriented perovskite substrates are shown in Fig. 33. The difference between the twinned and untwinned films is also evident along this azimuth.



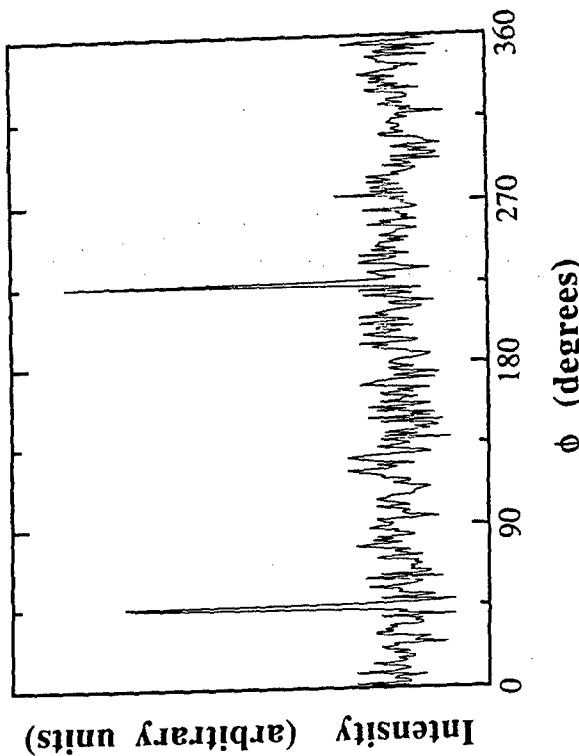
**Figure 32.** RHEED patterns observed along the  $<110>$  perovskite azimuths of  $\text{Bi}_2\text{Sr}_2\text{Ca}_{n-1}\text{Cu}_n\text{O}_{2n+4}$  films grown on vicinal and well oriented (001) perovskite substrates: (a) A  $\text{Bi}_2\text{Sr}_2\text{Ca}_2\text{Cu}_3\text{O}_{10}$  ( $n=3$ ) film on a vicinal  $\text{SrTiO}_3$  (001) substrate,  $\text{SrTiO}_3 [110]$  azimuth, (b) The same film shown in (a), but along the  $\text{SrTiO}_3 [1\bar{1}0]$  azimuth, and (c) A  $\text{Bi}_2\text{Sr}_2\text{CuO}_6$  ( $n=1$ ) film on a well oriented  $\text{LaAlO}_3$  (001) substrate,  $\text{LaAlO}_3 [110]$  azimuth. The RHEED pattern along the  $\text{LaAlO}_3 [1\bar{1}0]$  azimuth was identical to that shown in (c). Images from Refs. 94 and 340.

of nearly identical length in these  $\text{Bi}_2\text{Sr}_2\text{Ca}_{n-1}\text{Cu}_n\text{O}_{2n+4}$  materials. Instead, the observed x-ray diffraction pattern contains only two peaks, indicating that the incommensurate superlattice is aligned along only one of the  $<110>$ -type  $\text{SrTiO}_3$  surface directions. Specifically, the x-ray data indicate that the  $b$ -axis of the film runs up and down the substrate steps and not along the length of the substrate steps.



**Figure 33.** RHEED patterns observed along the  $<100>$  perovskite azimuths of  $\text{Bi}_2\text{Sr}_2\text{Ca}_{n-1}\text{Cu}_n\text{O}_{2n+4}$  films grown on vicinal and well oriented (001) perovskite substrates: (a) A  $\text{Bi}_2\text{Sr}_2\text{Ca}_2\text{Cu}_3\text{O}_{10}$  ( $n=3$ ) film on a vicinal  $\text{SrTiO}_3$  (001) substrate,  $\text{SrTiO}_3$  {100} azimuth and (b) A  $\text{Bi}_2\text{Sr}_2\text{CuO}_5$  ( $n=1$ ) film on a well oriented  $\text{LaAlO}_3$  (001) substrate,  $\text{LaAlO}_3$  {100} azimuth. The RHEED patterns along the [010] perovskite azimuths were identical to those shown in (a) and (b) for these two growths, respectively. Images from Refs. 94 and 340.

The absence of rotation and reflection twin boundaries in  $\text{Bi}_2\text{Sr}_2\text{Ca}_{n-1}\text{Cu}_n\text{O}_{2n+4}$  films grown on vicinal perovskite substrates is also evident from x-ray diffraction measurements. Just as the incommensurate superstructure along the  $b$ -axis of the orthorhombic subcell of these materials causes satellite streaks to occur in RHEED, it also produces satellite reflections in x-ray diffraction. In particular, the  $0\bar{2}1\bar{2}$  reflection of the  $\text{Bi}_2\text{Sr}_2\text{Ca}_2\text{Cu}_3\text{O}_{10}$  phase has satellite peaks on either side of it along the  $b^*$  reciprocal space axis, while the  $20\bar{1}2$  reflection does not have satellite peaks adjacent to it along the  $a^*$  reciprocal space axis. Figure 34 shows the observed x-ray diffraction intensity gathered by aligning the detector to a satellite reflection of the  $0\bar{2}1\bar{2}$  peak of a  $\text{Bi}_2\text{Sr}_2\text{Ca}_2\text{Cu}_3\text{O}_{10}$  film grown on a vicinal  $\text{SrTiO}_3$  (001) substrate and then rotating the  $b$ -axis of the 4-circle diffractometer around the [001] zone axis of the film. If the film contained rotation twin boundaries, this scan would have contained a diffraction peak every  $90^\circ$ . The presence of (110) reflection twin boundaries would also lead to x-ray diffraction peaks about every  $90^\circ$  since the  $a$ - and  $b$ -axes are



**Figure 34.** An x-ray diffraction  $\phi$ -scan of an incommensurate superlattice satellite peak of the  $0\bar{2}1\bar{2}$  peak of a  $\text{Bi}_2\text{Sr}_2\text{Ca}_2\text{Cu}_3\text{O}_{10}$  ( $n=3$ ) film grown on a misoriented  $\text{SrTiO}_3$  {100} substrate.  $\phi = 0$  was set parallel to  $\text{SrTiO}_3 <100>$ . This scan indicates that the  $b$ -axis of the  $\text{Bi}_2\text{Sr}_2\text{Ca}_2\text{Cu}_3\text{O}_{10}$  film runs up and down the steps of the misoriented substrate ( $45^\circ$  and  $225^\circ$  peaks) but not laterally along them (no peak at  $135^\circ$  or  $315^\circ$ ), indicating the absence of twin boundaries in the film (from Ref. 339).

Subsequent work using vicinal surfaces of  $\text{SrTiO}_3$  has not only confirmed these results and examined the microstructure in detail using TEM,[38][382][386] but has demonstrated that this technique may be utilized to fabricate virtually twin-free films of  $\text{Bi}_2\text{Sr}_2\text{Ca}_{n-1}\text{Cu}_n\text{O}_{2n+4}$  ( $111$ ),[383][384]  $(\text{La},\text{Sr})_2\text{CuO}_4$  (103),[385] and even the metallic perovskite  $\text{SrRuO}_3$  (110).<sup>[9]</sup> In an analogous manner, vicinal  $\text{SrTiO}_3$  (110) surfaces have been utilized

to prepare nearly untwinned  $\gamma\text{Ba}_2\text{Cu}_3\text{O}_{7-\delta}$  films,[393] vicinal  $\text{MgO}$  (110) surfaces with  $\text{CeO}_2$  buffer layers have been used to grow untwinned  $\text{Bi}_{2}\text{Sr}_2\text{Ca}_{n-1}\text{Cu}_n\text{O}_{2n+4}$  (01 $n$ ) films[385] and vicinal  $\text{LaSrGaO}_4$  (110) surfaces have enabled the growth of untwinned  $\text{Bi}_2\text{Sr}_2\text{CuO}_6$  (011) films.[387] Cleavage steps on  $\text{MgO}$  (100) have also been found to reduce the 4-fold symmetry of the substrate.[394] Alternatively, orthorhombic substrates, e.g.,  $\text{NdGaO}_3$  [385][386] and  $(\text{Y},\text{Nd})\text{AlO}_3$ , [171][387][389] and either anisotropic thermal expansion coefficients[397] or the application of mechanical stress[387][388] may be used for this purpose.

Note that the untwinned high  $T_c$  superconductor films grown on vicinal substrates are themselves vicinal. This not only allows the anisotropy in the transport properties to be investigated,[381][399] but with appropriate patterning, the current may be constrained to flow up or down these steps, which for the case of  $\text{Bi}_2\text{Sr}_{12}\text{Ca}_{n-1}\text{Cu}_n\text{O}_{2n+4}$  films, may lead to device possibilities since each step appears to be a weak link,[399] and the number of weak links in series connection is determined by the tilt of the substrate and length of the patterned region.

## 4.0 FUTURE DIRECTIONS

### 4.1 Hybrid MBE Techniques

As the MBE technique has been applied and adapted to the growth of high  $T_c$  superconductors, other thin film techniques have also been modified in order to achieve a customized layering capability of these materials. Layering control at the unit cell level has been demonstrated by reactive ion beam sputtering,[400] PLD,[401] and sputtering.[402][403] The pressures used in evaporation,[400] PLD,[401] and sputtering,[402][403] The pressures used in RHEED during shuttered growth,[386][404] Differential pumping has allowed the use of RHEED at the relatively high pressures used in reactive evaporation,[126][187] and PLD.[405] Another method enabling the use of RHEED observation during PLD is by supplying the high oxidant pressure to the substrate as brief pulses in synchronization with the PLD laser pulses. The resulting average background pressure is significantly lowered, making RHEED observation during PLD possible, as well as enabling the effects of altering the oxidation pulse timing to be studied.[406] The use of synchrotron X-ray radiation has allowed in-situ monitoring by diffraction techniques at the high pressures used in sputtering[407] and OMVPE.[408]

This monitoring has included the observation of x-ray intensity oscillations analogous to those present in RHEED.[408] Sequential deposition using multiple-target sputtering,[404][404][404][414] multiple target PLD,[415] reactive evaporation,[101] pulsed organometallic MBE,[416] and pulsed metal-organic chemical vapor deposition (MOCVD)[417] have been used to control the order in which the depositing species reach the substrate, in an effort to form customized and metastable structures in an analogous manner to MBE. While some aspects of these techniques are attractive, and the corresponding hybrid approaches (e.g., laser-MBE[418]-[420] and organometallic MBE[416]) will likely be utilized for the MBE growth of high  $T_c$  superconductors to a greater extent in the future, the layering control achieved by MBE remains unsurpassed for the controlled growth of high  $T_c$  superconductors which cannot be prepared by bulk methods, and for heterostructures containing custom-layered high  $T_c$  materials.

Some advantages of the hybrid laser-MBE technique are its ability to deposit materials with extremely low vapor pressures for in-situ patterning, or to deposit multi-component materials from a single target with faithful composition transfer. The latter capability is advantageous when a thick layer of a material that may be readily synthesized by bulk techniques is desired in a heterostructure which contains other layers, the growth of which requires the customized laying capability of MBE.

Utilizing gaseous precursors in high  $T_c$  MBE has similar advantages to metal-organic molecular beam epitaxy (MOMBE) and chemical beam epitaxy (CBE) over conventional MBE. However, the lack of gaseous precursors which may be easily transported to the growth chamber and reacted, particularly for the alkaline earth elements,[421] has been a significant obstacle to the widespread use of gaseous precursors for the MBE growth of high  $T_c$  superconductors. The development of suitable gaseous precursors remains an active area of research. As progress in precursor chemistry and their use in the growth of high  $T_c$  superconductors by MOCVD is made, these gaseous reagents may be more actively used in hybrid MBE approaches to the growth of high  $T_c$  superconductors, including hopefully, the growth of these materials by atomic layer epitaxy (ALE).[422] The use of surface chemistry in ALE growth to chemically limit the buildup of depositing species to a single complete monolayer has a distinct advantage over MBE, where even the most perfect composition control system results in the correct total number of species being deposited, but does not preclude their agglomeration (see Fig. 16). Clearly a deposition method in which surface absorption chemistry is used to accu-

rately fill each monolayer making up a custom-layered high  $T_c$  superconductor structure (i.e., ALE), is superior to a deposition method where purely physical methods (i.e., MBE) are utilized. Although some progress has been made in using absorption-controlled epitaxial methods for the growth of the high  $T_c$  superconductors  $(\text{Ba}, \text{Rb})\text{BiO}_3$  and  $(\text{Ba}, \text{K})\text{BiO}_3$ ,<sup>[115][29]</sup> and MOCVD researchers are working to develop suitable ALE reagents and find appropriate growth conditions,<sup>[421][423][424]</sup> the customized growth of high  $T_c$  superconductors by ALE remains a challenge.

#### 4.2 In-situ Monitoring Techniques

Further enhancements to the MBE technique which allow improved reproducibility and process control during the growth of high  $T_c$  superconductors will likely involve improving the resolution and accuracy of the currently used in-situ monitoring methods as well as incorporating other promising in-situ analysis techniques. The precision of atomic absorption spectroscopy for composition control has improved significantly over the last several years, and it is currently the best composition control method for use at the relatively high oxidant pressures used in the MBE growth of high  $T_c$  superconductors. With improvements in the intensity and stability of the light source used for atomic absorption spectroscopy, this technique should achieve much better composition control. The utility of RHEED oscillations as a composition control method would also be greatly enhanced if the effect of the shuttered supply of incident species on RHEED oscillations were understood sufficiently that the temporal behavior of the RHEED oscillation signal during growth could be used for composition control. RHEED oscillations are commonly used as a calibration method in the MBE growth of III-V and other semiconductor materials. However, unlike the growth of III-V materials, the crystal structures and lattice constants of the component binary oxides of high  $T_c$  superconductors are significantly different from each other and from the high  $T_c$  superconductors, making it impractical to do flux calibration by RHEED oscillations of the various binary oxide constituents of the high  $T_c$  material under study.

Two emerging in-situ composition analysis techniques which make use of the RHEED beam, and are thus quite compatible with the standard MBE geometry, are total-reflection-angle x-ray spectroscopy in RHEED (RHEED-TRAXS)<sup>[425]</sup> and reflection-electron energy loss spectroscopy (REELS).<sup>[426]</sup> Both are highly surface sensitive and give chemical information on the region of the sample upon which the RHEED beam is incident.

The former analyzes the energy and intensity of the x-rays emitted from the sample, as is done in EPMA, while the latter analyzes the energy and intensity of the electrons scattered from the sample. With monolayer elemental detection ability, the sensitivities of these techniques are excellent, however, the accuracy of the composition determination needs to be improved significantly for these methods to be useful for composition control during the growth of high  $T_c$  superconductors. RHEED-TRAXS has recently been applied to the MBE growth of high  $T_c$  superconductors.<sup>[427]</sup>

Another emerging technique for real-time composition control is the use of in-situ spectroscopic ellipsometry (SE) during thin film growth.<sup>[428][429]</sup> This optical method provides information on the optical properties of the growing film over a range of wavelengths, and its geometry is entirely compatible with MBE growth. Owing to the comparatively long penetration depth of light over the wavelength range used, SE differs from the aforementioned techniques in that it probes well into the film; it is a bulk-sensitive as opposed to a surface-sensitive technique. The variation of the optical properties (density and dielectric function) with thickness may be extracted from the SE data,<sup>[430]</sup> and if the film microstructure is fully dense and single phase, and the variation of the optical properties as a function of composition are known, as in the case of many semiconductor materials grown by MBE, the composition, thickness, and surface microstructure of the various layers making up the thin film sample may be calculated. The SE-determined surface microstructure may be used to distinguish between layer-by-layer and island growth, independently from RHEED. A useful feature of the SE technique is that the parameters extracted, thickness and composition, are overdetermined by the ellipsometry data taken at many different wavelengths, allowing the assumption of fully dense and single phase microstructure to be explicitly checked. Ellipsometry at a single wavelength has been used for closed-loop real-time composition control for the growth of III-V materials by MBE.<sup>[431]</sup> The use of a technique to a broader range of materials, perhaps including the MBE growth of high  $T_c$  superconductors. For composition sensitivity, it is desirable to perform SE in a wavelength range where the optical properties vary significantly with composition; this range lies in the infrared (IR) for many oxides. Spectroscopic ellipsometers that operate in the far-IR have been built and applied to oxides, including high  $T_c$  superconductors.<sup>[432]</sup> A related, but less complicated technique, reflectometry at a single wavelength, has been used in the MEE growth of III-V materials to monitor monolayer completion.<sup>[433]</sup> An abrupt change in slope of the reflectivity as

a function of deposited flux accompanies the completion of an MEE monolayer. The desire to accurately limit the flux deposited in each burst to an integral number of monolayers during MBE growth by sequential deposition indicates that such optical methods may also provide a means to better control the growth of high  $T_c$  superconductors. Although such optical methods have not yet been used in the MBE growth of high  $T_c$  superconductors, researchers growing  $\text{YBa}_2\text{Cu}_3\text{O}_{7-\delta}$  by sequential deposition MOCVD techniques<sup>[417]</sup> have utilized in-situ reflectometry to observe significant variation in the reflected light intensity accompanying the pulsed deposition and oxidation of the constituent fluxes.<sup>[424]</sup>

A distinct advantage of AA, RHEED-TRAXS, REELS, and SE over other composition control methods is that they can be used to measure either the flux incident upon the substrate (AA) or flux incorporated into (RHEED-TRAXS, REELS, and SE) the growing film *during* growth. Other composition control methods, e.g., quartz crystal microbalances, emission spectroscopic methods, mass-spectrometers, and ion gauges, when used during growth, rely on geometric factors to relate the flux at the position of the detector to the composition reaching the growing surface. Since these factors may change with time, gas pressure, and other process variables, it is advantageous to directly measure the flux reaching or, better yet, being incorporated into the film during growth.

A schematic diagram of what a future MBE system for the growth of high  $T_c$  superconductors might look like is shown in Fig. 35. In addition to the features common in today's MBE systems for the growth of high  $T_c$  superconductors, this system incorporates the hybrid laser-MBE technique (a combination of MBE and PLD) allowing a wider range of materials and growth conditions to be utilized as well as in-situ SE characterization.

## 5.0 CONCLUSIONS

The use of MBE for the growth of high  $T_c$  superconductors is still in its infancy and many hurdles, in particular accurate composition control, remain to be overcome for this technique to develop greater structural and doping control at the atomic layer level as well as reproducibility. Nonetheless, in the seven years since the discovery of high  $T_c$  superconductivity, MBE has become established as the premiere synthesis technique for these layered oxides when customized layering control is needed. As the complexity and metastability of desired structures increases, hopefully

aided by increased understanding of high  $T_c$  superconductivity and thus an enlightened design of new high  $T_c$  materials, the requirement for a controlled synthesis environment capable of atomic layer engineering of new superconductors and device heterostructures will become all the more important. MBE appears to be the most likely technique to meet this challenge.

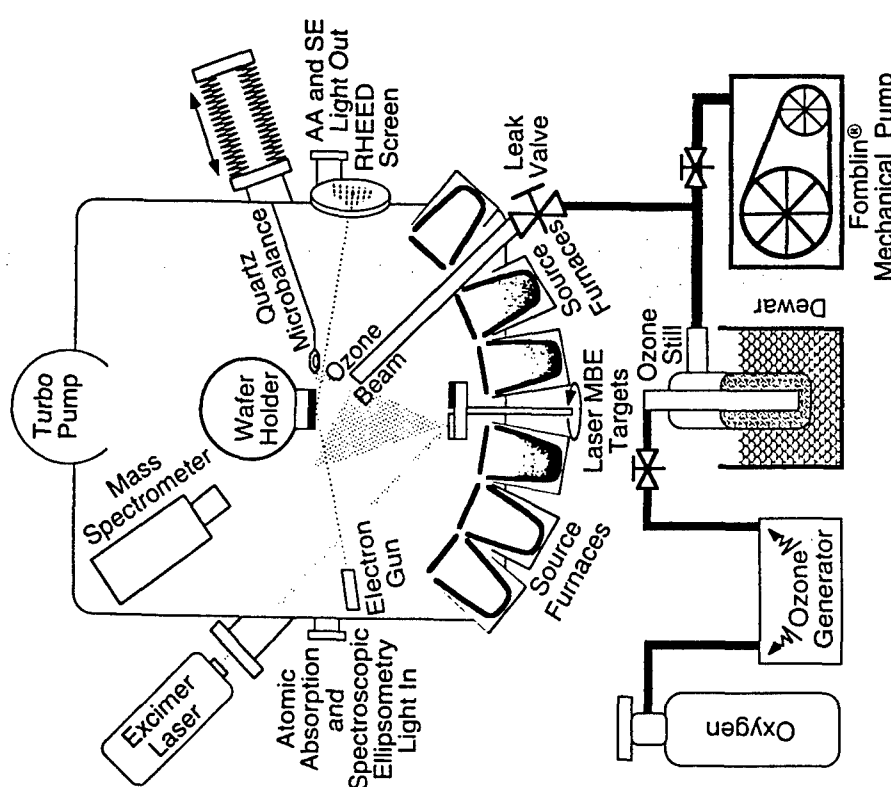


Figure 35. A schematic diagram of what added features a future MBE growth chamber might contain for the growth of high  $T_c$  superconductors. The growth chamber shown contains features commonly used, plus the ability to perform combined MBE and laser-MBE, and in-situ spectroscopic ellipsometry.

## ACKNOWLEDGMENTS

We gratefully acknowledge our many collaborators with whom, beginning in early 1987, we have worked toward the MBE growth of high  $T_c$  superconductors, especially E. S. Hellman, I. Bozovic, and J. N. Eckstein. In addition, we acknowledge stimulating interactions with the entire Stanford high  $T_c$  thin film group, and in particular R. H. Hammond, T. H. Geballe, and M. R. Beasley. The financial support of the Joint Services Electronics Program through contract DAAG29-84-K-0048, DARPA/ONR under contract N00014-88-C-0760, the National Science Foundation Material Research Laboratory Program through the Center of Materials Research at Stanford University, and the support of a Semiconductor Research Corporation Fellowship for DGS for the period of his thesis research are gratefully acknowledged. DGS acknowledges fruitful interactions with the IBM Zurich high  $T_c$  group, especially J. Mannhart and J. G. Bednorz, and the financial support of ONR through contract N00014-93-1-0512 during the preparation of this review chapter.

## REFERENCES

1. Bednorz, J. G. and Müller, K. A., *Z. Phys. B*, **64**:189–193 (1986); Bednorz, J. G., Takashige, M., and Müller, K. A., *Europhys. Lett.*, **3**:379–386 (1987)
2. Battlogg, B., Cava, R. J., Schneemeyer, L. F., and Espinosa, G. P., *IBM J. Res. Develop.*, **33**:208–214 (1989)
3. Ramesh, R., Inam, A., Chan, W. K., Wilkens, B., Myers, K., Remschmid, K., Hart, D. L., and Tarascon, J. M., *Science*, **252**:944–946 (1991)
4. Ramesh, R., Inam, A., Chan, W. K., Tillerot, F., Wilkens, B., Chang, C. C., Sands, T., Tarascon, J. M., and Keramidas, V. G., *Appl. Phys. Lett.*, **59**:3542–3544 (1991)
5. Ramesh, R., Chan, W. K., Wilkens, B., Gilchrist, H., Sands, T., Tarascon, J. M., Keramidas, V. G., Fork, D. K., Lee, J., and Safari, A., *Appl. Phys. Lett.*, **61**:1537–1539 (1992)
6. Fork, D. K., Ponce, F. A., Tramontana, J. C., and Geballe, T. H., *Appl. Phys. Lett.*, **58**:2294–2296 (1991)
7. Ramesh, R., Inam, A., Bonner, W. A., England, P., Wilkens, B. J., Meagher, B. J., Nazar, L., Wu, X. D., Hegde, M. S., Chang, C. C., Venkatesan, T., and Padamsee, H., *Thin Films, Appl. Phys. Lett.*, **55**:1138–1140 (1989)
8. Lichtenberg, F., Catana, A., Mannhart, J., and Schlom, D. G., *Appl. Phys. Lett.*, **60**:1138–1140 (1992)
9. Eom, C. B., Cava, R. J., Fleming, R. M., Phillips, J. M., van Dover, R. B., Marshall, J. H., Hsu, J. W. P., Krajewski, J. J., and Peck, W. F., Jr., *Science*, **258**:1766–1769 (1992)
10. Satyalakshmi, K. M., Mallya, R. M., Ramanathan, K. V., Wu, X. D., Brainard, B., Gautier, D. C., VasanthaCharya, N. Y., and Hegde, M. S., *Appl. Phys. Lett.*, **62**:1233–1235 (1993)
11. Dimos, D., Chaudhari, P., and Mannhart, J., *Phys. Rev. B*, **41**:4038–4049 (1990)
12. Suzuki, M. and Murakami, T., *Jpn. J. Appl. Phys.*, **26**:L524–L525 (1987)
13. Chaudhari, P., Koch, R. H., Laibowitz, R. B., McGuire, T. R., and Gambino, R. J., *Phys. Rev. Lett.*, **58**:2684–2686 (1987); Chaudhari, P., LeGoues, F. K., and Segmüller, A., *Science*, **238**:342–344 (1987)
14. Naito, M., Hammond, R. H., Oh, B., Hahn, M. R., Hsu, J. W. P., Rosenthal, P., Marshall, A. F., Beasley, M. R., Geballe, T. H., and Kapitulnik, A., *J. Mater. Res.*, **2**:713–725 (1987); Oh, B., Naito, M., Arnason, S., Rosenthal, P., Barton, R., Beasley, M. R., Geballe, T. H., Hammond, R. H., and Kapitulnik, A., *Appl. Phys. Lett.*, **51**:852–854 (1987)
15. Enomoto, Y., Murakami, T., Suzuki, M., and Moriwaki, K., *Jpn. J. Appl. Phys.*, **26**:L1248–L1250 (1987)
16. Char, K., Kent, A. D., Kapitulnik, A., Beasley, M. R., and Geballe, T. H., *Appl. Phys. Lett.*, **51**:1370–1372 (1987)
17. Webb, C., Weng, S.-L., Eckstein, J. N., Missert, N., Char, K., Schlom, D. G., Hellman, E. S., Beasley, M. R., Kapitulnik, A., and Harris, J. S., Jr., *Appl. Phys. Lett.*, **51**:1191–1193 (1987)
18. Kwo, J., Hsieh, T. C., Fleming, R. M., Hong, M., Liou, S. H., Davidson, B. A., and Feldman, L. C., *Phys. Rev. B*, **36**:4039–4042 (1987)
19. Dijkkamp, D., Venkatesan, T., Wu, X. D., Shaheen, S. A., Jisrawi, N., Min-Lee, Y. H., McLean, W. L., and Croft, M., *Appl. Phys. Lett.*, **51**:619–621 (1987)
20. See, for example: Cheung, J. and Horwitz, J., *MRS Bulletin*, **17**:30–36 (Feb. 1992); Chrisey, D. B. and Inam, A., *MRS Bulletin*, **17**:37–43 (Feb. 1992); Venkatesan, T., Wu, X. D., Muenchhausen, R., and Pique, A., *MRS Bulletin*, **17**:54–58 (Feb. 1992)

21. Cuomo, J. J., Gambino, R. J., Harper, J. M. E., and Kuptsis, J. D., *IBM J. Res. Develop.*, 21:580–583 (1977)
22. Gilbert, L. R., Messier, R., and Roy, R., *Thin Solid Films*, 54:129–136 (1978); Gilbert, L. R., Messier, R., and Krishnaswamy, S. V., *J. Vac. Sci. Technol.*, 17:389–391 (1980)
23. Rossnagel, S. M., and Cuomo, J. J., *Thin Film Processing and Characterization of High-Temperature Superconductors*, (J. M. E. Harper, R. J. Colton, and L. C. Feldman, eds.), pp. 106–113, American Institute of Physics, New York (1988)
24. Sandstrom, R. L., Gallagher, W. J., Dinger, T. R., Koch, R. H., Laibowitz, R. B., Kleinsasser, A. W., Gambino, R. J., Bumble, B., and Chisholm, M. F., *Appl. Phys. Lett.*, 53:444–446 (1988)
25. Li, H. C., Linker, G., Raizel, F., Smithey, R., and Geerk, J., *Appl. Phys. Lett.*, 52:1098–1100 (1988); Meyer, O., Weschenfelder, F., Geerk, J., Li, H. C., and Xiong, G. C., *Phys. Rev.*, B37:9757–9760 (1988)
26. Xi, X. X., Linker, G., Meyer, O., Nold, E., Obst, B., Raizel, F., Smithey, R., Strehlau, B., Weschenfelder, F., and Geerk, J., Z. *Phys.*, B74:13–19 (1989)
27. Eom, C. B., Sun, J. Z., Yamamoto, K., Marshall, A. F., Luther, K. E., Geballe, T. H., and Laderman, S. S., *Appl. Phys. Lett.*, 55:595–597 (1989)
28. Lathrop, D. K., Russek, S. E., and Buhrman, R. A., *Appl. Phys. Lett.*, 51:1554–1556 (1987); Tiez, L. A., de Cooman, B. C., Carter, C. B., Lathrop, D. K., Russek, S. E., and Buhrman, R. A., *J. Electron Microscop. Tech.*, 8:263–272 (1988)
29. Terashima, T., Iijima, K., Yamamoto, K., Bando, Y., and Mazaki, H., *Jpn. J. Appl. Phys.*, 27:L91–L93 (1988)
30. Wu, X. D., Inam, A., Venkatesan, T., Chang, C. C., Chase, E. W., Barboux, P., Tarascon, J. M., and Wilkins, B., *Appl. Phys. Lett.*, 52:754–756 (1988); Hwang, D. M., Venkatesan, T., Chang, C. C., Nazar, L., Wu, X. D., Inam, A., and Hegde, M. S., *Appl. Phys. Lett.*, 54:1702–1704 (1989)
31. Fujita, J., Yoshikake, T., Kamijo, A., Satoh, T., and Igarashi, H., *J. Appl. Phys.*, 64:1292–1295 (1988)
32. Koinuma, H., Kawasaki, M., Funabashi, M., Hasegawa, T., Kishio, K., Kitazawa, K., Fukui, K., and Nagata, S., *Appl. Phys.*, 62:1524–1526 (1987)
33. Lee, L.P., Char, K., Colclough, M.S., and Zaharchuk, G., *Appl. Phys. Lett.*, 59:3051–3053 (1991)
34. Triscone, J.-M., Fischer, Ø., Brunner, O., Antognazza, L., Kent, A. D., and Karkut, M. G., *Phys. Rev. Lett.*, 64:804–807 (1990)
35. Li, Q., Xi, X. X., Wu, X. D., Inam, A., Vadlamannati, S., McLean, W. L., Venkatesan, T., Ramesh, R., Hwang, D. M., Martinez, J. A., and Nazar, L., *Phys. Rev. Lett.*, 64:3086–3089 (1990)
36. Lowndes, D. H., Norton, D. P., and Budai, J. D., *Phys. Rev. Lett.*, 65:1160–1163 (1990)
37. Tabata, H., Kawai, T., and Kawai, S., *Phys. Rev. Lett.*, 70:2633–2636 (1993)
38. Terashima, T., Shimura, K., Bando, Y., Matsuda, Y., Fujiyama, A., and Komiyama, S., *Phys. Rev. Lett.*, 67:1362–1365 (1991)
39. Kitabatake, M., and Greene, J. E., *J. Appl. Phys.*, 73:3183–3194 (1993); Kitabatake, M., Fons, P., and Greene, J. E., *J. Vac. Sci. Technol.*, A8:3726–3735 (1990)
40. Wasa, K., Adachi, H., Hirochi, K., Ichikawa, Y., Matsushima, T., and Setsune, K., *J. Mater. Res.*, 6:1595–1604 (1991)
41. Sleight, A. W., *Physics Today*, 44:24–30 (1991)
42. Schliom, D. G., Eckstein, J. N., Hellman, E. S., Webb, C., Turner, F., Harris, J. S., Jr., Beasley, M. R., and Geballe, T. H., *Extended Abstracts, High-Temperature Superconductors II*, (D. W. Capone, II, W. H. Butler, B. Battlogg, and C. W. Chu, eds.), pp. 197–200, Materials Research Society, Pittsburgh (1988)
43. Spah, R. J., Hess, H. F., Stormer, H. L., White, A. E., and Short, K. T., *Appl. Phys. Lett.*, 53:441–443 (1988)
44. Schliom, D. G., Eckstein, J. N., Hellman, E. S., Streiffer, S. K., Harris, J. S., Jr., Beasley, M. R., Bravman, J. C., Geballe, T. H., Webb, C., von Dessonneck, K. E., and Turner, F., *Appl. Phys. Lett.*, 53:1660–1662 (1988)
45. Kwo, J., Hong, M., Trevor, D. J., Fleming, R. M., White, A. E., Farrow, R. C., Kortan, A. R., and Short, K. T., *Appl. Phys. Lett.*, 53:2683–2685 (1988)
46. Harris, J. S., Jr., Eckstein, J. N., Hellman, E. S., and Schlom, D. G., *J. Cryst. Growth*, 95:607–616 (1989)
47. See, for example, *The Technology and Physics of Molecular Beam Epitaxy*, (E. H. C. Parker, ed.), Plenum Press, New York (1985)
48. Müller-Buschbaum, H., *Angew. Chem. Int. Ed. Engl.*, 28:1472–1493 (1989)
49. Shannon, R. D., *Acta Cryst.*, A32:751–767 (1976)

50. Tokura, Y. and Arima, T., *Jpn. J. Appl. Phys.*, 29:2388–2402 (1990)
51. Cava, R. J., Batlogg, B., Krajewski, J. J., Farrow, R., Rupp, L. W., Jr., White, A. E., Short, K., Peck, W. F., and Kometani, T., *Nature*, 332:814–816 (1988)
52. Sleight, A. W., Gillson, J. L., and Bierstedt, P. E., *Solid State Comm.*, 17:27–28 (1975)
53. Petricek, V., Gao, Y., Lee, P., and Coppens, P., *Phys. Rev.*, B42:387–392 (1990)
54. Coppens, P., Lee, P., Gao, Y., and Sheu, H.-S., *J. Phys. Chem. Solids*, 52:1267–1272 (1991)
55. Cava, R. J., *Science*, 247:656–662 (1990)
56. Sleight, A. W., *Science*, 242:1519–1527 (1988)
57. Tokura, Y., Torrance, J. B., Huang, T. C., and Nazzal, A. I., *Phys. Rev.*, B38:7156–7159 (1988)
58. Torrance, J. B., Tokura, Y., Nazzal, A. I., Bezinge, A., Huang, T. C., and Parkin, S. S. P., *Phys. Rev. Lett.*, 61:1127–1130 (1988)
59. Rao, C. N. R., *Phil. Trans. R. Soc. London*, A336:595–624 (1991)
60. Tokura, Y., Takagi, H., and Uchida, S., *Nature*, 337:345–347 (1989)
61. Shafer, M. W. and Penney, T., *Eur. J. Solid State Inorg. Chem.*, 27:191–220 (1990)
62. Mannhart, J., *Mod. Phys. Lett.*, B6:555–571 (1992)
63. Sleight, A. W., *Physica*, C162–164:3–7 (1989)
64. Degterov, S. A. and Voronin, G. F., *Physica*, C178:213–220 (1991)
65. Karen, P., Braaten, O., and Kjekshus, A., *Acta Chem. Scand.*, 52:805–840 (1992)
66. Ahn, B. T., Lee, V. Y., Beyers, R., Gür, T. M., and Huggins, R. A., *Physica*, C167:529–537 (1990)
67. Beyers, R. and Ahn, B. T., *Annu. Rev. Mater. Sci.*, 21:335–372 (1991)
68. Majewsky, P., Hettich, B., Schulze, K., and Petzow, G., *Adv. Mater.*, 3:488–491 (1991)
69. *Phase Diagrams for High  $T_c$  Superconductors*, (J. D. Whitter, and R. S. Roth, eds.), pp. 136–145, Amer. Ceramic Soc., Westerville (1991). See in particular, figures S-198(B), S-205, S-211(B), and S-215(A).
70. Rubin, L. M., Orlando, T. P., Vander Sande, J. B., Gorman, G., Savov, R., Swope, R., and Beyers, R., *Appl. Phys. Lett.*, 61:1977–1979 (1992)

71. Tarascon, J. M., McKinnon, W. R., Barboux, P., Hwang, D. M., Bagley, B. G., Greene, L. H., Hull, G. W., LePage, Y., Stoffel, N., and Giroud, M., *Phys. Rev.*, B38:8885–8892 (1988)
72. See, for example, Eibl, O., *Physica*, C168:249–256 (1990). In this work, TEM analysis of samples produced by bulk synthesis methods yielding a majority of the  $n=3$   $\text{Bi}_2\text{Sr}_2\text{Ca}_{n-1}\text{Cu}_n\text{O}_{2n+4}$  phase revealed numerous intergrowths of  $n=1$  to  $n=7$ .
73. See, for example, Raveau, B., Michel, C., and Hervieu, M., *Advances in Superconductivity: Proceedings of the 1st International Symposium on Superconductivity (ISS '88)*, (K. Kitazawa, and T. Ishiguro, eds.), pp. 151–157, Springer-Verlag, Tokyo (1989). In this work, TEM analysis of samples produced by bulk synthesis methods yielding a majority of the  $n=4$   $\text{Tl}_2\text{Ba}_2\text{Ca}_n\text{Cu}_{n-1}\text{O}_{2n+4}$  phase revealed numerous intergrowths up to  $n=7$ .
74. Señaris-Rodríguez, M. A., Chippindale, A. M., Vázquez, A., Morán, E., and Alario-Franco, M. A., *Physica*, C172:477–480 (1991)
75. Cava, R. J., Siegrist, T., Hessen, B., Krajewski, J. J., Peck, W. F., Jr., Battlogg, B., Takagi, H., Waszczak, J. V., Schneemeyer, L. F., and Zandbergen, H. W., *J. Solid State Chem.*, 94:170–184 (1991)
76. Fu, W. T., Zandbergen, H. W., Xu, Q., van Ruitenberg, J. M., de Jongh, L. J., and van Tendeloo, G., *Solid State Comm.*, 70:1117–1121 (1989)
77. Holstein, W. L., Parisi, L. A., Fincher, C. R., and Gai, P. L., *Physica C*, 212:110–118 (1993)
78. Hyde, B. G. and Andersson, S., *Inorganic Crystal Structures*, Wiley-Interscience, New York (1989)
79. Udayakumar, K. R. and Cormack, A. N., *J. Am. Ceram. Soc.*, 71:C-469–C-471 (1988); Udayakumar, K. R. and Cormack, A. N., *J. Phys. Chem. Solids*, 50:55–60 (1989)
80. Tilley, R. J. D., *J. Solid State Chem.*, 21:293–30 (1977)
81. Gossard, A. C., Petroff, P. M., Weigmann, W., Dingle, R., and Savage, A., *Appl. Phys. Lett.*, 29:323–325 (1976)
82. Sakamoto, T., Funabashi, H., Ohta, K., Nakagawa, T., Kawai, N. J., Kojima, T., and Bando, Y., *Superlattices Microstruct.*, 1:347–352 (1985)
83. Kita, R., Hase, T., Itti, R., Sasaki, M., Morishita, T., and Tanaka, S., *Appl. Phys. Lett.*, 60:2684–2685 (1992)
84. Berkley, D. D., Goldman, A. M., Johnson, B. R., Morton, J., and Wang, T., *Rev. Sci. Instrum.*, 60:3769–3774 (1989)

85. Schlom, D. G., Lee, W. S., Ma, T., and Harris, J. S., Jr., *J. Vac. Sci. Technol.*, B7:296–298 (1989)
86. Coleman, E., Siegrist, T., and Yeh, J. J., *J. Electron. Mater.*, 19:235–239 (1990)
87. *The Oxide Handbook*, 2<sup>nd</sup> ed., (G. V. Samsonov, ed.) p. 153, IFI/Plenum, New York (1982)
88. Schlom, D. G., Marshall, A. F., Sizemore, J. T., Chen, Z. J., Eckstein, J. N., Bozovic, I., von Dessonneck, K. E., Harris, J. S., Jr., and Bravman, J. C., *J. Cryst. Growth*, 102:361–375 (1990)
89. Johnson, B. R., Beauchamp, K. M., Wang, T., Liu, J.-X., McGreer, K. A., Wan, J.-C., Tuominen, M., Zhang, Y.-J., McCartney, M. L., and Goldman, A. M., *Appl. Phys. Lett.*, 56:1911–1913 (1990)
90. Wang, H. S., Eissler, D., Dietsche, W., Fischer, A., and Ploog, K., *J. Cryst. Growth*, 126:565–577 (1993)
91. Nakayama, Y., Tsukada, I., and Uchinokura, K., *J. Appl. Phys.*, 70:4371–4377 (1991)
92. Appelboom, H. M., *Growth and Properties of Co-Evaporated Superconducting YBaCuO Thin Films*, Ph.D. Thesis, Delft University of Technology, Delft (1992)
93. Matijasevic, V. C., private communication
94. Schlom, D. G., *Molecular Beam Epitaxial Growth of Cuprate Superconductors and Related Phases*, Ph.D. Thesis, Stanford University, Stanford (1990)
95. Welch, K. M., *Capture Pumping Technology: An Introduction*, pp. 203–205, Pergamon Press, Oxford (1991)
96. Hellman, E. S., Hartford, E. H., and Fitzgerald, E. A., *J. Mater. Res.*, 7:795–800 (1992)
97. Humphreys, R. G., Satchell, J. S., Chew, N. G., Edwards, J. A., Goodyear, S. W., Blenkinsop, S. E., Dosser, O. D., and Cuillis, A. G., *Sci. Technol.*, 3:38–52 (1990); Humphreys, R. G., Satchell, J. S., Chew, N. G., Edwards, J. A., Goodyear, S. W., Keene, M. N., and Hedges, S. J., *Mater. Sci. Eng.*, B10:293–303 (1991)
98. Hammond, R. H., private communication
99. Haynes® is a registered trademark of Haynes International, Inc., Kokomo, Indiana.
100. Inconel® is a registered trademark of Inco Alloys International, Inc., Huntington, West Virginia.
101. Iijima, K., Terashima, T., Bando, Y., Kamigaki, K., and Terauchi, H., *J. Appl. Phys.*, 72:2840–2845 (1992)
102. Terashima, T., Bando, Y., Iijima, K., Yamamoto, K., Hirata, K., Hayashi, K., Kamigaki, K., and Terauchi, H., *Phys. Rev. Lett.*, 65:2684–2687 (1990)
103. Gerber, Ch., Anselmetti, D., Bednorz, J. G., Mannhart, J., and Schlom, D. G., *Nature*, 350:279–280 (1991)
104. Hawley, M., Raistrick, I. D., Beery, J. G., and Houlton, R. J., *Science*, 251:1587–1589 (1991)
105. Heinzelmann, H., Anselmetti, D., Wiesendanger, R., Güntherodt, H.-J., Kaldis, E., and Wisard, A., *Appl. Phys. Lett.*, 53:2447–2449 (1988)
106. Lang, H. P., Ramseyer, J. P., Brodbeck, D., Frey, T., Karpinski, J., Kaldis, E., and Wolf, Th., *Ultramicroscopy*, 42–44:715–720 (1992)
107. Kanai, M., Kawai, T., and Kawai, S., *Appl. Phys. Lett.*, 58:771–773 (1991)
108. Horikoshi, Y., Kawashima, M., and Yamaguchi, H., *Jpn. J. Appl. Phys.*, 25:L868–L870 (1986); Horikoshi, Y., Kawashima, M., and Yamaguchi, H., *Jpn. J. Appl. Phys.*, 27:169–179 (1988)
109. Bauer, E., *Techniques of Metals Research*, (R. F. Bunshah, ed.) II(2):501–558, Interscience, New York (1969)
110. Lagally, M. G., Savage, D. E., and Tringides, M. C., *Reflection High-Energy Electron Diffraction and Reflection Electron Imaging of Surfaces*, (P. K. Larsen and P. J. Dobson, eds.) pp. 139–174, Plenum Press, New York (1988)
111. Lindemer, T. B., Washburn, F. A., MacDougall, C. S., Feenstra, R., and Cavin, O. B., *Physica*, C178:93–104 (1991)
112. Matijasevic, V., Rosenthal, P., Shinohara, K., Marshall, A. F., Hammond, R. H., and Beasley, M. R., *J. Mater. Res.*, 6:682–698 (1991)
113. Humphreys, R. G., Chew, N. G., Satchell, J. S., Goodyear, S. W., Edwards, J. A., and Blenkinsop, S. E., *IEEE Trans. Magn.*, 27:1357–1360 (1991)
114. Degterov, S. A. and Voronin, G. F., *Physica*, C208:403–411 (1993)
115. Hellman, E. S. and Hartford, E. H., *J. Vac. Sci. Technol.*, B8:332–335 (1990)
116. Enomoto, Y., Murakami, T., and Moriwaki, K., *Jpn. J. Appl. Phys.*, 28:L1355–L1357 (1989)
117. Hellman, E. S. and Hartford, E. H., Jr., *Physica*, C190:31–34 (1991)
118. Cho, A. Y., *The Technology and Physics of Molecular Beam Epitaxy*, (E. H. C. Parker, ed.), pp. 1–13, Plenum Press, New York (1985)

119. Yoshida, S., *Critical Reviews™ in Solid State and Materials Sciences*, (D. E. Schuele and R. W. Hoffman, eds.), 11:287–316, CRC Press, Boca Raton (1984)
120. Terashima, T., Bando, Y., Iijima, K., Yamamoto, K., Hirata, K., Hayashi, K., Matsuda, Y., and Komiyama, S., *Appl. Phys. Lett.*, 56:677–679 (1990)
121. Coleman, E., Siegrist, T., Mixon, D. A., Trevor, P. L., and Trevor, D. H., *J. Vac. Sci. Technol., A9*:2408–2409 (1991)
122. Yokoyama, S., Ishibashi, T., Yamagami, M., and Kawabe, M., *Jpn. J. Appl. Phys.*, 30:L106–L109 (1990)
123. Satoh, T., Yoshitake, T., Miura, S., Fujita, J., Kubo, Y., and Igarashi, H., *Appl. Phys. Lett.*, 55:702–704 (1989)
124. Silver, R. M., Ogawa, E. T., Pan, S., and de Lozanne, A. L., *IEEE Trans. Magn.*, 27:1215–1218 (1991)
125. Berberich, F., Tate, J., Dietsche, W., and Kinder, H., *Appl. Phys. Lett.*, 53:925–926 (1988)
126. Baudenbacher, F., Karl, H., Berberich, P., and Kinder, H., *J. Less-Common Met.*, 164–165:269–278 (1990)
127. Schindler, W., van Hasselt, P., Tontsch, P., Markl, J., Burger, J., Bauer, P., and Saemann-Ischenko, G., *J. Cryst. Growth*, 127:1088–1090 (1993).
128. Herman, M. A. and Sitter, H., *Molecular Beam Epitaxy: Fundamentals and Current Status*, pp. 3–4, 31, Springer-Verlag, Berlin (1989)
129. Do, K. B., Arnason, S. B., Carey, G. P., Ahn, C. H., Beasley, M. R., Geballe, T. H., and Hammond, R. H., "Phase Stability of CuO and Cu<sub>2</sub>O Films Grown by Reactive Electron Beam Evaporation Using an ECR Atomic Oxygen Source," submitted to *Appl. Phys. Lett.* (1993). The O<sup>+</sup> partial pressure data from Fig. 3 of this reference was corrected for the beam nature of the incident fluxes (see Sec. 2.5) before plotting this data in Fig. 19.
130. Schlom, D. G., Eckstein, J. N., Bozovic, I., Chen, Z. J., Marshall, A. F., van Dessenbeck, K. E., and Harris, J. S., Jr., *SPIE*, 1285:234–247, SPIE, Bellingham (1990); *SPIE* 1287:152–165, SPIE, Bellingham (1990)
131. Ogihara, M., Abe, H., and Yamada, T., *Jpn. J. Appl. Phys.* 30:L703–L705 (1991). The NO<sub>2</sub> and O<sub>3</sub> partial pressure data from Fig. 2 of this reference was corrected for the beam nature of the incident fluxes (see Sec. 2.5) before plotting this data in Fig. 19. For this correction, it was assumed that the NO<sub>2</sub> and O<sub>3</sub> introduction tubes were perpendicular to the substrate surface (0=0°).
132. Nonaka, H., Shimizu, T., Hosokawa, S., Ichimura, S., and Arai, K., *SIA Surf. Interface Anal.*, 19:353–357 (1992). The pressure of NO<sub>2</sub> at the substrate position (110 mm from the NO<sub>2</sub> source) used in the copper oxidation experiments described in this reference and plotted in Fig. 19 was estimated from the NO<sub>2</sub> pressure measurements at a distance of 70 mm from the NO<sub>2</sub> source.
133. Chase, M. W., Jr., Davies, C. A., Downey, J. R., Jr., Frurip, D. J., McDonald, R. A., and Syverud, A. N., *JANAF Thermochemical Tables*, 3rd ed., American Chemical Society and American Institute of Physics (1985)
134. *American Institute of Physics Handbook*, 3rd ed., (D. E. Gray, ed.), pp. 7–6–7–8, McGraw-Hill, New York (1972)
135. Landolt-Bornstein: *Zahlenwerte und Funktionen aus Physik, Chemie, Astronomie, Geophysik, und Technik*, (A. Eucken, ed.), 1(1):369, Springer-Verlag, Berlin (1950)
136. Prasad, R., Venugopal, V., and Sood, D. D., *J. Chem. Thermodynamics*, 9:593–601 (1977)
137. Schilling, A., Cantoni, M., Guo, J. D., and Ott, H. R., *Nature*, 363:56–58 (1993)
138. Hashimoto, T., Koinuma, H., and Kishio, K., *Jpn. J. Appl. Phys.*, 30:1685–1686 (1991)
139. Kubinski, D. J., Hoffran, D. W., Soltis, R. E., and Logothetis, E. M., *J. Appl. Phys.*, 71:1860–1867 (1992)
140. Collins, D. M., private communication.
141. Schwarz, H., *Rev. Sci. Instrum.*, 32:194–199 (1961)
142. Loeb, L.B. *The Kinetic Theory of Gases: Being a Text and Reference Book Whose Purpose Is to Combine the Classical Deductions with Recent Experimental Advances in a Convenient Form for Student and Investigator*, 2nd ed., pp. 19, 106, McGraw-Hill, New York (1934)
143. Hellman, E. S., Schlom, D. G., Missert, N., Char, K., Harris, J. S., Jr., Beasley, M. R., Kapitulnik, A., Geballe, T. H., Eckstein, J. N., Weng, S. -L., and Webb, C., *J. Vac. Sci. Technol., B6*:799–803 (1988)
144. Yadavalli, S., Yang, M. H., and Flynn, C. P., *Phys. Rev. B*41:7961–7963 (1990)
145. McKee, R. A., Walker, F. J., Conner, J. R., Specht, E. D., and Zelman, D. E., *Appl. Phys. Lett.*, 59:782–784 (1991)
146. Muthe, K. P., Vyas, J. C., Kothiyal, G. P., Gandhi, D. P., Debnath, A. K., Gupta, S. K., Sabharwal, S. C., and Gupta, M. K., *J. Cryst. Growth*, 118:213–217 (1992)

147. Bormann, R. and Nölting, J., *Appl. Phys. Lett.*, 54:2148–2150 (1989)
148. Bormann, R. and Nölting, J., *Physica*, C162–164:81–82 (1989)
149. Miller, D. J., Chiarello, R. P., Kim, H. K., Roberts, T., You, H., Kampwirth, R. T., Gray, K. E., Zheng, J. Q., Williams, S., Chang, R. P. H., and Ketterson, J. B., *Appl. Phys. Lett.*, 59:3174–3176 (1991)
150. Missert, N., Hammond, R., Mooij, J. E., Matijasevic, V., Rosenthal, P., Geballe, T. H., Kapitulnik, A., Beasley, M. R., Laderman, S. S., Lu, C., Garwin, E., and Barton, R., *IEEE Trans. Magn.*, 25:2418–2421 (1989)
151. Yamamoto, K., Hammond, R. H., and Harris, J. S., Jr., *J. Vac. Sci. Technol.*, A9:2587–2593 (1991)
152. Chew, N. G., Goodyear, S. W., Edwards, J. A., Satchell, J. S., Blenkinsop, S. E., and Humphreys, R. G., *Appl. Phys. Lett.*, 57:2016–2018 (1990)
153. Kita, R., Hase, T., Takahashi, H., Kawaguchi, K., and Morishita, T., *J. Mater. Res.*, 8:321–323 (1993)
154. Eckstein, J. N., Bozovic, I., von Dessonneck, K. E., Schlam, D. G., Harris, J. S., Jr., and Baumann, S. M., *Appl. Phys. Lett.*, 57:931–933 (1990)
155. Kucera, J. T., Perkins, J. D., Uwai, K., Graybeal, J. M., and Orlando, T. P., *Rev. Sci. Instrum.*, 62:1630–1632 (1991)
156. Matijasevic, V. C., Appelboom, H. M., Mathu, F., Hadley, P., van der Marel, D., and Mooij, J. E., *IEEE Trans. Appl. Supercond.*, 3:1524–1527 (1993)
157. Ichimura, S., Hosokawa, S., Nonaka, H., and Arai, K., *J. Vac. Sci. Technol.*, A9:2369–2373 (1991)
158. Norimoto, K., Sekine, R., Mori, M., Hanada, T., Kudo, M., and Kawai, M., *Appl. Phys. Lett.*, 61:1971–1973 (1992)
159. Horváth, M., Blizky, L., and Hüttner, J., *Ozone*, pp. 56–57, 232, Elsevier, Amsterdam (1985), and references therein.
160. Watanabe, S., Kawai, M., and Hanada, T., *Jpn. J. Appl. Phys.*, 29:L1111–L1113 (1990)
161. Kawai, M., Mori, M., Hanada, T., Kudo, M., Ishizawa, N., Goda, T., and Teratani, S., *Physica*, C190:27–30 (1991)
162. Hosokawa, S., and Ichimura, S., *Rev. Sci. Instrum.*, 62:1614–1619 (1991)
163. Luzzau, P., Xu, X. Z., Laguës, M., Hess, N., Contour, J. P., Nanot, M., Queyroux, F., Touzeau, M., and Pagnon, D., *J. Vac. Sci. Technol.*, A8:3938–3940
164. Hill, D. M., Meyer, H. M., III, Weaver, J. H., and Nelson, D. L., *Appl. Phys. Lett.*, 53:1657–1659 (1988)
165. Stall, R. A., *J. Vac. Sci. Technol.*, B1:135–137 (1983)
166. Berkley, D. D., Johnson, B. R., Anand, N., Beauchamp, K. M., Conroy, L. E., Goldman, A. M., Maps, J., Mauersberger, K., Mecartheij, M. L., Morton, J., Tuominen, M., and Zhang, Y.-J., *Appl. Phys. Lett.*, 53:1973–1975 (1988)
167. Nakayama, Y., Ochiaizu, H., Maeda, A., Uchinokura, K., and Tanaka, S., *Jpn. J. Appl. Phys.*, 28:L1217–L1219 (1989)
168. Shimizu, T., Nonaka, H., Hosokawa, S., Ichimura, S., and Arai, K., *Physica*, C185–189:2003–2004 (1991)
169. Achutharaman, V. S., Beauchamp, K. M., Chandrasekhar, N., Spalding, G. C., Johnson, B. R., and Goldman, A. M., *Thin Solid Films*, 216:14–20 (1992)
170. Appelboom, H. M., Matijasevic, V. C., Mathu, F., Rietveld, G., Anczykowski, B., Peterse, W. J. A. M., Tuinstra, F., and Moolji, J. E., *Physica C*, 214:323–334 (1993)
171. Tsukada, I., Kobayashi, S., Koyama, I., Watanabe, H., and Uchinokura, K., *Jpn. J. Appl. Phys.*, 31:L1683–L1685 (1992)
172. Eckstein, J. N., Bozovic, I., Klausmeier-Brown, M. E., Virshup, G. F., and Ralls, K. S., *MRS Bulletin*, 17:27–33 (Aug. 1992); Bozovic, I., Eckstein, J. N., Virshup, G. F., Chaiken, A., Wall, M., Howell, R., and Fluss, M., *J. Supercond.*, 7:187–195 (1994)
173. Shimizu, T., Nonaka, H., and Arai, K., *Appl. Phys. Lett.*, 59:600–602 (1991)
174. Nonaka, H., Shimizu, T., and Arai, K., *Appl. Phys. Lett.*, 57:2850–2852 (1990)
175. Kawai, M., Watanabe, S., and Hanada, T., *J. Cryst. Growth*, 112:745–752 (1991)
176. Cook, G. A., Kiffer, A. D., Klumpp, C. V., Malik, A. H., and Spence, L. A., *Ozone Chemistry and Technology*, 21:44–52, *Advances in Chemistry Series*, Amer. Chem. Soc., Washington D.C. (1959)
177. Horváth, M., Blížký, L., and Hüttner, J., *Ozone*, pp. 215–230, Elsevier, Amsterdam (1985), and references therein.
178. Jenkins, A. C., *Ozone Chemistry and Technology*, 21:13–21, *Advances in Chemistry Series*, Amer. Chem. Soc., Washington D.C. (1959)
179. Waller, J. G. and McTurk, G., *J. Appl. Chem.*, 15:363–366 (1965)

180. Teflon® is a registered trademark of E. I. Du Pont de Nemours & Co., Inc., Wilmington, Delaware.
181. Kel-F® is a registered trademark of 3M, St. Paul, Minnesota.
182. Horváth, M., Blitzky, L., and Hüttner, J., *Ozone*, p. 236, Elsevier, Amsterdam (1985)
183. Carlson, D. J., Siegal, M. P., Phillips, J. M., Tiefel, T. H., and Marshall, J. H., *J. Mater. Res.*, 5:2797–2801 (1990)
184. Giedd, G. R. and Perkins, M. H., *Rev. Sci. Instrum.*, 31:773–775 (1960)
185. Sauerbrey, G., *Z. Phys.*, 155:206–222 (1959)
186. Lu, C. and Lewis, O., *J. Appl. Phys.*, 43:4385–4390 (1972); Lu, C., *J. Vac. Sci. Technol.*, 12:578–583 (1975); *Applications of Piezoelectric Quartz Microbalances*, Vol. 7, *Methods and Phenomena: Their Applications in Science and Technology Series*, (C. Lu and A. W. Czanderna, eds.), Elsevier, Amsterdam (1984)
187. Terashima, T., Iijima, K., Yamamoto, K., Hirata, K., Bando, Y., and Takada, T., *Jpn. J. Appl. Phys.*, 28:L987–L990 (1989)
188. Gogoi, C. A. and Cipro, C., *Surf. Coat. Technol.*, 37:339–348 (1989)
189. Hellman, E. S., Hartford, E. H., and Fleming, R. M., *Appl. Phys. Lett.*, 55:2120–2122 (1989)
190. Chang, L. L., Esaki, L., Howard, W. E., and Ludeke, R., *J. Vac. Sci. Technol.*, 10:11–16 (1973)
191. Fischer, H., Grob, M., Peter, G., and Koprio, J. A., *J. Vac. Sci. Technol.*, A6:2103–2108 (1988)
192. Appelboom, H. M., Hadley, P., van der Marel, D., and Mooij, J. E., *IEEE Trans. Magn.*, 27:1467–1470 (1991)
193. Lu, C., Lightner, M. J., and Gogoi, C. A., *J. Vac. Sci. Technol.*, 14:103–107 (1977)
194. Kobayashi, M., Kiyonaga, B., Ohsako, N., and Hayashi, Y., *Deposition Rate Monitoring of Oxide Superconductor Film by EIES Sensor*, in: *5th International Workshop on Future Electron Devices High-Temperature Superconducting Electron Devices* (1988)
195. Naito, M., *Physica*, C185–189:1977–1978 (1991)
196. Sakai, J., Chen, G., Hirama, K., Murakami, S., and Ishida, T., *Jpn. J. Appl. Phys.*, 27:319–322 (1988)
197. Sakai, J., Kato, K., Hirama, K., Murakami, S., and Ishida, T., *J. Cryst. Growth*, 95:621–624 (1989)
198. Stirling, A. J. and Westwood, W. D., *J. Appl. Phys.*, 41:742–748 (1970); Komietz, T. Y. and Wiegmann, W., *J. Vac. Sci. Technol.*, 12:933–936 (1975)
199. Lu, C., Missert, N., Mooij, J. E., Rosenthal, P., Matijasevic, V., Beasley, M. R., and Hammond, R. H., *High  $T_c$  Superconducting Thin Films, Devices, and Applications*, (G. Margaritondo, R. Joynt, and M. Onellion, eds.) pp. 163–170, American Institute of Physics (Conf. Proc. #182), New York (1989); Lu, C. and Guan, Y., "An Improved Method of Non-Intrusive Deposition Rate Monitoring by Atomic Absorption Spectroscopy for Physical Vapor Deposition Processes," to be published in *J. Vac. Sci. Technol. A*.
200. Cabanel, R., Schuhl, A., Crété, D. G., Tyc, S., and Touzeau, M., *Physica*, C180:38–41 (1991)
201. Klausmeier-Brown, M. E., Eckstein, J. N., Bozovic, I., and Virshup, G. F., *Appl. Phys. Lett.*, 60:657–659 (1992)
202. Beneroe, S. J., Ahn, C. H., Wang, M. M., Khlstrom, K. E., Do, K. B., Arnason, S. B., Fejer, M. M., Geballe, T. H., Beasley, M. R., and Hammond, R. H., *J. Vac. Sci. Technol. B*, 12:1217–1220 (1994)
203. Hammond, R. H., *IEEE Trans. Magn.*, 11:201–207 (1975)
204. Hellman, E. S., Schlom, D. G., Marshall, A. F., Streiffer, S. K., Harris, J. S., Jr., Beasley, M. R., Bravman, J. C., Geballe, T. H., Eckstein, J. N., and Webb, C., *J. Mater. Res.*, 4:476–495 (1989)
205. Hellman, E. S. and Hartford, E. H., Jr., *J. Vac. Sci. Technol. B*, 12:1178–1180 (1994)
206. Winefordner, J. D. and Vickers, T. J., *Anal. Chem.*, 36:161–165 (1964); McClintock, J. A. and Wilson, R. A., *J. Cryst. Growth*, 81:177–180 (1987)
207. Matijasevic, V., Garwin, E. L., and Hammond, R. H., *Rev. Sci. Instrum.*, 61:1747–1749 (1990)
208. Clampitt, R. and Hanley, P. E., *Supercond. Sci. Technol.*, 1:5–6 (1988)
209. Brown, J. D. and Packwook, R. H., *X-Ray Spectrom.*, 11:187–193 (1982)
210. Bastin, G. F., Heijligers, H. J. M., and van Loo, F. J. J., *Scanning*, 8:45–67 (1986)
211. Willich, P. and Obertop, D., *Philips Tech. Rev.*, 42:162–171 (1986)
212. Brown, J. D. and Packwook, R. H., *Appl. Surf. Sci.*, 26:294–305 (1986)

213. Bozovic, I., private communication.
214. DeVries, R. C., *Cubic Boron Nitride: Handbook of Properties*, p. 5, General Electric, Schenectady (1972)
215. Yasinskaya, G. A., *Refractories*, 2:70–72 (1965)
216. Naidich, Yu. V. and Kolesnichenko, G. A., *Poroshk. Metall. Mater. Vses. Konf. 9th*. (Proc. 9<sup>th</sup> All-Union Conf. on Powder Metallurgy) 142–145 (1968)
217. Zhu, W. J., Yue, J. J., Huang, Y. Z., and Zhao, Z. X., *Physica*, C205:118–122 (1993)
218. Li, R. K., Kremer, R. K., and Maier, J., *Physica*, C213:26–32 (1993); Uehara, M., Nakata, H., and Akimitsu, J., *Physica C*, 216:453–457 (1993)
219. Holland, L., *Vacuum Deposition of Thin Films*, pp. 110–111, Wiley, New York (1961)
220. Glang, R., *Handbook of Thin Film Technology*, (L. I. Maissel, and R. Glang, eds.) p. 1–37, McGraw-Hill, New York (1970)
221. *The Oxide Handbook*, 2<sup>nd</sup> ed., (G. V. Samsonov, ed.) p. 401, IFI/Plenum, New York (1982)
222. Davies, G. J. and Williams, D., *The Technology and Physics of Molecular Beam Epitaxy*, (E. H. C. Parker, ed.) pp. 15–46, Plenum Press, New York (1985)
223. Borodin, V. A., Sidorov, V. V., Steriopolo, T. A., and Tatarchenko, V. A., *J. Cryst. Growth*, 82:89–94 (1987)
224. Lamoreaux, R. H. and Hildenbrand, D. L., *J. Phys. Chem Ref. Data*, 16:419–443 (1987)
225. Farrow, R. F. C. and Williams, G. M., *Thin Solid Films*, 55:303–315 (1978)
226. Yvon, K. and François, M., *Z. Phys.*, B76:413–444 (1989)
227. Cava, R. J., Santoro, A., Johnson, D. W., Jr., Rhodes, W. W., *Phys. Rev.*, B35:6716–6720 (1987)
228. Maeta, H., Kato, T., Ono, F., Haruna, K., Tanaka, I., and Kojima, H., *Physica*, C185–189:1383–1384 (1991)
229. Fleming, R. M., Batlogg, B., Cava, R. J., and Rietman, E. A., *Phys. Rev.*, B35:7191–7194 (1987)
230. Beyers, R. and Shaw, T. M., *Solid State Phys.*, 42:135–212 (1989), and references therein.
231. Specht, E. D., Sparks, C. J., Dhre, A. G., Brynestad, J., Cavin, O. B., Kroeger, D. M., and Oye, H. A., *Phys. Rev.*, B37:7426–7434 (1988)

232. Arendt, R. H., Garbauskas, M. F., Meyer, C. A., Rotella, F. J., Jorgensen, J. D., and Hitterman, R. L., *Physica*, C182:73–78 (1991); Arendt, R. H., Garbauskas, M. F., Meyer, C. A., Rotella, F. J., Jorgensen, J. D., and Hitterman, R. L., *Physica*, C194:397–402 (1992)
233. Schneemeyer, L. F., Thomas, J. K., Siegist, T., Batlogg, B., Rupp, L. W., Opila, R. L., Cava, R. J., and Murphy, D. W., *Nature*, 335:421–423 (1988)
234. Fleming, R. M., Marsh, P., Cava, R. J., and Krajewski, J. J., *Phys. Rev.*, B38:7026–7028 (1988)
235. Landolt-Börnstein: *Numerical Data and Functional Relationships in Science and Technology, New Series*, (K.-H. Hellwege, ed.) Group III, 7:134, Springer-Verlag, Berlin (1975)
236. Giess, E. A., Sandstrom, R. L., Gallagher, W. J., Gupta, A., Shinde, S. L., Cook, R. F., Cooper, E. I., O'Sullivan, E. J. M., Roldan, J. M., Segmüller, A. P., and Angilello, J., *IBM J. Res. Develop.*, 34:916–926 (1990)
237. Taylor, D., *Trans. J. Br. Ceram. Soc.*, 84:181–188 (1985)
238. Touhoukian, Y. S., Kirby, R. K., Taylor, R. E., and Lee, T. Y. R., *Thermal Expansion: Nonmetallic Solids*, 13:570, *Thermophysical Properties of Matter*, Plenum, New York (1977)
239. Talvacchio, J., Wagner, G. R., and Talisa, S. H., *Microwave Journal*, 34:105–114 (July, 1991)
240. Geller, S. and Raccah, P. M., *Phys. Rev.*, B2:1167–1172 (1970)
241. Simon, R. W., Platt, C. E., Lee, A. E., Lee, G. S., Daly, K. P., Wire, M. S., Luine, J. A., and Urbanik, M., *Appl. Phys. Lett.*, 53:2677–2679 (1988)
242. Geller, S., Curlander, P. J., and Ruse, G. F., *Mat. Res. Bull.*, 9:637–644 (1974)
243. Sasaura, M., Miyazawa, S., and Mukaida, M., *J. Appl. Phys.*, 68:3643–3644 (1990)
244. Young, K. H., Negrete, G. V., Eddy, M. M., Sun, J. Z., James, T. W., Robinson, McD., and Smith, E. J., *Thin Solid Films*, 206:116–121 (1991)
245. Koren, G., Gupta, A., Giess, E. A., Segmüller, A., and Laibowitz, R. B., *Appl. Phys. Lett.*, 54:1054–1056 (1989)
246. Ingel, R. P. and Lewis, D., III, *J. Am. Ceram. Soc.*, 69:325–332 (1986)

247. Nielsen, T. H. and Leipold, M. H., *J. Am. Ceram. Soc.*, 47:155 (1964)
248. Tietz, L. A., Carter, C. B., Lathrop, D. K., Russek, S. E., Buhman, R. A., and Michael, J. R., *J. Mater. Res.*, 4:1072–1081 (1989)
249. Landolt-Börnstein: *Numerical Data and Functional Relationships in Science and Technology, New Series, Group III, (K. -H. Hellwege, ed.)* 7b:26, Springer-Verlag, Berlin (1975)
250. Tououlkian, Y. S., Kirby, R. K., Taylor, R. E., and Lee, T. Y. R., *Thermal Expansion: Nonmetallic Solids*, 13:288, *Thermophysical Properties of Matter*, Plenum, New York (1977)
251. Landolt-Börnstein: *Numerical Data and Functional Relationships in Science and Technology, New Series, Group III, (Hellwege, K. -H., ed.)* 7b:46, Springer-Verlag, Berlin (1975)
252. Tououlkian, Y. S., Kirby, R. K., Taylor, R. E., and Lee, T. Y. R., *Thermal Expansion: Nonmetallic Solids*, 13:176, *of Thermophysical Properties of Matter*, Plenum, New York (1977)
253. Talvacchio, J., Wagner, G. R., and Pohl, H. C., *Physica*, C162-164:659–660 (1989)
254. Char, K., Colclough, M. S., Garrison, S. M., Newman, N., and Zaharchuk, G., *Appl. Phys. Lett.*, 59:733–735 (1991)
255. Wu, X. D., Muenchausen, R. E., Nogar, N. S., Pique, A., Edwards, R., Wilkens, B., Ravi, T. S., Hwang, D. M., and Chen, C. Y., *Appl. Phys. Lett.*, 58:304–306 (1991)
256. Merchant, P., Jacobowitz, R. D., Tibbs, K., Taber, R. C., and Laderman, S. S., *Appl. Phys. Lett.*, 60:763–765 (1992)
257. Landolt-Börnstein: *Numerical Data and Functional Relationships in Science and Technology, New Series, Group III, (O. Madelung, ed.)* 22a:18, Springer-Verlag, Berlin (1987)
258. Tououlkian, Y. S., Kirby, R. K., Taylor, R. E., and Lee, T. Y. R., *Thermal Expansion: Nonmetallic Solids*, 13:154, *Thermophysical Properties of Matter*, Plenum, New York (1977)
259. Fork, D. K., Fenner, D. B., Connell, G. A. N., Phillips, J. M., and Geballe, T. H., *Appl. Phys. Lett.*, 57:1137–1139 (1990)
260. Fork, D. K., Fenner, D. B., Barton, R. W., Phillips, J. M., Connell, G. A. N., Boyce, J. B., and Geballe, T. H., *Appl. Phys. Lett.*, 57:1161–1163 (1990)
261. Landolt-Börnstein: *Numerical Data and Functional Relationships in Science and Technology, New Series, Group III, (O. Madelung, ed.)* 22a:88, Springer-Verlag, Berlin (1987)
262. Tououlkian, Y. S., Kirby, R. K., Taylor, R. E., and Lee, T. Y. R., *Thermal Expansion: Nonmetallic Solids*, 13:747, *Thermophysical Properties of Matter*, Plenum, New York (1977)
263. Nashimoto, K., Fork, D. K., and Geballe, T. H., *Appl. Phys. Lett.*, 60:1199–1201 (1992); Fork, D. K., Nashimoto, K., and Geballe, T. H., *Appl. Phys. Lett.*, 60:1621–1623 (1992)
264. Matthews, J. W., *Epitaxial Growth*, (J. W. Matthews, ed.) Part B, pp. 559–609, Academic Press, New York (1975)
265. Imam, A., Wu, X. D., Nazar, L., Hegde, M. S., Rogers, C. T., Venkatesan, T., Simon, R. W., Daly, K., Padamsee, H., Kirchgessner, J., Moffat, D., Rubin, D., Shu, Q. S., Kalokitis, D., Fathy, A., Pendrick, V., Brown, R., Brycki, B., Belohoubek, E., Drabeck, L., Gruner, G., Hammond, R., Gamble, F., Larson, B. M., and Bravman, J. C., *Appl. Phys. Lett.*, 56:1178–1180 (1990)
266. Alarco, J. A., Brorsson, G., Ivanov, Z. G., Nilsson, P.-Å., Olsson, E., and Löfgren, M., *Appl. Phys. Lett.*, 61:723–725 (1992)
267. Moeckly, B. H., Russek, S. E., Lathrop, D. K., Buhman, R. A., Li, J., and Mayer, J. W., *Appl. Phys. Lett.*, 57:1687–1689 (1990)
268. Berezin, A. B., Yuan, C. W., and de Lozanne, A. L., *Appl. Phys. Lett.*, 57:90–92 (1990)
269. Moeckly, B. H., Lathrop, D. K., Russek, S. E., Buhman, R. A., Norton, M. G., and Carter, C. B., *IEEE Trans. Magn.*, 27:1017–1020 (1991)
270. Char, K., Newman, N., Garrison, S. M., Barton, R. V., Taber, R. C., Laderman, S. S., and Jacobowitz, R. D., *Appl. Phys. Lett.*, 57:409–411 (1990)
271. Wang, F., Siegel, M., Smithey, R., Geerk, J., Linker, G., and Meyer, O., *High  $T_c$  Superconductor Thin Films*, (L. Correra, ed.), pp. 611–615, North-Holland, Amsterdam (1992)
272. Wu, X. D., Dye, R. C., Muenchausen, R. E., Folty, S. R., Maley, M., Rollett, A. D., Garcia, A. R., and Nogar, N. S., *Appl. Phys. Lett.*, 58:2165–2167 (1991)
273. Prusseit, W., Corsépius, S., Baudenbacher, F., Hirata, K., Berberich, P., and Kinder, H., *Appl. Phys. Lett.*, 61:1841–1843 (1992)
274. Grigoryeva, I. V. and Vinnikov, L. Ya., *J. Low Temp. Phys.*, 74:81–101 (1989)

275. Pan, V. M., Kaminsky, G. G., Kasatkina, A. L., Kuznetsov, M. A., Prokhorov, V. G., Svetchnikov, V. L., Tretiatchenko, C. G., Flis, V. S., Yushchenko, S. K., Matsui, V. I., and Melnikov, V. S., *Supercond. Sci. Technol.*, 5:S48–S54 (1992); Pan, V. M., Kasatkina, A. L., Svetchnikov, V. L., and Zandbergen, H. W., *Cryogenics*, 33:21–27 (1993); Pan, V.M., *J. Alloys Compd.*, 195:387–394 (1992)
276. Mannhart, J., Anselmetti, D., Bednorz, J. G., Catana, A., Gerber, Ch., Müller, K. A., and Schlim, D. G., *Z Phys.*, B86:177–181 (1992)
277. Gross, R., Gupta, A., Olsson, E., Segmüller, A., and Koren, G., *Appl. Phys. Lett.*, 57:203–205 (1990)
278. Gao, J., Häuser, B., and Rogalla, H., *J. Appl. Phys.*, 67:2512–2515 (1990)
279. Nagaishi, T., Itozaki, H., Tamaka, S., Matsuura, T., Ota, N., Fujimori, N., and Yazu, S., *Jpn. J. Appl. Phys.*, 30:L718–L721 (1991)
280. Pan, V. M., Solov'ev, V. F., and Taborov, V. F., *Supercond. Sci. Technol.*, 5:S192–S195 (1992)
281. Sasaoka, M., Mukaida, M., and Miyazawa, S., *Appl. Phys. Lett.*, 57:2728–2729 (1990)
282. Sasaoka, M. and Miyazawa, S., *J. Cryst. Growth*, 123:126–132 (1992)
283. Ralston, R. W., Kastner, M. A., Gallagher, W. J., and Battlogg, B., *IEEE Spectrum*, 29:50–55 (August 1992); Berkstresser, G. W., Valentino, A. J., and Brandle, C. D., *J. Cryst. Growth*, 109:457–466 (1991); Berkstresser, G. W., Valentino, A. J., and Brandle, C. D., *J. Cryst. Growth*, 109:467–471 (1991)
284. Hsu, Y. T., Applied Technology Enterprises, Columbia, SC, private communication.
285. Garrison, S. M., Newman, N., Cole, B. F., Char, K., and Barton, R. W., *Appl. Phys. Lett.*, 58:2168–2170 (1991); Garrison, S. M., Newman, N., Cole, B. F., Char, K., and Barton, R. W., *Appl. Phys. Lett.*, 59:3060 (1991)
286. Fork, D. K., Garrison, S. M., Hawley, M., and Geballe, T. H., *J. Mater. Res.*, 7:1641–1651 (1992)
287. Ramesh, R., Hwang, D., Ravi, T., Inam, A., Barner, J. B., Nazar, L., Chan, S. W., Chen, C. Y., Dutta, B., Venkatesan, T., and Wu, X. D., *Appl. Phys. Lett.*, 56:2243–2245 (1990); Ravi, T. S., Hwang, D. M., Ramesh, R., Chan, S. W., Nazar, L., Chen, C. Y., Inam, A., and Venkatesan, T., *Phys. Rev.*, B42:10141–10151 (1990)
288. Laderman, S. S., Taber, R. C., Jacobitz, R. D., Moll, J. L., Eom, C. B., Hylton, T. L., Marshall, A. F., Geballe, T. H., and Beasley, M. R., *Phys. Rev.*, B43:2922–2933 (1991)
289. Char, K., Colclough, M. S., Lee, L. P., and Zaharchuk, G., *Appl. Phys. Lett.*, 59:2177–2179 (1991)
290. Wu, X. D., Luo, L., Muenchhausen, R. E., Springer, K. N., and Folyn, S., *Appl. Phys. Lett.*, 60:1381–1383 (1992)
291. Hellman, E. S., Hartford, E. H., and Gyorgy, E. M., *Appl. Phys. Lett.*, 58:1335–1337 (1991)
292. Norton, M. G., Hellman, E. S., Hartford, E. H., Jr., and Carter, C. B., *J. Cryst. Growth*, 113:716–721 (1991); Norton, M. G., Hellman, E. S., Hartford, E. H., Jr., and Carter, C. B., *Physica*, C205:347–353 (1993)
293. Char, K., Newman, N., Garrison, S. M., Barton, R. W., and Zaharchuk, G., "Surface Resistance of Epitaxial  $\text{YBa}_2\text{Cu}_3\text{O}_7$  Thin Films on Sapphire," presented at the Applied Superconductivity Conference, Aspen (1990), unpublished.
294. Mogro-Campero, A., Hunt, B. D., Turner, L. G., Burrell, M. C., and Balz, W. E., *Appl. Phys. Lett.*, 52:584–586 (1988)
295. Madakson, P., Cuomo, J. J., Yee, D. S., Roy, R. A., and Scilla, G., *J. Appl. Phys.*, 63:2046–2053 (1988)
296. Venkatesan, T., Chase, E. W., Wu, X. D., Inam, A., Chang, C. C., and Shokoohi, F. K., *Appl. Phys. Lett.*, 53:243–245 (1988)
297. Fenner, D. B., Viano, A. M., Fork, D. K., Connell, G. A. N., Boyce, J. B., Ponce, F. A., and Tramontana, J. C., *J. Appl. Phys.*, 69:2176–2182 (1991)
298. Nordman, C. A., Wang, T., Chandrasekhar, N., Beauchamp, K. M., Achutharaman, V. S., Schulze, R. K., Spalding, G. C., Lin, Z.-H., Evans, J. F., and Goldman, A. M., *J. Appl. Phys.*, 70:5697–5699 (1991)
299. Filby, J. D. and Nielsen, S., *J. Appl. Phys.*, 18:1357–1382 (1967)
300. Manasevit, H. M., *J. Crystal Growth*, 22:125–148 (1974)
301. Manasevit, H. M., Miller, A., Morritt, F. L., and Nolder, R., *Trans. Metall. Soc., AIME* 233:540–549 (1965)
302. Manasevit, H. M. and Forbes, D. H., *J. Appl. Phys.*, 37:734–739 (1966)
303. Golecki, I., Manasevit, H. M., Moudy, L. A., Yang, J. J., and Mee, J. E., *Appl. Phys. Lett.*, 42:501–503 (1983); Manasevit, H. M., Golecki, I., Moudy, L. A., Yang, J. J., and Mee, J. E., *J. Electrochem. Soc.*, 130:1752–1758 (1983)

304. Ishida, M., Katakabe, I., Nakamura, T., and Otake, N., *Appl. Phys. Lett.*, 52:1326–1328 (1988); Sawada, K., Ishida, M., Nakamura, T., and Suzuki, T., *J. Cryst. Growth*, 95:494–499 (1989)
305. Iizuka, H., Yokoo, K., and Ono, S., *Appl. Phys. Lett.*, 61:2978–2980 (1992)
306. Ihara, M., Arimoto, Y., Jifuku, M., Kimura, T., Kodama, S., Yamawaki, H., and Yamaoka, T., *J. Electrochem. Soc.*, 129:2569–2573 (1982); Ihara, M., *Microelectron. Eng.*, 1:161–177 (1983)
307. Morita, M., Fukumoto, H., Imura, T., Osaka, Y., and Ichihara, M., *J. Appl. Phys.*, 58:2407–2409 (1985)
308. Legagneux, P., Garry, G., Dieumegard, D., Schwebel, C., Pellet, C., Gautherin, G., and Siejka, J., *Appl. Phys. Lett.*, 53:1506–1508 (1988)
309. Fukumoto, H., Imura, T., and Osaka, Y., *Jpn. J. Appl. Phys.*, 27:L1404–L1405 (1988)
310. Miura, S., Yoshitake, T., Matsubara, S., Miyasaka, Y., Shohata, N., and Satoh, T., *Appl. Phys. Lett.*, 53:1967–1969 (1988); Wu, X. D., Inam, A., Hegde, M. S., Wilkens, B., Chang, C. C., Hwang, D. M., Nazar, L., Venkatesan, T., Miura, S., Matsubara, S., Miyasaka, Y., and Shohata, N., *Appl. Phys. Lett.*, 54:754–756 (1989)
311. Inoue, T., Yamamoto, Y., Koyama, S., Suzuki, S., and Ueda, Y., *Appl. Phys. Lett.*, 56:1332–1333 (1990); Yamamoto, Y., Sato, M., Sakurai, Y., Nakajima, S., Inoue, T., and Ohsuna, T., *Jpn. J. Appl. Phys.*, 32:L620–L623 (1993)
312. Yoshimoto, M., Nagata, H., Tsukahara, T., and Koinuma, H., *Jpn. J. Appl. Phys.*, 29:L1199–L1202 (1990); Nagata, H., Tsukahara, T., Gonda, S., Yoshimoto, M., and Koinuma, H., *Jpn. J. Appl. Phys.*, 30:L1136–L1138 (1991); Nagata, H., Yoshimoto, M., Koinuma, H., Min, E., and Haga, N., *J. Cryst. Growth*, 123:1–4 (1992)
313. Luo, L., Wu, X. D., Dye, R. C., Muenchhausen, R. E., Folty, S. R., Coulter, Y., Maggiore, C. J., and Inoue, T., *Appl. Phys. Lett.*, 59:2043–2045 (1991)
314. Fork, D. K., Ponce, F. A., Tramontana, J. C., Newman, N., Phillips, J. M., and Geballe, T. H., *Appl. Phys. Lett.*, 58:2432–2434 (1991)
315. Burns, M. J., de la Houssaye, P. R., Russell, S. D., Garcia, G. A., Clayton, S. R., Ruby, W. S., and Lee, L. P., *Appl. Phys. Lett.*, 63:1282–1284 (1993)
316. Tseng, M. Z., Nguyen, C., Tarsa, E., Chang, L. D., Hu, E. L., and Kroemer, H., *Appl. Phys. Lett.*, 61:601–603 (1992)
317. Prusseit, W., Carsipius, S., Utz, B., Baudenbacher, F., Hirata, K., Berberich, P., Kinder, H., and Eibl, O., *IEEE Trans. Appl. Supercond.*, 3:1070–1073 (1993)
318. Goodyear, S. W., Satchell, J. S., Humphreys, R. G., Chew, N. G., and Edwards, J. A., *Physica*, C192:85–94 (1992)
319. Chandrasekhar, N., Agrawal, V., Achutharaman, V. S., and Goldman, A. M., *Appl. Phys. Lett.*, 60:2424–2426 (1992)
320. Agrawal, V., Chandrasekhar, N., Zhang, Y. J., Achutharaman, V. S., Mecartney, M. L., and Goldman, A. M., *J. Vac. Sci. Technol.*, A10:1531–1536 (1992)
321. Tanaka, S., Nakamura, T., Tokuda, H., and Iiyama, M., *Appl. Phys. Lett.*, 62:3040–3042 (1993)
322. Schlom, D. G., Anselmetti, D., Bednorz, J. G., Broom, R., Catana, A., Frey, T., Gerber, Ch., Güntherodt, H.-J., Lang, H. P., and Mannhart, J., *Z. Phys.*, B86:163–175 (1992)
323. Lang, H. P., Frey, T., and Güntherodt, H.-J., *Europhys. Lett.*, 15:667–670 (1991)
324. Baudenbacher, F., Hirata, K., Berberich, P., Kinder, H., Assmann, W., and Lang, H. P., *Physica*, C185–189:2177–2178 (1991)
325. Luo, L., Hawley, M. E., Maggiore, C. J., Dye, R. C., Muenchhausen, R. E., Chen, L., Schmidt, B., and Kaloyerous, A. E., *Appl. Phys. Lett.*, 62:485–486 (1993)
326. Schlom, D. G., Anselmetti, D., Bednorz, J. G., Gerber, Ch., and Mannhart, J., *J. Cryst. Growth*, 137:259–267 (1994)
327. Frank, F. C., *Disc. Farad. Soc.*, 5:48–79 (1949); Burton, W. K., Cabrera, N., and Frank, F. C., *Philos. Trans. R. Soc. London*, A243:299–358 (1951); Frank, F. C., *Adv. Phys.*, 1:91–109 (1952)
328. Verma, A. R., *Crystal Growth and Dislocations*, Butterworths, London (1953)
329. Baronnet, A., *J. Cryst. Growth*, 19:193–198 (1973)
330. Lowndes, D. H., Zheng, X.-Y., Zhu, S., Budai, J. D., and Warmack, R. J., *Appl. Phys. Lett.*, 61:852–854 (1992)
331. Satchell, J. S., Humphreys, R. G., Chew, N. G., Goodyear, S. W., Edwards, J. A., and Keene, M. N., *Physica*, C180:247–250 (1991)
332. Chew, N. G., Goodyear, S. W., Humphreys, R. G., Satchell, J. S., Edwards, J. A., and Keene, M. N., *Appl. Phys. Lett.*, 60:1516–1518 (1992)
333. Edwards, J. A., Satchell, J. S., Chew, N. G., Humphreys, R. G., Keene, M. N., and Dosser, O. D., *Appl. Phys. Lett.*, 60:2433–2435 (1992)

334. Kawai, M., private communication.
335. Inam, A., Rogers, C. T., Ramesh, R., Remschning, K., Farrow, L., Hart, D., Venkatesan, T., and Wilkens, B., *Appl. Phys. Lett.*, **57**:2484–2486 (1990)
336. Linker, G., Xi, X., Meyer, O., Li, Q., and Geerk, J., *Solid State Commun.*, **69**:249–253 (1989)
337. Eom, C. B., Marshall, A. F., Laderman, S. S., Jacobowitz, R. D., and Geballe, T. H., *Science*, **249**:1549–1552 (1990)
338. Terashina, T., Bando, Y., Iijima, K., Yamamoto, K., and Hirata, K., *Appl. Phys. Lett.*, **53**:2232–2234 (1988)
339. Schliom, D. G., Marshall, A. F., Harris, J. S., Jr., Bozovic, I., and Eckstein, J. N., *Advances in Superconductivity III: Proceedings of the 3rd International Symposium on Superconductivity (ISS '90)*, (K. Kajimura and H. Hayakawa, eds.) pp. 1011–1016, Springer-Verlag, Tokyo, (1991)
340. Eckstein, J. N., Bozovic, I., Schliom, D. G., and Harris, J. S., Jr., *Appl. Phys. Lett.*, **57**:1049–1051 (1990)
341. Eckstein, J. N., Bozovic, I., Klausmeier-Brown, M., Virshup, G., and Rails, K. S., *Thin Solid Films*, **216**:8–13 (1992)
342. Bozovic, I., Eckstein, J. N., Klausmeier-Brown, M. E., and Virshup, G., *J. Supercond.*, **5**:19–23 (1992)
343. Virshup, G. F., Klausmeier-Brown, M. E., Bozovic, I., and Eckstein, J. N., *Appl. Phys. Lett.*, **60**:2288–2290 (1992)
344. Klausmeier-Brown, M. E., Virshup, G. F., Bozovic, I., and Eckstein, J. N., *Appl. Phys. Lett.*, **60**:2806–2808 (1992)
345. Bodin, P., Sakai, S., and Kasai, Y., *Jpn. J. Appl. Phys.*, **31**:L949–L952 (1992)
346. Suzuki, K., Karaki, T., Iwashima, K., Shibata, M., Okada, H., Onnagawa, H., and Miyashita, K., *Jpn. J. Appl. Phys.*, **31**:L1339–L1341 (1992)
347. Tsukada, I., and Uchinokura, K., *Jpn. J. Appl. Phys.*, **30**:L1468–L1470 (1991)
348. Kasai, Y., and Sakai, S., *J. Cryst. Growth*, **115**:758–761 (1991)
349. Bozovic, I., Eckstein, J. N., Schliom, D. G., and Harris, J. S., *Science and Technology of Thin Film Superconductors 2*, (R. D. McConnell, and R. Noufi, eds.) pp. 267–272, Plenum Press, New York (1990)
350. Ikeda, Y., Ito, H., Shimomura, S., Oue, Y., Inaba, K., Hiroi, Z., and Takano, M., *Physica*, **C159**:93–104 (1989)

351. Roth, R. S., Rawn, C. J., Burton, B. P., and Beech, F., *J. Res. Natl. Inst. Stand. Technol.*, **95**:291–335 (1990)
352. Ishibashi, T., Okada, Y., Yokoyama, S., and Kawabe, M., *Jpn. J. Appl. Phys.*, **30**:3900–3903 (1991)
353. Sakai, S., Kasai, Y., and Bodin, P., *Jpn. J. Appl. Phys.*, **31**:L399–L401 (1992)
354. Chou, H., Chen, H. S., Kortan, A. R., Kimmerling, L. C., Thiel, F. A., and Wu, M. K., *Appl. Phys. Lett.*, **58**:2836–2838 (1991)
355. Betz, J., Piehler, A., Pechen, E. V., and Renk, K. F., *J. Appl. Phys.*, **71**:2478–2479 (1992)
356. Face, D. W., and Nestlerode, J. P., *Appl. Phys. Lett.*, **61**:1838–1840 (1992); Face, D. W., and Nestlerode, J. P., *IEEE Trans. Appl. Supercond.*, **3**:1516–1519 (1993)
357. Ahn, B. T., Lee, W. Y., and Beyers, R., *Appl. Phys. Lett.*, **60**:2150–2152 (1992)
358. Abe, H., Toda, F., and Ogiwara, M., *IEEE Electron Device Lett.*, **14**:100–102 (1993)
359. Cava, R. J., Siegrist, T., Peck, W. F., Jr., Krajewski, J. J., Battlogg, B., and Rosamilia, J., *Phys. Rev. B*, **44**:9746–9748 (1991)
360. Cava, R. J., Takagi, H., Zandbergen, H. W., Hessen, B., Krajewski, J. J., and Peck, W. F., Jr., *Phys. Rev. B*, **46**:14101–14104 (1992)
361. Xu, Q., Fu, W. T., van Ruitenbeek, J. M., and de Jongh, L. J., *Physica*, **C167**:271–277 (1990)
362. Warren, B. E., *X-ray Diffraction*, Dover, New York (1969, 1990). See in particular Eqs. 1.12, 2.5, 3.2, 3.24, and 4.7.
363. Hendricks, S., and Teller, E., *J. Chem. Phys.*, **10**:147–167 (1942)
364. Kuroda, K., Kojima, K., Tanioka, M., Yokoyama, K., and Hamanaka, K., *Jpn. J. Appl. Phys.*, **28**:1586–1592 (1989)
365. Kojima, K., Schliom, D. G., Kuroda, K., Tanioka, M., Hamanaka, K., Eckstein, J. N., and Harris, J. S., Jr., *Jpn. J. Appl. Phys.*, **29**:L1638–L1641 (1990)
366. Fujita, J., Tatsumi, T., Yoshitake, T., and Igarashi, H., *Science and Technology of Thin Film Superconductors*, (McConnell, R. D. and Wolf, S. A., eds.) pp. 175–184, Plenum, New York (1989); Fujita, J., Tatsumi, T., Yoshitake, T., and Igarashi, H., *Appl. Phys. Lett.*, **54**:2364–2366 (1989)
367. Krebs, H.-U., and Kehlenbeck, M., *Physica*, **C162**:164:119–120 (1989); Krebs, H.-U., Kehlenbeck, M., Steins, M., and Kupcik, V., *J. Appl. Phys.*, **69**:2405–2409 (1991)

368. Zhu, S., Lowndes, D. H., Chakoumakos, B. C., Budai, J. D., Christen, D. K., Zheng, X.-Y., Jones, E., and Warmack, B., *Appl. Phys. Lett.*, 63:409–411 (1993)
369. Lang, Ch., Hettich, B., Schwarz, M., Bestgen, H., and Elschner, S., *Physica*, C182:79–88 (1991)
370. Matsushima, T., Ichikawa, Y., Adachi, H., Setsune, K., and Wasa, K., *Solid State Commun.*, 76:1201–1204 (1990)
371. Horiuchi, K., Kawai, T., Kanai, M., and Kawai, S., *Jpn. J. Appl. Phys.*, 30:L1381–L1383 (1991)
372. Inoue, M., Yoshida, K., Ohbayashi, K., Takai, Y., and Hayakawa, H., *Physica*, C200:403–408 (1992)
373. Pargellis, A. N., Sharifi, F., Dynes, R. C., Miller, B., Hellman, E. S., Rosamilia, J. M., and Hartford, E. H., Jr., *Appl. Phys. Lett.*, 58:95–96 (1991)
374. Hellman, E. S., Martin, S., Hartford, E. H., Jr., Werder, D. J., Roessler, G. M., Jr., and Tedrow, P. M., *Physica*, C201:166–170 (1992)
375. Fink, R. L., Hilbert, C., and Kroger, H., *Appl. Phys. Lett.*, 62:3360–3362 (1993)
376. Kussmaul, A., Hellman, E. S., Hartford, E. H., Jr., and Tedrow, P. M., *Appl. Phys. Lett.*, 63:2824–2826 (1993)
377. Adachi, H., Ichikawa, Y., Hirochi, K., Matsushima, T., Setsune, K., and Wasa, K., *Jpn. J. Appl. Phys.*, 29:L81–L82 (1990)
378. The first report of GaAs grown directly on vicinal Si (100) was by: Metze, G. M., Choi, H. K., and Tsaur, B-Y., *Appl. Phys. Lett.*, 45:1107–1109 (1984). Although the vicinal nature of the Si (100) substrates used in a prior study is not stated, from the data presented it is likely that this earlier study of GaAs growth directly on silicon also used vicinal Si (100) surfaces: Wang, W. I., *Appl. Phys. Lett.*, 44:1149–1151 (1984)
379. Shibahara, K., Nishino, S., and Matsunami, H., *Appl. Phys. Lett.*, 50:1888–1890 (1987)
380. Budai, J. D., Chisholm, M. F., Feenstra, R., Lowndes, D. H., Norton, D. P., Boatner, L. A., and Christen, D. K., *Appl. Phys. Lett.*, 58:2174–2176 (1991)
381. Fujita, J., Yoshitake, T., Satoh, T., Miura, S., Tsuge, H., and Igashii, H., *Appl. Phys. Lett.*, 59:2445–2447 (1991)
382. Satoh, T., Fujita, J., Yoshitake, T., and Igashii, H., *Physica*, C191:359–362 (1992)
383. Kuroda, K., Wada, O., Tanimura, J., Kojima, K., Takami, T., Kataoka, M., Ogama, T., and Hamanaka, K., *Jpn. J. Appl. Phys.*, 30:L582–L584 (1991)
384. Wada, O., Kuroda, K., Tanimura, J., Kataoka, M., Kojima, K., Takami, T., Hamanaka, K., and Ogama, T., *Jpn. J. Appl. Phys.*, 30:L1881–L1883 (1991)
385. Tanimura, J., Kuroda, K., Kataoka, M., Wada, O., Takami, T., Kojima, K., and Ogama, T., *Jpn. J. Appl. Phys.*, 32:L254–L256 (1993)
386. Ishibashi, T., Song, K., Okada, Y., and Kawabe, M., *Jpn. J. Appl. Phys.*, 31:L406–L409 (1992)
387. Ishibashi, T., Fujita, T., Song, K., Okada, Y., and Kawabe, M., *J. Appl. Phys.*, 32:L257–L259 (1993)
388. Kwo, J., Fleming, R. M., Kao, H. L., Werder, D. J., and Chen, C. H., *Appl. Phys. Lett.*, 60:1905–1907 (1992)
389. Tsukada, I., and Uchinokura, K., *Physica*, B, 194–196:2329–2330 (1994)
390. Sunshine, S. A., Siegrist, T., Schneemeyer, L. F., Murphy, D. W., Cava, R. J., Battlogg, B., van Dover, R. B., Fleming, R. M., Glarum, S. H., Nakahara, S., Farrow, R., Krajewski, J. J., Zahurak, S. M., Waszczak, J. V., Marshall, J. H., Marsh, P., Rupp, L. W., Jr., and Peck, W. F., *Phys. Rev.*, B38:893–896 (1988)
391. Bordin, P., Capponi, J. J., Chaillout, C., Chenavas, J., Hewat, A. W., Hewat, E. A., Hodeau, J. L., Marezio, M., Tholence, J. L., and Tranqui, D., *Physica*, C156:189–192 (1988)
392. Eibl, O., *Physica*, C168:215–238 (1990)
393. Aarnink, W. A. M., Reuvekamp, E. M. C. M., Verhoeven, M. A. J., Pedyash, M. V., Gerritsma, G. J., van Silfhout, A., Rogalla, H., and Ryan, T. W., *Appl. Phys. Lett.*, 61:607–609 (1992)
394. Fujita, J., Yoshitake, T., Satoh, T., Ichihashi, T., and Igashii, H., *IEEE Trans. Magn.*, 27:1205–1210 (1991)
395. Scherer, T., Marienhoff, P., Henwig, R., Neuhaus, M., and Jutzi, W., *Physica*, C197:79–83 (1992)
396. Young, K. H. and Sun, J. Z., *Appl. Phys. Lett.*, 59:2448–2450 (1991)
397. Shlichta, P. J., *NASA Tech. Briefs*, 89-05:48 (1989); Shlichta, P. J., *NASA Technical Support Package NPO-17/6841*, NASA, BWI Airport (1989)
398. Takei, W. J., Wu, S. Y., and Francombe, M. H., *J. Cryst. Growth*, 28:188–198 (1975)

399. Fujita, J., Satoh, T., Yoshitake, T., Tsai, J. S., and Tsuge, H., *Extended Abstracts of the 1992 International Conference on Solid State Devices and Materials*, pp. 718–719, Business Center for Academic Societies Japan, Tokyo (1992)
400. Terashima, T., Shimura, K., Bando, Y., Iijima, K., Yamamoto, K., Hirata, K., Hayashi, K., Kamigaki, K., and Terauchi, H., *Advances in Superconductivity III: Proceedings of the 3rd International Symposium on Superconductivity (ISS '90)*, (K. Kajimura and H. Hayakawa, eds.) pp. 851–856, Springer-Verlag, Tokyo (1991); Kamigaki, K., Terashima, T., Shimura, K., Bando, Y., and Terauchi, H., *Physica*, C183:252–256 (1991)
401. Pennycook, S. J., Chisholm, M. F., Jesson, D. E., Norton, D. P., Lowndes, D. H., Feenstra, R., Kerchner, H. R., and Thomson, J. O., *Phys. Rev. Lett.*, 67:765–768 (1991)
402. Eibl, O., Hoenig, H. E., Triscone, J.-M., Fischer, Ø., Antognazza, L., and Brunner, O., *Physica*, C172:365–372 (1990)
403. Jia, C. L., Soltner, H., Jakob, G., Hahn, T., Adrian, H., and Urban, K., *Physica*, C210:1–15 (1993)
404. Fujita, J., Yoshitake, T., Igarashi, H., and Satoh, T., *Appl. Phys. Lett.*, 56:295–297 (1990)
405. Karl, H. and Stritzker, B., *Phys. Rev. Lett.*, 69:2939–2942 (1992)
406. Gupta, A. and Hussey, B. W., *Appl. Phys. Lett.*, 58:1211–1213 (1991); Chern, M. Y., Gupta, A., and Hussey, B. W., *Appl. Phys. Lett.*, 60:3045–3047 (1992); Chern, M. Y., Gupta, A., Hussey, B. W., and Shaw, T. M., *J. Vac. Sci. Technol. A*, 11:637–641 (1993)
407. Williams, S., Zheng, J. Q., Shih, M. C., Wang, X. K., Lee, S. J., Rippert, E. D., Maglic, S., Kaijyama, H., Segel, D., Dutta, P., Chang, R. P. H., Ketterson, J. B., Roberts, T., Lin, Y., Kampwirth, R. T., and Gray, K., *J. Appl. Phys.*, 72:4798–4804 (1992)
408. Fuoss, P. H., Kisker, D. W., Lamelas, F. J., Stephenson, G. B., Imperatori, P., and Brennan, S., *Phys. Rev. Lett.*, 69:2791–2794 (1992)
409. Adachi, H., Kohiki, S., Setsune, K., Mitsuyu, T., and Wasa, K., *Jpn. J. Appl. Phys.*, 27:L1883–1886 (1988)
410. Koinuma, H., Nagata, H., Takano, A., Kawasaki, M., and Yoshimoto, M., *Science and Technology of Thin Film Superconductors*, (R. D. McConnell, and S. A. Wolf, eds.) pp. 205–213, Plenum, New York (1989)

411. Nakamura, K., Sato, J., Kaise, M., and Ogawa, K., *Jpn. J. Appl. Phys.*, 28:L437–L440 (1989); Nakamura, K., Sato, J., and Ogawa, K., *Jpn. J. Appl. Phys.*, 29:L77–L80 (1990)
412. Kittl, J. A., Nieh, C. W., Lee, D. S., and Johnson, W. L., *Mater. Lett.*, 9:336–338 (1990); Kittl, J. A., Johnson, W. L., and Nieh, C. W., *J. Mater. Res.*, 7:2003–2016 (1992)
413. Ohbayashi, K., Anma, M., Takai, Y., and Hayakawa, H., *Jpn. J. Appl. Phys.*, 29:L2049–L2052 (1990); Ohtayashi, K., Yoshida, K., Anma, M., Takai, Y., and Hayakawa, H., *Jpn. J. Appl. Phys.*, 31:L953–L955 (1992)
414. Yang, K.-Y., Dilorio, M. S., Yoshizumi, S., Maung, M. A., Zhang, J., Tsai, P. K., and Maple, M. B., *Appl. Phys. Lett.*, 61:2826–2828 (1992)
415. Kanai, M., Kawai, T., Kawai, S., and Tabata, H., *Appl. Phys. Lett.*, 54:1802–1804 (1989)
416. Duray, S. J., Buchholz, D. B., Song, S. N., Richeson, D. S., Ketterson, J. B., Marks, T. J., and Chang, R. P. H., *Appl. Phys. Lett.*, 59:1503–1505 (1991)
417. Fujii, K., Zama, H., and Oda, S., *Jpn. J. Appl. Phys.*, 31:L787–L789 (1992)
418. Cheung, J. T. and Cheung, D. T., *J. Vac. Sci. Technol.*, 21:182–186 (1982); Cheung, J. T. and Sankur, H., *Critical Reviews™ in Solid State and Materials Sciences*, (J. E. Greene, ed.) 15:63–109, CRC Press, Boca Raton (1988)
419. Kanai, M., Horiuchi, K., Kawai, T., and Kawai, S., *Appl. Phys. Lett.*, 57:2716–2718 (1990); Kawai, T., Egami, Y., Tabata, H., and Kawai, S., *Nature*, 349:200 (1991); Tabata, H. and Kawai, T., *Thin Solid Films* 225:275–279 (1993)
420. Koinuma, H., Nagata, H., Tsukahara, T., Gonda, S., and Yoshimoto, M., *Appl. Phys. Lett.*, 58:2027–2029 (1991)
421. Leskelä, M., Mölsä, H., and Niinistö, L., *Supercond. Sci. Technol.*, 6:627–656 (1993)
422. *Atomic Layer Epitaxy*, (T. Suntola and M. Simpson, eds.) Blackie, Glasgow (1990)
423. Niinistö, L. and Leskelä, M., *Thin Solid Films*, 225:130–135 (1993)
424. Zama, H., Sakai, K., and Oda, S., *Jpn. J. Appl. Phys.*, 31:L1243–L1245 (1992); Oda, S., Zama, H., Fujii, K., Sakai, K., and Chen, Y. C., *Thin Solid Films*, 225:284–287 (1993)

425. Ino, S., Ichikawa, T., and Okada, S., *Jpn. J. Appl. Phys.*, 19:1451–1457 (1980)
426. Atwater, H. A. and Ahn, C. C., *Appl. Phys. Lett.* 58:269–271 (1991); Nikzad, S., Ahn, C. C., and Atwater, H. A., *J. Vac. Sci. Technol.*, B10:762–765 (1992)
427. Kamei, M., Aoki, Y., Usui, T., and Morishita, T., *Jpn. J. Appl. Phys.*, 31:1326–1328 (1992)
428. Kim, Y.-T., Collins, R. W., and Vedam, K., *Surf. Sci.*, 233:341–350 (1990); Collins, R. W. and Kim, Y.-T., *Anal. Chem.*, 62:887A–900A (1990); An, I., Nguyen, H. V., Nguyen, N. V., and Collins, R. W., *Phys. Rev. Lett.*, 65:2274–2277 (1990); Heyd, A. R., An, I., Collins, R. W., Cong, Y., Vedam, K., Bose, S. S., and Miller, D. L., *J. Vac. Sci. Technol.*, A 9:810–815 (1991)
429. Aspnes, D. E., Bhat, R., Caneau, C., Colas, E., Florez, L. T., Gregory, S., Harbison, J. P., Kamiya, I., Keramidas, V. G., Koza, M. A., *J. Cryst. Growth*, 120:71–77 (1992)
430. Vedam, K., McMarr, P. J., and Narayan, J., *Appl. Phys. Lett.*, 47:339–341 (1985); McMarr, P. J., Vedam, K., and Narayan, J., *J. Appl. Phys.*, 59:694–701 (1986)
431. Aspnes, D. E., Quinn, W. E., Tamargo, M. C., Pudensi, M. A. A., Schwarz, S. A., Brasil, M. J. S. P., Nahory, R. E., and Gregory, S., *Appl. Phys. Lett.*, 60:1244–1246 (1992)
432. Barth, K. -L. and Keilmann, F., *Rev. Sci. Instrum.*, 64:870–875 (1993)
433. Kobayashi, N. and Horikoshi, Y., *Jpn. J. Appl. Phys.*, 11:L1880–L1882 (1989); Horikoshi, Y., Kawashima, M., and Kobayashi, N., *J. Cryst. Growth*, 111:200–204 (1991)

## MBE Growth of Artificially-Layered Magnetic Metal Structures

*Robin F. C. Farrow, Ronald F. Marks, Gerald R. Harp,  
Dieter Weller, Thomas A. Rabedeau, Michael F.  
Toney, Stuart S. P. Parkin<sup>†</sup>*

### 1.0 INTRODUCTION

The artificially-layered structures considered here comprise one, several, or many magnetic films sandwiched by non-magnetic spacer films. In recent years, such structures have exhibited a variety of novel phenomena which are interesting from the standpoint of the physics of magnetism as well as for potential device applications. Collections of papers in this field, including reviews of specific topics, can be found in the proceedings of the Spring 1991 and 1993 *Symposia of the Materials Research Society* on magnetic surfaces, thin films, and multilayers,<sup>[1]</sup> and in the *Proceedings of the 1992 NATO Advanced Research Workshop* on structure and magnetism in systems of reduced dimension.<sup>[2]</sup> Interesting properties of artificially-layered magnetic structures include perpendicular magnetic anisotropy in films of Fe or Co that are a few monolayers thick, sandwiched by non-magnetic metals or simply left uncoated in ultra-high vacuum. In some cases, as for Co/Pt and Co/Pd multilayers, this perpendicular anisotropy persists to high temperatures ( $\geq 200^{\circ}\text{C}$ ) and has technological applications<sup>[3]</sup> in magneto-optical (MO) storage of information. Other interesting properties exhibited by these layered structures include the giant magnetoresistance (GMR) effect,<sup>[4]–[6]</sup> and oscillatory—AF

<sup>†</sup> This work was supported in part by the Office of Naval Research (Contracts N00014-87-C-0339 and N00014-92-C-0084).